frontiers | Research Topics

Point-of-care diagnostics technology and applications

Edited by
Nongyue He, Guangli Li, Zhiyang Li, Hongna Liu, Song Li and Yanqi Wu

Published in
Frontiers in Bioengineering and Biotechnology

ISSN 1664-8714
ISBN 978-2-8325-3191-4
DOI 10.3389/978-2-8325-3191-4

About Frontiers

Frontiers is more than just an open access publisher of scholarly articles: it is a pioneering approach to the world of academia, radically improving the way scholarly research is managed. The grand vision of Frontiers is a world where all people have an equal opportunity to seek, share and generate knowledge. Frontiers provides immediate and permanent online open access to all its publications, but this alone is not enough to realize our grand goals.

Frontiers journal series

The Frontiers journal series is a multi-tier and interdisciplinary set of open-access, online journals, promising a paradigm shift from the current review, selection and dissemination processes in academic publishing. All Frontiers journals are driven by researchers for researchers; therefore, they constitute a service to the scholarly community. At the same time, the *Frontiers journal series* operates on a revolutionary invention, the tiered publishing system, initially addressing specific communities of scholars, and gradually climbing up to broader public understanding, thus serving the interests of the lay society, too.

Dedication to quality

Each Frontiers article is a landmark of the highest quality, thanks to genuinely collaborative interactions between authors and review editors, who include some of the world's best academicians. Research must be certified by peers before entering a stream of knowledge that may eventually reach the public - and shape society; therefore, Frontiers only applies the most rigorous and unbiased reviews. Frontiers revolutionizes research publishing by freely delivering the most outstanding research, evaluated with no bias from both the academic and social point of view. By applying the most advanced information technologies, Frontiers is catapulting scholarly publishing into a new generation.

What are Frontiers Research Topics?

Frontiers Research Topics are very popular trademarks of the *Frontiers journals series*: they are collections of at least ten articles, all centered on a particular subject. With their unique mix of varied contributions from Original Research to Review Articles, Frontiers Research Topics unify the most influential researchers, the latest key findings and historical advances in a hot research area.

Find out more on how to host your own Frontiers Research Topic or contribute to one as an author by contacting the Frontiers editorial office: frontiersin.org/about/contact

Point-of-care diagnostics technology and applications

Topic editors

Nongyue He — Southeast University, China
Guangli Li — Hunan University of Technology, China
Zhiyang Li — Nanjing Drum Tower Hospital, China
Hongna Liu — iRepertore Inc., United States
Song Li — Hunan University of Technology, China
Yanqi Wu — Jamhuriya University of Science and Technology, Somalia

Citation

He, N., Li, G., Li, Z., Liu, H., Li, S., Wu, Y., eds. (2023). *Point-of-care diagnostics technology and applications*. Lausanne: Frontiers Media SA. doi: 10.3389/978-2-8325-3191-4

Table of contents

05 A Washing-Free and Easy-to-Operate Fluorescent Biosensor for Highly Efficient Detection of Breast Cancer-Derived Exosomes
Wenqin Chen, Yan Zhang, Kaili Di, Chang Liu, Yanyan Xia, Shijia Ding, Han Shen and Zhiyang Li

14 Research progress on detection techniques for point-of-care testing of foodborne pathogens
Sha Liu, Kaixuan Zhao, Meiyuan Huang, Meimei Zeng, Yan Deng, Song Li, Hui Chen, Wen Li and Zhu Chen

35 Highly efficient and automated isolation technology for extracellular vesicles microRNA
Kaili Di, Boyue Fan, Xinrui Gu, Rongrong Huang, Adeel Khan, Chang Liu, Han Shen and Zhiyang Li

44 Nucleic acid amplification strategies for volume-amplified magnetic nanoparticle detection assay
Zhongchao Huang, Jing Li, Hongwen Zhong and Bo Tian

52 Development of a high specificity typing method for the detection of herpes simplex virus
Zhu Chen, Kaixuan Zhao, Boyu Tan, Zengrui Tong, Ziyu He, Xiaofang Luo, Lei Cai, Hanming Wang, Polly H. M. Leung, Franklin Wang-Ngai Chow, Hui Chen and Yan Deng

61 An integrated digital PCR system with high universality and low cost for nucleic acid detection
Kangning Wang, Bin Li, Yu Guo, Yanqi Wu, Yan Li and Wenming Wu

73 Novel miniaturized fluorescence loop-mediated isothermal amplification detection system for rapid on-site virus detection
Yanqi Wu, Liping Bai, Chengfu Ye, Yuhong Guan, Kunming Yan, Hui Chen and Zhihong Jiang

81 A light-activated magnetic bead strategy utilized in spatio-temporal controllable exosomes isolation
Chenhan Wang, Duoteng Zhang, Haiyan Yang, Liang Shi, Lin Li, Changmin Yu, Jifu Wei and Qiang Ding

92 A miniaturized and integrated dual-channel fluorescence module for multiplex real-time PCR in the portable nucleic acid detection system
Yile Fang, Yue Wang, Xiangyi Su, Haoran Liu, Hui Chen, Zhu Chen, Lian Jin and Nongyue He

104 Advances in the use of nanomaterials for nucleic acid detection in point-of-care testing devices: A review
Ziyu He, Changsheng Liu, Zhongyu Li, Zhou Chu, Xiang Chen, Xupeng Chen and Yuan Guo

118 MicroRNAs in extracellular vesicles: Sorting mechanisms, diagnostic value, isolation, and detection technology
Dongjie Xu, Kaili Di, Boyue Fan, Jie Wu, Xinrui Gu, Yifan Sun, Adeel Khan, Peng Li and Zhiyang Li

138 Rapid classification of micro-particles using multi-angle dynamic light scatting and machine learning approach
Xu He, Chao Wang, Yichuan Wang, Junxiao Yu, Yanfeng Zhao, Jianqing Li, Mubashir Hussain and Bin Liu

151 Recent progress of microfluidic chips in immunoassay
Kaimin Wu, Xuliang He, Jinglei Wang, Ting Pan, Ran He, Feizhi Kong, Zhenmin Cao, Feiye Ju, Zhao Huang and Libo Nie

167 Clustered Regularly Interspaced Short Palindromic Repeats-Associated Proteins13a combined with magnetic beads, chemiluminescence and reverse transcription-recombinase aided amplification for detection of avian influenza a (H7N9) virus
Hongpan Xu, Lijun Peng, Jie Wu, Adeel Khan, Yifan Sun, Han Shen and Zhiyang Li

176 A CRISPR-Cas12a—Based platform for ultrasensitive, rapid, and highly specific detection of *Mycoplasma pneumonia* in clinical application
Nan Jia, Juan Zhou, Fei Xiao, Baoying Zheng, Xiaolan Huang, Chunrong Sun, Jin Fu, Zheng Xu, Min Chen and Yi Wang

187 Portable paper-based electrochemiluminescence test incorporating lateral-flow immunosensors for detection of interferon-γ levels
Shichao Yuan, Guihua Xie, Xiang Yang, Yu Chen and Hongbin Zhang

195 Rapid quantitative detection of *Klebsiella pneumoniae* in infants with severe infection disease by point-of-care immunochromatographic technique based on nanofluorescent microspheres
Ying Chen, Lulu Sha, Wenqing Li, Liuyan Zhou, Bing Pei, Xinyu Bian, Yongxin Ji, Yiping Liu, Li Wang and Huan Yang

208 Development of a biomarker signature using grating-coupled fluorescence plasmonic microarray for diagnosis of MIS-C
Michele Maltz-Matyschsyk, Clare K. Melchiorre, Katherine W. Herbst, Alexander H. Hogan, Kristina Dibble, Brandon O'Sullivan, Joerg Graf, Aishwarya Jadhav, David A. Lawrence, William T. Lee, Kyle J. Carson, Justin D. Radolf, Juan C. Salazar, Michael A. Lynes and Connecticut Children's COVID Collaborative

227 CRISPR-Cas and catalytic hairpin assembly technology for target-initiated amplification detection of pancreatic cancer specific tsRNAs
Jie Wu, Hongpan Xu, Fenghua Hu, Yiyue Jiang, Boyue Fan, Adeel Khan, Yifan Sun, Kaili Di, Xinrui Gu, Han Shen and Zhiyang Li

frontiers | Frontiers in Bioengineering and Biotechnology

ORIGINAL RESEARCH
published: 28 June 2022
doi: 10.3389/fbioe.2022.945858

A Washing-Free and Easy-to-Operate Fluorescent Biosensor for Highly Efficient Detection of Breast Cancer-Derived Exosomes

Wenqin Chen[1†], Yan Zhang[1†], Kaili Di[1], Chang Liu[1], Yanyan Xia[1], Shijia Ding[2], Han Shen[1]* and Zhiyang Li[1]**

[1]Department of Clinical Laboratory, Nanjing Drum Tower Hospital, The Affiliated Hospital of Nanjing University Medical School, Nanjing, China, [2]Key Laboratory of Clinical Laboratory Diagnostics (Ministry of Education), College of Laboratory Medicine, Chongqing Medical University, Chongqing, China

OPEN ACCESS

Edited by:
Mehmet Senel,
University of California, Irvine,
United States

Reviewed by:
Sajad Razavi Bazaz,
University of Technology Sydney,
Australia
Oleg Sergeevich Tutanov,
Institute of Chemical Biology and
Fundamental Medicine (RAS), Russia
Duanping Sun,
Guangdong Pharmaceutical
University, China

***Correspondence:**
Shijia Ding
dingshijia@163.com
Han Shen
shenhan10366@sina.com
Zhiyang Li
lizhiyangcn@qq.com

†These authors have contributed
equally to this work

Specialty section:
This article was submitted to
Biosensors and Biomolecular
Electronics,
a section of the journal
Frontiers in Bioengineering and
Biotechnology

Received: 17 May 2022
Accepted: 08 June 2022
Published: 28 June 2022

Citation:
Chen W, Zhang Y, Di K, Liu C, Xia Y,
Ding S, Shen H and Li Z (2022) A
Washing-Free and Easy-to-Operate
Fluorescent Biosensor for Highly
Efficient Detection of Breast Cancer-
Derived Exosomes.
Front. Bioeng. Biotechnol. 10:945858.
doi: 10.3389/fbioe.2022.945858

Traditional detection methods for protein tumor markers in the early screening of breast cancer are restricted by complicated operation procedures and unstable reproducibility. As one of alternative emerging tumor markers, exosomes play an important role in diagnosing and treating cancers at the early stage due to traceability of their origins and great involvement in occurrence and development of cancers. Herein, a washing-free and efficient fluorescent biosensor has been proposed to realize simple and straightforward analysis of breast cancer cell-derived exosomes based on high affinity aptamers and G quadruplex-hemin (G4-hemin). The whole reaction process can be completed by several simple steps, which realizes washing-free and labor-saving. With simplified operation procedures and high repeatability, the linear detection range for this developed fluorescent biosensing strategy to breast cancer cell-derived exosomes is from 2.5×10^5 to 1.00×10^7 particles/ml, and the limit of detection is down to 0.54×10^5 particles/ml.

Keywords: exosomes, fluorescence biosensing, aptamer, G4-hemin, tumor diagnosis

INTRODUCTION

Breast cancer has been the number one killer of women's health in recent years (Jordan, 2020; Houghton and Hankinson, 2021). Diagnosis of tumors usually relies on tissue biopsy in clinical, which requires very complex operation and may cause great harm to patients. Restricted by the complex operating procedures and instability of output results from current clinical detection methods, the reference value of marker proteins detection results, such as human epidermal growth factor receptor 2 (HER2) in the early screening of breast cancer has been reduced (Lamtha et al., 2021; Tang et al., 2021). Therefore, conceiving new detection strategies to make up for the deficiencies and achieve more effective early screening and diagnosis of breast cancer is an urgent problem. Liquid biopsy, as a promising approach, can detect tumor markers from blood, saliva, urine and other body fluids, avoiding the injury caused by surgical operation and puncture to patients. Current methods of liquid biopsy mainly include circulating tumor cell (CTC), circulating tumor DNA (ctDNA), exosomes, and extracellular free nucleic acids (Kilgour et al., 2020; Ahmadi and Rezaie, 2021). Exosomes (30–150 nm) are extracellular vesicles secreted into body fluids by various living cells and involved in signal transmission and regulation. In recent years, exosomes

have gradually become one of the most popular biomarkers for liquid biopsy due to the fact that they contain a variety of genetic materials from parental cells and their high participation in the occurrence and development of various diseases (Li et al., 2019b; Shen et al., 2020). Cells are stimulated to secrete more exosomes, far more than in normal physiological states. Moreover, overexpressed tumor-specific proteins are also present on the surface of tumor cell derived exosome membranes (Liang et al., 2020; Rezaie et al., 2022; Vahabi et al., 2022). Tumor cell-derived exosome specific protein or RNA markers can be used to indicate tumor development and invasion degree. Compared to other liquid biopsy targets such as CTC and ctDNA, exosomes are more abundant and stable due to the vesicles protection, which benefit to overcome the problem of easy degradation (Ignatiadis et al., 2021). Thanks to all above characteristics, exosomes undoubtedly become one of the biomarkers worthy of in-depth study and have far-reaching significance for early screening, preventive diagnosis and treatment of tumors.

Researchers have conceived a number of strategies to detect tumor cell-derived exosomes based on various detection platforms, such as electrochemistry (Huang et al., 2019), electrochemiluminescence (Li et al., 2021b), immunoassay (Wang et al., 2021) and thermophoresis (Timson, 2019), all of which obtained satisfactory detection results. However, these methods often require complicated and time-consuming washing steps, which make it difficult to guarantee the integrity of exosomal membranes and the repeatability of the experiment. In addition, most of these methods need to be tested by professionals on expensive ancillary equipment, which further increases capital and labor costs. Therefore, it is necessary to propose a new detection method to make up for the deficiencies of existing methods and achieve simple, cheap and sensitive detection of exosomes. Fluorescence detection is a natural luminescence reaction with extremely high sensitivity and wide linear range (Zhang et al., 2019; Huang et al., 2020). As a benefit from this, the interference of non-fluorescent components can be considerably avoided, which is the optimum choice for most trace target analysis (Casto-Boggess et al., 2022). Traditional fluorescence detection methods mostly use ready-made peroxidases such as HRP (Lu and Xu, 2019; Heo et al., 2021) and ALP (Han et al., 2020; Wu et al., 2022) to catalyze the substrate such as tyramine (Zhang et al., 2020a; Kang et al., 2020) and thioflavin T (Wu et al., 2018; Pramanik et al., 2021) to output fluorescent signals. The disadvantages of this method lie in that the enzyme protein is relatively unstable and has harsh requirements on reaction conditions, which make researchers turn their attention to the G4-hemin biomimetic enzyme (Li et al., 2021a; Huang et al., 2021). The advantages of G4-hemin are excellent catalytic performance, high structural flexibility and stability (Cao et al., 2020; Chen et al., 2020). Moreover, Just like G4-hemin, aptamer is one of the functional nucleic acids that can bind with corresponding ligand with high affinity and strong specificity, and is also a frequent visitor in the field of biosensing research (Connelly et al., 2021; Daems et al., 2021; Nakatsuka et al., 2021).

Herein, we proposed a simple and easy-to-operate biosensing strategy for efficient detection of breast cancer cell-derived exosomes based on fluorescence platform. First, in this strategy, we combined the high specificity of aptamer with excellent catalytic performance of G4-hemin through sophisticated structural design of the bicyclic capture probe. In addition, the whole reaction process requires only streamlined sample addition and no complicated washing steps are needed, which greatly saves time and labor costs. The washing-free and simple operation steps realize the highly sensitive detection of breast cancer cell-derived exosomes, which not only solves the problem of low repeatability in traditional detection methods, but also reduces the requirements for equipment and has the potential for clinical promotion.

EXPERIMENTAL

Reagents and Materials

Fetal Bovine Serum (FBS) and Dulbecco's Modified Eagle Medium (DMEM) were offered by Gibco (Gaithersburg, MD, United States, https://www.thermofisher.com). Phosphate buffer (PBS) was supplied by Thermo Fisher Scientific (Wilmington, United States, https://www.thermofisher.com). Monoclonal antibodies such as anti-CD63, anti-CD9 and anti-HER2 were obtained from Abcam (MA, United States, https://www.abcam.cn), and polyclonal antibody of HRP rabbit IgG were purchased from Beyotime (Jiangsu, China, https://www.beyotime.com). All of these antibodies were dissolved in 0.1% bovine serum albumin (BSA) solution. Hemin and tyramine were supplied by Sigma-Aldrich (St. Louis, United States, https://www.sigmaaldrich.com). We prepared dimethyl sulfoxide (DMSO) as stock solution to dissolve pure hemin, and then utilized HEPES (NaCl 200 mM, KCl 100 mM, DMSO 1%, Triton 0.05%) buffer solution to dilute the above hemin solution to different concentrations. Analytical reagent grade chemicals were utilized all through the experiment. As shown in **Supplementary Table S1**, all of the oligonucleotides were purified by high performance liquid chromatography. Next, the 30% hydrogen peroxide (H_2O_2) was supplied by Sangon Biotech. Co., Ltd. (Shanghai, China, https://www.sangon.com). We utilized the buffer of Tris-EDTA (TE) to dissolve and dilute all of the needed oligonucleotides for its suitable PH value and ion components. Lastly, we used the aqueous solutions supplied by the Millipore Milli-Q gradient ultrapure water system (Millipore Co., MA, United States, https://www.merckmillipore.com) all over the experiment.

Instruments

Fluorescence detections were carried out on a Cary Eclipse Fluorescence Spectrophotometer (Agilent Technologies, United States, https://www.agilent.com). Transmission Electron Microscope (TEM) image, Nanoparticle Tracking Analysis (NTA), the SDS-PAGE and gel imaging analysis for the characterization of tumor cell-derived exosomes was supported by H-7500 transmission electron microscope (Hitachi High-Technologies Co., Japan, https://www.hitachihightech.com),

ZetaView (Particle Metrix, Germany, https://www.particle-metrix.com), electrophoresis analyzer and ChemDoc XRS (Bio-Rad, United States, https://www.bio-equip.com), respectively.

Extraction Procedures for Exosomes

We obtained several needed tumor cell lines as the control subjects, such as SK-BR3, HeLa, MCF-7, LNCaP and HepG2 from the American Type Culture Collection (ATCC) (Rockville, United States, https://www.atcc.org). After addition of 1% streptomycin and penicillin and 10% FBS, the cell culture medium named Dulbecco's Modified Eagle Medium (DMEM) was used all over the experiment for tumor cell culture. All cells were cultured in a sterile environment throughout the whole process, and appropriate timing was selected for passage and cryopreservation according to the speed of cell growth and reproduction. We observed the growth state of the cells and when they grew well and covered about 80% of the culture dish, and then we reduced the nutrients from the cells and performed starvation culture. When the cells propagated in serum-free medium for 48 h, we proceeded to the next process of extracting exosomes. The cells were stressed in a nutrient-deficient growth environment and secreted far more exosomes than normal cells, so we got increased production of exosomes. Then we started the extraction process for exosomes (Zhang et al., 2020b). First, the cell culture medium for starvation culture was collected and centrifuged (10,000 ×g, 30 min) for preliminary purification to remove impurities such as cell debris with a large mass. The collected supernatant was then subjected to ultracentrifugation (100,000 ×g, 70 min) twice to continue purification of exosomes. It was critical to resuspend the pellet between the intervals of twice ultracentrifugation. After the first ultracentrifugation, the supernatant was discarded. Then, after adding 1 × PBS solution, the precipitate was resuspended before the second ultracentrifugation. Then, after the second ultracentrifugation, the supernatant was also discarded, and 100 μl 1 × PBS was added to resuspend the obtained exosome pellet. The step for extracting exosomes from clinical serum samples required an additional procedure on the basis of the above process. In general, the final exosome solution needed to be passed through a 0.22 μm filtration membrane to minimize the interference of other free-floating proteins and extracellular vesicles. The whole extraction process was carried out at 4°C to prevent exosome degradation. Finally, the extracted exosomes were characterized by TEM, NTA and western blot, and then stored at −80°C. The clinical samples were collected from the Affiliated Drum Tower Hospital of Nanjing University Medical School.

Fluorescent Biosensing of Exosome

For exosome recognition, 2 μl target exosome with various concentrations was added to a 97 μl reaction mixture containing 165 nM of G4 hairpin capture probe, and incubated at 37°C for 60 min. Then, hemin (98 μl, 154 nM), tyramine (2 μl, 160 mM), and freshly prepared H_2O_2 (1 μl, 200 mM) was added to the reaction mixture and reacted at room temperature for 10 min for G4-hemin biosensing. Finally, we scanned the above reaction products with a voltage of 600 V, and obtained the fluorescence emission spectrum between 330 and 500 nm under excitation wavelength of 320 nm.

RESULTS AND DISCUSSION

Design of Fluorescence Biosensor

The principle for detecting breast cancer cell-derived exosomes is shown in **Scheme 1**. First, the bicyclic capture probe was obtained by heating and annealing. The exosomes used in the experimental verification stage were extracted from cultured tumor cells by traditional ultracentrifugation. Different concentrations of exosomes were added to the capture probe solution, and the double rings were opened by the high affinity between the aptamer and HER2 protein over-expressed on the membrane of the SK-BR3-derived exosomes (Liu et al., 2019; Vajhadin et al., 2022). The terminal G4 sequence was exposed while tightly capture exosomes. After full reaction, hemin was added to generate G4-hemin catalytic enzyme. The best catalytic state was achieved by adjusting the optimal concentration ratio. Then, the addition of tyramine incited the catalysis of G4-hemin to output a fluorescent signal (Li et al., 2019a; Wang et al., 2020). Quantitative detection of exosomes was achieved by the fluorescence intensity. The highlight of this strategy is integration of target recognition, capture and signal output, which is reasonably reflected in the ingeniously designed bicyclic capture probe. More importantly, the washing-free and streamlined sample addition steps ensure the facile and efficient detection of breast cancer cell-derived exosomes.

Characterization of Exosomes

We chose Transmission Electron Microscope (TEM), Nanoparticle Tracking Analysis (NTA) and western blot to characterize the appearance, morphology and particle size distribution of the extracted breast cancer cell-derived exosomes, as shown in **Figure 1**. It can be seen from the TEM image on the left (**Figure 1A**) that the extracted exosomes were circular or elliptical vesicles with a double layer membrane. Meanwhile, we learned from the NTA characterization graph (**Figure 1B**) that the size of the extracted exosomes was mostly distributed between 75 and 200 nm, concentrated around 100 nm, which was consistent with information reported in the literatures (Le and Fan, 2021; Zhang et al., 2021). In addition, taking an authoritative literature as a guideline (Théry et al., 2018), we also performed western blot experiments to characterize common markers (CD63, CD9) and the specific marker HER2 on the membrane of SK-BR3 cell-derived exosomes. It can be seen from **Figure 1C** that these proteins are enriched in the target exosome membrane, which indicates the successful extraction process and supports the reliability of subsequent experiments.

Feasibility of Developed Biosensor

We then further verified the feasibility of this biosensor. As shown in **Figure 2**, the color of the solution changed only when the exosomes were present, from colorless to purple

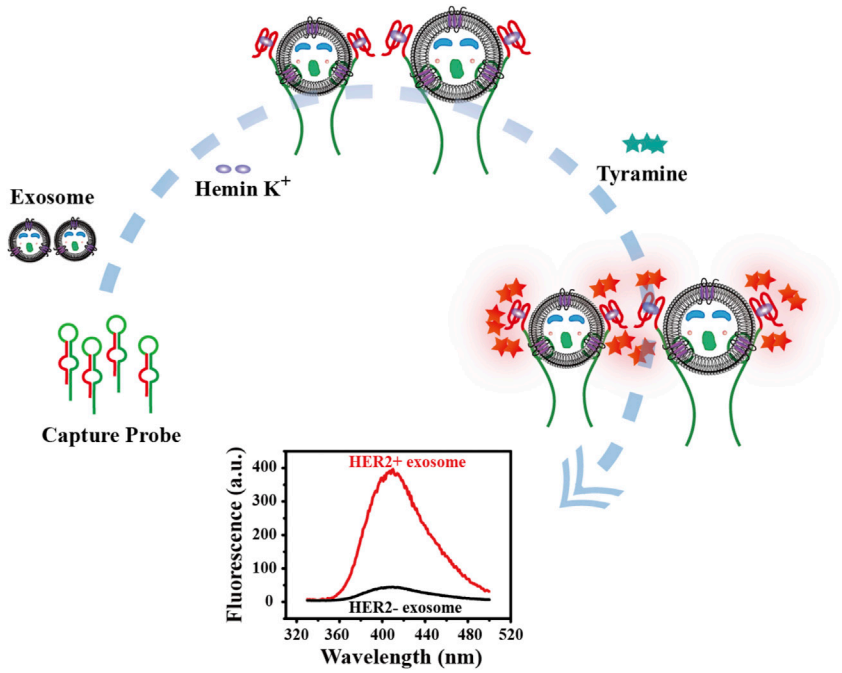

SCHEME 1 | Schematic diagram of principle for detection of tumor cell-derived exosomes.

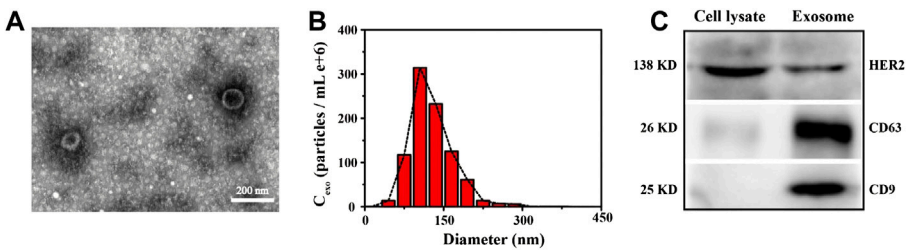

FIGURE 1 | Characterization of SK-BR3 cell exosomes by TEM **(A)**, NTA **(B)** and Western blot **(C)**, respectively. Scale bars = 200 nm. Cell lysate was set as a reference.

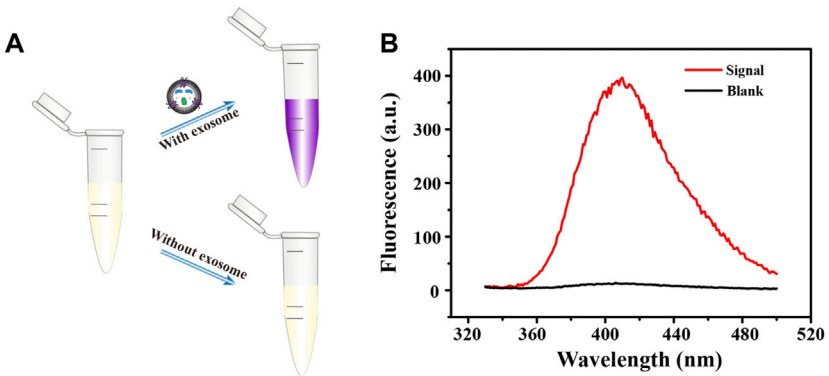

FIGURE 2 | Brief schematic **(A)** and fluorescence emission spectra **(B)** of fluorescent biosensing protocol in the detection of exosomes.

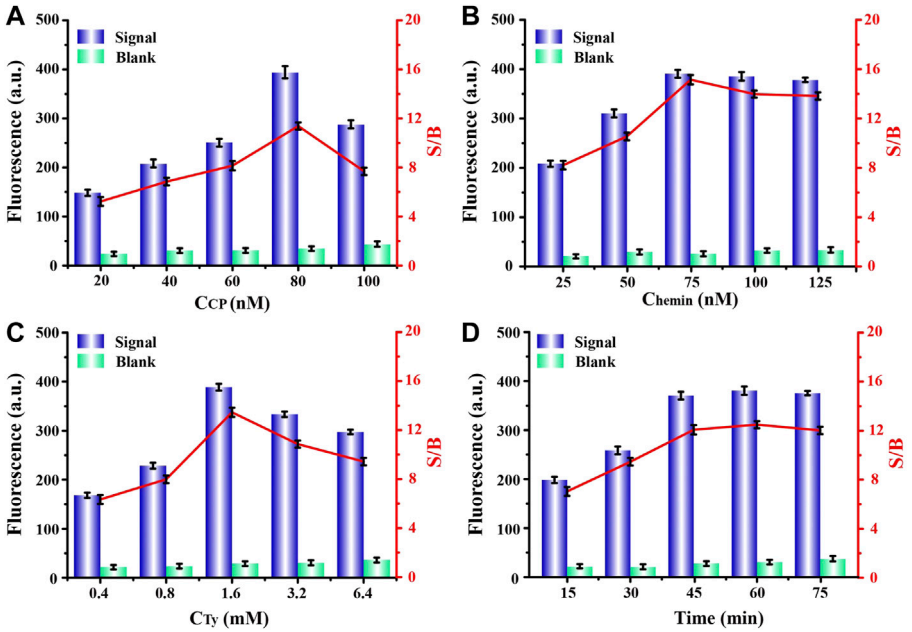

FIGURE 3 | Optimizations of experimental concentrations of **(A)** capture probe, **(B)** hemin, **(C)** tyramine, and **(D)** required reaction time for capture probe and exosomes, respectively.

(**Figure 2A**), and a strong fluorescent signal was produced (**Figure 2B**). By contrast, the color of the blank control did not change and the fluorescence signal was almost negligible, which indicates that only the target exosomes can open the bicyclic capture probe to release the G4 sequence. Thanks to the high specificity of aptamer and excellent catalytic performance of G4-hemin, the facile and sensitive detection of breast cancer cell-derived exosomes was achieved successfully. At the same time, the washing-free and simple operation procedure improved the reproducibility and repeatability of this detection method, broadening the future application range.

Optimization of Experimental Parameters

In order to achieve the best experimental results, we optimized a series of experimental conditions. First, the bicyclic capture probe was one of the most important components in this program, and its concentration had a significant impact on the signal output. Thereafter, we compared the fluorescence signals obtained from experiments using a range of probe concentrations. By observing **Figure 3A**, we can see that, when the probe had a concentration of 80 nM the obtained fluorescence signal was highest, and the signal-to-noise ratio also reached the maximum. When the concentration of the capture probe was further increased, the gradually enhanced steric hindrance limited the catalytic efficiency of G4-hemin to a certain extent, resulting in a decrease in the fluorescence intensity. Therefore, we chose 80 nM as the capture probe's optimal concentration for follow-up experiments. Next, the influence of hemin concentration cannot be ignored. The existence of hemin directly determines the formation and catalytic performance of G4-hemin (Ahmadi et al., 2021), which is an important key point of signal output in this scheme. It can be seen from **Figure 3B** that, only the 75 nM concentration of hemin obtained the highest signal and largest signal-to-noise ratio, so it was selected as suitable concentration. Additionally, in order to provide a resource-rich environment for maximum catalytic effect of G4-hemin, it was necessary to optimize the concentration of reaction substrate tyramine. We learned from **Figure 3C** that, too low tyramine concentration cannot meet the substrate requirements of the catalytic reaction, while too high tyramine concentration will also have a certain inhibitory effect on the catalytic reaction of G4-hemin. Therefore, according to the experimental results, to achieve the best signal output, the concentration of tyramine should be controlled to 1.6 mM. Finally, we also optimized the reaction time after adding the exosomes. It can be seen from **Figure 3D** that, when the reaction time was 60 min, the fluorescence signal and signal-to-noise ratio were both the highest, but when the reaction time was set for 45 min, the signal and signal-to-noise ratio obtained were hardly the same as the best state. After weighing the pros and cons, choosing a reaction time of 45 min was more efficient and time-saving.

Analytical Performance of Fluorescent Biosensor

To explore the analytical performance of this method, we carried out linear research subsequently. As shown in **Figure 4A**, after plenty of different concentrations of exosomes were detected, a set of fluorescence signals was also obtained. Through analysis, we learned that, the intensity of the fluorescence signal was positively correlated with concentration of target exosomes. Moreover, **Figure 4B** was a linear fitting for the fluorescence signal obtained in **Figure 4A** and the corresponding exosomal concentrations, which shows that there was a good linear correlation between

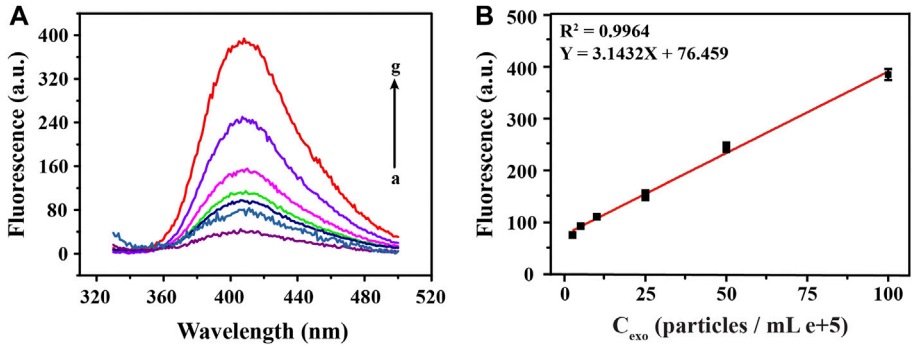

FIGURE 4 | Sensitivity analysis of fluorescence detection of exosomes at different concentrations. The corresponding fluorescence emission spectra **(A)** and linear fittings **(B)** obtained by detecting a series of different concentrations of exosomes (0, 2.5, 5, 10, 25, 50, 100 particles/mL e+5, from a to g).

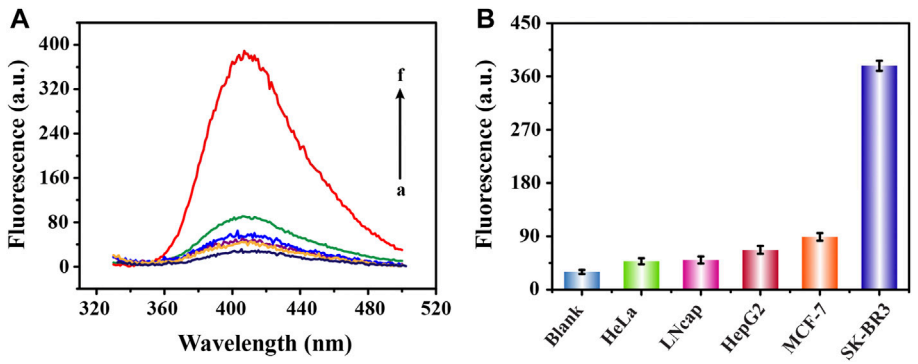

FIGURE 5 | Specific analysis of fluorescence detection of exosomes derived from different cells. Fluorescence emission spectra **(A)** and corresponding signal response diagrams **(B)** obtained from the detection of five cell-derived exosomes (100 × 10^5 particles/ml) (from b to f are HeLa, LNcap, HepG2, MCF-7 and SK-BR3 cell lines; a represents blank).

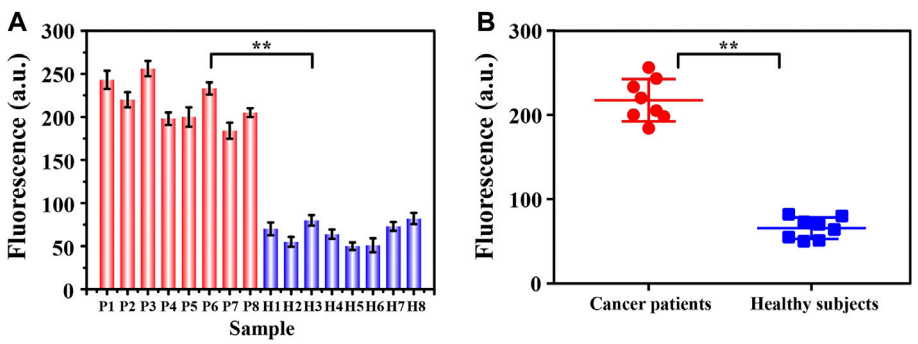

FIGURE 6 | The signal intensity **(A)** and corresponding scatter plots **(B)** of exosomes from two groups of clinical samples (breast cancer patients: P1~P8; healthy controls H1~H8) were analyzed by this fluorescence sensing method. By Student's unpaired *t*-test, the significance was determined. $^{**}p < 0.05$.

them. We obtained the regression equation between the exosome concentration (X) and corresponding fluorescence signal (Y) by linear fitting as Y = 3.1432 X + 76.459, with a correlation coefficient (R^2) of 0.9964. Then, according to the 3σ rule, which was defined as the mean value plus 3 times standard deviation of the blank (n = 3), the limit of detection (LOD) for exosomes was calculated to be 0.54 ×

10^5 particles/ml, comparable with other analytical methods (Karczmarczyk et al., 2016). Such a satisfactory detection performance was mainly attributed to the highly specific binding of the aptamer to the exosomal membrane protein and excellent catalytic performance of G4-hemin, which implies the rationality of the design for this strategy.

Specificity Analysis

In order to prove the high specificity of this biosensing strategy in the detection of SK-BR3 derived exosomes, we selected five different cancer cell-derived exosomes for specificity analysis. We learned from **Figure 5** that, compared with high fluorescence signal produced by SK-BR3 derived exosomes, the low signals of three lower-relevant cancer cell-derived exosomes (cervical cancer cells: HeLa, prostate cancer cells: LNcap and liver cancer cells: HepG2) were almost as negligible as the blank (Dahl et al., 2011; Liu et al., 2011; Feng et al., 2012). As another breast cancer cell of which expression of HER2 on the cell membrane is far less than that of SK-BR3, the signal obtained by MCF-7 cell-derived exosomes was slightly increased but was also far lower than that of SK-BR3 (Baumann et al., 2016). We also learned that, the affinity of aptamers was closely related to the expression of HER2 protein on exosome membrane. Such a high specific binding mode became a solid foundation for the successful release and assembly of G4-hemin as well as the subsequent display of catalytic performance.

Detection of Exosomes in Clinical Samples

Realizing the detection of trace targets in complex clinical samples is always the gold standard in judging whether a new method has the potential for clinical application. Inspired by this, we collected clinical serum samples for further analysis. As shown in **Figure 6**, we divided the collected samples into two groups, breast cancer patient group and healthy control group, each with eight samples. Apparently, we learned from the experimental results that the signals produced by the two groups of samples showed significant differences. The signals from the patient samples were all above 150 absorbance unit while the signals from the control group were all less than 100 absorbance unit, with relatively concentrated distribution. The statistically significant fluorescent signal difference between the two groups was learned easily from the scatter plot analysis in **Figure 6B** ($p < 0.05$), indicating the possibility for us to conduct preliminary screening of cancer patients through the intensity of the fluorescence signals. Aside from the simple and sensitive detection of exosomes, this method also has many notable advantages, including washing-free, time-saving, cost-effective and high repeatability. Furthermore, the detection of exosomes was completed with simple streamlined loading steps, which was easy to be transformed into clinical automated detection.

CONCLUSION

Liquid biopsy is developing rapidly in tumor early diagnosis and therapeutic monitoring. While most research currently focuses on circulating tumor cells and circulating tumor DNA, exosomes and other extracellular vesicles are also emerging as a potentially broader and complementary platform for research. Exosomes contain a variety of substances derived from tumor cells, which has aroused great interest in the study of exosomes as tumor biomarkers. In order to solve the current limitations of breast cancer diagnosis, we proposed a washing-free, simple, and highly operable fluorescent biosensor based on an ingeniously designed bicyclic capture probe for detection of breast cancer cell-derived exosomes. The high efficiency and sensitivity of this detection method is attributed to the high affinity of aptamers and the excellent catalytic performance of G4-hemin. More importantly, the application of this fluorescent sensing strategy for detection of clinical samples was successful. And the preliminary testing results of cancer patients and non-cancer patients were quite different, which shows a good degree of discrimination. Based on the above, it is possible for us to conduct preliminary screening of breast cancer patients through the differentiated detection results. It is worth mentioning that by replacing aptamers, the proposed method is suitable for detecting more different types of cell-derived exosomes and their subpopulations, which has a certain application value. Moreover, due to the advantages of washing-free, easy-to-operate and high reproducibility, our novel detection method has the potential to be designed as a portable instrument for point of care test in the near future to simplify the clinical diagnosis process.

However, how to efficiently design and optimize the washing-free probe to achieve multiple detection of the target is the direction of our further research, which was also the limitation of this detection strategy. Hopefully, we will solve this problem in subsequent experiments and continuously improve the performance of the detection method.

DATA AVAILABILITY STATEMENT

The original contributions presented in the study are included in the article/**Supplementary Material**, further inquiries can be directed to the corresponding authors.

ETHICS STATEMENT

The studies involving human participants were reviewed and approved by the Department of Clinical Laboratory, Nanjing Drum Tower Hospital, The Affiliated Hospital of Nanjing University Medical School, Nanjing 210008, China. The patients/participants provided their written informed consent to participate in this study.

AUTHOR CONTRIBUTIONS

WC: Conceptualization, methodology, software, and investigation, data curation, writing-original draft. YZ: Methodology, software, investigation, project administration, writing-review and editing. KD: Formal analysis, and software.

CL: Resources and software. YX: Conceptualization and data curation. SD: Resources and validation. HS: Supervision, methodology, data curation, and administration. ZL: Funding acquisition, supervision, administration, and data Curation.

FUNDING

This study was supported by the National Natural Science Foundation of China (Nos. 61971216 and 82002205), the Key Research and Development Project of Jiangsu Province (Nos. BE2019603, BE2020768, and BE2019761).

SUPPLEMENTARY MATERIAL

The Supplementary Material for this article can be found online at: https://www.frontiersin.org/articles/10.3389/fbioe.2022.945858/full#supplementary-material

REFERENCES

Ahmadi, M., and Rezaie, J. (2021). Ageing and Mesenchymal Stem Cells Derived Exosomes: Molecular Insight and Challenges. *Cell Biochem. Funct.* 39, 60–66. doi:10.1002/cbf.3602

Ahmadi, Y., Soldo, R., Rathammer, K., Eibler, L., and Barišić, I. (2021). Analyzing Criteria Affecting the Functionality of G-Quadruplex-Based DNA Aptazymes as Colorimetric Biosensors and Development of Quinine-Binding Aptazymes. *Anal. Chem.* 93, 5161–5169. doi:10.1021/acs.analchem.0c05052

Baumann, J., Wong, J., Sun, Y., and Conklin, D. S. (2016). Palmitate-induced ER Stress Increases Trastuzumab Sensitivity in HER2/neu-Positive Breast Cancer Cells. *BMC Cancer* 16, 551. doi:10.1186/s12885-016-2611-8

Cao, Y., Ding, P., Yang, L., Li, W., Luo, Y., Wang, J., et al. (2020). Investigation and Improvement of Catalytic Activity of G-Quadruplex/hemin DNAzymes Using Designed Terminal G-Tetrads with Deoxyadenosine Caps. *Chem. Sci.* 11, 6896–6906. doi:10.1039/d0sc01905d

Casto-Boggess, L. D., Golozar, M., Butterworth, A. L., and Mathies, R. A. (2022). Optimization of Fluorescence Labeling of Trace Analytes: Application to Amino Acid Biosignature Detection with Pacific Blue. *Anal. Chem.* 94, 1240–1247. doi:10.1021/acs.analchem.1c04465

Chen, Z., Luo, F., Li, L., Li, C., Zhu, Y., and Sun, X. (2020). Use of Tris-NH4Cl in Modified G4/hemin DNAzyme Assay with Duplexed Probes Extends Life of Colorized Radical Product. *Sensors Actuators B Chem.* 321, 128559. doi:10.1016/j.snb.2020.128559

Connelly, R. P., Madalozzo, P. F., Mordeson, J. E., Pratt, A. D., and Gerasimova, Y. V. (2021). Promiscuous Dye Binding by a Light-Up Aptamer: Application for Label-free Multi-Wavelength Biosensing. *Chem. Commun.* 57, 3672–3675. doi:10.1039/d1cc00594d

Daems, E., Moro, G., Campos, R., and De Wael, K. (2021). Mapping the Gaps in Chemical Analysis for the Characterisation of Aptamer-Target Interactions. *TrAC Trends Anal. Chem.* 142, 116311. doi:10.1016/j.trac.2021.116311

Dahl, M., Bouchelouche, P., Kramer-Marek, G., Capala, J., Nordling, J., and Bouchelouche, K. (2011). Sarcosine Induces Increase in HER2/neu Expression in Androgen-dependent Prostate Cancer Cells. *Mol. Biol. Rep.* 38, 4237–4243. doi:10.1007/s11033-010-0442-2

Feng, C., Zhou, L.-Y., Yu, T., Xu, G., Tian, H.-L., Xu, J.-J., et al. (2012). A New Anticancer Compound, Oblongifolin C, Inhibits Tumor Growth and Promotes Apoptosis in HeLa Cells through Bax Activation. *Int. J. Cancer* 131, 1445–1454. doi:10.1002/ijc.27365

Han, Y., Chen, J., Li, Z., Chen, H., and Qiu, H. (2020). Recent Progress and Prospects of Alkaline Phosphatase Biosensor Based on Fluorescence Strategy. *Biosens. Bioelectron.* 148, 111811. doi:10.1016/j.bios.2019.111811

Heo, Y., Shin, K., Park, M. C., and Kang, J. Y. (2021). Photooxidation-induced Fluorescence Amplification System for an Ultra-sensitive Enzyme-Linked Immunosorbent Assay (ELISA). *Sci. Rep.* 11, 5831. doi:10.1038/s41598-021-85107-7

Houghton, S. C., and Hankinson, S. E. (2021). Cancer Progress and Priorities: Breast Cancer. *Cancer Epidemiol. Biomarkers Prev.* 30, 822–844. doi:10.1158/1055-9965.EPI-20-1193

Huang, R., He, L., Li, S., Liu, H., Jin, L., Chen, Z., et al. (2020). A Simple Fluorescence Aptasensor for Gastric Cancer Exosome Detection Based on Branched Rolling Circle Amplification. *Nanoscale* 12, 2445–2451. doi:10.1039/c9nr08747h

Huang, R., He, L., Xia, Y., Xu, H., Liu, C., Xie, H., et al. (2019). A Sensitive Aptasensor Based on a Hemin/G-Quadruplex-Assisted Signal Amplification Strategy for Electrochemical Detection of Gastric Cancer Exosomes. *Small* 15, 1900735. doi:10.1002/smll.201900735

Huang, X., He, Z., Zhou, K., Zhi, H., and Yang, J. (2021). Fabrication of Bifunctional G-Quadruplex-Hemin DNAzymes for Colorimetric Detection of Apurinic/apyrimidinic Endonuclease 1 and microRNA-21. *Analyst* 146, 7379–7385. doi:10.1039/d1an01603b

Ignatiadis, M., Sledge, G. W., and Jeffrey, S. S. (2021). Liquid Biopsy Enters the Clinic - Implementation Issues and Future Challenges. *Nat. Rev. Clin. Oncol.* 18, 297–312. doi:10.1038/s41571-020-00457-x

Jordan, V. C. (2020). Molecular Mechanism for Breast Cancer Incidence in the Women's Health Initiative. *Cancer Prev. Res. (Phila).* 13, 807–816. doi:10.1158/1940-6207.CAPR-20-0082

Kang, L., Duan, J., He, F., Teng, J., Li, J., Yang, T., et al. (2021). Highly Sensitive Fluorescence Biosensing of BCR-ABL1 Fusion Gene Based on Exponential Transcription-Triggered Hemin Catalysis. *Talanta* 224, 121967. doi:10.1016/j.talanta.2020.121967

Karczmarczyk, A., Reiner-Rozman, C., Hageneder, S., Dubiak-Szepietowska, M., Dostálek, J., and Feller, K.-H. (2016). Fast and Sensitive Detection of Ochratoxin A in Red Wine by Nanoparticle-Enhanced SPR. *Anal. Chim. Acta* 937, 143–150. doi:10.1016/j.aca.2016.07.034

Kilgour, E., Rothwell, D. G., Brady, G., and Dive, C. (2020). Liquid Biopsy-Based Biomarkers of Treatment Response and Resistance. *Cancer Cell* 37, 485–495. doi:10.1016/j.ccell.2020.03.012

Lamtha, T., Tabtimmai, L., Bangphoomi, K., Kiriwan, D., Malik, A. A., Chaicumpa, W., et al. (2021). Generation of a Nanobody against HER2 Tyrosine Kinase Using Phage Display Library Screening for HER2-Positive Breast Cancer Therapy Development. *Protein Eng. Des. Sel.* 34, gzab030. doi:10.1093/protein/gzab030

Le, M.-C. N., and Fan, H. Z. (2021). Exosome Isolation Using Nanostructures and Microfluidic Devices. *Biomed. Mat.* 16, 022005. doi:10.1088/1748-605X/abde70

Li, J., Wu, H., Yan, Y., Yuan, T., Shu, Y., Gao, X., et al. (2021a). Zippered G-Quadruplex/hemin DNAzyme: Exceptional Catalyst for Universal Bioanalytical Applications. *Nucleic Acids Res.* 49, 13031–13044. doi:10.1093/nar/gkab1178

Li, J., Xiang, Y., Zhang, L., Huang, L., Teng, J., Ding, S., et al. (2019a). Dynamic DNA Self-Assembly Activated Hemin-Mimetic Enzyme System for Versatile Fluorescent Biosensing. *Sensors Actuators B Chem.* 288, 757–762. doi:10.1016/j.snb.2019.03.058

Li, R., An, Y., Jin, T., Zhang, F., and He, P. (2021b). Detection of MUC1 Protein on Tumor Cells and Their Derived Exosomes for Breast Cancer Surveillance with an Electrochemiluminescence Aptasensor. *J. Electroanal. Chem.* 882, 115011. doi:10.1016/j.jelechem.2021.115011

Li, Z., Hu, C., Jia, J., Xia, Y., Xie, H., Shen, M., et al. (2019b). Establishment and Evaluation of a Simple Size-Selective Method for Exosome Enrichment and Purification. *J. Biomed. Nanotechnol.* 15, 1090–1096. doi:10.1166/jbn.2019.2768

Liang, Y., Song, X., Li, Y., Chen, B., Zhao, W., Wang, L., et al. (2020). LncRNA BCRT1 Promotes Breast Cancer Progression by Targeting miR-1303/PTBP3 axis. *Mol. Cancer* 19, 85. doi:10.1186/s12943-020-01206-5

Liu, C., Zhao, J., Tian, F., Chang, J., Zhang, W., and Sun, J. (2019). λ-DNA- and Aptamer-Mediated Sorting and Analysis of Extracellular Vesicles. *J. Am. Chem. Soc.* 141, 3817–3821. doi:10.1021/jacs.9b00007

Liu, D., Xu, Y., Rao, Z., and Chen, Z. (2011). Preparation of Anti-HER2 Monoclonal Antibody-Paclitaxel Immunoconjugate and its Biological

Evaluation. *J. Huazhong Univ. Sci. Technol. Med. Sci.]* 31, 735–740. doi:10.1007/s11596-011-0669-8

Lu, H., and Xu, S. (2020). Ultrasensitive Turn on Molecularly Imprinted Fluorescence Sensor for Glycoprotein Detection Based on Nanoparticles Signal Amplification. *Sensors Actuators B Chem.* 306, 127566. doi:10.1016/j.snb.2019.127566

Nakatsuka, N., Abendroth, J. M., Yang, K.-A., and Andrews, A. M. (2021). Divalent Cation Dependence Enhances Dopamine Aptamer Biosensing. *ACS Appl. Mat. Interfaces* 13, 9425–9435. doi:10.1021/acsami.0c17535

Pramanik, S., Khamari, L., and Mukherjee, S. (2021). Differentiating a Least-Stable Single Nucleotide Mismatch in DNA via Metal Ion-Mediated Base Pairing and Using Thioflavin T as an Extrinsic Fluorophore. *J. Phys. Chem. Lett.* 12, 2547–2554. doi:10.1021/acs.jpclett.1c00146

Rezaie, J., Ahmadi, M., Ravanbakhsh, R., Mojarad, B., Mahbubfam, S., Shaban, S. A., et al. (2022). Tumor-derived Extracellular Vesicles: The Metastatic Organotropism Drivers. *Life Sci.* 289, 120216. doi:10.1016/j.lfs.2021.120216

Shen, M., Di, K., He, H., Xia, Y., Xie, H., Huang, R., et al. (2020). Progress in Exosome Associated Tumor Markers and Their Detection Methods. *Mol. Biomed.* 1, 3. doi:10.1186/s43556-020-00002-3

Tang, M., Schaffer, A. L., Kiely, B. E., Daniels, B., Lee, C. K., Simes, R. J., et al. (2021). Cardiac Assessment in Australian Patients Receiving (Neo)adjuvant Trastuzumab for HER2-Positive Early Breast Cancer: a Population-Based Study. *Breast Cancer Res. Treat.* 187, 893–902. doi:10.1007/s10549-021-06135-5

Théry, C., Witwer, K. W., Aikawa, E., Alcaraz, M. J., Anderson, J. D., Andriantsitohaina, R., et al. (2018). Minimal Information for Studies of Extracellular Vesicles 2018 (MISEV2018): a Position Statement of the International Society for Extracellular Vesicles and Update of the MISEV2014 Guidelines. *J. Extracell. Vesicles* 7, 1535750. doi:10.1080/20013078.2018.1535750

Timson, D. J. (2019). Myosin Va and Spermine Synthase: Partners in Exosome Transport. *Biosci. Rep.* 39, BSR20190326. doi:10.1042/BSR20190326

Vahabi, A., Rezaie, J., Hassanpour, M., Panahi, Y., Nemati, M., Rasmi, Y., et al. (2022). Tumor Cells-Derived Exosomal CircRNAs: Novel Cancer Drivers, Molecular Mechanisms, and Clinical Opportunities. *Biochem. Pharmacol.* 200, 115038. doi:10.1016/j.bcp.2022.115038

Vajhadin, F., Mazloum-Ardakani, M., Shahidi, M., Moshtaghioun, S. M., Haghiralsadat, F., Ebadi, A., et al. (2022). MXene-based Cytosensor for the Detection of HER2-Positive Cancer Cells Using CoFe2O4@Ag Magnetic Nanohybrids Conjugated to the HB5 Aptamer. *Biosens. Bioelectron.* 195, 113626. doi:10.1016/j.bios.2021.113626

Wang, C., Huang, C.-H., Gao, Z., Shen, J., He, J., MacLachlan, A., et al. (2021). Nanoplasmonic Sandwich Immunoassay for Tumor-Derived Exosome Detection and Exosomal PD-L1 Profiling. *ACS Sens.* 6, 3308–3319. doi:10.1021/acssensors.1c01101

Wang, L.-C., Hong, C.-Y., Lin, Z.-Z., Chen, X.-M., and Huang, Z.-Y. (2020). Aptamer-based Fluorometric Determination of Chloramphenicol by Controlling the Activity of Hemin as a Peroxidase Mimetic. *Anal. Methods* 12, 2391–2397. doi:10.1039/d0ay00389a

Wu, C., Wang, C., Zhang, T., Gao, G., Wei, M., Chen, Y., et al. (2022). Lysosome-Targeted and Fluorescence-Turned "On" Cytotoxicity Induced by Alkaline Phosphatase-Triggered Self-Assembly. *Adv. Healthc. Mater.* 11, 2101346. doi:10.1002/adhm.202101346

Wu, H., Zhou, X., Cheng, W., Yuan, T., Zhao, M., Duan, X., et al. (2018). A Simple Fluorescence Biosensing Strategy for Ultrasensitive Detection of the BCR-ABL1 Fusion Gene Based on a DNA Machine and Multiple Primer-like Rolling Circle Amplification. *Analyst* 143, 4974–4980. doi:10.1039/c8an01094c

Zhang, B., Sheng, W., Liu, Y., Huang, N., Zhang, W., and Wang, S. (2020a). Multiplexed Fluorescence Immunoassay Combined with Magnetic Separation Using Upconversion Nanoparticles as Multicolor Labels for the Simultaneous Detection of Tyramine and Histamine in Food Samples. *Anal. Chim. Acta* 1130, 117–125. doi:10.1016/j.aca.2020.07.043

Zhang, L., Gu, C., Wen, J., Liu, G., Liu, H., and Li, L. (2021). Recent Advances in Nanomaterial-Based Biosensors for the Detection of Exosomes. *Anal. Bioanal. Chem.* 413, 83–102. doi:10.1007/s00216-020-03000-0

Zhang, Y., Bi, J., Huang, J., Tang, Y., Du, S., and Li, P. (2020b). Exosome: A Review of Its Classification, Isolation Techniques, Storage, Diagnostic and Targeted Therapy Applications. *Ijn* 15, 6917–6934. doi:10.2147/IJN.S264498

Zhang, Z., Tang, C., Zhao, L., Xu, L., Zhou, W., Dong, Z., et al. (2019). Aptamer-based Fluorescence Polarization Assay for Separation-free Exosome Quantification. *Nanoscale* 11, 10106–10113. doi:10.1039/c9nr01589b

Conflict of Interest: The authors declare that the research was conducted in the absence of any commercial or financial relationships that could be construed as a potential conflict of interest.

Publisher's Note: All claims expressed in this article are solely those of the authors and do not necessarily represent those of their affiliated organizations, or those of the publisher, the editors and the reviewers. Any product that may be evaluated in this article, or claim that may be made by its manufacturer, is not guaranteed or endorsed by the publisher.

frontiers | Frontiers in Bioengineering and Biotechnology

TYPE Review
PUBLISHED 08 August 2022
DOI 10.3389/fbioe.2022.958134

OPEN ACCESS

EDITED BY
Long Ma,
Tianjin University of Science and Technology, China

REVIEWED BY
Zhirui Guo,
Nanjing Medical University, China
Tang Yongjun,
Shenzhen Polytechnic, China
Wenbo Lu,
Shanxi Normal University, China

*CORRESPONDENCE
Zhu Chen,
chenzhu220@163.com

SPECIALTY SECTION
This article was submitted to Biosensors and Biomolecular Electronics, a section of the journal Frontiers in Bioengineering and Biotechnology.

RECEIVED 31 May 2022
ACCEPTED 30 June 2022
PUBLISHED 08 August 2022

CITATION
Liu S, Zhao K, Huang M, Zeng M, Deng Y, Li S, Chen H, Li W and Chen Z (2022), Research progress on detection techniques for point-of-care testing of foodborne pathogens.
Front. Bioeng. Biotechnol. 10:958134.
doi: 10.3389/fbioe.2022.958134

Research progress on detection techniques for point-of-care testing of foodborne pathogens

Sha Liu[1], Kaixuan Zhao[1], Meiyuan Huang[2], Meimei Zeng[1], Yan Deng[1], Song Li[1], Hui Chen[1], Wen Li[3] and Zhu Chen[1]*

[1]Hunan Key Laboratory of Biomedical Nanomaterials and Devices, Hunan University of Technology, Zhuzhou, China, [2]Zhuzhou Hospital Affiliated to Xiangya School of Medicine, Department of Pathology, Central South University, Zhuzhou, China, [3]College of Food Science and Engineering, Central South University of Forestry and Technology, Changsha, China

The global burden of foodborne disease is enormous and foodborne pathogens are the leading cause of human illnesses. The detection of foodborne pathogenic bacteria has become a research hotspot in recent years. Rapid detection methods based on immunoassay, molecular biology, microfluidic chip, metabolism, biosensor, and mass spectrometry have developed rapidly and become the main methods for the detection of foodborne pathogens. This study reviewed a variety of rapid detection methods in recent years. The research advances are introduced based on the above technical methods for the rapid detection of foodborne pathogenic bacteria. The study also discusses the limitations of existing methods and their advantages and future development direction, to form an overall understanding of the detection methods, and for point-of-care testing (POCT) applications to accurately and rapidly diagnose and control diseases.

KEYWORDS

foodborne pathogens, rapid detection, immunoassay, molecular biology, POCT, microfluidic chip, biosensor

Introduction

Foodborne pathogens continue to cause many intestinal diseases in humans around the world, causing a huge health and economic burden (Ling et al., 2019; Akter et al., 2021; Prata et al., 2021; Qiu et al., 2021). Figures from the World Health Organization (WHO) estimate that about 2 billion people die each year from diarrhea or disease caused by contaminated food, and 30% of them are children under 5 years of age (Scallan Walter et al., 2020; Belina et al., 2021; Van Puyvelde et al., 2021). The United States has one of the safest food supplies in the world, yet one in four people gets sick from foodborne diseases every year (Hoffmann and Walter, 2020; Hoffmann et al., 2021; Ge et al., 2022). The frequency and importance of these foodborne diseases depend on interactions between foodborne pathogens, hosts, food, and the environment (Ishaq et al., 2021; Jahan et al., 2021; Saravanan et al., 2021; Zarkani and Schikora, 2021). Bacterial foodborne illnesses are caused by infections with bacterium, such as *Salmonella, Campylobacter* spp., *Escherichia coli, Shigella, Vibrio, Listeria monocytogenes* (LM) and *Clostridium*

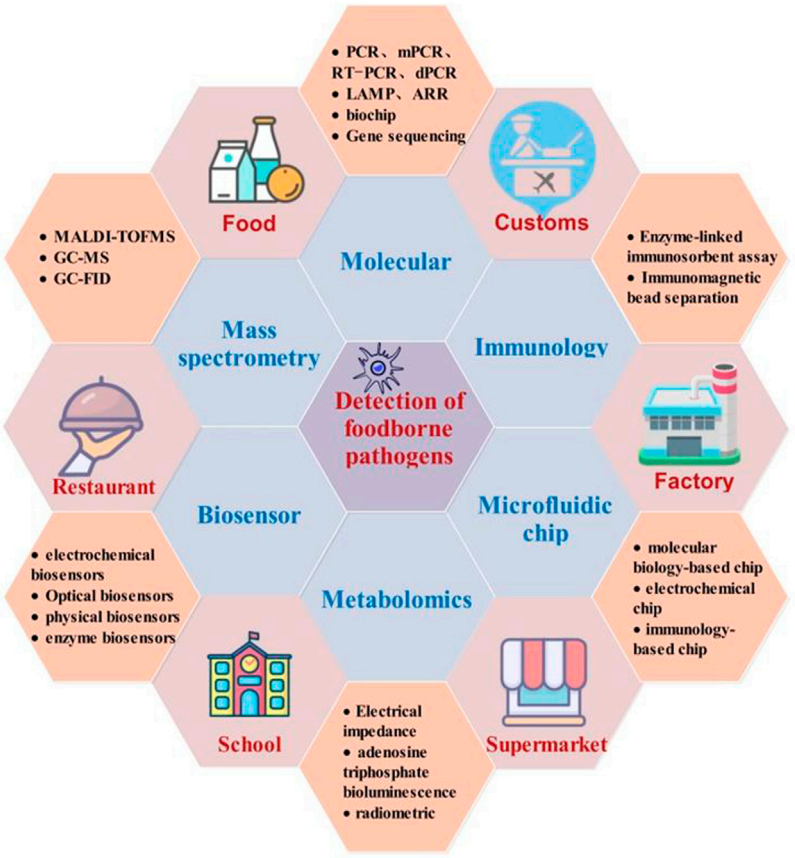

FIGURE 1
Summary based on detection methods of foodborne pathogenic bacteria.

botulinum, and *Clostridium perfringens* (Liu et al., 2019a; Xiao et al., 2019; Christopher et al., 2021; Fuochi et al., 2021; Kim et al., 2021a; Darbandi et al., 2022; Oyejobi et al., 2022). Viruses commonly reported are Norovirus and Hepatitis A, while examples of parasites involved are *Cryptosporidium* spp, *Giardia lamblia*, *Trichinella spiralis*, *Cyclospora* spp, *Toxoplasma canis,* and *Entamoeba histolytica* (Stryinski et al., 2020; Bozkurt et al., 2021; Lee and Yoon, 2021; Segeritz et al., 2021; Patel et al., 2022). Typical symptoms of foodborne illness include abdominal pain, diarrhea, vomiting, nausea, fever, difficulty breathing, and even death in severe cases (Abebe et al., 2020; Aik et al., 2020; Myintzaw et al., 2021; Sun et al., 2021; Janekrongtham et al., 2022). These symptoms are caused by ingested pathogens, such as foodborne infections (*Salmonellosis*, *Listeriosis*, etc.) (Gallo et al., 2020; Jang et al., 2021), or by microbial toxins produced in the host, such as toxic infections (*C. perfringens* food poisoning, etc.) (Rajkovic et al., 2020; Sharma et al., 2021). In the case of foodborne poisoning, toxins produced by pathogens in food cause symptoms (*C. botulinum* food poisoning, etc.) (Augustin et al., 2020; Walter et al., 2021). Poultry, ground meat, seafood, milk and dairy products, fruits, and vegetables have been blamed for most of the outbreaks (Leon Madrazo and Segura Campos, 2020; Visciano and Schirone, 2021; Singha et al., 2022).

Because foodborne pathogens pose a great threat to public health, it is therefore important to detect these pathogens (Dumen et al., 2020; Teffo and Tabit, 2020; Du et al., 2021a; Mi et al., 2021). Traditional methods for food pathogen detection mainly include plate separation, chemical analysis, and immunoassay (Wang et al., 2020a; Wang et al., 2020b; Han et al., 2021; Weng et al., 2021). However, these methods have more or less shortcomings, such as cumbersome steps, long detection cycle, high cost, and high requirements for a professional level of operators (Zhang et al., 2020a; Vidyadharani et al., 2021; Xie et al., 2021a; Nassarawa et al., 2022). Therefore, it is urgent to develop simple, sensitive, rapid, and low-cost methods for the detection of pathogenic bacteria in complex food samples.

Point-of-care testing (POCT) technology is a rapidly developing foodborne pathogen detection method in recent years that has advantages, such as simple operation, rapid operation, portability, and automation (Huang et al., 2018; Xu

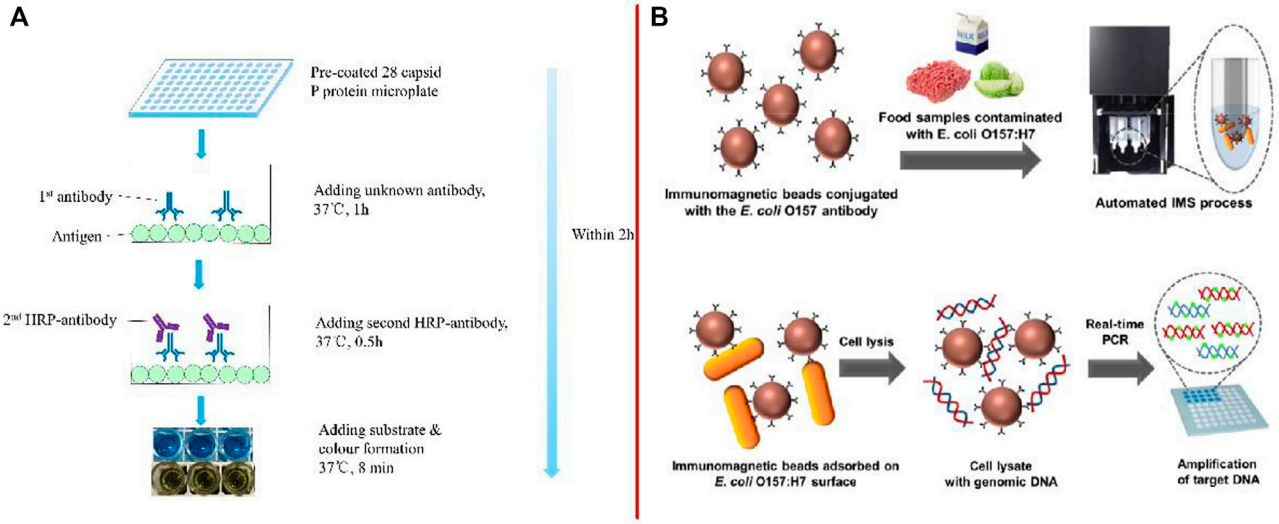

FIGURE 2
(A) Step-by-step schematic representation of ELISA (Zuo et al., 2021); **(B)** Schematic illustration of the detection method for *E. coli* O157: H7 using the automated IMS device combined with real-time PCR (Park et al., 2020).

et al., 2021). In this study, applications of POCT in the detection of foodborne pathogens based on biomolecules, immunoassay, gene sequencing, microfluidic, metabolism, biosensor, mass spectrometry, and related technologies in recent years have been reviewed (Figure 1). The principle, advantages, and disadvantages of each method and its application status are described. The existing problems and future development of rapid detection methods are also discussed. This study provides a reference for the development of rapid detection technology for foodborne pathogens and has certain significance for research on various disciplines and food safety supervision.

Immunological detection techniques

From its birth to its current development, the wide application of immunological detection technology determines its dominant position in the fields of biological science, food science, and clinical medicine. Its principle is based on antibody–antigen interaction, that is, the binding of specific antibodies (polyclonal antibody or monoclonal antibody) to their specific antigens (Jayan et al., 2020; Mishra et al., 2020; Wang et al., 2020c; Pires et al., 2021; Sohrabi et al., 2022).

Enzyme-linked immunosorbent assay

Enzyme-linked immunosorbent assay (ELISA) is a sensitive and specific analytical biochemical method that can be used for the detection and quantitative or qualitative analysis of analytes without requiring sophisticated or expensive equipment (Ferone et al., 2020; Nath et al., 2020; Rani et al., 2021; Kotsiri et al., 2022). At present, although traditional ELISA is widely used in scientific research and testing institutions and is the ideal method for the detection of viruses and antibodies (Leva-Bueno et al., 2020; Navarro et al., 2020; Xiao et al., 2021), this traditional method is time-consuming and also requires skilled operation techniques and sophisticated instruments (Luo et al., 2020a; Razmi et al., 2020; Huang et al., 2022). So the researchers changed the traditional approach.

Zuo et al. (2021) developed an indirect ELISA for testing the broad spectrum of anti-NoV antibodies (Figure 2A). The entire process of testing the spectrum of unknown antibodies required 2 h for completion. The intra-assay and inter-assay coefficients of variation were less than 10%. He et al. (2020) developed a sandwich-ELISA, which could detect 6 CFU/ml of *Salmonella enteritidis* (*S. enteritidis*) in milk after 10 h of enrichment. Zhao et al. (2020) developed a wax-printed paper-based enzyme-linked immunosorbent assay (P-ELISA) based on microfluidic paper-based analytical devices, with the whole operation time being less than 3 h and only needing 5 μl of samples for detection. The limit of detection for *E. coli* O157:H7 (*E. coli* O157:H7) reached 10^4 CFU/ml.

Immunomagnetic separation technology

Immunomagnetic separation (IMS) is an effective pre-concentration technique for food samples that can quickly

and selectively separate and concentrate target bacteria from complex food substrates (Liu et al., 2019c; Fang et al., 2021a; Nadar et al., 2021). The main principle is the surface of superparamagnetic particles after chemical modification, combined with target bacteria-specific active protein made of immunomagnetic bead separation (IMBS), and then the antibodies on IMBS will specifically identify and capture the target bacteria in the samples to be tested, which leads to the formation of IMBS-target bacteria complex (Ma et al., 2012; Jiang et al., 2013; Shen et al., 2021a; Zhang et al., 2021a). Finally, the complex is rapidly separated from other impurities in the sample by the force of a magnetic field, so as to achieve the efficient and accurate concentration of the target microorganism (Li et al., 2015; Wang and Lin, 2020; Wang et al., 2020d; Hou et al., 2020; Tang et al., 2020).

IMS technology has the characteristics such as strong specificity, high sensitivity, and fast separation speed (Pissuwan et al., 2020; Zhang et al., 2020b; Qi et al., 2022) and can be combined with a variety of other technologies (Yao et al., 2020; Zhai et al., 2021; Zhao et al., 2021a; Dester and Alocilja, 2022), such as ELISA, chemiluminescence immunoassay (CLIA), flow cytometry (FCM), immunochromatography (ICA), polymerase chain reaction (PCR), and other detection methods, to make the detection process more rapid and efficient (Yang et al., 2014a; He et al., 2017; Li et al., 2017; Lin et al., 2020; Nguyen and Kim, 2020; Sourri et al., 2022).

Moreover, Park et al. (2020) described the development of an automated IMS device combined with real-time PCR for detecting foodborne bacteria (Figure 2B). Target bacteria in the range of 10^1–10^2 colony-forming units per mg or g of sample can be detected in food samples, such as milk, ground beef, and cabbage, by using the proposed approach. Lv et al. (2021) developed an IMS technique by combining improved propidium monoazide and droplet digital PCR to detect the pathogenic viable but non-culturable *Cronobacter sakazakii* (*C. sakazakii*). The detection limit for this method in a background of powdered infant formula (PIF) was 5.6 copies/g. Jiang et al. (2020) first detected *Vibrio parahaemolyticus* (*V. parahaemolyticus*) in oysters by recombinant enzyme polymerase amplification (RPA) and side-flow (LF) combined with IMS. The method effectively combined sample preparation, amplification, and detection on one platform and could also detect *V. parahaemolyticus* within 15 min.

The IMS technology also has some limitations, such as the selected antigen target should have strong specificity, can specifically enrich the target bacteria, and avoid the enrichment of miscellaneous bacteria (Wang et al., 2020e; Zhai et al., 2020). Therefore, in order to rapidly develop in the field of foodborne pathogenic bacteria detection, specific antibodies from pathogenic bacteria must be screened.

Other immunological techniques

In addition to the above two immunological detection techniques, immuno chromatography (IC), immunodiffusion, immunofluorescence, Western blot, and Latex agglutination have all been applied in the detection of foodborne pathogens (Zhou et al., 2017; Li et al., 2018; Wu et al., 2020a; Morales-Pablos et al., 2020; Gao et al., 2021; Lopes-Luz et al., 2021; Wangman et al., 2021; Zhao et al., 2021b). Immunology technology has good specificity, high efficiency, low testing cost, and does not need the advantages of large instrument, but when the influenza virus contains competitive target bacteria in food material is very likely a false-positive result, the sensitivity is not high, these factors limit the immunology technology widely application in detection of foodborne pathogenic bacteria (Wang and Park, 2020; Zhao and Wu, 2020; Yan et al., 2021).

Molecular biology detection technology

Molecular biology detection technology is based on nucleic acid, through the detection of specific target pathogens DNA or RNA for detection purposes (Xi et al., 2014; Liu et al., 2017a; Foddai and Grant, 2020; Zheng and Tan, 2020; Kim and Oh, 2021). It is achieved by hybridizing the target sequence with complementary probes or primers (Yang et al., 2014b; Yang et al., 2017; Chen et al., 2020a; Wachiralurpan et al., 2020).

Temperature-changing amplification technology

Variable temperature amplification is a method based on PCR technology. Conventional PCR can only detect one pathogen at a time, but there are many pathogenic bacteria in food (Kim and Kim, 2021). Therefore, based on conventional PCR, dozens of different types of PCR methods were derived, mainly including multiple polymerase chain reaction (mPCR), real-time quantitative polymerase chain reaction (qPCR), and digital polymerase chain reaction technology (dPCR) (Tang et al., 2018; Mou et al., 2019a; Lei et al., 2020a; Cardoso et al., 2020; Huang et al., 2021a).

mPCR is based on traditional PCR, whereby multiple pairs of specific primers and templates are added into the same PCR reaction system (primers are specifically bound to corresponding templates) to amplify multiple DNA fragments with different sequences (Zhang et al., 2020c; Hossain et al., 2021; Bonny et al., 2022; Liu et al., 2022). Multiple DNA fragments amplified in the same reaction system can simultaneously detect multiple foodborne pathogens, reduce the number of experimental operations, shorten the detection time, and save reagents (Ma et al., 2020a; Yang et al., 2020a). He et al. (2022) developed a

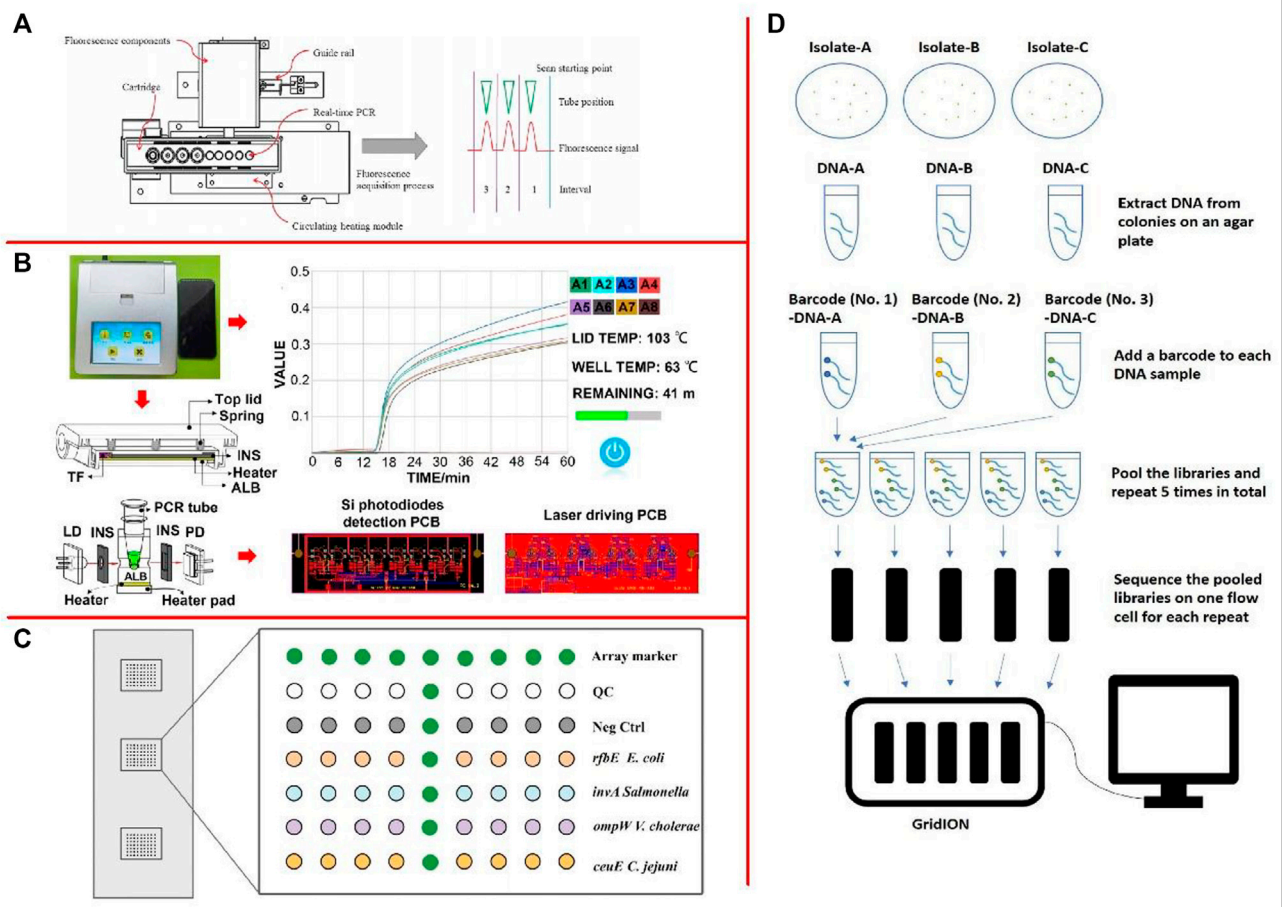

FIGURE 3
(A) Positions of the fluorescence detection module and the Peltier device, and the principle of fluorescence acquisition (Chen et al., 2017); **(B)** The design of the diagnostic device (Chen et al., 2022); **(C)** Layout of oligonucleotide probes on the detection microarray (Liu et al., 2017b); **(D)** An example of the workflow of multiplex ONT sequencing library preparation and sequencing (Wu et al., 2021).

detection system based on magnetic separation, mPCR, and capillary electrophoresis (CE) technologies for the simultaneous detection of four foodborne pathogens. The detection limit for bacterial DNA reached 10^{-5}–10^{-7} ng/μl and in the analysis of mocked food samples, the assay showed good sensitivity for bacterial detection ranging from 10^{1} to 10^{5} CFU/ml with excellent specificity.

mPCR is suitable for the detection of multiple foodborne pathogens with the same symptoms or easily contaminating the same food, which can standardize the detection of microorganisms in food (Du et al., 2020a; Ripolles-Avila et al., 2020). However, because multiple pairs of primers are amplified in the same system, each pair of primers affects each other, so the amplification effect and the actual number of amplified fragments in the actual operation of mPCR are often not satisfactory (Luo et al., 2020; Chen et al., 2021).

qPCR operates by adding fluorescent-labeled probes or fluorescent substances into the PCR system and monitors the accumulation of fluorescence signals in the whole PCR amplification process in real-time through the instrument. Finally, the method for quantitative analysis of samples with unknown concentrations was carried out through standard curves (Fu et al., 2020; Baoutina and Bhat, 2021; Wan et al., 2021). Moreover, Chen et al. (2017) presented a new POCT system based on magnetic nanoparticles that enable sample in-answer out (SIAO) automated real-time testing for pathogens (Figure 3A). Real-time PCR by the two methods (TaqMan-based probe and SYBR green dye) in the SIAO system was achievable by the manual method with comparable results. Xie and Liu. (2021) developed a double TaqMan real-time fluorescence quantitative PCR (DRT-PCR) method for their simultaneous enumeration within two kinds of powdered infant foods (PIFs). The dRT-PCR could quantify as low as 10^{2} and 10^{1} CFU/ml *C. sakazakii* and *Staphylococcus aureus* (*S. aureus*) in both pure cultures and spiked PIFs.

Compared with ordinary PCR, the nucleic acid amplification of qPCR technology is completed in a closed system, and no electrophoresis analysis is required after the amplification, which not only reduces the chances for sample contamination, but also avoids false-positive results caused by contamination and also shortens the detection time (Obande and Singh, 2020; Kim et al., 2021b). However, the experimental cost of real-time quantitative PCR is high, and the equipment required is expensive, which also requires the operator to have a high level of professional technology (Nunez-Bajo et al., 2020; Wang et al., 2021a).

dPCR does not require the establishment of a standard curve and concentration comparison by Ct value (the number of cycles that PCR fluorescence signal goes through when it reaches a set threshold) and is considered an absolute quantitative method (Grudlewska-Buda et al., 2020; Lei et al., 2021; Plante et al., 2021). Droplet digital PCR (ddPCR) is a new method that disperses a single target DNA molecule into multiple separated droplets, detects each droplet one by one after PCR amplification, and accurately quantifies DNA copy number (Lei et al., 2020b; Iwu et al., 2020). Du et al. (2021b) developed an effective pretreatment method based on an *in-situ* enrichment culture with an immunomagnetic separation step, combined with ddPCR technology to achieve rapid detection of trace *Salmonella* in milk, which allowed detecting as low as 10^{-1} CFU/ml level of *Salmonella*. ddPCR has the advantages of high sensitivity, high accuracy, high tolerance, and absolute quantification and has been widely used in rare mutation detection and gene expression detection in complex samples (Salipante and Jerome, 2020; Yang et al., 2020b).

Constant temperature amplification technology

At present, constant temperature amplification techniques applied to foodborne pathogenic microorganisms mainly include loop-mediated isothermal amplification (LAMP), recombinant enzyme-mediated nucleic acid amplification (RAA), RPA, and nucleic acid sequence-dependent amplification (NASBA) (Chen et al., 2018; Khan et al., 2019; Safenkova et al., 2020; He et al., 2021a; Hoang et al., 2021; Tian et al., 2022).

LAMP is a mature isothermal nucleic acid amplification technique in which the target sequence was amplified with two or three sets of primers at a constant temperature of 60–65°C (Prasannakumar et al., 2020; Wang et al., 2020f; Zhang et al., 2021b). Typically, four different primers are used to amplify six different regions on the target gene, which increases specificity (Xie et al., 2022). Another pair of "cyclic primers" can further accelerate the reaction. In addition to replication activity, polymerases with high chain displacement activity are required for amplification (Garafutdinov et al., 2020; Padzil et al., 2022). Liu et al. (2022) developed a LAMP method for LM detection using SYTO9 staining and image processing techniques. The detection limit of LM was 6 copies/μl. Chen et al. (2022) developed a novel Enter cytozoon hepatopenaei (EHP) field rapid detection device (size $18.8 \times 16.7 \times 6.6$ cm^3) based on magnesium pyrophosphate precipitation and LAMP (Figure 3B). The detection limit for EHP was 0.1 fg/μl. Moreover, Jin et al. (2020) developed a LAMP-based microdevice for performing high-throughput visual detection. The approach was able to perform simultaneous identification of six foodborne pathogens within 1 h. LAMP is an isothermal amplification technique with high practical value and detection efficiency, but it also has obvious disadvantages, such as false-positive results after the addition of ring primers (Yu et al., 2021a). Although the frequency of false-positive can be reduced by various methods, it is still impossible to avoid the high requirement and difficulty in primer design.

RAA is a technique for nucleic acid amplification using recombinant enzyme, single-chain binding protein, and DNA polymerase under isothermal conditions (optimal temperature 37°C) (Feng et al., 2022a; Hou et al., 2022; Zhang et al., 2022). The established RAA method can effectively shorten the detection time and does not require temperature change during nucleic acid amplification (Aman et al., 2020; Teklemariam et al., 2020; Li et al., 2021a). Li et al. (2021b) introduced the transcleavage activity of CRISPR/Cas12a into an electrochemical biosensor (ECRISPR), combined with RAA, to establish a cost-effective, specific, and ultrasensitive method, namely, RAA-based E-CRISPR. Under optimized conditions, the RAA-based E-CRISPR can detect as low as 0.68 aM of genomic DNA and 26 CFU/ml of LM in pure cultures. Xie et al. (2021b) proposed a modified propidium monoazide (PMAxx) dye combined with RAA for the rapid and real-time detection of viable *S. aureus*. The detection limit for viable *S. aureus* was 10^2 CFU/ml under 3 h enrichment and 10^1 CFU/ml under 6 h enrichment in artificially contaminated milk, respectively. Zhou et al. (2022) reported a novel CRISPR/Cas12a-based fluorescence enhanced lateral flow biosensor (LFB) in conjunction with functionalized quantum dots, combined with RAA, to establish low-cost, simple, and sensitive detection of *S. aureus*, namely, CRISPR/Cas-recombinase-assisted amplification-based LFB (CRA-LFB). The limit of detection was as low as 75 aM of genomic DNA, and 5.4×10^2 CFU/ml of *S. aureus* in pure cultures were detected. RAA has a great development advantage due to its lower requirements on environmental temperature, operating skills, and experimental equipment (Mu et al., 2021).

Biochip technology

Biochip technology was started in the 1980s. It is a micro biochemical analysis system of molecular microarray. It uses mechanical arm sampling technology or microelectronic lithography technology to construct up to tens of thousands

of different probes on the surface of a certain volume of the solid carrier to detect a variety of biological components (Li et al., 2013; Azizipour et al., 2020; Aladese and Jeong, 2021; Tahir et al., 2021). The biochip technology has the advantages such as diversification, high throughput, short detection time, and portability. At present, gene chip, protein chip technology, and liquid chip are widely used in the detection of foodborne pathogens (Pos et al., 2020; Qian et al., 2022).

Gene chip is the first developed and earliest researched and developed technology in biochip technology (Zeng et al., 2014; Chen et al., 2020b; Kumar et al., 2020; Ali et al., 2021). The sequencing principle for the gene chip is the hybridization sequencing method, by which hybridization with a group of nucleic acid probes with a known sequence of target nucleotide, and with a known sequence for nucleic acid sequencing are fixed on the surface of a substrate, (Zhang et al., 2020d; Hariharan and Prasannath, 2021; Taguchi et al., 2021). Liu et al. (2017b) developed a magnetic nanoparticle-enhanced oligonucleotide microarray assay for rapid and sensitive identification of *E. coli* O157:H7, *Salmonella enterica*, *Vibrio cholerae*, and *Campylobacter jejuni* (*C. jejuni*) in food (Figure 3C). In comparison with conventional single-stranded target preparation methods, this magnetic nanoparticles-based method yielded up to 15-fold increase in the hybridization signal and achieved 1 similar to 2 orders of magnitude enhancement on the limit of detection. Sarengaowa et al. (2020) developed an in situ-synthesized gene chip for the detection of foodborne pathogens on fresh-cut fruits and vegetables. The detection limit for the five target pathogens on fresh-cut cantaloupe and lettuce was approximately 3 log CFU/g without culturing and with a detection time of 24 h. Shen et al. (2020) performed the genome-wide DNA microarray analysis using *S. typhimurium* incubated with 0.001% epsilonpolylysine in 0.1% Bacto Soytone at 30°C for 2 h.

The high degree of automation of gene chip technology can analyze a large number of samples at one time, and the data are objective and reliable (Jia et al., 2021a). But the cost is high, with low detection sensitivity, poor repeatability, and narrow analysis scope (Zaczek-Moczydlowska et al., 2021).

Protein chip technology is a kind of protein microarray, which is different from gene chip to realize binding based on the principle of base complementary pairing. It uses the interaction between proteins, such as the reaction between antigen and antibody, enzyme and substrate, for detection (Khan et al., 2021; Zhou et al., 2021; Hang et al., 2022). With the continuous development and improved protein microarray technology, the technology has been gradually applied to the detection of foodborne pathogens. Liu et al. (2019c) constructed a protein chip to screen for antibody titers present in test sera raised against whole *C. jejuni* cells with over 1,400 individually purified GST-tagged *C. jejuni* proteins, representing over 86% of the proteome. These results indicated that the unbiased chip-based screen can reveal the full repertoire of host antibodies against microbial proteomes. Protein microarray technology is an emerging technology with bright development prospects, but there are still some problems in maintaining protein activity, protein fixation methods, and detection sensitivity (Xia et al., 2021), which need further research and optimization.

Liquid chips, also known as microsphere suspension chips, began in the mid-1990s, with their diverse fluorescent encoded microspheres, up to 100 different probes can be crosslinked by different ways of binding and hybridization (Jia et al., 2021b). Qualitative and quantitative detection of microsphere fluorescence coding and molecular fluorescence intensity by two different laser beams is a new generation of high-throughput molecular detection technology platform following DNA chip and protein microarray (Han et al., 2020; Li et al., 2020; Yin et al., 2020). Pang et al. (2019) established a microsphere-based suspension array (MSA) for the detection and identification of 55 *V. parahaemolyticus* K-serogroups based on CPSgc-specific genes. This system was then used to examine 845 publicly available *V. parahaemolyticus* genomes. Shi et al. (2019) established a rapid and accurate method based on mPCR combined with suspension array flexible sequence-tagged (xTAG) technology to simultaneously detect *S. typhimurium*, *Brucella* spp., *Bacillus* cereus, and *Shigella* spp. in raw milk. The results showed that the detection of milk samples demonstrated 100% specificity.

Gene sequencing

In molecular biology, DNA sequence analysis is the basis for further research and modification of target genes (Mou et al., 2019b; Uelze et al., 2020; Hu et al., 2021). At present, there are two types of mainstream technologies for sequencing: 1) Traditional sequencing technology, or first-generation sequencing technology, is represented by the Sanger sequencing method (Segerman, 2020; Kaprou et al., 2021). 2) The next-generation sequencing (NGS) technology developed in recent years is also known as high-throughput sequencing technology, and its sequencing principles include simultaneous sequencing and single-molecule sequencing (Reuter et al., 2015; Lu et al., 2020; Van Poelvoorde et al., 2020). Specifically, synthetization sequencing (also known as the second-generation sequencing technology) is represented by Roche's 454 technology, Illumina's Solexa, Hiseq technology, and ABI's Solid technology (Lewis et al., 2020; Shen et al., 2021b). Single-molecule sequencing (also known as third-generation sequencing technology) is based on Helicos Bioscience's HeliScope genetic analysis system, Pacific Biosciences' PacBio RS single-molecule real-time sequencing system, and Oxfold Nanopore Examples include Technologies' GridION and MinION (Yu et al., 2020; Gunther et al., 2021; Van Reckem et al., 2021). Single-cell sequencing technology is to sequence each individual cell through high-throughput sequencing

technology to obtain the genetic information of each individual cell (Davey and Valdivia, 2020; Peng et al., 2020a).

The principle for the Sanger sequencing method is to randomly cut genomic DNA into small fragments, and then many small fragments of DNA are cloned into plasmid vectors and transformed into *E. coli*. Finally, the cultured *E. coli* extracts plasmid for sequencing, and each sequencing reaction is completed in a reaction system for only a few microliters (Efimochkina and Sheveleva, 2022). Syromyatnikov et al. (2020) used high-throughput sequencing and Sanger sequencing of individual bacterial colonies to analyze the microbial content of commercially available butter brands. We identified a total of 94 amplicon sequence variants corresponding to different microbial taxa. Sanger sequencing technology is relatively common in small bacterial genome sequencing, plasmid sequencing, and other research fields, with its accuracy, precision target, and low throughput (Maguire et al., 2021). However, in large-scale sequencing tasks, Sanger sequencing technology has defects of low throughput, slow speed, and high cost, thus promoting high-throughput sequencing technology (Sheka et al., 2021).

High-throughput sequencing technology is a revolutionary improvement on traditional sequencing technology in history, which can simultaneously determine the molecular sequence of millions or even tens of millions of DNA (Cassotta et al., 2020; Chelliah et al., 2022). Muriuki et al. (2021) used 454 pyrosequencing, Illumina high-throughput sequencing of 16S rRNA gene in the analysis of total community DNA extracted from samples using the phenol-chloroform method. Uncultured *Candidatus* Koribacter and *Candidatus Solibacter* were also detected in the food samples. There was a significant difference in the microbial community structure among the sample types ($p < 0.1$). Gutierrez et al. (2021) sequenced 62 cases of Shiga toxin-producing *E. coli* (STEC) isolated from Chile using MiSeq Illumina. The results indicated that there may be local emerging STEC with unique features, nevertheless, no molecular markers were detected. Wu et al. (2021) evaluated the serotype prediction accuracy of using whole-genome sequencing (WGS) data from multiplex ONT sequencing (Figure 3D). This study demonstrated that accurate serotype prediction results could be obtained when multiplexing five or less *Salmonella* isolates with an average of 6 h of multiplex ONT sequencing, where each multiplexed isolate received at least 50× depth of genome coverage of sequencing data after demultiplexing.

The advantage of second-generation sequencing technology is that the cost is greatly reduced and the flux is greatly improved compared with the first generation, but the disadvantage is that the PCR process introduced will increase the sequencing error rate to a certain extent, and has a systematic bias, and the read length is relatively short (Kaavya et al., 2021). The third-generation sequencing technology is developed to solve the shortcomings of the second generation. Its fundamental feature is single-molecule sequencing, which does not require any PCR process, in order to effectively avoid system errors caused by PCR bias, while improving the read length, and maintaining the advantages of the second-generation technology of high throughput and low cost (Quijada et al., 2020).

Microfluidic detection technology

Microfluidics provides a powerful tool for testing applications with its advantages of portability, miniaturization, automation, multi-channel sample testing, minimization of hazardous material handling, and cost savings (Ragab and El-Kimary, 2021; Su et al., 2021; Tseng et al., 2021). In addition, all analytical processes, including sample preparation, reaction, separation, and detection are integrated into a microfluidic chip for field test applications (Fu et al., 2021; Xie et al., 2021c). Biosensors that use a variety of technologies combined with microfluidic chips to detect foodborne pathogens have been widely reported (Ali et al., 2020; Kaya et al., 2021). Many new microfluidic chips have been successfully developed for the detection of foodborne pathogens. At present, according to the detection principle, the microfluidic detection chips are mainly divided into three categories: molecular biology-based microfluidic detection chips, immunology-based microfluidic detection chips, and electrochemical microfluidic detection chips.

Xue et al. (2021) developed a microfluidic biosensor for rapid and sensitive detection of *Salmonella* using manganese dioxide nanoflowers (MnO_2 NFs), a microfluidic chip with a convergence-divergence spiral micromixer, and a smartphone app with a saturation calculation algorithm (Figure 4A). This biosensor was able to detect *Salmonella* from 4.4×10^1 to 4.4×10^6 CFU/ml in 45 min with a detection limit of 44 CFU/ml. Zhang et al. (2021b) have created an embedded paper-based microchip based on LAMP which can rapidly and sensitively detect foodborne pathogens (Figure 4B). The detection limit for *Salmonella* spp. in the sample measured by the microchip was approximately 12 CFU/ml. Song et al. (2020) developed a microfluidic platform to detect *S. aureus* by fluorescence labeling method and a self-made microfluidic chip, which has immune spheres were used to study the effect of capturing *S. aureus* (Figure 4C). Results showed that our platform can detect *S. aureus* at an injection rate of 5 μl/min reacted for 4 min and the detection limit of bacteria was 1.5×10^1 CFU/mul. Nguyen et al. (2020) proposed an integrated smartphone-based genetic analyzer. The LAMP mixture for Eriochrome Black T (EBT) colorimetric detection was injected into the LAMP chip to identify the *E. coli* O157:H7 (Figure 4D). The limit-of-detection (LOD) reached up to 10^1 copies/μl. Moreover, Asgari et al. (2022) developed a

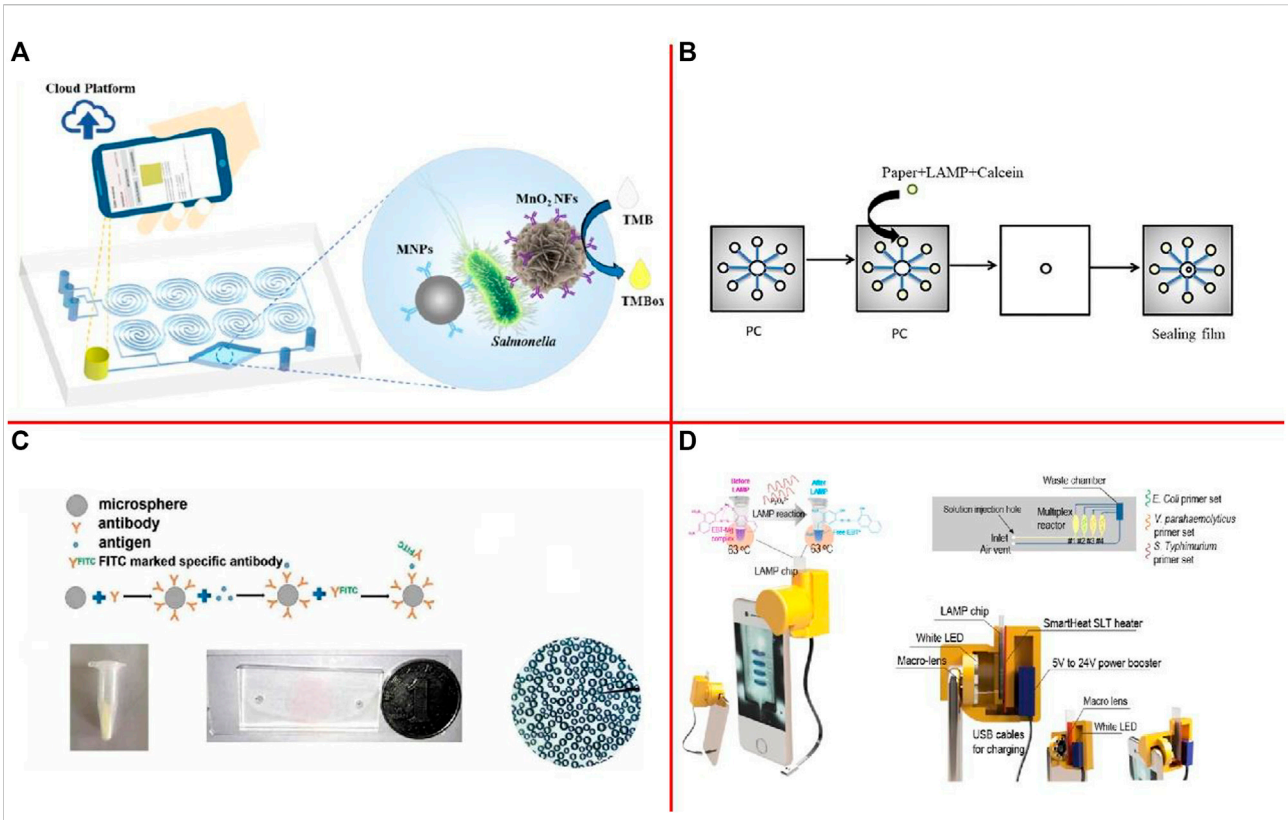

FIGURE 4
(A) Schematic of this Colorimetric Biosensor for Detection of *Salmonella* (Xue et al., 2021); **(B)** Making the process of the microchip (Zhang et al., 2021b); **(C)** The whole process of a microfluidic platform for detection of *S. aureus* by fluorescence labeling (Song et al., 2020); **(D)** Schematics of the i-Gene (Nguyen et al., 2020).

sensitive Surface-enhanced Raman spectroscopy (SERS)-based microfluidic simmunosensor to separate and detect *E. coli* O157:H7 in romaine lettuce. The limit of detection for *E. coli* O157:H7 in romaine lettuce was found to be 0.5 CFU/ml. Wang et al. (2022) demonstrated an ultrasensitive and simple microfluidic immunosensor for a point-of-care test of *S. aureus* based on stir bar enrichment and DNAzyme-assisted click reaction. The detection limit was 3 CFU/ml. Jiang et al. (2021) designed a thread-based microfluidic electrochemical aptasensor, fabricated and tested by using label-free aptamer immunosensing technology for rapid and highly sensitive detection of *V. parahaemolyticus* in seafood. The proposed aptasensor has a dynamic detection range of 10–10^6 CFU/ml, with a detection limit of 5.74 CFU/ml.

At present, microfluidic technology has shown great potential in environmental monitoring, food science, drug screening, disease diagnosis, and other fields, but there is still a long way to go to the market application. Therefore, the development of new materials and new processing methods is an important means to promote the development of microfluidic technology (Tsougeni et al., 2020).

Metabolic detection techniques

Metabolic detection is a common technique for the detection of foodborne pathogens (Castle et al., 2021). Its principle is to use various techniques to detect the variation characteristics of the amount and type of primary metabolites or secondary metabolites produced by different pathogenic bacteria in a specific cultural environment, to identify the pathogenic bacteria (Duarte-Sierra et al., 2020; Subjakova et al., 2021). According to different detection technologies, it can be divided into electrical impedance technology, radiometric technology adenosine triphosphate (ATP) bioluminescence technology, microcalorimeter technology, etc. (Mobed et al., 2020; McCuskey et al., 2022).

Electrical impedance technology

According to different metabolic activities of microorganisms in the growth process, electrical impedance technology is used to detect and identify microorganisms. Wang et al. (2020g) developed a sensitive

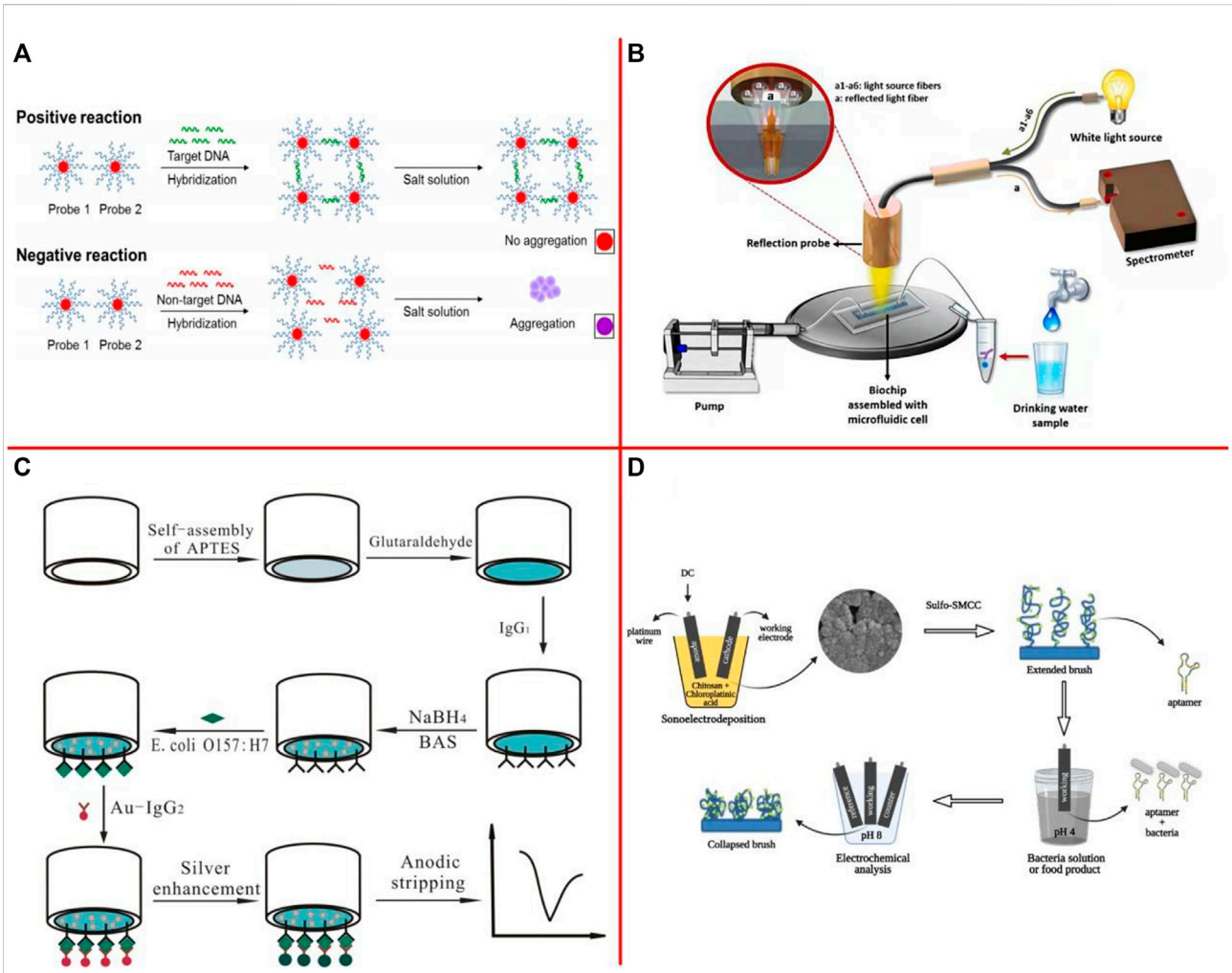

FIGURE 5
(A) The novel principles behind AuNPs optical biosensing and the schematic representation of DNA sandwich hybridization targeting ttrRSBCA locus of *Salmonella* spp. (Quintela et al., 2019); **(B)** Illustration of the white light reflectance spectroscopy (WLRS) optical setup and sensing and sensing principle (Angelopoulou et al., 2021); **(C)** Schematic diagram of electrochemical detection of *E. coli* O157:H7 by gold nanoparticle-catalyzed silver enhancement at porous pseudo-carbon paste electrode (Xu et al., 2012); **(D)** Fabrication, biofunctionalization, and sensing scheme of CHI/Pt aptasensor (Oliveira et al., 2021).

electrochemical aptasensor using aptamer coated gold interdigitated microelectrode for targeted capture and impedance measurement, and antibody-modified nickel nanowires (NiNWs) for target separation and impedance amplification. This electrochemical aptasensor was able to quantitatively detect *Salmonella* ranging from 10^2 to 10^6 CFU/ml in 2 h, with a detection limit of 80 CFU/ml. Wang et al. (2021b) developed a novel impedance immunosensor based on a metal-organic framework (Mn-MOF-74) to rapidly and sensitively detect LM in milk. The recoveries for L.m cells at concentration between 1.0×10^0 and 1.0×10^4 CFU/ml were 90.2%–101.7% in water and 88.5%–96.2% in milk. Wang et al. (2021c) developed a bacteria-imprinted conductive poly (3-thiopheneacetic acid) (BICP) film-based impedimetric sensor for the rapid, sensitive, and label-free detection of *S. aureus*.

Biosensor detection technology

Biosensor is an analysis device consisting of a biosensor and transducer. It mainly uses antigens (antibodies), various sensitive enzymes, alkaloids, and gene sequences to detect microorganisms (Shiba 2006; Wang et al., 2013; Liu et al., 2017c; Ma et al., 2020b; Guo et al., 2021; Das and Mishra, 2022). When the sample to be tested reacts with the above substances, biological interactions will occur, which can then be converted into measurable electrical signals by signal transducers, which can be read and

detected by signal amplifiers (Lai et al., 2018a; Lai et al., 2018b; Huang et al., 2021). According to different working principles, biosensors can be divided into optical biosensors, electrochemical biosensors, enzyme biosensors, physical biosensors, mechanical biosensors, and so on (Liu et al., 2018; Liu et al., 2019d; He et al., 2019; Ahovan et al., 2020; Naresh and Lee, 2021; Yu et al., 2021). Biosensors commonly used for rapid detection of foodborne pathogens include; optical biosensors and electrochemical biosensors (Tian et al., 2019; Wu et al., 2020b; Du et al., 2020b; Magesa et al., 2020; Mei et al., 2022).

Optical biosensors are widely used in the detection of foodborne pathogens due to their rapid detection and high sensitivity (Nie et al., 2014; Sun et al., 2021a; Wei et al., 2021). At present, the main optical sensing technologies include chemiluminescence, colorimetry, fluorescence, and surface plasmon resonance (Luan et al., 2020).

Quintela et al. (2019) developed a novel approach for simultaneous optical detection of various *Salmonella* spp. strains in contaminated complex matrices by utilizing oligonucleotide-functionalized AuNPs as a sensitive optical biosensing platform in combination with an efficient sample pooling and IMS system that ensure the detection of viable cells (Figure 5A). The results showed that the highly sensitive assay toward its target with a superior detection limit of <10 CFU/ml or g and 100% specificity. Srivastava et al. (2021) developed a nanophotonic structure with electric control-based photocatalytic nanocomposite to realize label-free optical detection of foodborne pathogens. The fabricated biosensor is capable of detecting *E. coli* bacteria concentrations of 5,000 CFU/ml. Angelopoulou et al. (2021) presented an optical biosensor for the detection of *S. typhimurium* lipopolysaccharide (LPS) and *Salmonella* bacteria in drinking water, based on white light reflectance spectroscopy (Figure 5B). The total assay duration was 15 min, while the achieved detection limits were 4 ng/ml for LPS and 320 CFU/ml for bacteria.

The electrochemical biosensor uses the electrode as a signal converter, and the target analyte performs an electrochemical reaction on the electrode interface, which causes the change of current, potential, impedance, or conductivity on the sensor surface (Deng et al., 2013a; Deng et al., 2013b; Upasham et al., 2021; Vidic and Manzano, 2021). Xu et al. (2012) described the fabrication of three different electrodes based on functional porous pseudo-carbon paste electrodes (PPCPEs) (Figure 5C). A linear relationship between the anodic stripping peak current and the concentration of *E. coli* O157: H7 from 1.0×10^3 to 1.0×10^7 cells/ml and a limit of detection as low as 8.0×10^2 cells/ml were obtained when PPCPE-CHO was used. The target analyte can be quantified by monitoring the change of these signals. Oliveira et al. (2021) developed a label-free and rapid electrochemical biosensor for LM detection using a new one-step simultaneous sonoelectrodeposition of platinum and chitosan (CHI/Pt) to create a biomimetic nanostructure that actuates under pH changes (Figure 5D). Actuation led to improved LM detection with a low limit of detection (33 CFU/10 ml in chicken broth). Feng et al. (2022b) constructed an electrochemical immunosensor for *Salmonella* detection by using a Fe_3O_4@graphene modified electrode. Under optimized experimental conditions, a good linear relationship was achieved in the *Salmonella* concentration range of 2.4×10^2 to 2.4×10^7 CFU/ml, and the limit of detection for the immunosensor was 2.4×10^2 CFU/ml.

Biosensor technology detection of microorganisms has rapid, sensitive, simple operation and low requirement for operating personnel, but biological sensors are used to identify biological molecules of the original life is relatively short, with high-cost production, so the use of biosensor technology is limited by some, and most is still in the development stage (Shen et al., 2021c).

Mass spectrometry

With the development of mass spectrometry, mass spectrometry (MS) is a new detection method of pathogenic bacteria, that has been developed gradually (Fang et al., 2021b). MS is a non-biochemical instrumental analysis method, which takes the characteristics of bacteria or their proteins as the research object and realizes the identification and detection of target bacteria by analyzing the characteristic ions generated after ionization.

Feucherolles et al. (2022) combined Matrix-assisted laser desorption/ionization time of flight mass spectrometry (MALDI-TOF MS) protein mass spectra with a prediction approach as an antimicrobial resistance (AMR) screening tool for relevant foodborne pathogens, such as *Campylobacter coli* and *C. jejuni*. A maximum sensitivity and precision of 92.3% and 81.2%, respectively, were reached. Moreover, Li et al. (2022) presented a novel strategy using mass tag-mediated surface engineering for simultaneous detection of multiple bacteria by MALDI-TOF MS. This strategy converted the detection of bacteria to the analysis of mass tags, allowing simultaneous detection of multiple bacteria and avoiding the dependence of microbial mass spectra databases. Dias et al. (2022) used gas chromatography-mass spectrometry (GC-MS) and gas chromatography-flame ionization detector (GC-FID) to determine the antibacterial activity of three essential oils (EOs) and their main components against foodborne pathogens and spoilage foods.

Among many detection technologies, the foodborne pathogenic bacteria MS has the highest detection rate at present, with fast detection speed and convenient operation, but there are still many problems in the actual detection process (Mangmee et al., 2020). In the detection process, it is necessary to improve the sensitivity and stability of foodborne pathogenic bacteria MS technology, so it is necessary to constantly debug spray voltage, flow rate, capillary temperature, and other issues to achieve the optimal state.

TABLE 1 Compare the methods of detecting foodborne pathogens.

Detection technology	Sensitivity	Specificity	Operation	Speed	Cost	Application	References
Immunology	202 CFU/ml	High	Easy to use	12 min	—	*C. sakazakii*	Gao et al. (2021)
	10 CFU/ml	High	Professionals to operate	65 min	—	*S. aureus*	Yao et al. (2020)
	100 CFU/ml	Extremely good	Professionals to operate	150 min	—	*V. parahaemolyticus*	Zhai et al. (2021)
	2 CFU/g	High	Easier to operate	4 h	—	*V. parahaemolyticus*	Jiang et al. (2020)
	10^4 CFU/ml	High	Easy to use	<3 h	Less costly than C-ELISA	*E. coli* O157:H7	Zhao et al. (2020)
	6 CFU/ml	Good	Professionals to operate	10 h	—	*S. enteritidis*	He et al. (2020)
Molecular	940 CFU/g	High	Professionals to operate	45 min	—	*L. monocytogenes*	Li et al. (2021b)
	1 CFU/ml	>80%	Professionals to operate	8 h	—	*Salmonella*	Du et al. (2021b)
	540 CFU/ml	Very high	Almost equipment-free	70 min	Low cost	*S. aureus*	Zhou et al. (2022)
	10 CFU/ml	Good	The whole operational procedure should be finished coherently	30 min	—	*S. typhimurium*, *Brucella* spp., *B. cereus* and *Shigella* spp.	Shi et al. (2019)
Microfluidics	15 CFU/ml	Good	Semi-automatic operation	about 1 h	—	*S. aureus*	Song et al. (2020)
	5.74 CFU/ml	High	Professionals to operate	about 30 min	—	*V. parahaemolyticus*	Jiang et al. (2021)
	44 CFU/ml	Good	Semi-automatic operation	45 min	—	*Salmonella*	Xue et al. (2021)
	0.5 CFU/ml	Good	Professionals to operate	about 1 h	A very low number of antibodies are needed	*E. coli* O157:H7	Asgari et al. (2022)
Metabolic	2 CFU/ml	High	Professionals to operate	10 min	Production cost of the BICP film was low	*S. aureus*	Wang et al. (2021c)
	80 CFU/ml	Good	Professionals to operate	2 h	—	*Salmonella*	Wang et al. (2020g)
	In water and milk are 7.1 and 9.2 CFU/ml	Good	Professionals to operate	within 1 h	—	*L. monocytogenes*	Wang et al. (2021b)
Biosensor	320 CFU/ml	High	Professionals to operate	15 min	The WLRS Biochip can be reused to reduce costs	*Salmonella*	Angelopoulou et al. (2021)
	240 CFU/ml	Excellent selectivity	Professionals to operate	1.5 h	—	*Salmonella*	Feng et al. (2022b)
	5,000 CFU/ml	Good	Professionals to operate	1 min	—	*E. coli*	Srivastava et al. (2021)
	<10 CFU/ml or g	High	Professionals to operate	<1 h	—	Various *Salmonella* spp	Quintela et al. (2019)

(Continued on following page)

TABLE 1 (*Continued*) Compare the methods of detecting foodborne pathogens.

Detection technology	Sensitivity	Specificity	Operation	Speed	Cost	Application	References
Mass Spectrometry	99.3% accuracy	High	Not require specially trained staff	The analysis time is longer than immunoassays and nucleic acid-based assays	Low cost per sample, but high initial cost of the instrument	Non-typhoidal *Salmonella* serovar screening	Mangmee et al. (2020)
	S. aureus (1,000 CFU/ml), E. coliO157:H7 (500 CFU/ml)	High	Professionals to operate	—	—	*E. coli* O157:H7 and *S. aureus*	Li et al. (2022)

C. sakazakii, *Cronobacter sakazakii*; *V. parahaemolyticus*, *Vibrio parahaemolyticus*; *S. aureus*, *Staphylococcus aureus*; *S. enteritidis*, *Salmonella enteritidis*; *S. Typhimurium*, *Salmonella Typhimurium*; *B. cereus*, *Bacillus. cereus*; *E.coli*, *Escherichia coli*; *E. coli* O157:H7, *Escherichia coli* O157:H7; C-ELISA, conventional enzyme-linked immunosorbent assay; BICP, bacteria-imprinted conductive poly; WLRS, white light reflectance spectroscopy.

Conclusion

In recent years, many methods for the detection of foodborne pathogens have been developed to address food safety and public health issues, especially with the increased consumption of fresh food and food with short shelf life. Rapid detection technologies are becoming more marketable (Freitas et al., 2020; Ezzatpanah et al., 2022). For example, many scholars have combined POCT technologies such as molecular immunology, bio-molecular, biosensor, and microfluidics to provide new approaches for rapid, low-cost, highly sensitive, and highly specific detection methods for foodborne pathogens (Cimafonte et al., 2020; Wang et al., 2021d; Zhang et al., 2021c). The POCT technology provides simple, fast, and sensitive platforms for the detection of foodborne pathogens and will become a powerful multi-functional tool for food safety, biological threat detection, and environmental monitoring. However, there are still shortcomings that require researchers to continuously improve the existing detection technologies (He et al., 2021b; Wagner et al., 2021). The sensitivity, specificity, ease of operation and detection speed, cost, and application of the techniques for detecting foodborne pathogens are given in Table 1.

With the advancement of science and technology, artificial intelligence, gene editing, nanotechnology, and other cutting-edge disciplines, the integration of these technologies and POCT technology in the rapid detection of foodborne pathogens will also become the future development trend (He et al., 2018; Chen et al., 2020c; Ding et al., 2020; Peng et al., 2020b; Yang et al., 2020c; Gong et al., 2021; Xiao et al., 2022). The following is the prospect of POCT technology in the future development trend: 1) the detection index is gradually transformed from biochemical and immunity to nucleic acid molecules, and from single to multiple indicators. 2) The devices are more miniaturized and integrated by the development of micro-nano fabrication and 3D printing and new materials technology. More and more functions can be integrated into a small device, such as integrate sample extraction and detection into a chip our cassette, etc. 3) The devices have the features of higher sensitivity and quicker time with the application of novel CRISPR method and gold nanoparticles and so on. 4) The devices will be more convenient and lower cost for the use of smart mobile phones, lateral flow dipsticks, or paper chips. Moreover, with the advance of cloud computing, Internet of things technology, devices make more intelligence.

The future detection technology for foodborne pathogenic bacteria will focus toward the integration of a variety of detection technologies, making flux detection faster, with higher sensitivity and repeatability, faster time, and lower cost. The future will also include wide promotion and standardization direction for these technologies, including production, processing, distribution, and sale of the whole production chain of food safety regulations.

Author contributions

All authors listed have made a substantial, direct, and intellectual contribution to the work, and approved it for publication.

Funding

This work was supported by the National Natural Science Foundation of China (No. 61901168), Hunan Provincial Natural Science Foundation of China (No. 2022JJ30229), China Postdoctoral Science Foundation (No. 2018M630498), and Education Department of Hunan Province (No. 21B0526).

Conflict of interest

The authors declare that the research was conducted in the absence of any commercial or financial relationships that could be construed as a potential conflict of interest.

Publisher's note

References

Abebe, E., Gugsa, G., and Ahmed, M. (2020). Review on major food-borne zoonotic bacterial pathogens. *J. Trop. Med.* 2020, 1–19. doi:10.1155/2020/4674235

Ahovan, Z. A., Hashemi, A., De Plano, L. M., Gholipourmalekabadi, M., and Seifalian, A. (2020). Bacteriophage based biosensors: Trends, outcomes and challenges. *Nanomaterials* 10, 501. doi:10.3390/nano10030501

Aik, J., Turner, R. M., Kirk, M. D., Heywood, A. E., and Newall, A. T. (2020). Evaluating food safety management systems in Singapore: A controlled interrupted time-series analysis of foodborne disease outbreak reports. *Food control.* 117, 107324. doi:10.1016/j.foodcont.2020.107324

Akter, R., Rahman, M. H., Bhattacharya, T., Kaushik, D., Mittal, V., Parashar, J., et al. (2021). Novel coronavirus pathogen in humans and animals: An overview on its social impact, economic impact, and potential treatments. *Environ. Sci. Pollut. Res.* 28, 68071–68089. doi:10.1007/s11356-021-16809-8

Aladese, A. D., and Jeong, H.-H. (2021). Recent developments in 3D printing of droplet-based microfluidics. *BioChip J.* 15, 313–333. doi:10.1007/s13206-021-00032-1

Ali, A. A., Altemimi, A. B., Alhelfi, N., and Ibrahim, S. A. (2020). Application of biosensors for detection of pathogenic food bacteria: A review. *Biosens. (Basel).* 10, 58. doi:10.3390/bios10060058

Ali, Q., Ahmar, S., Sohail, M. A., Kamran, M., Ali, M., Saleem, M. H., et al. (2021). Research advances and applications of biosensing technology for the diagnosis of pathogens in sustainable agriculture. *Environ. Sci. Pollut. Res.* 28, 9002–9019. doi:10.1007/s11356-021-12419-6

Aman, R., Mahas, A., and Mahfouz, M. (2020). Nucleic acid detection using CRISPR/cas biosensing technologies. *ACS Synth. Biol.* 9, 1226–1233. doi:10.1021/acssynbio.9b00507

Angelopoulou, M., Tzialla, K., Voulgari, A., Dikeoulia, M., Raptis, I., Kakabakos, S. E., et al. (2021). Rapid detection of *Salmonella typhimurium* in drinking water by a white light reflectance spectroscopy immunosensor. *Sensors* 21, 2683. doi:10.3390/s21082683

Asgari, S., Dhital, R., Aghvami, S. A., Mustapha, A., Zhang, Y., Lin, M., et al. (2022). Separation and detection of *E. coli* O157:H7 using a SERS-based microfluidic immunosensor. *Microchim. Acta* 189, 111. doi:10.1007/s00604-022-05187-8

Augustin, J.-C., Kooh, P., Bayeux, T., Guillier, L., Meyer, T., Jourdan-Da Silva, N., et al. (2020). Contribution of foods and poor food-handling practices to the burden of foodborne infectious diseases in France. *Foods* 9 (11), 1644. doi:10.3390/foods9111644

Azizipour, N., Avazpour, R., Rosenzweig, D. H., Sawan, M., and Ajji, A. (2020). Evolution of biochip technology: A review from lab-on-a-chip to organ-on-a-chip. *Micromachines* 11, 599. doi:10.3390/mi11060599

Baoutina, A., and Bhat, S. (2021). Novel design of nucleic acid standards for hydrolysis probe-based PCR with melting analysis. *Gene Ther*. doi:10.1038/s41434-021-00288-0

Belina, D., Hailu, Y., Gobena, T., Hald, T., and Njage, P. M. K. (2021). Prevalence and epidemiological distribution of selected foodborne pathogens in human and different environmental samples in Ethiopia: A systematic review and meta-analysis. *One Health Outlook* 3 (1), 19. doi:10.1186/s42522-021-00048-5

Bonny, S. Q., Hossain, M. A. M., Uddin, S. M. K., Pulingam, T., Sagadevan, S., Johan, M. R., et al. (2022). Current trends in polymerase chain reaction based detection of three major human pathogenic vibrios. *Crit. Rev. Food Sci. Nutr.* 62, 1317–1335. doi:10.1080/10408398.2020.1841728

Bozkurt, H., Kim-Yen, P.-T., van Ogtrop, F., Bell, T., and McConchie, R. (2021). Outbreaks, occurrence, and control of norovirus and hepatitis a virus contamination in berries: A review. *Crit. Rev. Food Sci. Nutr.* 61, 116–138. doi:10.1080/10408398.2020.1719383

Cardoso, G. V. F., Lima, J. S., de Oliveira, A. C. d. S., da Silva, J. B., Roos, T. B., de Moraes, C. M., et al. (2020). SYBR green qPCR technique for the detection of trypanosoma cruzi in acai pulp. *Foodborne Pathog. Dis.* 17, 466–469. doi:10.1089/fpd.2019.2745

Cassotta, M., Forbes-Hernandez, T. Y., Calderon Iglesias, R., Ruiz, R., Elexpuru Zabaleta, M., Giampieri, F., et al. (2020). Links between nutrition, infectious diseases, and microbiota: Emerging technologies and opportunities for human-focused research. *Nutrients* 12, 1827. doi:10.3390/nu12061827

Castle, L. M., Schuh, D. A., Reynolds, E. E., and Furst, A. L. (2021). Electrochemical sensors to detect bacterial foodborne pathogens. *ACS Sens.* 6, 1717–1730. doi:10.1021/acssensors.1c00481

Chelliah, R., Banan-MwineDaliri, E., Khan, I., Wei, S., Elahi, F., Yeon, S.-J., et al. (2022). A review on the application of bioinformatics tools in food microbiome studies. *Brief. Bioinform.* 23, bbac007. doi:10.1093/bib/bbac007

Chen, H., Wu, Y., Chen, Z., Hu, Z., Fang, Y., Liao, P., et al. (2017). Performance evaluation of a novel sample in-answer out (SIAO) system based on magnetic nanoparticles. *J. Biomed. Nanotechnol.* 13, 1619–1630. doi:10.1166/jbn.2017.2478

Chen, S., Li, J., Yang, L., and Zhong, C. (2020b). Research on healthcare and external medicine based on nano biochip technology. *Int. J. Nanotechnol.* 17, 106. doi:10.1504/ijnt.2020.110710

Chen, Y., Qian, C., Liu, C., Shen, H., Wang, Z., Ping, J., et al. (2020a). Nucleic acid amplification free biosensors for pathogen detection. *Biosens. Bioelectron. X.* 153, 112049. doi:10.1016/j.bios.2020.112049

Chen, Y., Wang, Z., Shi, Q., Huang, S., Yu, T., Zhang, L., et al. (2021). Multiplex PCR method for simultaneous detection of five pathogenic bacteria closely related to foodborne diseases. *3 Biotech.* 11, 219. doi:10.1007/s13205-021-02759-y

Chen, Z., Xiao, C., Qiu, H., Tan, X., Jin, L., He, Y., et al. (2020c). Recent advances of artificial intelligence in cardiovascular disease. *J. Biomed. Nanotechnol.* 16, 1065–1081. doi:10.1166/jbn.2020.2955

Chen, Z., Yang, T., Yang, H., Li, T., Nie, L., Mou, X., et al. (2018). A portable multi-channel turbidity system for rapid detection of pathogens by loop-mediated isothermal amplification. *J. Biomed. Nanotechnol.* 14, 198–205. doi:10.1166/jbn.2018.2524

Chen, Z., Zhao, K., He, Z., Luo, X., Qin, Z., Tan, Y., et al. (2022). Development and evaluation of a thermostatic nucleic acid testing device based on magnesium pyrophosphate precipitation for detecting Enterocytozoon hepatopenaei. *Chin. Chem. Lett.* 33, 4053–4056. doi:10.1016/j.cclet.2022.01.072

Christopher, A., Sarkar, D., and Shetty, K. (2021). Elicitation of stress-induced phenolic metabolites for antimicrobial applications against foodborne human bacterial pathogens. *Antibiot. (Basel).* 10 (2), 109. doi:10.3390/antibiotics10020109

Cimafonte, M., Fulgione, A., Gaglione, R., Papaianni, M., Capparelli, R., Arciello, A., et al. (2020). Screen printed based impedimetric immunosensor for rapid detection of *Escherichia coli* in drinking water. *Sensors* 20, 274. doi:10.3390/s20010274

Darbandi, A., Asadi, A., Ari, M. M., Ohadi, E., Talebi, M., Zadeh, M. H., et al. (2022). Bacteriocins: Properties and potential use as antimicrobials. *J. Clin. Lab. Anal.* 36, e24093. doi:10.1002/jcla.24093

Das, J., and Mishra, H. N. (2022). Recent advances in sensors for detecting food pathogens, contaminants, and toxins: A review. *Eur. Food Res. Technol.* 248, 1125–1148. doi:10.1007/s00217-021-03951-3

Davey, L., and Valdivia, R. H. (2020). Bacterial genetics and molecular pathogenesis in the age of high throughput DNA sequencing. *Curr. Opin. Microbiol.* 54, 59–66. doi:10.1016/j.mib.2020.01.007

Deng, Y., Wang, W., Ma, C., and Li, Z. (2013a). Fabrication of an electrochemical biosensor array for simultaneous detection of L-glutamate and acetylcholine. *J. Biomed. Nanotechnol.* 9, 1378–1382. doi:10.1166/jbn.2013.1633

Deng, Y., Wang, W., Zhang, L., Lu, Z., Li, S., Xu, L., et al. (2013b). Preparation and electrochemical behavior of L-glutamate electrochemical biosensor. *J. Biomed. Nanotechnol.* 9, 318–321. doi:10.1166/jbn.2013.1487

Dester, E., and Alocilja, E. (2022). Current methods for extraction and concentration of foodborne bacteria with glycan-coated magnetic nanoparticles: A review. *Biosens. (Basel).* 12 (2), 112. doi:10.3390/bios12020112

Dias, A. L. B., Fernandes, C. C., de Souza, J. H., Martins, C. H. G., Moreira, F. F., Crotti, A. E. M., et al. (2022). Antibacterial activity of essential oils from Brazilian

plants and their major constituents against foodborne pathogens and spoilage bacteria. *J. Essent. Oil Res.* 34, 195–202. doi:10.1080/10412905.2022.2032424

Ding, Z., Wang, Y., Zhou, Q., Ding, Z., Liu, J., He, Q., et al. (2020). Microstructure, wettability, corrosion resistance and antibacterial property of Cu-MTa_2O_5 multilayer composite coatings with different Cu incorporation contents. *Biomolecules* 10, 68. doi:10.3390/biom10010068

Du, H., Li, Z., Wang, Y., Yang, Q., and Wu, W. (2020b). Nanomaterial-based optical biosensors for the detection of foodborne bacteria. *Food Rev. Int.* 38, 655–684. doi:10.1080/87559129.2020.1740733

Du, H., Wang, X., Yang, Q., and Wu, W. (2021a). Quantum dot: Lightning invisible foodborne pathogens. *Trends Food Sci. Technol.* 110, 1–12. doi:10.1016/j.tifs.2021.01.065

Du, J., Wu, S., Niu, L., Li, J., Zhao, D., Bai, Y., et al. (2020a). A gold nanoparticles-assisted multiplex PCR assay for simultaneous detection of *Salmonella typhimurium*, Listeria monocytogenes and *Escherichia coli* O157:H7. *Anal. Methods* 12, 212–217. doi:10.1039/c9ay02282a

Du, M. H., Li, J. W., Liu, Q. J., Wang, Y. F., Chen, E. N., Kang, F. Y., et al. (2021b). Rapid detection of trace Salmonella in milk using an effective pretreatment combined with droplet digital polymerase chain reaction. *Microbiol. Res.* 251, 126838. doi:10.1016/j.micres.2021.126838

Duarte-Sierra, A., Tiznado-Hernandez, M. E., Jha, D. K., Janmeja, N., and Arul, J. (2020). Abiotic stress hormesis: An approach to maintain quality, extend storability, and enhance phytochemicals on fresh produce during postharvest. *Compr. Rev. Food Sci. Food Saf.* 19, 3659–3682. doi:10.1111/1541-4337.12628

Dumen, E., Ekici, G., Ergin, S., and Bayrakal, G. M. (2020). Presence of foodborne pathogens in seafood and risk ranking for pathogens. *Foodborne Pathog. Dis.* 17, 541–546. doi:10.1089/fpd.2019.2753

Efimochkina, N. R., and Sheveleva, S. A. (2022). Prospective molecular methods for sequencing microorganisms in the system of assessment and control of food safety. *Problems Nutr.* 91, 37–52. doi:10.33029/0042-8833-2022-91-1-37-52

Ezzatpanah, H., Gomez-Lopez, V. M., Koutchma, T., Lavafpour, F., Moerman, F., Mohammadi, M., et al. (2022). New food safety challenges of viral contamination from a global perspective: Conventional, emerging, and novel methods of viral control. *Compr. Rev. Food Sci. Food Saf.* 21, 904–941. doi:10.1111/1541-4337.12909

Fang, S., Liu, S., Song, J., Huang, Q., and Xiang, Z. (2021b). Recognition of pathogens in food matrixes based on the untargeted *in vivo* microbial metabolite profiling via a novel SPME/GC×GC-QTOFMS approach. *Food Res. Int.* 142, 110213. doi:10.1016/j.foodres.2021.110213

Fang, Y., Liu, H., Wang, Y., Su, X., Jin, L., Wu, Y., et al. (2021a). Fast and accurate control strategy for portable nucleic acid detection (PNAD) system based on magnetic nanoparticles. *J. Biomed. Nanotechnol.* 17, 407–415. doi:10.1166/jbn.2021.3028

Feng, K., Li, T., Ye, C., Gao, X., Yue, X., Ding, S., et al. (2022b). A novel electrochemical immunosensor based on Fe_3O_4@graphene nanocomposite modified glassy carbon electrode for rapid detection of Salmonella in milk. *J. Dairy Sci.* 105, 2108–2118. doi:10.3168/jds.2021-21121

Feng, Z.-S., Li, J.-Y., Zhang, J.-Y., Li, F.-Y., Guan, H.-X., Zhang, R.-Q., et al. (2022a). Development and evaluation of a sensitive recombinase aided amplification assay for rapid detection of Vibrio parahaemolyticus. *J. Microbiol. Methods* 193, 106404. doi:10.1016/j.mimet.2021.106404

Ferone, M., Gowen, A., Fanning, S., and Scannell, A. G. M. (2020). Microbial detection and identification methods: Bench top assays to omics approaches. *Compr. Rev. Food Sci. Food Saf.* 19, 3106–3129. doi:10.1111/1541-4337.12618

Feucherolles, M., Nennig, M., Becker, S. L., Martiny, D., Losch, S., Penny, C., et al. (2022). Combination of MALDI-TOF mass spectrometry and machine learning for rapid antimicrobial resistance screening: The case of Campylobacter spp. *Front. Microbiol.* 12, 804484. doi:10.3389/fmicb.2021.804484

Foddai, A. C. G., and Grant, I. R. (2020). Methods for detection of viable foodborne pathogens: Current state-of-art and future prospects. *Appl. Microbiol. Biotechnol.* 104, 4281–4288. doi:10.1007/s00253-020-10542-x

Freitas, J., Vaz-Pires, P., and Camara, J. S. (2020). *From aquaculture production to consumption: Freshness, safety, traceability and authentication, the four pillars of quality*, 518, 734857. doi:10.1016/j.aquaculture.2019.734857*Aquaculture*

Fu, L., Qian, Y., Zhou, J., Zheng, L., and Wang, Y. (2020). Fluorescence-based quantitative platform for ultrasensitive food allergen detection: From immunoassays to DNA sensors. *Compr. Rev. Food Sci. Food Saf.* 19, 3343–3364. doi:10.1111/1541-4337.12641

Fu, X., Sun, J., Liang, R., Guo, H., Wang, L., Sun, X., et al. (2021). Application progress of microfluidics-integrated biosensing platforms in the detection of foodborne pathogens. *Trends Food Sci. Technol.* 116, 115–129. doi:10.1016/j.tifs.2021.07.006

Fuochi, V., Emma, R., and Furneri, P. M. (2021). Bacteriocins, A natural weapon against bacterial contamination for greater safety and preservation of food: A review. *Curr. Pharm. Biotechnol.* 22, 216–231. doi:10.2174/1389201021666200704145427

Gallo, M., Ferrara, L., Calogero, A., Montesano, D., and Naviglio, D. (2020). Relationships between food and diseases: What to know to ensure food safety. *Food Res. Int.* 137, 109414. doi:10.1016/j.foodres.2020.109414

Gao, S., Wu, J., Wang, H., Hu, S., and Meng, L. (2021). Highly sensitive detection of Cronobacter sakazakii based on immunochromatography coupled with surface-enhanced Raman scattering. *J. Dairy Sci.* 104, 2748–2757. doi:10.3168/jds.2020-18915

Garafutdinov, R. R., Sakhabutdinova, A. R., Kupryushkin, M. S., and Pyshnyi, D. V. (2020). Prevention of DNA multimerization using phosphoryl guanidine primers during isothermal amplification with Bst exo- DNA polymerase. *Biochimie* 168, 259–267. doi:10.1016/j.biochi.2019.11.013

Ge, H., Wang, Y., and Zhao, X. (2022). Research on the drug resistance mechanism of foodborne pathogens. *Microb. Pathog.* 162, 105306. doi:10.1016/j.micpath.2021.105306

Gong, L., Zhao, L., Tan, M., Pan, T., He, H., Wang, Y., et al. (2021). Two-Photon fluorescent nanomaterials and their applications in biomedicine. *J. Biomed. Nanotechnol.* 17, 509–528. doi:10.1166/jbn.2021.3052

Grudlewska-Buda, K., Skowron, K., and Gospodarek-Komkowska, E. (2020). Comparison of the intensity of biofilm formation by Listeria monocytogenes using classical culture-based method and digital droplet PCR. *Amb. Express* 10, 75. doi:10.1186/s13568-020-01007-5

Gunther, N. W., Kanrar, S., and Uhlich, G. (2021). Complete genomic sequences of Campylobacter coli strains isolated from poultry sold in Pennsylvania farmers' markets. *Microbiol. Resour. Announc.* 10, e00015-21. doi:10.1128/mra.00015-21

Guo, W., Zhang, C., Ma, T., Liu, X., Chen, Z., Li, S., et al. (2021). Advances in aptamer screening and aptasensors' detection of heavy metal ions. *J. Nanobiotechnology* 19, 166. doi:10.1186/s12951-021-00914-4

Gutierrez, S., Diaz, L., Reyes-Jara, A., Yang, X., Meng, J., Gonzalez-Escalona, N., et al. (2021). Whole-genome phylogenetic analysis reveals a wide diversity of non-O157 STEC isolated from ground beef and cattle feces. *Front. Microbiol.* 11, 622663. doi:10.3389/fmicb.2020.622663

Han, A., Hao, S., Yang, Y., Li, X., Luo, X., Fang, G., et al. (2020). Perspective on recent developments of nanomaterial based fluorescent sensors: Applications in safety and quality control of food and beverages. *J. Food Drug Anal.* 28, 487–508. doi:10.38212/2224-6614.1270

Han, X., Liu, Y., Yin, J., Yue, M., and Mu, Y. (2021). Microfluidic devices for multiplexed detection of foodborne pathogens. *Food Res. Int.* 143, 110246. doi:10.1016/j.foodres.2021.110246

Hang, Y., Boryczka, J., and Wu, N. (2022). Visible-light and near-infrared fluorescence and surface-enhanced Raman scattering point-of-care sensing and bio-imaging: A review. *Chem. Soc. Rev.* 51, 329–375. doi:10.1039/c9cs00621d

Hariharan, G., and Prasannath, K. (2021). Recent advances in molecular diagnostics of fungal plant pathogens: A mini review. *Front. Cell. Infect. Microbiol.* 10, 600234. doi:10.3389/fcimb.2020.600234

He, L., Yang, H., Xiao, P., Singh, R., He, N., Liu, B., et al. (2017). Highly selective, sensitive and rapid detection of *Escherichia coli* O157: H7 using duplex PCR and magnetic nanoparticle-based chemiluminescence assay. *J. Biomed. Nanotechnol.* 13, 1243–1252. doi:10.1166/jbn.2017.2422

He, Q., Liu, J., Liu, X., Li, G., Deng, P., Liang, J., et al. (2018). Manganese dioxide Nanorods/electrochemically reduced graphene oxide nanocomposites modified electrodes for cost-effective and ultrasensitive detection of Amaranth. *Colloids Surfaces B Biointerfaces* 172, 565–572. doi:10.1016/j.colsurfb.2018.09.005

He, Q., Tian, Y., Wu, Y., Liu, J., Li, G., Deng, P., et al. (2019). Electrochemical sensor for rapid and sensitive detection of tryptophan by a Cu2O nanoparticles-coated reduced graphene oxide nanocomposite. *Biomolecules* 9, 176. doi:10.3390/biom9050176

He, S., Fong, K., Wang, S., and Shi, X. (2021b). Ethanol adaptation in foodborne bacterial pathogens. *Crit. Rev. Food Sci. Nutr.* 61, 777–787. doi:10.1080/10408398.2020.1746628

He, S., Huang, Y., Ma, Y., Yu, H., Pang, B., Liu, X., et al. (2022). Detection of four foodborne pathogens based on magnetic separation multiplex PCR and capillary electrophoresis. *Biotechnol. J.* 17, 2100335. doi:10.1002/biot.202100335

He, Y., Ren, Y., Guo, B., Yang, Y., Ji, Y., Zhang, D., et al. (2020). Development of a specific nanobody and its application in rapid and selective determination of Salmonella enteritidis in milk. *Food Chem. x.* 310, 125942. doi:10.1016/j.foodchem.2019.125942

He, Z., Tong, Z., Tan, B., He, X., Zhang, T., Guo, Y., et al. (2021a). Rapid detection of DNA methylation with a novel real-time fluorescence recombinase-aided

amplification assay. *J. Biomed. Nanotechnol.* 17, 1364–1370. doi:10.1166/jbn.2021.3111

Hoang, T. X., Phan, L. M. T., Vo, T. A. T., and Cho, S. (2021). Advanced signal-amplification strategies for paper-based analytical devices: A comprehensive review. *Biomedicines* 9, 540. doi:10.3390/biomedicines9050540

Hoffmann, S., Ashton, L., and Ahn, J.-W. (2021). Food safety: A policy history and introduction to avenues for economic research. *Appl. Econ. Perspect. Policy* 43, 680–700. doi:10.1002/aepp.13158

Hoffmann, S., and Walter, E. S. (2020). Acute complications and sequelae from foodborne infections: Informing priorities for cost of foodborne illness estimates. *Foodborne Pathog. Dis.* 17, 172–177. doi:10.1089/fpd.2019.2664

Hossain, M. A. M., Uddin, S. M. K., Sultana, S., Wahab, Y. A., Sagadevan, S., Johan, M. R., et al. (2021). Authentication of Halal and Kosher meat and meat products: Analytical approaches, current progresses and future prospects. *Crit. Rev. Food Sci. Nutr.* 62, 285–310. doi:10.1080/10408398.2020.1814691

Hou, L., Li, D., Zhang, N., Zhao, J., Zhao, Y., Sun, X., et al. (2022). Development of an isothermal recombinase-aided amplification assay for the rapid and visualized detection of *Klebsiella pneumoniae*. *J. Sci. Food Agric.* 102, 3879–3886. doi:10.1002/jsfa.11737

Hou, Y., Tang, W., Qi, W., Guo, X., and Lin, J. (2020). An ultrasensitive biosensor for fast detection of Salmonella using 3D magnetic grid separation and urease catalysis. *Biosens. Bioelectron. X.* 157, 112160. doi:10.1016/j.bios.2020.112160

Hu, L., Cao, G., Brown, E. W., Allard, M. W., Ma, L. M., Zhang, G., et al. (2021). Whole genome sequencing and protein structure analyses of target genes for the detection of Salmonella. *Sci. Rep.* 11, 20887. doi:10.1038/s41598-021-00224-7

Huang, F., Zhang, Y., Lin, J., and Liu, Y. (2021b). Biosensors coupled with signal amplification technology for the detection of pathogenic bacteria: A review. *Biosens. (Basel).* 11, 190. doi:10.3390/bios11060190

Huang, L., Zhang, D., Jiao, L., Su, E., and He, N. (2018). A new quality control method for lateral flow assay. *Chin. Chem. Lett.* 29, 1853–1856. doi:10.1016/j.cclet.2018.11.028

Huang, T., Shi, Y., Zhang, J., Han, Q., Xia, X.-S., Zhang, A. M., et al. (2021a). Rapid and simultaneous detection of five, viable, foodborne pathogenic bacteria by photoinduced PMAxx-coupled multiplex PCR in fresh juice. *Foodborne Pathog. Dis.* 18, 640–646. doi:10.1089/fpd.2020.2909

Huang, Y., Mu, X., Wang, J., Wang, Y., Xie, J., Ying, R., et al. (2022). The recent development of nanozymes for food quality and safety detection. *J. Mat. Chem. B* 10, 1359–1368. doi:10.1039/d1tb02667d

Ishaq, A. R., Manzoor, M., Hussain, A., Altaf, J., Rehman, S. U., Javed, Z., et al. (2021). Prospect of microbial food borne diseases in Pakistan: A review. *Braz. J. Biol.* 81, 940–953. doi:10.1590/1519-6984.232466

Iwu, C. D., Korsten, L., and Okoh, A. I. (2020). The incidence of antibiotic resistance within and beyond the agricultural ecosystem: A concern for public health. *Microbiologyopen* 9, e1035. doi:10.1002/mbo3.1035

Jahan, N. A., Lindsey, L. L., and Larsen, P. A. (2021). The role of peridomestic rodents as reservoirs for zoonotic foodborne pathogens. *Vector-Borne Zoonotic Dis.* 21, 133–148. doi:10.1089/vbz.2020.2640

Janekrongtham, C., Dejburum, P., Sujinpram, S., Rattanathumsakul, T., and Swaddiwudhipong, W. (2022). Outbreak of seafood-related food poisoning from undetectable Vibrio parahaemolyticus-like pathogen, Chiang Mai Province, Thailand, December 2020. *Trop. Med. Int. Health* 27, 92–98. doi:10.1111/tmi.13700

Jang, H.-J., Kim, H.-J., Park, J.-i., Yu, S.-N., Park, B. B., Ha, G.-J., et al. (2021). Comparative analysis of detection methods for food-borne pathogens in fresh-cut agricultural materials. *J. Life Sci.* 31 (1), 10–16. doi:10.5352/jls.2021.31.1.10

Jayan, H., Pu, H., and Sun, D.-W. (2020). Recent development in rapid detection techniques for microorganism activities in food matrices using bio-recognition: A review. *Trends Food Sci. Technol.* 95, 233–246. doi:10.1016/j.tifs.2019.11.007

Jia, X.-X., Li, S., Han, D.-P., Chen, R.-p., Yao, Z.-Y., Ning, B.-A., et al. (2021a). Development and perspectives of rapid detection technology in food and environment. *Crit. Rev. Food Sci. Nutr.* 62, 4706–4725. doi:10.1080/10408398.2021.1878101

Jia, X.-X., Yao, Z.-Y., Gao, Z.-X., and Fan, Z.-C. (2021b). The role of suspension array technology in rapid detection of foodborne pollutants: Applications and future challenges. *Crit. Rev. Anal. Chem.*, 1–14. doi:10.1080/10408347.2021.1882833

Jiang, H., Sun, Z., Guo, Q., and Weng, X. (2021). Microfluidic thread-based electrochemical aptasensor for rapid detection of Vibrio parahaemolyticus. *Biosens. Bioelectron. X.* 182, 113191. doi:10.1016/j.bios.2021.113191

Jiang, H., Zeng, X., Xi, Z., Liu, M., Li, C., Li, Z., et al. (2013). Improvement on controllable fabrication of streptavidin-modified three-layer core-shell Fe3O4@SiO2@Au magnetic nanocomposites with low fluorescence background. *J. Biomed. Nanotechnol.* 9, 674–684. doi:10.1166/jbn.2013.1575

Jiang, W., Ren, Y., Han, X., Xue, J., Shan, T., Chen, Z., et al. (2020). Recombinase polymerase amplification-lateral flow (RPA-LF) assay combined with immunomagnetic separation for rapid visual detection of Vibrio parahaemolyticus in raw oysters. *Anal. Bioanal. Chem.* 412, 2903–2914. doi:10.1007/s00216-020-02532-9

Jin, Z. J., Ding, G. T., Li, G. Y., Yang, G. X., Han, Y. H., Hao, N., et al. (2020). Rapid detection of foodborne bacterial pathogens using visual high-throughput microfluidic chip. *J. Chem. Technol. Biotechnol.* 95, 1460–1466. doi:10.1002/jctb.6331

Kaavya, R., Pandiselvam, R., Abdullah, S., Sruthi, N. U., Jayanath, Y., Ashokkumar, C., et al. (2021). Emerging non-thermal technologies for decontamination of Salmonella in food. *Trends Food Sci. Technol.* 112, 400–418. doi:10.1016/j.tifs.2021.04.011

Kaprou, G. D., Bergspica, I., Alexa, E. A., Alvarez-Ordonez, A., and Prieto, M. (2021). *Rapid Methods for Antimicrobial Resistance Diagnostics*, 10, 209. doi:10.3390/antibiotics10020209*Antibiotics-Basel*

Kaya, H. O., Cetin, A. E., Azimzadeh, M., and Topkaya, S. N. (2021). Pathogen detection with electrochemical biosensors: Advantages, challenges and future perspectives. *J. Electroanal. Chem. (Lausanne).* 882, 114989. doi:10.1016/j.jelechem.2021.114989

Khan, H., Khan, A., Liu, Y., Wang, S., Bibi, S., Xu, H., et al. (2019). CRISPR-Cas13a mediated nanosystem for attomolar detection of canine parvovirus type 2. *Chin. Chem. Lett.* 30, 2201–2204. doi:10.1016/j.cclet.2019.10.032

Khan, S., Burciu, B., Filipe, C. D. M., Li, Y., Dellinger, K., Didar, T. F., et al. (2021). DNAzyme-based biosensors: Immobilization strategies, applications, and future prospective. *Acs Nano* 15, 13943–13969. doi:10.1021/acsnano.1c04327

Kim, J.-H., and Oh, S.-W. (2021). Pretreatment methods for nucleic acid-based rapid detection of pathogens in food: A review. *Food control.* 121, 107575. doi:10.1016/j.foodcont.2020.107575

Kim, J. M., Park, J. S., Yoon, T. H., Park, J., and Park, K. S. (2021b). Nucleic acid lateral flow assay for simultaneous detection of hygiene indicator bacteria. *Anal. Bioanal. Chem.* 413, 5003–5011. doi:10.1007/s00216-021-03462-w

Kim, S.-O., and Kim, S.-S. (2021). Bacterial pathogen detection by conventional culture-based and recent alternative (polymerase chain reaction, isothermal amplification, enzyme linked immunosorbent assay, bacteriophage amplification, and gold nanoparticle aggregation) methods in food samples: A review. *J. Food Saf.* 41, e12870. doi:10.1111/jfs.12870

Kim, S. Y., Bang, H. W., and Choi, Y. S. (2021a). Distribution of pathogen resources by the national culture collection for pathogens in South Korea from 2015 to 2019. *Biopreserv. Biobank.* 19 (6), 511–524. doi:10.1089/bio.2020.0147

Kotsiri, Z., Vidic, J., and Vantarakis, A. (2022). Applications of biosensors for bacteria and virus detection in food and water-A systematic review. *J. Environ. Sci.* 111, 367–379. doi:10.1016/j.jes.2021.04.009

Kumar, H., Kuca, K., Bhatia, S. K., Saini, K., Kaushal, A., Verma, R., et al. (2020). Applications of nanotechnology in sensor-based detection of foodborne pathogens. *Sensors* 20, 1966. doi:10.3390/s20071966

Lai, Y., Deng, Y., Yang, G., Li, S., Zhang, C., Liu, X., et al. (2018a). Molecular imprinting polymers electrochemical sensor based on AuNPs/PTh modified GCE for highly sensitive detection of carcinomaembryonic antigen. *J. Biomed. Nanotechnol.* 14, 1688–1694. doi:10.1166/jbn.2018.2617

Lai, Y., Wang, L., Liu, Y., Yang, G., Tang, C., Deng, Y., et al. (2018b). Immunosensors based on nanomaterials for detection of tumor markers. *J. Biomed. Nanotechnol.* 14, 44–65. doi:10.1166/jbn.2018.2505

Lee, H., and Yoon, Y. (2021). Etiological agents implicated in foodborne illness world wide. *Food Sci. Anim. Resour.* 41, 1–7. doi:10.5851/kosfa.2020.e75

Lei, S., Chen, S., and Zhong, Q. (2021). Digital PCR for accurate quantification of pathogens: Principles, applications, challenges and future prospects. *Int. J. Biol. Macromol.* 184, 750–759. doi:10.1016/j.ijbiomac.2021.06.132

Lei, S., Gu, X., Xue, W., Rong, Z., Wang, Z., Chen, S., et al. (2020a). A 4-plex droplet digital PCR method for simultaneous quantification and differentiation of pathogenic and non-pathogenicVibrio parahaemolyticusBased on single intact cells. *Front. Microbiol.* 11, 1727. doi:10.3389/fmicb.2020.01727

Lei, S., Gu, X., Zhong, Q., Duan, L., and Zhou, A. (2020b). Absolute quantification of Vibrio parahaemolyticus by multiplex droplet digital PCR for simultaneous detection of tlh, tdh and ureR based on single intact cell. *Food control.* 114, 107207. doi:10.1016/j.foodcont.2020.107207

Leon Madrazo, A., and Segura Campos, M. R. (2020). Review of antimicrobial peptides as promoters of food safety: Limitations and possibilities within the food industry. *J. Food Saf.* 40 (6), e12854. doi:10.1111/jfs.12854

Leva-Bueno, J., Peyman, S. A., and Millner, P. A. (2020). A review on impedimetric immunosensors for pathogen and biomarker detection. *Med. Microbiol. Immunol.* 209, 343–362. doi:10.1007/s00430-020-00668-0

Lewis, E., Hudson, J. A., Cook, N., Barnes, J. D., and Haynes, E. (2020). Next-generation sequencing as a screening tool for foodborne pathogens in fresh produce. *J. Microbiol. Methods* 171, 105840. doi:10.1016/j.mimet.2020.105840

Li, F., Wang, Z., Huang, Y., Xu, H., He, L., Deng, Y., et al. (2015). Delivery of PUMA apoptosis gene using polyethyleneimine-SMCC-TAT/DNA nanoparticles: Biophysical characterization and *in vitro* transfection into malignant melanoma cells. *J. Biomed. Nanotechnol.* 11, 1776–1782. doi:10.1166/jbn.2015.2151

Li, F., Ye, Q., Chen, M., Xiang, X., Zhang, J., Pang, R., et al. (2021a). Cas12aFDet: A CRISPR/cas12a-based fluorescence platform for sensitive and specific detection of Listeria monocytogenes serotype 4c. *Anal. Chim. Acta X.* 1151, 338248. doi:10.1016/j.aca.2021.338248

Li, F., Ye, Q. H., Chen, M. T., Zhou, B. Q., Zhang, J. M., Pang, R., et al. (2021b). An ultrasensitive CRISPR/Cas12a based electrochemical biosensor for Listeria monocytogenes detection. *Biosens. Bioelectron. X.* 179, 113073. doi:10.1016/j.bios.2021.113073

Li, N., Zhang, W., Lin, J., Xing, G., Li, H., Lin, J.-M., et al. (2022). A specific mass-tag approach for detection of foodborne pathogens using MALDI-TOF mass spectrometry. *Anal. Chem.* 94, 3963–3969. doi:10.1021/acs.analchem.1c05069

Li, S., Liu, H., Deng, Y., Lin, L., and He, N. (2013). Development of a magnetic nanoparticles microarray for simultaneous and simple detection of foodborne pathogens. *J. Biomed. Nanotechnol.* 9, 1254–1260. doi:10.1166/jbn.2013.1610

Li, T., Yi, H., Liu, Y., Wang, Z., Liu, S., He, N., et al. (2018). One-step synthesis of DNA templated water-soluble Au-Ag bimetallic nanoclusters for ratiometric fluorescence detection of DNA. *J. Biomed. Nanotechnol.* 14, 150–160. doi:10.1166/jbn.2018.2491

Li, Y., Huang, T.-Y., Ye, C., Chen, L., Liang, Y., Wang, K., et al. (2020). Formation and control of the viable but non-culturable state of foodborne pathogen *Escherichia coli* O157:H7. *Front. Microbiol.* 11, 1202. doi:10.3389/fmicb.2020.01202

Li, Z., Wang, J., Yang, H., Chen, S., Ma, G., Zhang, X., et al. (2017). Ultrasensitive detection of gastric cancer plasma MicroRNAs via magnetic beads-based chemiluminescent assay. *J. Biomed. Nanotechnol.* 13, 1272–1280. doi:10.1166/jbn.2017.2426

Lin, L., Zheng, Q., Lin, J., Yuk, H.-G., and Guo, L. (2020). Immuno- and nucleic acid-based current technique for Salmonella detection in food. *Eur. Food Res. Technol.* 246, 373–395. doi:10.1007/s00217-019-03423-9

Ling, Y. Z., Zhu, Y. F., Fan, H. H., Zha, H. L., Yang, M., Wu, L., et al. (2019). Rapid method for detection of *Staphylococcus aureus* in feces. *J. Biomed. Nanotechnol.* 15, 1290–1298. doi:10.1166/jbn.2019.2781

Liu, F., Zhang, C., Wang, Y., and Chen, G. (2022). A review of the current and emerging detection methods of marine harmful microalgae. *Sci. Total Environ.* 815, 152913. doi:10.1016/j.scitotenv.2022.152913

Liu, H., Dong, H., Chen, Z., Lin, L., Chen, H., Li, S., et al. (2017b). Magnetic nanoparticles enhanced microarray detection of multiple foodborne pathogens. *J. Biomed. Nanotechnol.* 13, 1333–1343. doi:10.1166/jbn.2017.2418

Liu, J., Dong, S., He, Q., Yang, S., Xie, M., Deng, P., et al. (2019a). Facile preparation of Fe3O4/C nanocomposite and its application for cost-effective and sensitive detection of tryptophan. *Biomolecules* 9 (6), 245. doi:10.3390/biom9060245

Liu, J., Parrish, J. R., Hines, J., Mansfield, L., and Finley, R. L., Jr. (2019c). A proteome-wide screen of Campylobacter jejuni using protein microarrays identifies novel and conformational antigens. *PLoS One* 14, e0210351. doi:10.1371/journal.pone.0210351

Liu, M., Yu, X., Chen, Z., Yang, T., Yang, D., Liu, Q., et al. (2017a). Aptamer selection and applications for breast cancer diagnostics and therapy. *J. Nanobiotechnology* 15, 81. doi:10.1186/s12951-017-0311-4

Liu, S., He, X., Zhang, T., Zhao, K., Xiao, C., Tong, Z., et al. (2022). Highly sensitive smartphone-based detection of Listeria monocytogenes using SYTO9. *Chin. Chem. Lett.* 33 (4), 1933–1935. doi:10.1016/j.cclet.2021.11.051

Liu, Y., Deng, Y., Li, T., Chen, Z., Chen, H., Li, S., et al. (2018). Aptamer-based electrochemical biosensor for mercury ions detection using AuNPs-modified glass carbon electrode. *J. Biomed. Nanotechnol.* 14, 2156–2161. doi:10.1166/jbn.2018.2655

Liu, Y., Lai, Y., Yang, G., Tang, C., Deng, Y., Li, S., et al. (2017c). Cd-aptamer electrochemical biosensor based on AuNPs/CS modified glass carbon electrode. *J. Biomed. Nanotechnol.* 13, 1253–1259. doi:10.1166/jbn.2017.2424

Liu, Y., Li, T., Ling, C., Chen, Z., Deng, Y., He, N., et al. (2019b). Electrochemical sensor for Cd^{2+} and Pb^{2+} detection based on nano-porous pseudo carbon paste electrode. *Chin. Chem. Lett.* 30, 2211–2215. doi:10.1016/j.cclet.2019.05.020

Liu, Y., Li, T., Ling, C., Wang, Z., Jin, L., Zhao, Y., et al. (2019d). A simple visual method for DNA detection based on the formation of gold nanoparticles. *Chin. Chem. Lett.* 30, 2359–2362. doi:10.1016/j.cclet.2019.10.033

Lopes-Luz, L., Mendonca, M., Fogaca, M. B., Kipnis, A., Bhunia, A. K., Buhrer-Sekula, S., et al. (2021). Listeria monocytogenes: Review of pathogenesis and virulence determinants-targeted immunological assays. *Crit. Rev. Microbiol.* 47, 647–666. doi:10.1080/1040841x.2021.1911930

Lu, I. N., Muller, C. P., and He, F. Q. (2020). Applying next-generation sequencing to unravel the mutational landscape in viral quasispecies. *Virus Res.* 283, 197963. doi:10.1016/j.virusres.2020.197963

Luan, Y., Wang, N., Li, C., Guo, X., and Lu, A. (2020). Advances in the application of aptamer biosensors to the detection of aminoglycoside antibiotics. *Antibiot. (Basel).* 9, 787. doi:10.3390/antibiotics9110787

Luo, F., Li, Z., Dai, G., Lu, Y., He, P., Wang, Q., et al. (2020b). Simultaneous detection of different bacteria by microchip electrophoresis combined with universal primer-duplex polymerase chain reaction. *J. Chromatogr. A* 1615, 460734. doi:10.1016/j.chroma.2019.460734

Luo, K., Kim, H.-Y., Oh, M.-H., and Kim, Y.-R. (2020a). Paper-based lateral flow strip assay for the detection of foodborne pathogens: Principles, applications, technological challenges and opportunities. *Crit. Rev. Food Sci. Nutr.* 60, 157–170. doi:10.1080/10408398.2018.1516623

Lv, X., Wang, L., Zhang, J., He, X., Shi, L., Zhao, L., et al. (2021). Quantitative detection of trace VBNC Cronobacter sakazakii by immunomagnetic separation in combination with PMAxx-ddPCR in dairy products. *Food Microbiol.* 99, 103831. doi:10.1016/j.fm.2021.103831

Ma, B., Li, J., Chen, K., Yu, X., Sun, C., Zhang, M., et al. (2020a). Multiplex recombinase polymerase amplification assay for the simultaneous detection of three foodborne pathogens in seafood. *Foods* 9, 278. doi:10.3390/foods9030278

Ma, C., Li, C., He, N., Wang, F., Ma, N., Zhang, L., et al. (2012). Preparation and characterization of monodisperse core-shell Fe3O4 @ SiO2 microspheres and its application for magnetic separation of nucleic acids from *E. coli* BL21. *J. Biomed. Nanotechnol.* 8, 1000–1005. doi:10.1166/jbn.2012.1454

Ma, T., Huang, H., Guo, W., Zhang, C., Chen, Z., Li, S., et al. (2020b). Recent progress in Black phosphorus sensors. *J. Biomed. Nanotechnol.* 16, 1045–1064. doi:10.1166/jbn.2020.2963

Magesa, F., Wu, Y., Dong, S., Tian, Y., Li, G., Vianney, J. M., et al. (2020). Electrochemical sensing fabricated with Ta2O5 nanoparticle-electrochemically reduced graphene oxide nanocomposite for the detection of oxytetracycline. *Biomolecules* 10, 110. doi:10.3390/biom10010110

Maguire, M., Kase, J. A., Roberson, D., Muruvanda, T., Brown, E. W., Allard, M., et al. (2021). Precision long-read metagenomics sequencing for food safety by detection and assembly of Shiga toxin-producing *Escherichia coli* in irrigation water. *PLoS One* 16, e0245172. doi:10.1371/journal.pone.0245172

Mangmee, S., Reamtong, O., Kalambaheti, T., Roytrakul, S., and Sonthayanon, P. (2020). MALDI-TOF mass spectrometry typing for predominant serovars of non-typhoidal Salmonella in a Thai broiler industry. *Food control.* 113, 107188. doi:10.1016/j.foodcont.2020.107188

McCuskey, S. R., Chatsirisupachai, J., Zeglio, E., Parlak, O., Panoy, P., Herland, A., et al. (2022). Current progress of interfacing organic semiconducting materials with bacteria. *Chem. Rev.* 122, 4791–4825. doi:10.1021/acs.chemrev.1c00487

Mei, Y., He, C., Zeng, W., Luo, Y., Liu, C., Yang, M., et al. (2022). Electrochemical biosensors for foodborne pathogens detection based on carbon nanomaterials: Recent advances and challenges. *Food bioproc. Tech.* 15, 498–513. doi:10.1007/s11947-022-02759-7

Mi, F., Guan, M., Hu, C., Peng, F., Sun, S., Wang, X., et al. (2021). Application of lectin-based biosensor technology in the detection of foodborne pathogenic bacteria: A review. *Analyst* 146, 429–443. doi:10.1039/d0an01459a

Mishra, A., Tyagi, M., Pilloton, R., Jain, S., and Narang, J. (2020). Evolving techniques for the detection of Listeria monocytogenes: Underlining the electrochemical approach. *Int. J. Environ. Anal. Chem.* 100, 507–523. doi:10.1080/03067319.2019.1674502

Mobed, A., Hasanzadeh, M., Ahmadalipour, A., and Fakhari, A. (2020). Recent advances in the biosensing of neurotransmitters: Material and method overviews towards the biomedical analysis of psychiatric disorders. *Anal. Methods* 12, 557–575. doi:10.1039/c9ay02390a

Morales-Pablos, M. I., Mejia-Sanchez, P., Diaz-Aparicio, E., Palomares-Resendiz, E. G., Gutierrez-Hernandez, J. L., Reyna-Granados, J. R., et al. (2020). Risk factors associated with the seroprevalence of paratuberculosis in sheep flocks in the hot-arid region of Sonora, Mexico. *Trop. Anim. Health Prod.* 52, 1357–1363. doi:10.1007/s11250-019-02139-y

Mou, X., Chen, Z., Li, T., Liu, M., Liu, Y., Ali, Z., et al. (2019a). A highly sensitive strategy for low-abundance hepatitis B virus detection via one-step nested polymerase chain reaction, chemiluminescence technology and magnetic separation. *J. Biomed. Nanotechnol.* 15, 1832–1838. doi:10.1166/jbn.2019.2802

Mou, X., Sheng, D., Chen, Z., Liu, M., Liu, Y., Deng, Y., et al. (2019b). *In-situ* mutation detection by magnetic beads-probe based on single base extension and its

application in genotyping of hepatitis B virus pre-C region 1896nt locus single nucleotide polymorphisms. *J. Biomed. Nanotechnol.* 15, 2393–2400. doi:10.1166/jbn.2019.2862

Mu, D., Zhou, D., Xie, G., Liu, J., Xiong, Q., Feng, X., et al. (2021). The fluorescent probe-based recombinase-aided amplification for rapid detection of *Escherichia coli* O157:H7. *Mol. Cell. Probes* 60, 101777. doi:10.1016/j.mcp.2021.101777

Muriuki, S. W., Rengan, M. S., and Budambula, N. L. M. (2021). Prokaryotic diversity and potentially pathogenic bacteria in vended foods and environmental samples. *Ann. Microbiol.* 71, 27. doi:10.1186/s13213-021-01640-w

Myintzaw, P., Jaiswal, A. K., and Jaiswal, S. (2021). A review on campylobacteriosis associated with poultry meat consumption. *Food Rev. Int.*, 1–15. doi:10.1080/87559129.2021.1942487

Nadar, S. S., Kelkar, R. K., Pise, P. V., Patil, N. P., Patil, S. P., Chaubal-Durve, N. S., et al. (2021). The untapped potential of magnetic nanoparticles for forensic investigations: A comprehensive review. *Talanta* 230, 122297. doi:10.1016/j.talanta.2021.122297

Naresh, V., and Lee, N. (2021). A review on biosensors and recent development of nanostructured materials-enabled biosensors. *Sensors* 21, 1109. doi:10.3390/s21041109

Nassarawa, S. S., Luo, Z., and Lu, Y. (2022). Conventional and emerging techniques for detection of foodborne pathogens in horticulture crops: A leap to food safety. *Food bioproc. Tech.* 21, 1248–1267. doi:10.1007/s11947-021-02730-y

Nath, P., Kabir, A., Khoubafarin Doust, S., Kreais, Z. J., and Ray, A. (2020). Detection of bacterial and viral pathogens using photonic point-of-care devices. *Diagnostics* 10 (10), 841. doi:10.3390/diagnostics10100841

Navarro, A., Barcena, C., Pozo, P., Diez-Guerrier, A., Martinez, I., Polo, C., et al. (2020). Liver transudate, a potential alternative to detect anti-hepatitis E virus antibodies in pigs and wild boars (*Sus scrofa*). *Microorganisms* 8 (3), 450. doi:10.3390/microorganisms8030450

Nguyen, H. V., Nguyen, V. D., Liu, F., and Seo, T. S. (2020). An integrated smartphone-based genetic analyzer for qualitative and quantitative pathogen detection. *Acs Omega* 5, 22208–22214. doi:10.1021/acsomega.0c02317

Nguyen, Q. H., and Kim, M. I. (2020). Nanomaterial-mediated paper-based biosensors for colorimetric pathogen detection. *TrAC Trends Anal. Chem.* 132, 116038. doi:10.1016/j.trac.2020.116038

Nie, L., Liu, F., Ma, P., and Xiao, X. (2014). Applications of gold nanoparticles in optical biosensors. *J. Biomed. Nanotechnol.* 10, 2700–2721. doi:10.1166/jbn.2014.1987

Nunez-Bajo, E., Collins, A. S. P., Kasimatis, M., Cotur, Y., Asfour, T., Tanriverdi, U., et al. (2020). Disposable silicon-based all-in-one micro-qPCR for rapid on-site detection of pathogens. *Nat. Commun.* 11, 6176. doi:10.1038/s41467-020-19911-6

Obande, G. A., and Singh, K. K. B. (2020). Current and future perspectives on isothermal nucleic acid amplification technologies for diagnosing infections. *Infect. Drug Resist.* 13, 455–483. doi:10.2147/idr.S217571

Oliveira, D. A., Althawab, S., McLamore, E. S., and Gomes, C. L. (2021). One-step fabrication of stimuli-responsive chitosan-platinum brushes for Listeria monocytogenes detection. *Biosens. (Basel).* 11, 511. doi:10.3390/bios11120511

Oyejobi, G. K., Sule, W. F., Akinde, S. B., Khan, F. M., and Ogolla, F. (2022). Multidrug-resistant enteric bacteria in Nigeria and potential use of bacteriophages as biocontrol. *Sci. Total Environ.* 824, 153842. doi:10.1016/j.scitotenv.2022.153842

Padzil, F., Mariatulqabtiah, A. R., Tan, W. S., Ho, K. L., Isa, N. M., Lau, H. Y., et al. (2022). Loop-mediated isothermal amplification (LAMP) as a promising point-of-care diagnostic strategy in avian virus research. *Anim. (Basel).* 12, 76. doi:10.3390/ani12010076

Pang, Y., Guo, X., Tian, X., Liu, F. X., Wang, L., Wu, J. L., et al. (2019). Developing a novel molecular serotyping system based on capsular polysaccharide synthesis gene clusters of Vibrio parahaemolyticus. *Int. J. Food Microbiol.* 309, 108332. doi:10.1016/j.ijfoodmicro.2019.108332

Park, J. Y., Lim, M. C., Park, K., Ok, G., Chang, H. J., Lee, N. A., et al. (2020). Detection of *E. coli* O157:H7 in food using automated immunomagnetic separation combined with real-time PCR. *Processes* 8 (8), 908. doi:10.3390/pr8080908

Patel, A., Jenkins, M., Rhoden, K., and Barnes, A. N. (2022). A systematic review of zoonotic enteric parasites carried by flies, cockroaches, and dung beetles. *Pathogens* 11 (1), 90. doi:10.3390/pathogens11010090

Peng, L.-H., Zhou, L.-Q., Chen, X., and Piao, X. (2020b). A computational study of potential miRNA-disease association inference based on ensemble learning and kernel ridge regression. *Front. Bioeng. Biotechnol.* 8, 40. doi:10.3389/fbioe.2020.00040

Peng, L., Tian, X., Tian, G., Xu, J., Huang, X., Weng, Y., et al. (2020a). Single-cell RNA-seq clustering: Datasets, models, and algorithms. *RNA Biol.* 17, 765–783. doi:10.1080/15476286.2020.1728961

Pires, N. M. M., Dong, T., Yang, Z., and da Silva, L. F. B. A. (2021). Recent methods and biosensors for foodborne pathogen detection in fish: Progress and future prospects to sustainable aquaculture systems. *Crit. Rev. Food Sci. Nutr.* 61, 1852–1876. doi:10.1080/10408398.2020.1767032

Pissuwan, D., Gazzana, C., Mongkolsuk, S., and Cortie, M. B. (2020). Single and multiple detections of foodborne pathogens by gold nanoparticle assays. *Wiley Interdiscip. Rev. Nanomed. Nanobiotechnol.* 12 (1), e1584. doi:10.1002/wnan.1584

Plante, D., Barrera, J. A. B., Lord, M., Iugovaz, I., and Nasheri, N. (2021). Development of an RNA extraction protocol for norovirus from raw oysters and detection by qRT-PCR and droplet-digital RT-PCR. *Foods* 10, 1804. doi:10.3390/foods10081804

Pos, Z., Pos, O., Styk, J., Mocova, A., Strieskova, L., Budis, J., et al. (2020). Technical and methodological aspects of cell-free nucleic acids analyzes. *Int. J. Mol. Sci.* 21, 8634. doi:10.3390/ijms21228634

Prasannakumar, M. K., Parivallal, P. B., Manjunatha, C., Mahesh, H. B., Pramesh, D., Narayan, K. S., et al. (2020). Correction to: Loop-mediated isothermal amplification assay for pre-symptomatic stage detection of Xanthomonas axonopodis pv. punicae infection in pomegranate. *Australas. Plant Pathol.* 49, 475–476. doi:10.1007/s13313-020-00724-6

Prata, J. C., da Costa, J. P., Lopes, I., Andrady, A. L., Duarte, A. C., Rocha-Santos, T., et al. (2021). A One Health perspective of the impacts of microplastics on animal, human and environmental health. *Sci. Total Environ.* 777, 146094. doi:10.1016/j.scitotenv.2021.146094

Qi, W., Wang, L., Rong, N., Huo, X., Li, Y., Liao, M., et al. (2022). A lab-on-a-tube biosensor for automatic detection of foodborne bacteria using rotated Halbach magnetic separation and Raspberry Pi imaging. *Talanta* 239, 123095. doi:10.1016/j.talanta.2021.123095

Qian, S., Chen, Y., Xu, X., Peng, C., Wang, X., Wu, H., et al. (2022). Advances in amplification-free detection of nucleic acid: CRISPR/Cas system as a powerful tool. *Anal. Biochem.* 643, 114593. doi:10.1016/j.ab.2022.114593

Qiu, H., Zhang, Y., Li, Z., Jiang, P., Guo, S., He, Y., et al. (2021). Donepezil ameliorates pulmonary arterial hypertension by inhibiting M2-macrophage activation. *Front. Cardiovasc. Med.* 8, 639541. doi:10.3389/fcvm.2021.639541

Quijada, N. M., Hernandez, M., and Rodriguez-Lazaro, D. (2020). High-throughput sequencing and food microbiology. *Adv. Food Nutr. Res.* 91, 275–300. doi:10.1016/bs.afnr.2019.10.003

Quintela, I. A., de los Reyes, B. G., Lin, C. S., and Wu, V. C. H. (2019). Simultaneous colorimetric detection of a variety of Salmonella spp. in food and environmental samples by optical biosensing using oligonucleotide-gold nanoparticles. *Front. Microbiol.* 10, 1138. doi:10.3389/fmicb.2019.01138

Ragab, M. A. A., and El-Kimary, E. I. (2021). Recent advances and applications of microfluidic capillary electrophoresis: A comprehensive review (2017-mid 2019). *Crit. Rev. Anal. Chem.* 51, 709–741. doi:10.1080/10408347.2020.1765729

Rajkovic, A., Jovanovic, J., Monteiro, S., Decleer, M., Andjelkovic, M., Foubert, A., et al. (2020). Detection of toxins involved in foodborne diseases caused by Gram-positive bacteria. *Compr. Rev. Food Sci. Food Saf.* 19, 1605–1657. doi:10.1111/1541-4337.12571

Rani, A., Ravindran, V. B., Surapaneni, A., Mantri, N., and Ball, A. S. (2021). Review: Trends in point-of-care diagnosis for *Escherichia coli* O157:H7 in food and water. *Int. J. Food Microbiol.* 349, 109233. doi:10.1016/j.ijfoodmicro.2021.109233

Razmi, N., Hasanzadeh, M., Willander, M., and Nur, O. (2020). Recent progress on the electrochemical biosensing of *Escherichia coli* O157:H7: Material and methods overview. *Biosens. (Basel).* 10, 54. doi:10.3390/bios10050054

Reuter, J. A., Spacek, D. V., and Snyder, M. P. (2015). High-throughput sequencing technologies. *Mol. Cell* 58, 586–597. doi:10.1016/j.molcel.2015.05.004

Ripolles-Avila, C., Martinez-Garcia, M., Capellas, M., Yuste, J., Fung, D. Y. C., Rodriguez-Jerez, J.-J., et al. (2020). From hazard analysis to risk control using rapid methods in microbiology: A practical approach for the food industry. *Compr. Rev. Food Sci. Food Saf.* 19, 1877–1907. doi:10.1111/1541-4337.12592

Safenkova, I. V., Ivanov, A. V., Slutskaya, E. S., Samokhvalov, A. V., Zherdev, A. V., Dzantiev, B. B., et al. (2020). Key significance of DNA-target size in lateral flow assay coupled with recombinase polymerase amplification. *Anal. Chim. Acta X.* 1102, 109–118. doi:10.1016/j.aca.2019.12.048

Salipante, S. J., and Jerome, K. R. (2020). Digital PCR-an emerging technology with broad applications in microbiology. *Clin. Chem.* 66, 117–123. doi:10.1373/clinchem.2019.304048

Saravanan, A., Kumar, P. S., Hemavathy, R. V., Jeevanantham, S., Kamalesh, R., Sneha, S., et al. (2021). Methods of detection of food-borne pathogens: A review. *Environ. Chem. Lett.* 19, 189–207. doi:10.1007/s10311-020-01072-z

Sarengaowa, H. W., Feng, K., Jiang, A., Xiu, Z., Lao, Y., Li, Y., et al. (2020). An *in situ*-synthesized gene chip for the detection of food-borne pathogens on fresh-cut cantaloupe and lettuce. *Front. Microbiol.* 10, 3089. doi:10.3389/fmicb.2019.03089

Scallan Walter, E. J., McLean, H. Q., and Griffin, P. M. (2020). Hospital discharge data underascertain enteric bacterial infections among children. *Foodborne Pathog. Dis.* 17, 530–532. doi:10.1089/fpd.2019.2773

Segeritz, L., Anders, O., Middelhoff, T. L., Winterfeld, D. T., Maksimov, P., Schares, G., et al. (2021). New insights into gastrointestinal and pulmonary parasitofauna of wild eurasian lynx (Lynx lynx) in the harz mountains of Germany. *Pathogens* 10 (12), 1650. doi:10.3390/pathogens10121650

Segerman, B. (2020). The most frequently used sequencing technologies and assembly methods in different time segments of the bacterial surveillance and RefSeq genome databases. *Front. Cell. Infect. Microbiol.* 10, 527102. doi:10.3389/fcimb.2020.527102

Sharma, P. C., Sharma, D., Sharma, A., Bhagat, M., Ola, M., Thakur, V. K., et al. (2021). Recent advances in microbial toxin-related strategies to combat cancer. *Semin. Cancer Biol.* doi:10.1016/j.semcancer.2021.07.007

Sheka, D., Alabi, N., and Gordon, P. M. K. (2021). Oxford nanopore sequencing in clinical microbiology and infection diagnostics. *Brief. Bioinform.* 22, bbaa403. doi:10.1093/bib/bbaa403

Shen, C., Islam, M. T., Masuda, Y., Honjoh, K.-i., and Miyamoto, T. (2020). Transcriptional changes involved in inhibition of biofilm formation by epsilon-polylysine in Salmonella Typhimurium. *Appl. Microbiol. Biotechnol.* 104, 5427–5436. doi:10.1007/s00253-020-10575-2

Shen, Y. F., Xu, L. Z., and Li, Y. B. (2021c). Biosensors for rapid detection of Salmonella in food: A review. *Compr. Rev. Food Sci. Food Saf.* 20, 149–197. doi:10.1111/1541-4337.12662

Shen, Y., Nie, J., Kuang, L., Zhang, J., and Li, H. (2021b). DNA sequencing, genomes and genetic markers of microbes on fruits and vegetables. *Microb. Biotechnol.* 14, 323–362. doi:10.1111/1751-7915.13560

Shen, Y., Zhang, Y., Gao, Z. F., Ye, Y., Wu, Q., Chen, H.-Y., et al. (2021a). Recent advances in nanotechnology for simultaneous detection of multiple pathogenic bacteria. *Nano Today* 38, 101121. doi:10.1016/j.nantod.2021.101121

Shi, Y. X., Wang, Y., Tian, Y. F., Liu, W. S., Zhu, W. H., Sun, C. B., et al. (2019). Establishment of a method for the simultaneous detection of four foodborne pathogens using high-throughput suspension array xTAG technology. *Int. J. Food Sci. Technol.* 54, 2578–2585. doi:10.1111/ijfs.14169

Shiba, K. (2006). Functionalization of carbon nanomaterials by evolutionary molecular engineering: Potential application in drug delivery systems. *J. Drug Target.* 14, 512–518. doi:10.1080/10611860600845033

Singha, S., Thomas, R., Viswakarma, J. N., and Gupta, V. K. (2022). Foodborne illnesses of *Escherichia coli* O157origin and its control measures. *J. Food Sci. Technol.* doi:10.1007/s13197-022-05381-9

Sohrabi, H., Majidi, M. R., Khaki, P., Jahanban-Esfahlan, A., de la Guardia, M., Mokhtarzadeh, A., et al. (2022). State of the art: Lateral flow assays toward the point-of-care foodborne pathogenic bacteria detection in food samples. *Compr. Rev. Food Sci. Food Saf.* 21, 1868–1912. doi:10.1111/1541-4337.12913

Song, B., Wang, J. S., Yan, Z. J., Liu, Z. J., Pan, X. X., Zhang, Y. B., et al. (2020). Microfluidics for the rapid detection of *Staphylococcus aureus* using antibody-coated microspheres. *Bioengineered* 11, 1137–1145. doi:10.1080/21655979.2020.1831362

Sourri, P., Tassou, C. C., Nychas, G.-J. E., and Panagou, E. Z. (2022). Fruit juice spoilage by alicyclobacillus: Detection and control methods-A comprehensive review. *Foods* 11 (5), 747. doi:10.3390/foods11050747

Srivastava, S., Singh, L., Kaushik, V., Rajput, S., Jain, S., Pal, M. K., et al. (2021). Electrically controlled nanophotonic slot structure based on photocatalytic nanocomposite for optical detection of foodborne pathogens. *J. Light. Technol.* 39, 6670–6677. doi:10.1109/jlt.2021.3104409

Stryinski, R., Lopienska-Biernat, E., and Carrera, M. (2020). Proteomic insights into the biology of the most important foodborne parasites in europe. *Foods* 9 (10), 1403. doi:10.3390/foods9101403

Su, W., Liang, D., and Tan, M. (2021). Microfluidic strategies for sample separation and rapid detection of food allergens. *Trends Food Sci. Technol.* 110, 213–225. doi:10.1016/j.tifs.2021.02.004

Subjakova, V., Oravczova, V., Tatarko, M., and Hianik, T. (2021). Advances in electrochemical aptasensors and immunosensors for detection of bacterial pathogens in food. *Electrochim. Acta* 389, 138724. doi:10.1016/j.electacta.2021.138724

Sun, F., Zhang, J., Yang, Q., and Wu, W. (2021a). Quantum dot biosensor combined with antibody and aptamer for tracing food-borne pathogens. *Food Qual. Saf.* 5, fyab019. doi:10.1093/fqsafe/fyab019

Sun, L., Zhang, H., Chen, J., Chen, L., Qi, X., Zhang, R., et al. (2021b). Epidemiology of foodborne disease outbreaks caused by nontyphoidal Salmonella in zhejiang Province, China, 2010-2019. *Foodborne Pathog. Dis.* 18 (12), 880–886. doi:10.1089/fpd.2021.0006

Syromyatnikov, M. Y., Kokina, A. V., Solodskikh, S. A., Panevina, A. V., Popov, E. S., Popov, V. N., et al. (2020). High-throughput 16S rRNA gene sequencing of butter microbiota reveals a variety of opportunistic pathogens. *Foods* 9, 608. doi:10.3390/foods9050608

Taguchi, T., Ishikawa, M., Ichikawa, M., Tadenuma, T., Hirakawa, Y., Yoshino, T., et al. (2021). Amplification-free detection of bacterial genes using a signaling probe-based DNA microarray. *Biosens. Bioelectron. X.* 194, 113659. doi:10.1016/j.bios.2021.113659

Tahir, U., Shim, Y. B., Kamran, M. A., Kim, D.-I., and Jeong, M. Y. (2021). Nanofabrication techniques: Challenges and future prospects. *J. Nanosci. Nanotechnol.* 21, 4981–5013. doi:10.1166/jnn.2021.19327

Tang, C., He, Z., Liu, H., Xu, Y., Huang, H., Yang, G., et al. (2020). Application of magnetic nanoparticles in nucleic acid detection. *J. Nanobiotechnology* 18, 62. doi:10.1186/s12951-020-00613-6

Tang, Y., Ali, Z., Dai, J., Liu, X., Wu, Y., Chen, Z., et al. (2018). Single-nucleotide polymorphism genotyping of exoS in *Pseudomonas aeruginosa* using dual-color fluorescence hybridization and magnetic separation. *J. Biomed. Nanotechnol.* 14, 206–214. doi:10.1166/jbn.2018.2525

Teffo, L. A., and Tabit, F. T. (2020). An assessment of the food safety knowledge and attitudes of food handlers in hospitals. *BMC Public Health* 20 (1), 311. doi:10.1186/s12889-020-8430-5

Teklemariam, A. D., Samaddar, M., Alharbi, M. G., Al-Hindi, R. R., and Bhunia, A. K. (2020). Biosensor and molecular-based methods for the detection of human coronaviruses: A review. *Mol. Cell. Probes* 54, 101662. doi:10.1016/j.mcp.2020.101662

Tian, Y., Deng, P., Wu, Y., Ding, Z., Li, G., Liu, J., et al. (2019). A simple and efficient molecularly imprinted electrochemical sensor for the selective determination of tryptophan. *Biomolecules* 9, 294. doi:10.3390/biom9070294

Tian, Y., Liu, T., Liu, C., Xu, Q., and Liu, Q. (2022). Pathogen detection strategy based on CRISPR. *Microchem. J.* 174, 107036. doi:10.1016/j.microc.2021.107036

Tseng, C.-C., Kung, C.-T., Chen, R.-F., Tsai, M.-H., Chao, H.-R., Wang, Y.-N., et al. (2021). Recent advances in microfluidic paper-based assay devices for diagnosis of human diseases using saliva, tears and sweat samples. *Sensors Actuators B Chem.* 342, 130078. doi:10.1016/j.snb.2021.130078

Tsougeni, K., Kaprou, G., Loukas, C. M., Papadakis, G., Hamiot, A., Eck, M., et al. (2020). Lab-on-Chip platform and protocol for rapid foodborne pathogen detection comprising on-chip cell capture, lysis, DNA amplification and surface-acoustic-wave detection. *Sensors Actuators B Chem.* 320, 128345. doi:10.1016/j.snb.2020.128345

Uelze, L., Gruetzke, J., Borowiak, M., Hammerl, J. A., Juraschek, K., Deneke, C., et al. (2020). Typing methods based on whole genome sequencing data. *One Health Outlook* 2, 3. doi:10.1186/s42522-020-0010-1

Upasham, S., Banga, I. K., Jagannath, B., Paul, A., Lin, K.-C., Muthukumar, S., et al. (2021). Electrochemical impedimetric biosensors, featuring the use of Room Temperature Ionic Liquids (RTILs): Special focus on non-faradaic sensing. *Biosens. Bioelectron. X.* 177, 112940. doi:10.1016/j.bios.2020.112940

Van Poelvoorde, L. A., Saelens, X., Thomas, I., and Roosens, N. H. (2020). Next-generation sequencing: An eye-opener for the surveillance of antiviral resistance in influenza. *Trends Biotechnol.* 38, 360–367. doi:10.1016/j.tibtech.2019.09.009

Van Puyvelde, L., Aissa, A., Panda, S. K., De Borggraeve, W. M., Mukazayire, M. J., Luyten, W., et al. (2021). Bioassay-guided isolation of antibacterial compounds from the leaves of Tetradenia riparia with potential bactericidal effects on food-borne pathogens. *J. Ethnopharmacol.* 273, 113956. doi:10.1016/j.jep.2021.113956

Van Reckem, E., De Vuyst, L., Weckx, S., and Leroy, F. (2021). Next-generation sequencing to enhance the taxonomic resolution of the microbiological analysis of meat and meat-derived products. *Curr. Opin. Food Sci.* 37, 58–65. doi:10.1016/j.cofs.2020.09.004

Vidic, J., and Manzano, M. (2021). Electrochemical biosensors for rapid pathogen detection. *Curr. Opin. Electrochem.* 29, 100750. doi:10.1016/j.coelec.2021.100750

Vidyadharani, G., Vijaya Bhavadharani, H. K., Sathishnath, P., Ramanathan, S., Sariga, P., Sandhya, A., et al. (2021). Present and pioneer methods of early detection of food borne pathogens. *J. Food Sci. Technol.* 59, 2087–2107. doi:10.1007/s13197-021-05130-4

Visciano, P., and Schirone, M. (2021). Food frauds: Global incidents and misleading situations. *Trends Food Sci. Technol.* 114, 424–442. doi:10.1016/j.tifs.2021.06.010

Wachiralurpan, S., Chansiri, K., and Lieberzeit, P. A. (2020). Direct detection of Listeria monocytogenes DNA amplification products with quartz crystal microbalances at elevated temperatures. *Sensors Actuators B Chem.* 308, 127678. doi:10.1016/j.snb.2020.127678

Wagner, E., Fagerlund, A., Langsrud, S., Moretro, T., Jensen, M. R., Moen, B., et al. (2021). Surveillance of Listeria monocytogenes: Early detection, population

dynamics, and quasimetagenomic sequencing during selective enrichment. *Appl. Environ. Microbiol.* 87, e0177421. doi:10.1128/aem.01774-21

Walter, E. J. S., Griffin, P. M., Bruce, B. B., and Hoekstra, R. M. (2021). Estimating the number of illnesses caused by agents transmitted commonly through food: A scoping review. *Foodborne Pathog. Dis.* 18, 841–858. doi:10.1089/fpd.2021.0038

Wan, J., Zheng, L., Kong, L., Lu, Z., Tao, Y., Feng, Z., et al. (2021). Development of a rapid detection method for real-time fluorescent quantitative PCR of Salmonella spp. and Salmonella Enteritidis in ready-to-eat fruits and vegetables. *LWT* 149, 111837. doi:10.1016/j.lwt.2021.111837

Wang, B., and Park, B. (2020). Immunoassay biosensing of foodborne pathogens with surface plasmon resonance imaging: A review. *J. Agric. Food Chem.* 68, 12927–12939. doi:10.1021/acs.jafc.0c02295

Wang, D., Lian, F., Yao, S., Liu, Y., Wang, J., Song, X., et al. (2020e). Simultaneous detection of three foodborne pathogens based on immunomagnetic nanoparticles and fluorescent quantum dots. *Acs Omega* 5, 23070–23080. doi:10.1021/acsomega.0c02833

Wang, J., Tan, L., Bi, W., Shen, H., Li, D., Yu, Z., et al. (2022). Ultrasensitive microfluidic immunosensor with stir bar enrichment for point-of-care test of *Staphylococcus aureus* in foods triggered by DNAzyme-assisted click reaction. *Food Chem. x.* 378, 132093. doi:10.1016/j.foodchem.2022.132093

Wang, K., Wang, Z., Zeng, H., Luo, X., and Yang, T. (2020a). Advances in portable visual detection of pathogenic bacteria. *ACS Appl. Bio Mat.* 3, 7291–7305. doi:10.1021/acsabm.0c00984

Wang, L.-X., Fu, J.-J., Zhou, Y., Chen, G., Fang, C., Lu, Z. S., et al. (2020f). On-chip RT-LAMP and colorimetric detection of the prostate cancer 3 biomarker with an integrated thermal and imaging box. *Talanta* 208, 120407. doi:10.1016/j.talanta.2019.120407

Wang, L., Huo, X., Qi, W., Xia, Z., Li, Y., Lin, J., et al. (2020g). Rapid and sensitive detection of Salmonella Typhimurium using nickel nanowire bridge for electrochemical impedance amplification. *Talanta* 211, 120715. doi:10.1016/j.talanta.2020.120715

Wang, L., and Lin, J. (2020). Recent advances on magnetic nanobead based biosensors: From separation to detection. *TrAC Trends Anal. Chem.* 128, 115915. doi:10.1016/j.trac.2020.115915

Wang, L., Xue, L., Guo, R., Zheng, L., Wang, S., Yao, L., et al. (2020d). Combining impedance biosensor with immunomagnetic separation for rapid screening of Salmonella in poultry supply chains. *Poult. Sci.* 99, 1606–1614. doi:10.1016/j.psj.2019.12.007

Wang, M., Zhang, Y., Tian, F., Liu, X., Du, S., Ren, G., et al. (2021d). Overview of rapid detection methods for Salmonella in foods: Progress and challenges. *Foods* 10, 2402. doi:10.3390/foods10102402

Wang, N., Pan, G., Liu, P., Rong, S., Gao, Z., and Li, Q. (2021a). Advances and future perspective on detection technology of human norovirus. *Pathogens* 10, 1383. doi:10.3390/pathogens10111383

Wang, R., Wang, L., Yan, J., Luan, D., Sun, T., Wu, J., et al. (2021c). Rapid, sensitive and label-free detection of pathogenic bacteria using a bacteria-imprinted conducting polymer film-based electrochemical sensor. *Talanta* 226, 122135. doi:10.1016/j.talanta.2021.122135

Wang, S., Zhu, X., Meng, Q., Zheng, P., Zhang, J., He, Z., et al. (2021b). Gold interdigitated micro-immunosensor based on Mn-MOF-74 for the detection of Listeria monocytogens. *Biosens. Bioelectron. X.* 183, 113186. doi:10.1016/j.bios.2021.113186

Wang, W., Deng, Y., Li, S., Liu, H., Lu, Z., Zhang, L., et al. (2013). A novel acetylcholine bioensor and its electrochemical behavior. *J. Biomed. Nanotechnol.* 9, 736–740. doi:10.1166/jbn.2013.1577

Wang, Z., Cai, R., Gao, Z., Yuan, Y., and Yue, T. (2020c). Immunomagnetic separation: An effective pretreatment technology for isolation and enrichment in food microorganisms detection. *Compr. Rev. Food Sci. Food Saf.* 19, 3802–3824. doi:10.1111/1541-4337.12656

Wang, Z., Yao, X., Zhang, Y., Wang, R., Ji, Y., Sun, J., et al. (2020b). Functional nanozyme mediated multi-readout and label-free lateral flow immunoassay for rapid detection of *Escherichia coli* O157:H7. *Food Chem. x.* 329, 127224. doi:10.1016/j.foodchem.2020.127224

Wangman, P., Surasilp, T., Pengsuk, C., Sithigorngul, P., and Longyant, S. (2021). Development of a species-specific monoclonal antibody for rapid detection and identification of foodborne pathogen *Vibrio vulnificus*. *J. Food Saf.* 41. doi:10.1111/jfs.12939

Wei, L., Wang, Z., Feng, C., Xianyu, Y., and Chen, Y. (2021). Direct transverse relaxation time biosensing strategy for detecting foodborne pathogens through enzyme-mediated sol-gel transition of hydrogels. *Anal. Chem.* 93, 6613–6619. doi:10.1021/acs.analchem.0c03968

Weng, X., Zhang, C., and Jiang, H. (2021). Advances in microfluidic nanobiosensors for the detection of foodborne pathogens. *LWT* 151, 112172. doi:10.1016/j.lwt.2021.112172

Wu, X., Luo, H., Xu, F., Ge, C., Li, S., Deng, X., et al. (2021). Evaluation of Salmonella serotype prediction with multiplex nanopore sequencing. *Front. Microbiol.* 12, 637771. doi:10.3389/fmicb.2021.637771

Wu, Y., Deng, P., Tian, Y., Ding, Z., Li, G., Liu, J., et al. (2020a). Rapid recognition and determination of tryptophan by carbon nanotubes and molecularly imprinted polymer-modified glassy carbon electrode. *Bioelectrochemistry* 131, 107393. doi:10.1016/j.bioelechem.2019.107393

Wu, Y., Deng, P., Tian, Y., Feng, J., Xiao, J., Li, J., et al. (2020b). Simultaneous and sensitive determination of ascorbic acid, dopamine and uric acid via an electrochemical sensor based on PVP-graphene composite. *J. Nanobiotechnology* 18, 112. doi:10.1186/s12951-020-00672-9

Xi, Z., Huang, R., Deng, Y., and He, N. (2014). Progress in selection and biomedical applications of aptamers. *J. Biomed. Nanotechnol.* 10, 3043–3062. doi:10.1166/jbn.2014.1979

Xia, J., Qiu, S., Zeng, H., Liu, C., and Liu, Q. (2021). A rapid detection of *Escherichia coli* O157 : H7 by competition visual antigen macroarray. *J. Food Saf.* 4141 (1), e12872. doi:10.1111/jfs.12872

Xiao, C., Guo, Y., Zhao, K., Liu, S., He, N., He, Y., et al. (2022). Prognostic value of machine learning in patients with acute myocardial infarction. *J. Cardiovasc. Dev. Dis.* 9, 56. doi:10.3390/jcdd9020056

Xiao, X., Hu, S., Lai, X., Peng, J., and Lai, W. (2021). Developmental trend of immunoassays for monitoring hazards in food samples: A review. *Trends Food Sci. Technol.* 111, 68–88. doi:10.1016/j.tifs.2021.02.045

Xiao, Z., Chen, H., Chen, H., Wu, L., Yang, G., Wu, Y., et al. (2019). Advanced diagnostic strategies for *Clostridium difficile* infection (CDI). *J. Biomed. Nanotechnol.* 15, 1113–1134. doi:10.1166/jbn.2019.2782

Xie, G. Y., Zhou, D. G., Zhao, G. J., Feng, X. Y., Aguilar, Z. P., and Xu, H. Y. (2021b). Recombinase aided amplification with photoreactive DNA-binding dye for rapid detection of viable *Staphylococcus aureus*. *Lwt-Food Sci. Technol.* 135, 110249. doi:10.1016/j.lwt.2020.110249

Xie, M., Chen, T., Xin, X., Cai, Z., Dong, C., Lei, B., et al. (2022). Multiplex detection of foodborne pathogens by real-time loop-mediated isothermal amplification on a digital microfluidic chip. *Food control.* 136, 108824. doi:10.1016/j.foodcont.2022.108824

Xie, W., Wei, S., Zheng, Z., Jiang, Y., and Yang, D. (2021a). Recognition of defective carrots based on deep learning and transfer learning. *Food bioproc. Tech.* 14, 1361–1374. doi:10.1007/s11947-021-02653-8

Xie, X. Q., and Liu, Z. (2021). Simultaneous enumeration of Cronobacter sakazakii and *Staphylococcus aureus* in powdered infant foods through duplex TaqMan real-time PCR. *Int. Dairy J.* 117, 105019. doi:10.1016/j.idairyj.2021.105019

Xie, Z., Pu, H., and Sun, D.-W. (2021c). Computer simulation of submicron fluid flows in microfluidic chips and their applications in food analysis. *Compr. Rev. Food Sci. Food Saf.* 20, 3818–3837. doi:10.1111/1541-4337.12766

Xu, L. J., Du, J. J., Deng, Y., and He, N. Y. (2012). Electrochemical detection of *E. coli* O157:H7 using porous pseudo-carbon paste electrode modified with carboxylic multi-walled carbon nanotubes, glutaraldehyde and 3-aminopropyltriethoxysilane. *J. Biomed. Nanotechnol.* 8, 1006–1011. doi:10.1166/jbn.2012.1456

Xu, Y., Wang, T., Chen, Z., Jin, L., Wu, Z., Yan, J., et al. (2021). The point-of-care-testing of nucleic acids by chip, cartridge and paper sensors. *Chin. Chem. Lett.* 32, 3675–3686. doi:10.1016/j.cclet.2021.06.025

Xue, L., Jin, N. N., Guo, R. Y., Wang, S. Y., Qi, W. Z., Liu, Y. J., et al. (2021). Microfluidic colorimetric biosensors based on MnO2 nanozymes and convergence-divergence spiral micromixers for rapid and sensitive detection of Salmonella. *ACS Sens.* 6, 2883–2892. doi:10.1021/acssensors.1c00292

Yan, J., Lu, Y., Xie, S., Tan, H., Tan, W., Li, N., et al. (2021). Highly fluorescent N-doped carbon quantum dots derived from bamboo stems for selective detection of Fe3+ ions in biological systems. *J. Biomed. Nanotechnol.* 17, 312–321. doi:10.1166/jbn.2021.3034

Yang, , J., Zhang, N., Lv, J., Zhu, P., Pan, X., Hu, J., et al. (2020b). Comparing the performance of conventional PCR, RTQ-PCR, and droplet digital PCR assays in detection of Shigella. *Mol. Cell. Probes* 51, 101531. doi:10.1016/j.mcp.2020.101531

Yang, G., Huang, H., Xiao, Z., Zhang, C., Guo, W., Ma, T., et al. (2020c). A novel strategy for liquid exfoliation of ultrathin Black phosphorus nanosheets. *J. Biomed. Nanotechnol.* 16, 548–552. doi:10.1166/jbn.2020.2909

Yang, H. W., Liang, W. B., Si, J., Li, Z. Y., and He, N. Y. (2014a). Long spacer arm-functionalized magnetic nanoparticle platform for enhanced chemiluminescent detection of hepatitis B virus. *J. Biomed. Nanotechnol.* 10, 3610–3619. doi:10.1166/jbn.2014.2047

Yang, H. W., Liu, M., Jiang, H. R., Zeng, Y., Jin, L., Luan, T., et al. (2017). Copy number variation analysis based on gold magnetic nanoparticles and fluorescence multiplex ligation-dependent probe amplification. *J. Biomed. Nanotechnol.* 13, 655–664. doi:10.1166/jbn.2017.2386

Yang, S., Guo, H., Wei, B., Zhu, S., Cai, Y., Jiang, P., et al. (2014b). Association of miR-502-binding site single nucleotide polymorphism in the 3-untranslated region of SET8 and TP53 codon 72 polymorphism with non-small cell lung cancer in Chinese population. *Acta Biochimica Biophysica Sinica* 46, 149–154. doi:10.1093/abbs/gmt138

Yang, Y., Chen, Y., Tang, H., Zong, N., and Jiang, X. (2020a). Microfluidics for biomedical analysis. *Small Methods* 4, 1900451. doi:10.1002/smtd.201900451

Yao, S., Li, J., Pang, B., Wang, X., Shi, Y., Song, X., et al. (2020). Colorimetric immunoassay for rapid detection of *Staphylococcus aureus* based on etching-enhanced peroxidase-like catalytic activity of gold nanoparticles. *Microchim. Acta* 187, 504. doi:10.1007/s00604-020-04473-7

Yin, M., Jing, C., Li, H., Deng, Q., and Wang, S. (2020). Surface chemistry modified upconversion nanoparticles as fluorescent sensor array for discrimination of foodborne pathogenic bacteria. *J. Nanobiotechnology* 18, 41. doi:10.1186/s12951-020-00596-4

Yu, H., Guo, W., Lu, X., Xu, H., Yang, Q., Tan, J., et al. (2021b). Reduced graphene oxide nanocomposite based electrochemical biosensors for monitoring foodborne pathogenic bacteria: A review. *Food control.* 127, 108117. doi:10.1016/j.foodcont.2021.108117

Yu, J., Hou, Q., Li, W., Huang, W., Mo, L., Yao, C., et al. (2020). Profiling of the viable bacterial and fungal microbiota in fermented feeds using single-molecule real-time sequencing. *J. Anim. Sci.* 98, skaa029. doi:10.1093/jas/skaa029

Yu, Y., Li, R., Ma, Z., Han, M., Zhang, S., Zhang, M., et al. (2021a). Development and evaluation of a novel loop mediated isothermal amplification coupled with TaqMan probe assay for detection of genetically modified organism with NOS terminator. *Food Chem. x.* 356, 129684. doi:10.1016/j.foodchem.2021.129684

Zaczek-Moczydlowska, M. A., Beizaei, A., Dillon, M., and Campbell, K. (2021). Current state-of-the-art diagnostics for Norovirus detection: Model approaches for point-of-care analysis. *Trends Food Sci. Technol.* 114, 684–695. doi:10.1016/j.tifs.2021.06.027

Zarkani, A. A., and Schikora, A. (2021). Mechanisms adopted by Salmonella to colonize plant hosts. *Food Microbiol.* 99, 103833. doi:10.1016/j.fm.2021.103833

Zeng, Y., Tan, X., Zhang, L., Jiang, N., and Cao, H. (2014). Identification and expression of fructose-1, 6-bisphosphate aldolase genes and their relations to oil content in developing seeds of tea oil tree (camellia oleifera). *PLoS One* 9, e107422. doi:10.1371/journal.pone.0107422

Zhai, Y., Meng, X., Li, L., Liu, Y., Xu, K., Zhao, C., et al. (2021). Rapid detection of Vibrio parahaemolyticus using magnetic nanobead-based immunoseparation and quantum dot-based immunofluorescence. *RSC Adv.* 11, 38638–38647. doi:10.1039/d1ra07580b

Zhai, Y., Zhao, C., Li, L., Xu, K., Wang, J., Song, X., et al. (2020). Production of phage display-derived peptide and the application for DetectingVibrio parahaemolyticusby combined PCR technology. *Food Anal. Methods* 13, 1906–1917. doi:10.1007/s12161-020-01800-9

Zhang, J., Wang, Y., and Lu, X. (2021c). Molecular imprinting technology for sensing foodborne pathogenic bacteria. *Anal. Bioanal. Chem.* 413, 4581–4598. doi:10.1007/s00216-020-03138-x

Zhang, K., Deng, R., Gao, H., Teng, X., and Li, J. (2020d). Lighting up single-nucleotide variation *in situ* in single cells and tissues. *Chem. Soc. Rev.* 49, 1932–1954. doi:10.1039/c9cs00438f

Zhang, L., Jiang, H., Zhu, Z., Liu, J., and Li, B. (2022). Integrating CRISPR/Cas within isothermal amplification for point-of-Care Assay of nucleic acid. *Talanta* 243, 123388. doi:10.1016/j.talanta.2022.123388

Zhang, M. M., Liu, J. F., Shen, Z. Q., Liu, Y. X., Song, Y., Liang, Y., et al. (2021b). A newly developed paper embedded microchip based on LAMP for rapid multiple detections of foodborne pathogens. *BMC Microbiol.* 21, 197. doi:10.1186/s12866-021-02223-0

Zhang, M., Ye, J., He, J.-s., Zhang, F., Ping, J., Qian, C., et al. (2020a). Visual detection for nucleic acid-based techniques as potential on-site detection methods. A review. *Anal. Chim. Acta.* 1099, 1–15. doi:10.1016/j.aca.2019.11.056

Zhang, R., Belwal, T., Li, L., Lin, X., Xu, Y., Luo, Z., et al. (2020b). Nanomaterial-based biosensors for sensing key foodborne pathogens: Advances from recent decades. *Compr. Rev. Food Sci. Food Saf.* 19, 1465–1487. doi:10.1111/1541-4337.12576

Zhang, Y., Qu, Q., Rao, M., Zhang, N., Zhao, Y., Tao, F., et al. (2020c). Simultaneous identification of animal-derived components in meats using high-throughput sequencing in combination with a custom-built mitochondrial genome database. *Sci. Rep.* 10, 8965. doi:10.1038/s41598-020-65724-4

Zhang, Y., Ren, F., Wang, G., Liao, T., Hao, Y., Zhang, H., et al. (2021a). Rapid and sensitive pathogen detection platform based on a lanthanide-labeled immunochromatographic strip test combined with immunomagnetic separation. *Sensors Actuators B Chem.* 329, 129273. doi:10.1016/j.snb.2020.129273

Zhao, , T., Ji, P., and Kumar, G. D. (2021b). Pre-harvest treatment for reduction of foodborne pathogens and microbial load on tomatoes. *Food control.* 119, 107469. doi:10.1016/j.foodcont.2020.107469

Zhao, L., Guo, J., Li, S., and Wang, J. (2021a). The development of thermal immunosensing for the detection of food-borne pathogens *E. coli* O157:H7 based on the novel substoichiometric photothermal conversion materials MoO3-x NPs. *Sensors Actuators B Chem.* 344, 130306. doi:10.1016/j.snb.2021.130306

Zhao, X., and Wu, C. (2020). Recent advances in peptide nucleic acids for rapid detection of foodborne pathogens. *Food Anal. Methods* 13, 1956–1972. doi:10.1007/s12161-020-01811-6

Zhao, Y., Zeng, D., Yan, C., Chen, W., Ren, J., Jiang, Y., et al. (2020). Rapid and accurate detection of *Escherichia coli* O157:H7 in beef using microfluidic wax-printed paper-based ELISA. *Analyst* 145, 3106–3115. doi:10.1039/d0an00224k

Zheng, X. T., and Tan, Y. N. (2020). Recent development of nucleic acid nanosensors to detect sequence-specific binding interactions: From metal ions, small molecules to proteins and pathogens. *Sensors Int.* 1, 100034. doi:10.1016/j.sintl.2020.100034

Zhou, B. Q., Ye, Q. H., Li, F., Xiang, X. R., Shang, Y. T., Wang, C. F., et al. (2022). CRISPR/Cas12a based fluorescence-enhanced lateral flow biosensor for detection of *Staphylococcus aureus*. *Sensors Actuators B Chem.* 351, 130906. doi:10.1016/j.snb.2021.130906

Zhou, L., Peng, Y., Wang, Q., and Lin, Q. (2017). An ESIPT-based two-photon fluorescent probe detection of hydrogen peroxide in live cells and tissues. *J. Photochem. Photobiol. B Biol.* 167, 264–268. doi:10.1016/j.jphotobiol.2017.01.011

Zhou, X., Pu, H., and Sun, D.-W. (2021). DNA functionalized metal and metal oxide nanoparticles: Principles and recent advances in food safety detection. *Crit. Rev. Food Sci. Nutr.* 61, 2277–2296. doi:10.1080/10408398.2020.1809343

Zuo, Y. T., Xue, L., Gao, J. S., Liao, Y. Y., Jiang, Y. T., Li, Y., et al. (2021). Development and application of a novel rapid and throughput method for broad-spectrum anti-foodborne norovirus antibody testing. *Front. Microbiol.* 12, 670488. doi:10.3389/fmicb.2021.670488

frontiers | Frontiers in Bioengineering and Biotechnology

TYPE Original Research
PUBLISHED 10 August 2022
DOI 10.3389/fbioe.2022.948757

OPEN ACCESS

EDITED BY
Tailin Xu,
Shenzhen University, China

REVIEWED BY
Nan-Fu Chiu,
National Taiwan Normal University, Taiwan
Hui Yu,
Shanghai Jiao Tong University, China

*CORRESPONDENCE
Han Shen,
shenhan@njglyy.com
Zhiyang Li,
lizhiyangcn@qq.com

SPECIALTY SECTION
This article was submitted to Biosensors and Biomolecular Electronics, a section of the journal Frontiers in Bioengineering and Biotechnology

RECEIVED 20 May 2022
ACCEPTED 11 July 2022
PUBLISHED 10 August 2022

CITATION
Di K, Fan B, Gu X, Huang R, Khan A, Liu C, Shen H and Li Z (2022), Highly efficient and automated isolation technology for extracellular vesicles microRNA. *Front. Bioeng. Biotechnol.* 10:948757. doi: 10.3389/fbioe.2022.948757

Highly efficient and automated isolation technology for extracellular vesicles microRNA

Kaili Di[1], Boyue Fan[2], Xinrui Gu[1], Rongrong Huang[1], Adeel Khan[3], Chang Liu[1], Han Shen[1]* and Zhiyang Li[1]*

[1]Department of Laboratory Medicine, Affiliated Drum Tower Hospital, Medical School of Nanjing University, Nanjing, China, [2]Jiangsu Key Laboratory of Medical Science and Laboratory Medicine, School of Medicine, Jiangsu University, Zhenjiang, China, [3]State Key Laboratory of Bioelectronics, School of Biological Science and Medical Engineering, Southeast University, Nanjing, China

MicroRNA (miRNA) in extracellular vesicles (EVs) has great potential to be a promising marker in liquid biopsy. However, the present EV isolation methods, such as ultracentrifugation, have complicated and long-time operation, which impedes research on EV miRNA. The downstream complex miRNA extraction process will also significantly increase the detection cycle and loss. We first established a simple automated technique to efficiently extract target miRNAs in EVs from plasma based on Fe_3O_4@TiO_2 beads with high affinity and capture efficiency. We combined a heat-lysis method for quick and simple EV miRNA extraction and detection. The results indicated that our method has more RNA yield than TRIzol or a commercial kit and could complete EV enrichment and miRNA extraction in 30 min. Through the detection of miRNA-21, healthy people and lung cancer patients were distinguished, which verified the possibility of the application in clinical detection. The automated isolation technology for EV miRNA has good repeatability and high throughput, with great application potential in clinical diagnosis.

KEYWORDS

extracellular vesicles, microRNA, Fe_3O_4@TiO_2, isolation, lung cancer

Introduction

Extracellular vesicles (EVs) are vesicles released by most prokaryotic and eukaryotic cells containing proteins, lipids, and nucleic acids, which can be transported to distant cells (Yanez-Mo et al., 2015; Jan et al., 2019; Mathieu et al., 2019). EV-derived microRNAs (miRNAs) have been discovered to play an important role in gene expression regulation and disease progression (Yang et al., 2017). EV miRNAs have been extensively studied as a highly sensitive marker for different diseases, such as ovarian cancer (Maeda et al., 2020), lung cancer (Wu and Shen, 2020), and breast cancer (Volovat et al., 2020). Presently, several miRNA diagnostic kits have been developed and applied in clinical use. Given their unique high stability and specificity as biomarkers, EV miRNAs have great promise in early detection, prognosis, and monitoring of diseases (Preethi et al., 2022; Zhao et al., 2022).

EV isolation is a necessary and challenging step for research involving EV miRNAs. However, the lack of rapid and efficient techniques for EV isolation is a limitation that needs to be addressed urgently. Current isolation methods, including ultracentrifugation, size-exclusion chromatography, polymer precipitation, immunoaffinity etc., are time-limited, complex to operate, and require expensive equipment. After EV isolation, RNA extraction methods, such as TRIzol, will further reduce the extraction efficiency of EV miRNAs and prolong the detection period. In recent years, the development of various nanomaterials applied to detection technologies has brought convenience (Xiao et al., 2019; Yang et al., 2020). In particular, magnetic beads have shown great advantage as a fast and easy to operate detection method (Mou et al., 2015; Tang et al., 2018; Mou et al., 2019a; Mou et al., 2019b). Therefore, more efficient EV miRNA isolation methods should be developed and applied for EV analysis (Lu et al., 2021; Zhao et al., 2022). Titanium dioxide (TiO_2) is a nanomaterial widely used in many fields (Xin et al., 2021; Chen et al., 2022a; Gao et al., 2022; Li et al., 2022) and can combine with phosphorylated amino acid residues, including serine, tyrosine, and threonine (Liu et al., 2015). The surface of the TiO_2 beads is cationic and specifically binds to the phosphate groups on the phosphorylated modified peptide fragments. Recent researchers have suggested that TiO_2 is able to combine with the phosphate groups on the lipid bilayer membrane of EVs (Gao et al., 2019; Chen et al., 2022b).

In our study, Fe_3O_4@TiO_2 beads were used for EV rapid capture, and high capture efficiency of 80% was achieved. To better combine magnetic bead capture capacity and downstream biomarker detection for clinical application, we first designed an automated technique to efficiently extract target miRNAs in EVs from plasma. This unique approach involves three steps. First, EVs were specifically captured by Fe_3O_4@TiO_2. Second, EVs were directly cleaved by heating and releasing the target miRNAs. Finally, quantitative reverse transcription PCR (RT-qPCR) was used to amplify heat-released miRNAs.

Materials and methods

Materials

Primers and phosphate-buffered saline (PBS) were purchased from Sangon Biotech Co., Ltd. (Shanghai, China). Fe_3O_4@TiO_2 was obtained from Nanjing Xiuyuan Biotechnology Co., Ltd. (Jiangsu, China). Monoclonal anti-CD63 antibody, monoclonal calnexin antibody, and monoclonal TSG101 antibody were purchased from Abcam Co., Ltd. (Shanghai, China). A solution of 28 wt% ammonium hydroxide (NH_3•H_2O) and PKH26 Red Fluorescent Cell Linker Mini Kit were obtained from Sigma Co., Ltd. (Shanghai, China)., A 0.22-μm syringe-driven filter was purchased from Millipore (United States). Deionized water was processed by Ultrapure Millipore water (18.2 MΩ cm). High glucose Dulbecco's modified Eagle's medium (DMEM) and penicillin–streptomycin solution were purchased from Hyclone (UT, United States). Exosome-depleted fetal bovine serum (FBS) media supplement was purchased from System Biosciences, SBI (CA, United States).

All cell lines were purchased from the Shanghai Cell Bank, Chinese Academy of Sciences (Shanghai, China). Healthy human and lung cancer patient plasma samples were supplied by Nanjing University-affiliated Drum Tower Hospital. The samples were centrifuged at 1,500 g for 10 min at 4°C. The supernatant was collected and centrifuged at 2,000 g for 10 min at 4°C to remove platelets. The supernatant was centrifuged at 15,000 g for 30 min and stored at −80°C.

Isolation of model extracellular vesicles

A549 non–small cell lung cancer cells (NSCLC) and BEAS-2B normal human bronchial epithelial cells (NHBES) were cultured in DMEM medium supplemented with 1% (v/v) penicillin–streptomycin and 10% (v/v) with standard fetal bovine serum (FBS), at 5% CO_2 in culture bottles. When the cell density was up to 70%, we discarded the supernatant and washed the cells with PBS. Finally, cells were subcultured in DMEM containing 10% exosome-depleted FBS. The supernatant was collected after 24 h incubation.

Supernatants from the A549 and BEAS-2B cell cultures were collected and centrifuged at 300 g for 10 min to remove cell debris, followed by centrifugation at 2,000 g for 10 min. The supernatant was then transferred to ultracentrifuge tubes and centrifuged in an ultracentrifuge (Beckman Coulter, Brea, CA, United States) at 110,000 g at 4°C for 70 min twice. The pellet was resuspended in PBS and immediately stored at −80°C.

Characterization of extracellular vesicles

The EVs captured on Fe_3O_4@TiO_2 were eluted by 5% NH_3•H_2O for 10 min rotated on a rotator. After magnetic separation, the supernatant containing EVs was diluted with PBS and centrifuged at 2,000 g for 10 min in an Amicon Ultra100 kd ultrafiltration tube. EVs were recovered for subsequent analysis.

A total of 20 μl of the EV sample was incubated with 2% phosphotungstic acid on the copper mesh for 10 min at room temperature. After the copper mesh was dried, the EVs were photographed by transmission electron microscopy (TEM) (JEOL JEM-2100, Japan). For scanning electron microscopy (SEM) (Hitachi, Japan), 10 μl of EV sample–enriched Fe_3O_4@

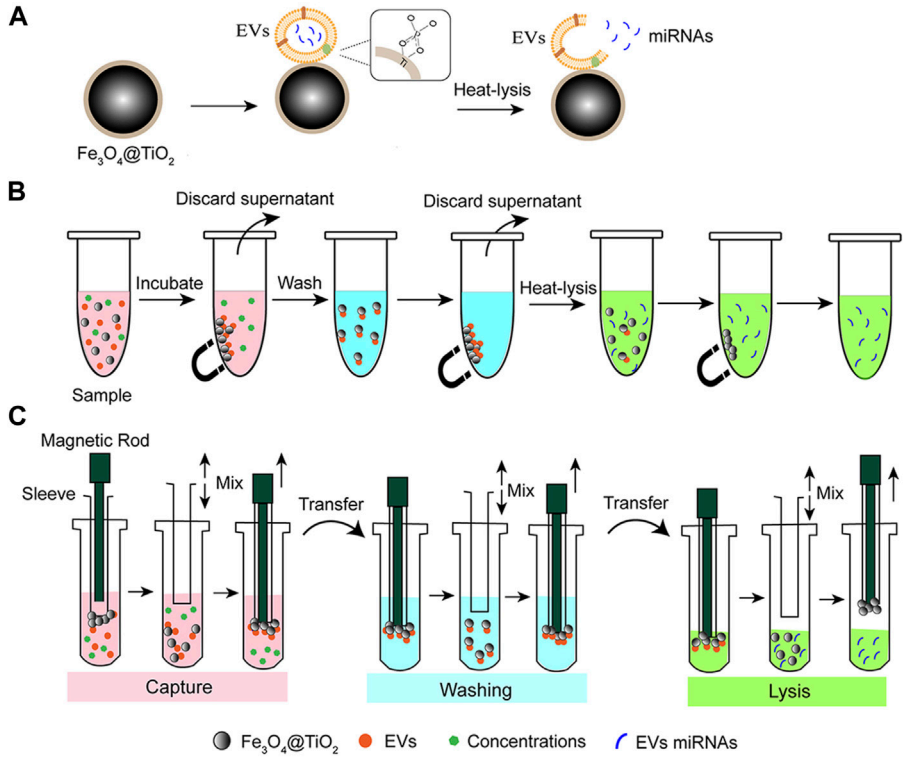

FIGURE 1
Schematic of EV miRNA isolation based on Fe_3O_4@TiO_2. **(A)** Principle for EV isolation based on Fe_3O_4@TiO_2. After capture, miRNAs were released from the EVs by the heat-lysis method. **(B)** Process of manual EV miRNA isolation. The sample was incubated with Fe_3O_4@TiO_2, and the beads were separated with magnets. Then, the supernatant was discarded after cleaning. Elution buffer was added to the beads to extract miRNAs. **(C)** Process of automated EV miRNA isolation. Binding buffer (pink), cleaning buffer (blue), and elution buffer (green).

TiO_2 was added to the clean tin foil paper. After drying at room temperature, the tin foil paper was glued to the conductive tape and photographed.

The particle size and concentration of the EVs were analyzed by using a ZetaView nanoparticles tracking analyzer (Particle Metrix, Germany). The EV sample was diluted with 1 × PBS to an appropriate concentration (10^7 ~ 10^9/ml). Data were recorded and analyzed at 11 positions.

Laser scanning confocal microscope

A laser scanning confocal microscope is used to observe the combination of stained EVs and magnetic beads. The model EVs from the A549 cell were incubated with 0.5 mg Fe_3O_4@TiO_2 beads for 10 min. After isolation, 20 μl of PE-labeled anti-CD63 antibodies was incubated with beads for 30 min in the dark. The beads were cleaned with 200 μl of PBS three times to remove uncombined antibodies. Fluorescence was observed and photographed by using a confocal laser microscope (Leica, Germany).

Extracellular vesicle microRNA extraction and detection

A schematic of the automatic isolation and detection of EVs based on Fe_3O_4@TiO_2 is shown in Figure 1C. First, the magnetic rod was used to transfer Fe_3O_4@TiO_2 to the sample. The magnetic rods were added on the cover immersed in the tube, followed by a frame shake up and down of the covers for better incubation and mixing. Upon completion of incubation, the magnetic rods dropped down into the cover. Once they slide in, the magnetic beads bind the cover again. The magnetic rods transfer the attached beads and the bound EVs into another tube containing the washing solution. Finally, the beads and the captured EVs were transferred into the elution solution for heat-lysis. The beads were removed, and the miRNAs from the EVs were left in the solution. To evaluate the recovery rate for the automatic instrument, we calculated the difference in the weight of the beads before and after the experiment. The miRNA-21 expression level was detected by RT-qPCR to evaluate the extraction effect. The primer sequences of RT-qPCR are shown in Supplementary Table S1.

A total of 500 µl of the A549 cell supernatant was incubated with Fe_3O_4@TiO_2. Different methods were used to compare the extraction effect of miRNA, including the heat-lysis method, TRIzol, and the miRNeasy Serum/Plasma Advanced Kit (Qiagen, Germany). In the heat-lysis method, 50 µl of RNase-free water was added to the magnetic beads after EV enrichment and heated in a metal bath at 95°C for 5 min. After magnetic separation, the supernatant was transferred for miRNA detection. For the TRIzol method, 600 µl of TRIzol lysis solution was added to the magnetic beads and then mixed with chloroform. After centrifugation, the upper aqueous phase was transferred and mixed with 500 µl isopropanol.Eighty percent ethanol was used to wash the RNA, followed by pouring out the supernatant carefully and drying precipitation. To dissolve the RNA, 50 µl of RNase-free water was added. For the commercial kit method, the RNA extraction followed steps miRNeasy Serum/Plasma as per the advanced kit instruction. Finally, 50 µl of RNase-free water was added, followed by centrifugation at full speed for 1 min to elute miRNA.

Extracellular vesicle miRNA-21 analysis

First, the expression differences of miRNA-21 in EVs from A549 cells and BEAS-2B cells were compared. A total of 500 µl of the supernatant from each cell was incubated with 1 mg Fe_3O_4@TiO_2 for 10 min. After washing, 50 µl RNase-free water was added to the magnetic beads, and miRNA was extracted using the heat-lysis method. Quantitative detection of miRNA-21 was performed by RT-qPCR. Each experiment was repeated three times.

An amount of 1 mg Fe_3O_4@TiO_2 was used to enrich the EVs from the plasma of lung cancer patients and healthy persons. Next, 50 µl of RNase-free water was added to the magnetic beads, and miRNA was extracted by the heat-lysis method. Quantitative detection of miRNA-21 was performed by RT-qPCR, and the results were normalized with U6 as an internal reference.

Results

Extracellular vesicle enrichment based on Fe_3O_4@TiO_2

The principle for EV isolation based on Fe_3O_4@TiO_2 is shown in Figure 1A. Fe_3O_4@TiO_2 beads were spherical and monodispersed under electron microscopy (Supplementary Figure S1). The diameter of Fe_3O_4@TiO_2 was observed to be approximately 300–500 nm. The elemental composition of magnetic beads is shown in the energy-dispersive X-ray (EDX) spectrum (Supplementary Figure S2). The model EV samples were prepared by ultracentrifugation from the A549 cell supernatant. As shown in Figure 1B, 1 mg Fe_3O_4@TiO_2 was added to 100 µl model EVs and incubated for 10 min on a rotator at room temperature. After incubation, the beads were separated and washed with PBS three times and finally resuspended in 100 µl PBS buffer.

TEM images showed that the EVs maintained a round-cup morphology typical structure (Figure 2A), and the EVs were 50–150 nm in diameter as detected by NTA (Figure 2B). The Fe_3O_4@TiO_2 beads captured with EVs were characterized by SEM (Figures 2C,D). The surface of the Fe_3O_4@TiO_2 beads became rough because they combined with EVs. After Fe_3O_4@TiO_2 was captured with PBS, EVs, and cell lysis, the beads were stained with the PE-labeled anti-CD63 antibody. The confocal laser scanning microscope (CLSM) pictures showed that red fluorescence was only observed when Fe_3O_4@TiO_2 was incubated with EVs, indicating that Fe_3O_4@TiO_2 had high affinity and specificity for EV capture (Figure 2E).

Optimization of capture conditions

To obtain high capture efficiency, we optimized capture conditions according to a previous research method (Pang et al., 2020). PKH26-stained EVs were incubated with Fe_3O_4@TiO_2 under different capture conditions. The fluorescence intensity for the supernatant after magnetic separation was detected. We optimized the amount of Fe_3O_4@TiO_2, incubation time, and pH value for the binding buffer. After incubation of EV samples and Fe_3O_4@TiO_2, the fluorescence intensity of the supernatant was detected after magnetic separation by using SpectraMax M5 Microplate Readers (Molecular Devices, United States).

The capture efficiency was calculated according to the ratio of the fluorescence value in the supernatant and fluorescence value in the initial EV sample. As shown in Figure 3A, the capture efficiency increased with increased incubation time, and we obtained the best capture efficiency in 10 min. Buffer pH had a significant effect on the capture process. We obtained the best capture efficiency at pH value 5 (Figure 3B), which may be due to the positive charge of Fe_3O_4@TiO_2, making it easier to combine with the EVs. The capture efficiency increased as the Fe_3O_4@TiO_2 amount was increased from 0.01 to 0.8 mg. For further downstream experiments, 0.5 mg was the best fit (Figure 3C). The maximum capture efficiency reached 80%. In addition, according to SDS-PAGE results, Fe_3O_4@TiO_2 beads can remove most impurity proteins in samples (Supplementary Figure S3). It indicated that Fe_3O_4@TiO_2 beads have high affinity and specificity for EVs.

Automatic extracellular vesicle microRNA extraction

A strategy for automated extraction of EV miRNA was proposed by combining the automatic instrument for the EV

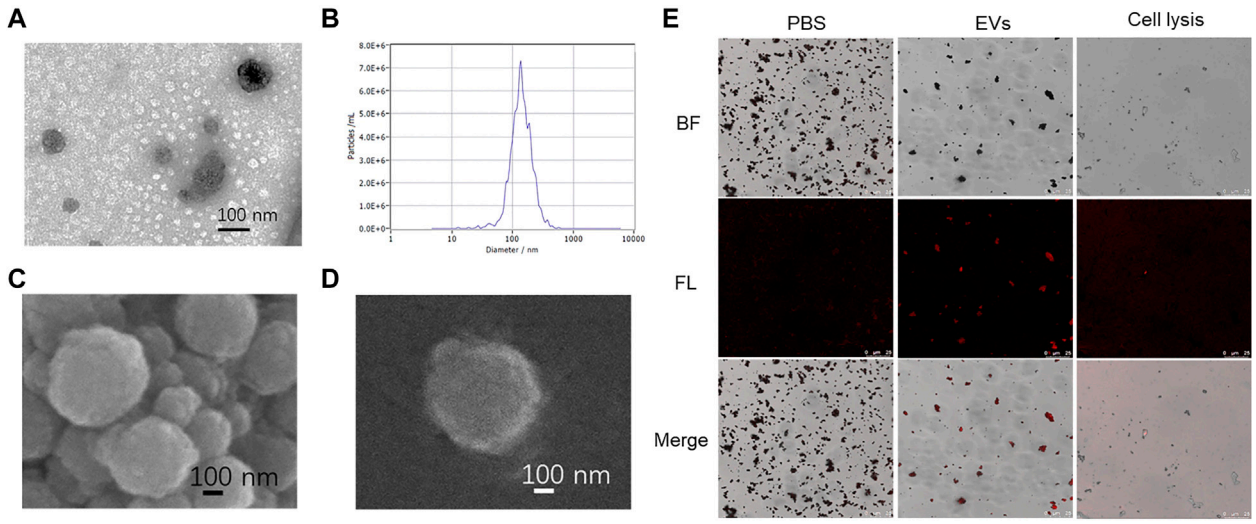

FIGURE 2
Characterization of EVs captured by Fe_3O_4@TiO_2. **(A)** TEM image of model EVs. **(B)** Particle size analysis of EVs. **(C)** SEM image of Fe_3O_4@TiO_2 after capture. **(D)** SEM image of single Fe_3O_4@TiO_2 after capture. **(E)** Confocal laser scanning microscope image of Fe_3O_4@TiO_2 captured with PBS, EVs, and cell lysis. EVs were stained with PE-labeled anti-CD63 antibody (red).

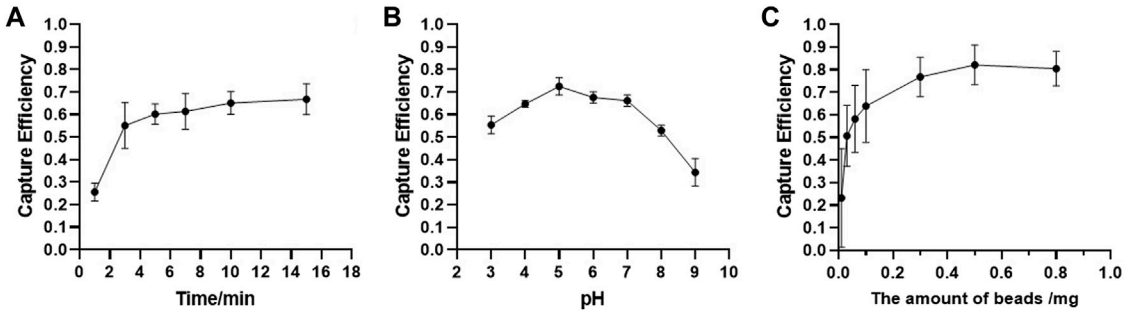

FIGURE 3
Optimization results for Fe_3O_4@TiO_2 capturing conditions. **(A)** Optimization results for incubation time. **(B)** Optimization results for binding buffer pH value. **(C)** Optimization results for bead amount.

extraction method based on Fe_3O_4@TiO_2 (Figure 1C). Figure 4A is the internal structure of the automatic instrument. In short, Fe_3O_4@TiO_2 beads were adsorbed onto magnetic rods in the machine that can help in the separation and cleaning of the beads. First, the magnetic rod was used to transfer the magnetic beads to the sample. The magnetic rods were added on the cover immersed in the tube, followed by a frame shake up and down of the covers for better incubation and mixing. Upon completion of incubation, the magnetic rods dropped down into the cover. Once they slide in, the magnetic beads bind the cover again. The magnetic rods transfer the attached beads and the bound EVs into another tube containing the washing solution, and the frame moves up and down for better cleaning. Finally, the beads and the captured EVs were transferred by the magnetic rod for heat-lysis. With the help of the magnetic rod, the beads were removed and the nucleic acid from the EVs was left in the solution.

Before RT-qPCR detection and analysis, the standard curve of miRNA-21 was performed to verify the reliability of the primers (Supplementary Figure S4). Good linearity and a single product band indicated that it could be used for the detection of miRNA-21. To find the optimal condition in the automated equipment, the miRNA extraction effects were compared to different mixing speed level and temperatures. The grade 3 mixing speed was selected because the CT mean value for miRNA-21 was minimum (Figure 4B). The CT value decreased gradually when the temperature was increased

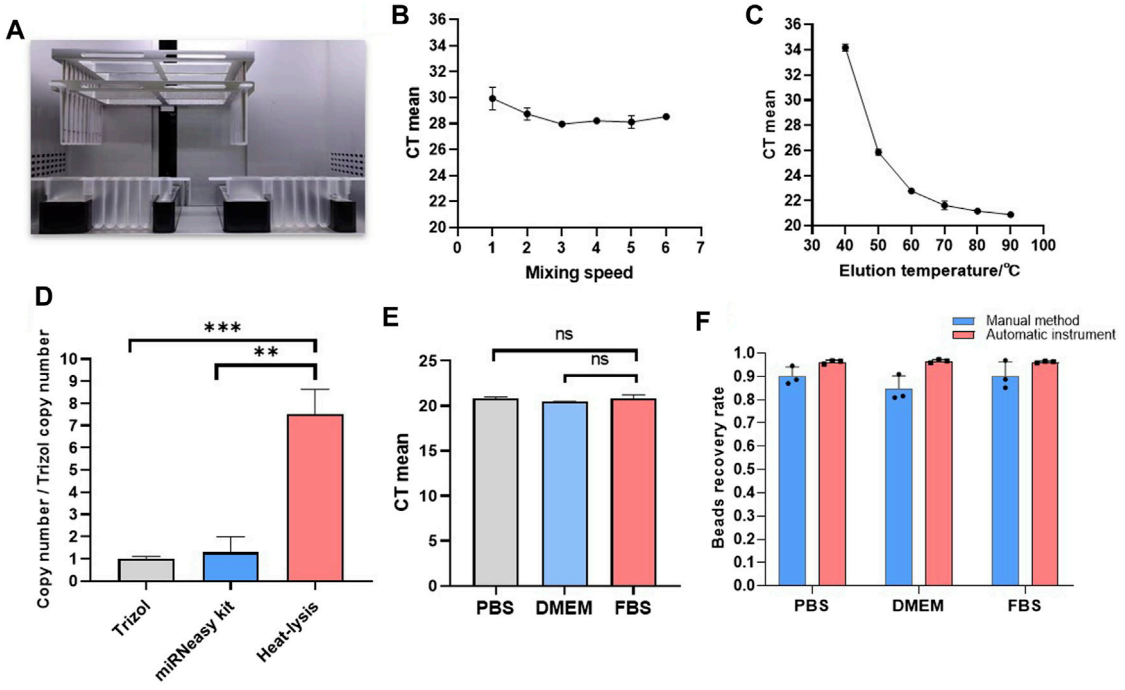

FIGURE 4
Automated EV isolation and miRNA extraction. **(A)** Internal structure of the automated instrument. **(B)** Optimization results for elution temperature. **(C)** Optimization results for mixing speed. **(D)** Copy number of miRNAs from different EV miRNA extraction methods. **(E)** CT values from EV miRNA extraction in different matrixes. **(F)** Recovery rate for magnetic beads by the manual method and automatic method (*$p < 0.05$, **$p < 0.01$, and ***$p < 0.001$, ns, non-significant).

(Figure 4C). So, we selected 90°C as the best lysis temperature. For verifying the advantages of this method in extraction, we compared the extraction effect of the heat-lysis method with TRIzol and the miRNeasy Serum/Plasma Advanced Kit. As shown in Figure 4D, the copy number of the heat-lysis method was about 7.5 times that of the TRIzol method and 5.8 times that of the kit method. Therefore, the heat-lysis method had better performance in EV miRNA extraction.

Different matrices were compared to study the influence factors for EV miRNA extraction, including PBS, DMEM, and exosome-free FBS. As shown in Figure 4E, the CT values for miRNA-21 extracted from the three matrices were the same, without significant difference. The results showed that the method for EV miRNA isolation by magnetic beads has wide adaptability. To compare the recovery rate for the automatic instrument and manual method, we calculated the weight ratio of the weight of the beads before and after the experiment. As shown in Figure 4F, the recovery rate for the magnetic beads on the automatic instrument reached up to 96%, while the highest recovery rate for the magnetic beads by the manual method was only 86%. The SD value for the instrumental method was also lower than that of the manual method, indicating that the recovery and repeatability of the instrumental method was better than that of the manual method. The repeatability of methods is particularly important in clinical testing. We used several human plasma samples ($n = 10$) to perform EV miRNA extraction and RT-qPCR detection of miRNA-21. All CT values were between mean ± 3 SD (Figure 5). The extraction of EV miRNA was confirmed to have good reproducibility by the repeated test.

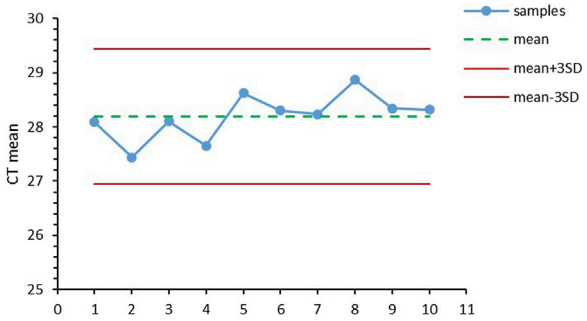

FIGURE 5
Repeated experimental results of automated EV miRNA isolation and detection ($n = 10$).

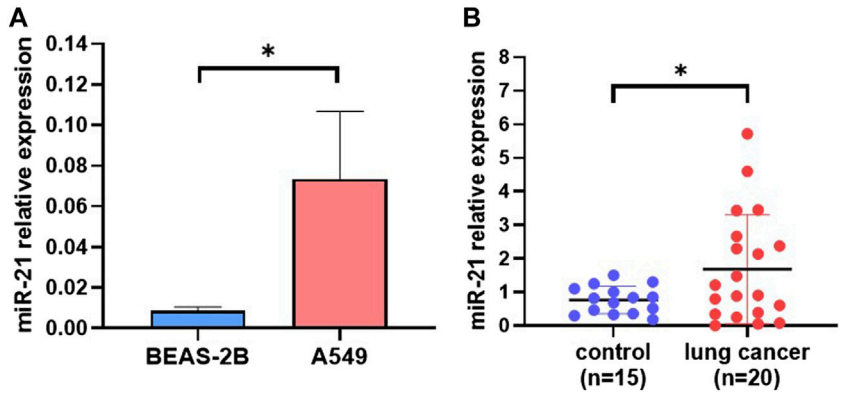

FIGURE 6
EV miRNA-21 analysis from different samples. **(A)** Difference in EV-derived miRNA-21 expression between A549 cells and Beas-2B cells (*p < 0.05). **(B)** Difference in plasma EV–derived miRNA-21 expression between healthy persons (n = 15) and lung cancer patients (n = 20) (*p < 0.05).

Extracellular vesicle miRNA-21 analysis

To demonstrate the possibility of applying this extraction method for research and clinical application, first, we verified it in a cell culture medium of human normal lung cell BEAS-2B and lung cancer cell A549. We found that the expression level of miRNA-21 in the EVs derived from A549 cells was significantly higher than that for the BEAS-2B cells (Figure 6A). Moreover, we compared the EV miRNA-21 expression from plasma after EV miRNA was extracted by the automated method based on Fe_3O_4@TiO_2. As shown in Figure 6B, the expression level of EV-derived miRNA-21 in the plasma from lung cancer patients was significantly higher than that of healthy persons. These results indicate that miRNA-21 can be used as a marker to distinguish lung cancer, which is consistent with the results from previous studies (Jin et al., 2017). This method can be used to detect clinical samples with advantages of more speed and convenience.

Discussion

The challenges of EV isolation methods, such as complicated operation and low recovery rate, limit research and application of EV miRNA. Recently, TiO_2 was discovered to have the ability to capture EVs. The Ti^{4+} on the surface of Fe_3O_4@TiO_2 can combine with the phosphate groups on the EV membrane (Pang et al., 2020). The recovery rate for the EVs was up to 80% based on Fe_3O_4@TiO_2 in 10 min. By contrast, the EV recovery rate for the ultracentrifugation method was less than 20% (Pang et al., 2020). Our research results showed that Fe_3O_4@TiO_2 successfully enriched EVs. The combination of magnetic beads and the automation method can obtain higher efficiency within less time (Supplementary Table S2) (Li et al., 2013).

The traditional TRIzol method or commercial kit is usually used to extract EV miRNA, which requires a large sample, cumbersome operation, and has poor repeatability. Considering that the enrichment of Fe_3O_4@TiO_2 reduced the components of proteins and nucleic acid pollutions, direct heat-lysis on the beads to extract RNA minimized the miRNA loss in a short time. The heat-lysis method has a significantly larger amount of EV miRNA. It has been reported that the RT-qPCR samples can be prepared by heat treatment of swab samples to diagnose COVID-19 (Bruce et al., 2020; Fomsgaard and Rosenstierne, 2020). Our experimental results show that miRNA-21 is highly expressed in EVs of lung cancer cells and plasma of lung cancer patients, consistent with other research studies (Bica-Pop et al., 2018).

In conclusion, we established a rapid and automatic EV miRNA extraction technology based on Fe_3O_4@TiO_2 beads, which will provide a very efficient tool for the clinical detection of EV miRNA. This method not only reduced the loss of nucleic acid during extraction steps but also avoided manual errors through automated procedures. We can effectively extract miRNA from only 50 µl plasma samples for detection, which is superior to TRIzol extraction technology and commercial kit. At present, the EV nucleic acid extraction method is relatively complex, and there is a large loss of nucleic acid in the operation process, which usually requires a 200 µl to 1 ml sample. The automated extraction method in our research has the advantages of high throughput, is fast, and requires less number of samples, which is very suitable for point-of-care testing (POCT) in clinical use. In addition to nucleic acid extraction, this method can be easily extended and used for the detection of various types of markers such as protein and lipid.

Data availability statement

The original contributions presented in the study are included in the article/Supplementary Material; further inquiries can be directed to the corresponding author.

Author contributions

ZL and KD: conceptualization and methodology. KD: data curation and writing—original draft preparation. XG and BF: visualization and investigation. RH and HS: supervision. CL: software and validation. KA: writing—reviewing and editing.

Funding

This study was supported by the National Natural Science Foundation of China (61971216, 82002242, and 81972310), the Key Research and Development Project of Jiangsu Province (BE2019603 and BE2020768), and Nanjing Important Science & Technology Specific Projects (2021-11005).

Conflict of interest

The authors declare that the research was conducted in the absence of any commercial or financial relationships that could be construed as a potential conflict of interest.

Publisher's note

All claims expressed in this article are solely those of the authors and do not necessarily represent those of their affiliated organizations, or those of the publisher, the editors, and the reviewers. Any product that may be evaluated in this article, or claim that may be made by its manufacturer, is not guaranteed or endorsed by the publisher.

Supplementary material

The Supplementary Material for this article can be found online at: https://www.frontiersin.org/articles/10.3389/fbioe.2022.948757/full#supplementary-material

References

Bica-Pop, C., Cojocneanu-Petric, R., Magdo, L., Raduly, L., Gulei, D., and Berindan-Neagoe, I. (2018). Overview upon miR-21 in lung cancer: focus on NSCLC. *Cell. Mol. Life Sci.* 75 (19), 3539–3551. doi:10.1007/s00018-018-2877-x

Bruce, E. A., Huang, M. L., Perchetti, G. A., Tighe, S., Laaguiby, P., Hoffman, J. J., et al. (2020). Direct RT-qPCR detection of SARS-CoV-2 RNA from patient nasopharyngeal swabs without an RNA extraction step. *PLoS Biol.* 18 (10), e3000896. doi:10.1371/journal.pbio.3000896

Chen, P., Zheng, H., Jiang, H., Liu, J., Tu, X., Zhang, W., et al. (2022). Oxygen-vacancy-rich phenanthroline/TiO_2 nanocomposites: an integrated adsorption, detection and photocatalytic material for complex pollutants remediation. *Chin. Chem. Lett.* 33 (2), 907–911. doi:10.1016/j.cclet.2021.07.002

Chen, Y., Chen, H., Yang, C., Wu, Y., Deng, C., and Sun, N. (2022). Specific enrichment of urinary exosomes and exosomal glycopeptides by coefficient affinity of integrated L-cysteine and titania. *Chin. Chem. Lett.* doi:10.1016/j.cclet.2022.03.075

Fomsgaard, A. S., and Rosenstierne, M. W. (2020). An alternative workflow for molecular detection of SARS-CoV-2 - escape from the NA extraction kit-shortage, copenhagen, denmark, march 2020. *Eurosurveillance* 25 (14), 2000398. doi:10.2807/1560-7917.es.2020.25.14.2000398

Gao, F., Jiao, F., Xia, C., Zhao, Y., Ying, W., Xie, Y., et al. (2019). A novel strategy for facile serum exosome isolation based on specific interactions between phospholipid bilayers and TiO(2). *Chem. Sci.* 10 (6), 1579–1588. doi:10.1039/c8sc04197k

Gao, K., Xu, R., Chen, Y., Zhang, Z., Shao, J., Ji, H., et al. (2022). TiO_2-carbon porous nanostructures for immobilization and conversion of polysulfides. *Chin. Chem. Lett.* doi:10.1016/j.cclet.2022.02.034

Jan, A. T., Rahman, S., Khan, S., Tasduq, S., and Choi, I. (2019). Biology, pathophysiological role, and clinical implications of exosomes: a critical appraisal. *Cells* 8 (2), 99. doi:10.3390/cells8020099

Jin, X., Chen, Y., Chen, H., Fei, S., Chen, D., Cai, X., et al. (2017). Evaluation of tumor-derived exosomal miRNA as potential diagnostic biomarkers for early-stage non-small cell lung cancer using next-generation sequencing. *Clin. Cancer Res.* 23 (17), 5311–5319. doi:10.1158/1078-0432.ccr-17-0577

Li, J., Li, X., Yu, S., Gao, S., Zhang, Y., Li, Y., et al. (2022). Photocatalytic fuel cell for simultaneous antibiotic wastewater treatment and electricity production by anatase TiO_2 nanoparticles anchored on Ni foam. *Chin. Chem. Lett.* doi:10.1016/j.cclet.2022.04.015

Li, S., Liu, H., Jia, Y., Mou, X., Deng, Y., Lin, L., et al. (2013). An automatic high-throughput single nucleotide polymorphism genotyping approach based on universal tagged arrays and magnetic nanoparticles. *J. Biomed. Nanotechnol.* 9 (4), 689–698. doi:10.1166/jbn.2013.1568

Liu, H., Zhou, J., and Huang, H. (2015). Amine-functionalized TiO_2 nanoparticles for highly selective enrichment of phosphopeptides. *Talanta* 143, 431–437. doi:10.1016/j.talanta.2015.05.019

Lu, Y., Tong, Z., Wu, Z., Jian, X., Zhou, L., Qiu, S., et al. (2021). Multiple exosome RNA analysis methods for lung cancer diagnosis through integrated on-chip microfluidic system. *Chin. Chem. Lett.* 33, 3188–3192. doi:10.1016/j.cclet.2021.12.045

Maeda, K., Sasaki, H., Ueda, S., Miyamoto, S., Terada, S., Konishi, H., et al. (2020). Serum exosomal microRNA-34a as a potential biomarker in epithelial ovarian cancer. *J. Ovarian Res.* 13 (1), 47. doi:10.1186/s13048-020-00648-1

Mathieu, M., Martin-Jaular, L., Lavieu, G., and Thery, C. (2019). Specificities of secretion and uptake of exosomes and other extracellular vesicles for cell-to-cell communication. *Nat. Cell Biol.* 21 (1), 9–17. doi:10.1038/s41556-018-0250-9

Mou, X., Chen, Z., Li, T., Liu, M., Liu, Y., Ali, Z., et al. (2019). A highly sensitive strategy for low-abundance hepatitis B virus detection via one-step nested polymerase chain reaction, chemiluminescence technology and magnetic separation. *J. Biomed. Nanotechnol.* 15 (8), 1832–1838. doi:10.1166/jbn.2019.2802

Mou, X., Li, T., Wang, J., Ali, Z., Zhang, Y., Chen, Z., et al. (2015). Genetic variation of BCL2 (rs2279115), NEIL2 (rs804270), LTA (rs909253), PSCA (rs2294008) and PLCE1 (rs3765524, rs10509670) genes and their correlation to gastric cancer risk based on universal tagged arrays and Fe_3O_4 magnetic nanoparticles. *J. Biomed. Nanotechnol.* 11 (11), 2057–2066. doi:10.1166/jbn.2015.2113

Mou, X., Sheng, D., Chen, Z., Liu, M., Liu, Y., Deng, Y., et al. (2019). *In-situ* mutation detection by magnetic beads-probe based on single base extension and its application in genotyping of hepatitis B virus pre-C region 1896nt locus single nucleotide polymorphisms. *J. Biomed. Nanotechnol.* 15 (12), 2393–2400. doi:10.1166/jbn.2019.2862

Pang, Y., Shi, J., Yang, X., Wang, C., Sun, Z., and Xiao, R. (2020). Personalized detection of circling exosomal PD-L1 based on Fe_3O_4@TiO_2 isolation and SERS immunoassay. *Biosens. Bioelectron.* 148, 111800. doi:10.1016/j.bios.2019.111800

Preethi, K. A., Selvakumar, S. C., Ross, K., Jayaraman, S., Tusubira, D., and Sekar, D. (2022). Liquid biopsy: exosomal microRNAs as novel diagnostic and prognostic biomarkers in cancer. *Mol. Cancer* 21 (1), 54. doi:10.1186/s12943-022-01525-9

Tang, Y., Ali, Z., Dai, J., Liu, X., Wu, Y., Chen, Z., et al. (2018). Single-Nucleotide polymorphism genotyping of exoS in *Pseudomonas aeruginosa* using dual-color fluorescence hybridization and magnetic separation. *J. Biomed. Nanotechnol.* 14 (1), 206–214. doi:10.1166/jbn.2018.2525

Volovat, S. R., Volovat, C., Hordila, I., Hordila, D. A., Mirestean, C. C., Miron, O. T., et al. (2020). MiRNA and LncRNA as potential biomarkers in triple-negative breast cancer: a review. *Front. Oncol.* 10, 526850. doi:10.3389/fonc.2020.526850

Wu, J., and Shen, Z. (2020). Exosomal miRNAs as biomarkers for diagnostic and prognostic in lung cancer. *Cancer Med.* 9 (19), 6909–6922. doi:10.1002/cam4.3379

Xiao, Z., Chen, H., Chen, H., Wu, L., Yang, G., Wu, Y., et al. (2019). Advanced diagnostic strategies for *Clostridium difficile* infection (CDI). *J. Biomed. Nanotechnol.* 15 (6), 1113–1134. doi:10.1166/jbn.2019.2782

Xin, Z., Zhao, X., Ji, H., Ma, T., Li, H., Zhong, S., et al. (2021). Amorphous carbon-linked TiO2/carbon nanotube film composite with enhanced photocatalytic performance: the effect of interface contact and hydrophilicity. *Chin. Chem. Lett.* 32 (7), 2151–2154. doi:10.1016/j.cclet.2020.11.054

Yanez-Mo, M., Siljander, P. R. M., Andreu, Z., Zavec, A. B., Borras, F. E., Buzas, E. I., et al. (2015). Biological properties of extracellular vesicles and their physiological functions. *J. Extracell. Vesicles* 4, 27066. doi:10.3402/jev.v4.27066

Yang, F., Ning, Z., Ma, L., Liu, W., Shao, C., Shu, Y., et al. (2017). Exosomal miRNAs and miRNA dysregulation in cancer-associated fibroblasts. *Mol. Cancer* 16 (1), 148. doi:10.1186/s12943-017-0718-4

Yang, G., Huang, H., Xiao, Z., Zhang, C., Guo, W., Ma, T., et al. (2020). A novel strategy for liquid exfoliation of ultrathin black phosphorus nanosheets. *J. Biomed. Nanotechnol.* 16 (4), 548–552. doi:10.1166/jbn.2020.2909

Zhao, Y., Fang, X., Bai, M., Zhang, J., Yu, H., Chen, F., et al. (2022). A microfluidic surface-enhanced Raman scattering (SERS) sensor for microRNA in extracellular vesicles with nucleic acid-tyramine cascade amplification. *Chin. Chem. Lett.* 33 (4), 2101–2104. doi:10.1016/j.cclet.2021.08.047

frontiers | Frontiers in Bioengineering and Biotechnology

TYPE Mini Review
PUBLISHED 10 August 2022
DOI 10.3389/fbioe.2022.939807

OPEN ACCESS

EDITED BY
Zhiyang Li,
Nanjing Drum Tower Hospital, China

REVIEWED BY
Alfredo De La Escosura-Muñiz,
University of Oviedo, Spain
Bingjie Zou,
China Pharmaceutical University, China

*CORRESPONDENCE
Bo Tian,
tianbo@csu.edu.cn

SPECIALTY SECTION
This article was submitted to Biosensors and Biomolecular Electronics, a section of the journal Frontiers in Bioengineering and Biotechnology

RECEIVED 09 May 2022
ACCEPTED 11 July 2022
PUBLISHED 10 August 2022

CITATION
Huang Z, Li J, Zhong H and Tian B (2022), Nucleic acid amplification strategies for volume-amplified magnetic nanoparticle detection assay. *Front. Bioeng. Biotechnol.* 10:939807. doi: 10.3389/fbioe.2022.939807

Nucleic acid amplification strategies for volume-amplified magnetic nanoparticle detection assay

Zhongchao Huang, Jing Li, Hongwen Zhong and Bo Tian*

Department of Biomedical Engineering, School of Basic Medical Science, Central South University, Changsha, Hunan, China

Magnetic nanoparticles (MNPs) can be quantified based on their magnetic relaxation properties by volumetric magnetic biosensing strategies, for example, alternating current susceptometry. Volume-amplified magnetic nanoparticle detection assays (VAMNDAs) employ analyte-initiated nucleic acid amplification (NAA) reactions to increase the hydrodynamic size of MNP labels for magnetic sensing, achieving attomolar to picomolar detection limits. VAMNDAs offer rapid and user-friendly analysis of nucleic acid targets but present inherence defects determined by the chosen amplification reactions and sensing principles. In this mini-review, we summarize more than 30 VAMNDA publications and classify their detection models for NAA-induced MNP size increases, highlighting the performances of different linear, cascade, and exponential NAA strategies. For some NAA strategies that have not yet been reported in VAMNDA, we predicted their performances based on the reaction kinetics and feasible detection models. Finally, challenges and perspectives are given, which may hopefully inspire and guide future VAMNDA studies.

KEYWORDS

magnetic biosensing, molecular amplification, magnetic nanoparticles, Brownian relaxation, homogeneous assays, volumetric sensing

Introduction

Magnetic micron/nano-sized particles stand out in comparison to alternative nanomaterials due to their unique properties, for example, easy manipulation, biocompatibility, signal stability, and high contrast (against the inherently negligible magnetic susceptibilities of biological objects), allowing for extensive applications in biomedical engineering (Gloag et al., 2019; Moerland et al., 2019; Cheng et al., 2021). Magnetic nanoparticles (MNPs), including micron-sized particles consisting of nanocomposites, can be directly analyzed as labels and transducers by magnetic sensors, facilitating an ideal mix-and-read biosensing approach that is attractive for on-site analysis and point-of-care testing (Schrittwieser et al., 2016; Xianyu et al., 2018). Based on the sensing principle, MNP detection sensors can be classified as surface-based and volumetric sensors (Issadore et al., 2014). Surface-based MNP sensing (e.g., micro-

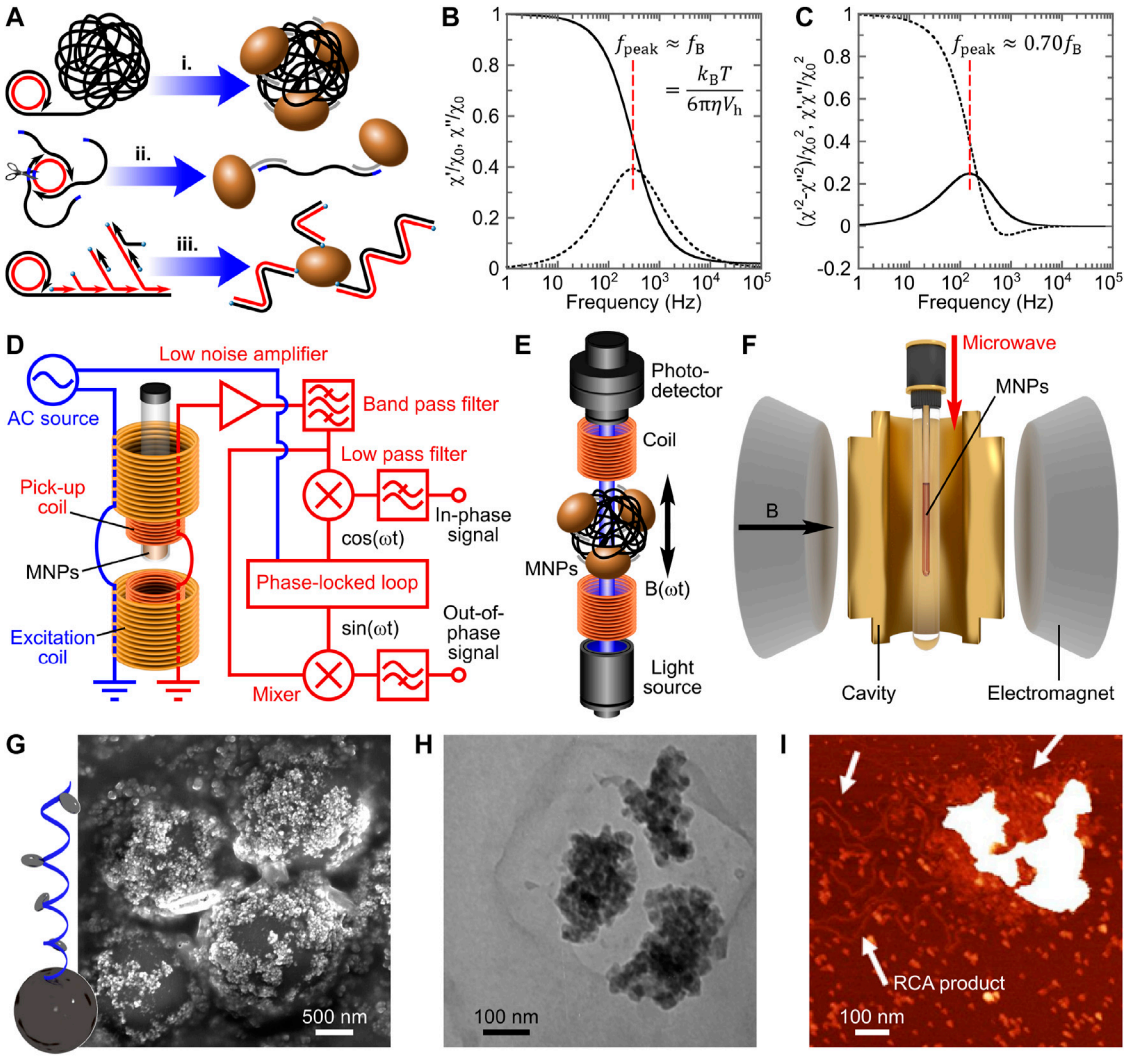

FIGURE 1
The basic principle of volume-amplified magnetic nanoparticle detection assays. **(A)** Three typical detection models for the nucleic acid amplification-based hydrodynamic size increase of MNPs, instanced by conventional, nicking-enhanced, and hyperbranched rolling circle amplification strategies, respectively. **(B)** Spectra of normalized in-phase and out-of-phase magnetic susceptibility (χ'/χ_0 and χ''/χ_0), represented by solid and dashed lines, respectively. **(C)** Spectra of normalized in-phase and out-of-phase optomagnetic output, corresponding to $(\chi'^2 - \chi''^2)/\chi_0^2$ and $\chi'\chi''/\chi_0^2$ in AC susceptometry, represented by solid and dashed lines, respectively. Panels **(B,C)** are adapted with permission from Tian et al. (2017), Copyright 2017, American Chemical Society. Detection schematics of **(D)** AC susceptometer (with a lock-in amplifier), **(E)** optomagnetic sensor, and **(F)** ferromagnetic resonance spectrometer. Panel **F** is adapted with permission from Tian et al. (2018a), Copyright 2018, American Chemical Society. **(G)** Scanning electron microscopy micrograph of core-satellite magnetic superstructures with 100 nm MNP satellites. Adapted with permission from Tian et al. (2018b), Copyright 2017, American Chemical Society. **(H)** Transmission electron microscopy micrograph of 130 nm MNPs aggregated by a DNA coil (only a salt precipitate can be observed). Adapted with permission from Akhtar et al. (2010), Copyright 2010, American Chemical Society. **(I)** Atomic force microscopy micrograph of 100 nm MNPs aggregated by a DNA coil. Adapted with permission from Oropesa-Nuñez et al. (2020), Copyright 2020, American Chemical Society.

Hall sensing and giant magnetoresistance sensing) detects the MNP's magnetic stray field induced by an external magnetic field. Due to the fast decay of the magnetic stray field with distance, only MNPs located close to the surface of the sensing element can be detected with the requirement of separation steps to remove unbound MNPs. In contrast, volumetric magnetic sensing could measure the presence and/or the property (e.g., relaxivity) changes of MNPs dispersed in the entire suspension, which is simple and convenient (Lee et al., 2015), especially when combined with homogeneous reaction strategies. The hydrodynamic size changes of MNPs are related to several magnetic properties such as Brownian relaxation frequency and magnetic anisotropy, allowing the volume-amplified magnetic nanoparticle detection assay (VAMNDA)

(Strömberg et al., 2008) based on different volumetric magnetic sensors.

Various nucleic acid amplification (NAA) strategies have been employed to increase the hydrodynamic volume of MNPs in VAMNDA. The hydrodynamic size increase of MNPs can be induced by analyte-initiated NAA in three detection models: (I) micrometer-sized single-stranded tandem amplicon coil-induced MNP aggregation, (II) amplicon monomer-mediated MNP linkage, and (III) double-stranded tandem amplicon chain-based MNP "hair growth," as illustrated in Figure 1A i, ii, and iii, respectively. In VAMNDA, the NAA-induced hydrodynamic size changes of MNPs are usually analyzed by alternating current (AC) susceptometry (or equivalent methodologies), measuring the susceptibility of MNPs exposed to an AC magnetic field. For commonly used MNPs with diameters of 30–300 nm, the MNP's relaxation process after switching off the external field is dominated by thermal rotational diffusion, that is, Brownian relaxation (Strömberg et al., 2007b). In AC susceptometry, for the simplest case, the Brownian relaxation frequency f_B of the MNP is found as the peak position of the out-of-phase magnetic susceptibility (χ'') spectrum shown in Figure 1B (Cole and Cole, 1941; Strömberg et al., 2007a): $f_{peak} \approx f_B = k_B T (6\pi\eta V_h)^{-1}$, where $k_B T$ is the thermal energy, η is the viscosity of the suspension, and V_h is the hydrodynamic volume of MNP. Accordingly, AC susceptometry can be applied for analyzing the concentration (related to the peak amplitude) and the hydrodynamic size (related to the peak frequency) of MNP objects, enabling the quantification of the target molecule initiating NAA. Most of the other magnetic sensing principles used in VAMNDA, such as optomagnetic sensor (Donolato et al., 2015a; Fock et al., 2017a, 2017b) and anisotropic magnetoresistance sensor (Østerberg et al., 2013a; 2013b, 2014), were designed referring to the AC susceptometry (Figure 1C). Detection schematics of AC susceptometer (with a lock-in amplifier), optomagnetic sensor, and ferromagnetic resonance spectrometer are illustrated in Figures 1D, E, and F, respectively. The critical performances of these VAMNDAs, for example, the limit of detection (LOD) and the total assay time, are determined mainly by the NAA strategy (Xiao et al., 2022). Herein, we introduce the concepts and performances of different NAA strategies employed in VAMNDAs, followed by the discussion of challenges and perspectives in this technique, which may hopefully inspire and guide future VAMNDA studies.

Rolling circle amplification

Owing to its simplicity, robustness, and high efficiency, rolling circle amplification (RCA) is the most widely adopted isothermal NAA in biomedical engineering (Ali et al., 2014; Soares et al., 2021; Yao et al., 2021). RCA is the most effective linear amplification due to (I) the conformational stresses that facilitate the strand displacement (Joffroy et al., 2018) and (II) the high polymerizing processivity of the polymerase (whereas in linear template-based amplification reactions, polymerases undergo cycles of diffusion-polymerization-dissociation). In phi29 polymerase-based RCA, ca. 10^5 nt-long single-stranded tandem amplicons (about 10^3 times amplification) can be synthesized in 1 h (Banér et al., 1998). Moreover, a single-nucleotide specific process, that is, padlock probe ligation, is usually employed to prepare circular templates for the following RCA, offering the whole reaction system an ability of single-nucleotide discrimination (Nilsson et al., 2000). RCA amplicons form micrometer-sized DNA coils in the aqueous solution, which can be quantified by VAMNDA model I (Figure 1A, i). Figure 1G shows a representative scanning electron microscopy micrograph of RCA coil-aggregated MNPs on the surface of microbeads, demonstrating the formation of micrometer-sized MNP aggregates (Tian et al., 2018b). RCA coil-aggregated MNPs have dramatically increased hydrodynamic volumes characterized by a χ'' peak located at low frequencies (usually out of the detection window). As the remaining unbound MNPs instead of the aggregated MNPs are detected, high signal homogeneity can be obtained, allowing multiplex detection employing MNP labels of different sizes (with distinguishable χ'' peaks) (Strömberg et al., 2009, 2014; Tian et al., 2017).

For RCA-based end-point VAMNDA, where an additional hybridization step is required to anneal probe-modified MNPs onto the coils, 1–10 pM, LODs were reported with total assay times around 2 h (including 1 h of RCA) and dynamic detection ranges of approximately two orders of magnitude (Donolato et al., 2015b; Bejhed et al., 2015; Blomgren et al., 2018; Sepehri et al., 2018; Tian et al., 2019b). By using a microfluidic sample handling system with a simultaneous differential sensor, Sepehri et al. improved the picomolar LOD to 45 fM, being the most sensitive conventional RCA-based VAMNDA (Sepehri et al., 2019). However, in the end-point detection format, MNPs can probably be stopped at the surface of RCA coils due to the multivalent binding reaction, resulting in a limited aggregation effect (Zardán Gómez de la Torre et al., 2010). Transmission electron microscopy and atomic force microscopy studies showed that only a few particles were bound to each RCA coil (Figures 1H, I), suggesting potentially higher sensitivity of the real-time MNP aggregation-based assay (Akhtar et al., 2010; Oropesa-Nuñez et al., 2020). In order to increase the MNP-to-coil ratio and shorten the total assay time, real-time VAMNDAs were presented by performing RCA and MNP hybridization simultaneously with magnetic incubation (i.e., applying magnetic actuation to enhance the binding kinetics) and optomagnetic phase lag sensing, which could achieve an LOD of 0.3 pM. within 90 min (Tian et al., 2019a; Minero et al., 2020).

Due to the steric hindrance and electrostatic repulsion, real-time RCA can hardly achieve the theoretical highest sensitivity (Zardán Gómez de la Torre et al., 2010). Nicking-enhanced RCA (NickRCA) performs nicking reactions during RCA, generating single-stranded amplicon monomers instead of amplicon coils (Li et al., 2010). Moreover, NickRCA allows several polymerases to act simultaneously on one single circular template, which further improves the amplification efficiency (Tian et al., 2019a).

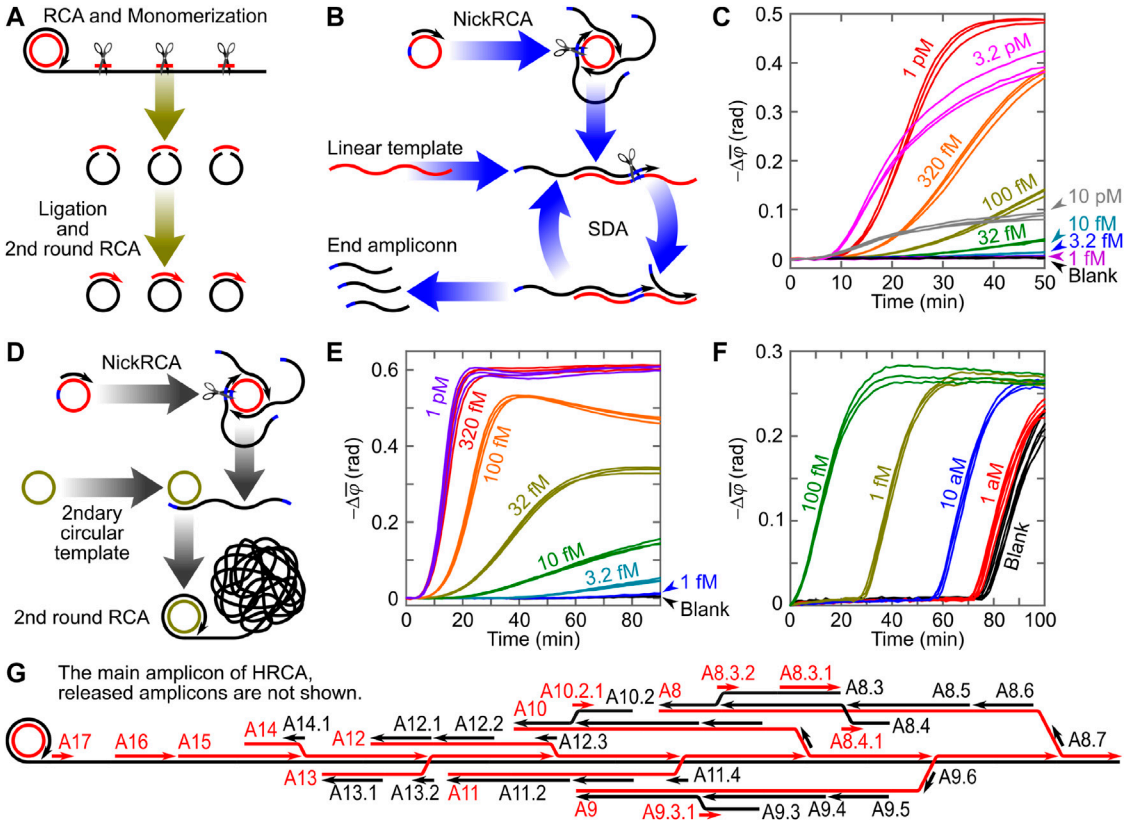

FIGURE 2
(A) Schematic illustration of conventional C2CA. **(B,C)** Schematic illustration and time-resolved optomagnetic signals (phase lag increases) of NECA-based VAMNDA. **(D,E)** Schematic illustration and time-resolved optomagnetic signals of HC2CA-based VAMNDA. **(F)** Time-resolved optomagnetic signals of PG-RCA-based VAMNDA. Panels **(C,E,F)** are adapted with permission from Tian et al. (2020a, 2020b, 2020c), Copyright 2020, Elsevier and Oxford University Press. **(G)** Illustration of HRCA processes on the RCA coil (amplicons that have already been released from the RCA coil are not shown). A8 means the eighth amplicon produced on the RCA coil (A1-A7 have been released), and A8.3 means the third amplicon produced on A8 (A8.1 and A8.2 have been released).

Amplicon monomers can bridge MNPs for turn-on measurement (detection model II, Figure 1A, ii). By real-time optomagnetic sensing of MNP phase lag in response to an AC field, NickRCA achieved an LOD of 15 fM target DNA with a total assay time of ca. 100 min (Tian et al., 2019a), which is the lowest LOD obtained by linear amplification-based VAMNDAs. As a comparison, optomagnetic analysis of synthetic DNA monomers (without NAA) presented an LOD of 50 pM. (Mezger et al., 2015), suggesting amplification of NickRCA of ca. 3×10^3 times.

Linear RCA-based VAMNDAs have been demonstrated for the quantification of bacterial/viral sequences (representing, e.g., influenza virus), discrimination of drug-resistance single-nucleotide mutations of *Mycobacterium tuberculosis*, and biplex detection of *Vibrio cholerae* and *Escherichia coli*. However, LODs at a 10^{-14} M range for nucleic acid targets are still inferior for many clinical applications (e.g., virus detection), suggesting the utilization of more efficient NAA strategies.

RCA-based cascade amplification

A cascade amplification strategy consists of tandemly performed amplification reactions, where the product of one amplification reaction is the trigger, primer, or template of the subsequent amplification reaction. Cascade amplification strategies are versatile to involve various tool enzymes at the expense of complicated strategy design (e.g., polymerases with exonucleolytic activity can digest the intermediate amplicons), especially for the one-pot homogeneous cascade amplification strategies that are preferred for VAMNDA. By stepwise performing n round of linear amplification reactions with the same amplification efficiency E_{li}, a cascade amplification obtains an ideal efficiency of $E_{ca} = (E_{li}/n)^n$. Therefore, under ideal conditions, the maximum cascade amplification efficiency, $E_{ca,\ max} = e^{E_{li}/e}$, can be achieved at $n = E_{li}/e$. However, for homogeneous cascade amplification, $E_{hca} = (E_{li})^n$. In reality,

however, considering the complicated design/operation and efficiency losses, only two to three reactions are tandemly incorporated for target detection.

Circle-to-circle amplification (C2CA, illustrated in Figure 2A) is a representative cascade amplification that converts RCA amplicon coils into multiple circular monomers (through endonuclease monomerization followed by ligation) as templates for subsequent RCA (Dahl et al., 2004). The ideal gain of C2CA (i.e., the quantity of generated amplicon) is $A_{C2CA} = E_{RCA}^{n}\prod_{i=1}^{n} t_i$, where E_{RCA} is the amplification efficiency of RCA and t_i is the reaction time of RCA round i. For immuno-recognition of *Bacillus globigii* spores followed by a proximity ligation assay and C2CA for VAMNDA, LODs of ca. 500 and 50 spores were reported by incorporating two and three RCA rounds, respectively (Zardán Gómez de la Torre et al., 2012). Other C2CA-based VAMNDA studies also suggested sub-femtomolar LODs for the bacterial DNA (synthetic and patient samples containing *Escherichia coli* sequences) but without showing a systematic dose-response curve or signal-noise analysis (Göransson et al., 2010; Mezger et al., 2015). Despite the high sensitivity, conventional C2CA requires tedious and time-consuming stepwise operations with different reaction temperatures (since monomerization and ligation are incompatible processes) and can only be analyzed in an end-point format (model I or II).

For homogeneous cascade amplification, nicking-assisted on- and off-loop enzymatic cascade amplification (NECA, illustrated in Figure 2B) comprises a NickRCA to generate primers of a subsequent strand-displacement amplification (SDA) for VAMNDA model II (Tian et al., 2020a). Both NickRCA and SDA were designed with the same template sequence: a padlock probe ligation process was employed to produce the circular template of NickRCA, leaving unligated padlock probe molecules in the suspension served as the template of SDA. Before all the templates are occupied, the ideal gain of NECA follows a quadratic function, $A_{NECA} = E_{NickRCA}E_{SDA}t^2$, where t is the reaction time and $E_{NickRCA}$ and E_{SDA} are the efficiencies of NickRCA and SDA, respectively. After all the templates are occupied, amplicons are produced linearly with time, resulting in a quadratic-linear time-resolved signal increase (Figure 2C) with an LOD of 2 fM (detecting a synthetic Dengue virus sequence) obtained in ca. 70 min (Tian et al., 2020a).

Homogeneous C2CA (HC2CA, illustrated in Figure 2D) employs NickRCA to produce primers for the subsequent RCA, combining two amplification reactions in a one-pot homogeneous reaction to eliminate additional monomerization and ligation steps (Tian et al., 2020b). However, the secondary circular template competes with the detection probe. Thus, the RCA coils can hardly be monitored before all circular templates are occupied (either by a primer or by an amplicon coil), indicated by a dead time during which no signal can be detected: $t_{dead} = \sqrt{2m(E_{NickRCA}E_{RCA}x)^{-1}}$, where m is the concentration of the circular template and x is the target concentration. For $t > t_{dead}$, a linearly increased signal can be observed (Figure 2E) with an ideal gain of $A_{HC2CA} = (t - t_{dead})\sqrt{2mE_{NickRCA}E_{RCA}x}$. For the quantification of a synthetic SARS-CoV-2 RdRp sequence based on detection model I, HC2CA presented an LOD of 0.4 fM with a total assay time of ca. 100 min (Tian et al., 2020b). Although sensitive and robust (against background amplification), homogeneous cascade amplification strategies such as NECA and HC2CA are difficult to design and optimize, which limits their applications.

Exponential amplification

An exponential amplification reaction, for example, the polymerase chain reaction (PCR), generates amplicons serving as the trigger, primer, or template of the reaction itself. NickRCA can react exponentially if the circular templates are added as reagents (instead of being prepared by padlock probe ligation), which is known as primer-generation RCA (PG-RCA) (Murakami et al., 2009). PG-RCA amplicons can trigger the formation of MNP dimers for detection model II, obtaining an attomolar LOD for a synthetic Dengue virus sequence (Figure 2F) (Tian et al., 2020c). However, the rapid generation of amplicon monomers requires real-time MNP binding. Otherwise, MNPs could be saturated by an excess amount of amplicons without a significant hydrodynamic size increase. Considering that some exponential NAAs include either high-temperature processes or molecular crowding agents, real-time VAMNDAs based on these NAAs are challenging. This may explain why PCR, EXPAR (exponential amplification reaction), and RPA (recombinase polymerase amplification) have not been reported in VAMNDA so far.

Loop-mediated isothermal amplification (LAMP) produces double-stranded amplicons of different lengths. By using biotinylated primers, LAMP amplicons can attach to the streptavidin-modified MNPs for VAMNDA model III, which can be achieved by either an end-point MNP binding or a real-time on-particle amplification, resulting in attomolar LODs for different synthetic (e.g., a Zika virus sequence) and real (e.g., Newcastle disease virus) targets within 30 min (Tian et al., 2016b, 2016c; Minero et al., 2017). Except for the amplicon-based detection, precipitation of $Mg_2P_2O_7$ (a by-product of LAMP) onto MNPs can also be utilized for VAMNDA, providing a sub-femtomolar LOD by using a ferromagnetic resonance spectrometer (Tian et al., 2018a). Similar to LAMP, hyperbranched RCA (HRCA) is an exponential amplification strategy producing double-stranded amplicons of different lengths. HRCA employs a pair of primers

to trigger SDA on the RCA coil (Figure 2G) with a gain of $A_{HRCA} \propto 2^{E_{SDA}t}$. Although HRCA has not yet been reported in VAMNDA, we predict that HRCA-based VAMNDA can be realized in the detection model III (Figure 1A, iii).

Challenges and perspectives

Existing VAMNDA models present inherence defects: model I requires long single-stranded amplicons that can hardly be produced with high efficiency; model II has to discriminate MNP dimers from a background of individual MNPs; model III is limited by the length distribution of amplicons and cannot distinguish false-positive amplicons. Moreover, the sensitivity of VAMNDA is determined mainly by the amplification efficiency of the NAA strategy, implying that exponential NAAs are preferred for lower LODs. However, due to the mispriming, *ab initio* DNA synthesis, and polymerase side-reactions, nonspecific synthesis of false-positive products is inevitable in highly effective NAA reactions, especially the exponential ones (Zyrina and Antipova, 2021). A CRISPR/Cas12a-based internal negative control system was reported in combination with VAMNDA, which could indicate the onset of nonspecific amplification (Tian et al., 2020c). Nevertheless, such a warning system cannot suppress nonspecific amplification. We expect that the problem of nonspecific synthesis can hopefully be solved in the future by applying highly accurate and programmable techniques such as DNA logic gates.

For the purpose of system automation and miniaturization, one-pot homogeneous reactions are preferred for VAMNDA. However, clinical applications of NAA strategies usually consist of a series of processes such as analyte extraction and purification. The lab-on-a-disc technique can integrate multi-step assays into a chip on which density gradient centrifugation and centrifugo-pneumatic valving can be processed, facilitating a compact and fully automated sample-to-answer biosensor (Uddin et al., 2018). In another RCA-based VAMNDA study (Garbarino et al., 2019), all the detection processes, including target capture, padlock probe ligation, molecular amplification, and optomagnetic detection, were integrated into a microfluidic chip containing three connected reaction chambers, below which a motorized permanent magnet was positioned to move analytes (captured by magnetic microparticles) along the fluid channel.

For homogeneous VAMNDAs without any washing/separation steps, the multiplex sensing can be realized by utilizing MNPs showing distinct relaxivities. As reviewed in a previous section, MNPs of different hydrodynamic volumes can be distinguished based on their characteristic χ'' peaks for multiplex detection. However, due to the influence of MNP uniformity, only biplex VAMNDAs using 100 (or 80) and 250 nm sized MNPs have been demonstrated by far (Strömberg et al., 2009; Tian et al., 2016a, 2017). Finding the third MNP size with a distinguishable magnetic signal is not easy: smaller MNPs have weaker magnetic responses, whereas larger MNPs are easier to sediment and less sensitive to size changes. In order to solve this problem, VAMNDA studies can be carried out on multi-transducer platforms that analyze signals of different energies with lock-in techniques, which requires more interdisciplinary collaborations in the future.

Portable and ease-of-use magnetic biosensing systems based on the VAMNDA concept have been commercialized for clinical applications, for example, one-drop-of-blood quantitative virus tests (blusense-diagnostics.com). However, these commercialized biosensors were realized based on the (target antibody-induced) immuno-agglutination but not NAA, which could probably be explained by the lack of reliable and sensitive homogeneous isothermal amplification strategies with proper controls of background amplification. Nevertheless, some NAA-based VAMNDAs were verified by testing clinical samples such as virus specimens (vaccine and tissue) (Tian et al., 2016b) and bacterium specimens (urine) (Mezger et al., 2015), implying potential applications in diagnosis.

Conclusion

Following the trends of nanoscience, magnetics, and sensing techniques over the last decade, VAMNDAs have undergone a pronounced evolution toward point-of-care testing. However, despite the rapidly improved biosensing performances, technical challenges remain. We herein provide an overview of VAMNDA and introduce the concepts and performances of different NAA strategies employed in this technique. Thereafter, limitations and prospects toward point-of-care applications are discussed. We hope that this mini-review will motivate studies to help solve the current limitations that are preventing VAMNDA from clinical applications.

Author contributions

ZH: conceptualization, supervision, manuscript review and editing. JL and HZ: data analysis, manuscript review and editing. BT: project administration, funding acquisition, and original draft.

Funding

This work was financially supported by the National Natural Science Foundation of China (no. 32101214), the Hunan Provincial Natural Science Foundation of China (no. 2022JJ40582), and the Fundamental Research Funds for the Central Universities of Central South University (no. 202045006).

Conflict of interest

The authors declare that the research was conducted in the absence of any commercial or financial relationships that could be construed as a potential conflict of interest.

Publisher's note

References

Akhtar, S., Strömberg, M., Zardán Gómez de la Torre, T., Russell, C., Gunnarsson, K., Nilsson, M., et al. (2010). Real-space transmission electron microscopy investigations of attachment of functionalized magnetic nanoparticles to DNA-coils acting as a biosensor. *J. Phys. Chem. B* 114, 13255–13262. doi:10.1021/jp105756b

Ali, M. M., Li, F., Zhang, Z., Zhang, K., Kang, D. K., Ankrum, J. A., et al. (2014). Rolling circle amplification: A versatile tool for chemical biology, materials science and medicine. *Chem. Soc. Rev.* 43, 3324–3341. doi:10.1039/c3cs60439j

Banér, J., Nilsson, M., Mendel-Hartvig, M., and Landegren, U. (1998). Signal amplification of padlock probes by rolling circle replication. *Nucleic Acids Res.* 26, 5073–5078. doi:10.1093/nar/26.22.5073

Bejhed, R. S., Zardán Gómez de la Torre, T., Donolato, M., Hansen, M. F., Svedlindh, P., and Strömberg, M. (2015). Turn-on optomagnetic bacterial DNA sequence detection using volume-amplified magnetic nanobeads. *Biosens. Bioelectron.* 66, 405–411. doi:10.1016/j.bios.2014.11.048

Blomgren, J., Ahrentorp, F., Ilver, D., Jonasson, C., Sepehri, S., Kalaboukhov, A., et al. (2018). Development of a sensitive induction-based magnetic nanoparticle biodetection method. *Nanomaterials* 8, 887. doi:10.3390/nano8110887

Cheng, H. W., Tsao, H. Y., Chiang, C. S., and Chen, S. Y. (2021). Advances in magnetic nanoparticle-mediated cancer immune-theranostics. *Adv. Healthc. Mat.* 10, 2001451. doi:10.1002/adhm.202001451

Cole, K. S., and Cole, R. H. (1941). Dispersion and absorption in dielectrics I. Alternating current characteristics. *J. Chem. Phys.* 9, 341–351. doi:10.1063/1.1750906

Dahl, F., Banér, J., Gullberg, M., Mendel-Hartvig, M., Landegren, U., and Nilsson, M. (2004). Circle-to-circle amplification for precise and sensitive DNA analysis. *Proc. Natl. Acad. Sci. U. S. A.* 101, 4548–4553. doi:10.1073/pnas.0400834101

Donolato, M., Antunes, P., Bejhed, R. S., Zardán Gómez de la Torre, T., Østerberg, F. W., Strömberg, M., et al. (2015a). Novel readout method for molecular diagnostic assays based on optical measurements of magnetic nanobead dynamics. *Anal. Chem.* 87, 1622–1629. doi:10.1021/ac503191v

Donolato, M., Antunes, P., Zardán Gómez de la Torre, T., Hwu, E. T., Chen, C. H., Burger, R., et al. (2015b). Quantification of rolling circle amplified DNA using magnetic nanobeads and a Blu-ray optical pick-up unit. *Biosens. Bioelectron.* 67, 649–655. doi:10.1016/j.bios.2014.09.097

Fock, J., Jonasson, C., Johansson, C., and Hansen, M. F. (2017a). Characterization of fine particles using optomagnetic measurements. *Phys. Chem. Chem. Phys.* 19, 8802–8814. doi:10.1039/c6cp08749c

Fock, J., Parmvi, M., Strömberg, M., Svedlindh, P., Donolato, M., and Hansen, M. F. (2017b). Comparison of optomagnetic and AC susceptibility readouts in a magnetic nanoparticle agglutination assay for detection of C-reactive protein. *Biosens. Bioelectron.* 88, 94–100. doi:10.1016/j.bios.2016.07.088

Garbarino, F., Minero, G. A. S., Rizzi, G., Fock, J., and Hansen, M. F. (2019). Integration of rolling circle amplification and optomagnetic detection on a polymer chip. *Biosens. Bioelectron.* 142, 111485. doi:10.1016/j.bios.2019.111485

Gloag, L., Mehdipour, M., Chen, D., Tilley, R. D., and Gooding, J. J. (2019). Advances in the application of magnetic nanoparticles for sensing. *Adv. Mat.* 31, 1904385. doi:10.1002/adma.201904385

Göransson, J., Zardán Gómez de la Torre, T., Strömberg, M., Russell, C., Svedlindh, P., Strømme, M., et al. (2010). Sensitive detection of bacterial DNA by magnetic nanoparticles. *Anal. Chem.* 82, 9138–9140. doi:10.1021/ac102133e

Issadore, D., Park, Y. I., Shao, H., Min, C., Lee, K., Liong, M., et al. (2014). Magnetic sensing technology for molecular analyses. *Lab. Chip* 14, 2385. doi:10.1039/c4lc00314d

Joffroy, B., Uca, Y. O., Prešern, D., Doye, J. P. K., and Schmidt, T. L. (2018). Rolling circle amplification shows a sinusoidal template length-dependent amplification bias. *Nucleic Acids Res.* 46, 538–545. doi:10.1093/nar/gkx1238

Lee, H., Shin, T. H., Cheon, J., and Weissleder, R. (2015). Recent developments in magnetic diagnostic systems. *Chem. Rev.* 115, 10690–10724. doi:10.1021/cr500698d

Li, J., Deng, T., Chu, X., Yang, R., Jiang, J., Shen, G., et al. (2010). Rolling circle amplification combined with gold nanoparticle aggregates for highly sensitive identification of single-nucleotide polymorphisms. *Anal. Chem.* 82, 2811–2816. doi:10.1021/ac100336n

Mezger, A., Fock, J., Antunes, P., Østerberg, F. W., Boisen, A., Nilsson, M., et al. (2015). Scalable DNA-based magnetic nanoparticle agglutination assay for bacterial detection in patient samples. *ACS Nano* 9, 7374–7382. doi:10.1021/acsnano.5b02379

Minero, G. A. S., Nogueira, C., Rizzi, G., Tian, B., Fock, J., Donolato, M., et al. (2017). Sequence-specific validation of LAMP amplicons in real-time optomagnetic detection of Dengue serotype 2 synthetic DNA. *Analyst* 142, 3441–3450. doi:10.1039/c7an01023k

Minero, G. A. S., Bagnasco, M., Fock, J., Tian, B., Garbarino, F., and Hansen, M. F. (2020). Automated on-chip analysis of tuberculosis drug-resistance mutation with integrated DNA ligation and amplification. *Anal. Bioanal. Chem.* 412, 2705–2710. doi:10.1007/s00216-020-02568-x

Moerland, C. P., Van IJzendoorn, L. J., and Prins, M. W. J. (2019). Rotating magnetic particles for lab-on-chip applications-a comprehensive review. *Lab. Chip* 19, 919–933. doi:10.1039/C8LC01323C

Murakami, T., Sumaoka, J., and Komiyama, M. (2009). Sensitive isothermal detection of nucleic-acid sequence by primer generation-rolling circle amplification. *Nucleic Acids Res.* 37, e19. doi:10.1093/nar/gkn1014

Nilsson, M., Barbany, G., Antson, D. O., Gertow, K., and Landegren, U. (2000). Enhanced detection and distinction of RNA by enzymatic probe ligation. *Nat. Biotechnol.* 18, 791–793. doi:10.1038/77367

Oropesa-Nuñez, R., Zardán Gómez de la Torre, T., Stopfel, H., Svedlindh, P., Strömberg, M., and Gunnarsson, K. (2020). Insights into the formation of DNA-magnetic nanoparticle hybrid structures: Correlations between morphological characterization and output from magnetic biosensor measurements. *ACS Sens.* 5, 3510–3519. doi:10.1021/acssensors.0c01623

Østerberg, F. W., Rizzi, G., and Hansen, M. F. (2013a). On-chip measurements of Brownian relaxation of magnetic beads with diameters from 10 nm to 250 nm. *J. Appl. Phys.* 113, 154507. doi:10.1063/1.4802657

Østerberg, F. W., Rizzi, G., Zardán Gómez de la Torre, T., Strömberg, M., Strømme, M., Svedlindh, P., et al. (2013b). Measurements of Brownian relaxation of magnetic nanobeads using planar Hall effect bridge sensors. *Biosens. Bioelectron.* 40, 147–152. doi:10.1016/j.bios.2012.07.002

Østerberg, F. W., Rizzi, G., Donolato, M., Bejhed, R. S., Mezger, A., Strömberg, M., et al. (2014). On-chip detection of rolling circle amplified DNA molecules from Bacillus globigii spores and *Vibrio cholerae*. *Small* 10, 2877–2882. doi:10.1002/smll.201303325

Schrittwieser, S., Pelaz, B., Parak, W. J., Lentijo-Mozo, S., Soulantica, K., Dieckhoff, J., et al. (2016). Homogeneous biosensing based on magnetic particle labels. *Sensors Switz.* 16, 828. doi:10.3390/s16060828

Sepehri, S., Eriksson, E., Kalaboukhov, A., Zardán Gómez de la Torre, T., Kustanovich, K., Jesorka, A., et al. (2018). Volume-amplified magnetic bioassay integrated with microfluidic sample handling and high-T_c SQUID magnetic readout. *Apl. Bioeng.* 2, 016102. doi:10.1063/1.4999713

Sepehri, S., Zardán Gómez de la Torre, T., Schneiderman, J. F., Blomgren, J., Jesorka, A., Johansson, C., et al. (2019). Homogeneous differential magnetic assay. *ACS Sens.* 4, 2381–2388. doi:10.1021/acssensors.9b00969

Soares, R. R. G., Madaboosi, N., and Nilsson, M. (2021). Rolling circle amplification in integrated microsystems: An uncut gem toward massively multiplexed pathogen diagnostics and genotyping. *Acc. Chem. Res.* 54, 3979–3990. doi:10.1021/acs.accounts.1c00438

Strömberg, M., Gunnarsson, K., Johansson, H., Nilsson, M., Svedlindh, P., and Strømme, M. (2007a). Interbead interactions within oligonucleotide functionalized ferrofluids suitable for magnetic biosensor applications. *J. Phys. D. Appl. Phys.* 40, 1320–1330. doi:10.1088/0022-3727/40/5/002

Strömberg, M., Gunnarsson, K., Valizadeh, S., Svedlindh, P., and Strømme, M. (2007b). Aging phenomena in ferrofluids suitable for magnetic biosensor applications. *J. Appl. Phys.* 101, 023911. doi:10.1063/1.2424522

Strömberg, M., Göransson, J., Gunnarsson, K., Nilsson, M., Svedlindh, P., and Strømme, M. (2008). Sensitive molecular diagnostics using volume-amplified magnetic nanobeads. *Nano Lett.* 8, 816–821. doi:10.1021/nl072760e

Strömberg, M., Zardán Gómez de la Torre, T., Göransson, J., Gunnarsson, K., Nilsson, M., Svedlindh, P., et al. (2009). Multiplex detection of DNA sequences using the volume-amplified magnetic nanobead detection assay. *Anal. Chem.* 81, 3398–3406. doi:10.1021/ac900561r

Strömberg, M., Zardán Gómez de la Torre, T., Nilsson, M., Svedlindh, P., and Strømme, M. (2014). A magnetic nanobead-based bioassay provides sensitive detection of single- and biplex bacterial DNA using a portable AC susceptometer. *Biotechnol. J.* 9, 137–145. doi:10.1002/biot.201300348

Tian, B., Bejhed, R. S., Svedlindh, P., and Strömberg, M. (2016a). Blu-ray optomagnetic measurement based competitive immunoassay for Salmonella detection. *Biosens. Bioelectron.* 77, 32–39. doi:10.1016/j.bios.2015.08.070

Tian, B., Ma, J., Zardán Gómez de la Torre, T., Bálint, Á., Donolato, M., Hansen, M. F., et al. (2016b). Rapid Newcastle disease virus detection based on loop-mediated isothermal amplification and optomagnetic readout. *ACS Sens.* 1, 1228–1234. doi:10.1021/acssensors.6b00379

Tian, B., Qiu, Z., Ma, J., Zardán Gómez de la Torre, T., Johansson, C., Svedlindh, P., et al. (2016c). Attomolar Zika virus oligonucleotide detection based on loop-mediated isothermal amplification and AC susceptometry. *Biosens. Bioelectron.* 86, 420–425. doi:10.1016/j.bios.2016.06.085

Tian, B., Ma, J., Qiu, Z., Zardán Gómez de la Torre, T., Donolato, M., Hansen, M. F., et al. (2017). Optomagnetic detection of MicroRNA based on duplex-specific nuclease-assisted target recycling and multilayer core-satellite magnetic superstructures. *ACS Nano* 11, 1798–1806. doi:10.1021/acsnano.6b07763

Tian, B., Liao, X., Svedlindh, P., Strömberg, M., and Wetterskog, E. (2018a). Ferromagnetic resonance biosensor for homogeneous and volumetric detection of DNA. *ACS Sens.* 3, 1093–1101. doi:10.1021/acssensors.8b00048

Tian, B., Qiu, Z., Ma, J., Donolato, M., Hansen, M. F., Svedlindh, P., et al. (2018b). On-particle rolling circle amplification-based core-satellite magnetic superstructures for MicroRNA detection. *ACS Appl. Mat. Interfaces* 10, 2957–2964. doi:10.1021/acsami.7b16293

Tian, B., Fock, J., Minero, G. A. S., Garbarino, F., and Hansen, M. F. (2019a). Ultrasensitive real-time rolling circle amplification detection enhanced by nicking-induced tandem-acting polymerases. *Anal. Chem.* 91, 10102–10109. doi:10.1021/acs.analchem.9b02073

Tian, B., Han, Y., Fock, J., Strömberg, M., Leifer, K., and Hansen, M. F. (2019b). Self-assembled magnetic nanoparticle–graphene oxide nanotag for optomagnetic detection of DNA. *ACS Appl. Nano Mat.* 2, 1683–1690. doi:10.1021/acsanm.9b00127

Tian, B., Fock, J., Minero, G. A. S., and Hansen, M. F. (2020a). Nicking-assisted on-loop and off-loop enzymatic cascade amplification for optomagnetic detection of a highly conserved dengue virus sequence. *Biosens. Bioelectron.* 160, 112219. doi:10.1016/j.bios.2020.112219

Tian, B., Gao, F., Fock, J., Dufva, M., and Hansen, M. F. (2020b). Homogeneous circle-to-circle amplification for real-time optomagnetic detection of SARS-CoV-2 RdRp coding sequence. *Biosens. Bioelectron.* 165, 112356. doi:10.1016/j.bios.2020.112356

Tian, B., Minero, G. A. S., Fock, J., Dufva, M., and Hansen, M. F. (2020c). CRISPR-Cas12a based internal negative control for nonspecific products of exponential rolling circle amplification. *Nucleic Acids Res.* 48, e30. doi:10.1093/nar/gkaa017

Uddin, R., Donolato, M., Hwu, E. T., Hansen, M. F., and Boisen, A. (2018). Combined detection of C-reactive protein and PBMC quantification from whole blood in an integrated lab-on-a-disc microfluidic platform. *Sensors Actuators B Chem.* 272, 634–642. doi:10.1016/j.snb.2018.07.015

Xianyu, Y., Wang, Q., and Chen, Y. (2018). Magnetic particles-enabled biosensors for point-of-care testing. *TrAC Trends Anal. Chem.* 106, 213–224. doi:10.1016/j.trac.2018.07.010

Xiao, X., Yuan, C., Li, T., Fock, J., Svedlindh, P., and Tian, B. (2022). Optomagnetic biosensors: Volumetric sensing based on magnetic actuation-induced optical modulations. *Biosens. Bioelectron.* 215, 114560. doi:10.1016/j.bios.2022.114560

Yao, C., Zhang, R., Tang, J., and Yang, D. (2021). Rolling circle amplification (RCA)-based DNA hydrogel. *Nat. Protoc.* 16, 5460–5483. doi:10.1038/s41596-021-00621-2

Zardán Gómez de la Torre, T., Strömberg, M., Russell, C., Göransson, J., Nilsson, M., Svedlindh, P., et al. (2010). Investigation of immobilization of functionalized magnetic nanobeads in rolling circle amplified DNA coils. *J. Phys. Chem. B* 114, 3707–3713. doi:10.1021/jp911251k

Zardán Gómez de la Torre, T., Ke, R., Mezger, A., Svedlindh, P., Strømme, M., and Nilsson, M. (2012). Sensitive detection of spores using volume-amplified magnetic nanobeads. *Small* 8, 2174–2177. doi:10.1002/smll.201102632

Zyrina, N. V., and Antipova, V. N. (2021). Nonspecific synthesis in the reactions of isothermal nucleic acid amplification. *Biochem. Mosc.* 86, 887–897. doi:10.1134/S0006297921070099

frontiers | Frontiers in Bioengineering and Biotechnology

TYPE Original Research
PUBLISHED 17 August 2022
DOI 10.3389/fbioe.2022.955713

OPEN ACCESS

EDITED BY
Hongna Liu,
iRepertore Inc., United States

REVIEWED BY
Xinjiang Cao,
Anyang Institute of Technology, China
Bin Liu,
Nanjing Medical University, China
Qi You,
Nanjing University, China

*CORRESPONDENCE
Ziyu He,
18774657648@163.com
Yan Deng,
hndengyan@126.com

SPECIALTY SECTION
This article was submitted to Biosensors and Biomolecular Electronics, a section of the journal Frontiers in Bioengineering and Biotechnology

RECEIVED 29 May 2022
ACCEPTED 18 July 2022
PUBLISHED 17 August 2022

CITATION
Chen Z, Zhao K, Tan B, Tong Z, He Z, Luo X, Cai L, Wang H, Leung PHM, Chow FW-N, Chen H and Deng Y (2022), Development of a high specificity typing method for the detection of herpes simplex virus. *Front. Bioeng. Biotechnol.* 10:955713. doi: 10.3389/fbioe.2022.955713

Development of a high specificity typing method for the detection of herpes simplex virus

Zhu Chen[1], Kaixuan Zhao[1], Boyu Tan[1], Zengrui Tong[1], Ziyu He[2]*, Xiaofang Luo[3], Lei Cai[4], Hanming Wang[5], Polly H. M. Leung[6], Franklin Wang-Ngai Chow[6], Hui Chen[1] and Yan Deng[1]*

[1]Hunan Key Laboratory of Biomedical Nanomaterials and Devices, Hunan University of Technology, Zhuzhou, China, [2]Department of Scientific Research, Zhuzhou Hospital Affiliated to Xiangya School of Medical, Central South University, Zhuzhou, China, [3]College of Chemistry and Bioengineering, Hunan University of Science and Engineering, Yongzhou, China, [4]Guangzhou Wondfo iCubate Biotech Co. Ltd., Guangzhou, China, [5]Wondfo Biotech Co. Ltd., Guangzhou, China, [6]Department of Health Technology and Informatics, The Hong Kong Polytechnic University, Hong Kong, China

Herpes disease is caused by Herpes simplex virus (HSV). It has become one of the global health problems. This paper reports a method for HSV type testing. First specific primers sequence for HSV-1 and HSV-2 were selected, designed, and synthesized. Then, these amplification products were proved by sequencing and analysis. Lastly, we optimized the reaction system and PCR reaction program by orthogonal design and sensitivity testing. Results showed that the lowest concentration in HSV-type testing is about 6.67×10^6 copies/ml. Moreover, the specificity of detection was very high. So, this method has very great potentials for HSV type testing in clinical practice.

KEYWORDS

HSV-1, HSV-2, orthogonal design, primer design, HSV typing

Introduction

Herpes disease, caused by Herpes Simplex Virus (HSV), has become one of the global health problems (Looker et al., 2017). HSV can cause high infant morbidity and infant mortality with mother-to-child transmission (James and Kimberlin, 2015). It includes Herpes simplex virus type 1 (HSV-1) and Herpes simplex virus type 2 (HSV-2), which are double-stranded DNA viruses belonging to the Herpesviridae family (Salvatore et al., 2019), causing persistent infection in the trigeminal or lumbosacral ganglia (Christine et al., 2016). Besides, the HSV-associated disease becomes malignant when the virus gets access to the central nervous system, which may result in herpes encephalitis (Koujah et al., 2018). HSV-1 mainly causes infection of skin other than genital organs, mucosa (oral mucosa), and organs (brain). HSV-2 mainly causes genital musoca skin infection. However, in these years, it is found that HSV-1 can be transmitted *via* sexual contact and genital herpes may also occur due to transmission of HSV-1 by oral-genital contact (Christian et al., 2019; Khan et al., 2019), which means that the line between HSV-1 and HSV-2 infection has become increasingly blurred and both viruses can infect genital epithelial cells and produce the same pathological mechanisms. And given that the latest

TABLE 1 Sequence information for plasmid used for polymerase chain reaction.

Primer name	Sequence information (5′–3′)	Amplification length (bp)
Plasmid-HSV-1	GTCATTCAGATATCCTGTCTGCTCTACGACCTGTCCACCACCGCCCTGGAGCACGTCCTCCTGTTTTCG CTCGGTTCCTGCGACCTCCCCGAATCCCACCTGAACGAGCTGGCGGCCAGGGGCCTGCCCACGCCCGTG GTTCTGGAATTCGACAGCGAATTCGAGATGCTGTTGGCCTTCATGACCCTTGTGAAACAGTACGGCCCC GAGTTCGTGACCGGGTACAACATCATCAACTTCGACTGGCCCTTCTTGCTGGCCAAGCTGACGGACATT TACAAGGTCCCCCTGGACGGGTACGGCCGCATGAACGGCCGGGGCGTGTTTCGCGTGTGGGACATA GGCCAGAGCCACTTCCAGAAGCGCAGCAAGATAAAGGTGAACGGCATGGTGAACATCGACATGTAC GGGATTATAACCGACAAGATCAAGCTCTCGAGCTACAAGCTCAACGCCGTGGCCGAAGCCGTCCTGAAG GACAAGAAGAAGG	490
Plasmid-HSV-2	CAGCCCTCGCCCCTGGGTCGGGAGGCGGTGGAACAGTTCTTCCGGCACGTGCGCGCCCAGCTGAACATC CGCGAGTACGTAAAGCAAAACGTCACCCCCAGGGAAACCGCCCTGGCGGGAGACGCGGCCGCCGCC TACCTGCGCGCGCGCACGTATGCCCCGGCGGCCCTCACGCCCGCCCCCGCGTACTGCGGGGTCGCAGAC TCGTCCACCAAAATGATGGGACGTCTGGCGGAAGCAGAAAGGCTCCTAGTCCCCCACGGCTGGCCC GCGTTCGCACCAACAACCCCCGGGGACGACGCGGGGGGCGGCACTGCCGCCCCCCAGACCTGCGGA ATCGTCAAGCGCCTCCTCAAGCTGGCCGCCACGGAGCAGCAGGGCACGACGCCCCCGGCGATCGCG GCTCTCATGCAGGACGCGTCGGTCCAAACCCCCCTGCCCGTGTACAGGATTACCATGTCCCCGACCGGC CAGGCGTTTGCCGCGGCGG	490

TABLE 2 Sequence information of the primers used for polymerase chain reaction.

Primer name	Sequence information (5′–3′)	Amplification length (bp)
PCR-H1-F	ATATCCTGTCTGCTCTACGACCTGTCCACCAC	469
PCR-H1-R	TCCTTCAGGACGGCTTCGGCCACGGCGTTGAG	
PCR-H2-F	AAATGATGGGACGTCTGGCGGAAGCAGAAAGG	267
PCR-H2-R	GCAAACGCCTGGCCGGTCGGGGACATGGTAA	

TABLE 3 Reaction system information for optimization by orthogonal design (μl).

Number	dd H_2O	PCR MIX	Primer 1	Primer 2	DNA
1	7.0	15.0	1.5	1.0	0.5
2	10.0	12.5	1.2	0.8	0.5
3	13.0	10.0	0.9	0.6	0.5
4	7.0	15.0	1.25	1.25	0.5
5	10.0	12.5	1.0	1.0	0.5
6	13.0	10.0	0.75	0.75	0.5
7	7.0	15.0	1.0	1.5	0.5
8	10.0	12.5	0.8	1.2	0.5
9	13.0	10.0	0.6	0.9	0.5

literature reports that the HSV-2 has infected more than 700 million people worldwide, early selection of appropriate methods for accurate diagnosis of HSV is particularly important (Dropulic et al., 2019; Harfouche et al., 2021; Rice, 2021).

At present, HSV detection methods mainly include cytology, immunology, molecular biology detection and so on. For example; 1) Virus isolation and culture is a reliable basis for definitive diagnosis of HSV infection in clinical practice today, but its operation is cumbersome and the time is long, and also needs other methods to assist identification (Qi et al., 2020; Wijesinghe et al., 2021). 2) Immunoassay has high specificity and insufficient sensitivity, which may lead to false negative (Chauhan et al., 2018; Fatima et al., 2021). 3) Nucleic acid detection methods in molecular biology have outstanding advantages, such as high sensitivity and specificity (Chen

TABLE 4 Information for polymerase chain reaction program optimization by orthogonal design.

Nos	Degeneration temperature (°C)	Degeneration time (s)	Annealing temperature (°C)	Annealing time (s)	Extension temperature (°C)	Extension time (s)
1	95	20	57	25	72	25
2	95	20	58	30	72	35
3	95	20	59	35	72	45
4	95	20	60	40	72	55
5	95	25	57	25	72	25
6	95	25	58	30	72	35
7	95	25	59	35	72	45
8	95	25	60	40	72	55
9	95	30	57	25	72	25
10	95	30	58	30	72	35
11	95	30	59	35	72	45
12	95	30	60	40	72	55
13	95	35	57	25	72	25
14	95	35	58	30	72	35
15	95	35	59	35	72	45
16	95	35	60	40	72	55

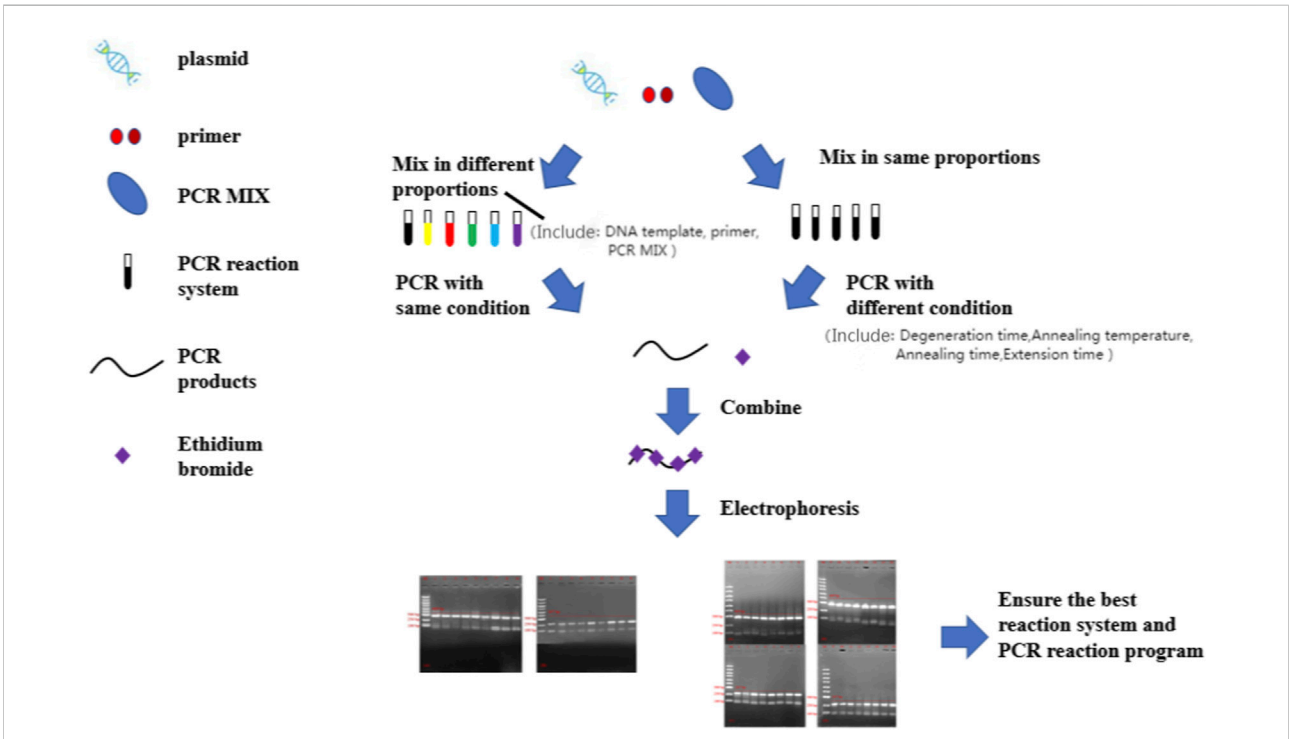

FIGURE 1
The flowchart for optimization of a high specificity typing PCR method. PCR, polymerase chain reaction.

et al., 2020; Tang et al., 2020; Chen et al., 2022; Liu et al., 2022). So, this study aimed to design a PCR typing detection method for detecting HSV-1 or HSV-2 in the same reaction system (Figure 1), and it has high specificity and is difficult to appear with false positive. This work hopes to provide some new ideas for researchers in HSV-type identification in clinical practice.

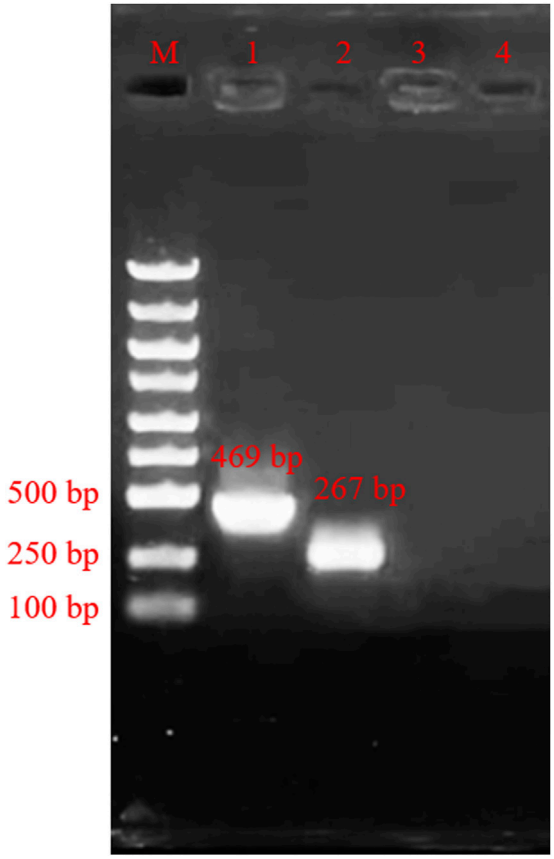

FIGURE 2
Agarose gel electrophoresis of amplification product. M: Marker; Lane 1, primers PCR-H1-F and primer PCR-H1-R; Lane 2, primers PCR-H2-F and primer PCR-H2-R; Lane 3, Negative control of primers PCR-H1-F and primer PCR-H1-R; Lane 4, Negative control of primers PCR-H2-F and primer PCR-H2-R.

Materials and methods

Materials

We chose the CDS region of HSV-1 and HSV-2 as the target gene sequence. Then we compared homologous sequences on NCBI to identify the target sequence. The plasmids from HSV-1 and plasmid from HSV-2 were synthesized by Sangon Biotech (Shanghai, China) (Table 1). The MIX used for PCR (including Taq DNA polymerase, dNTPs, buffer, etc.) was a 2x concentrated PCR amplification premixed solution purchased from Sangon Biotech (Shanghai, China). PCR not only removes the complex operation process by adding templates and primers to the system, but also saves time. According to the design principles for PCR primers, those primers were designed by using primer 5 software for our selected gene regions (Table 2).

Design primer for PCR assays

We design the two pairs of designed primers for PCR and verify them useful. The reaction components for PCR assays were as follows: 12.5 μl PCR Mix, 10 μl dd H_2O, 0.5 μl HSV-1 template or HSV-2 template, 1 μl primer 1-F and 1 μl primer 1-R or 1 μl primer 2-F and 1 μl primer 2-R. It was amplified in Eppendorf Master cycler PCR instrument (Eppendorf, Hamburg, Germany) for predegeneration at 72°C for 5 min, and then 35 cycles at 95°C 30 s, 58°C for 30 s, and 72°C 30 s, followed by a final extension at 72°C for 10 min. The PCR products were sequenced by Sangon Biotech (Shanghai, China), after being analyzed by 1% agarose gel.

PCR typing assays

To verify whether the typing PCR was feasible. The reaction components for the PCR assays were as follows:12.5 μl PCR Mix, 10 μl dd H_2O, 0.5 μl HSV-1 template or HSV-2 template, 0.5 μl primer 1-F, 0.5 μl primer 1-R, 0.5 μl primer 2-F, 0.5 μl primer 2-R. It was amplified in Eppendorf Master cycler PCR instrument (Eppendorf, Hamburg, Germany) for predegeneration at 95°C for 5 min, and then 35 cycles at 95°C 30 s, 58°C for 30 s, and 72°C 30 s, followed by a final extension at 72°C for 10 min. Finally, the PCR products were analyzed by 1% agarose gel.

Optimization of reaction system by orthogonal design

Referring to others' work (Zeng et al., 2015; Zeng et al., 2016; Tang et al., 2018; Mou et al., 2019; Gong et al., 2021), the gradient experiments for single factor and multilevel orthogonal design were integrated and results from the two experiments were analyzed to find the best PCR reaction system (Table 3).

Optimization of PCR reaction program by orthogonal design

As shown in Table 4, the gradient experiments for single factor and multilevel orthogonal design were integrated and results from the two experiments were analyzed to find the best PCR reaction conditions. The predegeneration was at 95°C for 5 min and final extension was at 72°C for 10 min.

Sensitivity experimental design

We diluted the plasmid of HSV-1 and plasmid from HSV-2 at 6.67×10^{10} copies/ml to 6.67×10^{6} copies/ml concentrations in a 10-fold gradient with dd H_20. Plasmids

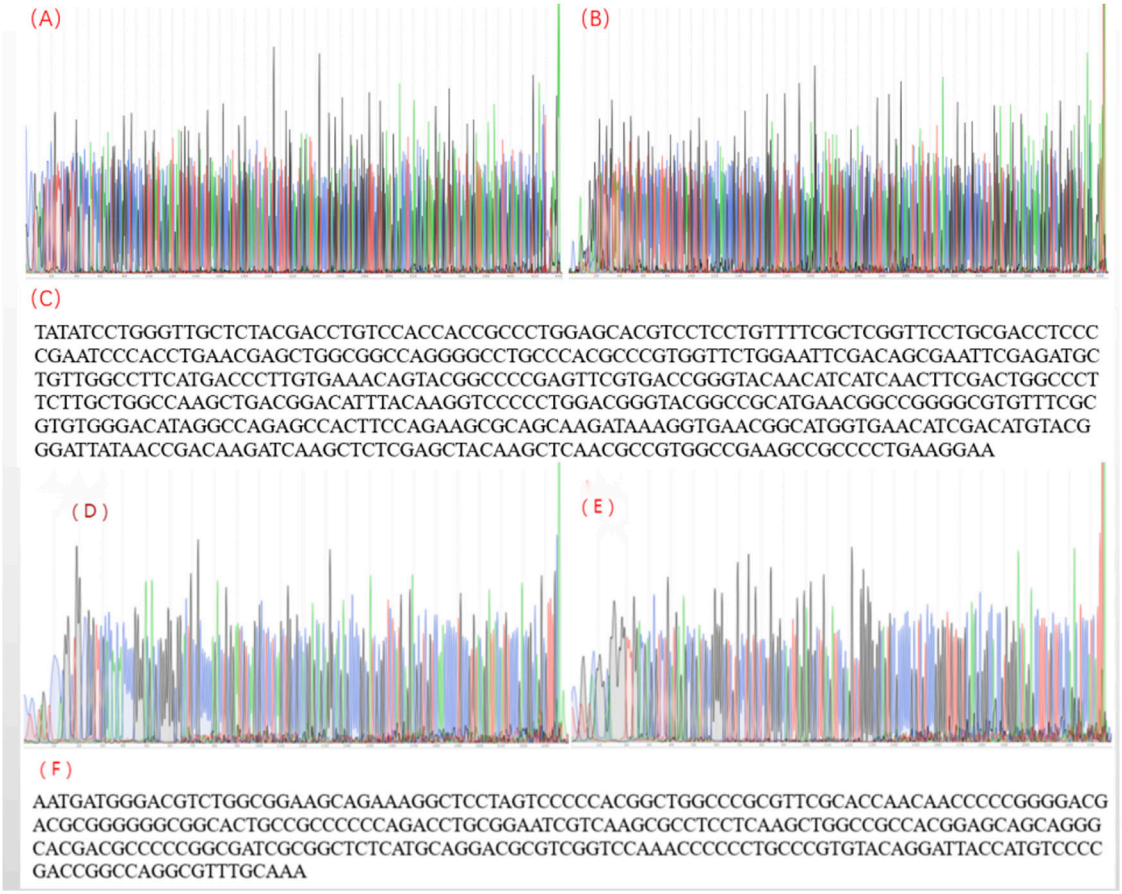

FIGURE 3
The sequencing result for herpes simplex virus polymerase chain reaction products. **(A)** The sequencing peak map for HSV-1-F; **(B)** The sequencing peak map for HSV-1-R; **(C)** Assembling from sequencing data of herpes simplex virus 1; **(D)** The sequencing peak map for HSV-2-F; **(E)** The sequencing peak map for HSV-2-R; **(F)** Assembling from sequencing data for herpes simplex virus 2.

(from 6.67 × 10^8 copies/ml to 6.67 × 10^5 copies/ml) with different concentrations were added into the reaction system. It was then amplified in a PCR instrument (Eppendorf, Hamburg, Germany) for predegeneration at 95°C for 5 min, and then 35 cycles at 95°C 20 s, 59°C for 35 s, and 72°C 45 s, followed by a final extension at 72°C for 10 min.

Results and discussion

The feasibility of primers

The results from verifications of our designed primers are shown in Figure 2 below. The location of the bands was correct, and the bands had high specificity. Then the products were sent to company (Shanghai, China) for sequencing. The sequencing results are shown in Figure 3, and the results are correct. The designed primers were then used for subsequent experiments.

PCR typing system detection

Using the confirmed reaction system, we added the HSV-1 template plasmids into tube-1, and template plasmids from HSV-2 into tube-2. We then added dd H_2O into tube-3 as a negative control. The results are shown in Figure 4. The obtained bands' specificity was high, and nonspecific amplification did not appear in our result.

Optimization of reaction system

Nine different combinations of experiments were analyzed and optimized due to differences in the templates, primers, and MIX. As shown in Figure 5, we can see that 1, 2, 3, 4, 5, and 7 bands for HSV-1 were greater than 6, 8, and 9. 5, 7, 8, and 9 for the nine HSV-2 systems were significantly brighter than for other systems. Combining above analysis, system 5 (12.5 μl PCR Mix,

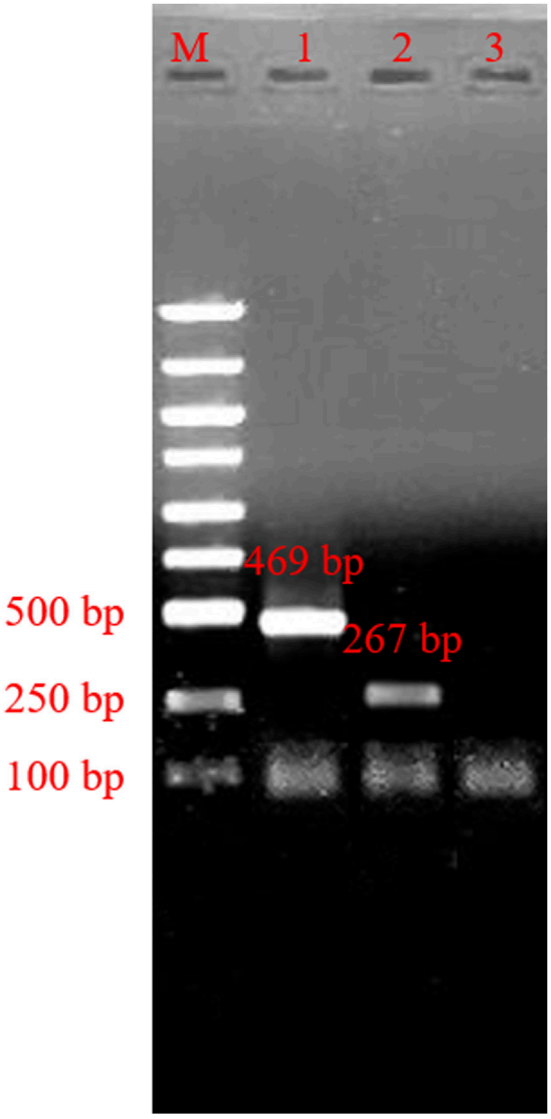

FIGURE 4
Agarose gel electrophoresis of typing polymerase chain reaction product. M: marker; line 1, typing polymerase chain reaction product of herpes simplex virus 1; line 2, typing polymerase chain reaction product of herpes simplex virus 2; Lane 3, Negative control.

10 μl dd H_2O, 0.5 μl HSV-1 template or HSV-2 template, 0.5 μl primer 1-F, 0.5 μl primer 1-R, 0.5 μl primer 2-F, 0.5 μl primer 2-R) was the best choice.

Optimization of the PCR reaction program

Different combinations of 16 sets of PCR reaction programs were analyzed and optimized, and the results are shown in Figure 6. In HSV-2's program optimization, the third program band was brighter than in the other programs. With HSV-1's program optimization, the difference in the results was small. Combining both analyses, the third program band was clear, and had good stability. So, program 3 (degeneration time 20 s, annealing temperature 59 degrees, annealing time 35 s, extension time 45 s) was the best reaction program.

Sensitivity inspection

The primer length designed in this experiment was more than 30 bp, slightly larger than the traditional PCR primer design length (The traditional PCR primer design length is about 15–30 bp). It enhanced the specificity of PCR amplification, leading to a certain decrease in the amplification efficiency as shown by results in Figure 7. 6.67×10^8 copies/ml-6.67×10^6 copies/ml can get bands, 6.67×10^5 copies/ml can't get bands, so the lowest concentration in HSV-type testing is about 6.67×10^6 copies/ml.

Conclusion

The current study on HSV detection was based on the HSV typing PCR reaction system and optimization of reaction procedures. Since the line between HSV-1 and HSV-2 infection has become increasingly blurred, it was necessary to establish a PCR reaction system suitable for HSV typing detection. The system is influenced by multiple aspects, including interactions of DNA concentration, primers concentration, and 2 × Taq PCR Master Mix content. This experiment is slightly different from the establishment and optimization of traditional PCR reaction system (Yang et al., 2020). The traditional PCR reaction system is a single-factor investigation method to determine the content of various components in the system. Although the herein results are intuitive, it ignores the integrity of the system (the mutual influence and internal connection between each component). The experiment adopts the orthogonal optimization method, which makes up for the deficiency of single-factor investigation, takes into account the intrinsic correlation of components, shortens the time to optimize the experimental method and saves energy. The establishment and optimization of traditional PCR reaction system usually examines the influence of five factors on the system, including (DNA template, primer, Tap DNA primer, polymerase, Mg^{2+}, dNTP), this experiment adopted 2 × Taq PCR Master Mix, to transform the original complex 5 factors into 3 factors, simplifying the establishment and optimization of the reaction system and facilitating subsequent experiments. This HSV typing detection system with high availability of HSV with high stability was verified by suitable target genes and designed primers.

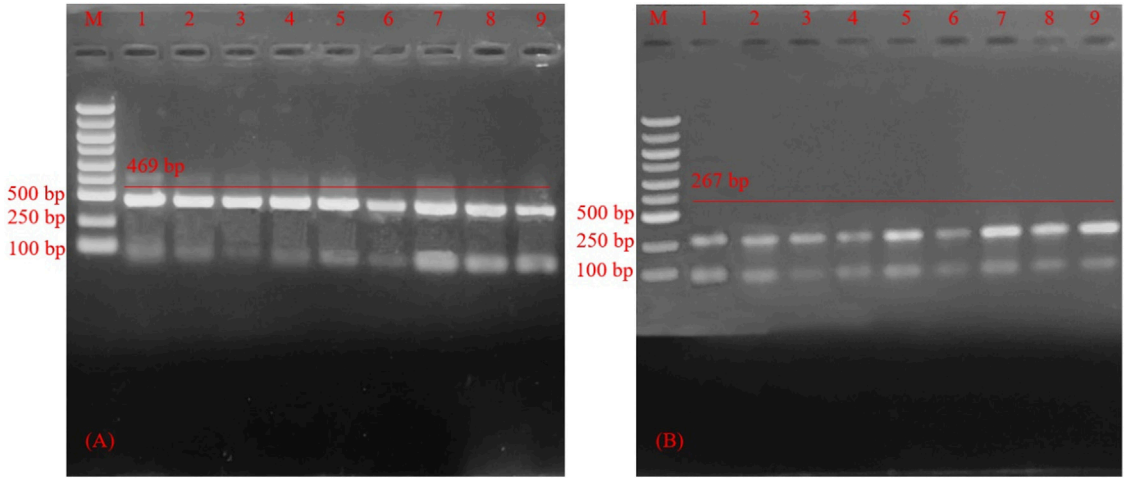

FIGURE 5
Agarose gel electrophoresis of polymerase chain reaction product of reaction system optimization **(A)** Agarose gel electrophoresis for polymerase chain reaction product of optimization of herpes simplex virus -1 reaction system. M: Marker; Lane 1–9, primers PCR-H1-F and PCR-H1-R PCR product of optimization of herpes simplex virus 1 reaction system. **(B)** Agarose gel electrophoresis for polymerase chain reaction product optimization of herpes simplex virus 2 reaction system. M: Marker; Lane 1–9, polymerase chain reaction product of optimization of herpes simplex virus 2 reaction system.

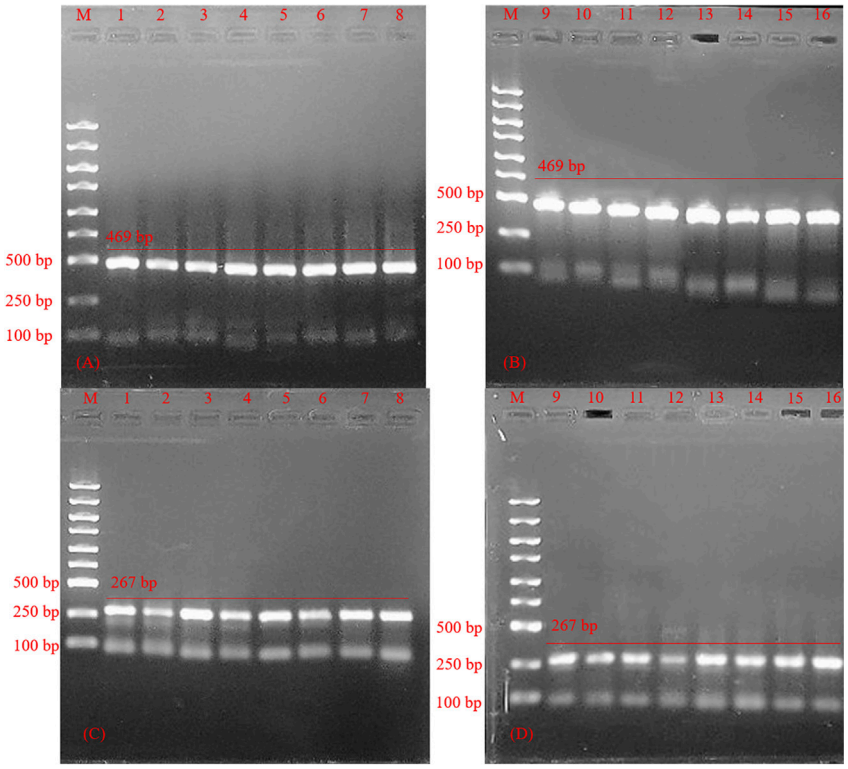

FIGURE 6
Agarose gel electrophoresis for polymerase chain reaction product optimization of polymerase chain reaction program. **(A,B)** Product of herpes simplex virus 1; M: marker; line 1–16, PCR product optimization of polymerase chain reaction program for herpes simplex virus 1; **(C,D)** Product of herpes simplex virus 2; M: marker; line 1–16, polymerase chain reaction product optimization of polymerase chain reaction program for herpes simplex virus 2.

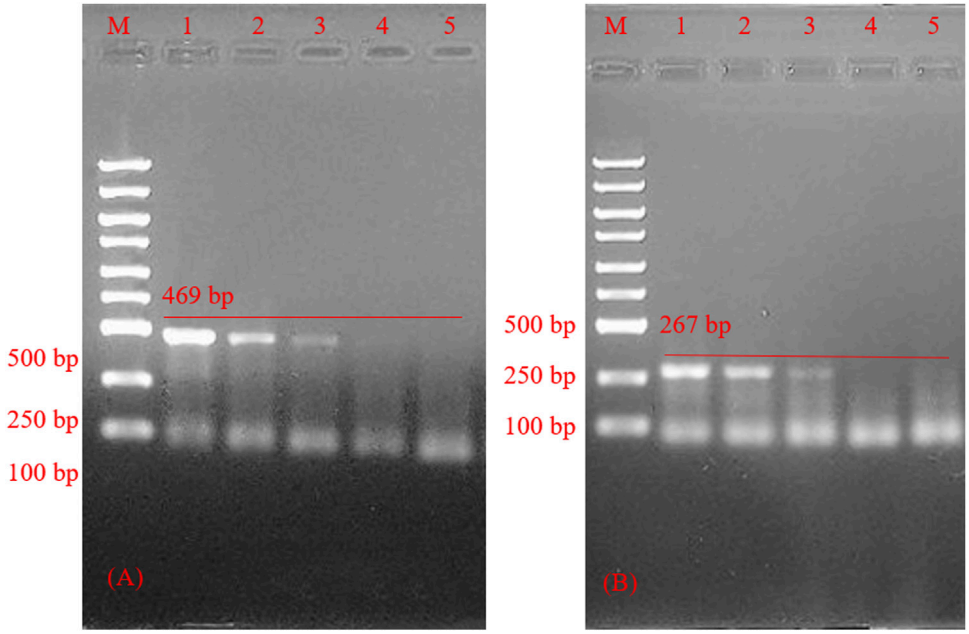

FIGURE 7
Agarose gel electrophoresis of polymerase chain reaction product sensitivity inspection. **(A)** Sensitivity inspection of herpes simplex virus 1. polymerase chain reaction product optimization of herpes simplex virus 1 reaction system; M: marker; line 1–4, Sensitivity inspection of herpes simplex virus 1 reaction system; line 5, negative control. **(B)** Sensitivity inspection of herpes simplex virus 2. M: marker; line 1–4, Sensitivity inspection of herpes simplex virus 1 reaction system; line 5, negative control.

Data availability statement

The original contributions presented in the study are included in the article/Supplementary Materials, further inquiries can be directed to the corresponding authors.

Author contributions

ZC and ZYH proposed the research idea. BYT, ZRT, and KXZ participated in the PCR experiment subjects and wrote the first draft. ZYH and HC design the HSV-typing PCR Primers. XFL and LC participated the sequence and statistical analysis. PHML and FWNC prepared the Figures and Tables. ZC and YD provides research materials, reagents, patients, experimental samples, instruments, etc. All authors contributedto revising and editing the manuscript and approved the submitted version.

Funding

This work was supported by the grant from the National Natural Science Foundation of China (61901168), Hunan Provincial Natural Science Foundation of China (2022JJ30229), Educational project of Hunan Province of China (Nos 21B0526, 21B0736). Hunan Key Research and Development Program (No. 2021SK 2003).

Conflicts of interest

Author LC was employed by Guangzhou Wondfo iCubate Biotech Co. Ltd. Author HW was employed by Wondfo Biotech Co., Ltd.

The remaining authors declare that the research was conducted in the absence of any commercial or financial relationships that could be construed as a potential conflict of interest.

Publisher's note

All claims expressed in this article are solely those of the authors and do not necessarily represent those of their affiliated organizations, or those of the publisher, the editors and the reviewers. Any product that may be evaluated in this article, or claim that may be made by its manufacturer, is not guaranteed or endorsed by the publisher.

References

Chauhan, V., Goyal, k., and Singh, M. (2018). Identification of broadly reactive epitopes targeting major glycoproteins of Herpes simplex virus (HSV) 1 and 2 - an immunoinformatics analysis. *Infect. Genet. Evol.* 61, 24–35. doi:10.1016/j.meegid.2018.03.004

Chen, H., Xiao, Z., Chu, Z., Jin, L., Li, S., Deng, Y., et al. (2020). Novel detection of norovirus and double *Clostridium difficile* in a closed cartridge system. *J. Biomed. Nanotechnol.* 16, 954–964. doi:10.1166/jbn.2020.2933

Chen, Z., Zhao, K. X., He, Z. Y., Jin, L., Wu, Z., Yan, J., et al. (2022). Development and evaluation of a thermostatic nucleic acid testing device based on magnesium pyrophosphate precipitation for detecting enterocytozoon hepatopenaei. *Chin. Chem. Lett.* 33, 4053–4056. doi:10.1016/j.cclet.2022.01.072

Christian, M. Z., David, M., Knipe, P. E., and Pellett, R. H. (2019). Classification of human Herpesviridae proteins using domain-architecture aware inference of orthologs (DAIO). *Virology* 529, 29–42. doi:10.1016/j.virol.2019.01.005

Christine, J., Sami, L., and Gottlieb, A. W. (2016). Status of vaccine research and development of vaccines for herpes simplex virus. *Vaccine* 34, 2948–2952. doi:10.1016/j.vaccine.2015.12.076

Dropulic, L., Oestreich, M., Pietz, H., Laing, K., Hunsberger, S., Lumbard, K., et al. (2019). A randomized, double-blinded, placebo-controlled, phase 1 study of a replication-defective herpes simplex virus (HSV) type 2 vaccine, HSV529, in adults with or without HSV infection. *J. Infect. Dis.* 220, 990–1000. doi:10.1093/infdis/jiz225

Fatima, S., Kumari, A., and Dwivedi, V. (2021). Advances in adjunct therapy against tuberculosis: Deciphering the emerging role of phytochemicals. *MedComm* 2, 494–513. doi:10.1002/mco2.82

Gong, Y., Nie, L., and Dai, L. (2021). Beyond proteins: Ubiquitylation of lipopolysaccharide to fight bacteria. *MedComm* 2, 855–857. doi:10.1002/mco2.86

Harfouche, M., Abu-Hijleh, F. M., James, C., Looker, K. J., and Abu-Raddad, L. J. (2021). Epidemiology of herpes simplex virus type 2 in sub-saharan africa: Systematic review, meta-analyses, and meta-regressions. *Eclinicalmedicine* 35, 100876. doi:10.1016/j.eclinm.2021.100876

James, S. H., and Kimberlin, D. W. (2015). Neonatal herpes simplex virus infection. *Infect. Dis. Clin. North Am.* 29, 391–400. doi:10.1016/j.idc.2015.05.001

Khan, H., Khan, A., Liu, Y., Wang, S., Bibi, S., Xu, H., et al. (2019). CRISPR-Cas13a mediated nanosystem for attomolar detection of canine parvovirus type 2. *Chin. Chem. Lett.* 30, 2201–2204. doi:10.1016/j.cclet.2019.10.032

Koujah, L., Suryawanshi, R. K., and Shukla, D. (2018). Pathological processes activated by herpes simplex virus-1 (HSV-1) infection in the cornea. *Cell. Mol. Life Sci.* 76, 405–419. doi:10.1007/s00018-018-2938-1

Liu, S., He, X., Zhang, T., Zhao, K., Xiao, C., Tong, Z., et al. (2022). Highly sensitive smartphone-based detection of Listeria monocytogenes using SYTO9. *Chin. Chem. Lett.* 33, 1933–1935. doi:10.1016/j.cclet.2021.11.051

Looker, K. J., Magaret, A. S., May, M. T., Turner, K. M. E., Vickerman, P., Newman, L. M., et al. (2017). First estimates of the global and regional incidence of neonatal herpes infection. *Lancet Glob. Health* 5, 300–309. doi:10.16/S2214-109X(16)30362-X

Mou, X. B., Sheng, D. N., Chen, Z., Liu, M., Liu, Y., Deng, Y., et al. (2019). *In-situ* mutation detection by magnetic beads-probe based on single base extension and its application in genotyping of hepatitis B virus pre-C region 1896nt locus single nucleotide polymorphisms. *J. Biomed. Nanotechnol.* 15, 2393–2400. doi:10.1166/jbn.2019.2862

Qi, J., He, J., Liu, C., Jin, S., Gao, R., Yang, X., et al. (2020). Pulmonary Staphylococcus aureus infection regulates breast cancer cell metastasis via neutrophil extracellular traps (NETs) formation. *MedComm* 1, 188188–201201. doi:10.1002/mco2.22

Rice, S. A. (2021). Release of HSV-1 cell-free virions: Mechanisms, regulation, and likely role in human-human transmission. *Viruses* 13, 2395. doi:10.3390/v13122395

Salvatore, C., Luca, F., Alberto, B., Cesare, D., Giulia, A., Francesca, G., et al. (2019). Herpes virus, oral clinical signs and QoL: Systematic review of recent data. *Viruses* 11, 463. doi:10.3390/v11050463

Tang, C. L., He, Z. Y., Liu, H. M., Xu, Y., Huang, H., Yang, G. J., et al. (2020). Application of magnetic nanoparticles in nucleic acid detection. *J. Nanobiotechnology* 18, 62. doi:10.1186/s12951-020-00613-6

Tang, Y. J., Ali, Z. S., Dai, J. G., Liu, X. L., Wu, Y. Q., Chen, Z., et al. (2018). Single-nucleotide polymorphism genotyping of ExoS in Pseudomonas aeruginosa using dual-color fluorescence hybridization and magnetic separation. *J. Biomed. Nanotechnol.* 14, 206–214. doi:10.1166/jbn.2018.2525

Wijesinghe, V. N., Farouk, I. A., Zabidi, N. Z., Puniyamurti, A., Choo, W. S., and Lal, S. K. (2021). Current vaccine approaches and emerging strategies against herpes simplex virus (HSV). *Expert Rev. Vaccines* 20, 1077–1096. doi:10.1080/14760584.2021.1960162

Yang, J., Zhang, N., Lv, J., Zhu, P., Pan, X., Hu, J. Q. G., et al. (2020). Comparing the performance of conventional PCR, RTQ-PCR, and droplet digital PCR assays in detection of Shigella. *Mol. Cell. Probes* 51, 101531. doi:10.1016/j.mcp.2020.101531

Zeng, B., Huang, X., Huang, L. K., Zhang, J., Yan, H. D., Luo, D., et al. (2015). Optimization of SCoT-PCR reaction system in dactylis glomerata by orthogonal design. *Genet. Mol. Res.* 14, 3052–3061. doi:10.4238/2015.April.10.15

Zeng, B., Yan, H. D., Huang, L. K., Wang, Y. C., Wu, J. H., Huang, X., et al. (2016). Orthogonal design in the optimization of a start codon targeted (SCoT) PCR system in roegneria kamoji ohwi. *Genet. Mol. Res.* 15, 15048968. doi:10.4238/gmr15048968

frontiers | Frontiers in Bioengineering and Biotechnology

TYPE Original Research
PUBLISHED 19 August 2022
DOI 10.3389/fbioe.2022.947895

OPEN ACCESS

EDITED BY
Guangli Li,
Hunan University of Technology, China

REVIEWED BY
Tao Liu,
Wuhan University, China
Sheena Kumari,
Durban University of Technology, South Africa

*CORRESPONDENCE
Wenming Wu,
wuwenming627@163.com

†These authors have contributed equally to this work

SPECIALTY SECTION
This article was submitted to Biosensors and Biomolecular Electronics, a section of the journal Frontiers in Bioengineering and Biotechnology

RECEIVED 19 May 2022
ACCEPTED 25 July 2022
PUBLISHED 19 August 2022

CITATION
Wang K, Li B, Guo Y, Wu Y, Li Y and Wu W (2022), An integrated digital PCR system with high universality and low cost for nucleic acid detection.
Front. Bioeng. Biotechnol. 10:947895.
doi: 10.3389/fbioe.2022.947895

An integrated digital PCR system with high universality and low cost for nucleic acid detection

Kangning Wang[1†], Bin Li[2†], Yu Guo[3], Yanqi Wu[4], Yan Li[1] and Wenming Wu[1*]

[1]Institute of Biological and Medical Engineering, Guangdong Academy of Sciences, Guangzhou, China, [2]Institute of Microbiology Chinese Academy of Sciences, Beijing, China, [3]School of Mechanical and Electrical Engineering, Guangdong University of Technology, Guangzhou, China, [4]State Key Laboratory of Quality Research in Chinese Medicine, Macau University of Science and Technology, Taipa, China

Digital PCR is the most advanced PCR technology. However, due to the high price of the digital PCR analysis instrument, this powerful nucleic acid detection technology is still difficult to be popularized in the general biochemistry laboratory. Moreover, one of the biggest disadvantages of commercial digital PCR systems is the poor versatility of reagents: each instrument can only be used for a few customized kits. Herein, we built a low-cost digital PCR system. The system only relies on low-cost traditional flat-panel PCR equipment to provide temperature conditions for commercial dPCR chips, and the self-made fluorescence detection system is designed and optically optimized to meet a wide range of reagent requirements. More importantly, our system not only has a low cost (<8000 US dollars) but also has a much higher universality for nucleic acid detection reagents than the traditional commercial digital PCR system. In this study, several samples were tested. The genes used in the experiment were plasmids containing UPE-1a fragment, TP53 reference DNA, hepatitis B virus DNA, leukemia sample, SARS-COV-2 DNA, and SARS-COV-2 RNA. Under the condition that DNA can be amplified normally, the function of the dPCR system can be realized with simpler and low-price equipment. Some DNA cannot be detected by using the commercial dPCR system because of the special formula when it is configured as the reaction solution, but these DNA fluorescence signals can be clearly detected by our system, and the concentration can be calculated. Our system is more applicable than the commercial dPCR system to form a new dPCR system that is smaller and more widely applicable than commercially available machinery.

KEYWORDS

SARS-CoV-2 virus, digital PCR, dPCR chip, fluorescence detection, absolute quantification

Introduction

Polymerase chain reaction (PCR), a method for enzymatic synthesis of specific DNA *in vitro*, has been proposed for 20 years. PCR reaction procedure consists of denaturation, annealing, and extension for one cycle. After several cycles, the target DNA can be massively amplified in a short time. To date, PCR has developed into the conventional key technology in the field of molecular biology, greatly promoting the development of various fields of life sciences. Especially in the late 1990s, the quantitative real-time PCR (qPCR) technology (Ginzinger, 2002; Arya et al., 2005; Ma et al., 2013) and related products from *in vitro* synthesis of quantitative and qualitative/detection techniques developed into a highly sensitive, specific, and accurate quantitative analysis technology.

Considering the rapid development over the past decades, the qPCR technology has been used for the diagnosis of many diseases (Coulson et al., 2008; Taniguchi et al., 2009; van Eijk et al., 2011; Song et al., 2012; Moreira et al., 2013). However, there are many factors that affect the amplification efficiency during PCR amplification. There is no guarantee that the amplification efficiency will remain constant during the reaction. In other words, the amplification efficiency may be different between the work samples and the standard samples. This results in the fact that the cyclic threshold (CT) on which quantitative analysis depends is not constant. Therefore, the quantification of the qPCR is only "relative quantification," and its accuracy and reproducibility still cannot meet the requirements of quantitative analysis of molecular biology.

At the end of the 20th century, Vogelstein et al. proposed the concept of digital PCR (dPCR) by dividing a sample into tens to tens of thousands of different reaction units, where each unit contained one or more copies of the target molecule (DNA template) (Sanders et al., 2011; Whale et al., 2012; Hudecova, 2015; Schuler et al., 2016; Sreejith et al., 2018). The target molecule is subjected to PCR amplification in each reaction unit, and the fluorescence signal of each reaction unit is statistically analyzed after the amplification. Unlike qPCR, digital PCR does not depend on CT values, so it is not affected by the amplification efficiency. At the end of the amplification, the average concentration (content) of each reaction unit can be calculated by direct counting or employing the Poisson distribution formula. Under the control of less than 5%, digital PCR can realize absolute quantitative analysis without standard samples and curves. Droplet dPCR (Pinheiro et al., 2011; Tian et al., 2015; Gou et al., 2018; Song et al., 2018) is actually a miniaturized traditional PCR amplification. In this technique, the reaction solution is uniformly introduced into the reaction chamber or through hole, and each chamber or through hole is scanned using microfluidic chip technology and fluorescence signal. The method is similar to the detection method of the gene chip to calculate the content of the target sequence. However, the droplet dPCR technology is widely used due to its maturity.

During the past 10 years, different companies have explored different technologies and methods to realize digital PCR automation. At present, the available digital platforms are mainly different in the number of liquid separations, droplet generation methods, and special equipment required. BioMark™HD system provides a matrix dedicated to digital integrated fluid circuits (IFCs), which can distribute samples in multiple separate reaction chambers. QuantStudio 3D system uses a silicon chip composed of a single reaction hole arranged in a certain order, which can distribute samples according to its matrix. CONSTELLATION® digital PCR system uses a microporous plate using sealed compression axis; the micropipette separates the sample liquid channel into a separate microfluidic chamber. Other digital PCR platforms such as QX200™DropletDigital™PCR and RainDropplus™ digital PCR systems use oil-in-water emulsification to partition. The water phase is composed of primers, probes, or fluorescent dyes and mixed into super premixes; the samples and mineral oil are put into specially designed scaffolds, the droplet generator uses microfluidics to generate pressure, and the water phase and oil phase are sucked into the output channel. In this process, droplets are formed, and each droplet is read in a specific droplet reader one by one. The Naica system from Stilla Technologie™ company combines the array and emulsification methods. In this system, the sample passes through the channel of the chip and forms droplets inside the chip, which becomes an ideal digital PCR technology platform.

At present, dPCR technology, also regarded as liquid biopsy, is mainly used for detecting trace DNA. Its clinical applications include tumor fluid biopsy, (Sacher et al., 2016; Conteduca et al., 2017; van Ginkel et al., 2017; Wang et al., 2018), noninvasive prenatal screening (Tan et al., 2019), early diagnosis of infectious diseases, (Cao et al., 2019), transplant rejection monitoring (Beck et al., 2013) and other fields. The detection object of tumor liquid biopsy is the circulating tumor DNA (ctDNA) in blood or other body fluids, which not only realizes non-invasive diagnosis and detection but also can monitor the course of the disease and guide the treatment. dPCR is a powerful tool to detect low abundance mutations. At present, ctDNA detection technology based on dPCR has achieved encouraging results in the research of nonsmall cell lung cancer, (Sacher et al., 2016), prostate cancer, (Conteduca et al., 2017), head and neck squamous cell carcinoma, and other tumors (HNSCC) (van Ginkel et al., 2017).

In this study, we realized the function of the dPCR system by using the simple traditional plane PCR instrument and detection system, which made the whole system simpler, smaller, and cheaper. Moreover, the detection range of commercial dPCR is limited due to the need for specific reagent formulation. But the system is more user-friendly and accurate.

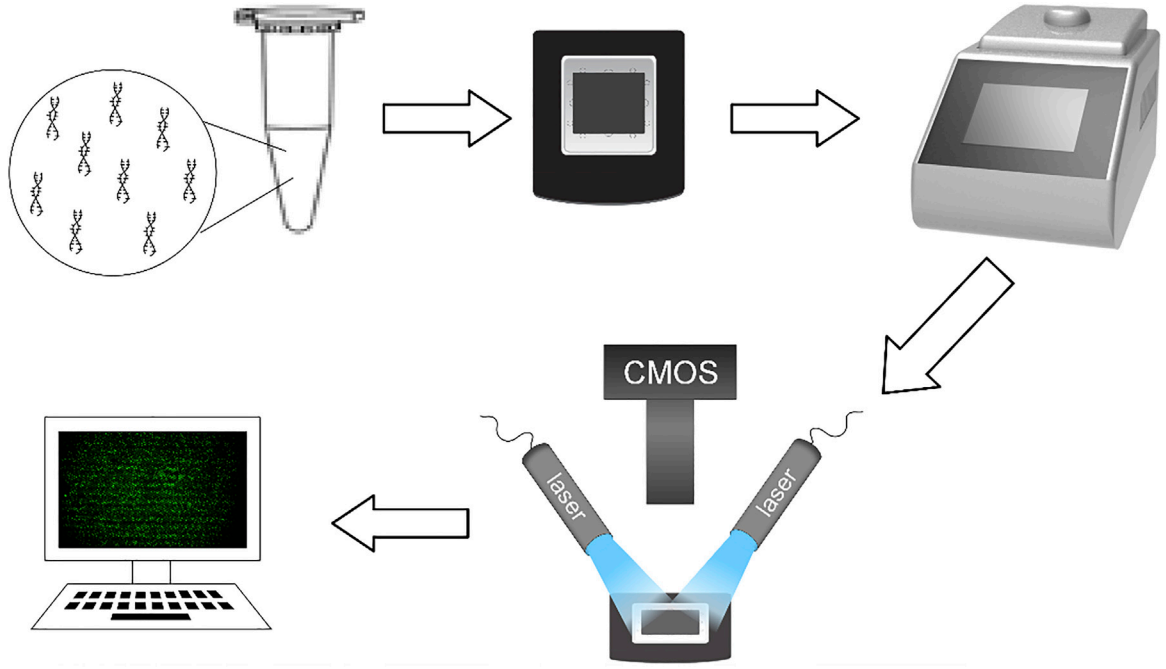

FIGURE 1
Flow chart of dPCR system.

Materials and method

Reagents

In this study, several samples were tested. The genes used in the experiment were plasmids containing SARS-COV-2 DNA fragment (N gene) provided by Sangon Biotech (Shanghai) Co., Ltd. (abbreviated as SARS-COV-2 DNA in the following description), plasmids containing UPE-1a fragment (abbreviated as UPE DNA in the following description), RNA sample of SARS-COV-2 (abbreviated as SARS-COV-2 RNA in subsequent narratives) provided by Wuhan Institute of Virology, Chinese Academy Of Sciences, TP53 reference DNA (abbreviated as TP53 DNA in the following description) provided by RainSure biology company, hepatitis B virus DNA (abbreviated as HBV DNA in the following description) provided by Northeast Pharmaceutical Company, and the genetic sample of a leukemia patient provided by First Bethune Hospital of Jilin University (abbreviated as leukemia sample in the following description). 2x ddPCR Supermix for probes (NO dUTP) was produced from Bio Rad. Before the experiment, the sample was configured as a mixture of reaction solution according to the formula in the instruction manual. Some of the mixture was coated in the dPCR chip as the experimental group. After all the preparations, the dPCR chips with DNA samples distributed were placed in the conventional planar PCR (BIOER Gene Touch TC-EA) for amplification (Figure 1). A part of the reaction solution was tested by the commercial dPCR system (RainSure), and the results were used as the standard to measure the success of the experiment.

Digital Polymerase chain reaction chip

Droplet dPCR does not depend on the cyclic threshold to determine the number of targets. Therefore, the difference in PCR efficiency between biological samples will not affect the quantitative results.

Although the principle of dPCR technology is not complicated, it is difficult to break through in the early stage of sample distribution in the first step, and the quantity and uniformity of distribution are very low, which greatly limits the development of dPCR. Until the last few years, with the emergence of water-in-oil emulsified droplets, integrated fluidic circuit (IFC), nanofabrication, and other technologies, dPCR technology has finally broken through the technical bottleneck and successfully commercialized. Among them, the droplet dPCR technology is represented by Life Technology's QuantStudio 3D system. Using high-density nanoliter fluidic chip technology, a standard PCR reaction is evenly distributed to up to 20,000 individual reaction holes in the chip. Each reaction well contains or does not contain one or more copies of the target molecule (DNA template) so as to realize "single molecule

template PCR amplification." The fluorescence signal of each reaction chamber is scanned by a method similarly to a gene chip to calculate the content of the target sequence. Currently, each chip is integrated with 10,000–40,000 (BioMark HD) reaction chambers or 20,000 (QuantStudio 3D) reaction well. However, the high price of PCR machines has deterred many organizations that need them from buying them.

In this study, only the chip of QuantStudio 3D system was selected as the reflecting container, and the denaturation, renaturation, and elongation temperatures required for polymerase chain reaction were provided in other cheaper devices.

Twenty thousand reaction wells of QuantStudio® 3D Digital PCR 20K chip are fabricated on a 10 square millimeter silicon wafer to make dPCR chips. Each well is a regular hexagon with a diagonal length of 60 μm. Each reaction well is isolated from its neighbors. Fixed reaction volume minimizes upfront sample manipulation.

Image acquisition and processing

In our former fluorescence detection system, the high-power blue LED with a power of 3 W was used as the fluorescence excitation light source, and a narrow-band filter with a central wavelength of 480 nm was installed in front of the excitation light source to ensure that it could excite the fluorescence, but it would not generate redundant noise. A 20-megapixel CMOS (complementary metal oxide semiconductor) was selected as the fluorescence receiving device. An optical lens and a narrow-band filter with a central wavelength of 520 nm were installed in the front-end of the CMOS to receive the fluorescence signal, and the real-time image was displayed on the PC connected with it. But in the experiment, we found that LED cannot provide enough light energy for the microdroplets in the chip, which led to the fact that the fluorescence signal could not be detected by CMOS in the initial experiment. In order to solve the abovementioned problems, we chose higher energy and more concentrated laser (Anford T850AD1670GD-P488 60 mW) as the light source for excitation fluorescence. The advantages of laser, such as small volume, light weight, good monochromaticity, high energy concentration, and reliability, were just suitable for our requirements of excitation light source. The lens was used to irradiate the dPCR chip as evenly as possible. Therefore, two small lasers with a central wavelength of 488 nm were selected as excitation sources and placed symmetrically on both sides of the chip. CMOS was placed in the center of two small lasers, which was convenient to collect the fluorescence information in the chip. Of course, for weak fluorescence detection, the appropriate optical barrel is indispensable. The optical tube received the fluorescence as much as possible and projected it on the sensitive element of the receiver. At the same time, it was important for enlarging the chip to be observed to an appropriate size.

Concentration calculation

Digital PCR technology is an absolute quantitative technology of nucleic acid molecules. The principle is to distribute the PCR reaction system to a large number of micro reactors. Each micro reactor contains or does not contain one or more copies of the target nucleic acid molecules (DNA templates) for "single molecule template" PCR amplification. At the end of amplification, the number of positive reaction units (judged by terminal fluorescence signal) and the number of copies of target genes in the original samples were calculated by statistical method. The workflow mainly includes four steps (as shown in the figure below): PCR/RT-PCR reaction premixing sample DNA/RNA, reaction premixing liquid dispersion or division, PCR amplification, fluorescence signal acquisition, and data analysis. Digital PCR disperses the sample DNA into 25,000–30,000 microdrops so that each microdrop does not contain or contains one or more copies of the target molecule (DNA template). All microdrops are randomly spread in the sapphire chip in the form of a 2D array. After amplification, the number of template copies in the original sample was calculated by counting the number of positive reaction holes. Because the target DNA molecules are randomly distributed in the positive reaction units and directly count and count the positive reaction units, it is not the true copy number of the target DNA molecules. Each reaction unit may contain two or more target molecules. We used Poisson probability distribution Eq. 1 to calculate.

$$\mathrm{p} = \frac{e^{-\lambda}}{k!}\lambda^{k}, \lambda = 0,\ 1,\ 2\ldots, \tag{1}$$

In the above Eq. 1, λ is the average number of copies of starting DNA molecules contained in each reaction unit, and *p* is the probability of each reaction unit containing k copy target molecules under certain λ conditions. λ is determined by the dilution coefficient m (or the number of zones) of the sample solution, i.e., λ = cm, where c is the original copy number of the sample. When k = 0, i.e., without the target DNA molecule, *p* is the ratio between the number of reaction units without fluorescent signal and the total number of reaction units, i.e., the ratio of negative reaction units. Eq. 1 can be simplified as Eq. 2:

$$\mathrm{p} = e^{-\lambda}\,(k > 0,\ \lambda) = 1 - e^{-\lambda}\,(k = 0,\ \lambda) = 1 - e^{-cm} \tag{2}$$

Through the end-point method, the total number of reaction units n and the number of positive reaction units f with fluorescence signal can be reached, so the proportion of negative reaction units is Eq. 3:

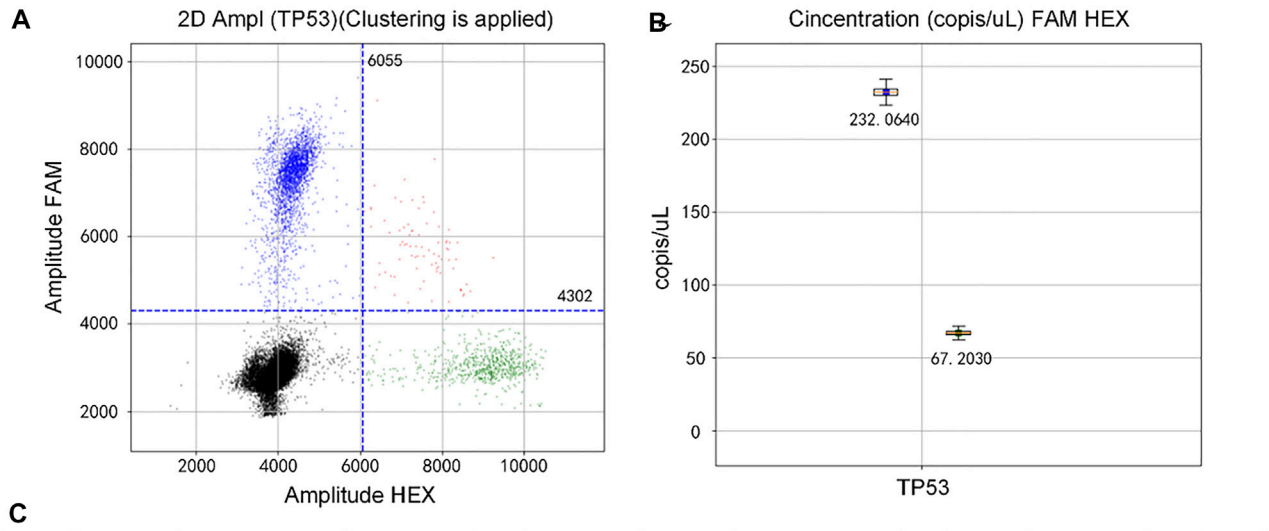

C

Well	ExptType	SampleName	TargetType	TargetName	Channel	Concentration (copies/ul)	Positives	Negatives	Accepted Droplets
B01	MUT	TP53rainsure	Unknown		FAM	232. 064	2542	15601	18143
B01	MUT	TP53rainsure	Unknown		HEX	67. 203	776	17367	18143

FIGURE 2
(A) Scatter plot by RainSure dPCR; **(B)** Initial DNA concentration calculated by RainSure dPCR; **(C)** Microdroplet data derived by RainSure dPCR.

$$p = \frac{n - f}{n} \tag{3}$$

Taking the logarithm with e as the base on both sides of the abovestated formula, the following equation is obtained:

$$cm = -\ln\left(1 - \frac{f}{n}\right) \tag{4}$$

When using the method of digital PCR to carry out the absolute quantitative analysis of nucleic acid, only through the proportion of negative reaction units and the dilution coefficient (or partition number) of samples, the average number of nucleic acid copies of reaction units can be determined, thus realizing the accurate quantitative analysis of DNA.

Results and discussion

In order to prove the applicability of the proposed dPCR device, we designed multiple sets of control experiments to analyze the gene fragments by using dPCR. First, we prepared UPE-1a plasmid DNA from Wuhan Virus Research Institute and a TP53 reference DNA sample from Swiss Biosciences at a concentration. The dPCR reaction mixture was prepared for each panel. The 20 μl of reaction mixture containing UPE-1a DNA included the following: 10 μl of 2x ddPCR SuperMix (No dUTP), 1 μl of Mntant FAM probe, 2 μl of reference STD DNA, and 7 μl of sterile double distilled water. The reaction mixture containing TP53 reference DNA included the following: 10 μl of 2x ddPCR SuperMix for probes (NO dUTP), 0.75 μl of upEF, 0.75 μl of upER, 0.5 μl of upEP (FAM), 1 μl of template solution, and 7 μl of sterile double distilled water. The 20 μl of reaction mixture containing the leukemia sample included the following: 10 μl of 2x ddPCR SuperMix (No dUTP), 2 μl of a mixture of primer and probe, 1 μl of leukemia sample, and 7 μl of sterile double distilled water. The 20 μl of reaction mixture containing SARS-COV-2 DNA included the following: 10 μl of 2x ddPCR SuperMix (No dUTP), 1 μl of a mixture of primer and probe, 1 μl of SARS-COV-2 DNA, and 8 μl of sterile double distilled water. The 50 μl of reaction mixture containing SARS-COV-2 RNA included the following: 10 μl of 5x One-step RT-PCR buffer, 5 μl of Solution I (10x), 2 μl of Abstart Taq (with dNTP), 2.5 μl of a mixture of primer and probe, 20 μl of SARS-COV-2 RNA, and 10.5 μl of sterile double distilled water. In the experiment, 15 μl of the mixture was placed on a special blade, the mixture was evenly applied to the chip, and finally, the sealing oil was injected (immersion fluid) to prevent evaporation of the mixture during heating.

The thermal-cycling scheme of UPE DNA, TP53 reference DNA, leukemia sample, and SARS-COV-2 DNA starts from the pre-denaturation of 95°C for 10 min, the denaturation temperature is 94°C, lasting for 30 s, and the renaturation and extension temperature is 55°C, maintaining for 60 sb with 40 cycles. SARS-

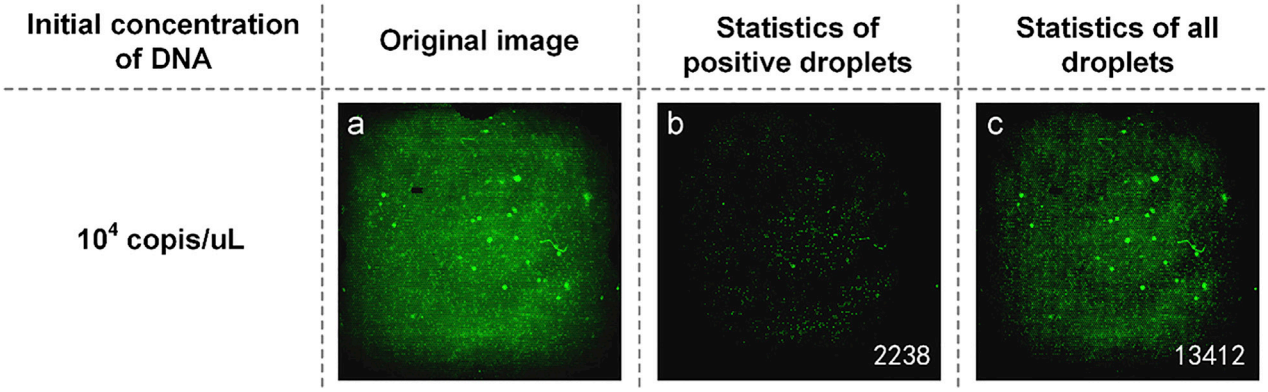

FIGURE 3
(A) Original fluorescence image of TP53 DNA; **(B)** Image processed by software and the number of positive droplets; **(C)** Statistics of all droplets with TP53 DNA.

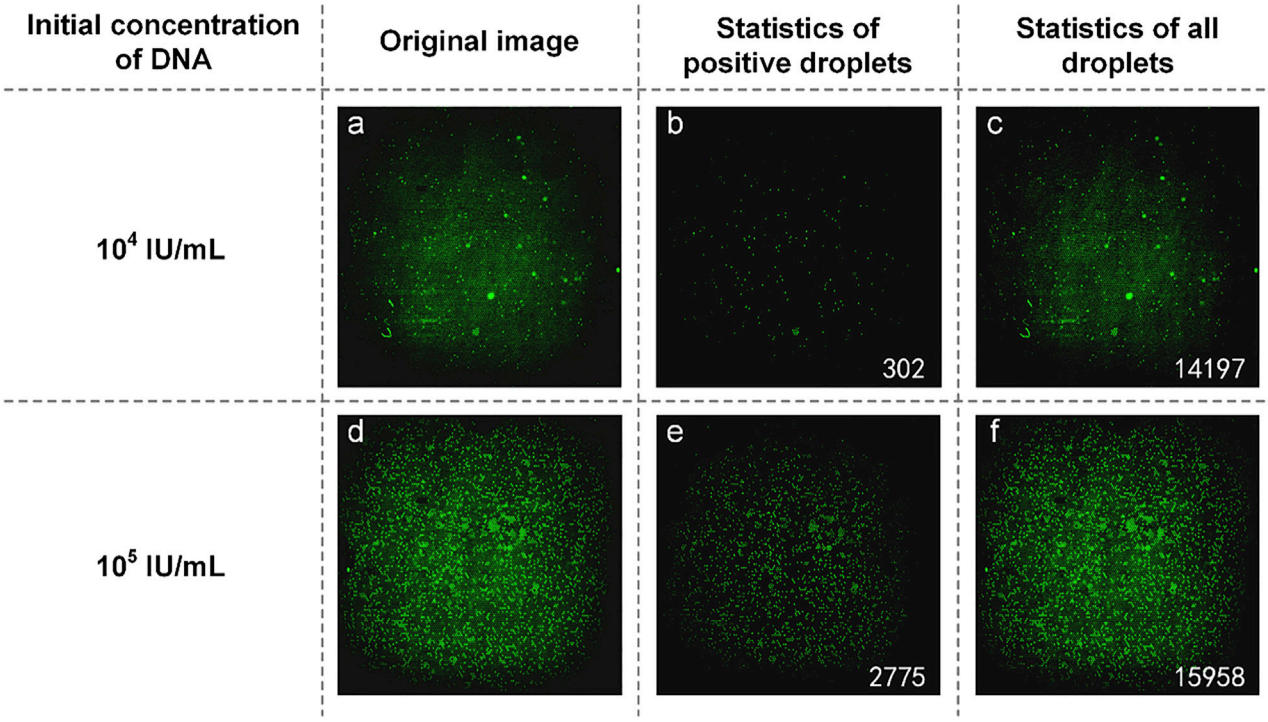

FIGURE 4
(A) Original image of HBV DNA with an initial concentration of 10^4 IU/ml; **(B)** Image processed by software and the number of positive droplets with low-concentration DNA; **(C)** Statistics of all droplets containing HBV DNA with an initial concentration of 10^4 IU/ml; **(D)** Original image of HBV DNA with a concentration of 10^5 IU/ml; **(E)** Image processed by software and the number of positive droplets with high-concentration DNA; **(F)** Statistics of all droplets containing HBV DNA with an initial concentration of 10^5 IU/ml.

COV-2 RNA added a reverse transcription process at 55°C for 30 min. HBV DNA is replicated by two steps: 94°C of denaturation temperature lasts for 10 s, 60°C of renaturation and extension temperature lasts for 30 s. The experiment lasts 40 cycles. In order to make the PCR reaction more stable, the temperature change rate the of *in-situ* PCR instrument was set to 0.5°C/s. During the experiment, we found that although the excitation light source was replaced by a small laser, the cover of the dPCR

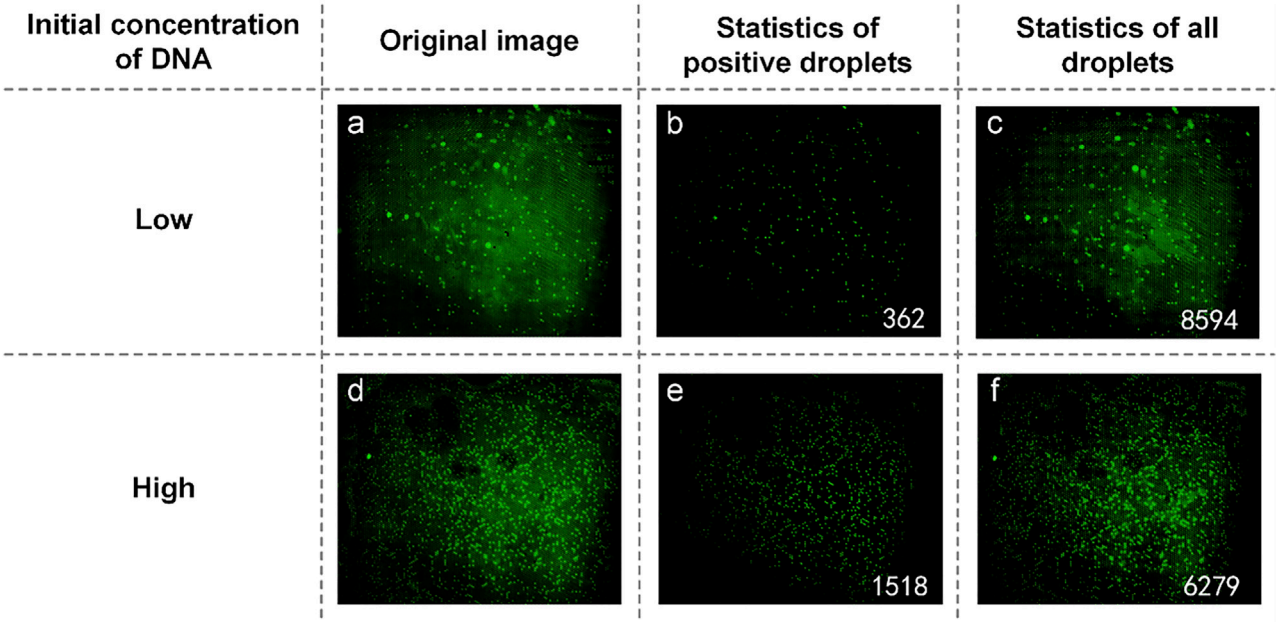

FIGURE 5
(A) Original image of UPE DNA with low concentration; **(B)** Image processed by software and the number of positive droplets with low-concentration DNA; **(C)** Statistics of all droplets containing UPE DNA with low concentration; **(D)** Original image of UPE DNA with high concentration; **(E)** Image processed by software and the number of positive droplets with high-concentration DNA; **(F)** Statistics of all droplets containing UPE DNA with high concentration.

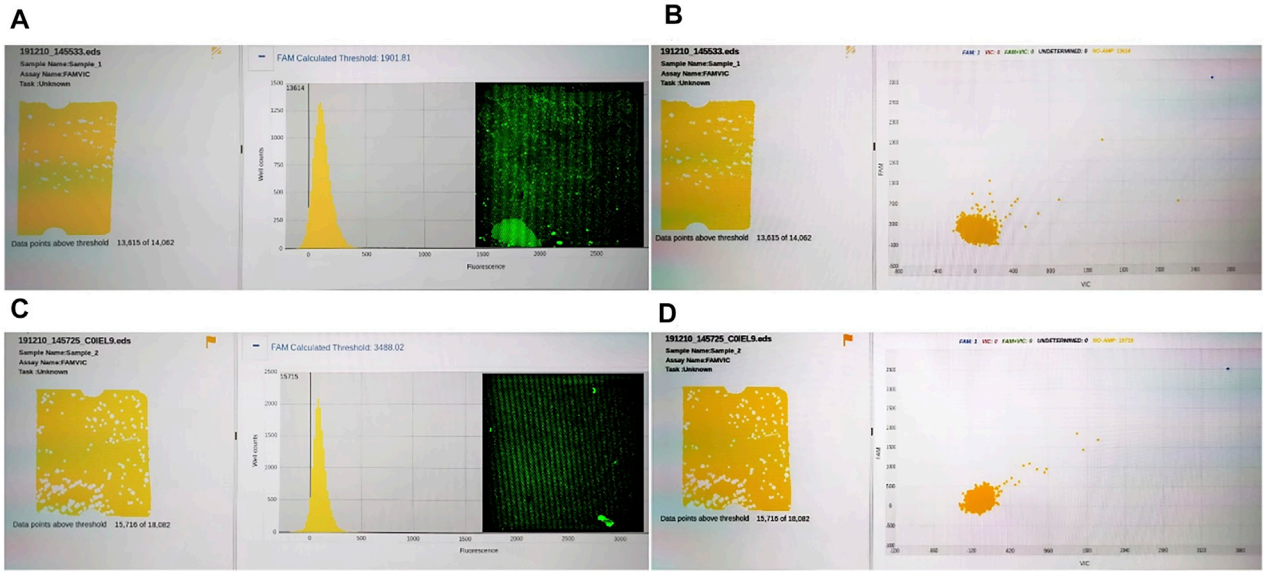

FIGURE 6
(A) Fluorescence intensity distribution of HBV DNA; **(B)** Fluorescence intensity distribution of HBV DNA; **(C)** Fluorescence intensity distribution of UPE DNA; **(D)** Fluorescence intensity distribution of UPE DNA.

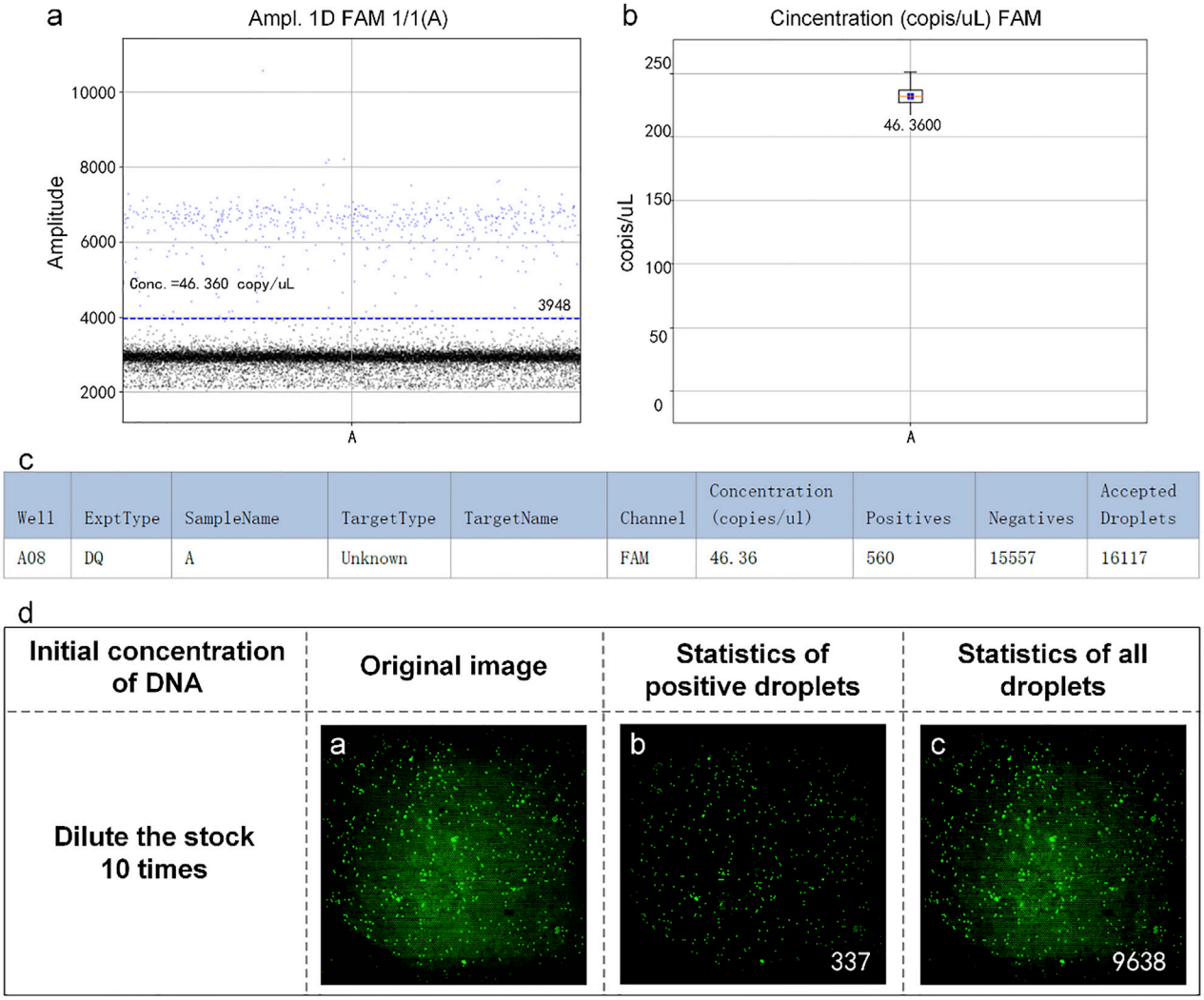

FIGURE 7
(A) Scatter plot by RainSure dPCR; **(B)** Initial DNA concentration calculated by RainSure dPCR; **(C)** Microdroplet data derived by RainSure dPCR; **(D)** Test results obtained with our system.

chip would still block part of the light energy irradiated on the droplet. Therefore, we increased the number of lasers to two and placed the lasers symmetrically on both sides to avoid weak light energy and uneven distribution caused by irradiation on one side while not interfering with image acquisition.

The prepared reaction liquid mixture (FAM channel) was evenly coated on the dPCR chip, the sealing cover was covered, and the sealing oil was injected. Then, the chip was placed in the PCR machine, and the thermal cycle was set as described earlier. The heat cover temperature was set to 80°C. After thermal cycling, the dPCR chip was placed in the fluorescence observation system to observe the fluorescence.

The initial concentration of TP53 DNA was 10^4 copies/μl. In the experiment, the mixture was divided into two parts. One of them was detected by RainSure dPCR as the control group. The other was coated on the dPCR chip as the experimental group and placed in the plane PCR instrument for amplification. If the results of the two methods are similar, it will be proved that our method can replace the expensive dPCR equipment very well. Figure 2A shows that the fluorescence could be easily identified after amplification. In the FAM channel, the DNA concentration was 232.0640 copies/μl (Figure 2B). Details of the droplet are given in Figure 2C.

Another part of the reaction solution was amplified in the dPCR chip. The fluorescent image captured by the detection device is shown in Figure 3A. The brightness of the image was still uneven, and there was a difference between the center brightness and the edge brightness, which made it difficult to count the microdroplets. We used MATLAB to write the image

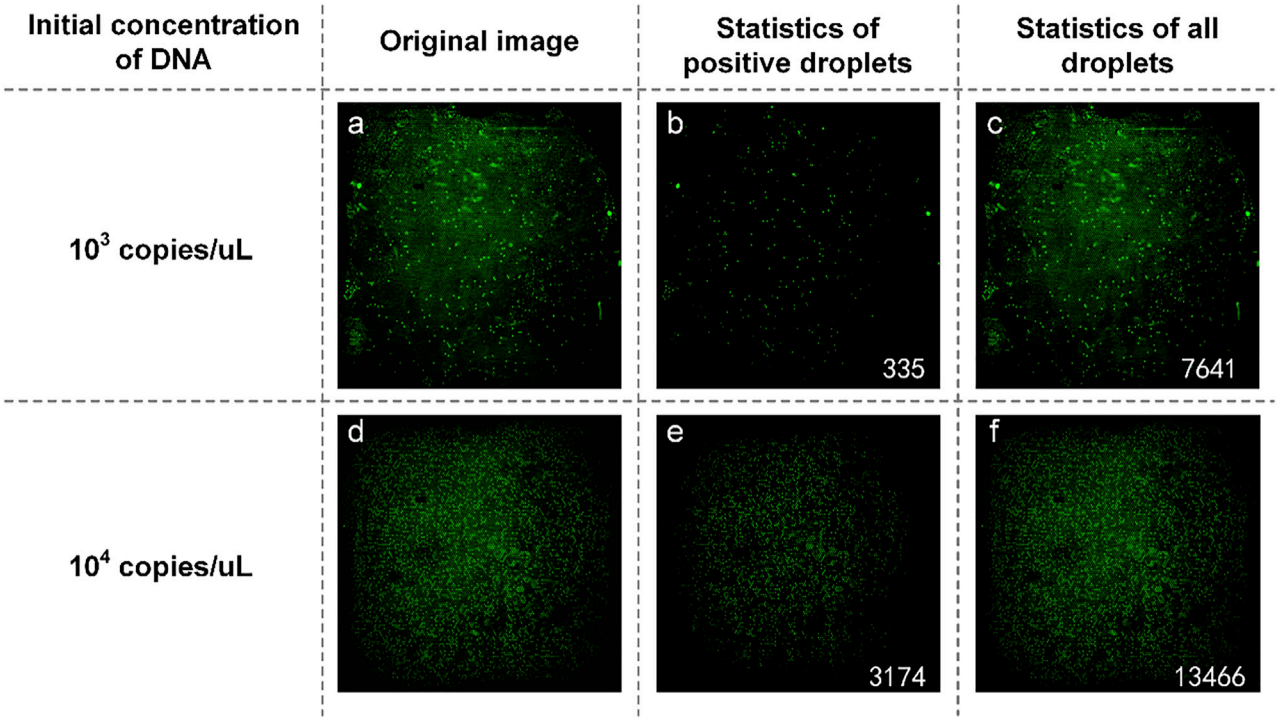

FIGURE 8
(A) Original image of SARS-COV-2 DNA with a concentration of 10^3 copies/μl; **(B)** Image processed by software and the number of positive droplets with a concentration of 10^3 copies/μl; **(C)** Statistics of all droplets containing SARS-COV-2 with a concentration of 10^3 copies/μl; **(D)** Original image of SARS-COV-2 DNA with a concentration of 10^4 copies/μl; **(E)** Image processed by software and the number of positive droplets with a concentration of 10^4 copies/μl; **(F)** Statistics of all droplets containing SARS-COV-2 DNA with a concentration of 10^4 copies/μl.

processing program, which was used to distinguish the original image's positive droplets from the negative droplets (Figures 3B and C). The number of positive droplets was 2,238, and the number of all droplets was 13,412. This proves that our method is available.

The detection of a kind of DNA only showed that our method can quantify DNA by dPCR chip, without using a specific dPCR system. We also wanted to prove that such a combination could be used to detect reagents that could not be detected by commercial dPCR systems, breaking the detection limitations.

The mixture of reaction solution containing HBV DNA could not be added to the reagents used in commercial dPCR, resulting in the concentration of HBV DNA not being detected by commercial dPCR. Therefore, we used the concentration ratio of the reaction liquid mixture itself to verify the results. In the experiment, DNA with an initial concentration of 1:10 was selected to prepare the mixture of the reaction solution. The experimental data are shown in Figure 4. From the original image (Figures 4A and D), the proportion of the number of positive droplets corresponding to the two initial concentrations of DNA was close to 1:10 by eyes. After analyzing the image, the accurate number of positive droplets and the total number of droplets were obtained. The number of positive droplets containing HBV DNA with an initial concentration of 10^4 IU/ml is 302 (Figure 4B), and the number of all droplets containing HBV DNA with an initial concentration of 10^4 IU/ml is 14,197 (Figure 4C). The concentration of DNA in the mixture of the reaction solution was 21.9404 copies/μl by using the quantitative formula of dPCR. the number of positive droplets containing HBV DNA with an initial concentration of 10^5 IU/ml is 2,775 (Figure 4E), and the number of all droplets containing HBV DNA with an initial concentration of 10^5 IU/ml is 15,958 (Figure 4F). The concentration of DNA in the mixture was 194.9308 copies/μl. The results showed that the ratio of DNA concentration calculated was close to 1:10, and the initial DNA concentration was 1:10. In consideration of the errors caused by the imprecise volume of each component in the configuration process of the reaction liquid mixture, as well as the errors produced in the sample loading process of the mixture, the test results are accurate.

UPE DNA was provided without explicitly indicating the initial DNA concentration. Here, it is expressed as high and low concentrations, and low concentration DNA was obtained by diluting the high concentration DNA 10-fold. Therefore, the relationship between the initial calculated DNA concentration of about 10 times proves the success of the experiment. Figures 5A and D are initial fluorescence images of UPE DNA. After

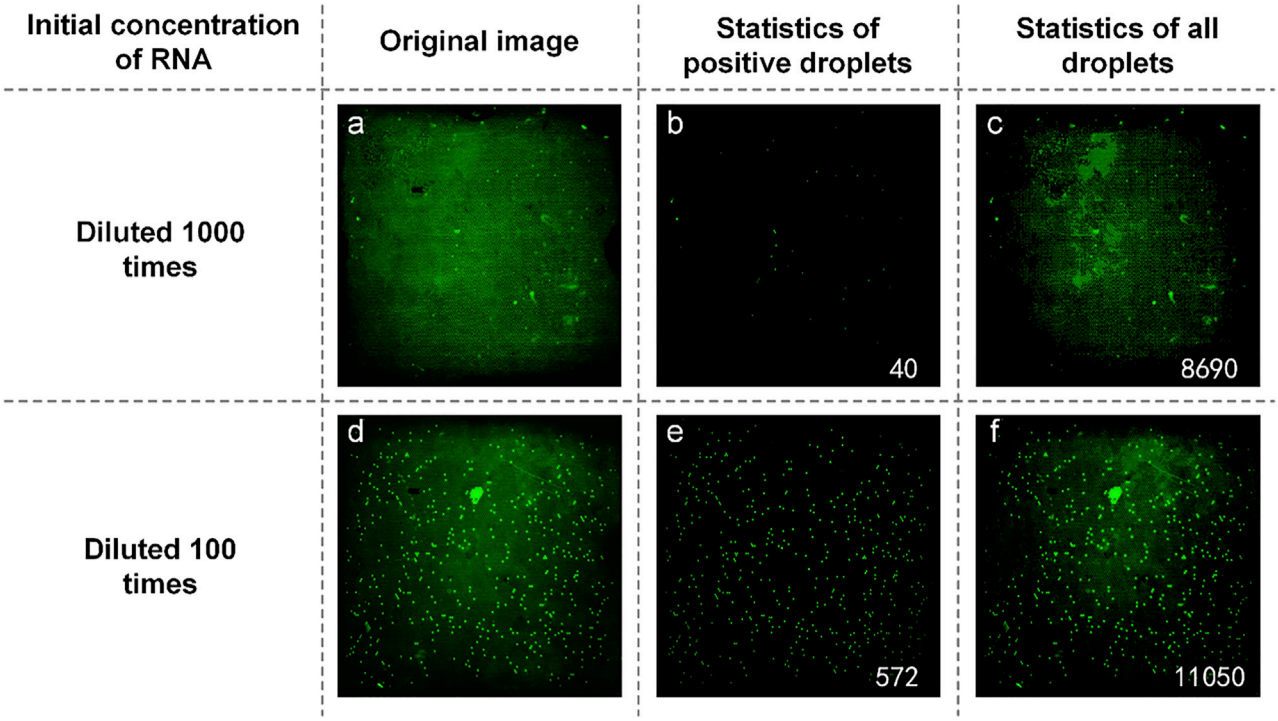

FIGURE 9
(A) Original image of SARS-COV-2 RNA with a concentration of diluted 1,000 times; **(B)** Image processed by software and the number of positive droplets with a concentration of diluted 1,000 times; **(C)** Statistics of all droplets containing SARS-COV-2 RNA with a concentration of diluted 1,000 times; **(D)** Original image of SARS-COV-2 RNA with a concentration of diluted 100 times; **(E)** Image processed by software and the number of positive droplets with a concentration of diluted 100 times; **(F)** Statistics of all droplets containing SARS-COV-2 RNA with a concentration of diluted 100 times.

processing and analyzing the image, we found that the number of positive droplets containing UPE DNA with low concentration (Figure 5B) was 362, and the number of all droplets containing UPE DNA with low concentration (Figure 5C) was 8,594. The concentration of DNA was 43.9136 copies/μl. Figures 5E and F show that the number of positive droplets containing UPE DNA with high concentration was 1,518, and the number of all droplets containing UPE DNA with high concentration was 6,279. After calculation, the concentration of DNA was 282.4010 copies/μl. The concentration of the two reaction mixtures was approximately 1:7, so for UPE DNA, our system could detect the presence of DNA, but the accuracy of the concentration calculation was not high enough.

To compare the universality of reagents between our system and commercial instruments, we compared the results of QuantStudio 3D digital PCR system and RainSure digital PCR system. The results showed that RainSure digital PCR system could detect TP53 DNA matched with it (picture 2), but it could not get the detection results of HBV DNA. In addition, for QuantStudio 3D digital PCR system, 20 μl of reaction solution containing HBV DNA and UPE DNA, respectively, in the abovementioned experiments was reserved, respectively. The reaction solution was coated in the dPCR chip according to the operating instructions. The chip was placed in the corresponding dPCR system for reaction and detection. Figure 6 shows that no amplification signal of dPCR chip was detected. Among them, Figures 6A and B are the detection results of the dPCR chip containing HBV DNA. Figures 6C and D are the detection results of the dPCR chip containing UPE DNA. The droplets in the detection results were all negative; the reaction solution did not contain the target DNA. Then, the chips were taken out from the detection device and placed in our detection system to observe the fluorescence. In the results, we observed not only the negative drops but also the positive ones. These images were added to Figures 6A and C, and the DNA in the results corresponds to Figures 6A and C, respectively.

The reaction mixtures containing the leukemia sample were divided into two portions. One served as the control group detected by the RainSure dPCR system, while the other was spread on the dPCR chip as an experimental group and placed in a planar PCR instrument for amplification. The scatter plot given by the commercial instrument showed that the demarcation line of the fluorescence brightness of the negative droplet from the positive droplet was obvious (Figure 7A), and the sample concentration was 46.36 copies/μl (Figure 7B), of which, the

number of positive droplets was 560, and the total number of droplets was 16,117 (Figure 7C). Figure 7D illustrates the test results given by our system: the number of positive droplets is 337, and the total number of droplets is 9,975. The measured sample concentration was calculated to be 42.96 copies/μl.

In early 2020, COVID-19 swept the world. Therefore, we performed the test for the detection ability of the SARS-COV-2 sample. Similar to HBV DNA, the mixture of reaction solutions that we used containing the SARS-COV-2 sample was also not detectable by the RainSure dPCR system. Therefore, the validation method is the same as that for HBV DNA. Samples with an initial concentration difference of 10 times were selected for detection.

The plasmid containing SARS-COV-2 DNA was tested first. In the experiment, SARS-COV-2 DNA at an initial concentration of 1:10 was selected to prepare the reaction solution mixture. They are spread on dPCR chips and placed in a planar PCR instrument for amplification. As shown in Figure 8, the number of positive droplets of the reaction solution mixture with an initial concentration of 10^3 copies/μl was 335 (Figure 8B), the total number of droplets was 7,976 (Figure 8C), and the sample concentration was 53.64 copies/μl. The number of positive droplets of the reaction solution mixture with the initial concentration of 10^4 copies/μl was 3,174 (Figure 8E), the total amount of droplets was 16,640 (Figure 8F), and the sample concentration was 264.55 copies/μl. The two concentrations differed numerically by an order of magnitude, so the detection was successful.

We also obtained samples containing SARS-COV-2 RNA from the Wuhan Institute of Virology and prepared a reaction mixture with an initial concentration ratio of 1:10. They were spread on dPCR chips and placed in a planar PCR instrument for amplification. As shown in Figure 9, the number of positive droplets of the reaction solution mixture added with the sample diluted 1000-fold was 40 (Figure 9B), the total number of droplets was 4,730 (Figure 9C), and the sample concentration was 10.62 copies/μl. The number of positive droplets of the reaction mixture of samples diluted 100-fold was 572 (Figure 9E), the total number of droplets was 11,622 (Figure 9F), and the sample concentration was 63.09 copies/μl. The two concentrations differ by an order of magnitude numerically, so our system can quantitatively detect SARS-COV-2.

Conclusion

In this study, the commercial dedicated dPCR chip is combined with the cheaper traditional planar PCR instrument and the fluorescence detection system built by the team to build a dPCR system with a lower price and wider application range. This makes the dPCR chip out of the dedicated system. Under the condition that DNA can be amplified normally, dPCR function can be realized with simpler equipment by using traditional planar PCR apparatus to provide thermal cycling conditions. The experiment proved that traditional planar PCR can provide suitable reaction conditions for dPCR chips. Under the detection system, the amplified microdroplets can be clearly distinguished, and the detection results are accurate, which is consistent with those of commercial PCR systems. During the experiment, we also found that, for commercial dPCR systems, some DNA cannot be detected due to the special formulation and reagents (such as HBV DNA, UPE DNA, and SARS-COV-2 sample) when they are configured as reaction solutions. But the fluorescence signal of such DNA can be clearly detected by our system, and the concentration can be calculated. In addition, we used TEC to build our own thermal cycling device, and the dPCR chips were used for testing. Experiments showed that the DNA in the chip can be amplified under this thermal cycling device, and the result was accurate. In general, our system used cheaper and simpler equipment to realize the functions of expensive and complex commercial dPCR systems. Moreover, our system has a wider detection range than commercial dPCR systems (RainSure dPCR system).

Data availability statement

The original contributions presented in the study are included in the article/Supplementary Material; further inquiries can be directed to the corresponding author.

Author contributions

WW and KW contributed to the conception and design of the study. BL performed the statistical analysis and wrote the first draft of the manuscript. YG organized the database and wrote sections of the manuscript. YW and YL contributed to manuscript revision and submitted it. All authors contributed to manuscript revision, read, and approved the submitted version.

Funding

This project is supported by the talent program from Guangdong Academy of Sciences (2021GDASYL-20210102012) and GDAS' Project of Science and Technology Development (2022GDASZH-2022010110).

Conflict of interest

The authors declare that the research was conducted in the absence of any commercial or financial relationships that could be construed as a potential conflict of interest.

Publisher's note

References

Arya, M., Shergill, I. S., Williamson, M., Gommersall, L., Arya, N., and Patel, H. R. (2005). Basic principles of real-time quantitative PCR. *Expert Rev. Mol. Diagn.* 55 (2), 209–219. doi:10.1586/14737159.5.2.209

Beck, J., Bierau, S., Balzer, S., Andag, R., Kanzow, P., Schmitz, J., et al. (2013). Digital droplet PCR for rapid quantification of donor DNA in the circulation of transplant recipients as a potential universal biomarker of graft injury. *Clin. Chem.* 59 (12), 1732–1741. doi:10.1373/clinchem.2013.210328

Cao, G., Tan, C., Zhang, Y., Kong, X., Sun, X., Ma, Y., et al. (2019). Digital droplet polymerase chain reaction analysis of common viruses in the aqueous humour of patients with Posner-schlossman syndrome in Chinese population. *Clin. Exp. Ophthalmol.* 47 (4), 513–520. doi:10.1111/ceo.13440

Conteduca, V., Wetterskog, D., Sharabiani, M., Grande, E., Fernandez-Perez, M., Jayaram, A., et al. (2017). Androgen receptor gene status in plasma DNA associates with worse outcome on enzalutamide or abiraterone for castration-resistant prostate cancer: a multi-institution correlative biomarker study. *Ann. Oncol.* 28 (7), 1508–1516. doi:10.1093/annonc/mdx155

Coulson, D. T., Brockbank, S., Quinn, J. G., Murphy, S., Ravid, R., Irvine, G. B., et al. (2008). Identification of valid reference genes for the normalization of RT qPCR gene expression data in human brain tissue. *BMC Mol. Biol.* 9 (1), 46. doi:10.1186/1471-2199-9-46

Ginzinger, D. G. (2002). Gene quantification using real-time quantitative PCR: an emerging technology. *Exp. Hematol.* 30 (6), 503–512. doi:10.1016/s0301-472x(02)00806-8

Gou, T., Hu, J., Wu, W., Ding, X., Zhou, S., Fang, W., et al. (2018). Smartphone-based mobile digital PCR device for DNA quantitative analysis with high accuracy. *Biosens. Bioelectron.* 120, 144–152. doi:10.1016/j.bios.2018.08.030

Hudecova, I. (2015). Digital PCR analysis of circulating nucleic acids. *Clin. Biochem.* 48 (15), 948–956. doi:10.1016/j.clinbiochem.2015.03.015

Ma, Z., Liu, Q., Yang, H., Runyan, R. B., Eisenberg, C. A., Xu, M., et al. (2013). Laser patterning for the study of MSC cardiogenic differentiation at the single-cell level. *Light. Sci. Appl.* 2 (5), e68. doi:10.1038/lsa.2013.24

Moreira, O. C., Ramírez, J. D., Velázquez, E., Melo, M. F. D., Lima-Ferreira, C., Guhl, F., et al. (2013). Towards the establishment of a consensus real-time qPCR to monitor trypanosoma cruzi parasitemia in patients with chronic chagas disease cardiomyopathy: A substudy from the BENEFIT trial. *Acta Trop.* 125 (1), 23–31. doi:10.1016/j.actatropica.2012.08.020

Pinheiro, L. B., Coleman, V. A., Hindson, C. M., Herrmann, J., Hindson, B. J., Bhat, S., et al. (2011). Evaluation of a droplet digital polymerase chain reaction format for DNA copy number quantification. *Anal. Chem.* 84 (2), 1003–1011. doi:10.1021/ac202578x

Sacher, A. G., Paweletz, C., Dahlberg, S. E., Alden, R. S., O'Connell, A., Feeney, N., et al. (2016). Prospective validation of rapid plasma genotyping for the detection of EGFR and KRAS mutations in advanced lung cancer. *JAMA Oncol.* 2 (8), 1014–1022. doi:10.1001/jamaoncol.2016.0173

Sanders, R., Huggett, J. F., Bushell, C. A., Cowen, S., Scott, D. J., and Foy, C. A. (2011). Evaluation of digital PCR for absolute DNA quantification. *Anal. Chem.* 83 (17), 6474–6484. doi:10.1021/ac103230c

Schuler, F., Trotter, M., Geltman, M., Schwemmer, F., Wadle, S., Domínguez-Garrido, E., et al. (2016). Digital droplet PCR on disk. *Lab. Chip* 16 (1), 208–216. doi:10.1039/c5lc01068c

Song, J., Bai, Z., Han, W., Zhang, J., Meng, H., Bi, J., et al. (2012). Identification of suitable reference genes for qPCR analysis of serum microRNA in gastric cancer patients. *Dig. Dis. Sci.* 57 (4), 897–904. doi:10.1007/s10620-011-1981-7

Song, Q., Sun, J., Mu, Y., Xu, Y., Zhu, Q., Jin, Q. J. S., et al. (2018). A new method for polydimethylsiloxane (PDMS) microfluidic chips to maintain vacuum-driven power using Parylene C. *Sens. Actuators B Chem.* 256, 1122–1130. doi:10.1016/j.snb.2017.10.006

Sreejith, K. R., Ooi, C. H., Jin, J., Dao, D. V., and Nguyen, N.-T. (2018). Digital polymerase chain reaction technology – recent advances and future perspectives. *Lab. Chip* 18 (24), 3717–3732. doi:10.1039/c8lc00990b

Tan, C., Chen, X., Wang, F., Wang, D., Cao, Z., Zhu, X., et al. (2019). A multiplex droplet digital PCR assay for non-invasive prenatal testing of fetal aneuploidies. *Analyst* 144 (7), 2239–2247. doi:10.1039/c8an02018c

Taniguchi, K., Kajiyama, T., and Kambara, H. (2009). Quantitative analysis of gene expression in a single cell by qPCR. *Nat. Methods* 6 (7), 503–506. doi:10.1038/nmeth.1338

Tian, Q., Yu, B., Mu, Y., Xu, Y., Ma, C., Zhang, T., et al. (2015). An integrated temporary negative pressure assisted microfluidic chip for DNA isolation and digital PCR detection. *RSC Adv.* 5 (100), 81889–81896. doi:10.1039/c5ra18166f

van Eijk, R., Licht, J., Schrumpf, M., Yazdi, M. T., Ruano, D., Forte, G. I., et al. (2011). Rapid KRAS, EGFR, BRAF and PIK3CA mutation analysis of fine needle aspirates from non-small-cell lung cancer using allele-specific qPCR. *PLoS ONE* 6 (3), e17791. doi:10.1371/journal.pone.0017791

van Ginkel, J. H., Huibers, M. M., van Es, R. J., de Bree, R., and Willems, S. M. (2017). Droplet digital PCR for detection and quantification of circulating tumor DNA in plasma of head and neck cancer patients. *BMC Cancer* 17 (1), 428. doi:10.1186/s12885-017-3424-0

Wang, Z., Cheng, Y., An, T., Gao, H., Wang, K., Zhou, Q., et al. (2018). Detection of EGFR mutations in plasma circulating tumour DNA as a selection criterion for first-line gefitinib treatment in patients with advanced lung adenocarcinoma (BENEFIT): a phase 2, single-arm, multicentre clinical trial. *Lancet Respir. Med.* 6 (9), 681–690. doi:10.1016/s2213-2600(18)30264-9

Whale, A. S., Huggett, J. F., Cowen, S., Speirs, V., Shaw, J., Ellison, S., et al. (2012). Comparison of microfluidic digital PCR and conventional quantitative PCR for measuring copy number variation. *Nucleic Acids Res.* 40 (11), e82. doi:10.1093/nar/gks203

frontiers | Frontiers in Bioengineering and Biotechnology

TYPE Original Research
PUBLISHED 24 August 2022
DOI 10.3389/fbioe.2022.964244

OPEN ACCESS

EDITED BY
Hongna Liu,
iRepertore Inc., United States

REVIEWED BY
Zhishan Yuan,
Guangdong University of Technology, China
Nathan A. Tanner,
New England Biolabs, United States
Mohammad Soleimani,
Aja University of Medical Sciences, Iran

*CORRESPONDENCE
Zhihong Jiang,
zhjiang@must.edu.mo

SPECIALTY SECTION
This article was submitted to Biosensors and Biomolecular Electronics, a section of the journal Frontiers in Bioengineering and Biotechnology

RECEIVED 08 June 2022
ACCEPTED 21 July 2022
PUBLISHED 24 August 2022

CITATION
Wu Y, Bai L, Ye C, Yuhong Guan, Kunming Yan, Chen H and Jiang Z (2022), Novel miniaturized fluorescence loop-mediated isothermal amplification detection system for rapid on-site virus detection.
Front. Bioeng. Biotechnol. 10:964244.
doi: 10.3389/fbioe.2022.964244

Novel miniaturized fluorescence loop-mediated isothermal amplification detection system for rapid on-site virus detection

Yanqi Wu[1,2], Liping Bai[1], Chengfu Ye[2], Yuhong Guan[2], Kunming Yan[2], Hui Chen[3] and Zhihong Jiang[1]*

[1]State Key Laboratory of Quality Research in Chinese Medicine, Macau University of Science and Technology, Taipa, China, [2]Shenzhen LemnisCare Medical Technology Co., Ltd, Shenzhen, China, [3]Hunan Key Laboratory of Biomedical Nanomaterials and Devices, Hunan University of Technology, Zhuzhou, China

New pathogen outbreaks have progressed rapidly and are highly infectious in recent years, increasing the urgency of rapid and accurate detection of pathogenic microorganisms. Based on the point-of-care testing (POCT) requirements, in this study, a real-time fluorescent loop-mediated isothermal amplification (LAMP) detection system was developed and applied to pathogen detection. The system is compact and portable, with good uniformity and reproducibility, and it can detect pathogens rapidly and effectively. For norovirus detection, the linear range was 10^0–10^6 copies/μL. The system can achieve the theoretical sensitivity of LAMP detection, conclusions could be obtained within 35 min, and quantitative detection was possible. The test results of 45 clinical samples were consistent with quantitative PCR (qPCR) and clinical results, and the accuracy could reach 100%. This system has the characteristics of portability, speed, and POCT accuracy, and the cost is much lower than that of commercial qPCR. Therefore, it is suitable for remote areas or places with relatively poor conditions and environments requiring on-site conditions. It can also be widely used to detect various epidemics and unexpected diseases.

KEYWORDS

LAMP, POCT, norovirus, fluorescence detection, aerosol pollution

1 Introduction

In recent years, due to the continuous emergence of new pathogens such as Zika virus, Ebola virus, SARS, and COVID-19 etc. (Liao et al., 2017; Al-Saud et al., 2020), rapid and highly infectious outbreaks of new pathogens have made rapid and accurate identification of pathogenic microorganisms and diagnosis of infectious disease an urgent need (Chen et al., 2018; Demrba et al., 2021). The technology of diagnosing diseases has been developing continuously, from the earliest culture method to hematological analysis, specific protein detection, immunological antigen, and antibody detection, to pathogen mass spectrometry and nucleic acid analysis (Hussain et al., 2020) six; the methods are

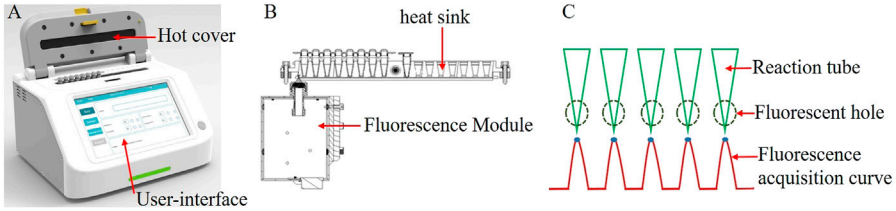

FIGURE 1
(A) Overall schematic of the system; **(B)**. Schematic of the heat trap and fluorescence modules; **(C)**. Multi-channel fluorescence signal acquisition curve.

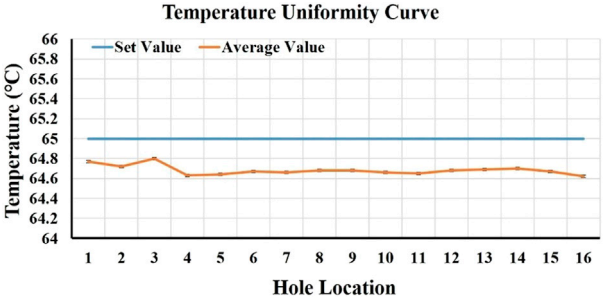

FIGURE 2
16-well temperature uniformity curve.

becoming increasingly accurate. Compared with traditional etiological diagnostic methods with higher detection values but a slower detection process, nucleic acid testing is currently the leading technology for pathogen diagnosis (Tang et al., 2020; Fang et al., 2021; Xu et al., 2021).

The application of the mainstream polymerase chain reaction (PCR) and its derivative technologies in various nucleic acid testing is unsuitable for on-site application due to high instrument requirements and complicated operations (He et al., 2017). Various high-efficiency, high-sensitivity, and specific isothermal amplification technologies can meet the needs of on-site detection, such as low equipment requirements and simple operation (Chen et al., 2017; Liu et al., 2019). Presently, the main isothermal amplification technologies are rolling circle amplification (RCA) (Gu et al., 2018; Zhao et al., 2020), loop-mediated isothermal amplification (LAMP) (Chen et al., 2018), strand displacement amplification (SDA), nucleic acid sequence-based amplification (NASBA), helix-dependent amplification (HAD), and recombinase polymerase amplification technology (RPA) (Knox and Beddoe, 2021; Wei et al., 2022). Although these technologies have their limitations, LAMP is currently the most widely used. LAMP technology enables simple and rapid nucleic acid amplification. Due to its extremely high amplification efficiency, several products and byproducts are generated in a short time, which is more convenient for detection. Common detection methods include gel electrophoresis, turbidity, colloidal gold test strip, metal ion indicator, and fluorescence detection methods. The principle of fluorescence detection is the same as that of real-time fluorescent PCR. Through fluorescent probes or dyes, the amplification speed of LAMP is more than that of PCR and LOD of LAMP method is theoretically comparable to the real-time fluorescent PCR method.

On the other hand, with the advancement of medical means and the continuous improvement of the degree of automation, society has paid more attention to the usage scenarios of point-of-care testing (POCT) in recent years (Chen et al., 2019; Liu et al., 2022). The core of this concept is that the tests that can only be performed in laboratories or hospitals can be transferred to people's homes, being a part of their daily lives, without the need for professional personnel to operate, simplifying testing procedures, reducing testing cost and time, and at the same time, meeting the requirements of accuracy. However, this concept requires a high degree of integration and automation of medical instruments, as well as good portability. Compared with the cumbersome process of the traditional clinical laboratory and the inability to implement rapid on-site testing, POCT realizes the miniaturization of the instrument, the simplicity of operation, and the real-time testing on-site. The fluorescent LAMP detection method combined with the POCT detection instrument can realize the rapid, accurate, and efficient detection of pathogen nucleic acid in remote areas or places with relatively poor conditions. Many businesses are dedicated to the research of POCT systems, high accuracy, miniaturization, and portability are their consistent goals. For example, ABBOTT specializes in point-of-care solutions and its ID NOW™ isothermal nucleic acid amplification detector can simultaneously detect influenza A and B viruses within 15 min without the need for expensive laboratory equipment (Masciotra et al., 2013; van den Berk et al., 2003). Lucira's Lucira COVID-19 all-in-one test kit utilizes RT-LAMP technology to detect the N gene RNA of SARS-CoV-2, generating a signal from several RNA copies in less than 30 min, generated by the process of amplification A change in pH, followed by a change in the color of the dye in the

TABLE 1 RT-LAMP and RT-qPCR reaction conditions.

RT-LAMP		RT-qPCR	
Experimental components	Condition setting	Experimental components	Condition setting
10X Isothermal amplification buffer II, 2.5 μl		2x Buffer, 12.5 μl	50°C, 10 min 95°C, 5 min 95°C, 15 s 60°C, 30 s 45 cycles 60°C fluorescence collection
MgSO4 (100 mm), 1.5 μl		Enzyme mix, 1 μl	
dNTP Mix (10 mm), 3.5 μl	65 C 45 min,Fluorescence is collected every minute	Forward primer (20 μm), 1 μl	
FIP/BIP primers (40 μm), 1 μl		Reverse primer (20 μm), 1 μl	
F3/B3 primers (20 μm), 1 μl		Probe (10 μm), 1 μl	
LF/LB primers (20 μm), 1 μl		Nuclease-free water, 3.5 μl	
Nuclease-free water 7 μl		DNA or RNA Sample 5 μl	
NEB LAMP dye (50x), 0.5 μl			
Bst 3.0 DNA polymerase (8 U/μl), 2 μl			
DNA or RNA sample, 5 μl			
Total, 25 μl		Total, 25 μl	

reaction mixture, enables accurate self-diagnosis at home (2021). The Cue™ COVID-19 Test Cartridge Pouch developed by Cue Health can produce test results in 20 min and transmit the results to the smart devices of users and doctors (2021). Research shows that the product has a sensitivity and specificity of up to 98%. Among these products, methods such as immunochromatography, LAMP and Real-time PCR are used to achieve rapid detection of individual samples, and the reagents and consumables can be discarded for one-time use. The above-mentioned platforms are very fast and convenient for POCT applications, but for some remote or under-condition areas or places, the cost of a single detection of these instruments increases due to the specificity of consumables or reagents; on the other hand, the small quantitative testing is often also required for POCT. Therefore, we hope to design a rapid detection system with low throughput and strong versatility.

In order to meet the needs of on-site nucleic acid detection of a small number of samples, we developed a portable fluorescent LAMP detection system that can rapidly and effectively detect pathogens. Herein, after introducing the system structure and evaluating and verifying its performance, we applied the system to actual sample detection. Compared with those of laboratory detection methods, the results show that the system's accuracy, sensitivity, and stability can meet the needs of nucleic acid testing and enable early diagnosis of pathogens on the spot, providing an effective basis for disease prevention, control, and precise treatment.

2 System structure

Overall system dimensions: The portable fluorescent LAMP detection system has a length, width, and height of 240 × 180 × 150 mm, respectively, and a weight of 3.6 kg, with an internally integrated heat sink, heating module, fluorescent module, and display module (Figure 1A). There are two eight-row heat sink holes, which can detect 16 samples simultaneously. Unlike the commercial Roche and ABI fluorescence detection instruments, which read the fluorescence from the top, this system reads the fluorescence from the side. By opening a 3-mm small hole on the lower side of each heat sink hole, the fluorescence module collects and detects the fluorescence signal when it passes through each well by sliding, as shown in Figure 1B. At present, we have tested the fluorescent channel suitable for SYBR/FAM, which can be detected by their similar fluorescent probes or dyes. The collected fluorescence signal will have a maximum fluorescence value in each well, and this maximum value is selected as the fluorescence value of the well in this reaction time period, as shown in Figure 1C. The heating module is mainly made up of a heat sink and heat cover heating. The heat sink heating adopts a thermoelectric cooler, while the heat cover heating adopts a thin film heater. The display module integrates a human–computer interaction interface through which the user can set the experimental parameters, including reaction temperature, time, sample well information, etc., and display the fluorescence detection curve in real-time during the experiment.

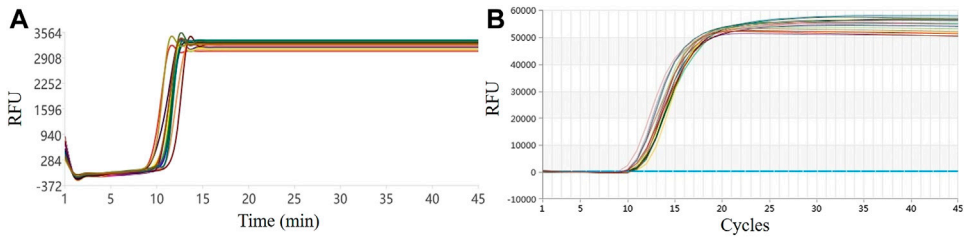

FIGURE 3
Six-well uniformity test results: **(A)** Our system. **(B)** Commercial qPCR instrument.

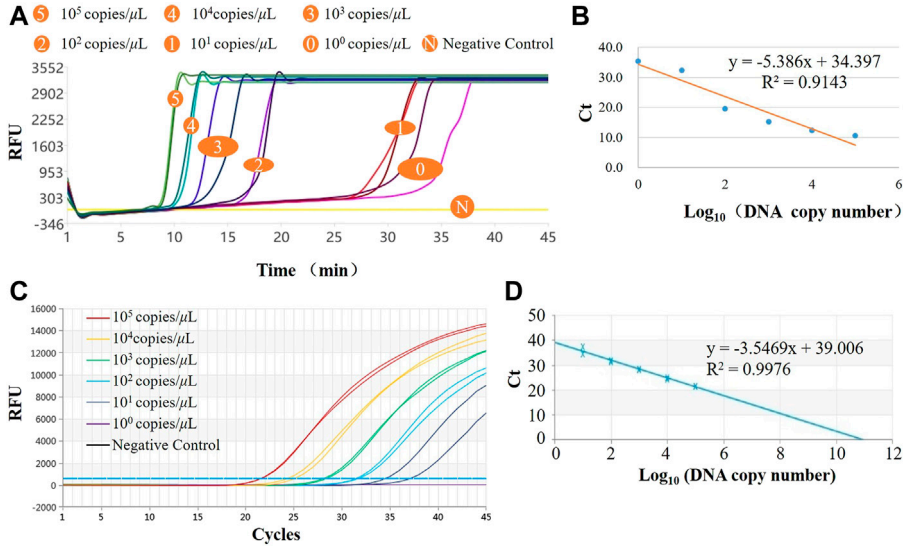

FIGURE 4
Results of norovirus sensitivity. **(A)** LAMP amplification curves of six concentration gradients in the system; **(B)** Standard curve for LAMP assay; **(C)** qPCR amplification curves of six concentration gradients in the system; **(D)** Standard curve for qPCR assay.

3 System performance

The main factors that affect the experimental results are temperature, fluorescence signal acquisition, etc. Therefore, it is necessary to evaluate the performance of the entire system from hardware and experiments.

3.1 Temperature

Temperature, especially its uniformity, stability of the heat sink, and the heating speed, are important factors that affect the amplification effect of LAMP. To test the temperature of 16 sample wells, two eight-row 0.2 ml centrifuge tubes (Aixin Biotechnology (Hangzhou) Co., Ltd, Hangzhou, China) were placed in a heat trap, 50 μL of pure water was added to each centrifuge tube, and the heat sink temperature was set to 65°C. The temperature of the liquid in each centrifuge tube was then measured. Each hole was tested every 5 s for 10 consecutive times. We analyzed the average temperature, standard deviation (SD), coefficient of variation (CV) values, etc., of each hole. The test results are depicted in Figure 2. It shows that among the 16 holes, the minimum average temperature was 64.62°C, and the maximum was 64.8°C, the temperature fluctuation of 10 measurements per well was less than 0.3°C, the maximum temperature difference from the set temperature did not exceed 0.5°C, and the CV value was 0.07–0.15%. The setting temperature was 27–65°C, and it took 15 s to reach the set temperature for the first time, indicating that the heating rate can reach 2.53°C/s. The temperature test results revealed that the temperature uniformity of the 16 wells

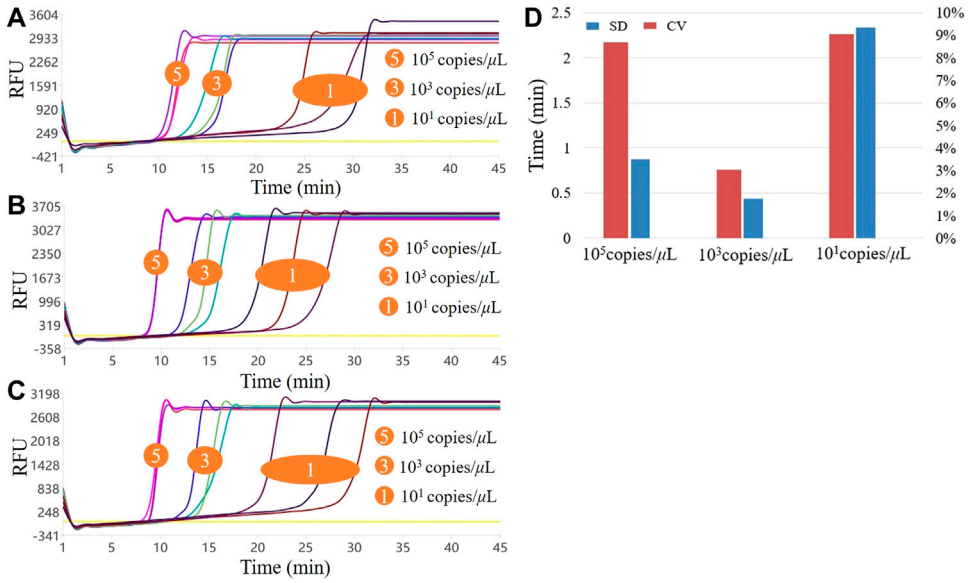

FIGURE 5
Results of the three LAMP experiments with high, medium, and low concentrations. **(A–C)** show the three LAMP amplification curves, respectively; **(D)**. Stability of the three LAMP experiments.

was good, the temperature control was stable, and the heating rate was fast, which did not affect the amplification.

3.2 Evaluation and verification of RT-LAMP performance

To test the usability of the system, the sensitivity, detection limit, uniformity, and repeatability stability of the system were tested and evaluated and compared with commercial qPCR instruments Gentier 96E (Xi'an Tianlong Technology Co., Ltd, Xi'an, China), and the results were compared with qPCR detection. The LAMP and qPCR reagents were purchased from commercial kits (Shenzhen LemnisCare Medical Technology Co., LTD, Shenzhen, China). Table 1 describes the reagents and conditions for RT-LAMP and RT-qPCR detection.

3.2.1 Uniformity

We diluted the norovirus GII standard to 10^4 copies/μL for the LAMP experiment, prepared 16 reaction solutions according to the experimental components in Table 1, distributed them into two eight-row 0.2 ml centrifuge tubes, put the centrifuge tubes into the system, set up the system according to the reaction conditions in Table 1, and observed the real-time fluorescence amplification curve of 16 wells. Simultaneously, we ran the same test on Gentier 96E (Xi'an Tianlong Technology Co., Ltd, Xi'an, China). The uniformity of the system was assessed by the time to threshold (Tt) values of the amplification curves and the coincidence of the curves.

3.2.2 Sensitivity and detection limit

We diluted the norovirus standard with sterile water in a 10-fold gradient to six concentrations (10^5–10^0copies/μL), configured the reaction solution according to Table 1, set a negative control, configured two copies of each concentration, and put them into the test system. Then, we configured the reaction solution according to the qPCR system in Table 1, added the same standard substance, and performed qPCR detection using the Tianlong real-time fluorescence PCR instrument. The detection limit of the system and the difference from qPCR detection were determined by amplification curve and Tt and Ct values.

3.2.3 Stability

Three different concentrations of standards were selected for testing, wherein the high, medium, and low concentrations were 10^5copies/μL, 10^3copies/μL, and 10^1copies/μL, respectively. The reaction solution was configured according to the system in Table 1, a negative control was established, and three copies of each concentration were configured and introduced into the system for detection. The experiment was repeated thrice to detect the high, medium, and low concentrations. First, the stability was initially assessed by the amplification curve of the three experiments, and

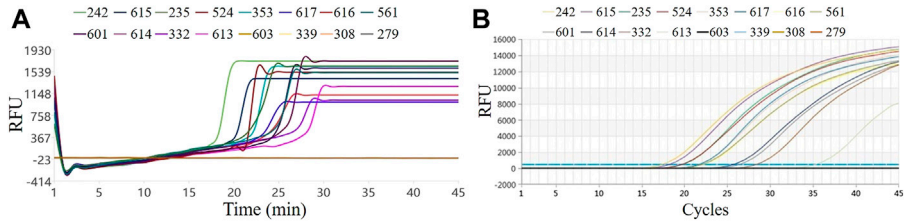

FIGURE 6
Results of clinical samples by RT-LAMP and RT-qPCR. **(A)** RT-LAMP on our system; **(B)** RT-qPCR on the commercial instrument.

then the detection results of the three experiments were put together to compare the CV value of the average Tt. The Tt value refers to the calculation of the real-time fluorescent PCR Ct value, and the baseline was calculated according to the negative control fluorescence value of each experiment group.

3.2.4 RT-LAMP and RT-qPCR for the detection of clinical samples

We collected 45 cases of norovirus diarrhea samples from the Guangdong Provincial People's Hospital, performed nucleic acid extraction for clinical samples, adopted the magnetic bead method using a nucleic acid extraction kit (Shenzhen LemnisCare Medical Technology Co., LTD, Shenzhen, China), and performed the RT-LAMP test on this system. We set the reaction system and reaction conditions as stated in Table 1. Simultaneously, we conducted RT-qPCR test to compare the test results.

4 Results and discussion

4.1 Homogeneity assessment

The 16-well LAMP real-time fluorescence amplification curve of this system and the amplification curve on a commercial qPCR instrument are shown in Figure 3. From the shape of the curve, the overlap of the two amplification curves is high. According to the Tt value, the average value of the reaction of 16 wells in this system was 12.56, the SD was 0.73, and the CV was 5.81%; the LAMP experimental results on a commercial qPCR instrument revealed an average Ct value of 9.83, an SD of 0.38, and a CV of 3.88%, as shown in Figure 3B. Compared with the commercial qPCR instrument, the CV was only 1.93% different, indicating that the overall uniformity of the system is good.

4.2 Sensitivity and detection linear range evaluation

The LAMP amplification curves of six concentration gradients are shown in Figure 4A. From the shape of the amplification curve, it could be observed that the amplification efficiency was stable and high, and the sensitivity could reach 10^0 copies/μL, i.e., copy numbers within 10 can be detected. The minimum detection limit detection time was <35 min. The logarithm of the plasmid concentration has an obvious linear relationship with the Tt value. As shown in Figure 4B, the R^2 value is 0.9143, indicating that the system also has potential quantitative performance. The real-time PCR amplification curves of the same six concentration gradients are shown in Figure 4C, and the standard curve is shown in Figure 4D. It could be observed from the amplification curve that the detection line of real-time fluorescent PCR was 10^1 copies/μL, and the whole PCR process took about 90 min. From the perspective of the linearity of the standard curve, LAMP is worse than qPCR, which is primarily reflected in low concentration detection. Also, its amplification efficiency was not as good following high concentration detection, and the amplification was unstable, resulting in a decrease in the overall linearity, although it was basically a linear relationship. Quantitative detection was possible. In terms of detection time, LAMP was superior to the gold standard qPCR; In terms of sensitivity, theoretically qPCR assays can detect to <10 copies, which means that LOD (Limits of Detection) of LAMP and qPCR are comparable. This system uses the LAMP method for pathogen detection, which meets the actual needs in terms of accuracy and speed and is competitive in POCT.

4.3 Stability assessment

Stability is also a crucial performance indicator of detection methods and systems. The system uses high, medium, and low concentration standard samples that are repeated three times to ensure reproducibility. The amplification curves of the three assays are shown in Figures 5A,C. From the overall perspective of the curved shape, the high, medium, and low concentrations of the three experiments could be amplified normally, the curve shape similarity was high, and the reproducibility between batches was high concentration > medium concentration > low concentration.

We calculated the SD and CV values of the Tt values for the three experiments at three concentrations. As shown in Figure 5D, the CVs of the high, medium, and low concentrations were 8.69, 3.02, and 9.05%, respectively. The performance was medium concentration > high concentration > low concentration. The above CV values were <10%, indicating that the overall amplification efficiency of the system was reproducible. Additionally, the detection results of the repeatable experiments on commercial PCR instruments were consistent with those in this system, so the stability of this system for point-of-care diagnosis of norovirus meets the requirements and could be applied to real-time qualitative monitoring of the virus, with high specificity, sensitivity, and rapidity.

4.4 Rt-LAMP and RT-qPCR for the detection of clinical samples

The results of temperature, uniformity, sensitivity, and reproducibility show that the system can be used for pathogen detection in a stable, fast, convenient, and portable manner. We further verified the performance of the system to test actual samples. We tested 45 clinical norovirus diarrhea samples, including 12 positive and 33 negative samples. We selected three negative and 12 positive samples for testing in this system, and the results are shown in Figure 6. Figure 6A represents the RT-LAMP amplification curve, and Figure 6B is the RT-qPCR amplification curve. The Ct value of RT-qPCR curve and the Tt value of the RT-LAMP curve were in the same order, indicating that the RT-LAMP and RT-qPCR detection results of this batch of clinical samples on the system are consistent. From the comparison between the Tt value and the time to reach the plateau phase, it was revealed that LAMP could reach the plateau phase within 5 min after the Tt value starts, while qPCR could reach the plateau phase after at least 15 cycles. Therefore, LAMP has an absolute advantage in the overall response time, making this system ideal for rapid on-site pathogen detection.

We discovered that the uniformity and stability of this system were not significantly different from those of commercial equipment after summarizing the above performance test and evaluation results. The linear range detected by this system was 10^0–10^6 copies/μL, and the sensitivity of the system can be similar to that of commercial PCR instruments. Furthermore, the detection of 45 clinical samples was consistent with the qPCR and clinical results, and the accuracy could reach 100%. Another outstanding performance of this system is that it could significantly reduce the detection time and improve the amplification efficiency when detecting pathogens. For raw data on performance testing, please check Supplementary Tables S1, S2 and Supplementary Figures S1–S4 in the Supplementary Materials.

5 Conclusion

Summarily, in this study, we successfully developed a real-time fluorescent RT-LAMP detection system and applied it to pathogen detection. The whole system is compact and portable, and it can rapidly and effectively detect pathogens. For the norovirus detection, the entire process could be completed within 45 min, and the system can achieve the theoretical sensitivity of LAMP detection, test results could be determined within 35 min, and quantitative testing was possible. The overall uniformity and reproducibility of the system were good, and the detection results of clinical samples were consistent with the RT-qPCR and clinical results. Moreover, the cost is much lower than that of commercial qPCR, and it uses conventional reagent consumables and has 16 sample detection holes, making it very suitable for areas where medical conditions are relatively scarce or need on-site environments. It can also be used to detect various epidemiological and unexpected diseases such as novel coronavirus, monkeypox virus, African swine fever, etc. Thus, these show that this system has the characteristics of portability, speed, and accuracy of a POCT.

Data availability statement

The original contributions presented in the study are included in the article/Supplementary Material, further inquiries can be directed to the corresponding author.

Author contributions

ZJ: Ideas, formulation or evolution of overarching research goals and aims; YW: System mechanical structure design; LB: Management and coordination responsibility for the research activity planning and execution; CY: System Hardware Control Design; YG: Investigation conducting a research and investigation process, specifically performing the experiments, or data/evidence collection; KY: System screen user interface design and algorithm research; HC: Verification, whether as a part of the activity or separate, of the overall replication/reproducibility of results/experiments and other research outputs.

Funding

This research was financially funded by the Science and Technology Development Fund, Macau SAR [File No. 0065/2020/A2, SKL-QRCM(MUST)-2020-2022].

Conflict of interest

Authors YW, CY, YG, and KY were employed by the company Shenzhen LemnisCare Medical Technology Co., Ltd.

The remaining authors declare that the research was conducted in the absence of any commercial or financial relationships that could be construed as a potential conflict of interest.

Publisher's note

All claims expressed in this article are solely those of the authors and do not necessarily represent those of their affiliated organizations, or those of the publisher, the editors and the reviewers. Any product that may be evaluated in this article, or claim that may be made by its manufacturer, is not guaranteed or endorsed by the publisher.

Supplementary material

The Supplementary Material for this article can be found online at: https://www.frontiersin.org/articles/10.3389/fbioe.2022.964244/full#supplementary-material

References

Al-Saud, H., Al-Romaih, K., Bakheet, R., Mahmoud, L., Al-Harbi, N., Alshareef, I., et al. (2020). Automated SARS-COV-2 RNA extraction from patient nasopharyngeal samples using a modified DNA extraction kit for high throughput testing. *Ann. Saudi Med.* 40, 373–381. doi:10.5144/0256-4947.2020.373

Chen, H., Liu, K., Li, Z., and Wang, P. (2019). Point of care testing for infectious diseases. *Clin. Chim. Acta* 493, 138–147. doi:10.1016/j.cca.2019.03.008

Chen, H., Wu, Y., Chen, Z., Hu, Z., Fang, Y., Liao, P., et al. (2017). Performance evaluation of a novel sample in–answer out (SIAO) system based on magnetic nanoparticles. *J. Biomed. Nanotechnol.* 13, 1619–1630. doi:10.1166/jbn.2017.2478

Chen, Z., Yang, T., Yang, H., Li, T., Nie, L., Mou, X., et al. (2018). A portable Multi-channel turbidity system for rapid detection of pathogens by loop-mediated isothermal amplification. *J. Biomed. Nanotechnol.* 14, 198–205. doi:10.1166/jbn.2018.2524

Demrba, Y. S., Sareyypolu, B., Ztrk, H., Ksmal, G., and Zkul, A. (2021). The role of bio-detection dogs in prevention and diagnosis of infectious disease: A systematic review. *Veteriner Fakültesi derg* 68, 185–192. doi:10.33988/auvfd.834133

Fang, Y., Liu, H., Wang, Y., Su, X., Jin, L., Wu, Y., et al. (2021). Fast and accurate control strategy for portable nucleic acid detection (PNAD) system based on magnetic nanoparticles. *J. Biomed. Nanotechnol.* 17, 407–415. doi:10.1166/jbn.2021.3028

Gu, L., Yan, W., Liu, L., Wang, S., Zhang, X., and Lyu, M. (2018). Research progress on rolling circle amplification (RCA)-Based biomedical sensing. *Pharm. (Basel)* 11, 35. doi:10.3390/ph11020035

He, L., Yang, H., Xiao, P., Singh, R., He, N., Liu, B., et al. (2017). Highly selective, sensitive and rapid detection of *Escherichia coli* O157:H7 using duplex PCR and magnetic nanoparticle-based chemiluminescence assay. *J. Biomed. Nanotechnol.* 13, 1243–1252. doi:10.1166/jbn.2017.2422

Hussain, M., Chen, Z., Lv, M., Xu, J., Dong, X., Zhao, J., et al. (2020). Rapid and label-free classification of pathogens based on light scattering, reduced power spectral features and support vector machine. *Chin. Chem. Lett.* 31, 3163–3167. doi:10.1016/j.cclet.2020.04.038

Knox, A., and Beddoe, T. (2021). Isothermal Nucleic Acid Amplification Technologies for the Detection of Equine Viral Pathogens. *Anim. (Basel)* 11, 2150. doi:10.3390/ani11072150

Liao, Y., Xu, B., Wang, J., and Liu, X. (2017). A new method for assessing the risk of infectious disease outbreak. *Sci. Rep.* 7, 40084. doi:10.1038/srep40084

Liu, S., He, X., Zhang, T., Zhao, K., Xiao, C., Tong, Z., et al. (2022). Highly sensitive smartphone-based detection of Listeria monocytogenes using SYTO9. *Chin. Chem. Lett.* 33, 1933–1935. doi:10.1016/j.cclet.2021.11.051

Liu, Y., Li, T., Ling, C., Wang, Z., Jin, L., Zhao, Y., et al. (2019). A simple visual method for DNA detection based on the formation of gold nanoparticles. *Chin. Chem. Lett.* 30, 2359–2362. doi:10.1016/j.cclet.2019.10.033

Masciotra, S., Luo, W., Youngpairoj, A. S., Kennedy, M. S., Wells, S., Ambrose, K., et al. (2013). Performance of the alere Determine™ HIV-1/2 Ag/Ab combo rapid test with specimens from HIV-1 seroconverters from the US and HIV-2 infected individuals from ivory coast. *J. Clin. Virology* 58, e54-e58. doi:10.1016/j.jcv.2013.07.002

Tang, C., He, Z., Liu, H., Xu, Y., Huang, H., Yang, G., et al. (2020). Application of magnetic nanoparticles in nucleic acid detection. *J. Nanobiotechnology* 18, 62. doi:10.1186/s12951-020-00613-6

van den Berk, G. E., Frissen, P. H., Regez, R. M., and Rietra, P. J. (2003). Evaluation of the rapid immunoassay determine HIV 1/2 for detection of antibodies to human immunodeficiency virus types 1 and 2. *J. Clin. Microbiol.* 41, 3868–3869. doi:10.1128/jcm.41.8.3868-3869.2003

Wei, Z., Wang, X., Feng, H., Ji, F., Bai, D., Dong, X., et al. (2022). Isothermal nucleic acid amplification technology for rapid detection of virus. *Crit. Rev. Biotechnol.*, 1–18. doi:10.1080/07388551.2022.2030295

Xu, Y., Wang, T., Chen, Z., Jin, L., Wu, Z., Yan, J., et al. (2021). The point-of-care-testing of nucleic acids by chip, cartridge and paper sensors. *Chin. Chem. Lett.* 32, 3675–3686. doi:10.1016/j.cclet.2021.06.025

Zhao, S., Luo, J., Zeng, X., Li, K., Yuan, R., Zhu, L., et al. (2020). Rolling circle amplification (RCA)-Mediated genome-wide ihpRNAi mutant library construction in Brassica napus. *Int. J. Mol. Sci.* 21, 7243. doi:10.3390/ijms21197243

frontiers | Frontiers in Bioengineering and Biotechnology

TYPE Original Research
PUBLISHED 06 September 2022
DOI 10.3389/fbioe.2022.1006374

OPEN ACCESS

EDITED BY
Zhiyang Li,
Nanjing Drum Tower Hospital, China

REVIEWED BY
Fernando Soto,
Stanford University, United States
Xianguang Ding,
Nanjing University of Posts and Telecommunications, China

*CORRESPONDENCE
Qiang Ding,
dingqiang@njmu.edu.cn
Changmin Yu,
iamcmyu@njtech.edu.cn
Jifu Wei,
weijifu@njmu.edu.cn

†These authors have contributed equally to this work and share first authorship

SPECIALTY SECTION
This article was submitted to Biosensors and Biomolecular Electronics, a section of the journal Frontiers in Bioengineering and Biotechnology

RECEIVED 29 July 2022
ACCEPTED 15 August 2022
PUBLISHED 06 September 2022

CITATION
Wang C, Zhang D, Yang H, Shi L, Li L, Yu C, Wei J and Ding Q (2022), A light-activated magnetic bead strategy utilized in spatio-temporal controllable exosomes isolation.
Front. Bioeng. Biotechnol. 10:1006374.
doi: 10.3389/fbioe.2022.1006374

A light-activated magnetic bead strategy utilized in spatio-temporal controllable exosomes isolation

Chenhan Wang[1†], Duoteng Zhang[2†], Haiyan Yang[1†], Liang Shi[1], Lin Li[2], Changmin Yu[2*], Jifu Wei[3*] and Qiang Ding[1*]

[1]Jiangsu Breast Disease Center, The First Affiliated Hospital with Nanjing Medical University, Nanjing, China, [2]Key Laboratory of Flexible Electronics (KLOFE) and Institute of Advanced Materials (IAM), Nanjing Tech University (NanjingTech), Nanjing, China, [3]Department of Pharmacy, Jiangsu Cancer Hospital and Jiangsu Institute of Cancer Research and The Affiliated Cancer Hospital of Nanjing Medical University, Nanjing, China

Tumor-derived exosomes are considered as a key biomarker in the field of liquid biopsy. However, conventional separation techniques such as ultracentrifugation, co-precipitation and column chromatography cannot isolate samples with high throughput, while traditional immunomagnetic separation techniques, due to steric effect of magnetic beads, reducing sensitivity of exosomes optical detection. Herein, we provide a novel and simple nanoplatform for spatiotemporally controlling extraction and elution of exosomes *via* magnetic separation and light-activated cargo release. In this system, magnetic beads are co-modified by photoresponsive groups -nitrobenzyl group and aptamers that are compatible with CD63-a highly expressed exosomal surface-specific protein. Through exosomes extracted from cell model and nude mice xenograft tumor model morphological characterization and proteomic analysis, results showed that our novel magnetic bead system outperformed current ultracentrifugation in serum exosome extraction in terms of extraction time, yield, and proportion of populations with high CD63 expression. This strategy may be a powerful tool for exosome isolation in clinical liquid biopsies of cancer disease.

KEYWORDS

exosome, cancer, magnetic separation, light-activated release, liquid biopsy

Introduction

Liquid biopsy is an emerging adjunctive detection method, which uses biological information carried by body fluid components such as blood, urine, sweat, et al. (Willms et al., 2018; Wang C et al., 2020; Descamps et al., 2022; Markou et al., 2022). Exosomes, a type of small extracellular vesicles with a size of 30–150 nm, are well-documented to participate in tumor development, e.g., stimulating the growth of tumor cells, suppressing anti-tumor immunity, promoting tumor cell migration and metastasis, et al. (Liu et al., 2018; Hofmann et al., 2020; Liao and Li, 2020; Chen et al., 2022; He et al., 2022). They are

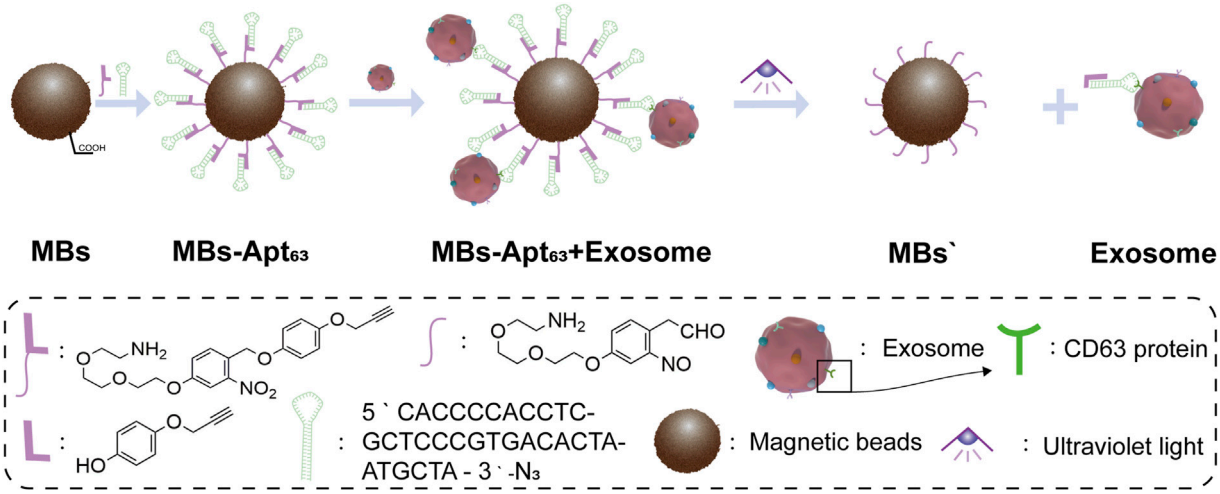

FIGURE 1
Schematic illustration of our ultraviolet-responsive nanomagnetic beads for binding and separation of exosomes.

appealing to liquid biopsy due to following advantages: *1*) possessing diverse tumor biological information, such as RNAs, DNAs, and proteins; *2*) secreted by and indicating the activity of living tumor cells; *3*) easy to preserve and identify *via* their surface markers (Gurunathan et al., 2019; Sung et al., 2020; Yu et al., 2021). In fact, in some tumors, such as prostate and breast cancer, exosome-based liquid biopsies have shown significant prognostic value (Ibsen et al., 2017; Guo et al., 2020; Shen et al., 2020; Puhka et al., 2022).

Currently, exosomes are mainly isolated through ultracentrifugation (UC) (Momen-Heravi et al., 2013; Wang S et al., 2020; Xie et al., 2020; Yang et al., 2020). UC is normally time- and labor-consuming, and depends on availability of instrument. Some emerging exosome isolation methods, such as size separation-based chromatography column, microfluidic, immunosorbent-based kit *etc.* (Momen-Heravi et al., 2013; Gurunathan et al., 2019; Shen et al., 2020). These methods are cumbersome in extraction procedures and are not suitable for simple high-throughput detection (Lu et al., 2022; Zhao et al., 2022; Zhu et al., 2022). To solve the issues of centrifugal method, some new separation methods have been developed, such as magnetic bead system based on immunological binding and magnetic separation. Notably, in order to elute the captured exosomes from magnetic beads, non-physiological conditions of extreme ion concentrations are commonly involved, which may cause irreversible damage to exosomes during isolation and subsequently result in false information (Gao et al., 2019; Choi et al., 2022). Moreover, exosome detection methods based on magnetic separation have obvious steric hindrance due to large particle sizes of magnetic beads and exosomes. Detection technologies using fluorescence or chemiluminescence will weaken fluorescence signals due to masking or quenching effect of magnetic beads (Yang et al., 2015). Therefore, the development of a new magnetic bead system for efficient and gentle separation of exosomes has become an urgent need in the field of liquid biopsy.

Light is noninvasive, spatiotemporally controllable, and biocompatible, which is widely used as a trigger in clinical imaging diagnosis and treatment. This inspired us to exploit light-activated degradation to elude exosomes, which would allow spatial, temporal, and rate control by manipulating the location, timing, and intensity of applied light. Herein, we developed a novel strategy using magnetic bead-based capture and light-activated elution for spatiotemporally controllable exosome isolation from serum. As shown in Figure 1, we anchored CD63 aptamer on the surface of magnetic beads *via* light-sensitive nitrobenzene group, which was cleaved by ultraviolet (UV) light at around 365 nm (Chang et al., 2009; Kobayashi et al., 2012; Lai et al., 2016; Wang et al., 2017; Hentzen et al., 2020). CD63 is member of tetraspanins that is considered to be a reliable exosome surface marker. It plays important roles in membrane transport and has been proved to be a biomarker for breast cancer exosomes (Song et al., 2020; Mathieu et al., 2021). After incubation with serum from breast cancer-bearing mice, our magnetic bead system can selectively bind with the CD63 protein on exosomes, and subsequently isolate the target exosomes with external magnetic field. Finally, the structurally and functionally intact exosomes would be eluted from magnetic beads by regulating light excitation. This nanodevice provides a controllable strategy for separating exosomes from serum, allowing us to maximally preserve the value of exosomes for liquid biopsy and clinical studies. At the same time, the magnetic bead sorting method based on optical control strategy also provides a new platform for exosome detection of liquid homogeneous substances in the future.

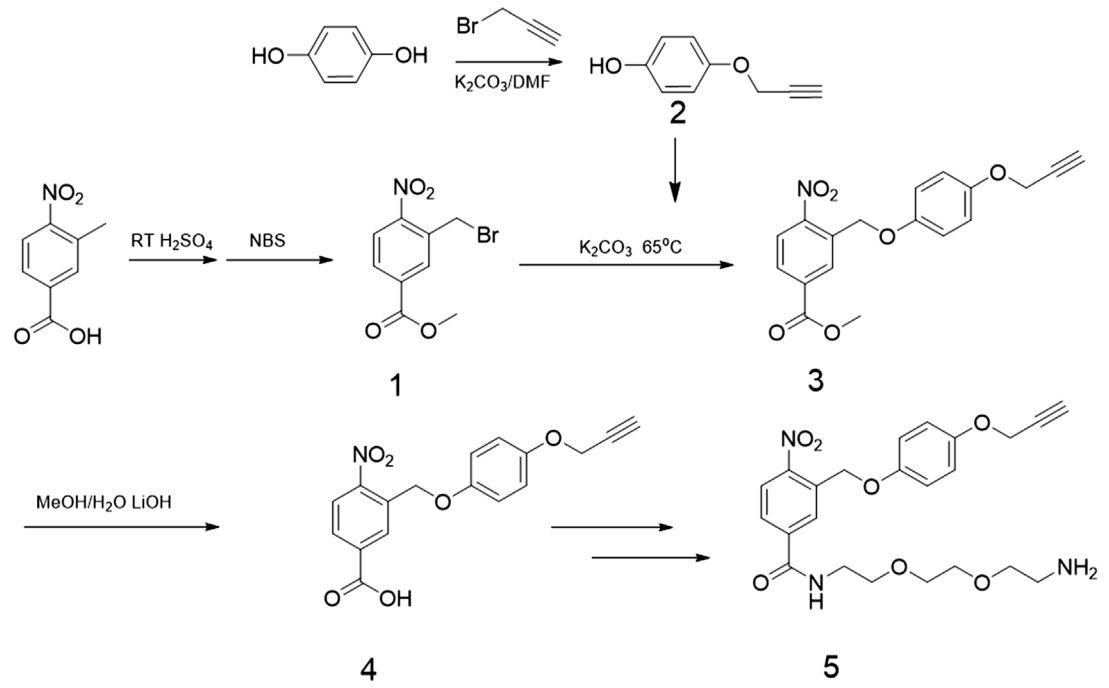

FIGURE 2
Synthesis routes of photo responsive ligands.

Materials and methods

Materials and reagents

Magnetic beads (CSMN Beads-100, MBs, 100 nm) were purchased from So-Fe Biomedicine (Shanghai, China). The rest of chemical reagents used in the synthesis of nanodevices were purchased from Sinopharm Chemical Reagent Co. (Shanghai, China) and Sigma (Shanghai, China). SUM-1315 cells line was purchased from the Chinese Academy of Sciences (Shanghai, China). DMEM medium (11965092), Penicillin/streptomycin (15140122), and FBS (10099141C) were purchased from GIBCO (Shanghai, China). Anti-CD9 (13,403) primary antibodies were purchased from Cell Signaling Technology (Shanghai, China). Anti-CD63 (ab22595) and anti-calnexin (ab134045) primary antibodies were purchased from Abcam (Shanghai, China). Antirabbit HRP secondary antibodies (a0208), Enhanced-chemiluminescence (ECL) kits (P0018FS), and BCA kit (P0012S) were purchased from Beyotime. Biotechnology (Shanghai, China). CD63 aptamer with azide group was synthesized by Sangon (Shanghai, China), with the following sequence: 5′-CAC CCC ACC TCG CTC CCG TGA CAC TAA TGC TA-3′-N_3 (Zhang Z et al., 2019).

Synthesis of magnetic bead system (MBs-Apt_{63})

Magnetic nanoparticle solution (600 μl, 5 mg/ml) was added to a 1.5 ml centrifuge tube. The nanoparticles were precipitated to bottom of the centrifuge tube with magnets, and supernatant was removed. After being washed with water three times, the nanoparticles were redispersed in 3 ml of 2-morpholinoethanesulfonic acid (MES) buffer with ultrasound. 1-(3-Dimethylaminopropyl)-3-ethylcarbodiimide hydrochloride (EDC) (dissolved with MES, 2.5 mg/ml, 2 ml) and N-hydroxy succinimide (NHS) (dissolved with MES, 5 mg/ml, 1 ml) were then added, followed by sonication for 15 s. The centrifuge tube was sealed by sealing film and shaken at 37°C for 45 min. After that, the nanoparticles were deposited to the bottom of the centrifuge tube and washed twice with phosphate buffered saline (PBS) buffer. The nanoparticles were redispersed in 6 ml PBS. Compound 5 (the compound codes mentioned in this paper were shown in Figure 2) in dimethyl sulfoxide (DMSO) (60 μl, 100 mg/ml) was added to the centrifuge tube and mixed by ultrasound. The mixture was oscillated at 37°C for 12 h. After removal of the supernatant, the CD63 aptamer with azide group was added into the nanoparticles' aqueous solution at a 1:1 M ratio. 1 mol% copper sulfate pentahydrate and 5 mol% sodium ascorbates were added and

solution was shaken at room temperature for 8 h to get the final magnetic bead system (MBs-Apt_{63}).

Cell culture

SUM-1315 cells tested negative for *mycoplasma* were cultured in DMEM supplemented with 10% FBS and 1% penicillin–streptomycin. All cells were cultured in an incubator under 5% CO_2 at 37°C.

Agarose gel electrophoresis

The aptamer-MBs mixture system was loaded into each well of the agarose gel and separated *via* electrophoresis. Target oligonucleotides were detected with Gel-Red kits.

Isolation of exosomes by UC from cell supernatant and serum

Exosomes were extracted from the supernatant of SUM-1315 cells or serum in the following steps: centrifugation was performed at 4°C at 2,000 × *g* for 10 min, and the supernatant was kept and centrifuged at 10,000 × *g* for another 30 min to further remove the debris. These samples were transferred to UC tubes and centrifuged at 110,000 × *g* for 75 min, followed by removal of the supernatant. The precipitates were resuspended and diluted with 1×PBS, and filtered through 0.22 μm membrane. The product was centrifugated again at 110,000 × *g* for 75 min, and the supernatant was discarded. The pellets were resuspended with 1×PBS and stored at −80°C for further use.

Isolation of exosomes by MBs -Apt_{63}

Magnetic beads (0.1 μg) were added to every 500 μl of exosome suspension or serum to capture exosomes. The binding process was carried out on a shaker. After 20 min, the EP tube was put in a tube rack with a permanent magnet placed against the tube bottom. The supernatant was discarded. After 5 min of precipitation, and the pellets were resuspended in PBS and placed under UV light for 20 min. After elution of the exosomes, the bare magnetic beads were removed by permanent magnets after of 5 min's adsorption time, and the exosome-containing supernatant was retained in 500 μl PBS.

Transmission electron microscope (TEM)

PBS solution (20 μl) containing exosomes was added to a carbon-coated copper grid and adsorbed. After cleaning with PBS, the copper grid was fixed in 1% glutaraldehyde for 2 min. The excess solution was removed by using paper towel to blot the edges of each grid. Then the sample was negatively stained with saturated uranyl acetate solution and incubated at room temperature for 1min. The unevaporated solution is removed with paper towel. The samples were observed under a transmission electron microscope.

Nanoparticle tracking analysis (NTA)

Nanoparticle tracking analysis was performed on ZetaVIEW S/N 17-310 and all NTA measurements were performed using the same setup to ensure consistent results. The exosomes were diluted in PBS to obtain 50 particles in each field of vision for optimal counting.

Dynamic light scattering (DLS)

Dynamic light scattering (DLS) measurements were conducted on a Nano ZS instrument (Malvern, United Kingdom). All samples were resuspended in PBS, and measured with the same instrument setup.

Western blotting

Exosome suspension (10 μl) was loaded into SDS-PAGE and then separated by electrophoresis. Proteins were transferred onto polyvinylidene fluoride membranes and blocked with 5% skim milk. The primary anti-CD63 and anti-CD9 antibodies were used, followed by incubation with HRP-conjugated secondary antibodies. Target proteins were detected with enhanced-ECL kits.

Animal models

BALB/C-nude mice (female, 4 weeks) were purchased from Model Animal Research Center, Nanjing University. The animal experiment was approved by the Ethics Committee of Nanjing Medical University. We confirmed that all animal experiments are complied with National Institutes of Health guide for the care and use of Laboratory animals (NIH Publications No. 8023, revised 1978). The animals were raised at 25°C with 60% humidity. 2×10^6 of sum-1315 cells were inoculated into the back of each nude mouse. 10 days later, blood was collected from the posterior venous cluster of the eyeball. The blood was placed at room temperature for 2 h and centrifuged at 3000 rpm for 10 min at 4°C, and the upper serum was preserved. The serum of nude mice was stored at −80°C.

High sensitivity flow cytometry

Exosomes were incubated with 20 μl fluorescently labeled antibody (CD63) at 37°C for 30 min in dark. Then 1 ml of pre-cooled PBS (4°C) was added, followed by centrifugation at 110,000 *g* for 70 min. The supernatant was carefully removed and 1 ml of pre-cooled PBS (4°C) was added to resuspend. The solution was then centrifuged at 110,000 *g* at 4°C for 70 min, and the supernatant was carefully removed, followed by resuspension of pellets in 50 μl of precooled PBS (4°C) for analysis.

Proteomic analysis of exosomes

Exosome suspension was treated with 7 M urea, 2%SDS, and 1× Protease Inhibitor Cocktail. Protein concentration was determined using the BCA protein detection kit, and then the sample was processed with nuclease digestion, reduction/alkylation, acetone precipitation, and lysine-C/trypsin digestion. Desalination was carried out in the monospin column using 0.1% trifluoroacetic acid (TFA) and acetonitrile. After vacuum drying, 0.1%FA was added to redissolve the sample, and a 1–2 μg of sample was analyzed. The separation was performed with Easy-NLC 1000 (Thermo Scientific, United States) using an analytical column (C18, 1.9 μm, 75 μm × 20 cm) at a flow rate of 300 NL/min. Orbitrap Fusion Lumos (Thermo Scientific, United States) was used as a mass spectrometer. Data Dependent Acquisition (DDA) model was used for tandem mass spectrometry. The full-scan resolution was 60,000 (FWHM), the mass-charge ratio range was set to M/Z 350-1800, and the impact energy was set to 30% in HCD fragmentation mode. The original mass spectrometry data were collected and analyzed using the mass informatics platform Proteome Discoverer 2.4 (Thermo Fisher).

Statistics

Origin 2019 and GraphPad Prism 8.0 were used for statistical calculation of all histograms, and one-way anova was used for calculation of mean and variance.

Results

Synthesis of UV-responsive magnetic bead system (MBs-Apt$_{63}$)

The 2-nitrobenzyl groups were used as photo-cleavable linkers to anchor CD63 aptamers onto MBs. The detailed synthesis route is shown in Figure 2, and the chemical synthesis steps of photoresponsive ligands are described in Supplementary Material S1. The structure of MBs-Apt$_{63}$ is shown in Figure 1. Firstly, the photo-cleavable linkers were anchored onto the surface of MBs *via* a moderate amination reaction. To selectively capture exosomes, CD63 aptamers were finally conjugated with the MBs through click reaction. The final UV-responsive magnetic bead system (MBs-Apt$_{63}$) was characterized for Zeta potential, infrared spectroscopy, and dynamic light scattering (DLS) size (Supplementary Figure S2 and Supplementary Figure S10).

Magnetic beads respond to UV *in vitro*

We measured the UV responsiveness of the magnetic beads with a concentration at the range of 0–10 μg/ml, while the time of exposure to UV light was between 0 and 30 min. In Figures 3A,B, it was found that within the range of 0–10 μg/ml, the light-responsive groups of magnetic beads were highly sensitive to and effectively cleaved by UV light. The CD63 aptamers were rapidly released from MBs-Apt$_{63}$ under irradiation, which also showed obvious time dependence. With increased exposure time, the amount of released free aptamers increased, and reached the maximum after 15 min of UV exposure.

Preparation and validation of exosomes

To test the ability of MBs-Apt$_{63}$ to capture exosomes, we firstly extracted tumor exosomes from the cultural medium of breast cancer cell line SUM-1315 by UC. Western blotting analysis of exosomes showed the presence of CD9, CD63 (two common surface markers of exosomes) and calnexin (endoplasmic reticulum protein), indicating the successful preparation (Figure 3C). In DLS analysis, the exosomes showed an average size of 56 nm (Figure 3D), in line with characteristic particle size of exosomes (30–150 nm). Finally, we used TEM to observe the morphology of exosomes (Figures 3E,F), which displayed a typical lipid bilayer structure and a size in the range of 50–100 nm.

Capturing exosomes with MBs-Apt$_{63}$ and elution with UV light

The process of isolating exosomes from cell supernatant or serum is shown in Figure 4A, which involves beads binding and exosome elution. DLS analysis was performed after MBs binding to exosomes and UV-triggered elution, which showed a size of 250 and 190 nm, respectively. (Figures 4B,C). In Figure 4C, the magnetic bead components were not removed in the system after ultraviolet dissociation. This reduced shift in maximum peak particle size from 256 to 190 nm indicated

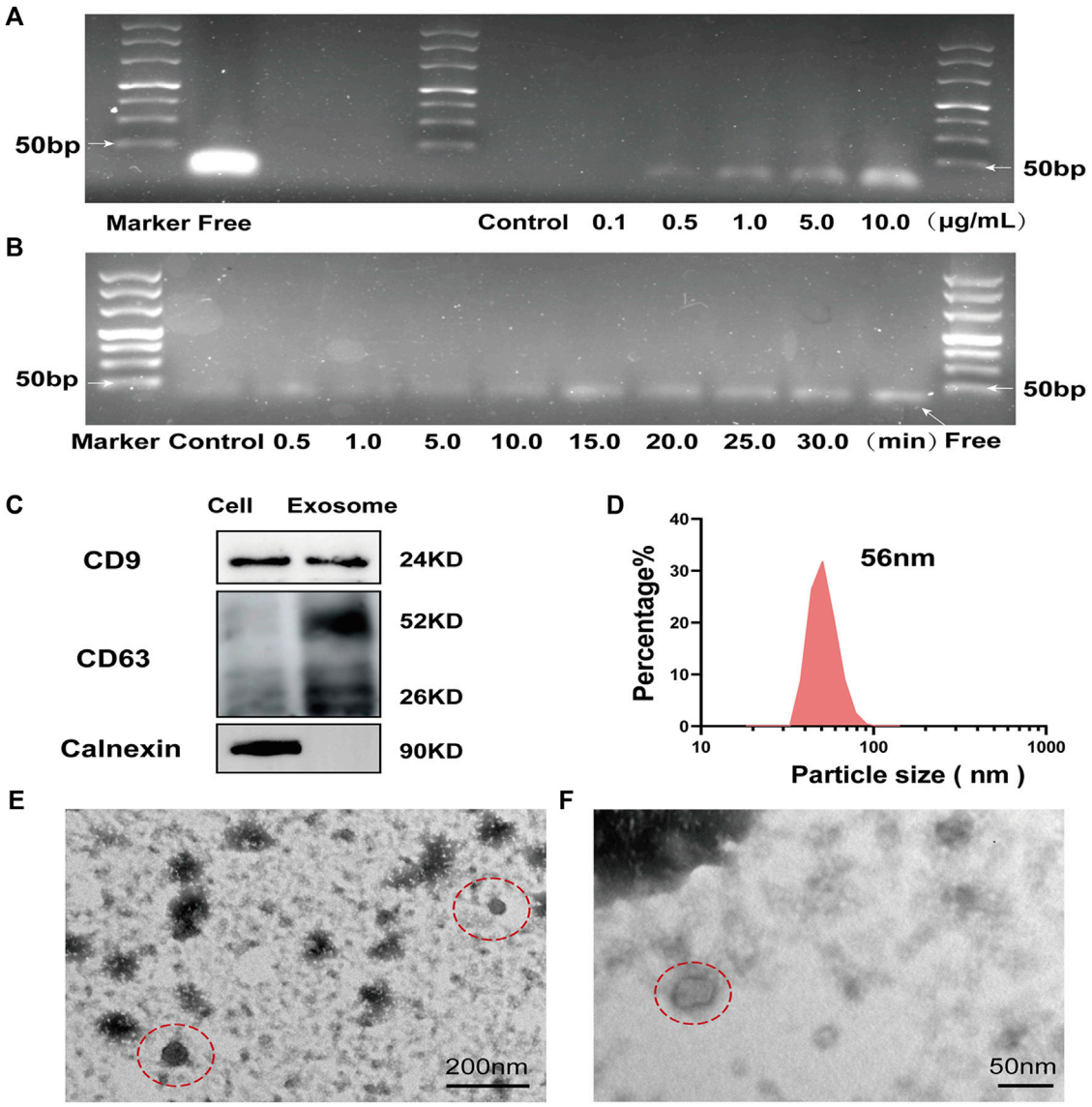

FIGURE 3
Response of MBs-Apt$_{63}$ to UV *in vitro* and identification of exosomes **(A)** Agarose gel electrophoresis (molecular weight of free aptamer = 32 bp) of MBs-Apt$_{63}$ at different concentrations after UV exposure; **(B)** Agarose gel electrophoresis of MBs-Apt$_{63}$ (10.0 μg/ml) after exposure to UV for different times (molecular weight of free aptamer = 32 bp). **(C)** The expression of CD9, CD63 and calnexin determined by western blotting; **(D)** The particle size of breast cancer cell exosomes characterized by DLS; **(E,F)** Transmission electron microscopy image of breast cancer exosomes (magnification = 50000× in **C** and 100000× in **D**, exosomes are shown in the red dotted circle).

the elution of exosomes from the MBs after UV exposure. To further elaborate the binding and elution processes, TEM was used to observe the MBs-exosome complex before and after UV-triggered cargo release. Typical MBs bound to many exosomes were clearly seen before exposure to UV light (Figure 4D), whereas only purified exosomes could be observed after UV-induced release of exosomes and removal of magnetic beads by permanent magnets (Figure 4E).

Application of MBs-Apt$_{63}$ in the separation of serum exosomes from breast cancer

To evaluating the performance of this novel MBs system in isolating serum exosomes, we established mice models of triple-negative breast cancer using human breast cancer SUM-1315 cells. We collected the serum when the tumor grew to about 800 mm^3, and then isolated exosomes with MBs-Apt$_{63}$ and conventional UC respectively. We firstly analyzed the particle

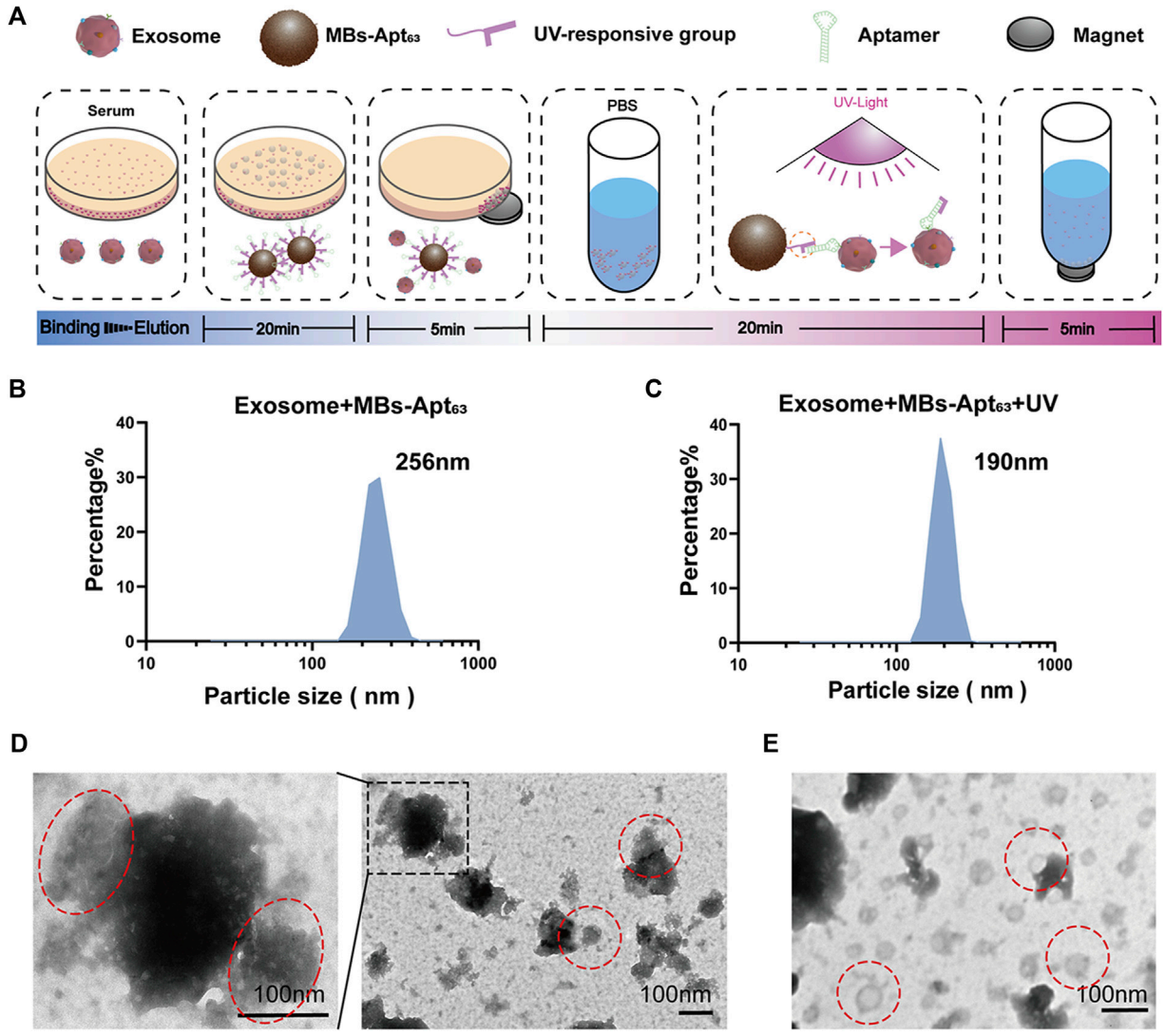

FIGURE 4
Capturing exosomes by and elution of exosomes from MBs-Apt$_{63}$. **(A)** Schematic diagram for extracting exosomes from serum and cell supernatant with MBs-Apt$_{63}$; **(B)** DLS characterization after incubating exosomes with MBs-Apt$_{63}$; **(C)** DLS characterization after exposing the MBs-exosome complex to UV light; **(D)** Transmission electron microscopy image of exosomes bound to MBs-Apt$_{63}$ (left, 100000×, right, 25000×). Positions of exosomes and MBs-Apt$_{63}$ are marked in red; **(E)** Transmission electron microscopy image of exosomes eluted from MBs-Apt$_{63}$ by UV light.

size distribution (Figure 5A) and particle concentration of exosomes (Figure 5B) with NTA. Results showed that the particle size distribution of exosomes isolated by MBs-Apt$_{63}$ and UC was similarly uniform, both of which were about 100 nm. While the serum concentration of exosomes acquired by UC is lower compared with that by MBs-Apt$_{63}$ (2.5×10^9/ml versus 4.0×10^9/ml) according to the particle count analysis, indicating higher efficiency of MBs-Apt$_{63}$ in extracting serum exosomes.

Next, we used the high sensitivity flow cytometry (HSFC) system to analyze the expression of CD63 on exosomes separated by UC and MBs-Apt$_{63}$ (Figure 5C). The results showed that the expression abundance of CD63 was 4.9% in exosomes extracted by MBs-Apt$_{63}$, which is much higher (0.4%) in exosomes separated by UC method. Therefore, the light strategy in MBs-Apt$_{63}$ system improved the purity of exosomes with high expression of CD63.

In exosome-based liquid biopsies, diagnostic value ultimately comes from biomarkers in exosomes. In this study, proteins in exosomes separated by UC and magnetic beads were both analyzed by liquid mass spectrometry. We conducted a database search and comparison according to Proteome

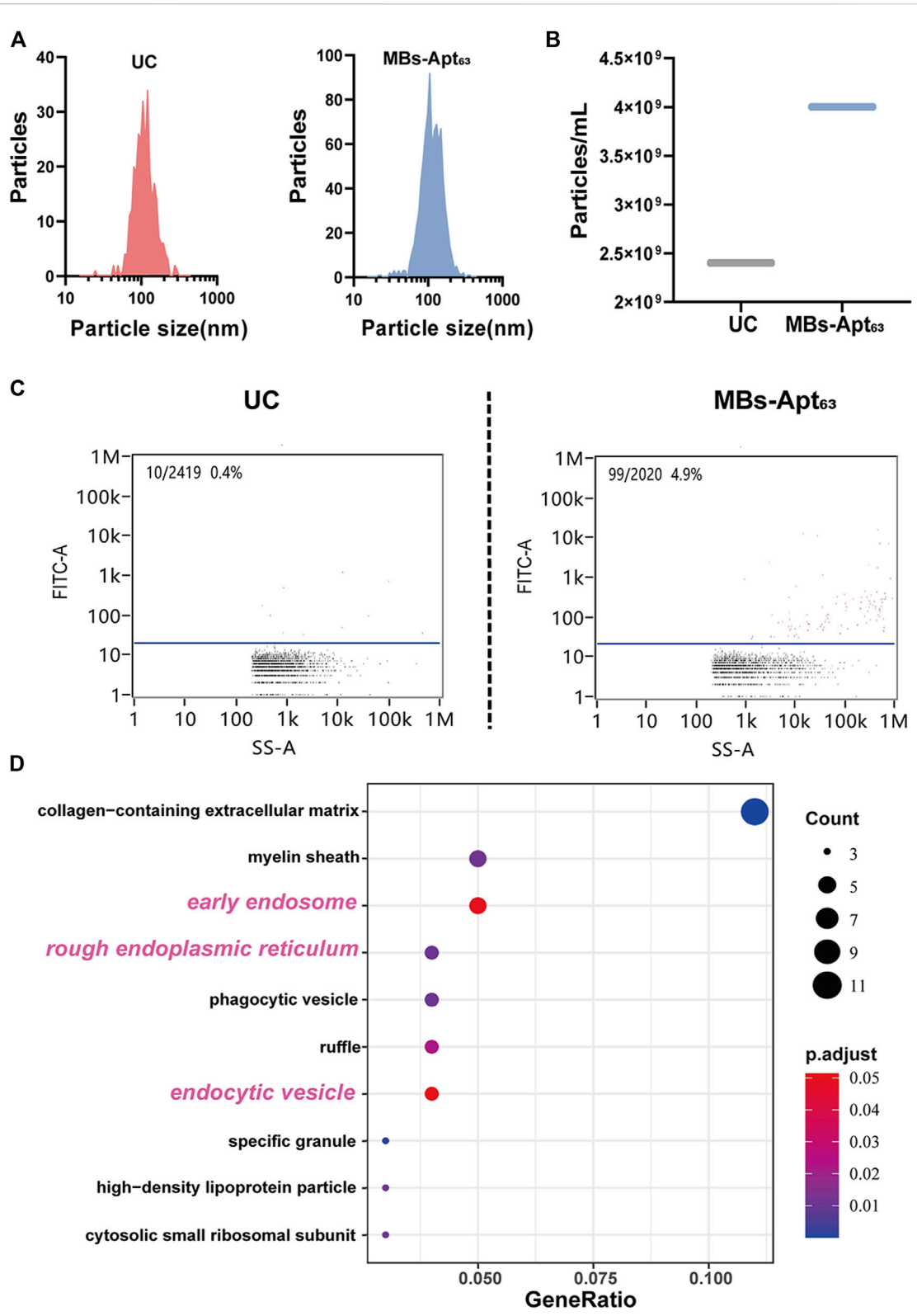

FIGURE 5
Evaluation of MBs-Apt$_{63}$ in the isolation of serum tumor exosomes. **(A)** Particle size distributions of exosomes extracted by UC and MBs-Apt$_{63}$. **(B)** Average serum exosome concentrations prepared by UC or MBs-Apt$_{63}$; **(C)** Expression abundance of CD63 in exosomes isolated by UC and MBs-Apt$_{63}$. Results were obtained from nanoflow flow test; **(D)** GO analysis of proteins from exosomes separated by MBs-Apt$_{63}$ or UC. Top 10 GO components are displayed that are most enriched in exosomes separated by MBs-Apt$_{63}$ ($p < 0.05$ as significance).

Discoverer 2.4 system. Specific database search parameters are shown in Supplementary Table S2. The relevant quality control information is shown in Supplementary Figure S5. 1044 proteins were identified in the exosomes isolated by UC, while only 677 proteins were detected in the exosomes separated by magnetic beads (Supplementary Table S3). To verify that our optically controlled MBs-Apt_{63} preserved more exosome-related proteins, we performed GO analysis on high-expression set of exosome proteins extracted by MBs-Apt_{63} versus UC. The screening criteria for differential proteins between the two groups were:

(1), Inter-group ratio ≥ 4 (2), Unique Peptides ≥ 2.

Among the top 10 GO components that were significantly higher in exosomes extracted by MBs-Apt_{63}, three are related to exosome formation, including rough endoplasmic reticulum, early endosomes, and endocytic vesicles (Figure 5D), indicating a higher expression abundance of exosome-related proteins in CD63 positive exosomes separated by MBs-Apt_{63}.

Discussions

In this study, we developed a facile light-responsive magnetic bead sorting system for extracting exosomes from breast cancer. In our strategy, 2-nitrobenzene is designed as the surface ligand of the magnetic beads, whose UV responsiveness allows for spatiotemporal control of exosome separation with minimum interference with serum composition. From a practical perspective, it requires less time and smaller sample volume, and does not need sophisticated instruments. More importantly, this system can largely improve the efficiency of exosome isolation, maximizing the purity and integrity of the exosomes. At the same time, without the interference of magnetic beads, exosomes in the real liquid environment can greatly improve the efficiency of the labeled enzyme and substrate reaction. In addition, the masking the effect of magnetic beads themselves will be eliminated. Therefore, this method should be able to improve the sensitivity of subsequent detection.

Previous studies have reported considerable progress in the field of liquid biopsy, particularly some nanomaterial-based liquid biopsy techniques (Zhang P et al., 2019; Tian et al., 2019; Huang et al., 2020; Xia et al., 2020; Chen et al., 2021; He et al., 2021). On this basis, some studies have significantly improved the sensitivity of liquid biopsies, while others have looked at reducing the amount of fluid used in this process (Huang et al., 2019; Li et al., 2019; Kim et al., 2020; Jiang et al., 2021). In this study, the operation mode and sample requirements of liquid biopsy were further simplified. Firstly, the extraction method of exosomes by illumination and magnetic separation does not require additional reagents and processing time, which ensures reproducibility of extraction procedures, making our magnetic bead system can be used in large quantities in clinical practice. Secondly, the spatiotemporally controllable extraction method provides a simple exosome release strategy to remove the steric effect based on magnetic bead fixation, so that magnetic bead-based exosome detection can achieve better detection efficiency in the liquid phase reaction system. At the same time, as most research on UV response devices, the wavelength of UV light used in this study is about 254 nm. It has been shown in some studies that there is no relevant evidence to confirm that 254 nm ultraviolet light will cause damage to proteins under certain conditions of time and intensity (O'Brien et al., 2014; Cannon et al., 2014).

Our experimental results basically demonstrate the clinical application prospect of the system. Compared with traditional ultracentrifugation, the number of exosomes extracted from serum by our system increased by 60%. At the same time, the purity of proteins represented by CD63 was increased by 10 times. Through proteomic analysis, we also confirmed that the MBs-Apt_{63} preserved more protein components from exosomes. It indicated that, compared with traditional exosome extraction methods in the field of liquid biopsy for clinical cancer patients, this system can obtain the information of tumor in patients' serum in a relatively comprehensive way, thus providing more reference value for implementation of diagnosis and treatment process. In the future, by changing the aptamers, our strategy provides a flexible approach to pathological analysis of breast cancer for personalized medicine, and its large-scale application can also supply a new platform for broadening the application scope of liquid biopsy of cancer. At the same time, this light-activated magnetic bead strategy also establishes the possibility to nondestructively enrich specific functional cell exosomes for cancer disease treatment (Fang et al., 2022).

Data availability statement

The original contributions presented in the study are included in the article/Supplementary Material; further inquiries can be directed to the corresponding authors.

Ethics statement

The animal study was reviewed and approved by Ethics Committee of Nanjing Medical University.

Author contributions

QD and CY conceived the idea and supervised the research; CW and DZ designed the experiments; CW, DZ, and HY carried out specific experimental operations; CW, DZ, QD, JW, LL, and CY co-wrote the paper; LS provides clinical consulting and data

analysis; All authors discussed the results and commented on the manuscript.

Funding

This study was supported by the National Natural Science Foundation of China (81972486).

Conflict of interest

The authors declare that the research was conducted in the absence of any commercial or financial relationships that could be construed as a potential conflict of interest.

Publisher's note

Supplementary material

The Supplementary Material for this article can be found online at: https://www.frontiersin.org/articles/10.3389/fbioe.2022.1006374/full#supplementary-material

References

Cannon, J. R., Cammarata, M. B., Robotham, S. A., Cotham, V. C., Shaw, J. B., Fellers, R. T., et al. (2014). Ultraviolet photodissociation for characterization of whole proteins on a chromatographic time scale. *Anal. Chem.* 86, 2185–2192. doi:10.1021/ac403859a

Chang, D. J., Yoon, E. Y., Lee, G. B., Kim, S. O., Kim, W. J., Kim, Y. M., et al. (2009). Design, synthesis and identification of novel colchicine-derived immunosuppressant. *Bioorg. Med. Chem. Lett.* 19, 4416–4420. doi:10.1016/j.bmcl.2009.05.054

Chen, W., Li, Z., Cheng, W., Wu, T., Li, J., Li, X., et al. (2021). Surface plasmon resonance biosensor for exosome detection based on reformative tyramine signal amplification activated by molecular aptamer beacon. *J. Nanobiotechnology* 19, 450. doi:10.1186/s12951-021-01210-x

Chen, W., Zhang, Y., Di, K., Liu, C., Xia, Y., Ding, S., et al. (2022). A washing-free and easy-to-operate fluorescent biosensor for highly efficient detection of breast cancer-derived exosomes. *Front. Bioeng. Biotechnol.* 10, 945858. doi:10.3389/fbioe.2022.945858

Choi, D. Y., Park, J. N., Paek, S. H., and Choi, S. C. (2022). Detecting early-stage malignant melanoma using a calcium switch-enriched exosome subpopulation containing tumor markers as a sample. *Biosens. Bioelectron. X.* 198, 113828. doi:10.1016/j.bios.2021.113828

Descamps, L., Le Roy, D., and Deman, A. L. (2022). Microfluidic-based technologies for CTC isolation: a review of 10 years of intense efforts towards liquid biopsy. *Int. J. Mol. Sci.* 23, 1981. doi:10.3390/ijms23041981

Fang, Z. W., Zhang, X. Y., Wu, J., and Huang, H. (2022). Exosome based miRNA delivery strategy for disease treatment. *Chin. Chem. Lett.* 33, 1693–1704. doi:10.1016/j.cclet.2021.11.050

Gao, F., Jiao, F., Xia, C., Zhao, Y., Ying, W., Xie, Y., et al. (2019). A novel strategy for facile serum exosome isolation based on specific interactions between phospholipid bilayers and TiO2. *Chem. Sci.* 10, 1579–1588. doi:10.1039/c8sc04197k

Guo, S., Xu, J., Estell, A. P., Ivory, C. F., Du, D., Lin, Y., et al. (2020). Paper-based ITP technology: An application to specific cancer-derived exosome detection and analysis. *Biosens. Bioelectron. X.* 164, 112292. doi:10.1016/j.bios.2020.112292

Gurunathan, S., Kang, M. H., Jeyaraj, M., Qasim, M., and Kim, J. H. (2019). Review of the isolation, characterization, biological function, and multifarious therapeutic approaches of exosomes. *Cells* 8, 307. doi:10.3390/cells8040307

He, L., Huang, R., Xiao, P., Liu, Y., Jin, L., Liu, H., et al. (2021). Current signal amplification strategies in aptamer-based electrochemical biosensor: A review. *Chin. Chem. Lett.* 32, 1593–1602. doi:10.1016/j.cclet.2020.12.054

He, L., Yu, X., Huang, R., Jin, L., Liu, Y., Deng, Y., et al. (2022). A novel specific and ultrasensitive method detecting extracellular vesicles secreted from lung cancer by padlock probe-based exponential rolling circle amplification. *Nano Today* 22, 101334. doi:10.1016/j.nantod.2021.101334

Hentzen, N. B., Mogaki, R., Otake, S., Okuro, K., and Aida, T. (2020). Intracellular photoactivation of caspase-3 by molecular glues for spatiotemporal apoptosis induction. *J. Am. Chem. Soc.* 142, 8080–8084. doi:10.1021/jacs.0c01823

Hofmann, L., Ludwig, S., Vahl, J. M., Brunner, C., Hoffmann, T. K., and Theodoraki, M. N. (2020). The emerging role of exosomes in diagnosis, prognosis, and therapy in head and neck cancer. *Int. J. Mol. Sci.* 21, 4072. doi:10.3390/ijms21114072

Huang, R., He, L., Xia, Y., Xu, H., Liu, C., Xie, H., et al. (2019). A sensitive aptasensor based on a Hemin/G-Quadruplex-assisted signal amplification strategy for electrochemical detection of gastric cancer exosomes. *Small* 15, e1900735. doi:10.1002/smll.201900735

Huang, R., He, L., Li, S., Liu, H., Jin, L., Chen, Z., et al. (2020). A simple fluorescence aptasensor for gastric cancer exosome detection based on branched rolling circle amplification. *Nanoscale* 12, 2445–2451. doi:10.1039/c9nr08747h

Ibsen, S. D., Wright, J., Lewis, J. M., Kim, S., Ko, S. Y., Ong, J., et al. (2017). Rapid isolation and detection of exosomes and associated biomarkers from plasma. *ACS Nano* 11, 6641–6651. doi:10.1021/acsnano.7b00549

Jiang, K. M., Wu, Y. A., Li, Z. H., Chen, J., Shi, M., and Meng, H. (2021). Molecular recognition triggered aptamer cascade for ultrasensitive detection of exosomes in clinical serum samples. *Chin. Chem. Lett.* 32, 1827–1830. doi:10.1016/j.cclet.2020.11.031

Kim, Y. B., Yang, J. S., Lee, G. B., and Moon, M. H. (2020). Evaluation of exosome separation from human serum by frit-inlet asymmetrical flow field-flow fractionation and multiangle light scattering. *Anal. Chim. Acta X.* 1124, 137–145. doi:10.1016/j.aca.2020.05.031

Kobayashi, T., Komatsu, T., Kamiya, M., Campos, C., Gonzalez-Gaitan, M., Terai, T., et al. (2012). Highly activatable and environment-insensitive optical highlighters for selective spatiotemporal imaging of target proteins. *J. Am. Chem. Soc.* 134, 11153–11160. doi:10.1021/ja212125w

Lai, J., Yu, A., Yang, L., Zhang, Y., Shah, B. P., and Lee, K. B. (2016). Development of photoactivated fluorescent N-hydroxyoxindoles and their application for cell-selective imaging. *Chem. Eur. J.* 22, 6361–6367. doi:10.1002/chem.201600547

Li, Z., Hu, C., Jia, J., Xia, Y., Xie, H., Shen, M., et al. (2019). Establishment and evaluation of a simple size-selective method for exosome enrichment and purification. *J. Biomed. Nanotechnol.* 15, 1090–1096. doi:10.1166/jbn.2019.2768

Liao, H., and Li, H. (2020). Advances in the detection technologies and clinical applications of circulating tumor DNA in metastatic breast cancer. *Cancer Manag. Res.* 12, 3547–3560. doi:10.2147/cmar.s249041

Liu, C., Xu, X., Li, B., Situ, B., Pan, W., Hu, Y., et al. (2018). Single-exosome-counting immunoassays for cancer diagnostics. *Nano Lett.* 18, 4226–4232. doi:10.1021/acs.nanolett.8b01184

Lu, Y. X., Tong, Z. D., Mao, H. J., Jian, X., Zhou, L., Qiu, S., et al. (2022). Multiple exosome RNA analysis methods for lung cancer diagnosis through integrated on-chip microfluidic system. *Chin. Chem. Lett.* 33, 3188–3192. doi:10.1016/j.cclet.2021.12.045

Markou, A., Tzanikou, E., and Lianidou, E. (2022). The potential of liquid biopsy in the management of cancer patients. *Semin. Cancer Biol.* 22, 00069–00079. doi:10.1016/j.semcancer.2022.03.013

Mathieu, M., Névo, N., Jouve, M., Valenzuela, J. I., Maurin, M., Verweij, F. J., et al. (2021). Specificities of exosome versus small ectosome secretion revealed by live intracellular tracking of CD63 and CD9. *Nat. Commun.* 12, 4389–4407. doi:10.1038/s41467-021-24384-2

Momen-Heravi, F., Balaj, L., Alian, S., Mantel, P. Y., Halleck, A. E., Trachtenberg, A. J., et al. (2013). Current methods for the isolation of extracellular vesicles. *Biol. Chem.* 394, 1253–1262. doi:10.1515/hsz-2013-0141

O'Brien, J. P., Li, W., Zhang, Y., and Brodbelt, J. S. (2014). Characterization of native protein complexes using ultraviolet photodissociation mass spectrometry. *J. Am. Chem. Soc.* 37, 12920–12928. doi:10.1021/ja505217w

Puhka, M., Thierens, L., Nicorici, D., Forsman, T., Mirtti, T., af Hallstrom, T., et al. (2022). Exploration of extracellular vesicle miRNAs, targeted mRNAs and pathways in prostate cancer: Relation to disease status and progression. *Cancers (Basel).* 14, 532. doi:10.3390/cancers14030532

Shen, M., Di, K., He, H., Xia, Y., Xie, H., Huang, R., et al. (2020). Progress in exosome associated tumor markers and their detection methods. *Mol. Biomed.* 1, 3. doi:10.1186/s43556-020-00002-3

Song, Z., Mao, J., Barrero, R. A., Wang, P., Zhang, F., and Wang, T. (2020). Development of a CD63 aptamer for efficient cancer immunochemistry and immunoaffinity-based exosome isolation. *Molecules* 25, 5585–5601. doi:10.3390/molecules25235585

Sung, B. H., von Lersner, A., Guerrero, J., Krystofiak, E. S., Inman, D., Pelletier, R., et al. (2020). A live cell reporter of exosome secretion and uptake reveals pathfinding behavior of migrating cells. *Nat. Commun.* 11, 2092. doi:10.1038/s41467-020-15747-2

Tian, X., Shen, H., Li, Z., Wang, T., and Wang, S. (2019). Tumor-derived exosomes, myeloid-derived suppressor cells, and tumor microenvironment. *J. Hematol. Oncol.* 12, 84. doi:10.1186/s13045-019-0772-z

Wang, L., Chen, B., Peng, P., Hu, W., Liu, Z., Pei, X., et al. (2017). Fluorescence imaging mitochondrial copper(II) via photocontrollable fluorogenic probe in live cells. *Chin. Chem. Lett.* 28, 1965–1968. doi:10.1016/j.cclet.2017.07.016

Wang, C., Senapati, S., and Chang, H. C. (2020). Liquid biopsy technologies based on membrane microfluidics: High-yield purification and selective quantification of biomarkers in nanocarriers. *Electrophoresis* 41, 1878–1892. doi:10.1002/elps.202000015

Wang, S., Khan, A., Huang, R., Ye, S., Di, K., Xiong, T., et al. (2020). Recent advances in single extracellular vesicle detection methods. *Biosens. Bioelectron. X.* 154, 112056. doi:10.1016/j.bios.2020.112056

Willms, E., Cabanas, C., Mager, I., Wood, M. J. A., and Vader, P. (2018). Extracellular vesicle heterogeneity: Subpopulations, isolation techniques, and diverse functions in cancer progression. *Front. Immunol.* 9, 738. doi:10.3389/fimmu.2018.00738

Xia, Y., Hu, X., Di, K., Liu, C., Tan, T., Lin, Y., et al. (2020). Combined detection of exosome concentration and tumor markers in gastric cancer. *J. Biomed. Nanotechnol.* 16, 252–258. doi:10.1166/jbn.2020.2887

Xie, H., Di, K., Huang, R., Khan, A., Xia, Y., Xu, H., et al. (2020). Extracellular vesicles based electrochemical biosensors for detection of cancer cells: A review. *Chin. Chem. Lett.* 31, 1737–1745. doi:10.1016/j.cclet.2020.02.049

Yang, H., Liang, W., He, N., Deng, Y., and Li, Z. (2015). Chemiluminescent labels released from long spacer arm-functionalized magnetic particles: a novel strategy for ultrasensitive and highly selective detection of pathogen infections. *ACS Appl. Mat. Interfaces* 7, 774–781. doi:10.1021/am507203s

Yang, Q., Cheng, L., Hu, L., Lou, D., Zhang, T., Li, J., et al. (2020). An integrative microfluidic device for isolation and ultrasensitive detection of lung cancer-specific exosomes from patient urine. *Biosens. Bioelectron. X.* 163, 112290. doi:10.1016/j.bios.2020.112290

Yu, W., Hurley, J., Roberts, D., Chakrabortty, S., Enderle, D., Noerholm, M., et al. (2021). Exosome-based liquid biopsies in cancer: opportunities and challenges. *Ann. Oncol.* 32, 466–477. doi:10.1016/j.annonc.2021.01.074

Zhang, Z., Tang, C., Zhao, L., Xu, L., Zhou, W., Dong, Z., et al. (2019). Aptamer-based fluorescence polarization assay for separation-free exosome quantification. *Nanoscale* 11, 10106–10113. doi:10.1039/c9nr01589b

Zhang, P., Zhou, X., He, M., Shang, Y., Tetlow, A. L., Godwin, A. K., et al. (2019). Ultrasensitive detection of circulating exosomes with a 3D-nanopatterned microfluidic chip. *Nat. Biomed. Eng.* 3, 438–451. doi:10.1038/s41551-019-0356-9

Zhao, Y., Fang, X. X., Zhao, Y. X., Zhang, J., Yu, H., Chen, F., et al. (2022). A microfluidic surface-enhanced Raman scattering (SERS) sensor for microRNA in extracellular vesicles with nucleic acid-tyramine cascade amplification. *Chin. Chem. Lett.* 33, 2101–2104. doi:10.1016/j.cclet.2021.08.047

Zhu, F. J., Ji, Y. H., Lu, Y., Li, L., Bai, X., Liu, X., et al. (2022). Microfluidics-based technologies for the analysis of extracellular vesicles at the single-cell level and single-vesicle level. *Chin. Chem. Lett.* 33, 2893–2900. doi:10.1016/j.cclet.2021.09.058

frontiers | Frontiers in Bioengineering and Biotechnology

TYPE Original Research
PUBLISHED 12 September 2022
DOI 10.3389/fbioe.2022.996456

OPEN ACCESS

EDITED BY
Eden Morales-Narváez,
Centro de Investigaciones en Optica, Mexico

REVIEWED BY
Semra Akgönüllü,
Hacettepe University, Turkey
Guangyao Zhang,
Qingdao University, China

*CORRESPONDENCE
Nongyue He,
nyhe1958@163.com

†These authors have contributed equally to this work

SPECIALTY SECTION
This article was submitted to Biosensors and Biomolecular Electronics, a section of the journal Frontiers in Bioengineering and Biotechnology

RECEIVED 17 July 2022
ACCEPTED 29 August 2022
PUBLISHED 12 September 2022

CITATION
Fang Y, Wang Y, Su X, Liu H, Chen H, Chen Z, Jin L and He N (2022), A miniaturized and integrated dual-channel fluorescence module for multiplex real-time PCR in the portable nucleic acid detection system. *Front. Bioeng. Biotechnol.* 10:996456. doi: 10.3389/fbioe.2022.996456

A miniaturized and integrated dual-channel fluorescence module for multiplex real-time PCR in the portable nucleic acid detection system

Yile Fang[1†], Yue Wang[1†], Xiangyi Su[1], Haoran Liu[1], Hui Chen[2], Zhu Chen[2], Lian Jin[2] and Nongyue He[1,2*]

[1]State Key Laboratory of Bioelectronics, School of Biological Science and Medical Engineering, Southeast University, Nanjing, China, [2]Economical Forest Cultivation and Utilization of 2011 Collaborative Innovation Center in Hunan Province, Hunan Key Laboratory of Biomedical Nanomaterials and Devices, Hunan University of Technology, Zhuzhou, China

A portable nucleic acid detection (PNAD) system based on real-time polymerase chain reaction (real-time PCR) has been developed for point-of-care testing (POCT) of infectious disease pathogens. In order to achieve "sample-in, result-out" while keeping the system compact, the hardware system integrates optical, thermal and motion control modules in a limited space for nucleic acid extraction, purification, amplification and detection. Among these hardware modules, the fluorescence module is one of the most important modules, because its performance directly affects the accuracy and sensitivity of the testing results. In this paper, a miniaturized, high-sensitivity and integrated dual-channel fluorescence module have been proposed for the homemade PNAD system. Based on the principle of confocal optical path, two group of excitation-emission optical paths of different wavelengths are integrated in a small space. In terms of circuitry, a current-light dual negative feedback light emitting diode (LED) drive circuit is applied to improve the stability of the excited light source. All optical and electronic components are integrated in a metal box of 55 mm × 45 mm × 15 mm, that helps miniaturize the detection system. Two different modules have been assembled to fit various fluorescent dyes or probes with the set of excitation and emission as follow: module 1#: 470 nm/525 nm, 570 nm/630 nm; module 2#: 520 nm/570 nm, 630 nm/690 nm. Finally, hepatitis B virus (HBV) concentration gradient detection and multiplex detection of different gene targets of SARS-CoV-2 are carried out on the PNAD system equipped with these two fluorescence modules for evaluating their performances. Compared with the commercial real-time PCR instrument, our fluorescence module has good stability and detection sensitivity.

KEYWORDS

fluorescence detection, confocal optical path, LED drive circuit, real-time PCR, point-of-care testing

Introduction

Nowadays, the Corona Virus Disease 2019(COVID-19) ravages the world with clinical manifestations ranging from cough and fever to pneumonia and even death, and its high infection and mortality rates bring great inconvenience and loss to people's lives and the global economy (Bedford et al., 2020; Benmalek et al., 2021). The detection methods for COVID-19 mainly include antigen testing and nucleic acid testing (Cui and Zhou, 2020; Mathuria et al., 2020; Pokhrel et al., 2020; Rai et al., 2021). The antigen test measures some of the viral proteins and indicates the presence of pathogens. Compared with the nucleic acid method, antigen test is simple to perform and has a shorter turnaround time, but its low sensitivity makes unreliable results. Nucleic acid test detects viruses by amplifying the targeted nucleic acids and is used to confirm the presence of viruses that are difficult to culture, making it the gold standard test for COVID-19 microbiological diagnosis (Zhu et al., 2020; Song et al., 2021). But traditional nucleic acid testing is only suitable for large centralized diagnostic laboratories which require multiple devices to complete. The rapid development of COVID-19 and the limited capabilities of laboratory-based molecular detection make point-of-care testing (POCT) urgently needed in the diagnosis of COVID-19 outside the laboratory setting (Li and Ren, 2020; Tang et al., 2020). The greatest merit of POCT is that it could realize fast tests with low cost, providing sufficient time for the implementation of necessary preventive and therapeutic measures (Chen et al., 2018; Hanson et al., 2020; Deng et al., 2021; Huang et al., 2021; Wang et al., 2021).

Based on the above background, our group has developed a portable nucleic acid detection (PNAD) system (Figure 1A), which can automatically perform nucleic acid extraction and real-time PCR without manual intervention to achieve "sample-in, result-out" (Chen et al., 2017; Fang et al., 2021). As shown in Figure 1B, there are three core functional modules in this system including motion control module, thermal control module and fluorescence module, in which the fluorescence module is the crux of real-time PCR, because its sensitivity and stability determine whether real-time PCR can accurately quantify DNA templates. Meanwhile, its structure needs to be as compact as possible for miniaturization and portability.

Fluorescence is a photoluminescence phenomenon. When a substance absorbs incoming light, the energy of the photon is transferred to the molecule. After excitation occurs, the electrons of the molecule jump from a low energy level to a high energy level, i.e., from the ground state to an excited single or excited triplet state. Molecules in excited states are unstable and must be released by radiative transfer or non-radiative transfer to return to the ground state. The energy in the radiative transfer is released as photons (Ishikawa-Ankerhold at al., 2012; Fu et al., 2020). Compared to other optical detection techniques, fluorescence detection has high sensitivity, specificity and accuracy. Besides, fluorescence detection is immune to electromagnetic, pressure and temperature interference, so it also has a high stability. With the development of fluorescence detection technology, portable instruments based on fluorescence are developed and applied in various fields. However, fluorescence modules reported in the literature and used in commercial equipment either only have a single excitation light or a split structure with separate light sources and detectors. For example, Novak et al. (Novak et al., 2007) developed a fluorescence detection module consisting of a blue LED, excitation and detection filters, dichroic mirrors, and photodiodes. Katzmeier et al. (Katzmeier et al., 2019) reported a pocket-sized fluorescence detector for POCT, the detection unit of which includes an excitation light and a photodetector. Both of the above mentioned had only one excitation source and didn't allow for multiple detection. Alam et al. (Alam et al., 2019) designed a portable fluorometer for detection of breast cancer cells, the excitation source and the detector are placed on opposite sides of the sample in a linear fashion. This separated structure was not favorable to integration.

In this study, a miniaturized, high-sensitivity and integrated dual-channel fluorescence module was designed for special

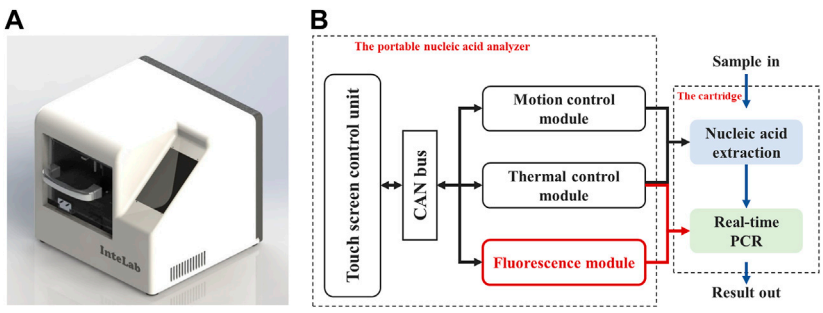

FIGURE 1
Homemade portable nucleic acid detection (PNAD) system. **(A)** 3D rendering of the PNAD device. **(B)** Functional block diagram of the PNAD system including motion control module, thermal control module and fluorescence module to achieve "sample-in, result-out".

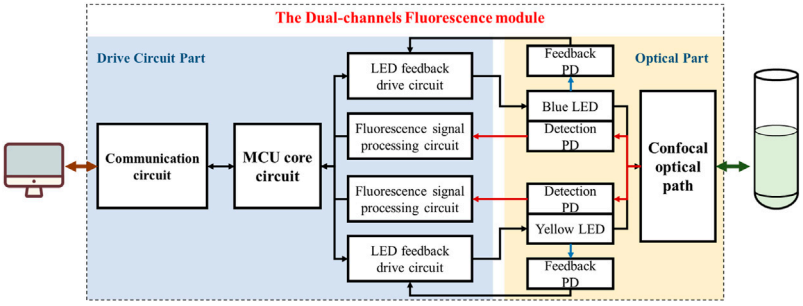

FIGURE 2
The Functional block diagram of the dual-channel fluorescence module, which can be divided into two partitions of drive circuit and optical path (Take module 1# as an example).

requirements of the homemade PNAD system. The optical path was based on a confocal structure, which enables the excitation and emission of light without interference. Different from split structure, the excitation light source and detector of this module were located on the same side to make the structure more compact. Due to the generally weak fluorescence signal, it is crucial that the light source and detector should be stable and sensitive. A current-light dual negative feedback drive circuit was used to adjust the light intensity of the light emitting diode (LED) for its stability. As for the detection portion, the fluorescence signal was processed by amplification, filtering and analogue-to-digital (A/D) to confirm the accuracy and stability of the fluorescence data. After fabrication, two fluorescence modules containing 4 different fluorescence channels were integrated into the PNAD system, and hepatitis B virus (HBV) concentration gradient detection and multiplex detection of different gene targets of SARS-CoV-2 have been carried out for evaluating the performance of the modules. The results showed that the fluorescence module has excellent has excellent linearity with R2 greater than 0.99 and reproducibility with coefficient of variation (CV) less than 2%. And this fluorescence has good homogeneity of each channels compared with the commercial StepOnePlus.

Materials and methods

Architecture of the fluorescence module

Figure 2 shows the functional block diagram of the fluorescence module. The whole module can be divided into two parts of a drive circuit and an optical path. As for the first part, a STM32 series microcontroller (STM32F103C8T6, STMicroelectronics) was used as the microprogrammed control unit (MCU) of the module, which realized data and commands interaction with outside through controller area network (CAN) bus while controlled the excitation LEDs by outputting signals through the input/output (I/O) ports. A current-light dual negative feedback LED drive circuit was designed to enhance the stability of the excitation light. Moreover, a fluorescence signal processing circuit was designed to perform amplification, filtering and analog-to-digital (A/D) conversion on optoelectronic signals from detection photodiodes (PD). In terms of the optical part, LEDs, PDs and other optical elements such as filters, dichroic mirrors and lens were fixed on the confocal light path. The module integrated two similar excitation/emission optical path and corresponding drive circuits for achieving dual-channel measurement.

The module was executed as follows: First, the MCU controlled the LED to excit the sample through excitation light path. Then, the sample absorbed the specific frequency of photons and emitted the fluorescence. After passing through the emission light path, the fluorescence signal was received by the detection photodiode and converted into electrical signal, which was then processed by the photoelectric signal processing circuit for amplification, filtering, and finally transmitted to the host computer through the communication unit after analog-to-digital (A/D) conversion.

Optical design and components selection

Common optical systems used for fluorescence detection include light sources, focusing lenses, filters, dichroic mirrors and photodetectors. It is important to select an appropriate excitation light according to the requirements of application, which affects the sensitivity and selectivity of detection. Real-time PCR commonly used excitation light sources are xenon lamps, mercury lamps, lasers and high-power LEDs (Spibey et al., 2001; Shin et al., 2021), different lights have their own applications due to their characteristics. For example, xenon lamps and mercury lamps are applied to high power analysis systems with high luminous intensity, but their large size is not allowed in

TABLE 1 Fluorescence dyes excitation and emission wavelengths.

	LED	Fluorescence dye	Excitation light (nm)	Emission light (nm)
Module 1	LB W5SM	FAM	450–490	510–530
	LY W5SM	Texas Red	560–590	610–650
Module 2	LT W5SM	HEX	515–535	560–580
	LR W5SM	Cy5	620–650	675–690

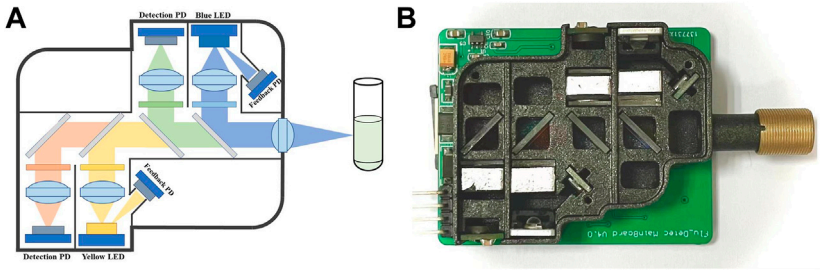

FIGURE 3
Optical path of the dual-channel fluorescence module (Take module 1# as an example). **(A)** Schematic diagram of optical path: two excitation lights (blue and yellow) and two emitted lights (green and orange) forms a confocal light path with the help of four dichroic mirrors. **(B)** Photograph of the optical path, consistent with the schematic.

miniaturized instruments. Lasers have high brightness and good monochromaticity but their prices are expensive. Compared with other lights, LED is more suitable for portable systems with low-cost, small size, low energy consumption, long life, etc. Therefore, we chose high-power monochromatic LEDs of different wavelengths as light sources (LB W5SM, LY W5SM, LT W5SM, LR W5SM, OSRAM GmbH.). The wavelength of these 4 LEDs and corresponding fluorescence dyes are listed in Table 1. As for photoelectric sensors, the mainstream photodetectors include avalanche diode (APD), charge-coupled device (CCD), photomultiplier tube (PMT) and photodiodes (PD). APD has high gain, high quantum efficiency but narrow spectral response range, CCD can scan all fluorescent signals at the same time but with low sensitivity, PMT would be a good choice profits from its fast response and low noise without considering price. In contrast, PD is the most suitable detector in our system because of its high sensitivity, low noise and low-cost (Song et al., 2010; Ryu et al., 2011; Abdallah et al., 2014; Zhan et al., 2019), so the silicon PDs (S1337-33BR, Hamamatsu Photonics Co., Ltd.) were chosen as the detector.

To make the module more compact while reducing the interference of external stray light and improving the signal-to-noise ratio (Xie and Yang, 2019; Peng et al., 2021), an optical structure based on confocal light paths was designed as shown in Figure 3A. Figure 3B shows the photograph of the optical path, in which all of the optical elements were installed in a 3D printing box. In order to make the emitted light unaffected by the excitation light, bandpass filters of corresponding wavelengths were set in front of the LEDs and the PDs. In addition, dichroic mirrors in the main optical path were set to separate the lights from each channel.

The bandpass filters and the dichroic mirrors were set as follows:

Module 1# channel 1#

The bandpass filter with center wavelength (CWL) of 470 ± 20 nm (BP-470, Shanghai Mega-9 Photoelectric Co., Ltd.) and the dichroic mirror with central wavelength of 500 (DM-500, Shanghai Mega-9 Photoelectric Co., Ltd.) nm were applied for excitation light; The bandpass filter with CWL of 525 ± 20 nm (BP-525) and the dichroic mirror with central wavelength of 550 nm (DM-550) were applied for emission light;

Module 1# channel 2#

The bandpass filter with center wavelength (CWL) of 570 ± 20 nm (BP-570) and the dichroic mirror with central wavelength of 600 nm (DM-600) were applied for excitation light; The bandpass filter with CWL of 630 ± 20 nm (BP-630) and the dichroic mirror with central wavelength of 650 (DM-650) nm were adopted for emission light;

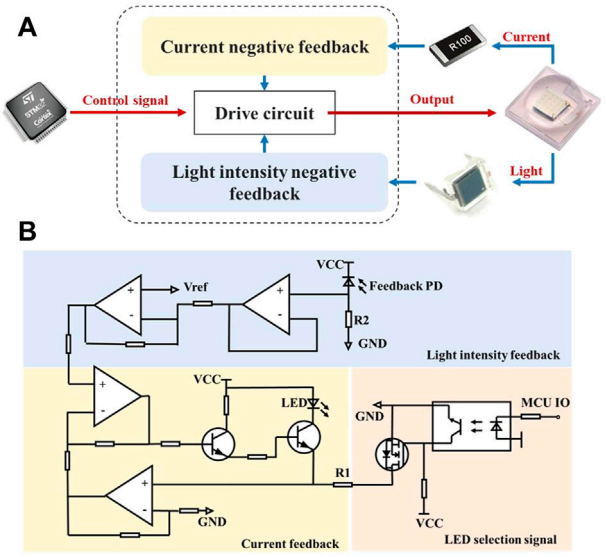

FIGURE 4
The current-light dual negative feedback LED drive circuit. **(A)** Working schematic block diagram of the circuit, the current-light dual negative feedback is realized by sampling the current and the light intensity of the LED. **(B)** Schematic of the circuit which can be divided into three partitions of current feedback, light intensity feedback and LED selection.

Module 2# channel 1#

The bandpass filter with center wavelength (CWL) of 520 ± 20 nm (BP-520) and the dichroic mirror with central wavelength of 550 (DM-550) nm were adopted for excitation light; The bandpass filter with CWL of 570 ± 20 nm (BP-570) and the dichroic mirror with central wavelength of 600 nm (DM-600) were adopted for emission light;

Module 2# channel 2#

The bandpass filter with center wavelength (CWL) of 630 ± 20 nm (BP-630) and the dichroic mirror with central wavelength of 650 nm (DM-650) were adopted for excitation light; The bandpass filter with CWL of 680 ± 20 nm (BP-680) and the dichroic mirror with central wavelength of 700 (DM-700) nm were adopted for emission light; To achieve light focusing, convex lenses (GL12-006–006, Beijing Golden Way Scientific Co., Ltd.) were also set in front of the LED and the PD, and a focusing lens (GL11-006–008, Beijing Golden Way Scientific Co., Ltd.) was set at the excitation and acquisition ends to make the excitation light focus at the sample.

The current-light dual negative feedback LED drive circuit

According to the principle of fluorescence detection, the stability of the detected fluorescence signal is affected by the fluctuation of the excitation light. Therefore, a current-light dual negative feedback LED drive circuit was designed to provide stable excitation light.

The schematic block diagram is shown in Figure 4A, the current and light intensity adjust the drive circuit together to make the output stable. Due to the negative temperature coefficient of LED, the forward voltage drop will decrease as the temperature rises resulting in an increase of the forward current when driven by a constant voltage source. Meanwhile, a slight change in the forward voltage will cause a large change in the forward current because of volt-ampere non-linearity, so that the LED luminous flux will also be changed. Therefore, constant current source is more appropriate for the LED driver, which can avoid fluctuations in the supply current and thus ensure the stability of the light source. With increased usage time and temperature changes, LED will experience light decay and its light intensity will then diminish. To solve this problem, light intensity negative feedback was added on the basis of current negative feedback.

Figure 4B is the schematic of the drive circuit, which can be divided into three parts: 1) on-off control area: control signal from the MCU controlled LED via a MOSFET (YJL3400A, Yangzhou Yangjie Electronic Technology Co., Ltd.); 2) current feedback area: sampled by a resister R1, LED current was converted to voltage and put into negative feedback, and finally the current was regulated by the output characteristics of a triode (BCP56-16T3G, ON Semiconductor). 3) light intensity feedback area: a feedback PD (BPW 34 BS, OSRAM GmbH.) generated photocurrent when receiving excitation light, which was sampled by a resistor R2 and then connected to feedback terminal. In short, the current negative feedback will increase current when it decreases, and the light intensity negative feedback will increase current to strengthen light when light weakens, and vice versa.

Fabrication and integration of the module

The exploded view of the overall structure is shown in Figure 5A, all the optical components were placed in a 3D printing box, above which was the control circuit board. The optical path and the circuitry were assembled into a complete unit by soldering the LED board and the PD board to the main circuit board. This assembly was then placed inside a metal box to isolate electromagnetic noise in environment. Two fluorescence modules (Figure 5B) with different wavelengths of excitation light were fabricated and integrated into the PNAD system (Figure 5C) for multiplex real-time PCR. Under the driving of the stepping motor, the fluorescence modules can scan and detect the signal of multiple reaction tubes.

Reagents and methods for performance evaluation

The two fluorescence modules were installed in the homemade PNAD system after fabrication. Then, HBV and

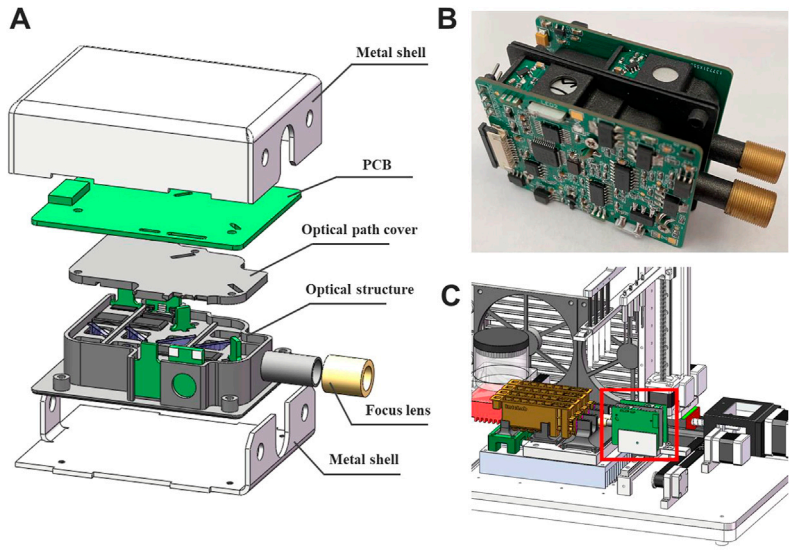

FIGURE 5
(A) The three-dimensional (3D) illustration of the fluorescence module in an exploded view, which includes metal shell, PCB, optical path cover, optical structure and focus lens. **(B)** The photograph of two fluorescence modules combined together. **(C)** Integration of the fluorescence module (in the red box) with a homemade portable nucleic acid detection system.

SARS-Cov-2 real-time reverse transcription PCR (real-time RT-PCR) were performed on this system. Meanwhile, the same sample was amplified and detected in StepOnePlus real-time PCR system (Applied Biosystems, America) under the same conditions for reliable results. The reagents used in the experiments include magnetic bead RNA extraction kit (Z-ME-0010, Shanghai Zhijiang Biotechnology Co., Ltd.), hepatitis B virus (HBV) nucleic acid assay kit (Z-HD-2002-02, Shanghai Zhijiang Biotechnology Co., Ltd.), 2019-nCoV nucleic acid test kit (Z-RR-0479-02-50, Shanghai Zhijiang Biotechnology Co., Ltd.) and Sterilized ddH_2O (Sangon Biotech).

Experimental methods are as follows:

1) Serum samples containing 5×10^6 IU/ml (standard sample in the HBV nucleic acid assay kit) were selected for testing. First, the viral RNA was extracted by the RNA extraction kit. After that, purified HBV RNA was diluted 10×, 100×, 1,000×, and a total 4 concentrations of samples were obtained before and after dilution. Then, 10 μL of each sample was added to 40 μL of the PCR mix, blended and centrifuged. Finally, real-time RT-PCR was performed by the PNAD system and StepOnePlus. The reaction conditions of real-time RT-PCR were: 37°C 2 min, 94°C 2 min, 93°C 15 s 45 cycles and 60°C 60 s. The first channel (excitation: 470 nm and emission: 520 nm) was used to detect the fluorescence signal.
2) SARS-CoV-2 positive control sample of the test kit were extracted by the extraction kit. Then 5 μL of purified RNA and 20 μL of PCR mix were blended to form 25 μL amplification system. Finally, multiplex real-time RT-PCR was performed by the PNAD system and StepOnePlus to test ORFlab gene, N gene, E gene and the internal standard target of SARS-CoV-2. The reaction conditions of real-time RT-PCR were: 45°C 2 min, 95°C 3 min, 95°C 15 s, 45 cycles and 58°C 30 s. The first channel (excitation: 470 nm and emission: 520 nm) was used to detect ORFlab gene, the second channel (excitation: 520 nm and emission: 570 nm) was used to detect N gene, the third channel (excitation: 570 nm and emission: 630 nm) was used to detect E gene, and the fourth channel (excitation: 630 nm and emission: 690 nm) was used to detect the internal standard target.

The fluorescence module designed in this paper was used for fluorescence excitation and detection. It took 200 ms to detect each sample tube, 5 raw fluorescence data were collected and averaged as the final fluorescence value. Finally, the fluorescence values of each cycle were plotted as real-time PCR curves for further analysis.

Results and discussion

Optical path simulation results and analysis

In order to further analyze the feasibility of the optical path, the transmission efficiency and detector received light intensity were simulated by the ZEMAX software. And the optical paths of

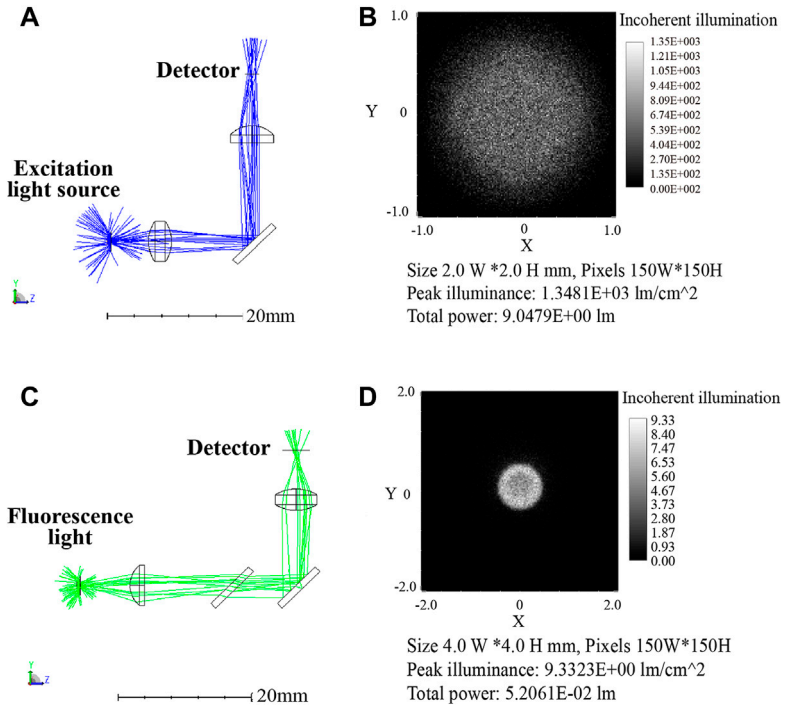

FIGURE 6
First channel optical paths (excitation/emission: 470 nm/525 nm) simulation diagram **(A)** 3D layout of the excitation optical path. **(B)** Image of the excitation optical path detector with 9.05 l m total power. **(C)** 3D layout of the emission optical path. **(D)** Image of the emission optical path detector with 5.2 × 10^{-2} lm total power.

TABLE 2 Results of the first channel simulation analysis.

	Light source	Light intensity (lm)	Receiving light intensity (lm)	With transmittance (95%) (lm)
Simulation	LED (470 nm)	100	9.05	7.76 (3 optical elements)
	Fluorescence (520 nm)	1	0.052	0.042 (4 optical elements)
Actual parameters	LB W5SM	15–33	1.36–2.99	1.16–2.56
	FAM	0.75–1.65	0.04–0.86	0.031–0.069

the two channels were simulated separately, with each channel divided into two optical paths: excitation and emission. The first channel optical paths simulation diagram is shown in Figure 6, Figure 6A indicates the 3D layout of the excitation optical, where the excitation light was collimated by a focusing lens, reflected by a dichroic mirror, and then focused by a plano-convex lens onto a detector. Figure 6B shows the light spot on the detector that was set up to evaluate the excitation light intensity at the sample. Likewise, Figure 6C presents the 3D layout of the emission light path, compared with the excitation light path, an additional dichroic mirror was set to separate the excitation light from the emission light. Figure 6D shows the light spot on the detector which represented the light received by the PD in the actual module.

Table 2 displays the results of the simulation, ignoring transmittance and reflectance, with the setting power of 100 l m, the LED light intensity reached to the reagent was 9.05 l m after passing through the optical elements. Calculated with 95% transmittance, the light intensity was 7.76 l m after 3 optical elements. The fluorescence intensity was set to 1 l m and picked up by the detector with the intensity of 0.042 l m after optical path loss. Corresponding the above relationships to the actual parameters, the blue LED (LB W5SM) output at I = 350 mA was 15–33 l m, so the blue light projected to the reagent was

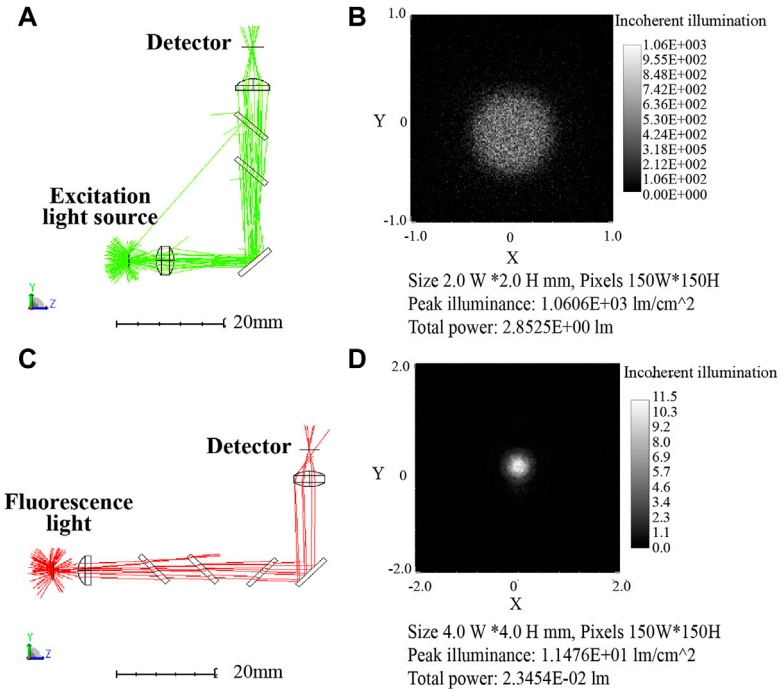

FIGURE 7
Second channel optical path (excitation/emission: 570 nm/630 nm) simulation diagram. **(A)** 3D layout of the excitation optical path with 2.85 l m total power. **(B)** Image of the excitation optical path detector. **(C)** 3D layout of the emission optical path. **(D)** Image of the emission optical path detector with 2.35 × 10^{-2} lm total power.

TABLE 3 Results of the second channel simulation analysis.

	Light source	Light intensity (lm)	Receiving light intensity (lm)	With transmittance (95%) (lm)
Simulation	LED (570 nm)	100	2.85	2.21 (5 optical elements)
	Fluorescence (630 nm)	1	0.023	0.017 (6 optical elements)
Actual parameters	LY W5SM	39–82	1.11–2.34	0.86–1.81
	Texas Red	0.56–1.18	0.012–0.027	0.01–0.02

1.16–2.56 l m. Assumed with 65% fluorescence quantum efficiency of the reagent dye, the fluorescence intensity was 0.75–1.65 l m and the intensity reaching the detector was 0.031–0.069 l m. The PD (S1337-33BR, 5.7 cm^2 detection area) had a current of 4.4–6.2 μA at 100 lx illumination, so the luminous flux on the detector surface at 100 lx was 5.7c×10^{-4} lm which was far less than 0.031 l m. Therefore, it can be considered that the fluorescence from samples was excited by the 470 nm excitation light, and then returned to the PD with very weak intensity which was still detectable despite significant losses.

Similarly, second channel optical path simulation diagram is shown in Figure 7 and the its results are displayed in Table 3. The Yellow LED (LY W5SM) output was 39–82 l m and the fluorescence emitted from reagent was 0.56–1.18 l m. The light intensity received by the detector after six optical elements was 0.01–0.02 l m, much larger than 5.7 × 10^{-4} lm (the luminous flux on the PD at 100 lx). Although the second channel lost more light energy than the first, the faint fluorescence also can be detected by the PD, demonstrating the viability of the optical path.

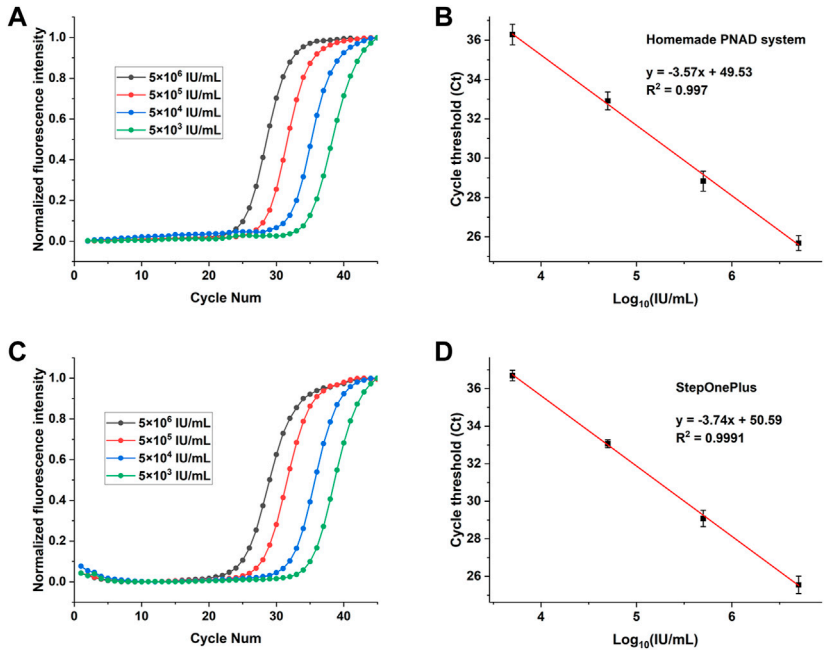

FIGURE 8
Real-time fluorescence PCR curves (left) and their standard curves (right) for detection of HBV with concentrations ranging from 5×10^6 IU/ml to 5×10^3 IU/ml. **(A)** and **(B)**: The real-time PCR curves and standard curves for Ct values from the homemade PNAD system. **(C,D)**: The fluorescence curves and standard curves for Ct values from StepOnePlus system.

TABLE 4 Ct value and reproducibility of HBV concentration gradient test from the PNAD system and StepOnePlus system.

Concentration	PNAD system		StepOnePlus	
	Average ct value	CV(%)	Average ct value	CV(%)
5×10^6 IU/ml	25.68	1.483	25.55	1.827
5×10^5 IU/ml	28.93	1.756	29.08	1.495
5×10^4 IU/ml	32.91	1.383	33.06	0.629
5×10^3 IU/ml	36.29	1.876	36.69	0.762

HBV concentration gradient test

Figure 8 shows the HBV concentration gradient test results from PNAD system and StepOnePlus. Real-time RT-PCR curves for HBV with concentration range from 5×10^6 IU/ml to 5×10^3 IU/ml are shown in Figures 8A,C, and standard curves for Ct values are shown in Figures 8B,D. In order to compare the results more visually, all original fluorescence data were baseline subtracted and normalized. In Figures 8A,C, the curves were aesthetically smooth and had the same trend for each concentration of HBV tested. Figures 8B,D indicates that standard curves from the PNAD system and StepOnePlus both had excellent linearity within the selected concentration range, and both had a determination coefficient $R^2 > 0.99$. Table 4 shows the results of Ct values and their reproducibility, the Ct values of HBV from the PNAD system and StepOnePlus were similar, and the CV of PNAD was within 2% which can be considered that the PNAD system equipped with this fluorescence module was fully comparable to the commercial StepOnePlus.

SARS-CoV-2 multi-target test

To further validate performance of the 4 channels of the two fluorescence modules, the 2019-nCoV nucleic acid test kit was used to test ORFlab gene, N gene, E gene and the internal

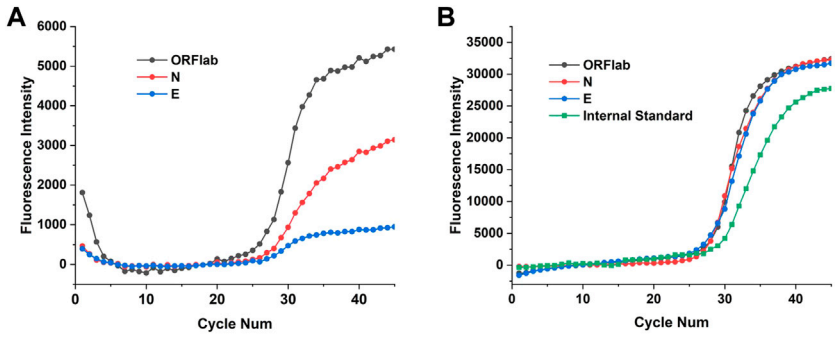

FIGURE 9
Multiplex real-time fluorescence PCR curves for detection of different targets of SARS-CoV-2. **(A)** Fluorescence curves of ORFlab gene, N gene and E gene of SARS-CoV-2 from StepOnePlus system. **(B)** Fluorescence curves of ORFlab gene, N gene, E gene and internal standard target from the homemade PNAD system.

TABLE 5 Ct value of different targets of SARS-CoV-2 from the PAND system and StepOnePlus system.

	Ct			
Target	**ORFlab**	**N**	**E**	**Internal standard**
StepOnePlus	27.83	27.97	27.86	\
PNAD System	27.67	28.12	27.82	30.32

standard target of SARS-CoV-2. These four targets corresponding to the fluorescence channels are: FAM (470 nm/520 nm), HEX (520 nm/570 nm), TEXAS Red (570 nm/630 nm) and Cy5 (630 nm/690 nm), which coincided with the detection channels of the two fluorescence modules. Multiplex real-time fluorescence PCR curves for different genes of SARS-CoV-2 from StepOnePlus and the PNAD system are shown in the Figure 9. It should be noted that since there was no Cy 5 channel in StepOnePlus system, so the curve corresponding to the internal standard target was absence. Comparing with the curves from StepOnePlus system (Figure 9A), fluorescence curves from the PNAD system (Figure 9B) are smoother both in baseline and exponential growth periods, which means that under the driving of the current-light dual negative feedback LED circuit the excitation LED of the designed fluorescence module is highly stable. In addition, comparing with Figure 9A, the difference in signal gain of these curves was smaller in Figure 9B due to the compensation for optical loss by strengthening excitation light and amplifying fluorescence signal gain in the designed fluorescence module. The Ct values of each curves are displayed in Table 5, as for 3 different genes of SARS-CoV-2, the similar results of the PNAD system and StepOnePlus further indicate the homogeneity of each channels in fluorescence module.

Conclusion

We developed a miniaturized, high-sensitivity and integrated dual-channel fluorescence module that was extremely suitable for portable nucleic acid detection system for real-time PCR. The dual-channel fluorescence module integrated drive circuit board and all of the optical elements in a minute (55 mm × 45 mm × 15 mm) metal box. Based on confocal optical path, a single module realized dual channels fluorescence exciting and detecting by integrating two set excitation-emission optical paths at different wavelengths. The stability of fluorescence signal is enhanced by the improvement of the LED stability which is provided by a current-light dual negative feedback LED circuit. In addition, the signal differences of each curves are smaller due to the compensation for optical loss by strengthening excitation light and amplifying fluorescence signal gain. After fabrication, we installed the two fluorescence modules on the homemade PNAD system to perform HBV concentration gradient test and multiplex test for different gene targets of SARS-CoV-2. The homemade PNAD system showed excellent linear response to HBV within the concentration range from 5×10^6 IU/ml to 5×10^3 IU/ml, the correlation coefficient R^2 was greater than 0.99. Besides, it had good reproducibility with CV less than 2%. A comparison of the SARS-CoV-2 test results between our modules and StepOnePlus shows that this module performs better in stability and homogeneity across different channels.

Currently, four dichroic mirrors are used in the optical path to distinguish excitation light from emission light, which greatly causes the loss of light energy. If more channels of fluorescence detection want to be achieved, the current optical path structure is not the most preferable solution. Because more detection channels mean more excitation sources, detectors and optical components such as dichroic mirrors and filters, there will be more losses in the optical path. So, we are considering the use of

optical fiber to achieve the separation of excitation and emission light, which may reduce the loss of light energy. In addition to being integrated into a homemade PNAD system for real-time PCR, the fluorescence module designed in this paper can be adapted to different applications such as water quality monitoring, food safety checking and clinical testing by changing the LEDs and filters.

Data availability statement

The raw data supporting the conclusions of this article will be made available by the authors, without undue reservation.

Author contributions

YF and YW contributed to conception and design of the study. YF provided the conceptualization and methodology and authored the software. YW designed and debugged the circuits, performed the data analysis and wrote the first draft. XS, HL, HC, LJ, and ZC wrote sections of the manuscript. NH acquired funding and provided guidance All authors contributed to manuscript revision, read, and approved the submitted version.

Funding

This research was financially supported by the NSFC (62071119), the Open Funding of State Key Laboratory of Oral Diseases (SKLOD2022OF05), and the Jiangsu Provincial Key Research and Development Program (No. BA2020016).

Conflict of interest

The authors declare that the research was conducted in the absence of any commercial or financial relationships that could be construed as a potential conflict of interest.

Publisher's note

All claims expressed in this article are solely those of the authors and do not necessarily represent those of their affiliated organizations, or those of the publisher, the editors and the reviewers. Any product that may be evaluated in this article, or claim that may be made by its manufacturer, is not guaranteed or endorsed by the publisher.

References

Abdallah, Z., Rumeau, A., Fernandez, A., Cibiel, G., and Llopis, O. (2014). Nonlinear equivalent-circuit modeling of a fast photodiode. *IEEE Phot. Technol. Lett.* 26 (18), 1840–1842. doi:10.1109/lpt.2014.2337352

Alam, M. W., Wahid, K. A., Goel, R. K., and Lukong, K. E. (2019). Development of a low-cost and portable smart fluorometer for detecting breast cancer cells. *Biomed. Opt. Express* 10 (2), 399–410. doi:10.1364/BOE.10.000399

Bedford, J., Enria, D., Giesecke, J., Heymann, D. L., Ihekweazu, C., Kobinger, G., et al. (2020). COVID-19: Towards controlling of a pandemic. *Lancet* 395 (10229), 1015–1018. doi:10.1016/S0140-6736(20)30673-5

Benmalek, E., Elmhamdi, J., and Jilbab, A. (2021). Comparing CT scan and chest X-ray imaging for COVID-19 diagnosis. *Biomed. Eng. Adv.* 1, 100003. doi:10.1016/j.bea.2021.100003

Chen, H., Wu, Y., Chen, Z., Hu, Z., Fang, Y., Liao, P., et al. (2017). Performance evaluation of a novel sample in-answer out (SIAO) system based on magnetic nanoparticles. *J. Biomed. Nanotechnol.* 13 (12), 1619–1630. doi:10.1166/jbn.2017.2478

Chen, Z., Yang, T., Yang, H., Li, T., Nie, L., Mou, X., et al. (2018). A portable multi-channel turbidity system for rapid detection of pathogens by loop-mediated isothermal amplification. *J. Biomed. Nanotechnol.* 14 (1), 198–205. doi:10.1166/jbn.2018.2524

Cui, F., and Zhou, H. S. (2020). Diagnostic methods and potential portable biosensors for coronavirus disease 2019. *Biosens. Bioelectron. X.* 165, 112349. doi:10.1016/j.bios.2020.112349

Deng, H., Jayawardena, A., Chan, J., Tan, S. M., Alan, T., and Kwan, P. (2021). An ultra-portable, self-contained point-of-care nucleic acid amplification test for diagnosis of active COVID-19 infection. *Sci. Rep.* 11 (1), 15176. doi:10.1038/s41598-021-94652-0

Fang, Y., Liu, H., Wang, Y., Su, X., Jin, L., Wu, Y., et al. (2021). Fast and accurate control strategy for portable nucleic acid detection (PNAD) system based on magnetic nanoparticles. *J. Biomed. Nanotechnol.* 17 (3), 407–415. doi:10.1166/jbn.2021.3028

Fu, L., Qian, Y., Zhou, J., Zheng, L., and Wang, Y. (2020). Fluorescence-based quantitative platform for ultrasensitive food allergen detection: From immunoassays to DNA sensors. *Compr. Rev. Food Sci. Food Saf.* 19 (6), 3343–3364. doi:10.1111/1541-4337.12641

Hanson, K. E., Azar, M. M., Banerjee, R., Chou, A., Colgrove, R. C., Ginocchio, C. C., et al. (2020). Molecular testing for acute respiratory tract infections: Clinical and diagnostic recommendations from the IDSA's diagnostics committee. *Clin. Infect. Dis.* 71 (10), 2744–2751. doi:10.1093/cid/ciaa508

Huang, L., Su, E., Liu, Y., He, N., Deng, Y., Jin, L., et al. (2021). A microfluidic device for accurate detection of hs-cTnI. *Chin. Chem. Lett.* 32 (4), 1555–1558. doi:10.1016/j.cclet.2020.09.055

Ishikawa-Ankerhold, H. C., Ankerhold, R., and Drummen, G. P. (2012). Advanced fluorescence microscopy techniques--FRAP, FLIP, FLAP, FRET and FLIM. *Molecules* 17 (4), 4047–4132. doi:10.3390/molecules17044047

Katzmeier, F., Aufinger, L., Dupin, A., Quintero, J., Lenz, M., Bauer, L., et al. (2019). A low-cost fluorescence reader for *in vitro* transcription and nucleic acid detection with Cas13a. *PLoS One* 14 (12), e0220091. doi:10.1371/journal.pone.0220091

Li, C., and Ren, L. (2020). Recent progress on the diagnosis of 2019 novel coronavirus. *Transbound. Emerg. Dis.* 67 (4), 1485–1491. doi:10.1111/tbed.13620

Mathuria, J. P., Yadav, R., and Rajkumar, Y. (2020). Laboratory diagnosis of SARS-CoV-2 - a review of current methods. *J. Infect. public health* 13 (7), 901–905. doi:10.1016/j.jiph.2020.06.005

Novak, L., Neuzil, P., Pipper, J., Zhang, Y., and Lee, S. (2007). An integrated fluorescence detection system for lab-on-a-chip applications. *Lab. Chip* 7 (1), 27–29. doi:10.1039/b611745g

Peng, Y. M., Pan, J. Z., and Fang, Q. (2021). Handheld laser-induced fluorescence detection systems with different optical configurations. *Talanta* 230, 122329. doi:10.1016/j.talanta.2021.122329

Pokhrel, P., Hu, C., and Mao, H. (2020). Detecting the coronavirus (COVID-19). *ACS Sens.* 5 (8), 2283–2296. doi:10.1021/acssensors.0c01153

Rai, P., Kumar, B. K., Deekshit, V. K., Karunasagar, I., and Karunasagar, I. (2021). Detection technologies and recent developments in the diagnosis of COVID-19 infection. *Appl. Microbiol. Biotechnol.* 105 (2), 441–455. doi:10.1007/s00253-020-11061-5

Ryu, G., Huang, J., Hofmann, O., Walshe, C. A., Sze, J. Y. Y., McClean, G. D., et al. (2011). Highly sensitive fluorescence detection system for microfluidic lab-on-a-chip. *Lab. Chip* 11 (9), 1664. doi:10.1039/c0lc00586j

Shin, Y.-H., Teresa Gutierrez-Wing, M., and Choi, J.-W. (2021). Review—recent progress in portable fluorescence sensors. *J. Electrochem. Soc.* 168 (1), 017502. doi:10.1149/1945-7111/abd494

Song, Q., Sun, X., Dai, Z., Gao, Y., Gong, X., Zhou, B., et al. (2021). Point-of-care testing detection methods for COVID-19. *Lab. Chip* 21 (9), 1634–1660. doi:10.1039/d0lc01156h

Song, T., Zhang, B., and Luo, Q. Q. (2010). Photoeletric conversion circuit design and optimization. *Electro-Opt. Technol. Appl.* 25 (06), 46–48.

Spibey, C. A., Jackson, P., and Herick, K. (2001). A unique charge-coupled device/xenon arc lamp based imaging system for the accurate detection and quantitation of multicolour fluorescence. *Electrophoresis* 22 (5), 829–836. doi:10.1002/1522-2683()22:5<829::AID-ELPS829>3.0.CO;2-U

Tang, C., He, Z., Liu, H., Xu, Y., Huang, H., Yang, G., et al. (2020). Application of magnetic nanoparticles in nucleic acid detection. *J. Nanobiotechnology* 18 (1), 62. doi:10.1186/s12951-020-00613-6

Wang, C., Liu, M., Wang, Z., Li, S., Deng, Y., and He, N. (2021). Point-of-care diagnostics for infectious diseases: From methods to devices. *Nano Today* 37, 101092. doi:10.1016/j.nantod.2021.101092

Xie, X. R., and Yang, B. (2019). Optical system design of multichannel PCR fluorescene detector. *Opt. Tech.* 45 (5), 531–534. doi:10.13741/j.cnki.11-1879/o4.2019.05.004

Zhan, X., Liu, Q., Wang, Y., Tian, H., Hu, A., He, X., et al. (2019). Coupled equivalent circuit for high-speed photodiodes. *IEEE Electron Device Lett.* 40 (10), 1654–1657. doi:10.1109/led.2019.2937677

Zhu, H., Zhang, H., Ni, S., Korabecna, M., Yobas, L., and Neuzil, P. (2020). The vision of point-of-care PCR tests for the COVID-19 pandemic and beyond. *TrAC Trends Anal. Chem.* 130, 115984. doi:10.1016/j.trac.2020.115984

frontiers | Frontiers in Bioengineering and Biotechnology

TYPE Review
PUBLISHED 13 October 2022
DOI 10.3389/fbioe.2022.1020444

OPEN ACCESS

EDITED BY
Guangli Li,
Hunan University of Technology, China

REVIEWED BY
Xianbo Mou,
Ningbo University, China
Xinjiang Cao,
Anyang Institute of Technology, China
Qi You,
Nanjing University, China

*CORRESPONDENCE
Yuan Guo,
guoyuan0815@163.com

SPECIALTY SECTION
This article was submitted to Biosensors and Biomolecular Electronics, a section of the journal Frontiers in Bioengineering and Biotechnology

RECEIVED 16 August 2022
ACCEPTED 23 September 2022
PUBLISHED 13 October 2022

CITATION
He Z, Liu C, Li Z, Chu Z, Chen X, Chen X and Guo Y (2022), Advances in the use of nanomaterials for nucleic acid detection in point-of-care testing devices: A review.
Front. Bioeng. Biotechnol. 10:1020444.
doi: 10.3389/fbioe.2022.1020444

Advances in the use of nanomaterials for nucleic acid detection in point-of-care testing devices: A review

Ziyu He[1], Changsheng Liu[1], Zhongyu Li[2], Zhou Chu[1], Xiang Chen[3], Xupeng Chen[1] and Yuan Guo[4]*

[1]Department of Scientific Research, Zhuzhou Hospital Affiliated to Xiangya School of Medicine, Central South University, Zhuzhou, China, [2]Department of Blood Transfusion, Zhuzhou Hospital Affiliated to Xiangya School of Medicine, Central South University, Zhuzhou, China, [3]Department of Clinical Laboratory, Zhuzhou Hospital Affiliated to Xiangya School of Medicine, Central South University, Zhuzhou, China, [4]Department of Cardiovascular Medicine, Zhuzhou Hospital Affiliated to Xiangya School of Medicine, Central South University, Zhuzhou, China

The outbreak of the coronavirus (COVID-19) has heightened awareness of the importance of quick and easy testing. The convenience, speed, and timely results from point-of-care testing (POCT) in all vitro diagnostic devices has drawn the strong interest of researchers. However, there are still many challenges in the development of POCT devices, such as the pretreatment of samples, detection sensitivity, specificity, and so on. It is anticipated that the unique properties of nanomaterials, e.g., their magnetic, optical, thermal, and electrically conductive features, will address the deficiencies that currently exist in POCT devices. In this review, we mainly analyze the work processes of POCT devices, especially in nucleic acid detection, and summarize how novel nanomaterials used in various aspects of POCT products can improve performance, with the ultimate aims of offering new ideas for the application of nanomaterials and the overall development of POCT devices.

KEYWORDS

nanomaterial, nucleic acid detection, point-of-care testing devices, sensor, nucleic acid enrichment

Introduction

Point-of-care testing (POCT), which refers to detection immediately after sampling—without the need for professional personnel and equipment—has the advantages of being in real-time, fast, low cost, and so on (Buckle et al., 2021; Xu et al., 2021). Operators do not need to be medical professionals, and testing does not need to be in a fixed site, but can take place anywhere, e.g., in an emergency room, ambulance, outdoors or in the home (Ferreira et al., 2018; Yan et al., 2021). WHO has defined the criteria for POCT products as "ASSURED" (i.e., affordable, sensitive, specific, user-friendly, rapid and robust, equipment-free, and deliverable to end-users) (Land et al., 2019). However, there is a challenge in fulfilling these criteria, especially the sensitivity and

specificity of the device. Thus, novel methods are urgently needed to ensure the rapid development of POCT devices.

Nanomaterials can be defined as materials possessing at least one external dimension within the nanometer scale of 1–100 nm (Suan Ng et al., 2022). Due to their special features, nanomaterials offer a wide range of possibilities in various fields, such as biocompatibility, fluorescence, electrical and thermal conductivity, and magnetism (Guo et al., 2018; Li et al., 2020; Tang et al., 2020; Gong N et al., 2021; Li J et al., 2022a). Meanwhile, nanomaterials have different shapes and can be divided into four types: 0D (e.g., spherical nanomaterials), 1D (e.g., nanotubes and nanowires), 2D (e.g., graphenes), and 3D (e.g., nanoprisms and nanoflowers). In line with their advantages and disadvantages, nanomaterials have been applied in different fields, such as the diagnosis of disease, detection of metal ions, and so on (Lai et al., 2018; Quesada-Gonzalez et al., 2018; Ma et al., 2020; Li J et al., 2021). Owing to their specific features, nanomaterials have also become integral in enhancing the performance of POCT devices.

In recent years, nanomaterials have been applied in multiple POCT devices to improve the efficiency of nucleic acid detection, especially in the face of the coronavirus (COVID-19) pandemic. Kim et al. (2021) found nanomaterial-based thin films were superior transducers that can reliably detect about 100 copies of the virus without being disturbed by interfering agents in a virus culture medium (WHO considers a viral load under 10^6 copies/mL negative). Interestingly, the relations between various thin film properties and the sensitivity of immunosensors were systematically analyzed using a special calculation method that showed good correlation. Hasanzadeh et al. (2021) introduced the application of nanomaterials in protective equipment, the loading and delivery of vaccines, and COVID-19 detection equipment. Xiao C et al. (2022) also systematically elaborated relevant studies regarding the use of nanomaterials in preventing viral spread, preparing vaccines, and diagnosing coronavirus. These works show that nanomaterials have penetrated all stages in the diagnosis and treatment of COVID-19, and hence their integration with POCT devices will be an increasing trend in the future detection market.

A clear understanding of the core technology of POCT devices is of paramount importance. The sensor as receiver controls the accuracy and sensitivity of the devices, because it can register the measured information and output as an electrical signal or in other required forms. A nanosensor is also a type of sensor, and has the advantages of miniaturization, digitalization, intelligence, multi-functionality, systematization, and network capacity, which shows its good application prospects in the development of POCT devices (Yang et al., 2018; Wu et al., 2020b; Li Q et al., 2021; Suan Ng et al., 2022; Xiao M. F et al., 2022). As Mitasha has described, using various biomolecules to detect specific analytes, activatable sensors in POCT products can be divided into immunological-based tests, nucleic acid (NA)-based tests, and other biomarker-based tests (Bharadwaj et al., 2021). Activatable sensors can improve specificity and sensitivity compared to traditional detection, hence providing more comprehensive information and obtaining faster detection speed (Wiraja et al., 2019; Ma et al., 2020; Xie et al., 2020). Therefore, the advantages of activatable sensors all meet the demands for POCT, and are widely used in POCT devices.

The NA-based nanosensor is an activatable sensor, which not only targets NA or proteins (e.g. aptamer), but can also combine antisense oligonucleotides or interfering RNAs to serve both therapeutic and diagnostic purposes (theragnostic) (Liu et al., 2017; Xie et al., 2020; He et al., 2021; Khan et al., 2021). Use of an NA-based sensor as a screening tool to detect COVID-19 produces highly specific and sensitive results (Dronina et al., 2021; Zhang M et al., 2022). In recent decades, the NA-based sensor has been used as a detector to assess heavy metal ion concentration, where it has also demonstrated good performance (Liu et al., 2018; Guo et al., 2021; Chen et al., 2022). In summary, deeper insights into POCT devices and their application include disease diagnosis and therapy, pathogen diagnosis, heavy metal ion monitoring, and so on (Cho et al., 2018; Zeng et al., 2020; Kim H et al., 2021; Mo et al., 2021; Jani and Peter., 2022). However, using a NA-based sensor to achieve the purpose of detection in POCT, to meet the abovementioned WHO-defined criteria, requires greater accuracy and shorter response times, and can, to a certain extent, be achieved by combination with nanomaterials.

In this review, we firstly clarify the current status and trends in POCT in recent years to elicit the latest information, as these aspects have been broadly reviewed in general terms (Prattis et al., 2021; Zhang N et al., 2022). Moreover, we focus on introducing the role of nanomaterials in the work processes of POCT devices, as illustrated in Figure 1, including loading the sample, detection, and data display. In relation to detection especially, we elaborate two functions: amplification and non-amplification, and highlight the important role of nanomaterials in these functions. Overall, this work aims to promote further development of POCT devices, and in particular, POCT devices related to nucleic acid detection. It also offers new ideas for the continued development of POCT devices with high sensitivity, low assay cost, and low power requirements.

Loading the sample

To reduce interference material in the sample, and to avoid influence on the determination of the result, sample purification is an important step that cannot be ignored. Currently, for the extraction and purification of NA, common methods are magnetic bead-based, column-based, and phenol-chloroform-based (Mou et al., 2019; Wang S et al., 2021; White et al., 2022). In the early days of POCT devices, few researchers considered the project of integrating sample preprocessing into POCT devices. It is well known that the complex and time-consuming sample

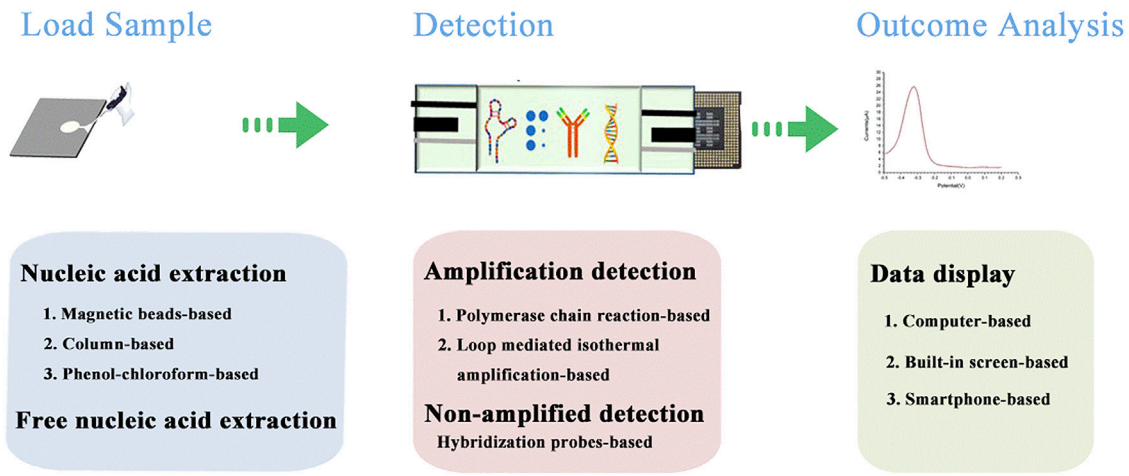

FIGURE 1
The schematic diagram of POCT device detection process.

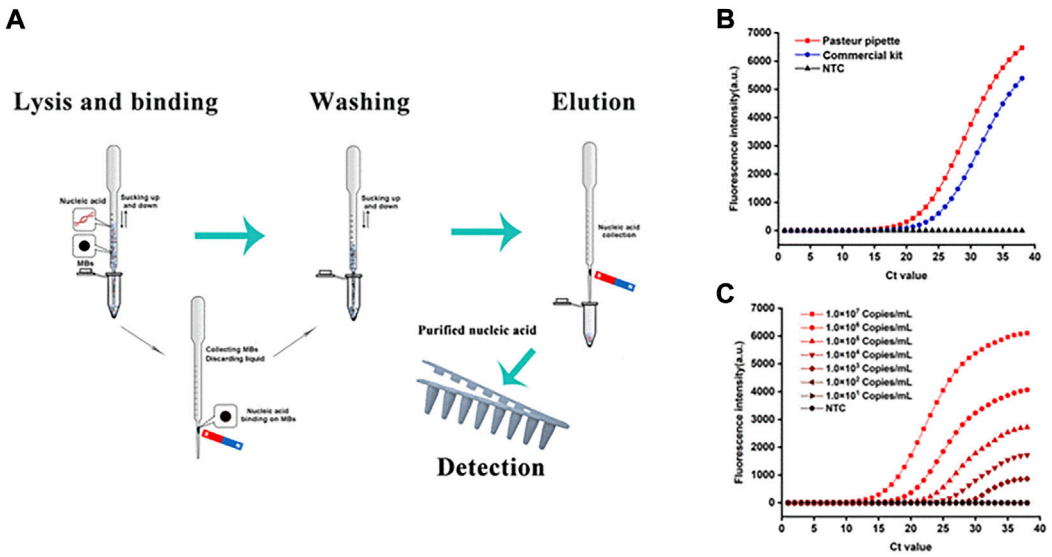

FIGURE 2
Nucleic acid extraction in Pasteur pipette system and detection results. **(A)** The schematic illustration of lysis and binding step, washing step, elution step and nucleic acid extraction in Pasteur pipette system, and detection step. **(B)** Comparison of extraction effect between Pasteur pipette system and the commercial kit. **(C)** The sensitivity of the Pasteur pipette system. Copyright 2021 Elsevier Inc.

preparation process should be performed by professionals, because direct loading of samples under unpurified conditions can cause high false positives and negative results. These processes are difficult to promote, which hinders further development of POCT technology.

The application of nanomaterials can speed up and automate sample purification, which also helps users simplify sample pre-processing and hence improve accuracy in the POCT procedure. Magnetic nanoparticles have a pivotal position, particularly in NA purification (He et al., 2017; Tang et al., 2018; Dong et al., 2020). A variety of extraction methods involving magnetic nanomaterials are emerging. Kang et al. (2021) developed a simple NA purification system performed in a plastic Pasteur pipette, using magnetic nanoparticles that enter the NA extraction process, as shown in Figure 2. Unlike traditional approaches, the system could complete NA extraction from

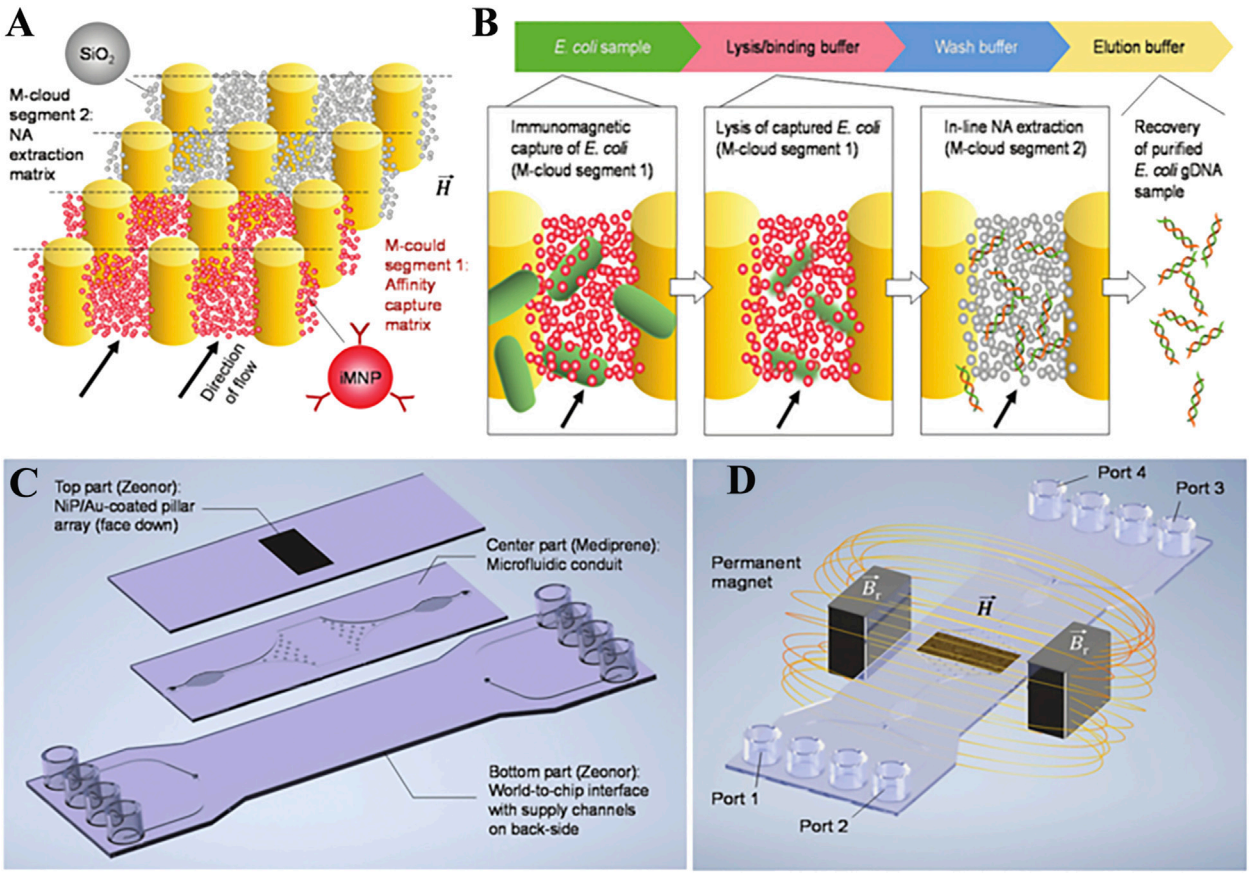

FIGURE 3
Concept of *in situ* microbial capture and DNA isolation. **(A)** Schematic illustration of segmented, multifunctional M-cloud configuration used within this work. **(B)** Flow chart detailing the order in which assay components are introduced to the M-cloud, along with illustrations of the main steps. **(C)** Schema of the microfluidic chip developed for process integration. **(D)** Illustration of the experimental setup used to generate M-cloud capture regions inside the microfluidic chip. Copyright 2022 Royal Society of Chemistry.

various samples, including swabs, serum, milk, and pork, in 15 min without assistance from electrical instruments, and the obtained extract had a lower limit for subsequent amplification detection. The system satisfies the requirements for POCT and offers a new idea for integrated detection in POCT devices.

There is a similar study from Pearlman et al. (2020), and work is ongoing to improve the capturing ability of magnetic beads. Bacteria have a different cell surface hydrophobicity, and when the contact angle of the material and water is approximately 90°, the highest bacterial adhesion is shown (Krasowska and Sigler., 2014; Li et al., 2019). In line with this feature, Lee et al., (2021) synthesized tryptamine-functionalized magnetic nanoparticles. Their strategy was to adopt the enrichment of bacteria before DNA extraction. The result demonstrated the extraction efficiency of 1 CFU/ml was 10 times better than that of the commercial kit, and that the process had good stability and accuracy. A novel g-Fe_2O_3/PEDOT hybrid nanocomposite was synthesized by da Silva et al. (2021). Here modified nanomagnetic beads were used to extract the DNA from blood and bacteria, and the yields after verification were 6.4 mg and 7.3 mg, respectively, and the captured DNA could be directly used for downstream experiments, such as PCR amplification, without being detached from the nanocomposite.

The limitation of magnetic nanoparticles is their slow response to external magnetic stimuli, which means that they need to form larger magnetic complexes by using high nanoparticle concentrations or have long incubation times (Burklund et al., 2020). Poncelet et al. (2021) developed suspended magnetic nanoparticle assemblies (M-clouds) for DNA extraction. The detailed principle is shown in Figure 3. The M-clouds have a strong magnetic field, and can enable almost instant contact between capture sites and the target analyte when the sample solution is flowing. The real result shows that the efficiency of *E.coli* capture and DNA extraction by M-cloud devices was in the range of 17.3–34.1% when the

concentration was 10^3 CFU/ml in environmental water samples. Extraction reagents surely also affect the efficiency of DNA capture (Tang et al., 2013; He et al., 2019). In short, the purpose of pre-test treatment for complex samples is to improve the purity and yield of NA, and all the work has been done to this end. The purification and enrichment of bio samples to obtain high quantity NA is crucial for downstream detection and analysis. Pre-processing of complex samples is therefore essential, and from proper processing it will be easier to obtain highly accurate detection results.

Detection

Obtaining high-quality DNA is the first step in optimizing detection results, but improvement in the sensitivity and specificity of detection should not be ignored. Therefore, researchers are taking great pains to improve detection methods in order to obtain more exact outcomes. At present, there are two methods for NA detection: amplification and non-amplification. They each have their advantages and disadvantages, which are unavoidable to some extent. Researchers strive to improve these advantages and reduce the disadvantages. The use of nanomaterials can help to address some of the key issues, and in the next section we mainly introduce NA detection methods based on use of nanomaterials in POCT devices.

Amplification

Exponential amplification in NA detection helps researchers obtain sufficient information from low NA levels. Zhang W et al. (2022) reviewed the application of different nanomaterials (0D, 1D, 2D, and 3D) in isothermal NA amplification, and identified the following advantages of nanomaterials: increasing the activity and stability of the amplification enzyme, activating the activity of enzymes, inhibiting nonspecific amplification, and promoting helicase-dependent denaturation. These advantages are all driving forces in promoting the development of POCT devices.

POCT devices have some limitations, such as complex temperature controls, considerable weight, and high background signals. To solve these problems, more novel technologies have been developed. For example, in the work of Lee et al. (2020), a novel system based on a nanogap-embedded, active whispering-gallery mode resonator was developed to detect the product of recombinase polymerase amplification. Resonators are the core components of detection systems. At present, nano-gap active resonators, disk resonators, and ring resonators are the most common. Ultra-high quality factor optical resonators (Chen et al., 2017) are among the disk resonators, while silicon microring resonators (Park et al., 2013) are ring resonators. Detailed parameter comparisons are given in Table 1, with nanogap active resonators possessing higher sensitivity and lower background signals compared to other resonators. Meanwhile, the author thinks the system can become a POCT device by combining it with a visible LED source, because the size and performance of the entire system fits the demands for POCT devices. Direct detection without NA extraction has become a hot topic, because of the simplified detection steps, shortened detection time, and decreased detection costs, although distractions in the sample or impure NA will affect the detection results.

Similarly, Yi et al. (2021) have synthesized a nanoporous hydrogel with self-cleaning properties for application to direct NA analysis without the need for any sample pretreatment. The detection principle is shown in Figure 4. The inhibitor was adsorbed and removed by the formation of a cross-linking network structure of hydrogel, and next an amplification reaction was produced. The method gives us the new idea that nanoporous hydrogel can become a sort of “dustman” in removing some adverse factors and achieving an efficient NA amplification reaction. Appropriately amplifying the detection signal is necessary. For example, Yang et al. (2020), reviewed detection signal amplification strategies for nanomaterial-based photoelectrochemical (PEC) biosensors, and put forward PEC instruments that are simpler, more cost-effective, with higher analytical detection performance and easier miniaturization. In addition, the PEC sensors can reduce background signals, and have higher sensitivity than conventional electrochemical methods. Alafeef et al. (2021) synthesized the antisense oligonucleotide (ASO)-capped gold nanoparticles (AuNPs) to detect the product of loop-mediated isothermal amplification. By using clinical sample evolution, the accuracy, sensitivity, and specificity of the detection were >98.4%, >96.6%, and 100%, respectively, with a detection limit of 10 copies/μL.

Rolling circle amplification (RCA) is an isothermal NA amplification method and has ultrahigh specificity for nucleotide variants. Tian et al. (2020), performed two rounds of RCA, and the product of the second round of RCA combined magnetic nanoparticles to generate amplicon coils. The opto magnetic signal can then be charged with the increased amplification product, thus achieving real-time NA detection. Similarly, Wang et al. proposed a lateral flow gene assay (LFGA), combining recombinase polymerase amplification (RPA) and nucleic acid lateral flow (NALF), to directly detect a DNA sample using an oligonucleotide probe. The detection process is described in detail in Figure 5. AuNPs were applied as a dye in RPA amplification product analysis. The whole detection process was completed under 37–42°C in 30 min. This work provides a portable POCT platform without the need for any costly instruments (Wang Z et al., 2021).

These results show that nanomaterials make a contribution to POCT devices in the matter of NA amplification detection, mainly concerning amplified detection signals and reduced nonspecific amplification, and a large body of literature

TABLE 1 Comparison of the nano-gap active resonator with other resonators.

Types	Nano-gap active Resonator	Disk resonator	Ring resonator
Pump source	LED/CW laser	Tunable laser	Tunable laser
Coupling scheme	Light illumination in free-space	Tapered fiber	Bus waveguide
Primer state	Immobilized	Immobilized	Immobilized
Amplification condition	Isothermal (38 or 43°C)	Not tested	Isothermal (38 or 43°C)
Background signal	No	Yes	Yes
Target detection time	10 min	20 min	20 min
Detection limit (copies/reaction)	10^0	10^1 to 10^2	10^1 to 10^2

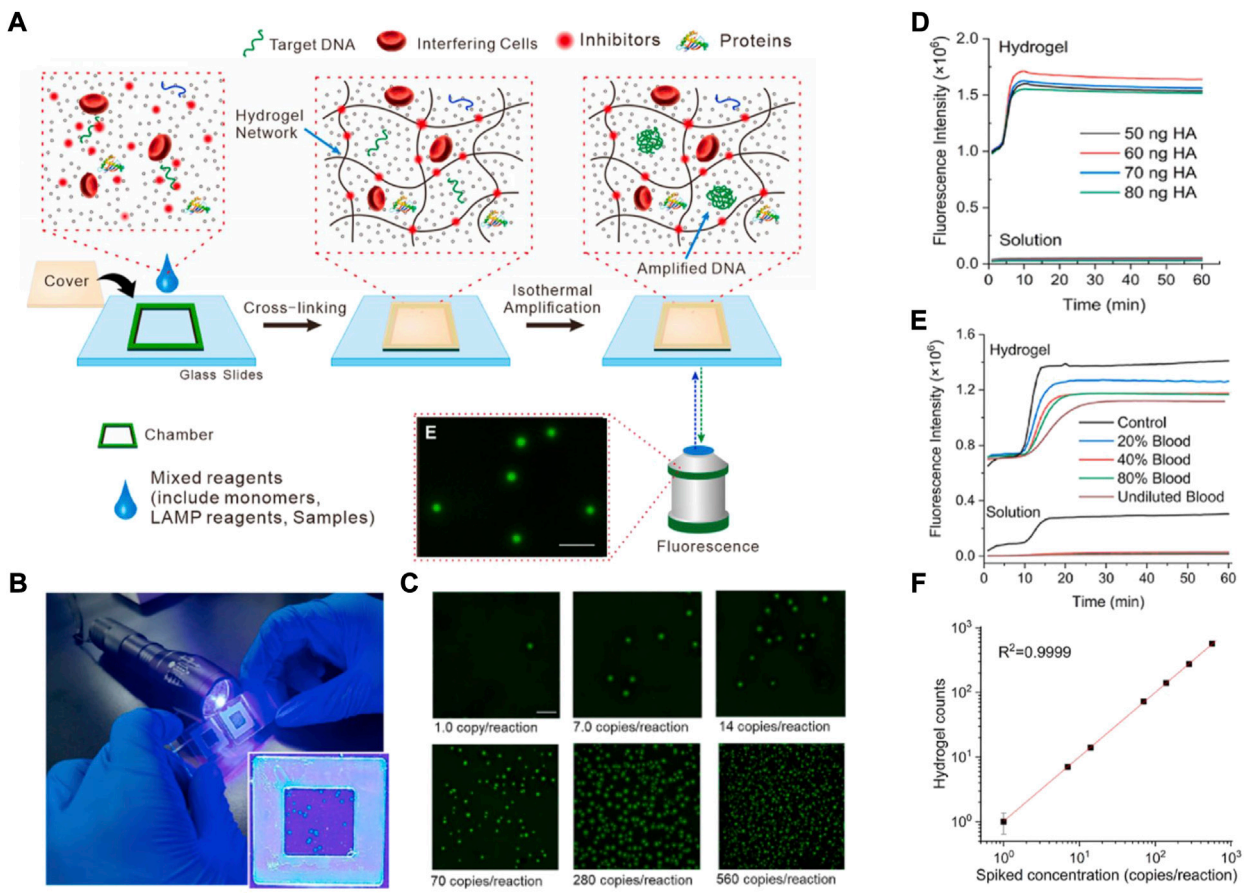

FIGURE 4
(A) Schematic illustration of isothermal amplification inside the nano porous hydrogel for digital LAMP in complex matrices. **(B)** The photograph for naked-eye counts of amplicon dots in the hydrogel under the LED flashlight. **(C)** Endpoint fluorescence images of hydrogel after LAMP reaction for unprocessed whole blood spiked with a series concentration of the *E.coli* genome. Scale bar of 1 mm. **(D)** The impact of different concentrations of whole blood on LAMP reaction performed in the hydrogel or solution. **(E)** The impact of different concentrations of HA on LAMP reaction in the hydrogel or solution. **(F)** Comparison of hydrogel counts to the spiked *E. coli* genome concentration in unprocessed blood. LAMP: loop-mediated isothermal amplification. Copyright 2021 Elsevier B.V.

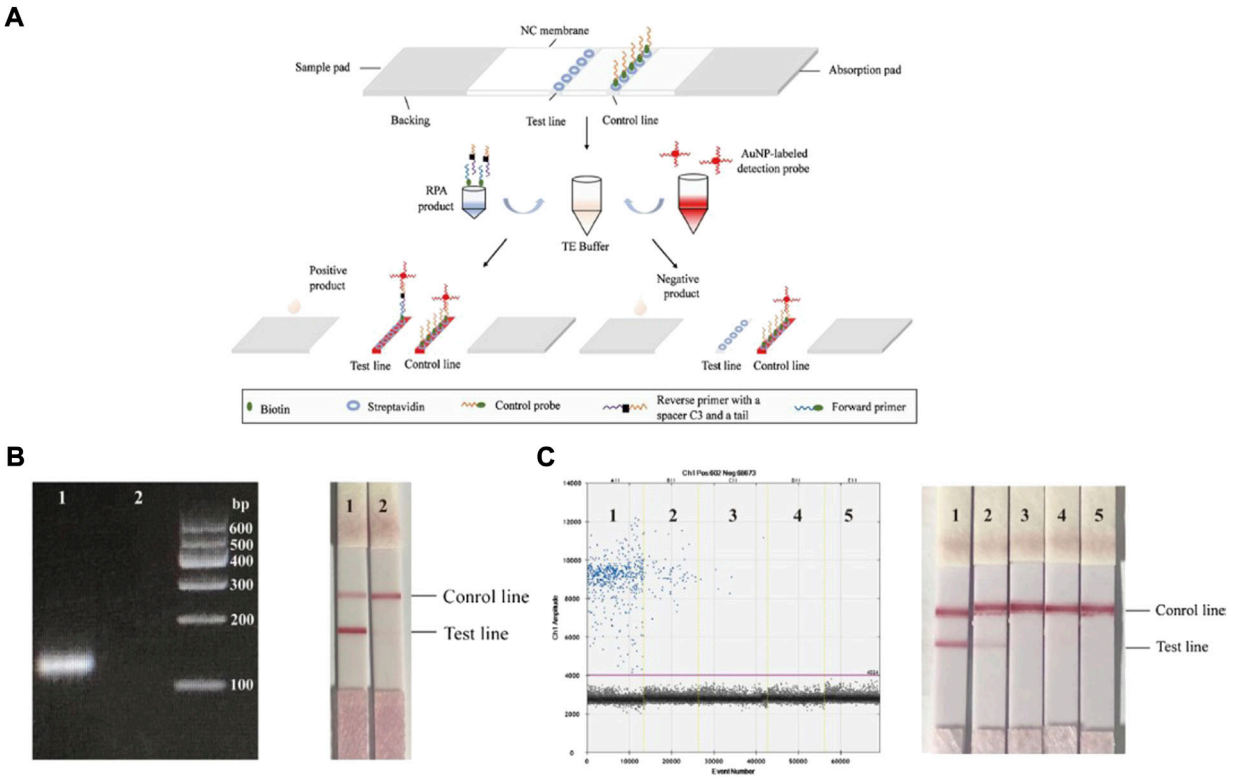

FIGURE 5
(A) The principle of lateral flow gene assay. The RPA product and the AuNP-labeled detection probe were added to TE buffer, and then the mixed droplets were added to the sample pad of the strip. In the presence of positive products, there will be two red lines on both the test line and control line. In the presence of negative products, there will be only one red line on the control line. **(B)** The detection result of sample, Lane 1: target DNA; Lane 2: double-distilled H_2O. **(C)** A series of tenfold DNA diluents from 10^1 to 10^4 extracted from blood infected with ASFV were used to determine the LOD, Lane 1: 10-fold dilution; Lane 2: 10^2-fold dilution; Lane 3: 10^3-fold dilution; Lane 4: 10^4-fold dilution; Lane 5: NTC. Copyright 2022 Springer Nature Switzerland AG.

supports this result (Jiang et al., 2013; Nie et al., 2014; Yang et al., 2017; Jiang et al., 2018; Wu et al., 2020a). Overall, nanomaterials have made an outstanding contribution in optimizing NA amplification, and can not only improve the accuracy of detection, but can also shorten detection time and optimize the detection process. Amplification detection requires enzyme assistance, and enzymes need a separate chamber in order to work, and specifically, most reactions require temperature to activate the enzymes. This means that POCT products need to be larger to some extent and are more difficult to operate. However, the above methods can be applied to miniaturized instruments to achieve POCT detection.

Non-amplification

Direct detection of NA without amplification is more suitable for POCT devices. Meanwhile, the requirement for sample purification is also lower without the involvement of an amplifying enzyme. Nevertheless, here the greatest limitation is low sensitivity, and how to capture more NA in samples and collect as many real signals as possible are some of the problems that researchers need to think about (Mondal et al., 2021; Sun 2022). AuNPs can be designed to suit diversified functionalization options, due to easy surface modification (Lai et al., 2018; Sarfraz and Khan, 2021; Li J et al., 2022b; Liu Y et al., 2022).

AuNPs have the feature of localized surface plasmon resonance, which give them a signal 10- to 10,000-times higher than fluorescent dyes or quantum dots, and this can be detected in simple dark-field microscope. Li et al. (2016) developed a nonamplification sandwich assay for NA detection, and the detection principle is shown in Figure 6. The result shows the length and concentration of target DNA: while the dose of AuNPs can affect the detection efficiency, the detection rate of the target DNA is almost unaffected in a complex matrix containing a variety of proteins and other contaminants. Interestingly, the limit of detection of a clinic sample is 3 fM, and only requires a simple dark-field microscope, which shows that the assay has high simplicity and sensitivity.

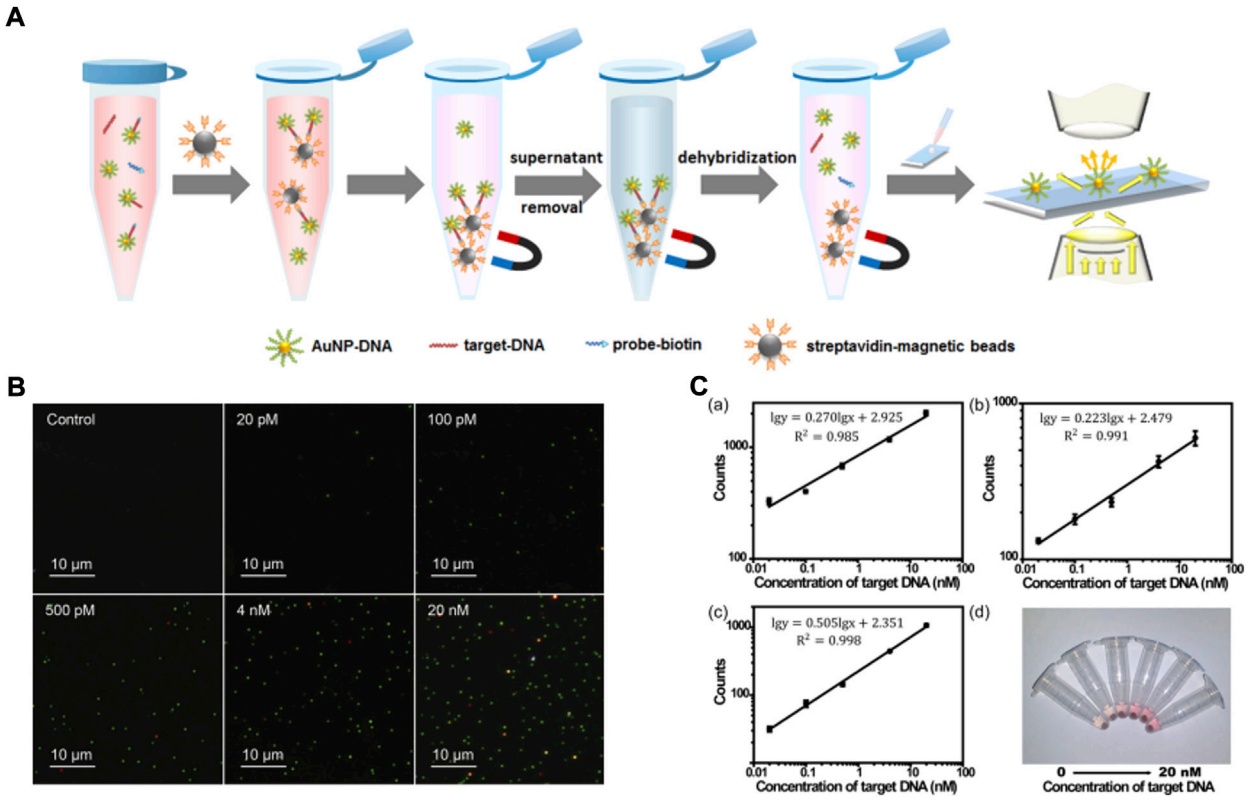

FIGURE 6
(A) The schematic illustration of nucleic acid extraction method combining the sandwich-type DNA hybridization strategy and magnetic separation. **(B)** Dark-field images of AuNP-DNA with different concentrations of 40-nucleotide target DNA. **(C)** Automatic counting results for target DNA with different lengths: (a) 24 nucleotides, (b) 40 nucleotides, and (c) 60 nucleotides; (d) the photograph of the supernatant with different concentrations of 40-nucleotide target DNA (from left to right, 0 p.m., 20 p.m., 100 p.m., 500 p.m., 4 nM, and 20 nM). Copyright 2016 American Chemical Society. Copyright 2021 Elsevier B.V.

Ota et al. (2021) used 4-cyano-N-(2-mercaptoethyl) benzamide (4CMB) and oligonucleotides to modify the surface of gold nanorods and finally form a sandwich structure which can detect the target DNA under 1 nM. The limitations of the structure are that the concentration of target DNA is unquantifiable and needs the auxiliary detection of a micro-Raman spectroscope.

A DNA nanostructure is a technique for artificially designing and producing useful NA structures, which, as a bridge, connect the relationship between optoelectronics, thermology dynamics, and genetic information (Zhang et al., 2020; Henry and Stephanopoulos, 2021; Li S et al., 2021; Qin et al., 2022). Although not active, a DNA nanostructure has these advantages: low toxicity, high resistance to degradation in biological media, and an ideal ability to enter cells without transfection agents. These advantages make it a good tool for detecting the NA in live cells (Zhou et al., 2021; Li G et al., 2022a; Li G et al., 2022b). Li et al. (2019) assembled a DNA tetrahedral structure using oligonucleotides to protect the DNAzyme and fluorescent probe. To prevent the uncontrollability of the DNAzyme, the author designed a unique structure to lock its activity, with specific miRNA as the "key" to activating the DNAzyme. The DNAzyme can obtain the dissociated fluorescent signal by separating out the fluorescence-quenched structure, thus achieving the purpose of fluorescence detection. This detection method, compared with its nonamplification molecular beacon counterpart, exhibited at least 10 times higher detection sensitivity (the limit of detection is 16 p.m.) and was able to distinguish miRNA targets from corresponding family members. Of course, the structures can not only detect the miRNA, but are also applied in NA detection, especially short fragment NA. Non-amplification makes NA detection convenient and speedy, and with its shortcomings addressed by some of the above work, is an important part of the development of POCT technology.

In summary, non-amplification NA detection still has huge difficulties, especially for samples with low levels of NA, but it has advantages for direct detection in complex samples. Therefore, it is important to select appropriate detection methods for POCT products, given the method has an important relationship with

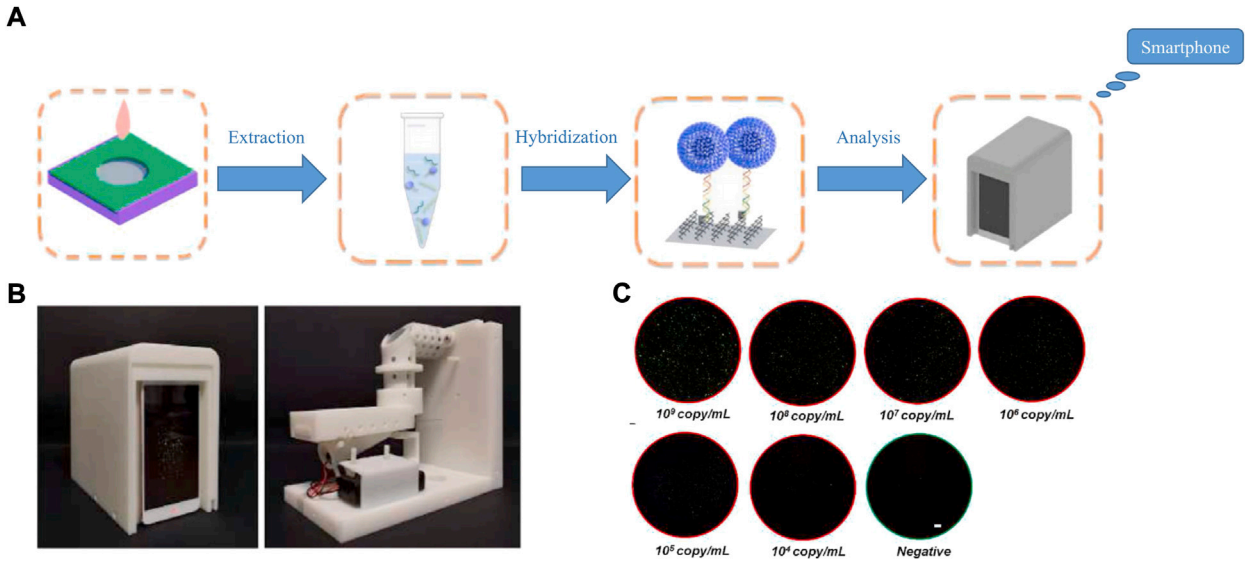

FIGURE 7
(A) Flow chart of the amplification-free smartphone-based detecting technique. **(B)** Portable fluorescence nucleic acid detector. **(C)** Captured FoVs corresponding to different virus concentration. White bar represents 1 μm. Copyright 2021 Elsevier B.V.

the samples tested. When developing new POCT products, it is essential to consider the object for detection.

Data display

In this section, we only discuss the forms of data presentation, and not how the data is processed. The data display has very little to do with the nanomaterial, but it is an integral part of POCT, especially in terms of the user experience. Currently, the personal computer (PC) and built-in touch screen are the two main forms for presenting data visualization, but their disadvantages cannot be ignored. For example, the PC is an expensive and bulky device compared with some POCT products, which is bad news for users. The built-in touch screen solves the problem of needing the supplementary PC, but the use of screens in POCT devices, while on the one hand increasing the instrument's size, on the other offers a poor user experience.

Given its popularity, the smartphone is a good choice as a tool for data display. Its characteristics, such as simplicity, affordability and user-friendliness, makes it acceptable to the public. Meanwhile, three data transmission modes, wired, wireless, and Bluetooth, can meet user needs in different situations. Furthermore, smartphones are widely used as detector and analysis devices (Pujari 2021; Pujari et al., 2021; Zhang Z et al., 2022), due to their built-in high-definition cameras. Li Y et al. (2021) built a novel optical detection system for use with a smartphone. Fluorescent images are taken from the camera of a smartphone, and the application is driven by an Android smartphone to analyze the fluorescent signal, and ultimately obtain detection results. The specific detection process and results are shown in Figure 7. Liu S et al. (2022) did the same thing, choosing SYTO9 as a fluorescence reagent to stain the amplification product, which was then observed and analyzed by smartphone. Their result was exciting, and the limit of detection for pathogenic bacteria was 6 copies/mL in the green channel, with the whole process carried out under a constant temperature. Powerful smartphones have brought benefits to productivity, and the lives of people in all aspects, and provide a new idea for the development of POCT. The strong fluorescence of nanomaterials (Li et al., 2018; Mei et al., 2021; Ye et al., 2021) means they can be accurately captured by smartphones, which might create a trend in POCT development in the future.

However, in order to obtain accurate test results, an adequate fluorescence signal and sensitive detection are indispensable. It is also worth noting the smartphone is not professional camera equipment, and can experience data loss or sensitivity decrease, and should thus be treated with caution when used as a detector.

Discussion and conclusion

Nanomaterials have attracted increased attention due to their unique physical and chemical properties, generating considerable

interest in many fields, including biotechnology, catalysis, electronics, optics, and drug-loading (Liu et al., 2020; Gong L et al., 2021; Zhang M et al., 2021; Choi et al., 2022; Gao et al., 2022; Pang et al., 2022). In this review, we focused on the area of NA detection in POCT devices. There is no doubt that the high efficiency and accuracy of NA detection can greatly improve the performance of POCT devices. It is thus important to obtain high quality NA and highly sensitive identification processes. Nanomaterials play a crucial role in NA detection, with detection results showing high performance in terms of sensitivity and selectivity. A lot of the literature reveals that modified nanomaterials not only improve detection capability (about 10–1000 fold compared to routine PCR), but also address the complexity of the sample (Chen et al., 2020; Fang et al., 2021; Liu et al., 2021; Zhang C et al., 2022), such as in the detection of *Salmonella* Typhimurium in complex food environments using a novel fluorescent platform of DNA-stabilized silver nanoclusters. The authors assessed the effectiveness of the main method in terms of sensitivity, specificity, and detection rate in complex samples and their results showed that the detection rate had a linear concentration range of *Salmonella* Typhimurium from 4.6×10^2 to 4.6×10^7 CFU/ml, with the limit of detection reaching 6.6×10^2 CFU/ml in food samples (Yang et al., 2021). When novel nanomaterials are applied in NA detection, the detection limit for biomolecules is one of the key parameters in evaluating the feasibility of the assay. Hence researchers want to improve the sensitivity of detection by combining the specificity and versatility of NA with the intrinsic properties of nanomaterials. In summary, the design of nanomaterials has become a primary research goal in the biomedical field. With advancements in the artificial intelligence age, new smart technologies have an indispensable place in POCT devices. Sow et al. (2020) summarized the advantages of using smart materials in different work stages of POCT devices, but the challenge presented by high signal-to-noise ratio and accurate detection of analytes in the POCT platform still exists. In general, the main means of promoting the POCT industry in the future will be to use the characteristics of the nanomaterials combined with suitable detection methods.

At the same time, the limitations of the use of nanomaterials also attracts the attention of researchers. Toxicity, stability, and biocompatibility are major problems hindering *in vivo* application, and when it comes to *in vitro* testing, stability is the primary consideration (Ahmed et al., 2021; Jobdeedamrong et al., 2021; Li Y et al., 2021; Zhang Q et al., 2021). No matter how well designed, the deviation in repeated experiment results is too large, which leads to the greatly reduced reliability of such experimental results. Agglomeration of nanoparticles is another main factor that may affect their stability (Magesa et al., 2020; Sun et al., 2021; Diephuis et al., 2022). These properties are nevertheless beneficial in many fields, such as vascular tissue engineering (Rahimnejad et al., 2021). In terms of NA detection, aggregation will affect the efficiency of extraction and detection, and cause the failure of the POCT device. Moreover, the environmental pollution caused by the degradation-resistant nanomaterials should not be ignored, for as the food chain circulates, it accumulates, and eventually enters the body and harms human health. Therefore, easily degradable, non-toxic, and highly stable nanomaterials are the focus for researchers, and the key factors driving the sustainable development of the field.

Application of nanomaterials in POCT devices has become a hot topic for research in recent years, owing in part to the impact of COVID-19, which further stimulated POCT device development. POCT devices represent the future trend in the field of molecular diagnosis, given there is no need for a fixed testing site, as reagents and instruments are portable and can be operated in a timely manner. A problem was posed: i.e., the need to ensure that requirements for speed, quality, and cost all are met in COVID-19 detection (Ding et al., 2020). Beach et al. (2021) thought that POCT could become a key diagnostic tool for health-care providers carrying out COVID-19 rapid-testing, and they identified what needed attention when using POCT devices for detection, such as an established quality assurance framework and the evaluation of clinical performance. While POCT devices have many advantages as a detection tool, they are still a long way from reaching the diagnostic market and being widely used. Therefore, according to the WHO-defined ASSURED criteria, integrating appropriate detection methods to be applied in different fields will shape the direction of our efforts.

Operable paper-based POCT devices have advantages, such as self-driven flow, high surface to volume ratio, and superb biocompatibility. Researchers have thus intensively studied these, and some have produced products that have become commercialized (Liu et al., 2021). For example, Jia et al. (2021) commented on applications of a paper-based POCT device, putting forward reagent storage and sample preparation as the key research directions for the device, in the hope it would have high accuracy while basically meeting WHO's ASSURED criteria through the endeavors of academia and industry.

Overall, we mainly introduced herein the application of POCT devices to NA testing. The detection aspect is crucial in POCT devices, owing to the development of detection technology closely related to obtaining high quality data. Of course, the other two aspects, loading sampling and data display, cannot be ignored either. Nanomaterials have been widely used in POCT devices, so we have summarized their advantages and use in various parts of these devices, so that researchers might learn about the latest developments in relation to NA detection. However, POCT devices still have their challenges, including low accuracy of detection, the requirement for specialized reagents, and lack of a uniform evaluation system. Of note, in NA detection, fully enclosed detection can reduce the hazards of nucleic acid aerosols, and hence increase the credibility of the

result. Some POCT devices associated with NA detection are only a simple combination of a nucleic acid extraction instrument and detector. Strictly speaking, they do not belong to the category of POCT devices. Therefore, developing uniform industry standards is a priority. Second, improving the accuracy and sensitivity of POCT devices will be the future developmental trend, while the use of nanomaterials will be the intrinsic driving force promoting the development of POCT devices. The review we have presented here will be helpful to researchers in promoting POCT products, and will also provide new ideas for creating better healthcare systems for current and future types of disease detection.

Author contributions

The author contributions as follows: ZH: writing, original draft preparation, and methodology; CL, ZL, and ZC: investigation; XC and XC: visualization and figure processing; YG: supervision and funding acquisition. All authors reviewed the final manuscript.

Funding

This work was supported by Hunan Health Committee Scientific Research Project of China (Grant No. 202103010009).

Conflict of interest

The authors declare that the research was conducted in the absence of any commercial or financial relationships that could be construed as a potential conflict of interest.

Publisher's note

All claims expressed in this article are solely those of the authors and do not necessarily represent those of their affiliated organizations, or those of the publisher, the editors, and the reviewers. Any product that may be evaluated in this article, or claim that may be made by its manufacturer, is not guaranteed or endorsed by the publisher.

References

Ahmed, J., Gultekinoglu, M., Bayram, C., Kart, D., Ulubayram, K., and Edirisinghe, M. (2021). Alleviating the toxicity concerns of antibacterial cinnamon-polycaprolactone biomaterials for healthcare-related biomedical applications. *MedComm* 2, 236–246. doi:10.1002/mco2.71

Alafeef, M., Moitra, P., Dighe, K., and Pan, D. (2021). Rna-extraction-free nano-amplified colorimetric test for point-of-care clinical diagnosis of Covid-19. *Nat. Protoc.* 16, 3141–3162. doi:10.1038/s41596-021-00546-w

Beach, L. A., Fung, A. W. S., Knauer, M. J., Shaw, J. L. V., and Taher, J. (2021). Rapid Covid-19 testing: Speed, quality and cost. Can you have all three? *Clin. Biochem.* 95, 13–14. doi:10.1016/j.clinbiochem.2021.05.009

Bharadwaj, M., Bengtson, M., Golverdingen, M., Waling, L., and Dekker, C. (2021). Diagnosing point-of-care diagnostics for neglected tropical diseases. *PLoS Negl. Trop. Dis.* 15, e0009405. doi:10.1371/journal.pntd.0009405

Buckle, P., Micocci, M., Tulloch, J., Kierkegaard, P., Parvulescu, P., Thompson, C., et al. (2021). Covid-19 point-of-care testing in care homes: What are the lessons for policy and practice? *Age Ageing* 50, 1442–1444. doi:10.1093/ageing/afab101

Burklund, A., Petryk, J. D., Hoopes, P. J., and Zhang, J. X. J. (2020). Microfluidic enrichment of bacteria coupled to contact-free lysis on a magnetic polymer surface for downstream molecular detection. *Biomicrofluidics* 14, 034115. doi:10.1063/5.0011908

Chen, D., Kovach, A., Shen, X., Poust, S., and Armani, A. M. (2017). On-chip ultra-high-q silicon oxynitride optical resonators. *ACS Photonics* 4, 2376–2381. doi:10.1021/acsphotonics.7b00752

Chen, M., Nguyen, T. T., Varongchayakul, N., Grazon, C., Chern, M., Baer, R. C., et al. (2020). Surface immobilized nucleic acid-transcription factor quantum dots for biosensing. *Adv. Healthc. Mat.* 9, e2000403. doi:10.1002/adhm.202000403

Chen, Z., Zhao, K., He, Z., Luo, X., Qin, Z., Tan, Y., et al. (2022). Development and evaluation of a thermostatic nucleic acid testing device based on magnesium pyrophosphate precipitation for detecting enterocytozoon hepatopenaei. *Chin. Chem. Lett.* 33, 4053–4056. doi:10.1016/j.cclet.2022.01.072

Cho, I. H., Lee, J., Kim, J., Kang, M. S., Paik, J. K., Ku, S., et al. (2018). Current technologies of electrochemical immunosensors: Perspective on signal amplification. *Sensors (Basel).* 18, 207. doi:10.3390/s18010207

Choi, S. H., Lee, J. S., Choi, W. J., Seo, J. W., and Choi, S. J. (2022). Nanomaterials for iot sensing platforms and point-of-care applications in South Korea. *Sensors (Basel)* 22, 610. doi:10.3390/s22020610

da Silva, R. J., Pedro, G. C., Gorza, F. D. S., Maciel, B. G., Ratkovski, G. P., Mojica-Sanchez, L. C., et al. (2021). DNA purification using a novel gamma-fe2o3/pedot hybrid nanocomposite. *Anal. Chim. Acta X.* 1178, 338762. doi:10.1016/j.aca.2021.338762

Diephuis, W. R., Molloy, A. L., Boltz, L. L., Porter, T. B., Aragon Orozco, A., Duron, R., et al. (2022). The effect of agglomeration on arsenic adsorption using iron oxide nanoparticles. *Nanomater. (Basel)* 12, 1598. doi:10.3390/nano12091598

Ding, H., Yin, S., Cheng, Y., Cai, Y., Huang, W., and Deng, W. (2020). Neurologic manifestations of nonhospitalized patients with Covid-19 in wuhan, China. *MedComm* 1, 253–256. doi:10.1002/mco2.13

Dong, H., Tang, C., He, Z., Liu, H., Xu, Y., Huang, H., et al. (2020). Rapid identification of diarrheagenic escherichia coli based on barcoded magnetic bead hybridization. *Chin. Chem. Lett.* 31, 1812–1816. doi:10.1016/j.cclet.2020.03.002

Dronina, J., Bubniene, U. S., and Ramanavicius, A. (2021). The application of DNA polymerases and cas9 as representative of DNA-modifying enzymes group in DNA sensor design (review). *Biosens. Bioelectron. X.* 175, 112867. doi:10.1016/j.bios.2020.112867

Fang, Y., Liu, H., Wang, Y., Su, X., Jin, L., Wu, Y., et al. (2021). Fast and accurate control strategy for portable nucleic acid detection (pnad) system based on magnetic nanoparticles. *J. Biomed. Nanotechnol.* 17, 407–415. doi:10.1166/jbn.2021.3028

Ferreira, C. E. S., Guerra, J. C. C., Slhessarenko, N., Scartezini, M., Franca, C. N., Colombini, M. P., et al. (2018). Point-of-care testing: General aspects. *Clin. Lab.* 64, 1–9. doi:10.7754/Clin.Lab.2017.170730

Gao, Y., Chen, X., Tian, T., Zhang, T., Gao, S., Zhang, X., et al. (2022). A lysosome-activated tetrahedral nanobox for encapsulated sirna delivery. *Adv. Mat.*, e2201731. doi:10.1002/adma.202201731

Gong, L., Zhao, L., Tan, M., Pan, T., He, H., Wang, Y., et al. (2021). Two-photon fluorescent nanomaterials and their applications in biomedicine. *J. Biomed. Nanotechnol.* 17, 509–528. doi:10.1166/jbn.2021.3052

Gong, N., Sheppard, N. C., Billingsley, M. M., June, C. H., and Mitchell, M. J. (2021). Nanomaterials for t-cell cancer immunotherapy. *Nat. Nanotechnol.* 16, 25–36. doi:10.1038/s41565-020-00822-y

Guo, L., Wang, T., Chen, Z., He, N., Chen, Y., and Yuan, T. (2018). Light scattering based analyses of the effects of bovine serum proteins on interactions of magnetite spherical particles with cells. *Chin. Chem. Lett.* 29, 1291–1295. doi:10.1016/j.cclet.2017.11.017

Guo, W., Zhang, C., Ma, T., Liu, X., Chen, Z., Li, S., et al. (2021). Advances in aptamer screening and aptasensors' detection of heavy metal ions. *J. Nanobiotechnology* 19, 166. doi:10.1186/s12951-021-00914-4

Hasanzadeh, A., Alamdaran, M., Ahmadi, S., Nourizadeh, H., Bagherzadeh, M. A., Mofazzal Jahromi, M. A., et al. (2021). Nanotechnology against Covid-19: Immunization, diagnostic and therapeutic studies. *J. Control. Release* 336, 354–374. doi:10.1016/j.jconrel.2021.06.036

He, L., Huang, R., Xiao, P., Liu, Y., Jin, L., Liu, H., et al. (2021). Current signal amplification strategies in aptamer-based electrochemical biosensor: A review. *Chin. Chem. Lett.* 32, 1593–1602. doi:10.1016/j.cclet.2020.12.054

He, L., Yang, H., Xiao, P., Singh, R., He, N., Liu, B., et al. (2017). Highly selective, sensitive and rapid detection of Escherichia Coli O157:H7 using duplex pcr and magnetic nanoparticle-based chemiluminescence assay. *J. Biomed. Nanotechnol.* 13, 1243–1252. doi:10.1166/jbn.2017.2422

He, Z., Tang, C., Chen, X., Liu, H., Yang, G., Xiao, Z., et al. (2019). Based on magnetic beads to develop the kit for extraction of high-quality cell-free DNA from blood of breast cancer patients. *Mat. express* 9, 956–961. doi:10.1166/mex.2019.1579

Henry, S. J. W., and Stephanopoulos, N. (2021). *Functionalizing DNA nanostructures for therapeutic applications*, 13. Wiley Interdiscip Rev Nanomed Nanobiotechnol, e1729. doi:10.1002/wnan.1729

Jani, I. V., and Peter, T. F. (2022). Nucleic acid point-of-care testing to improve diagnostic preparedness. *Clin. Infect. Dis.* 75, 723–728. doi:10.1093/cid/ciac013

Jiang, H., Zeng, X., Xi, Z., Liu, M., Li, C., Li, Z., et al. (2013). Improvement on controllable fabrication of streptavidin-modified three-layer core-shell fe_3o_4@sio_2@au magnetic nanocomposites with low fluorescence background. *J. Biomed. Nanotechnol.* 9, 674–684. doi:10.1166/jbn.2013.1575

Jiang, P., Wang, Y., Zhao, L., Ji, C., Chen, D., and Nie, L. (2018). Applications of gold nanoparticles in non-optical biosensors. *Nanomater. (Basel)* 8, 977. doi:10.3390/nano8120977

Jobdeedamrong, A., Theerasilp, M., Nasongkla, N., and Crespy, D. (2021). Nanocapsules with excellent biocompatibility and stability in protein solutions. *Biomater. Sci.* 9, 5781–5784. doi:10.1039/d1bm00510c

Kang, J., Li, Y., Zhao, Y., Wang, Y., Ma, C., and Shi, C. (2021). Nucleic acid extraction without electrical equipment *via* magnetic nanoparticles in pasteur pipettes for pathogen detection. *Anal. Biochem.* 635, 114445. doi:10.1016/j.ab.2021.114445

Khan, M. I., Nur, S. M., Adhami, V., and Mukhtar, H. (2021). Epigenetic regulation of rna sensors: Sentinels of immune response. *Semin. Cancer Biol.* 83, 413–421. doi:10.1016/j.semcancer.2020.12.028

Kim, H., Huh, H. J., Park, E., Chung, D. R., and Kang, M. (2021). Multiplex molecular point-of-care test for syndromic infectious diseases. *BioChip J.* 15, 14–22. doi:10.1007/s13206-021-00004-5

Kim, S. Y, S. Y., Lee, J. C., Seo, G., Woo, J. H., Lee, M., Nam, J., et al. (2021). Computational method-based optimization of carbon nanotube thin-film immunosensor for rapid detection of sars-cov-2 virus. *Small Sci.* 2, 2100111. doi:10.1002/smsc.202100111

Krasowska, A., and Sigler, K. (2014). How microorganisms use hydrophobicity and what does this mean for human needs? *Front. Cell. Infect. Microbiol.* 4, 112. doi:10.3389/fcimb.2014.00112

Lai, Y., Deng, Y., Yang, G., Li, S., Zhang, C., and Liu, X. (2018). Molecular imprinting polymers electrochemical sensor based on aunps/pth modified gce for highly sensitive detection of carcinomaembryonic antigen. *J. Biomed. Nanotechnol.* 14, 1688–1694. doi:10.1166/jbn.2018.2617

Land, K. J., Boeras, D. I., Chen, X. S., Ramsay, A. R., and Peeling, R. W. (2019). Reassured diagnostics to inform disease control strategies, strengthen health systems and improve patient outcomes. *Nat. Microbiol.* 4, 46–54. doi:10.1038/s41564-018-0295-3

Lee, E. Y., Kim, Y., Koo, B., Noh, G. S., Lee, H., and Shin, Y. (2020). A novel nucleic acid amplification system based on nano-gap embedded active disk resonators. *Sensors Actuators B Chem.* 320, 128351. doi:10.1016/j.snb.2020.128351

Lee, S. Y., Chen, F., and Lee, T. Y. (2021). Tryptamine-functionalized magnetic nanoparticles for highly sensitive detection of salmonella typhimurium. *Analyst* 146, 2559–2566. doi:10.1039/d0an02458a

Li, C., Xue, C., Wang, J., Luo, M., Shen, Z., and Wu, Z. S. (2019). Oriented tetrahedron-mediated protection of catalytic DNA molecular-scale detector against *in vivo* degradation for intracellular mirna detection. *Anal. Chem.* 91, 11529–11536. doi:10.1021/acs.analchem.9b00860

Li, Q., Xia, Y., Wan, X., Yang, S., Cai, Z., Ye, Y., et al. (2020). Morphology-dependent mno2/nitrogen-doped graphene nanocomposites for simultaneous detection of trace dopamine and uric acid. *Mater. Sci. Eng. C* 109, 110615. doi:10.1016/j.msec.2019.110615

Li, T., Xu, X., Zhang, G., Lin, R., Chen, Y., Li, C., et al. (2016). Nonamplification sandwich assay platform for sensitive nucleic acid detection based on aunps enumeration with the dark-field microscope. *Anal. Chem.* 88, 4188–4191. doi:10.1021/acs.analchem.6b00535

Li, T., Yi, H., Liu, Y., Wang, Z., Liu, S., He, N., et al. (2018). One-step synthesis of DNA templated water-soluble au-ag bimetallic nanoclusters for ratiometric fluorescence detection of DNA. *J. Biomed. Nanotechnol.* 14, 150–160. doi:10.1166/jbn.2018.2491

Li, Z., and Guo, Z. (2019). Bioinspired surfaces with wettability for antifouling application. *Nanoscale* 11, 22636–22663. doi:10.1039/c9nr05870b

Li, G., Qi, X., Wu, J., Xu, L., Wan, X., Liu, Y., et al. (2022a). Ultrasensitive, label-free voltammetric determination of norfloxacin based on molecularly imprinted polymers and au nanoparticle-functionalized black phosphorus nanosheet nanocomposite. *J. Hazard. Mat.* 436, 129107. doi:10.1016/j.jhazmat.2022.129107

Li, G., Qi, X., Zhang, G., Wang, S., Li, K., Wu, J., et al. (2022b). Low-cost voltammetric sensors for robust determination of toxic cd(ii) and pb(ii) in environment and food based on shuttle-like α-fe2o3 nanoparticles decorated β-bi2o3 microspheres. *Microchem. J.* 179, 107515. doi:10.1016/j.microc.2022.107515

Li, J., Lai, Y., Li, M., Chen, X., Zhou, M., Wang, W., et al. (2022a). Repair of infected bone defect with clindamycin-tetrahedral DNA nanostructure complex-loaded 3d bioprinted hybrid scaffold. *Chem. Eng. J.* 435, 134855. doi:10.1016/j.cej.2022.134855

Li, J., Wu, X., Li, Y., Wang, X., Huang, H., Jian, D., et al. (2021). Amplification-free smartphone-based attomolar hbv detection. *Biosens. Bioelectron. X.* 194, 113622. doi:10.1016/j.bios.2021.113622

Li, J., Yao, Y., Wang, Y., Xu, J., Zhao, D., Liu, M., et al. (2022b). Modulation of the crosstalk between schwann cells and macrophages for nerve regeneration: A therapeutic strategy based on a multifunctional tetrahedral framework nucleic acids system. *Adv. Mat.*, 2202513. doi:10.1002/adma.202202513

Li, Q., Wu, J. T., Liu, Y., Qi, X. M., Jin, H. G., Yang, C., et al. (2021). Recent advances in black phosphorus-based electrochemical sensors: A review. *Anal. Chim. Acta X.* 1170, 338480. doi:10.1016/j.aca.2021.338480

Li, S., Liu, Y., Tian, T., Zhang, T., Lin, S., Zhou, M., et al. (2021). Bioswitchable delivery of microrna by framework nucleic acids: Application to bone regeneration. *Small* 17, e2104359. doi:10.1002/smll.202104359

Li, Y., Yang, H. P., Chen, S., Wu, X. J., and Long, Y. F. (2021). Simple preparation of carbon dots and application in cephalosporin detection. *J. Nanosci. Nanotechnol.* 21, 6024–6034. doi:10.1166/jnn.2021.19520

Liu, J., Chen, J., Wu, D., Huang, M., Chen, J., Pan, R., et al. (2021). Crispr-/cas12a-mediated liposome-amplified strategy for the surface-enhanced Raman scattering and naked-eye detection of nucleic acid and application to food authenticity screening. *Anal. Chem.* 93, 10167–10174. doi:10.1021/acs.analchem.1c01163

Liu, M., Yu, X., Chen, Z., Yang, T., Yang, D., Liu, Q., et al. (2017). Aptamer selection and applications for breast cancer diagnostics and therapy. *J. Nanobiotechnology* 15, 81. doi:10.1186/s12951-017-0311-4

Liu, Y., Deng, Y., Li, T., Chen, Z., Chen, H., Li, S., et al. (2018). Aptamer-based electrochemical biosensor for mercury ions detection using aunps-modified glass carbon electrode. *J. Biomed. Nanotechnol.* 14, 2156–2161. doi:10.1166/jbn.2018.2655

Liu, Y., Sun, Y., Li, S., Liu, M., Qin, X., Chen, X., et al. (2020). Tetrahedral framework nucleic acids deliver antimicrobial peptides with improved effects and less susceptibility to bacterial degradation. *Nano Lett.* 20, 3602–3610. doi:10.1021/acs.nanolett.0c00529

Liu, S., He, X., Zhang, T., Zhao, K., Xiao, C., Tong, Z., et al. (2022). Highly sensitive smartphone-based detection of listeria monocytogenes using syto9. *Chin. Chem. Lett.* 33, 1933–1935. doi:10.1016/j.cclet.2021.11.051

Liu, Y., Li, T., Yang, G., Deng, Y., Mou, X., and He, N. (2022). A simple aunps-based colorimetric aptasensor for chlorpyrifos detection. *Chin. Chem. Lett.* 33, 1913–1916. doi:10.1016/j.cclet.2021.11.025

Ma, T., Huang, H., Guo, W., Zhang, C., Chen, Z., Li, S., et al. (2020). Recent progress in black phosphorus sensors. *J. Biomed. Nanotechnol.* 16, 1045–1064. doi:10.1166/jbn.2020.2963

Magesa, F., Wu, Y., Dong, S., Tian, Y., Li, G., Vianney, J. M., et al. (2020). Electrochemical sensing fabricated with TA_2O_5 nanoparticle-electrochemically reduced graphene oxide nanocomposite for the detection of oxytetracycline. *Biomolecules* 10, 110. doi:10.3390/biom10010110

Mei, X., Wang, D., Zhang, L., Li, J., and Dong, C. (2021). Synthesis of carbon dots for al(3+) sensing in water by fluorescence assay. *Luminescence* 36, 1469–1475. doi:10.1002/bio.4088

Mo, X., Wang, X., Zhu, Z., Yu, Y., Chang, D., Zhang, X., et al. (2021). Quality management for point-of-care testing of pathogen nucleic acids: Chinese expert consensus. *Front. Cell. Infect. Microbiol.* 11, 755508. doi:10.3389/fcimb.2021.755508

Mondal, S., Feirer, N., Brockman, M., Preston, M. A., Teter, S. J., Ma, D., et al. (2021). A direct capture method for purification and detection of viral nucleic acid

enables epidemiological surveillance of sars-cov-2. *Sci. Total Environ.* 795, 148834. doi:10.1016/j.scitotenv.2021.148834

Mou, X. S., Chen, Z., Liu, M., Liu, Y., Deng, Yan, et al. (2019). *In-situ* mutation detection by magnetic beads-probe based on single base extension and its application in genotyping of Hepatitis B virus pre-c region 1896nt locus single nucleotide polymorphisms. *J. Biomed. Nanotechnol.* 15, 2393–2400. doi:10.1166/jbn.2019.2862

Nie, L., Liu, F., Ma, P., and Xiao, X. (2014). Applications of gold nanoparticles in optical biosensors. *J. Biomed. Nanotechnol.* 10, 2700–2721. doi:10.1166/jbn.2014.1987

Ota, R., Takagi, N., Imaizumi, Y., Waku, T., and Kobori, A. (2021). Sandwich-type detection of nucleic acids by bioorthogonal sers probes. *Nucleosides Nucleotides Nucleic Acids* 40, 166–177. doi:10.1080/15257770.2020.1849718

Pang, R., Zhu, Q., Wei, J., Meng, X., and Wang, Z. (2022). Enhancement of the detection performance of paper-based analytical devices by nanomaterials. *Molecules* 27, 508. doi:10.3390/molecules27020508

Park, M. K., Kee, J. S., Quah, J. Y., Netto, V., Song, J., Fang, Q., et al. (2013). Label-free aptamer sensor based on silicon microring resonators. *Sensors Actuators B Chem.* 176, 552–559. doi:10.1016/j.snb.2012.08.078

Pearlman, S. I., Leelawong, M., Richardson, K. A., Adams, N. M., Russ, P. K., Pask, M. E., et al. (2020). Low-resource nucleic acid extraction method enabled by high-gradient magnetic separation. *ACS Appl. Mat. Interfaces* 12, 12457–12467. doi:10.1021/acsami.9b21564

Poncelet, L., Malic, L., Clime, L., Geissler, M., Morton, K. J., Nassif, C., et al. (2021). Multifunctional magnetic nanoparticle cloud assemblies for *in situ* capture of bacteria and isolation of microbial DNA. *Analyst* 146, 7491–7502. doi:10.1039/d1an01297e

Prattis, I., Hui, E., Gubeljak, P., Kaminski Schierle, G. S., Lombardo, A., and Occhipinti, L. G. (2021). Graphene for biosensing applications in point-of-care testing. *Trends Biotechnol.* 39, 1065–1077. doi:10.1016/j.tibtech.2021.01.005

Pujari, A. (2021). Smartphone ophthalmoscopy: Is there a place for it? *Clin. Ophthalmol.* 15, 4333–4337. doi:10.2147/OPTH.S243103

Pujari, A., Saluja, G., Agarwal, D., Sinha, A., Kumar, A., and Sharma, N. (2021). Clinical role of smartphone fundus imaging in diabetic retinopathy and other neuro-retinal diseases. *Curr. Eye Res.* 46, 1605–1613. doi:10.1080/02713683.2021.1958347

Qin, X., Xiao, L., Li, N., Hou, C., Li, W., Li, J., et al. (2022). Tetrahedral framework nucleic acids-based delivery of microrna-155 inhibits choroidal neovascularization by regulating the polarization of macrophages. *Bioact. Mat.* 14, 134–144. doi:10.1016/j.bioactmat.2021.11.031

Rahimnejad, M., Nasrollahi Boroujeni, N., Jahangiri, S., Rabiee, N., Rabiee, M., Makvandi, P., et al. (2021). Prevascularized micro-/nano-sized spheroid/bead aggregates for vascular tissue engineering. *Nanomicro. Lett.* 13, 182. doi:10.1007/s40820-021-00697-1

Sarfraz, N., and Khan, I. (2021). Plasmonic gold nanoparticles (aunps): Properties, synthesis and their advanced energy, environmental and biomedical applications. *Chem. Asian J.* 16, 720–742. doi:10.1002/asia.202001202

Suan Ng, S., Ling Lee, H., Bothi Raja, P., and Doong, R. A. (2022). Recent advances in nanomaterial-based optical biosensors as potential point-of-care testing (poct) probes in carcinoembryonic antigen detection. *Chem. Asian J.* 17, e202200287. doi:10.1002/asia.202200287

Sun, H., Jiao, R., An, G., Xu, H., and Wang, D. (2021). Influence of particle size on the aggregation behavior of nanoparticles: Role of structural hydration layer. *J. Environ. Sci.* 103, 33–42. doi:10.1016/j.jes.2020.10.007

Sun, X. (2022). Glucose detection through surface-enhanced Raman spectroscopy: A review. *Anal. Chim. Acta X.* 1206, 339226. doi:10.1016/j.aca.2021.339226

Tang, C., He, Z., Liu, H., Xu, Y., Huang, H., Yang, G., et al. (2020). Application of magnetic nanoparticles in nucleic acid detection. *J. Nanobiotechnology* 18, 62. doi:10.1186/s12951-020-00613-6

Tang, Y., Ali, Z., Dai, J., Liu, X., Wu, Y., Chen, Z., et al. (2018). Single-nucleotide polymorphism genotyping of exos in pseudomonas aeruginosa using dual-color fluorescence hybridization and magnetic separation. *J. Biomed. Nanotechnol.* 14, 206–214. doi:10.1166/jbn.2018.2525

Tang, Y., Li, Z., He, N., Zhang, L., Ma, C., Li, X., et al. (2013). Preparation of functional magnetic nanoparticles mediated with peg-4000 and application in pseudomonas aeruginosa rapid detection. *J. Biomed. Nanotechnol.* 9, 312–317. doi:10.1166/jbn.2013.1493

Tian, B., Gao, F., Fock, J., Dufva, M., and Hansen, M. F. (2020). Homogeneous circle-to-circle amplification for real-time optomagnetic detection of sars-cov-2 rdrp coding sequence. *Biosens. Bioelectron. X.* 165, 112356. doi:10.1016/j.bios.2020.112356

Wang, S., Shanthan, G., Bouzga, M. M., Thi Dinh, H. M., Haas, C., and Fonnelop, A. E. (2021). Evaluating the performance of five up-to-date DNA/rna co-extraction methods for forensic application. *Forensic Sci. Int.* 328, 110996. doi:10.1016/j.forsciint.2021.110996

Wang, Z., Yu, W., Xie, R., Yang, S., and Chen, A. (2021). A strip of lateral flow gene assay using gold nanoparticles for point-of-care diagnosis of african swine fever virus in limited environment. *Anal. Bioanal. Chem.* 413, 4665–4672. doi:10.1007/s00216-021-03408-2

White, T. J., Rye, M. S., and Tay, J. W. (2022). Developmental validation of an efficient differential separation method incorporating the i-sep ® DL spin column with high sperm DNA recovery for the processing of sexual assault samples. *J. Forensic Sci.* 67, 1679–1689. doi:10.1111/1556-4029.15043

Wiraja, C., Yeo, D. C., Lio, D. C. S., Zheng, M., and Xu, C. (2019). Functional imaging with nucleic-acid-based sensors: Technology, application and future healthcare prospects. *Chembiochem* 20, 437–450. doi:10.1002/cbic.201800430

Wu, Y., Deng, P., Tian, Y., Ding, Z., Li, G., Liu, J., et al. (2020a). Rapid recognition and determination of tryptophan by carbon nanotubes and molecularly imprinted polymer-modified glassy carbon electrode. *Bioelectrochemistry* 131, 107393. doi:10.1016/j.bioelechem.2019.107393

Wu, Y., Deng, P., Tian, Y., Feng, J., Xiao, J., Li, J., et al. (2020b). Simultaneous and sensitive determination of ascorbic acid, dopamine and uric acid *via* an electrochemical sensor based on pvp-graphene composite. *J. Nanobiotechnology* 18, 112. doi:10.1186/s12951-020-00672-9

Xiao, C., Guo, Y., Zhao, K., Liu, S., He, N., He, Y., et al. (2022). Prognostic value of machine learning in patients with acute myocardial infarction. *J. Cardiovasc. Dev. Dis.* 9, 56. doi:10.3390/jcdd9020056

Xiao, M. F, M. F., Zeng, C., Li, S. H., and Yuan, F. L. (2022). Applications of nanomaterials in Covid-19 pandemic. *Rare Met.* 41, 1–13. doi:10.1007/s12598-021-01789-y

Xie, H., Di, K., Huang, R., Khan, A., Xia, Y., Xu, H., et al. (2020). Extracellular vesicles based electrochemical biosensors for detection of cancer cells: A review. *Chin. Chem. Lett.* 31, 1737–1745. doi:10.1016/j.cclet.2020.02.049

Xu, Y., Wang, T., Chen, Z., Jin, L., Wu, Z., Yan, J., et al. (2021). The point-of-care-testing of nucleic acids by chip, cartridge and paper sensors. *Chin. Chem. Lett.* 32, 3675–3686. doi:10.1016/j.cclet.2021.06.025

Yan, T., Zhang, G., Chai, H., Qu, L., and Zhang, X. (2021). Flexible biosensors based on colorimetry, fluorescence, and electrochemistry for point-of-care testing. *Front. Bioeng. Biotechnol.* 9, 753692. doi:10.3389/fbioe.2021.753692

Yang, G., Lai, Y., Xiao, Z., Tang, C., and Deng, Y. (2018). Ultrasensitive electrochemical immunosensor of carcinoembryonic antigen based on gold-label silver-stain signal amplification. *Chin. Chem. Lett.* 29, 1857–1860. doi:10.1016/j.cclet.2018.11.030

Yang, H., Liu, M., Jiang, H., Zeng, Y., Jin, L., Luan, T., et al. (2017). Copy number variation analysis based on gold magnetic nanoparticles and fluorescence multiplex ligation-dependent probe amplification. *J. Biomed. Nanotechnol.* 13, 655–664. doi:10.1166/jbn.2017.2386

Yang, L., Zhang, S., Liu, X., Tang, Y., Zhou, Y., and Wong, D. K. Y. (2020). Detection signal amplification strategies at nanomaterial-based photoelectrochemical biosensors. *J. Mat. Chem. B* 8, 7880–7893. doi:10.1039/d0tb01191f

Yang, X., Wang, L., Pang, L., Fu, S., Qin, X., Chen, Q., et al. (2021). A novel fluorescent platform of DNA-stabilized silver nanoclusters based on exonuclease iii amplification-assisted detection of salmonella typhimurium. *Anal. Chim. Acta X.* 1181, 338903. doi:10.1016/j.aca.2021.338903

Ye, H. L., Shang, Y., Wang, H. Y., Ma, Y. L., He, X. W., Li, W. Y., et al. (2021). Determination of fe ion and cellular bioimaging based on a novel photoluminescent silicon nanoparticles. *Talanta* 230, 122294. doi:10.1016/j.talanta.2021.122294

Yi, C., Luo, Z., Lu, Y., Belwal, T., Pan, X., and Lin, X. (2021). Nanoporous hydrogel for direct digital nucleic acid amplification in untreated complex matrices for single bacteria counting. *Biosens. Bioelectron. X.* 184, 113199. doi:10.1016/j.bios.2021.113199

Zeng, Q., Qi, X., Zhang, M., Tong, X., Jiang, N., Pan, W., et al. (2020). Efficient decontamination of heavy metals from aqueous solution using pullulan/polydopamine hydrogels. *Int. J. Biol. Macromol.* 145, 1049–1058. doi:10.1016/j.ijbiomac.2019.09.197

Zhang, T., Tian, T., Zhou, R., Li, S., Ma, W., Zhang, Y., et al. (2020). Design, fabrication and applications of tetrahedral DNA nanostructure-based multifunctional complexes in drug delivery and biomedical treatment. *Nat. Protoc.* 15, 2728–2757. doi:10.1038/s41596-020-0355-z

Zhang, C., Belwal, T., Luo, Z., Su, B., and Lin, X. (2022). Application of nanomaterials in isothermal nucleic acid amplification. *Small* 18, e2102711. doi:10.1002/smll.202102711

Zhang, M., Cui, X., and Li, N. (2022). Smartphone-based mobile biosensors for the point-of-care testing of human metabolites. *Mat. Today Bio* 14, 100254. doi:10.1016/j.mtbio.2022.100254

Zhang, M., Shao, S., Yue, H., Wang, X., Zhang, W., Chen, F., et al. (2021). High stability au nps: From design to application in nanomedicine. *Int. J. Nanomedicine* 16, 6067–6094. doi:10.2147/IJN.S322900

Zhang, N., Li, J., Liu, B., Zhang, D., Zhang, C., Guo, Y., et al. (2022). Signal enhancing strategies in aptasensors for the detection of small molecular contaminants by nanomaterials and nucleic acid amplification. *Talanta* 236, 122866. doi:10.1016/j.talanta.2021.122866

Zhang, Q., Lin, S., Wang, L., Peng, S., Tian, T., Li, S., et al. (2021). Tetrahedral framework nucleic acids act as antioxidants in acute kidney injury treatment. *Chem. Eng. J.* 413, 127426. doi:10.1016/j.cej.2020.127426

Zhang, W., He, Y., Feng, Z., and Zhang, J. (2022). Recent advances of functional nucleic acid-based sensors for point-of-care detection of sars-cov-2. *Microchim. Acta* 189, 128. doi:10.1007/s00604-022-05242-4

Zhang, Z., Ma, P., Ahmed, R., Wang, J., Akin, D., Soto, F., et al. (2022). Advanced point-of-care testing technologies for human acute respiratory virus detection. *Adv. Mat.* 34, e2103646. doi:10.1002/adma.202103646

Zhou, M., Zhang, T., Zhang, B., Zhang, X., Gao, S., Zhang, T., et al. (2021). A DNA nanostructure-based neuroprotectant against neuronal apoptosis *via* inhibiting toll-like receptor 2 signaling pathway in acute ischemic stroke. *ACS Nano* 16, 1456–1470. doi:10.1021/acsnano.1c09626

frontiers | Frontiers in Bioengineering and Biotechnology

TYPE Review
PUBLISHED 17 October 2022
DOI 10.3389/fbioe.2022.948959

OPEN ACCESS

EDITED BY
Eden Morales-Narváez,
Centro de Investigaciones en Optica, Mexico

REVIEWED BY
Cuncong Zhong,
University of Kansas, United States
Ciro Tetta,
Unicyte AG, Switzerland

*CORRESPONDENCE
Peng Li,
lipeng@yangtzeu.edu.cn
Zhiyang Li,
lizhiyangcn@qq.com

†These authors have contributed equally to this study

SPECIALTY SECTION
This article was submitted to Biosensors and Biomolecular Electronics, a section of the journal Frontiers in Bioengineering and Biotechnology

RECEIVED 20 May 2022
ACCEPTED 30 September 2022
PUBLISHED 17 October 2022

CITATION
Xu D, Di K, Fan B, Wu J, Gu X, Sun Y, Khan A, Li P and Li Z (2022), MicroRNAs in extracellular vesicles: Sorting mechanisms, diagnostic value, isolation, and detection technology. *Front. Bioeng. Biotechnol.* 10:948959. doi: 10.3389/fbioe.2022.948959

MicroRNAs in extracellular vesicles: Sorting mechanisms, diagnostic value, isolation, and detection technology

Dongjie Xu[1†], Kaili Di[2†], Boyue Fan[3], Jie Wu[3], Xinrui Gu[2], Yifan Sun[3], Adeel Khan[4], Peng Li[1*] and Zhiyang Li[2*]

[1]College of Animal Science, Yangtze University, Jingzhou, China, [2]Department of Laboratory Medicine, Affiliated Drum Tower Hospital, Medical School of Nanjing University, Nanjing, China, [3]Jiangsu Key Laboratory of Medical Science and Laboratory Medicine, School of Medicine, Jiangsu University, Zhenjiang, China, [4]State Key Laboratory of Bioelectronics, School of Biological Science and Medical Engineering, National Demonstration Center for Experimental Biomedical Engineering Education (Southeast University), Southeast University, Nanjing, China

MicroRNAs (miRNAs) are a class of short, single-stranded, noncoding RNAs, with a length of about 18–22 nucleotides. Extracellular vesicles (EVs) are derived from cells and play a vital role in the development of diseases and can be used as biomarkers for liquid biopsy, as they are the carriers of miRNA. Existing studies have found that most of the functions of miRNA are mainly realized through intercellular transmission of EVs, which can protect and sort miRNAs. Meanwhile, detection sensitivity and specificity of EV-derived miRNA are higher than those of conventional serum biomarkers. In recent years, EVs have been expected to become a new marker for liquid biopsy. This review summarizes recent progress in several aspects of EVs, including sorting mechanisms, diagnostic value, and technology for isolation of EVs and detection of EV-derived miRNAs. In addition, the study reviews challenges and future research avenues in the field of EVs, providing a basis for the application of EV-derived miRNAs as a disease marker to be used in clinical diagnosis and even for the development of point-of-care testing (POCT) platforms.

KEYWORDS

extracellular vesicles, microRNAs, liquid biopsy biomarkers, sorting mechanisms, diagnostic value, isolation and detection technology

1 Introduction

Extracellular vesicles (EVs) are membrane-enclosed entities shed by majority of cells. EVs range in size, from 50 nm to 2 μm, and are abundant in almost all human body fluids. EVs are enriched with bioactive components such as protein, nucleic acid, and lipids. The enriched EVs and their content can specifically relate to the onset and prognosis of a plethora of diseases (Joyce et al., 2016; Bebelman et al., 2018; Momen-Heravi et al., 2018). EVs can also be used as a tumor detection marker for tumor (Xie et al., 2020a).

MicroRNAs (miRNAs) are a class of short noncoding RNAs with a length of about 18–22 nucleotides that are widely produced by all eukaryotic cells (Friedman et al., 2009; Cortez et al., 2011). A large number of these miRNAs exist in body fluids, including plasma (Mitchell et al., 2008), urine (Bandini, 2021), saliva (Kamal et al., 2020), bronchoalveolar lavage fluid (Groot and Lee, 2020), amniotic fluid (Keller et al., 2011), and semen (Ruiz-Plazas et al., 2021). Circulating miRNAs are stable in body fluids and can be protected by binding to argonaute (AGO) proteins, high-density lipoprotein (HDL), and/or encapsulated in EVs (Wagner et al., 2013; Qu et al., 2016; Groot and Lee, 2020). The microRNA can control protein expression by binding to mRNA (Song et al., 2018; Gui et al., 2021; Ferri et al., 2022). The EVs from diseased sources have been proven to have unique miRNA expression profiles. In addition, specific miRNA expression characteristics not only reflect the presence of diseases at early stages but can also reflect the dynamic development of diseases at late stages, as well as diseases prognosis and drug resistance (Hu et al., 2010). With maturity of miRNA from EV research, miRNA is gradually employed for clinical diagnosis. For instance, about seven kinds of miRNA detection kits are available for diagnosing early-stage hepatocellular carcinoma (HCC) based on a plasma miRNA panel found by the Jia Fan group. Similarly, pancreatic cancer miRNA-25 detection kits have also obtained China Food and Drug Administration (CFDA) approval (Zhou et al., 2011). Herein, we mainly introduce EV-derived miRNA sorting mechanisms, diagnostic value, isolation, and detection technology (Figure 1).

2 Mechanisms for microRNA sorting in extracellular vesicles

Most prokaryotic and eukaryotic cells rain EVs. EVs can be divided into three types on the basis of their biogenesis (Figure 2). Exosomes, with a diameter of about 30–150 nm, originate in the multivesicular body (MVB) of endosomes, which subsequently migrate to the plasma membrane and fuse, causing exosomes to be released into the extracellular space. Microvesicles of about 100–1,000 nm diameter are formed from direct outward germination of the plasma membrane. Apoptotic bodies with a 50 nm–2 μm diameter are formed from cell apoptosis (Cocucci and Meldolesi, 2015; Thery et al., 2018; Gurunathan et al., 2019; Yuan and Li, 2019; Kalluri and LeBleu, 2020). They contain different types of biomolecules, including proteins, lipids, and

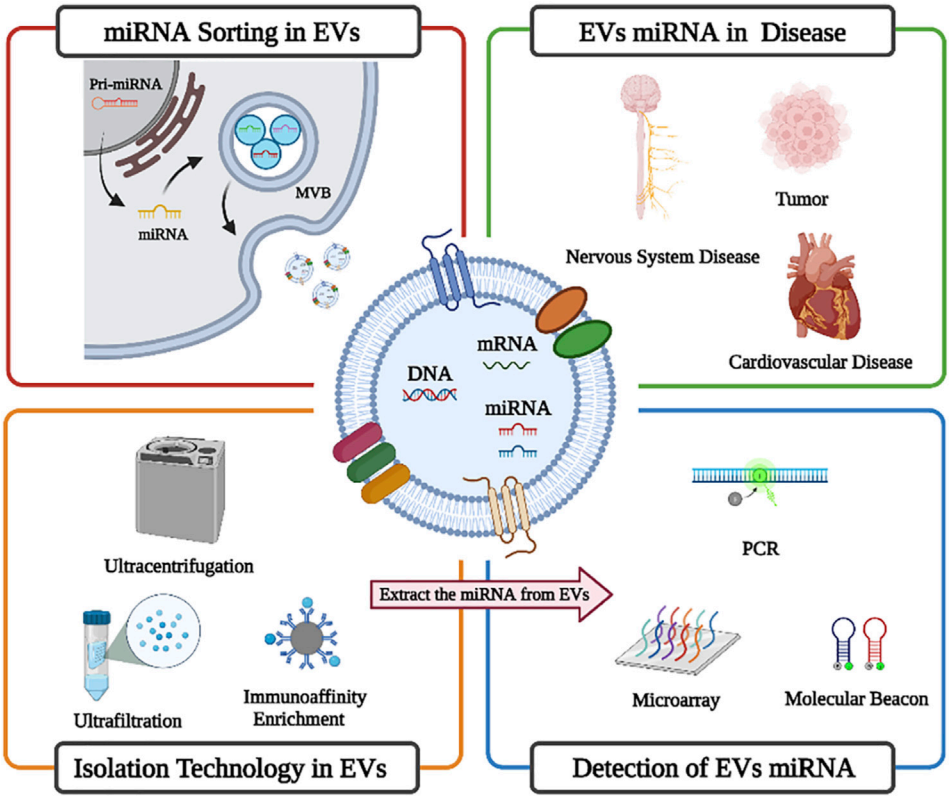

FIGURE 1
Brief overview of EV-derived miRNA sorting mechanisms, diagnostic value, isolation, and detection technology (created with BioRender.com).

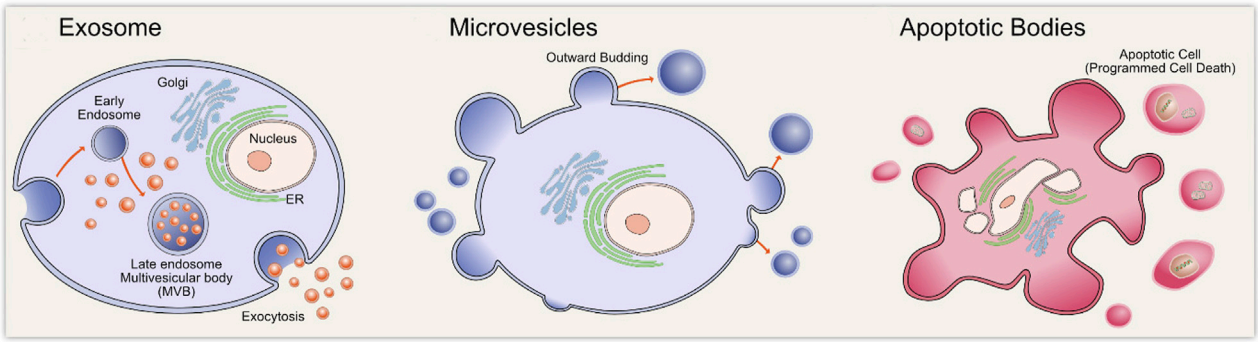

FIGURE 2
Diagrammatic overview of the three types of extracellular vesicles biogenesis including exosomes biogenesis, microvesicles biogenesis, and apoptotic bodies biogenesis. Reprinted with permission from Gurunathan et al. (2019).

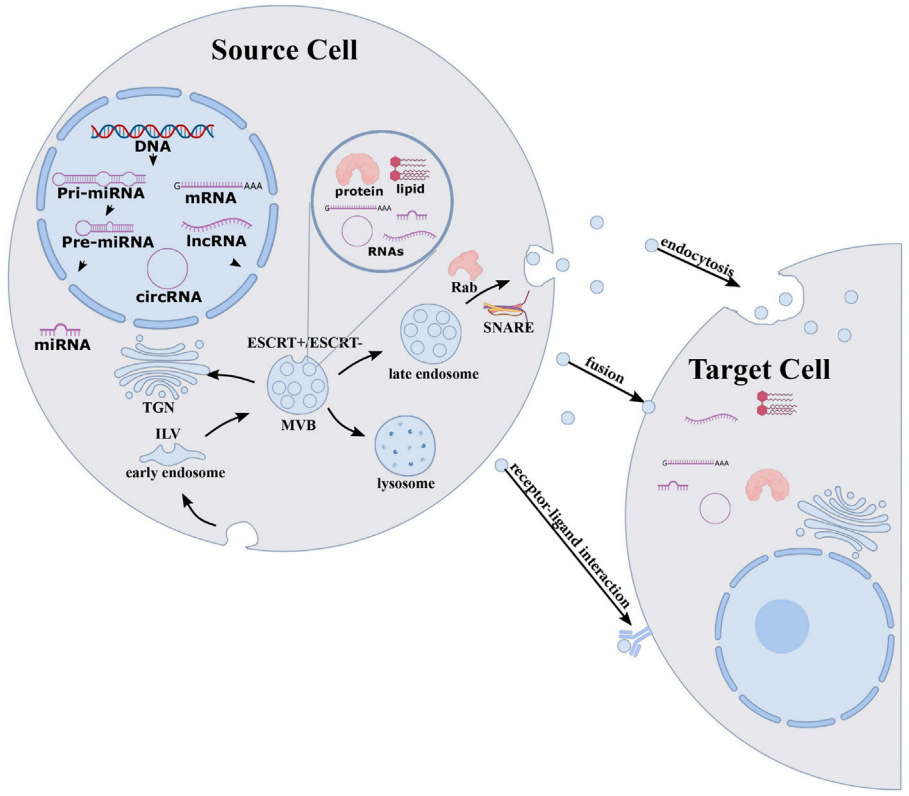

FIGURE 3
sorting mechanism for exosomal miRNAs. MiRNA originates in nucleus and enzymatically processed to form mature miRNA that are loaded into the MVBs through endosomal sorting complex required to transport ESCRT-dependent or ESCRT-independent pathways. MVBs of endosomes migrate to the plasma membrane and fuse, causing exosome and exosomal cargoes to be released into the extracellular space and delivered to target cells. Reprinted with permission from Yue et al. (2020).

nucleic acids. These substances can be protected by the EV membrane structure and thus transported to distant cells (Yanez-Mo et al., 2015; Jan et al., 2019; Mathieu et al., 2019). EVs have been shown to have multiple biological functions, including immune response, antigen presentation, and intracellular communication (Lasser et al., 2011; Tomasetti

et al., 2017; Mathieu et al., 2019). EVs are enriched with noncoding RNAs, including miRNAs, tRNA, rRNA, mitochondrial RNA, circular RNA (circRNA), and long noncoding RNA (lncRNA) (Michaela and Aigner, 2021; Yu et al., 2022). Extracellular miRNA mainly exists in the EVs (Zhang et al., 2015), and although the detailed mechanisms by which the miRNAs are packaged into the EVs are largely unknown, they are thought to be selectively classified into the EVs (Turchinovich et al., 2013; O'Brien et al., 2020; Makarova et al., 2021). Both miRNA and pre-miRNA can be secreted into exosomes and microvesicles in protein-bound and protein-free forms. Exosomal miRNAs are secreted by various pathways, including sequence-dependent or sequence-independent classification of miRNAs into MVB. Usually, the miRNA begins in the nucleus and is processed by enzymes (Figure 3) and transported to the outside of the cell through exosomes (Lee et al., 2012; Sun et al., 2018; Yue et al., 2020). Various studies have shown that there is more than one mechanism for miRNA sorting (Montecalvo et al., 2012; Kosaka et al., 2013; Tran, 2016). For example, Kosaka et al. (2013) demonstrated that neurilemphospholipase 2 (nSMase2) can regulate the secretion of exosome miRNA and promote angiogenesis and metastasis in the tumor microenvironment. Montecalvo et al. (2012) demonstrated that dendritic cells (DC cells) release exosomes with different miRNAs according to degree of maturity, and they found that exosomes release miRNAs into the cytoplasm after fusion with target DC cells. MiRNAs derived from EVs perform different functions in different target cells, such as miR-21, which is associated with senescent fibrosis of the kidneys (Liu et al., 2020) and is also highly expressed in breast cancer cells (Lee et al., 2019). Therefore, more research is still needed to reveal the generation mechanism and biological impact of EV-derived miRNAs.

3 Diagnostic value of extracellular vesicle-derived microRNA in diseases

MiRNA is correlated with the occurrence and development of many diseases (Peng et al., 2020), including tumor, neurological diseases, cardiovascular diseases, and many other diseases. The EV-derived miRNAs have many unique advantages as biomarkers (Schwarzenbach, 2017; Sanz-Rubio et al., 2018). First, the expression profile of EV-derived miRNA is similar to that of cells from which it originates (Chaput and Thery, 2011). MiRNAs are transported to recipient cells through EVs to achieve regulatory functions (Skog et al., 2008). Second, many EVs exist in various biological body fluids, which is convenient for sampling and screening diseases (Cai et al., 2015). Third, the EV lipid membranes protect miRNA from degradation and remain stable in body fluids (Yu et al., 2021). Moreover, EV-derived miRNA is considered highly sensitive and specific diagnostic tools for numerous diseases (Jin et al., 2017).

3.1 Extracellular vesicle-derived microRNA in tumor

The ability of tumor to proliferate and metastasize is related to the intercellular communication mediating in tumor microenvironment (TME) (Chiarugi and Cirri, 2016; Tian et al., 2019; Tan et al., 2020). The EVs secreted by cancer cells can mediate intercellular communication and are mediators of key signals in TME, playing an essential role in realizing intercellular material transport and information transmission in TME (Bao et al., 2018; Harmati et al., 2019; Xie et al., 2020b; Yekula et al., 2020). The EVs derived from tumor cells can participate in the proliferation and migration of tumor cells by activating a variety of signaling pathways, changing the physiological state of target cells and affecting the tumor microenvironment (Qu et al., 2020). MiRNA encapsulated in EVs can also enhance tumor invasiveness and metastasis (Mao et al., 2018a; Bao et al., 2018; Ludwig et al., 2020).

In a variety of tumor diseases, such as bladder cancer (Piao et al., 2021), ovarian cancer (Taylor and Gercel-Taylor, 2008), non-small-cell lung cancer (Wu and Shen, 2020), breast cancer (Volovat et al., 2020), prostate cancer (Sobhani et al., 2020), pancreatic cancer (Savareh et al., 2020), and gastric cancer (Cheng et al., 2020), the levels of miRNA in the EVs obtained from plasma of tumor patients were significantly higher than those of healthy controls. Certain disease-related miRNAs are selectively incorporated into the EVs, with significant differences in the miRNAs content compared to cells (Baglio et al., 2015). miRNA-224 enclosed in EVs is the diagnostic and prognostic marker for hepatocellular carcinoma (Cui et al., 2019). Zhou et al. (2017) identified six miRNAs (miR-19b-3p, miR-21-5p, miR-221-3p, miR-584-5p, miR-425-5p, and miR-409-3p) differentially expressed in exosomes from patients' plasma with lung adenocarcinoma, which can distinguish patients with lung adenocarcinoma from healthy individuals. Jin et al. (2017) found that the expression of let-7b-5p and miR-486-5p in EVs could distinguish between non-small-cell lung cancer (NSCLC) patients and healthy individuals rather than in the supernatant without EVs. These studies have shown that the use of EV-derived miRNAs in serum as biomarkers has exceptional high stability and specificity (Moloudizargari et al., 2021) and can be used for the early detection, prognosis, and monitoring of cancer.

3.2 Extracellular vesicle-derived microRNAs in cardiovascular disease

EV-derived miRNA plays an important role in the occurrence and progression of cardiovascular diseases

(Hergenreider et al., 2012; Murugesan et al., 2021; Zhang and Huang, 2021), such as atherosclerosis, acute coronary syndrome, heart failure (HF), myocardial ischemia-reperfusion injury, and pulmonary hypertension (Matkovich et al., 2009; Tian et al., 2017; Kalayinia et al., 2021; Zheng et al., 2021). Ren et al. (2020) found that the EVs from adventitial fibroblasts (AFs) regulate vascular smooth muscle cell (VSMC) proliferation by transporting miR55-5P and angiotensin converting enzyme (ACE), which plays a vital role in vascular remodeling.

EV-derived miRNA-30 members are key modulators of complex biological processes in a variety of cardiovascular diseases, including ischemic heart disease, heart failure, hypertension, and arrhythmias. They are attractive diagnostic and prognostic biomarkers in the cardiovascular field (Mao et al., 2018b). Studies have shown that the EV-derived miRNA (miR-17-5p, miR-126-5p, and miR-145-3p) can be of diagnostic value for acute myocardial infarction (AMI), and a combination of three miRNAs can improve the area under curve (AUC) and receiver operating characteristic curve (ROC) values, providing higher accuracy in the diagnosis of AMI (Xue et al., 2019; Mir et al., 2021).

3.3 Extracellular vesicle-derived microRNAs in nervous system diseases

At present, the pathogenesis of inflammatory diseases of the central nervous system [including neurodegenerative diseases (Ruan et al., 2021; Xiao et al., 2021)] and autoimmune diseases (Xu et al., 2022) has not been completely clarified, but more and more studies have begun to focus on the role of EVs in autoimmune diseases and research on treatment of EVs (Guo et al., 2019; Chu et al., 2020; Dar et al., 2021; Saeedi et al., 2021; Xia et al., 2021). Studies have found that multiple miRNAs are involved in neuroinflammation and neurological diseases, such as Parkinson's disease (Xie et al., 2020c), Alzheimer's disease (AD) (Dong et al., 2021), amyotrophic lateral sclerosis (Liu et al., 2022), and depression (Trotta et al., 2018; Chen and Wang, 2021). The blood–brain barrier (BBB) is the barrier between plasma and brain tissue, which can prevent harmful substances from entering the brain tissue from blood (He et al., 2018). The EVs act as transporters for miRNAs that cross the endothelial layer of the BBB, facilitating communication through biological fluids between the brain and distant organs (Montecalvo et al., 2013; Xia et al., 2021). Neurons and neurological cells release EVs, and their cargo can function in cellular communication and neuroinflammation by delivering mRNAs, miRNAs, and proteins (Gupta and Pulliam, 2014; Pegtel et al., 2014; Markoutsa et al., 2022). The EVs have been identified as a potential cell-to-cell carrier of misfolded proteins associated with neurodegenerative diseases in the central nervous system in most neurodegenerative diseases, and Aβ peptide, viral protein, alpha synuclein, tau, and superoxide dismutase (SOD) pathogenic aggregates are released from cells as exosomes (Saman et al., 2012; Schneider and Simons, 2013). These proteins form aggregates (amyloid and ion-like proteins) that escape normal degradation mechanisms. Cerebrospinal fluid (CSF) reflects physiological and pathological changes in the brain and is the best indicator for most central nervous system diseases, but sampling difficulties are unsuitable for disease screening. Compared with CSF, blood is easier to obtain, thus avoiding the invasive process of sample collection, and it is more suitable as a screening marker for neurological diseases. Moreover, Cheng et al. (2015) performed an unbiased next-generation sequencing (NGS) analysis of serum EV-derived miRNAs, identifying an AD-specific 16-miRNA signature that differ between healthy and AD patients, and used a random forest model to predict clinical classification with 87% sensitivity and 77% specificity (Lv et al., 2013).

3.4 Extracellular vesicle-derived microRNAs in kidney diseases

Recent studies have shown that the EV-miRNAs play an important role in kidney diseases and can also be a valuable biomarker for diagnosis. It was found that miR-29c in EVs can be related to renal function, and there are differences in the expression of EVs-miR-29c in patients with varying degrees of renal fibrosis (Lv et al., 2013). Similarly, miR-200b in nonproximal tubulo-derived urinary exosomes is expressed differently in normal people and patients with renal fibrosis, which can be used as a biomarker for renal fibrosis and can replace traditional invasive renal biopsy for diagnosis of renal fibrosis (Yu et al., 2018). It has been validated by sequencing and qPCR of EV-derived miRNAs that significant differences exist in the expression of miR-215-5p, miR-378i, miR-365b-3p, and miR-135b-5p in the urinary exosomes of immunoglobulin A nephropathy patients and healthy controls (Min et al., 2017). MiR-18a-5p was highly expressed in the acute phase of injury, and miR-132-3p was upregulated during the transition between acute and fibrotic injury; miR-146b-5p is highly expressed in the high fibrosis phase (Pellegrini et al., 2015). These studies suggest that miRNA has the potential to act as markers for kidney disease.

3.5 Extracellular vesicles-derived microRNAs in liver diseases

EVs can be produced by all types of cells in the liver, are involved in transmitting information between liver cells, and the EVs produced by liver cells are loaded with miRNAs that can be used in diagnosing liver-related diseases. Another research group verified by a mouse model of alcoholic hepatitis that miR-192, miR-122, miR-30a, miR-744, miR-1246, miR-30b, and miR-130a

were elevated in alcohol-fed mice. Further testing was then carried out in human patients yielding results consistent with animal models showing that the EV-miRNAs are potential biomarkers of alcoholic hepatitis (Momen-Heravi et al., 2015). Elevated levels of miR-122 and miR-192 in EVs were found in models of nonalcoholic fatty liver mice, which could be used as a promising diagnostic marker (Newman et al., 2022). Another group found that higher expression of miR-19a in exosomes was also observed in serum from hepatocytes and patients with chronic hepatitis C virus (HCV) fibrosis infected with HCV compared with healthy volunteers and patients with non-HCV-associated liver disease (Devhare et al., 2017). These studies help us understand the role of EV-miRNAs in the development of liver disease.

4 Advances in isolation technology of microRNAs in extracellular vesicles

There are many miRNA binding to free proteins in that body fluid environment; therefore, for detection of EV-derived miRNAs, it is necessary to isolate the EVs first and then use TRIzol and other methods to isolate and purify EV-derived miRNAs (Hu et al., 2018; Yang et al., 2018). These steps take much time, and it is imperative to realize the timely detection of miRNA. Herein, we first introduce the purification technology for EV and then discuss the miRNA purification technology.

4.1 Progress of extracellular vesicle isolation and purification technology

The isolation method for EVs is very important for subsequent analysis of EV miRNA. Currently, there are many isolation methods for EVs. However, ultracentrifugation (UC), density gradient centrifugation (DGC), size exclusion chromatography (SEC), co-precipitation, and immunoaffinity enrichment are the most widely used methods. The summary of the contemporary methods for EV isolation is as follows.

4.1.1 Ultracentrifugation

A differential ultracentrifugation method was proposed by Dr. Thery in France for the separation of EVs based on physical and chemical properties of EVs (Thery et al., 2006). It is considered a classical (Momen-Heravi, 2017) and gold standard EV isolation method (Royo et al., 2020). Most researchers isolate EVs by UC (Gardiner et al., 2016). The differential ultracentrifugation method is mainly used to separate the EVs from other components by continuously increasing centrifugal force on samples and removing cells and cell fragments. Many studies have proved its reliability. The usually used ultracentrifugation speed is 110,000 g for centrifugal force to centrifuge the sample twice for 70 min and finally blow and mix into the buffer (Lobb et al., 2015). Although EV researchers have widely used differential ultracentrifugation, it still has many drawbacks. First, this method requires expensive instruments. Second, centrifugation can easily lead to EV aggregation and will be mixed with non-EV impurities, such as protein polymers and viruses. Especially in sticky body fluids such as plasma, there are more impurities. Third, the high-speed process of ultracentrifugation will cause damage to EVs to a certain extent, and the longtime of ultracentrifugation may lead to EV morphological changes (Issman et al., 2013). The EVs extracted by UC have high purity and are conducive to downstream detection, but due to limitations of current instrumentation and extraction efficiency, it is difficult to use the separation of large number of clinical specimens' samples, which is mainly used for researchers' research. Density gradient centrifugation (DGC) and UC have similar principles in isolating the EVs; DGC can maintain the integrity of EVs, but it still has the corresponding disadvantages of UC, whereas the DGC is to form a specific density gradient medium in a centrifuge tube. At present, sucrose and iodoxanol are commonly used, and the density of medium increases from top to bottom. Under a certain centrifugal force, the smaller the density, the higher the distribution. Finally, the particles of different densities will stagnate in the corresponding iso density area. Density gradient centrifugation has a higher resolution and is often used to separate EVs with higher purity (Ashley et al., 2018). Some HDLs can still be co-separated, although density gradient centrifugation has a higher purity for EVs than ultrafast centrifugation (Yuana et al., 2014; Greening et al., 2015). DGC can isolate higher purity EVs, but it introduces exogenous components and has the same disadvantages as UC, which is not conducive for extraction of large clinical samples and detection of miRNAs.

4.1.2 Size exclusion chromatography

The SEC separation method is based on the particle size. Each molecule can pass through the hole in the polymer bead according to its size on a chromatographic column with a special pore size matrix. Molecules with smaller radius can enter the hole, and the elution speed is slow. Molecules with larger radii cannot enter the hole and move through the column more quickly. Most of the EVs can be eluted before soluble components (Boing et al., 2014). The size of interception aperture depends on the choice of the exclusion matrix. For example, with an aperture of about 60 nm for agarose 2B, SEC can remove 99% of soluble plasma proteins and > 95% of HDL without causing EV aggregation, preserving its integrity and biological activity (Boing et al., 2014). Plasma proteins are difficult to remove by differential ultracentrifugation or precipitators, which is simpler and less time-consuming than density gradient centrifugation. However, the SEC removes most of the overabundant soluble plasma proteins (Monguio-Tortajada et al., 2019). Moreover, some non-EV components

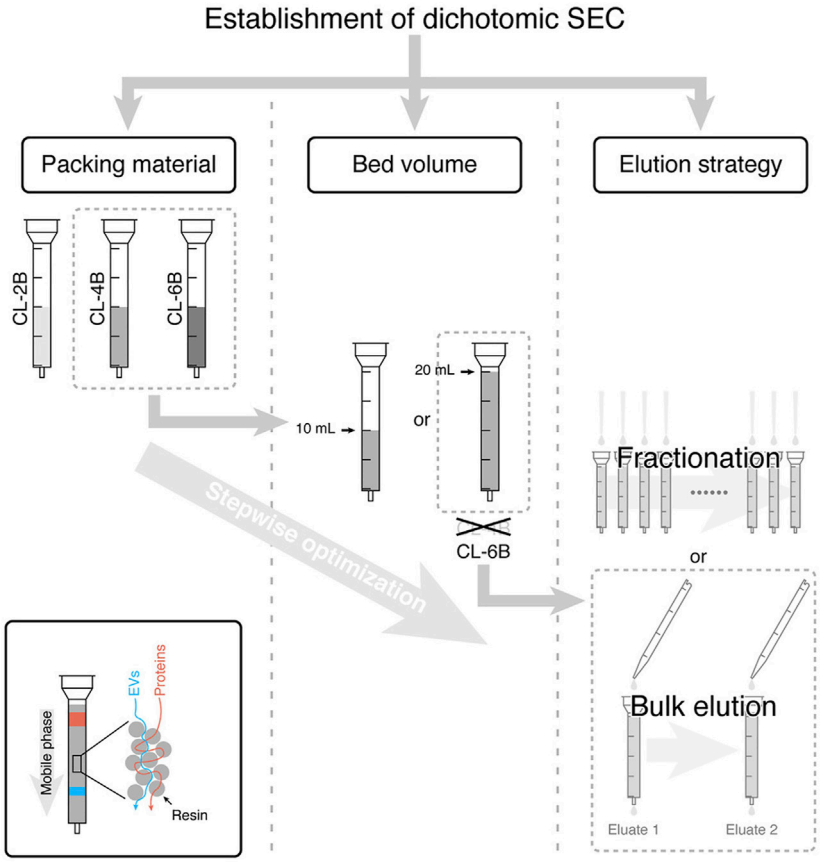

FIGURE 4
SEC-based EV isolation workflow and the underlying principle. In this study, CL-6B was demonstrated to be the best one from three Sepharose CL resins with the bed volume of 20 ml, and two bulk elution steps were sufficient for isolation of EVs. Reprinted with permission from Guo et al. (2021).

mainly particles above the interceptor aperture, including viruses, protein polymers, and some large proteins such as chylomicrons, are also separated together. Koh et al. (2018) used ultracentrifugation and SEC to enrich the EVs from the plasma for clinical application. Guo et al. (2021) established a simplified dichotomic SEC method that only requires two bulk elutions to get the EVs in the Eluate 1 and proteins in the Eluate 2. This dichotomic SEC has fascinating potential for EV preparation for clinical testing and/or basic research (Figure 4).

4.1.3 Ultrafiltration

The ultrafiltration method is simple and efficient and does not affect the biological activity of EVs (Taylor and Shah, 2015). This size-based separation method involves the use of a membrane filter with a specific pore size, such as a membrane filter with a typical pore size of 0.22 μm to collect EVs from the filtrate. For the sample to pass through the filter, negative pressure or centrifugal force is usually used as pressure. Ultrafiltration has a short time and a high recovery rate, effectively concentrating the EVs in large samples such as the culture medium (Haraszti et al., 2018). We have made a small extraction and filtration device for rapid extraction of EVs (Li et al., 2019). First, negative pressure was applied to remove large membrane fragments through a filter membrane with a pore size of 600 nm, and then the filtrate was used to remove small impurities through a filter membrane with a pore size of 20 nm. Chen et al. (2021) proposed a new ultrafiltration strategy: the exosome detection method *via* an ultrafast isolation system (EXODUS), which introduced dual coupled harmonic oscillations into a dual-membrane filter configuration to generate s-waves. The inhibition of the scaling effect improved the treatment speed, yield, and purity and helped achieving nonblocking and ultrafast purification of EVs. Ultrafiltration and a high recovery rate can effectively concentrate EVs in large volume samples. However, this method requires complex equipment and is not easy to be popularized. Ultrafiltration only separates the EVs by size and lacks specificity; therefore, it cannot remove many impurities

with similar particle sizes to EVs. When passing through the filter membrane, the EVs are stocked on the filter membrane, resulting in an inevitable loss.

4.1.4 Co-precipitation

Recently, the polymer co-precipitation method, which changes the solubility of exosomes and precipitates them (Rider et al., 2016), has attracted many researchers' attention for its simple and rapid use. Commercial kits based on polymer co-precipitation (e.g., ExoQuick and total exosome isolation) have been developed for EV extraction and isolation. Once the reagents are introduced, the solubility of EVs is significantly reduced and easily precipitated. Under the action of low centrifugal force, the precipitated EVs can be easily separated, thus avoiding the time-consuming centrifugal operation. The precipitation method can save more time, and the concentration of exosomes is 2.5-fold higher than ultracentrifugation (Coughlan et al., 2020). The total exosome isolation kit is commonly used for serum EV separation as an example. After mixing 30 μl of precipitant with 100 μl of serum sample, the sample is incubated at 4°C for 30 min and centrifuged at 10,000 g for 5 min to precipitate EVs. However, this method is not conducive to large-scale clinical application and may co-precipitate many organelle-related proteins, such as endoplasmic reticulum and lysosome, which is not conducive to a downstream analysis (Li et al., 2021). In addition, as additional components need to be added to the sample during extraction, the collected EVs cannot be directly used for subsequent cell culture or transport, limiting the application of EVs. The EVs is isolated by co-precipitation and will be mixed with protein impurities and require centrifuges. The method is not conducive to extraction of a large number of clinical specimens and miRNA detection.

4.1.5 Immunoaffinity enrichment

The specificity and simplicity of immunoaffinity capture is an attractive method. To enrich EVs, antibodies specific to EV specific markers, such as CD9, CD63, CD81, epidermal growth factor receptor (EGFR), and epithelial cell adhesion molecule (EpCAM), are fixed on the surface of various vectors, such as an ELISA plate, and a magnetic bead or chip (Choi et al., 2021). Taking the exosome CD63 isolation kit (Life Technologies) as an example, the magnetic beads coated with anti-CD63 monoclonal antibodies are mixed with the sample and then incubated at 2–8°C for 18–22 h. After magnetic separation, the magnetic beads are cleaned with a washing buffer to remove the impurities, and the magnetic beads enriched with EVs could be directly used for flow cytometry detection (Oksvold et al., 2015). The immunoaffinity capture method can isolate specific subgroups of EVs, obtain high purity EVs, and have many advantages, such as simple operation. However, the incubation time between magnetic beads and samples is more extended, usually taking hours or even overnight. In addition, due to the strong affinity of antigen–antibody binding, it is challenging to separate immune magnetic beads from the EVs, which is not conducive to a subsequent functional analysis. Moreover, this method can only extract the EVs subgroup from the corresponding antigen, which is accompanied by the risk of bias. In combination with other labeling methods, such as fluorescent labeling, it can be used for the detection of EVs. It is an isolation method that is expected to be used for clinical applications. However, this method can only specifically enrich the EVs corresponding high antigen expression, which may cause the loss of EV-related miRNA information.

4.1.6 Field flow fractionation

Field flow fractionation (FFF) is a kind of technology that can separate and characterize different size particles. Unlike size exclusion chromatography, FFF separation is performed in a single phase. The samples flow in the FFF channel in a parabolic form. Particles have the highest velocity in the center, and velocity decreases as they get closer to the channel wall. Zhang and Lyden (2019) successfully isolated EVs of different sizes from cell supernatant using the asymmetric flow field flow separation (AF4) technique. The particles in the sample first gather to one side of the channel under the action of an external field. The particles will remain at different distances from the tube wall due to their size, and smaller particles farther from the side wall flow faster and are thus eluded earlier than larger particles. This way, the EVs of different sizes can be obtained at specific periods. The sample preparation process of the asymmetric flow–flow separation method is cumbersome, resulting in low flux. The high initial sample concentration requirement and time-consuming operation also limit its wide application. This method has less damage to EVs and can sort out the EVs of different particle sizes. Some proteins of the same particle size may be adulterated. In studying EVs of different size, it has a potential application value.

4.1.7 Acoustic-based isolation method

Acoustic waves have high precision and biocompatibility in processing cells and other biological particles and can be used in combination with microfluidic technology for EV separation (Lee et al., 2015b). The acoustic-based microfluidics EV separation method typically uses ultrasonic waves to apply to particles in a sample (Huang et al., 2021). Under sound pressure, the particles are separated according to their physical properties, such as size and density, under different forces (Iliescu et al., 2019; Hassanpour Tamrin et al., 2021). Ku et al. (2018) captured the EVs by scattering between the microparticles in the resonance cavity and EVs by an ultrasonic wave. The integrated acoustic device is capable of fast operation, label-less, contactless, and continuous separation of EVs. Researchers also developed an integrated acoustic device that can directly separate the EVs from blood samples (Wu et al., 2017). The device combines acoustic wave and microfluidic technology into two separate modules.

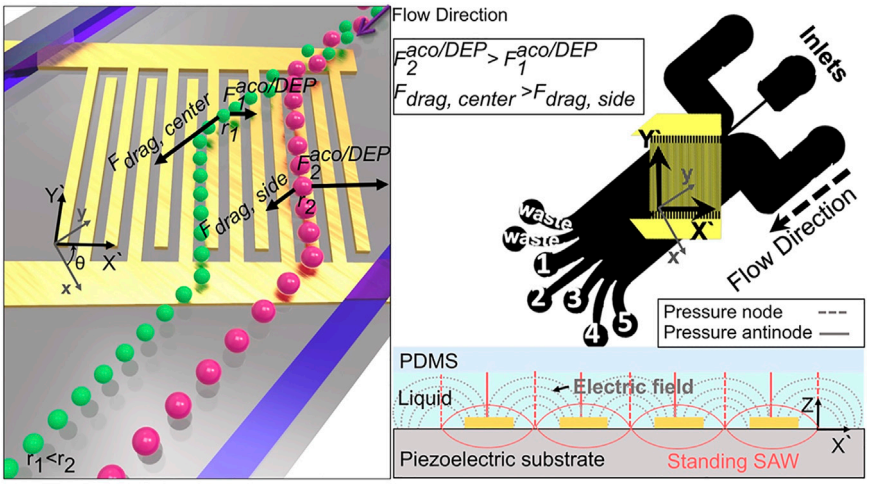

FIGURE 5
Schematic illustrates the working mechanism of the system. Left image shows that particles of different sizes are subjected to different forces in the acoustic and electric fields, causing the separation of particles of different sizes. The right one is the schematic diagram of PDMS microchannel device and the side view of electric and acoustic field around the electrodes (Tayebi et al., 2021).

The first module can remove substances larger than 1 μm in diameter, such as cells, and the second module can separate larger microvesicles and apoptotic bodies from exosomes. By adjusting the input power and flow rate, the interception size of the two separation modules can be adjusted to flexibly adjust the obtained particle size, and the application range is more expansive. Tayebi et al. (2021) demonstrated a method for sorting the exosomes (<200 nm) and microvesicles (>300 nm) using both electrical and acoustic forces, with EV purification resulting in more than 95% purity and 81% recovery (Figure 5).

4.1.8 Metallic oxide-based isolation method

Titanium dioxide (TiO_2) can combine with phosphorylated amino acid residues including serine, tyrosine, and threonine (Liu et al., 2015). Under acidic conditions, the surface of the TiO_2 beads is cationic and specifically binds to the phosphate groups on phosphorylated modified peptide fragments. TiO_2 materials have been extensively studied in the research field of phosphorylated proteins (Mancera-Arteu et al., 2020). Gao et al., 2019a reported a strategy to isolate serum exosome based on TiO_2 microspheres. They compare serum exosome proteins from pancreatic cancer patients and healthy donors, identifying 59 significantly upregulated proteins (Gao et al., 2019a). Researchers also achieved the rapid enrichment of EVs from the serum using TiO_2 magnetic beads to further recognize the EVs expressing PD-L1, supporting the TiO_2 good ability for enriching EVs (Peng et al., 2020). Xiang et al., 2021 combined ultrafiltration and TiO_2 to enrich EVs from many urine samples and conducted liquid chromatography–mass spectrometry (LC–MS) to identify proteins (Xiang et al., 2021). Dao et al. (2022) synthesized chimeric nanocomposites of lactoferrin conjugated 2,2-bis (methylol) propionic acid dendrimer-modified magnetic nanoparticles (LF-bis-MPA-MNPs) to isolate the EVs by electrostatic interaction, physical absorption, and biorecognition. The mechanism of EV isolation by LF-bis-MPA-MNPs is shown in Figure 6. The metallic oxide-based isolation method has many significant advantages for EV separation. First, the high affinity makes the incubation time concise. Second, the EVs can be separated by magnetic separation only after combining with magnetic beads. The EVs have a high recovery rate and easy operation and do not require many samples to meet downstream analysis requirements. It is expected to be used in POCT for EVs in the future by combining with other detection methods.

4.1.9 Absorbent polymer-based method

Super absorbent polymer (SAP) is a hydrogel with strong water absorption ability. There is a particular size space where relatively small molecules will be sucked into with water, while the EVs and other large size particles are excluded for concentration and purification. Some researchers developed a method to concentrate the EVs by SAP beads and successfully enriched the EVs from culture medium and urine (Yang et al., 2021). The principle is shown in Figure 7, where the method is simple and efficient without special equipment that can be used in the separation and purification of EVs in large volume samples, such as cell supernatant or urine. Compared with polymer co-precipitation, ultrafiltration and other methods, the method has advantages such as shorter concentration time and lower cost. However, the purity of EVs obtained is low and there is protein contamination with particle sizes similar to those of EVs. It is difficult to be directly applied to complex samples, such as blood. This method is simple to operate and highly scalable, which can be widely used in therapeutic or diagnostic applications that require EV enrichment.

There are two main aspects of application of EV-related miRNAs: one is the study on mechanism of action for target cells

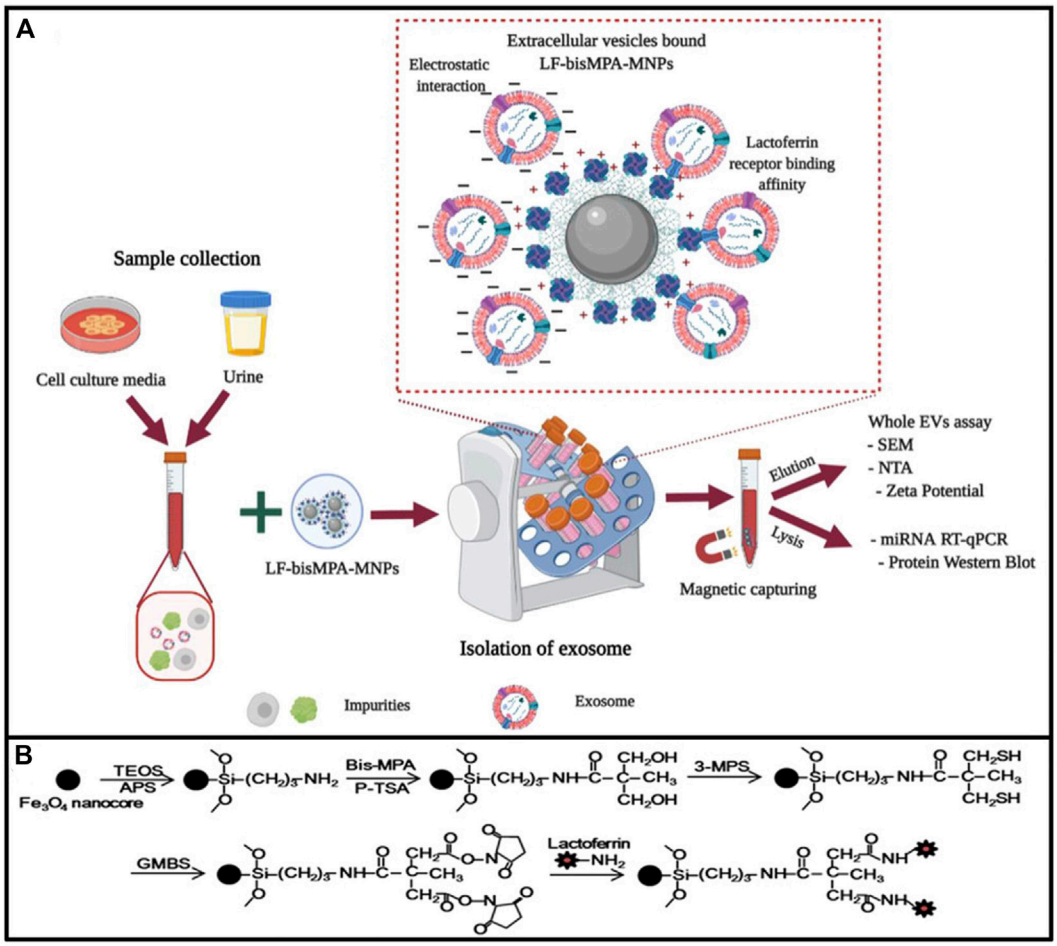

FIGURE 6
Diagrammatic elucidation of EV isolation by LF-bis-MPA-MNPs. **(A)** LF-bis-MPA-MNPs mediated EV isolation from cell culture media (CCM) and human urine. **(B)** Elucidation of LF-bis-MPA-MNPs synthesis and modification principal. Reprinted with permission from Dao et al. (2022).

and the other is the detection of potential markers for disease. The impact of free protein and free protein-bound miRNA contamination on downstream experiments should be considered, as well as cost, flux, and automation. However, the tolerance of different experimental purposes and influence weight of related factors are different. For different applications, we can use the most suitable separation method, and the advantages and disadvantages of different isolation methods for application of EV-related miRNAs are as in Table 1.

4.2 Extraction and purification methods for microRNA

There are different isolation methods for EV, and there are also different separation and purification methods for miRNA (Chomczynski and Sacchi, 2006; Rio et al., 2010; Duy et al., 2015). The core of RNA separation is to improve the purity of extracted EV-derived miRNA and reduce the losses (Lin et al., 2022). TRIzol method can extract miRNA from the EVs. TRIzol is a reagent whose main component is phenol that can maintain RNA integrity during sample lysis or homogenization. After adding chloroform, the solution is divided into aqueous and organic phases. RNA can then be precipitated in the aqueous phase with isopropyl alcohol (Burgos et al., 2013). But the main issue with precipitation-based isolation is the incomplete removal of phenols and salts. Some miRNAs may be lost during the extraction (Kim et al., 2012), but the reagent chloroform is dangerous. The TRIzol method accompanied by column purification (Brown et al., 2018) has high efficiency. Using the solid phase to isolate the EV miRNA, such as magnetic beads (Xu et al., 2018; Mahmudunnabi et al., 2022), can make the process simple. The high salt concentration is also

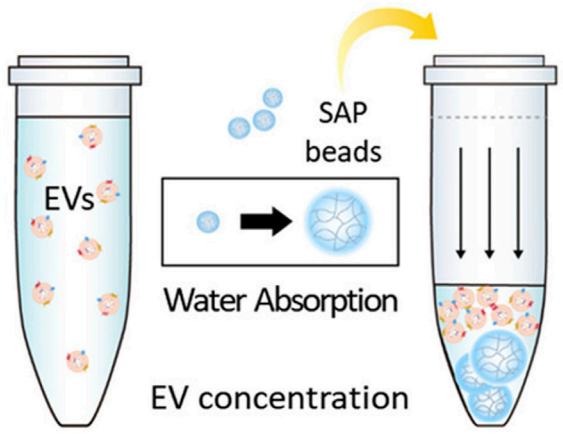

FIGURE 7
EVs enrichment *via* SAP bead. Small molecules are sucked into SAP with water, whereas EVs and other large size particles are excluded for concentration and purification. Reprinted with permission from Yang et al. (2021).

different sources refers to different extraction methods. Therefore, a fast and simple EV-derived miRNA extraction method is needed.

5 Advances in detection of extracellular vesicles–derived microRNA

Current techniques for qualitative and quantitative analysis of miRNAs in samples have developed. Quantitative reverse transcription polymerase chain reaction (qRT-PCR) based on amplification is the typical method for miRNA detection in EV. Furthermore, many other strategies have been established, including molecular beacon *in situ* (MB *in situ*), surface-enhanced Raman scatting (SERS), microarray, next-generation sequencing (NGS), and isothermal amplification. Except NGS, the above methods can detect specific miRNAs by probe or primer that is specifically complementary to the target miRNA.

TABLE 1 Summary of EV isolation methods.

Isolation method	Isolation mechanism	Advantages	Disadvantages	References
Ultracentrifugation	Density	Gold standard method, widely used	EVs yields are low Long process	Thery et al. (2006), Lobb et al. (2015), Nigro et al. (2021)
Density gradient centrifugation	Density	High purity	Cumbersome operation; time-consuming	Ashley et al. (2018)
Size exclusion chromatography	Particle size	Used for large-scale samples	Each consumable can only handle samples from the same source, which is too costly if used for the separation of different clinical samples	(Boing et al. (2014), Guo et al. (2021)
Ultrafiltration	Particle size	The separation steps are simple and fast	Cannot remove similar-sized protein particles	(Haraszti et al. (2018), Li et al. (2019), Chen et al. (2021)
Co-precipitation	Surface charge	Simple and fast separation steps	Contamination of organelle-related proteins, not conducive to downstream detection	Rider et al. (2016), Ludwig et al. (2018)
Immunoaffinity enrichment	Antigen–antibody	Obtain EVs expressing specific proteins	Bind to free proteins and affects the capture efficiency of EVs; low recovery	Choi et al. (2021)
Field flow fractionation	Molecular weight	Wide range of separations	Special equipment; low-throughput	Zhang and Lyden, (2019)
Acoustic-based isolation method	Sound wave	The separation steps are simple and fast	Not suitable for complex samples	Lee et al. (2015b), Tayebi et al. (2021)
Metallic oxide-based isolation method	electrostatic interaction, physically absorption and biorecognition	Fast and simple; small sample volume; Low cost	Not conducive to downstream detection	Gao et al. (2019a), Dao et al. (2022)
Absorbent polymer-based method	Particle size	High-efficiency, No special equipment	Low purity; not suitable for complex samples	Yang et al. (2021)

necessary to solve, which can influence the downstream analysis. McAlexander and fellow researchers (McAlexander et al., 2013) compared different RNA extraction methods and drew the conclusion that not all extraction methods are good. RNA extraction from

5.1 Quantitative reverse transcription polymerase chain reaction

Currently, the most widespread application for detection of extracellular vesicle miRNA is qRT-PCR (Drula et al., 2020),

which is regarded as a gold standard for the detection of gene expression. Quantification of RNA molecules by qRT-PCR unusually consists of two steps: first, the complementary DNA with RNA targets is synthesized by reverse transcriptase (RT), and then PCR amplification is performed using cDNA as a template. The amplification process is monitored in real time by detecting the fluorescence of specific dye of double-stranded DNA or a specific fluorescent probe. Currently, there is no accepted internal reference for EVs that is commonly used in cellular miRNA, such as gene U6 is not stably expressed in the EVs; therefore, it is crucial to find the stably expressed internal reference genes, which is suitable for samples before analyzing the miRNA. Fang et al. (2021) designed a portable nucleic acid detection (PNAD) system and realized the sample processing and PCR in a single device. Compared to traditional PCR techniques, droplet digital PCR (ddPCR) makes a technical improvement, solving the problem of sensitivity in detecting low copy number of transcripts (Hindson et al., 2013). The reaction system was divided into thousands of oil droplets, which encapsulated all reagents, but only one copy of the template was amplified. The fluorescence signal from each droplet was measured by the ddPCR instrument. ddPCR has higher accuracy and reproducibility for serum miRNA (Hindson et al., 2013). Moreover, researchers have recently shown that the ddPCR has higher sensitivity, repeatability, and accuracy in detecting miRNA in urine exosomes, compared with qPCR (Wang et al., 2019). The ddPCR is sensitive to detecting nucleic acids with low copy numbers, but it requires special instruments and costs highly. Moreover, Zhou et al. (2021) detected the EV-derived miRNA in the plasma of patients with endometrial cancer (EC) by PCR and found that mir-15a-5p, mir-106b-5p, and mir107 were significantly upregulated in the exosomes isolated from plasma samples of EC patients, compared with healthy controls.

5.2 Molecular beacon *in situ*

A series of situ detection methods for miRNAs in exosomes were developed by molecular beacon (MB) (Zhai et al., 2018; Oliveira et al., 2019; Mao et al., 2022). The MB is able to bind to target RNA specifically, resulting in failure of quenching group and generation of fluorescence. The fluorescence intensity has a direct correlation with concentration of hybridizing molecular beacon with miRNA (Lee et al., 2018). These methods neither need RNA extraction nor amplification process, showing characteristics of simple operation. They only need the incubation of the sample with the beacon without removing the unbound beacon, but there is a false negative problem caused by low concentration (Lee et al., 2015a; He et al., 2019). Gao et al. (2019b) have reported a virus-mimicking fusogenic vesicle packaging MB by membrane disposal MB hybridized with target miRNAs in the exosomes for *in situ* detection.

5.3 Surface-enhanced Raman scatting

Surface-enhanced Raman scatting (SERS) can stimulate signals from small molecules on the metal surface (Kneipp et al., 1996). It can also be used for miRNA detection and classification and have several advantages, such as high sensitivity for detecting very low-level analytes with specific molecular fingerprints (Driskell et al., 2008). More and more research focus on detection of EV-derived miRNA using SERS. A recent study used a modified dual SERS biosensor to detect miRNAs isolated from exosomes. Biosensor uses the SERS label of Fe_3O_4@Ag-DNA-Au@Ag@DTNB that possesses DNA oligonucleotides complemented with target miRNA. Target miRNA hybridizes with DNA oligonucleotides on nanoparticles labeled SERS, and then DNA from the miRNA/DNA duplexes is selectively cleaved by duplex-specific nuclease. Cutting causes the separation of SERS label from the substrate, and the quenching reaction can be detected and low detection limit of 1 a.m. copy number can be achieved (Pang et al., 2019). Researchers reported an *in situ* platform for directly detecting exosomal miRNAs from serum samples (Jiang et al., 2021a). They used Au@DTNB-modified [DTNB is the Raman reporter molecule 5,5′-dithiobis-(2-nitrobenzoic acid)] locked nucleic acids (LNAs) to introduce into exosomes and bind to targeted miRNAs to generate SERS signals. The SERS signal is enhanced by Fe_3O_4@TiO_2 enrichment of exosomes. As shown in Figure 8, target miRNAs can be directly qualified *in situ* with a detection limit of 0.21 fM based on the platform, which is better or comparable to qRT-PCR. The SERS detection has the advantages of being fast, simple, and inexpensive. More portable SERS detection equipment will appear in the future.

5.4 Microarray

Microarray is based on a predesigned label probe that hybridizes with the target cDNA sequence (Sevenler et al., 2018). Total RNA was herein extracted from the EVs isolated from the sample, and then a cDNA library that complements with RNA was constructed. To realize the detection of miRNA, cDNA is mixed up with the label probe fixed on the chip, and complementary sequence is hybridized with the labeled probe in the microarray, while the relative gene expression level is quantified according to the hybridization signal intensity (Li et al., 2020). Microarray has been widely used in the analysis of miRNA in EVs. Nakamaru et al. (2020) analyzed the expression of EV-derived miRNA in type 1 autoimmune pancreatitis (AIP) samples, chronic pancreatitis (CP), and healthy adult (HC) samples by microarray technology and found that mir-21-5p was highly expressed in AIP compared with control group. Roman-Canal et al., 2019 used TaqMan open array technology to analyze the expression of miRNAs related EVs and found that 210 miRNAs were differentially expressed in the

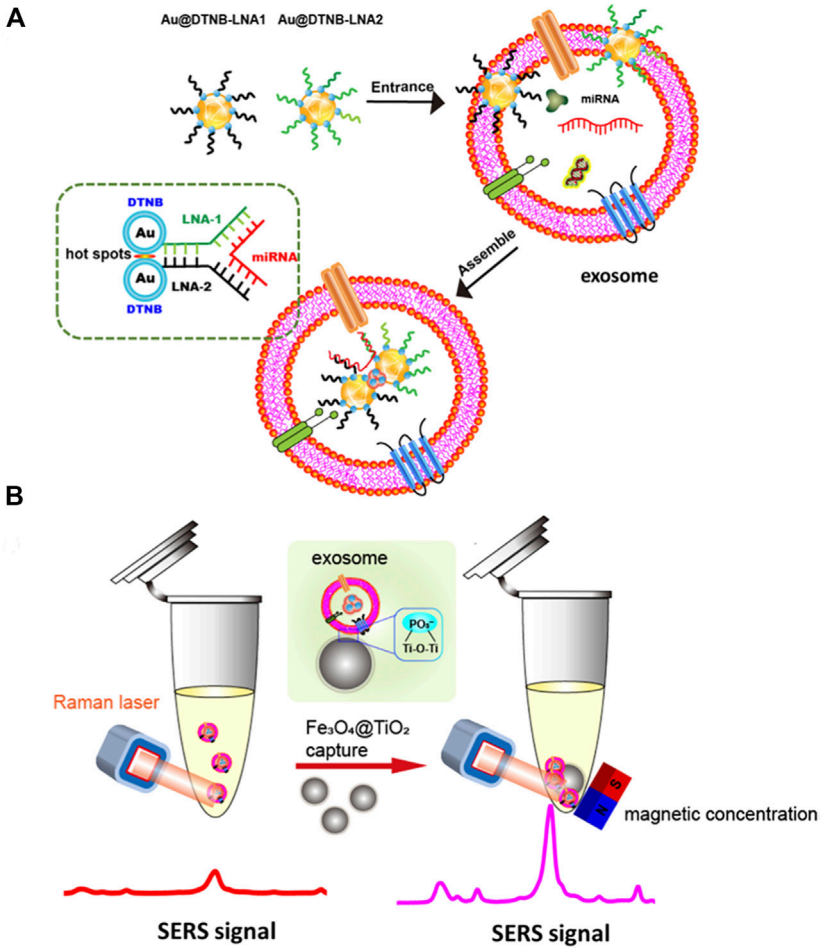

FIGURE 8
Exosomal miRNA *in situ* detection using SERS biosensor combined with Fe_3O_4@TiO_2-based concentration. SERS tags are adsorbed to exosomes and bind to the target exosomal miRNA **(A)**. The hot spots and SERS intensity increase, and SERS intensity increases as Fe_3O_4@TiO_2 captures exosome for *in situ* detection of exosomal miRNAs **(B)**. Reprinted with permission from Jiang et al. (2021a).

EVs isolated from peritoneal lavage fluid of patients with colorectal cancer (CRC) (Roman-Canal et al., 2019). Although the miRNA chip can analyze a large number of sequences simultaneously; however, it has low sensitivity, narrow dynamic range, high cost, and extended operation.

5.5 Next-generation sequencing

NGS is a high-throughput sequencing method that is the leading technology in transcriptome analysis (Alexandra et al., 2022; Griffin et al., 2022). It can sequence the base pair of DNA or RNA. First, RNA in the sample needs to be extracted and purified. Universal adaptors are often connected to the 5′ and 3′ ends of each RNA strand, and then reverse transcription and PCR amplification, and finally, the products are sequenced. NGS technology overcomes some limitations of microarray to study miRNA in EVs, such as requiring many samples being unable to detect unknown miRNA, and has higher sensitivity and accuracy than microarray. NGS is usually used to screen the disease-related specific miRNA. In another study, researchers analyzed the noncoding RNA expression profile of prostate cancer metastatic cells (PC3) and EVs by NGS technology and found that miR-10a-5p and miR-29b-3p from the EVs in the plasma sample from patients with prostate cancer were significantly overexpressed (Worst et al., 2020). Sequencing technology can find the new gene sequences, but it is not suitable as the standard detection technology because of its long cycle, high cost, and complex data analysis.

5.6 Isothermal amplification technique

In recent years, isothermal amplification has become a popular method for detecting miRNA (Zhao et al., 2015; Reid et al., 2018). It is

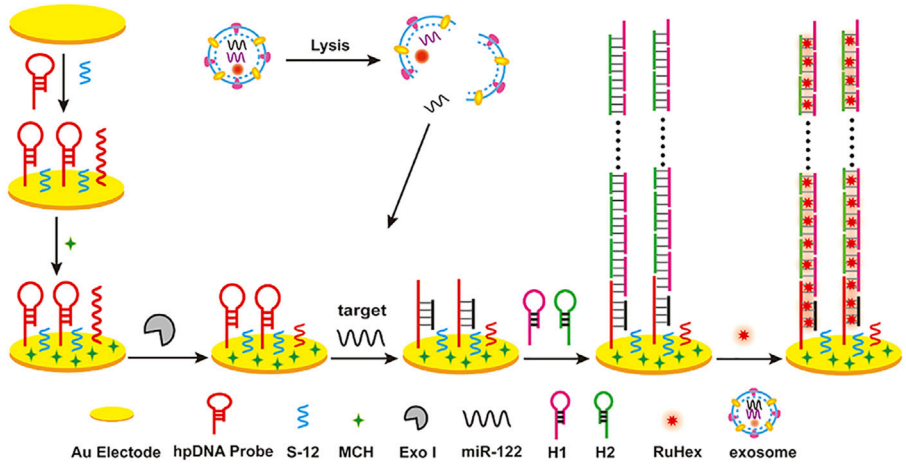

FIGURE 9
Exosomal miRNA detection by an electrochemical sensing platform harnessing HCR as a signal amplification strategy. Reprinted with permission from Guo et al. (2020).

easy for isothermal amplification methods to have allowed nucleic acid amplification to be carried out, and isothermal amplification has had a profound impact on the way molecular diagnostics operate (Glokler et al., 2021). Because it does not need a thermal cycler, isothermal amplification is more suitable for short-sequence RNA. MiRNA is used as the primer extended on the template, triggering sequence amplification or template for primer design (Deng et al., 2017). As described in the overviews (Gines et al., 2020), isothermal amplification is usually divided into enzyme and enzyme-free methods. Enzymatic isothermal amplification includes loop-mediated isothermal amplification (LAMP), nuclear acid sequence-based amplification (NASBA), rolling circle amplification (RCA), exponential amplification reaction (EXPAR), and duplex-specific nuclease amplification reaction (DSNAR). Recent studies show a sensitive detection method for miRNA in various exosomes using RCA technology to detect miRNA-21, miRNA-122, and miRNA-155 (Wang et al., 2021) in exosomes at the same time. Compared with conventional methods, it has the advantage of multiple detection and simplicity of RCA. Enzyme-free isothermal amplification methods for miRNA detection include catalytic hairpin assembly (CHA) and hybrid chain reaction (HCR) (Gines et al., 2020). Guo et al. (2020) developed a label-free sensitive electrochemical detection method based on HCR for signal amplification to detect miRNA-122 in exosomes (Figure 9), and the detection limit was as low as 53 a.m.

Table 2 shows the advantages and disadvantages of current detection methods for miRNA. With fast development of quantitative detection technology, the emergence of EV miRNA has become a particular and sensitive diagnostic and prognostic biomarker that is expected to be used for noninvasive detection of diseases.

6 Summary and future prospect

In this review, we have discussed the mechanisms for miRNA sorting in EVs and diagnostic value of EV-derived miRNA in diseases. We then summarized the isolation methods for EVs and EVs' miRNA-related detection technologies. Moreover, we also illuminated the advantages and disadvantages of each method, that can be valuable for deciding the most suitable isolation and detection methods in different situations.

Ample progress has been made in studies on EV-derived miRNAs in a plethora of diseases, but there are still many challenges with unclear mechanisms. However, the current EV-derived miRNA extraction technology still has many challenges to solve. First, the inefficient EV separation method may lead to the loss of many EVs, affecting the downstream analysis of EVs contents. Second, the EV-derived miRNA extraction refers to extraction method for miRNA from cells and body fluids. For example, the TRIzol method is widely used to extract nucleic acids, but it has limitations such as complicated operation and high miRNA loss, which hinder the application of EV-derived miRNA for clinical diagnosis.

Many disease-related EV miRNAs have been discovered, and detection of EV miRNA has made significant progress and is now close to commercial application. It has significant social value and economic benefits to develop a new method for automatic, rapid isolation of EVs and extraction of miRNA in large samples. In the aspect of EV isolation, the method can be improved to get EVs with high purity by employing various methods, such as using magnetic beads or microfluidics technology. For the miRNA detection, the application of multiple detections of different EVs' miRNA and detection of EV miRNA in combination with EV-related membrane proteins, DNA, or

TABLE 2 Summary of EV-derived miRNA detection methods.

Method	Time	Advantages	Disadvantages	References
RT-qPCR	>2 h	Gold standard method, high sensitivity	Time-consuming for heating, many other influencing factor	Jiang et al. (2021b)
ddPCR	>2 h	High sensitivity	Special equipment, unable to popularize	Wang et al. (2019), Zhou et al. (2021)
MB *in situ*	<1 h	Simple operation, no amplification, *in situ*	Low sensitivity	Lee et al. (2018)
SERS	~1 h	Low cost and simple operation	High requirements for chip manufacturing, Low repeatability, special equipment, unable to popularize	Pang et al. (2019)
Microarray	~2 days	Detect many sequences at once	High cost and time-consuming for a small number of samples, unable to popularize	Nakamaru et al. (2020), Tan et al. (2021)
NGS	3–7 days	Find unknown miRNA	Time-consuming and high cost	Selmaj et al. (2017)
Enzymatic isothermal amplification	>1 h	High amplification efficiency without heating	Complex primer design, not easy to realize multiple detection	Wang et al. (2021)
Enzyme free isothermal amplification	>2 h	No enzyme, low cost	Complex primer design	Guo et al. (2020)

glycoproteins can improve the sensitivity and specificity of the detection methods. Detection of miRNA from a single EV ensures the integrity of the EV structure and information without extraction of RNA, which is the direction for future development. For some EV-derived miRNAs associated with acute diseases, the development of simple, rapid, and sensitive miRNA extraction and detection POCT technology is also one of the future research directions.

Author contributions

Writing—original draft preparation and writing: DX and KD. Review and suggestion: BF, JW, XG, YS, and AK. Supervision and conceptualization: PL and ZL. All authors have agreed to be accountable for the content of the work.

Funding

This study was supported by the National Natural Science Foundation of China (61971216), Key Research and Development Project of Jiangsu Province (BE2019603, BE2019761, BE2022692 and BE2020768), Nanjing Important Science & Technology Specific Projects (2021-11005), Nanjing Science and Technology Development Plan Project (202205066), the National Natural Science Foundation of China (82103578) and Doctoral Program of Entrepreneurship and Innovation of Jiangsu Province (JSSCBS20211509).

Conflict of interest

The authors declare that the research was conducted in the absence of any commercial or financial relationships that could be construed as a potential conflict of interest.

Publisher's note

All claims expressed in this article are solely those of the authors and do not necessarily represent those of their affiliated organizations, or those of the publisher, the editors, and the reviewers. Any product that may be evaluated in this article, or claim that may be made by its manufacturer, is not guaranteed or endorsed by the publisher.

References

Alexandra, M. M., Luca, S., Nancy, B., Katherine, H., Hamza, A., Johnathan, R., et al. (2022). Next-generation sequencing of cerebrospinal fluid for clinical molecular diagnostics in pediatric, adolescent and young adult (AYA) brain tumor patients. *Neuro. Oncol.*, noac035. doi:10.1093/neuonc/noac035

Ashley, J., Cordy, B., Lucia, D., Fradkin, L. G., Budnik, V., and Thomson, T. (2018). Retrovirus-like gag protein Arc1 binds RNA and traffics across synaptic boutons. *Cell* 172 (1-2), 262–274. e11. doi:10.1016/j.cell.2017.12.022

Baglio, S. R., Rooijers, K., Koppers-Lalic, D., Verweij, F. J., Lanzon, M. P., Zini, N., et al. (2015). Human bone marrow- and adipose-mesenchymal stem cells secrete exosomes enriched in distinctive miRNA and tRNA species. *Stem Cell Res. Ther.* 6, 127. doi:10.1186/s13287-015-0116-z

Bandini, E. (2021). Urinary microRNA and mRNA in tumors. *Methods Mol. Biol.* 2292, 57–72. doi:10.1007/978-1-0716-1354-2_6

Bao, L. L., You, B., Shi, S., Shan, Y., Zhang, Q. C., Yue, H. J., et al. (2018). Metastasis-associated miR-23a from nasopharyngeal carcinoma-derived exosomes

mediates angiogenesis by repressing a novel target gene TSGA10. *Oncogene* 37 (21), 2873–2889. doi:10.1038/s41388-018-0183-6

Bebelman, M. P., Smit, M. J., Pegtel, D. M., and Baglio, S. R. (2018). Biogenesis and function of extracellular vesicles in cancer. *Pharmacol. Ther.* 188, 1–11. doi:10.1016/j.pharmthera.2018.02.013

Boing, A. N., van der Pol, E., Grootemaat, A. E., Coumans, F. A., Sturk, A., and Nieuwland, R. (2014). Single-step isolation of extracellular vesicles by size-exclusion chromatography. *J. Extracell. Vesicles* 3 (1), 23430. doi:10.3402/jev.v3.23430

Brown, R. A. M., Epis, M. R., Horsham, J. L., Kabir, T. D., Richardson, K. L., and Leedman, P. J. (2018). Total RNA extraction from tissues for microRNA and target gene expression analysis: Not all kits are created equal. *BMC Biotechnol.* 18 (1), 16. doi:10.1186/s12896-018-0421-6

Burgos, K. L., Javaherian, A., Bomprezzi, R., Ghaffari, L., Rhodes, S., Courtright, A., et al. (2013). Identification of extracellular miRNA in human cerebrospinal fluid by next-generation sequencing. *RNA* 19 (5), 712–722. doi:10.1261/rna.036863.112

Cai, X., Janku, F., Zhan, Q. M., and Fan, J. B. (2015). Accessing genetic information with liquid biopsies. *Trends Genet.* 31 (10), 564–575. doi:10.1016/j.tig.2015.06.001

Chaput, N., and Thery, C. (2011). Exosomes: Immune properties and potential clinical implementations. *Semin. Immunopathol.* 33 (5), 419–440. doi:10.1007/s00281-010-0233-9

Chen, Y. C., Zhu, Q. F., Cheng, L. M., Wang, Y., Li, M., Yang, Q. S., et al. (2021). Exosome detection via the ultrafast-isolation system: Exodus. *Nat. Methods* 18 (2), 212–218. doi:10.1038/s41592-020-01034-x

Chen, Y. H., and Wang, H. Y. (2021). The association between migraine and depression based on miRNA biomarkers and cohort studies. *Curr. Med. Chem.* 28 (27), 5648–5656. doi:10.2174/0929867327666201117100026

Cheng, J. Y., Yang, A. M., Cheng, S. J., Feng, L., Wu, X., Lu, X. H., et al. (2020). Circulating miR-19a-3p and miR-483-5p as novel diagnostic biomarkers for the early diagnosis of gastric cancer. *Med. Sci. Monit.* 26, e923444. doi:10.12659/msm.923444

Cheng, L., Doecke, J. D., Sharples, R. A., Villemagne, V. L., Fowler, C. J., Rembach, A., et al. (2015). Prognostic serum miRNA biomarkers associated with Alzheimer's disease shows concordance with neuropsychological and neuroimaging assessment. *Mol. Psychiatry* 20 (10), 1188–1196. doi:10.1038/mp.2014.127

Chiarugi, P., and Cirri, P. (2016). Metabolic exchanges within tumor microenvironment. *Cancer Lett.* 380 (1), 272–280. doi:10.1016/j.canlet.2015.10.027

Choi, E. S., Al Faruque, H., Kim, J. H., Kim, K. J., Choi, J. E., Kim, B. A., et al. (2021). CD5L as an extracellular vesicle-derived biomarker for liquid biopsy of lung cancer. *Diagnostics* 11 (4), 620. doi:10.3390/diagnostics11040620

Chomczynski, P., and Sacchi, N. (2006). The single-step method of RNA isolation by acid guanidinium thiocyanate-phenol-chloroform extraction: Twenty-something years on. *Nat. Protoc.* 1 (2), 581–585. doi:10.1038/nprot.2006.83

Chu, X. L., Liu, D. X., Li, T. T., Ke, H. F., Xin, D. Q., Wang, S. H., et al. (2020). Hydrogen sulfide-modified extracellular vesicles from mesenchymal stem cells for treatment of hypoxic-ischemic brain injury. *J. Control. Release* 328, 13–27. doi:10.1016/j.jconrel.2020.08.037

Cocucci, E., and Meldolesi, J. (2015). Ectosomes and exosomes: Shedding the confusion between extracellular vesicles. *Trends Cell Biol.* 25 (6), 364–372. doi:10.1016/j.tcb.2015.01.004

Cortez, M. A., Bueso-Ramos, C., Ferdin, J., Lopez-Berestein, G., Sood, A. K., and Calin, G. A. (2011). MicroRNAs in body fluids-the mix of hormones and biomarkers. *Nat. Rev. Clin. Oncol.* 8 (8), 467–477. doi:10.1038/nrclinonc.2011.76

Coughlan, C., Bruce, K. D., Burgy, O., Boyd, T. D., Michel, C. R., Garcia-Perez, J. E., et al. (2020). Exosome isolation by ultracentrifugation and precipitation and techniques for downstream analyses. *Curr. Protoc. Cell Biol.* 88 (1), e110. doi:10.1002/cpcb.110

Cui, Y., Xu, H. F., Liu, M. Y., Xu, Y. J., He, J. C., Zhou, Y., et al. (2019). Mechanism of exosomal microRNA-224 in development of hepatocellular carcinoma and its diagnostic and prognostic value. *World J. Gastroenterol.* 25 (15), 1890–1898. doi:10.3748/wjg.v25.i15.1890

Dao, T. N. T., Kim, M. G., Koo, B., Liu, H. F., Jang, Y. O., Lee, H. J., et al. (2022). Chimeric nanocomposites for the rapid and simple isolation of urinary extracellular vesicles. *J. Extracell. Vesicles* 11 (2), e12195. doi:10.1002/jev2.12195

Dar, G. H., Mendes, C. C., Kuan, W. L., Speciale, A. A., Conceicao, M., Gorgens, A., et al. (2021). GAPDH controls extracellular vesicle biogenesis and enhances the therapeutic potential of EV mediated siRNA delivery to the brain. *Nat. Commun.* 12 (1), 6666. doi:10.1038/s41467-021-27056-3

Deng, R. J., Zhang, K. X., and Li, J. H. (2017). Isothermal amplification for MicroRNA detection: From the test tube to the cell. *Acc. Chem. Res.* 50 (4), 1059–1068. doi:10.1021/acs.accounts.7b00040

Devhare, P. B., Sasaki, R., Shrivastava, S., Di Bisceglie, A. M., Ray, R., and Ray, R. B. (2017). Exosome-mediated intercellular communication between hepatitis C virus-infected hepatocytes and hepatic stellate cells. *J. Virol.* 91, e02225–e02216. doi:10.1128/jvi.02225-16

Dong, Z. W., Gu, H. J., Guo, Q., Liang, S., Xue, J., Yao, F., et al. (2021). Profiling of serum exosome miRNA reveals the potential of a miRNA panel as diagnostic biomarker for Alzheimer's Disease. *Mol. Neurobiol.* 58 (7), 3084–3094. doi:10.1007/s12035-021-02323-y

Driskell, J. D., Seto, A. G., Jones, L. P., Jokela, S., Dluhy, R. A., Zhao, Y. P., et al. (2008). Rapid microRNA (miRNA) detection and classification via surface-enhanced Raman spectroscopy (SERS). *Biosens. Bioelectron. X.* 24 (4), 917–922. doi:10.1016/j.bios.2008.07.060

Drula, R., Ott, L. F., Berindan-Neagoe, I., Pantel, K., and Calin, G. A. (2020). MicroRNAs from liquid biopsy derived extracellular vesicles: Recent advances in detection and characterization methods. *Cancers* 12 (8), 2009. doi:10.3390/cancers12082009

Duy, J., Koehler, J. W., Honko, A. N., and Minogue, T. D. (2015). Optimized microRNA purification from TRIzol-treated plasma. *BMC Genomics* 16, 95. doi:10.1186/s12864-015-1299-5

Fang, Y. L., Liu, H. R., Wang, Y., Su, X. Y., Jin, L., Wu, Y. Q., et al. (2021). Fast and accurate control strategy for portable nucleic acid detection (PNAD) system based on magnetic nanoparticles. *J. Biomed. Nanotechnol.* 17 (3), 407–415. doi:10.1166/jbn.2021.3028

Ferri, C., Di Biase, A., Bocchetti, M., Zappavigna, S., Wagner, S., Le Vu, P., et al. (2022). MiR-423-5p prevents MALAT1-mediated proliferation and metastasis in prostate cancer. *J. Exp. Clin. Cancer Res.* 41 (1), 20. doi:10.1186/s13046-021-02233-w

Friedman, R. C., Farh, K. K. H., Burge, C. B., and Bartel, D. P. (2009). Most mammalian mRNAs are conserved targets of microRNAs. *Genome Res.* 19 (1), 92–105. doi:10.1101/gr.082701.108

Gao, F. Y., Jiao, F. L., Xia, C. S., Zhao, Y., Ying, W. T., Xie, Y. P., et al. (2019a). A novel strategy for facile serum exosome isolation based on specific interactions between phospholipid bilayers and TiO2. *Chem. Sci.* 10 (6), 1579–1588. doi:10.1039/c8sc04197k

Gao, X., Li, S., Ding, F., Fan, H., Shi, L., Zhu, L., et al. (2019b). Rapid detection of exosomal MicroRNAs using virus-mimicking fusogenic vesicles. *Angew. Chem. Int. Ed.* 58 (26), 8719–8723. doi:10.1002/anie.201901997

Gardiner, C., Di Vizio, D., Sahoo, S., Thery, C., Witwer, K. W., Wauben, M., et al. (2016). Techniques used for the isolation and characterization of extracellular vesicles: Results of a worldwide survey. *J. Extracell. Vesicles* 5, 32945. doi:10.3402/jev.v5.32945

Gines, G., Menezes, R., Xiao, W. J., Rondelez, Y., and Taly, V. (2020). Emerging isothermal amplification technologies for microRNA biosensing: Applications to liquid biopsies. *Mol. Aspects Med.* 72, 100832. doi:10.1016/j.mam.2019.11.002

Glokler, J., Lim, T. S., Ida, J., and Frohme, M. (2021). Isothermal amplifications - a comprehensive review on current methods. *Crit. Rev. Biochem. Mol. Biol.* 56 (6), 543–586. doi:10.1080/10409238.2021.1937927

Greening, D. W., Xu, R., Ji, H., Tauro, B. J., and Simpson, R. J. (2015). A protocol for exosome isolation and characterization: Evaluation of ultracentrifugation, density-gradient separation, and immunoaffinity capture methods. *Methods Mol. Biol.* 1295, 179–209. doi:10.1007/978-1-4939-2550-6_15

Griffin, J. R., Jun, T., Liaw, B. C.-H., Guin, S., Tsao, C.-K., Patel, V. G., et al. (2022). Clinical utility of next-generation sequencing for prostate cancer in the context of a changing treatment landscape. *J. Clin. Oncol.* 40 (6), 112. doi:10.1200/JCO.2022.40.6_suppl.112

Groot, M., and Lee, H. (2020). Sorting mechanisms for microRNAs into extracellular vesicles and their associated diseases. *Cells* 9 (4), 1044. doi:10.3390/cells9041044

Gui, C. P., Liao, B., Luo, C. G., Chen, Y. H., Tan, L., Tang, Y. M., et al. (2021). circCHST15 is a novel prognostic biomarker that promotes clear cell renal cell carcinoma cell proliferation and metastasis through the miR-125a-5p/EIF4EBP1 axis. *Mol. Cancer* 20 (1), 169. doi:10.1186/s12943-021-01449-w

Guo, J. H., Wu, C. H., Lin, X. Y., Zhou, J., Zhang, J. Y., Zheng, W. T., et al. (2021). Establishment of a simplified dichotomic size-exclusion chromatography for isolating extracellular vesicles toward clinical applications. *J. Extracell. Vesicles* 10 (11), e12145. doi:10.1002/jev2.12145

Guo, Q. Q., Yu, Y. Q., Zhang, H., Cai, C. X., and Shen, Q. M. (2020). Electrochemical sensing of exosomal MicroRNA based on hybridization chain reaction signal amplification with reduced false-positive signals. *Anal. Chem.* 92 (7), 5302–5310. doi:10.1021/acs.analchem.9b05849

Guo, S. W., Perets, N., Betzer, O., Ben-Shaul, S., Sheinin, A., Michaelevski, I., et al. (2019). Intranasal delivery of mesenchymal stem cell derived

exosomes loaded with phosphatase and tensin homolog siRNA repairs complete spinal cord injury. *ACS Nano* 13 (9), 10015–10028. doi:10.1021/acsnano.9b01892

Gupta, A., and Pulliam, L. (2014). Exosomes as mediators of neuroinflammation. *J. Neuroinflammation* 11, 68. doi:10.1186/1742-2094-11-68

Gurunathan, S., Kang, M. H., Jeyaraj, M., Qasim, M., and Kim, J. H. (2019). Review of the isolation, characterization, biological function, and multifarious therapeutic approaches of exosomes. *Cells* 8 (4), 307. doi:10.3390/cells8040307

Haraszti, R. A., Miller, R., Stoppato, M., Sere, Y. Y., Coles, A., Didiot, M. C., et al. (2018). Exosomes produced from 3D cultures of MSCs by tangential flow filtration show higher yield and improved activity. *Mol. Ther.* 26 (12), 2838–2847. doi:10.1016/j.ymthe.2018.09.015

Harmati, M., Gyukity-Sebestyen, E., Dobra, G., Janovak, L., Dekany, I., Saydam, O., et al. (2019). Small extracellular vesicles convey the stress-induced adaptive responses of melanoma cells. *Sci. Rep.* 9, 15329. doi:10.1038/s41598-019-51778-6

Hassanpour Tamrin, S., Sanati Nezhad, A., and Sen, A. (2021). Label-free isolation of exosomes using microfluidic technologies. *ACS Nano* 15 (11), 17047–17079. doi:10.1021/acsnano.1c03469

He, D. G., Wang, H. Z., Ho, S. E. L., Chan, H. G., Hai, L., He, X. X., et al. (2019). Total internal reflection-based single-vesicle *in situ* quantitative and stoichiometric analysis of tumor-derived exosomal microRNAs for diagnosis and treatment monitoring. *Theranostics* 9 (15), 4494–4507. doi:10.7150/thno.33683

He, Q. G., Liu, J., Liang, J., Liu, X. P., Li, W., Liu, Z., et al. (2018). Towards improvements for penetrating the blood-brain barrier-recent progress from a material and pharmaceutical perspective. *Cells* 7 (4), 24. doi:10.3390/cells7040024

Hergenreider, E., Heydt, S., Treguer, K., Boettger, T., Horrevoets, A. J. G., Zeiher, A. M., et al. (2012). Atheroprotective communication between endothelial cells and smooth muscle cells through miRNAs. *Nat. Cell Biol.* 14 (3), 249–256. doi:10.1038/ncb2441

Hindson, C. M., Chevillet, J. R., Briggs, H. A., Gallichotte, E. N., Ruf, I. K., Hindson, B. J., et al. (2013). Absolute quantification by droplet digital PCR versus analog real-time PCR. *Nat. Methods* 10 (10), 1003–1005. doi:10.1038/nmeth.2633

Hu, Y., Rao, S. S., Wang, Z. X., Cao, J., Tan, Y. J., Luo, J., et al. (2018). Exosomes from human umbilical cord blood accelerate cutaneous wound healing through miR-21-3p-mediated promotion of angiogenesis and fibroblast function. *Theranostics* 8 (1), 169–184. doi:10.7150/thno.21234

Hu, Z. B., Chen, X., Zhao, Y., Tian, T., Jin, G. F., Shu, Y. Q., et al. (2010). Serum microRNA signatures identified in a genome-wide serum microRNA expression profiling predict survival of non-small-cell lung cancer. *J. Clin. Oncol.* 28 (10), 1721–1726. doi:10.1200/jco.2009.24.9342

Huang, L., Su, E. B., Liu, Y., He, N. Y., Deng, Y., Jin, L., et al. (2021). A microfluidic device for accurate detection of hs-cTnI. *Chin. Chem. Lett.* 32 (4), 1555–1558. doi:10.1016/j.cclet.2020.09.055

Iliescu, F. S., Vrtacnik, D., Neuzil, P., and Iliescu, C. (2019). Microfluidic technology for clinical applications of exosomes. *Micromachines* 10 (6), 392. doi:10.3390/mi10060392

Issman, L., Brenner, B., Talmon, Y., and Aharon, A. (2013). Cryogenic transmission electron microscopy nanostructural study of shed microparticles. *PLoS One* 8 (12), e83680. doi:10.1371/journal.pone.0083680

Jan, A. T., Rahman, S., Khan, S., Tasduq, S. A., and Choi, I. (2019). Biology, pathophysiological role, and clinical implications of exosomes: A critical appraisal. *Cells* 8 (2), 99. doi:10.3390/cells8020099

Jiang, S. Q., Li, Q., Wang, C. W., Pang, Y. F., Sun, Z. W., and Xiao, R. (2021a). *In situ* exosomal MicroRNA determination by target-triggered SERS and Fe3O4@TiO2-based exosome accumulation. *ACS Sens.* 6 (3), 852–862. doi:10.1021/acssensors.0c01900

Jiang, X., Li, J. Y., Zhang, B. Q., Hu, J. M., Ma, J. L., Cui, L. L., et al. (2021b). Differential expression profile of plasma exosomal microRNAs in women with polycystic ovary syndrome. *Fertil. Steril.* 115 (3), 782–792. doi:10.1016/j.fertnstert.2020.08.019

Jin, X. C., Chen, Y. F., Chen, H. B., Fei, S. R., Chen, D. D., Cai, X. N., et al. (2017). Evaluation of tumor-derived exosomal miRNA as potential diagnostic biomarkers for early-stage non-small cell lung cancer using next-generation sequencing. *Clin. Cancer Res.* 23 (17), 5311–5319. doi:10.1158/1078-0432.Ccr-17-0577

Joyce, D. P., Kerin, M. J., and Dwyer, R. M. (2016). Exosome-encapsulated microRNAs as circulating biomarkers for breast cancer. *Int. J. Cancer* 139 (7), 1443–1448. doi:10.1002/ijc.30179

Kalayinia, S., Arjmand, F., Maleki, M., Malakootian, M., and Singh, C. P. (2021). MicroRNAs: Roles in cardiovascular development and disease. *Cardiovasc. Pathol.* 50, 107296. doi:10.1016/j.carpath.2020.107296

Kalluri, R., and LeBleu, V. S. (2020). The biology, function, and biomedical applications of exosomes. *Science* 367 (6478), eaau6977. doi:10.1126/science.aau6977

Kamal, N., Awang, R. A. R., Mohamad, S., and Shahidan, W. N. S. (2020). Plasma- and saliva exosome profile reveals a distinct MicroRNA signature in chronic periodontitis. *Front. Physiol.* 11, 587381. doi:10.3389/fphys.2020.587381

Keller, S., Ridinger, J., Rupp, A. K., Janssen, J. W. G., and Altevogt, P. (2011). Body fluid derived exosomes as a novel template for clinical diagnostics. *J. Transl. Med.* 9, 86. doi:10.1186/1479-5876-9-86

Kim, Y. K., Yeo, J., Kim, B., Ha, M., and Kim, V. N. (2012). Short structured RNAs with low GC content are selectively lost during extraction from a small number of cells. *Mol. Cell* 46 (6), 893–895. doi:10.1016/j.molcel.2012.05.036

Kneipp, K., Wang, Y., Kneipp, H., Itzkan, I. I., Dasari, R. R., and Feld, M. S. (1996). Population pumping of excited vibrational states by spontaneous surface-enhanced Raman scattering. *Phys. Rev. Lett.* 76 (14), 2444–2447. doi:10.1103/PhysRevLett.76.2444

Koh, Y. Q., Almughlliq, F. B., Vaswani, K., Peiris, H. N., and Mitchell, M. D. (2018). Exosome enrichment by ultracentrifugation and size exclusion chromatography. *Front. Biosci.* 23, 4621–4874. doi:10.2741/4621

Kosaka, N., Iguchi, H., Hagiwara, K., Yoshioka, Y., Takeshita, F., and Ochiya, T. (2013). Neutral sphingomyelinase 2 (nSMase2)-dependent exosomal transfer of angiogenic microRNAs regulate cancer cell metastasis. *J. Biol. Chem.* 288 (15), 10849–10859. doi:10.1074/jbc.M112.446831

Ku, A., Lim, H. C., Evander, M., Lilja, H., Laurell, T., Scheding, S., et al. (2018). Acoustic enrichment of extracellular vesicles from biological fluids. *Anal. Chem.* 90 (13), 8011–8019. doi:10.1021/acs.analchem.8b00914

Lasser, C., Alikhani, V. S., Ekstrom, K., Eldh, M., Paredes, P. T., Bossios, A., et al. (2011). Human saliva, plasma and breast milk exosomes contain RNA: Uptake by macrophages. *J. Transl. Med.* 9, 9. doi:10.1186/1479-5876-9-9

Lee, J. H., Kim, J. A., Kwon, M. H., Kang, J. Y., and Rhee, W. J. (2015a). *In situ* single step detection of exosome microRNA using molecular beacon. *Biomaterials* 54, 116–125. doi:10.1016/j.biomaterials.2015.03.014

Lee, J., Kwon, M. H., Kim, J. A., and Rhee, W. J. (2018). Detection of exosome miRNAs using molecular beacons for diagnosing prostate cancer. *Artif. Cells Nanomedicine Biotechnol.* 46 (3), S52–S63. doi:10.1080/21691401.2018.1489263

Lee, J. U., Kim, W. H., Lee, H. S., Park, K. H., and Sim, S. J. (2019). Quantitative and specific detection of exosomal miRNAs for accurate diagnosis of breast cancer using a surface-enhanced Raman scattering sensor based on plasmonic head-flocked gold nanopillars. *Small* 15, 1804968. doi:10.1002/smll.201804968

Lee, K., Shao, H., Weissleder, R., and Lee, H. (2015b). Acoustic purification of extracellular microvesicles. *ACS Nano* 9 (3), 2321–2327. doi:10.1021/nn506538f

Lee, Y., El Andaloussi, S., and Wood, M. J. A. (2012). Exosomes and microvesicles: Extracellular vesicles for genetic information transfer and gene therapy. *Hum. Mol. Genet.* 21, R125–R134. doi:10.1093/hmg/dds317

Li, M., Lou, D. D., Chen, J. Y., Shi, K. Q., Wang, Y., Zhu, Q. F., et al. (2021). Deep dive on the proteome of salivary extracellular vesicles: Comparison between ultracentrifugation and polymer-based precipitation isolation. *Anal. Bioanal. Chem.* 413 (2), 365–375. doi:10.1007/s00216-020-03004-w

Li, P., Luo, X. D., Xie, Y., Li, P. F., Hu, F. Y., Chu, J. F., et al. (2020). GC-derived EVs enriched with MicroRNA-675-3p contribute to the MAPK/PD-L1-Mediated tumor immune escape by targeting CXXC4. *Mol. Ther. - Nucleic Acids* 22, 615–626. doi:10.1016/j.omtn.2020.08.020

Li, Z. Y., Hu, C. Y., Jia, J., Xia, Y. Y., Xie, H., She, M. J., et al. (2019). Establishment and evaluation of a simple size-selective method for exosome enrichment and purification. *J. Biomed. Nanotechnol.* 15 (5), 1090–1096. doi:10.1166/jbn.2019.2768

Lin, Z., Wong, A., and Alam, S. (2022). Extraction of exosomes and exosomal miRNA from mesenchymal stem cells. *Methods Mol. Biol.* 2455, 333–341. doi:10.1007/978-1-0716-2128-8_25

Liu, H., Zhou, J., and Huang, H. (2015). Amine-functionalized TiO(2) nanoparticles for highly selective enrichment of phosphopeptides. *Talanta* 143, 431–437. doi:10.1016/j.talanta.2015.05.019

Liu, J.-R., Cai, G.-Y., Ning, Y.-C., Wang, J.-C., Lv, Y., Guo, Y.-N., et al. (2020). Caloric restriction alleviates aging-related fibrosis of kidney through downregulation of miR-21 in extracellular vesicles. *Aging* 12, 18052–18072. doi:10.18632/aging.103591

Liu, J. M., Zhou, F. H., Guan, Y. J., Meng, F. D., Zhao, Z. H., Su, Q., et al. (2022). The biogenesis of miRNAs and their role in the development of amyotrophic lateral sclerosis. *Cells* 11 (3), 572. doi:10.3390/cells11030572

Lobb, R. J., Becker, M., Wen, S. W., Wong, C. S., Wiegmans, A. P., Leimgruber, A., et al. (2015). Optimized exosome isolation protocol for cell culture supernatant and human plasma. *J. Extracell. Vesicles* 4 (1), 27031. doi:10.3402/jev.v4.27031

Ludwig, A. K., De Miroschedji, K., Doeppner, T. R., Borger, V., Ruesing, J., Rebmann, V., et al. (2018). Precipitation with polyethylene glycol followed by washing and pelleting by ultracentrifugation enriches extracellular vesicles from tissue culture supernatants in small and large scales. *J. Extracell. Vesicles* 7 (1), 1528109. doi:10.1080/20013078.2018.1528109

Ludwig, N., Rubenich, D. S., Zareba, L., Siewiera, J., Pieper, J., Braganhol, E., et al. (2020). Potential roles of tumor cell- and stroma cell-derived small extracellular vesicles in promoting a pro-angiogenic tumor microenvironment. *Cancers* 12 (12), 3599. doi:10.3390/cancers12123599

Lv, L.-L., Cao, Y.-H., Ni, H.-F., Xu, M., Liu, D., Liu, H., et al. (2013). MicroRNA-29c in urinary exosome/microvesicle as a biomarker of renal fibrosis. *Am. J. Physiology-Renal Physiology* 305, F1220–F1227. doi:10.1152/ajprenal.00148.2013

Mahmudunnabi, R. G., Umer, M., Seo, K. D., Park, D. S., Chung, J. H., Shiddiky, M. J. A., et al. (2022). Exosomal microRNAs array sensor with a bioconjugate composed of p53 protein and hydrazine for the specific lung cancer detection. *Biosens. Bioelectron. X.* 207, 114149. doi:10.1016/j.bios.2022.114149

Makarova, J., Turchinovich, A., Shkurnikov, M., and Tonevitsky, A. (2021). Extracellular miRNAs and cell-cell communication: Problems and prospects. *Trends Biochem. Sci.* 46 (8), 640–651. doi:10.1016/j.tibs.2021.01.007

Mancera-Arteu, M., Lleshi, N., Sanz-Nebot, V., Gimenez, E., and Benavente, F. (2020). Analysis of glycopeptide biomarkers by on-line TiO2 solid-phase extraction capillary electrophoresis-mass spectrometry. *Talanta* 209, 120563. doi:10.1016/j.talanta.2019.120563

Mao, D., Zheng, M., Li, W., Xu, Y., Wang, C., Qian, Q., et al. (2022). Cubic DNA nanocage-based three-dimensional molecular beacon for accurate detection of exosomal miRNAs in confined spaces. *Biosens. Bioelectron.* 204, 114077. doi:10.1016/j.bios.2022.114077

Mao, L., Li, X., Gong, S., Yuan, H. Y., Jiang, Y., Huang, W. J., et al. (2018a). Serum exosomes contain ECRG4 mRNA that suppresses tumor growth via inhibition of genes involved in inflammation, cell proliferation, and angiogenesis. *Cancer Gene Ther.* 25 (9-10), 248–259. doi:10.1038/s41417-018-0032-3

Mao, L., Liu, S. M., Hu, L., Jia, L., Wang, H. R., Guo, M. M., et al. (2018b). miR-30 family: A promising regulator in development and disease. *Biomed Res. Int.* 2018, 1–8. doi:10.1155/2018/9623412

Markoutsa, E., Mayilsamy, K., Gulick, D., Mohapatra, S. S., and Mohapatra, S. (2022). Extracellular vesicles derived from inflammatory-educated stem cells reverse brain inflammation-implication of miRNAs. *Mol. Ther.* 30 (1), 816–830. doi:10.1016/j.ymthe.2021.08.008

Mathieu, M., Martin-Jaular, L., Lavieu, G., and Thery, C. (2019). Specificities of secretion and uptake of exosomes and other extracellular vesicles for cell-to-cell communication. *Nat. Cell Biol.* 21 (1), 9–17. doi:10.1038/s41556-018-0250-9

Matkovich, S. J., Van Booven, D. J., Youker, K. A., Torre-Amione, G., Diwan, A., Eschenbacher, W. H., et al. (2009). Reciprocal regulation of myocardial microRNAs and messenger RNA in human cardiomyopathy and reversal of the microRNA signature by biomechanical support. *Circulation* 119 (9), 1263–1271. doi:10.1161/circulationaha.108.813576

McAlexander, M. A., Phillips, M. J., and Witwer, K. W. (2013). Comparison of methods for miRNA extraction from plasma and quantitative recovery of RNA from cerebrospinal fluid. *Front. Genet.* 4, 83. doi:10.3389/fgene.2013.00083

Michaela, S., and Aigner, A. (2021). Nucleic acid delivery with extracellular vesicles. *Adv. Drug Deliv. Rev.* 173, 89–111. doi:10.1016/j.addr.2021.03.005

Min, Q.-H., Chen, X.-M., Zou, Y.-Q., Zhang, J., Li, J., Wang, Y., et al. (2017). Differential expression of urinary exosomal microRNAs in IgA nephropathy. *J. Clin. Lab. Anal.* 32, e22226. doi:10.1002/jcla.22226

Mir, R., Elfaki, I., Khullar, N., Waza, A. A., Jha, C., Mir, M. M., et al. (2021). Role of selected miRNAs as diagnostic and prognostic biomarkers in cardiovascular diseases, including coronary artery disease, myocardial infarction and atherosclerosis. *J. Cardiovasc. Dev. Dis.* 8 (2), 22. doi:10.3390/jcdd8020022

Mitchell, P. S., Parkin, R. K., Kroh, E. M., Fritz, B. R., Wyman, S. K., Pogosova-Agadjanyan, E. L., et al. (2008). Circulating microRNAs as stable blood-based markers for cancer detection. *Proc. Natl. Acad. Sci. U. S. A.* 105 (30), 10513–10518. doi:10.1073/pnas.0804549105

Moloudizargari, M., Hekmatirad, S., Mofarahe, Z. S., and Asghari, M. H. (2021). Exosomal microRNA panels as biomarkers for hematological malignancies. *Curr. Problems Cancer* 45 (5), 100726. doi:10.1016/j.currproblcancer.2021.100726

Momen-Heravi, F., Getting, S. J., and Moschos, S. A. (2018). Extracellular vesicles and their nucleic acids for biomarker discovery. *Pharmacol. Ther.* 192, 170–187. doi:10.1016/j.pharmthera.2018.08.002

Momen-Heravi, F. (2017). Isolation of extracellular vesicles by ultracentrifugation. *Methods Mol. Biol.* 1660, 25–32. doi:10.1007/978-1-4939-7253-1_3

Momen-Heravi, F., Saha, B., Kodys, K., Catalano, D., Satishchandran, A., and Szabo, G. (2015). Increased number of circulating exosomes and their microRNA cargos are potential novel biomarkers in alcoholic hepatitis. *J. Transl. Med.* 13, 261. doi:10.1186/s12967-015-0623-9

Monguio-Tortajada, M., Galvez-Monton, C., Bayes-Genis, A., Roura, S., and Borras, F. E. (2019). Extracellular vesicle isolation methods: Rising impact of size-exclusion chromatography. *Cell. Mol. Life Sci.* 76 (12), 2369–2382. doi:10.1007/s00018-019-03071-y

Montecalvo, A., Larregina, A. T., and Morelli, A. E. (2013). Methods of analysis of dendritic cell-derived exosome-shuttle microRNA and its horizontal propagation between dendritic cells. *Methods Mol. Biol.* 1024, 19–40. doi:10.1007/978-1-62703-453-1_3

Montecalvo, A., Larregina, A. T., Shufesky, W. J., Stolz, D. B., Sullivan, M. L. G., Karlsson, J. M., et al. (2012). Mechanism of transfer of functional microRNAs between mouse dendritic cells via exosomes. *Blood* 119 (3), 756–766. doi:10.1182/blood-2011-02-338004

Murugesan, S., Saravanakumar, L., Powell, M. F., Rajasekaran, N. S., Kannappan, R., and Berkowitz, D. E. (2021). Role of exosomal microRNA signatures: An emerging factor in preeclampsia-mediated cardiovascular disease. *Placenta* 103, 226–231. doi:10.1016/j.placenta.2020.10.033

Nakamaru, K., Tomiyama, T., Kobayashi, S., Ikemune, M., Tsukuda, S., Ito, T., et al. (2020). Extracellular vesicles microRNA analysis in type 1 autoimmune pancreatitis: Increased expression of microRNA-21. *Pancreatology* 20 (3), 318–324. doi:10.1016/j.pan.2020.02.012

Newman, L. A., Useckaite, Z., Johnson, J., Sorich, M. J., Hopkins, A. M., and Rowland, A. (2022). Selective isolation of liver-derived extracellular vesicles redefines performance of miRNA biomarkers for non-alcoholic fatty liver disease. *Biomedicines* 10, 195. doi:10.3390/biomedicines10010195

Nigro, A., Finardi, A., Ferraro, M. M., Manno, D. E., Quattrini, A., Furlan, R., et al. (2021). Selective loss of microvesicles is a major issue of the differential centrifugation isolation protocols. *Sci. Rep.* 11 (1), 3589. doi:10.1038/s41598-021-83241-w

O'Brien, K., Breyne, K., Ughetto, S., Laurent, L. C., and Breakefield, X. O. (2020). RNA delivery by extracellular vesicles in mammalian cells and its applications. *Nat. Rev. Mol. Cell Biol.* 21 (10), 585–606. doi:10.1038/s41580-020-0251-y

Oksvold, M. P., Neurauter, A., and Pedersen, K. W. (2015). Magnetic bead-based isolation of exosomes. *Methods Mol. Biol.* 1218, 465–481. doi:10.1007/978-1-4939-1538-5_27

Oliveira, G. P. d., Zigon, E., Rogers, G., Davodian, D., Lu, S., Jovanovic-Talisman, T., et al. (2019). Detection of extracellular vesicle RNA using molecular beacons. *iScience* 23 (1), 100782. doi:10.1016/j.isci.2019.100782

Pang, Y. F., Wang, C. G., Lu, L. C., Wang, C. W., Sun, Z. W., and Xiao, R. (2019). Dual-SERS biosensor for one-step detection of microRNAs in exosome and residual plasma of blood samples for diagnosing pancreatic cancer. *Biosens. Bioelectron. X.* 130, 204–213. doi:10.1016/j.bios.2019.01.039

Pegtel, D. M., Peferoen, L., and Amor, S. (2014). Extracellular vesicles as modulators of cell-to-cell communication in the healthy and diseased brain. *Phil. Trans. R. Soc. B* 369 (1652), 20130516. doi:10.1098/rstb.2013.0516

Pellegrini, K. L., Gerlach, C. V., Craciun, F. L., Ramachandran, K., Bijol, V., Kissick, H. T., et al. (2015). Application of small RNA sequencing to identify microRNAs in acute kidney injury and fibrosis. *Toxicol. Appl. Pharmacol.* 312, 42–52. doi:10.1016/j.taap.2015.12.002

Peng, L. H., Zhou, L. Q., Chen, X., and Piao, X. (2020). A computational study of potential miRNA-disease association inference based on ensemble learning and kernel ridge regression. *Front. Bioeng. Biotechnol.* 8, 40. doi:10.3389/fbioe.2020.00040

Piao, X. M., Cha, E. J., Yun, S. J., and Kim, W. J. (2021). Role of exosomal miRNA in bladder cancer: A promising liquid biopsy biomarker. *Int. J. Mol. Sci.* 22 (4), 1713. doi:10.3390/ijms22041713

Qu, L., Ding, J., Chen, C., Wu, Z. J., Liu, B., Gao, Y., et al. (2016). Exosome-transmitted lncARSR promotes sunitinib resistance in renal cancer by acting as a competing endogenous RNA. *Cancer Cell* 29 (5), 653–668. doi:10.1016/j.ccell.2016.03.004

Qu, X. Y., Li, J. W., Chan, J., and Meehan, K. (2020). Extracellular vesicles in head and neck cancer: A potential new trend in diagnosis, prognosis, and treatment. *Int. J. Mol. Sci.* 21 (21), 8260. doi:10.3390/ijms21218260

Reid, M. S., Le, X. C., and Zhang, H. Q. (2018). Exponential isothermal amplification of nucleic acids and assays for proteins, cells, small molecules, and enzyme activities: An EXPAR example. *Angew. Chem. Int. Ed.* 57 (37), 11856–11866. doi:10.1002/anie.201712217

Ren, X. S., Tong, Y., Qiu, Y., Ye, C., Wu, N., Xiong, X. Q., et al. (2020). MiR155-5p in adventitial fibroblasts-derived extracellular vesicles inhibits vascular smooth muscle cell proliferation via suppressing angiotensin-converting enzyme expression. *J. Extracell. Vesicles* 9 (1), 1698795. doi:10.1080/20013078.2019.1698795

Rider, M. A., Hurwitz, S. N., and Meckes, D. G. (2016). ExtraPEG: A polyethylene glycol-based method for enrichment of extracellular vesicles. *Sci. Rep.* 6, 23978. doi:10.1038/srep23978

Rio, D. C., Ares, M., Jr., Hannon, G. J., and Nilsen, T. W. (2010). Purification of RNA using TRIzol (TRI reagent). *Cold Spring Harb. Protoc.* 2010 (6), pdb.prot5439. pdb prot5439. doi:10.1101/pdb.prot5439

Roman-Canal, B., Tarragona, J., Moiola, C. P., Gatius, S., Bonnin, S., Ruiz-Miro, M., et al. (2019). EV-associated miRNAs from peritoneal lavage as potential diagnostic biomarkers in colorectal cancer. *J. Transl. Med.* 17, 208. doi:10.1186/s12967-019-1954-8

Royo, F., Thery, C., Falcon-Perez, J. M., Nieuwland, R., and Witwer, K. W. (2020). Methods for separation and characterization of extracellular vesicles: Results of a worldwide survey performed by the ISEV rigor and standardization subcommittee. *Cells* 9 (9), 1955. doi:10.3390/cells9091955

Ruan, J., Miao, X. M., Schluter, D., Lin, L., and Wang, X. (2021). Extracellular vesicles in neuroinflammation: Pathogenesis, diagnosis, and therapy. *Mol. Ther.* 29 (6), 1946–1957. doi:10.1016/j.ymthe.2021.04.020

Ruiz-Plazas, X., Altuna-Coy, A., Alves-Santiago, M., Vila-Barja, J., Garcia-Fontgivell, J. F., Martinez-Gonzalez, S., et al. (2021). Liquid biopsy-based exo-oncomiRNAs can predict prostate cancer aggressiveness. *Cancers* 13 (2), 250. doi:10.3390/cancers13020250

Saeedi, S., Nagy, C., Ibrahim, P., Theroux, J. F., Wakid, M., Fiori, L. M., et al. (2021). Neuron-derived extracellular vesicles enriched from plasma show altered size and miRNA cargo as a function of antidepressant drug response. *Mol. Psychiatry* 26 (12), 7417–7424. doi:10.1038/s41380-021-01255-2

Saman, S., Kim, W., Raya, M., Visnick, Y., Miro, S., Saman, S., et al. (2012). Exosome-associated tau is secreted in tauopathy models and is selectively phosphorylated in cerebrospinal fluid in early alzheimer disease. *J. Biol. Chem.* 287 (6), 3842–3849. doi:10.1074/jbc.M111.277061

Sanz-Rubio, D., Martin-Burriel, I., Gil, A., Cubero, P., Forner, M., Khalyfa, A., et al. (2018). Stability of circulating exosomal miRNAs in healthy subjects. *Sci. Rep.* 8, 10306. doi:10.1038/s41598-018-28748-5

Savareh, B. A., Aghdaie, H. A., Behmanesh, A., Bashiri, A., Sadeghi, A., Zali, M., et al. (2020). A machine learning approach identified a diagnostic model for pancreatic cancer through using circulating microRNA signatures. *Pancreatology* 20 (6), 1195–1204. doi:10.1016/j.pan.2020.07.399

Schneider, A., and Simons, M. (2013). Exosomes: Vesicular carriers for intercellular communication in neurodegenerative disorders. *Cell Tissue Res.* 352 (1), 33–47. doi:10.1007/s00441-012-1428-2

Schwarzenbach, H. (2017). Clinical relevance of circulating, cell-free and exosomal microRNAs in plasma and serum of breast cancer patients. *Oncol. Res. Treat.* 40 (7-8), 423–429. doi:10.1159/000478019

Selmaj, I., Cichalewska, M., Namiecinska, M., Galazka, G., Horzelski, W., Selmaj, K. W., et al. (2017). Global exosome transcriptome profiling reveals biomarkers for multiple sclerosis. *Ann. Neurol.* 81 (5), 703–717. doi:10.1002/ana.24931

Sevenler, D., Daaboul, G. G., Kanik, F. E., Unlu, N. L., and Unlu, M. S. (2018). Digital microarrays: Single-molecule readout with interferometric detection of plasmonic nanorod labels. *ACS Nano* 12 (6), 5880–5887. doi:10.1021/acsnano.8b02036

Skog, J., Wurdinger, T., van Rijn, S., Meijer, D. H., Gainche, L., Sena-Esteves, M., et al. (2008). Glioblastoma microvesicles transport RNA and proteins that promote tumour growth and provide diagnostic biomarkers. *Nat. Cell Biol.* 10 (12), 1470–1476. doi:10.1038/ncb1800

Sobhani, N., Sirico, M., Generali, D., Zanconati, F., and Scaggiante, B. (2020). Circulating cell-free nucleic acids as prognostic and therapy predictive tools for metastatic castrate-resistant prostate cancer. *World J. Clin. Oncol.* 11 (7), 450–463. doi:10.5306/wjco.v11.i7.450

Song, J. Y., Ma, Q. X., Hu, M., Qian, D. M., Wang, B., and He, N. N. (2018). The inhibition of miR-144-3p on cell proliferation and metastasis by targeting TOP2A in HCMV-positive glioblastoma cells. *Molecules* 23 (12), 3259. doi:10.3390/molecules23123259

Sun, Z. Q., Shi, K., Yang, S. X., Liu, J. B., Zhou, Q. B., Wang, G. X., et al. (2018). Effect of exosomal miRNA on cancer biology and clinical applications. *Mol. Cancer* 17, 147. doi:10.1186/s12943-018-0897-7

Tan, L. N., Zhao, M., Wu, H. J., Zhang, Y. Z., Tong, X. L., Gao, L. H., et al. (2021). Downregulated serum exosomal miR-451a expression correlates with renal damage and its intercellular communication role in systemic lupus erythematosus. *Front. Immunol.* 12, 630112. doi:10.3389/fimmu.2021.630112

Tan, S. M., Xia, L. Z., Yi, P., Han, Y. Q., Tang, L., Pan, Q., et al. (2020). Exosomal miRNAs in tumor microenvironment. *J. Exp. Clin. Cancer Res.* 39 (1), 67. doi:10.1186/s13046-020-01570-6

Tayebi, M., Yang, D. H., Collins, D. J., and Ai, Y. (2021). Deterministic sorting of submicrometer particles and extracellular vesicles using a combined electric and acoustic field. *Nano Lett.* 21 (16), 6835–6842. doi:10.1021/acs.nanolett.1c01827

Taylor, D. D., and Gercel-Taylor, C. (2008). MicroRNA signatures of tumor-derived exosomes as diagnostic biomarkers of ovarian cancer. *Gynecol. Oncol.* 110 (1), 13–21. doi:10.1016/j.ygyno.2008.04.033

Taylor, D. D., and Shah, S. (2015). Methods of isolating extracellular vesicles impact down-stream analyses of their cargoes. *Methods* 87, 3–10. doi:10.1016/j.ymeth.2015.02.019

Thery, C., Amigorena, S., Raposo, G., and Clayton, A. (2006). Isolation and characterization of exosomes from cell culture supernatants and biological fluids. *Curr. Protoc. Cell Biol.* 30, Unit 3.22. Chapter 3Unit 3 22. doi:10.1002/0471143030.cb0322s30

Thery, C., Witwer, K. W., Aikawa, E., Alcaraz, M. J., Anderson, J. D., Andriantsitohaina, R., et al. (2018). Minimal information for studies of extracellular vesicles 2018 (MISEV2018): A position statement of the international society for extracellular vesicles and update of the MISEV2014 guidelines. *J. Extracell. Vesicles* 7 (1), 1535750. doi:10.1080/20013078.2018.1535750

Tian, J., An, X. J., and Niu, L. (2017). Role of microRNAs in cardiac development and disease. *Exp. Ther. Med.* 13 (1), 3–8. doi:10.3892/etm.2016.3932

Tian, X. Y., Shen, H., Li, Z. Y., Wang, T. T., and Wang, S. J. (2019). Tumor-derived exosomes, myeloid-derived suppressor cells, and tumor microenvironment. *J. Hematol. Oncol.* 12 (1), 84. doi:10.1186/s13045-019-0772-z

Tomasetti, M., Lee, W., Santarelli, L., and Neuzil, J. (2017). Exosome-derived microRNAs in cancer metabolism: Possible implications in cancer diagnostics and therapy. *Exp. Mol. Med.* 49, e285. doi:10.1038/emm.2016.153

Tran, N. (2016). Cancer exosomes as miRNA factories. *Trends Cancer* 2 (7), 329–331. doi:10.1016/j.trecan.2016.05.008

Trotta, T., Panaro, M. A., Cianciulli, A., Mori, G., Di Benedetto, A., and Porro, C. (2018). Microglia-derived extracellular vesicles in Alzheimer's disease: A double-edged sword. *Biochem. Pharmacol.* 148, 184–192. doi:10.1016/j.bcp.2017.12.020

Turchinovich, A., Samatov, T. R., Tonevitsky, A. G., and Burwinkel, B. (2013). Circulating miRNAs: Cell-cell communication function? *Front. Genet.* 4, 119. doi:10.3389/fgene.2013.00119

Volovat, S. R., Volovat, C., Hordila, I., Hordila, D. A., Mirestean, C. C., Miron, O. T., et al. (2020). MiRNA and LncRNA as potential biomarkers in triple-negative breast cancer: A review. *Front. Oncol.* 10, 526850. doi:10.3389/fonc.2020.526850

Wagner, J., Riwanto, M., Besler, C., Knau, A., Fichtlscherer, S., Roxe, T., et al. (2013). Characterization of levels and cellular transfer of circulating lipoprotein-bound MicroRNAs. *Arterioscler. Thromb. Vasc. Biol.* 33 (6), 1392–1400. doi:10.1161/atvbaha.112.300741

Wang, C., Ding, Q., Plant, P., Basheer, M., Yang, C., Tawedrous, E., et al. (2019). Droplet digital PCR improves urinary exosomal miRNA detection compared to real-time PCR. *Clin. Biochem.* 67, 54–59. doi:10.1016/j.clinbiochem.2019.03.008

Wang, Z. L., Zong, S. F., Liu, Y., Qian, Z. T., Zhu, K., Yang, Z. Y., et al. (2021). Simultaneous detection of multiple exosomal microRNAs for exosome screening based on rolling circle amplification. *Nanotechnology* 32 (8), 085504. doi:10.1088/1361-6528/abc7d4

Worst, T. S., Previti, C., Nitschke, K., Diessl, N., Gross, J. C., Hoffmann, L., et al. (2020). miR-10a-5p and miR-29b-3p as extracellular vesicle-associated prostate cancer detection markers. *Cancers* 12 (1), 43. doi:10.3390/cancers12010043

Wu, J., and Shen, Z. J. (2020). Exosomal miRNAs as biomarkers for diagnostic and prognosticin lung cancer. *Cancer Med.* 9 (19), 6909–6922. doi:10.1002/cam4.3379

Wu, M. X., Ouyang, Y. S., Wang, Z. Y., Zhang, R., Huang, P. H., Chen, C. Y., et al. (2017). Isolation of exosomes from whole blood by integrating acoustics and microfluidics. *Proc. Natl. Acad. Sci. U. S. A.* 114 (40), 10584–10589. doi:10.1073/pnas.1709210114

Xia, W., Xie, J., Cai, Z. Q., Liu, X. H., Wen, J., Cui, Z. K., et al. (2021). Damaged brain accelerates bone healing by releasing small extracellular vesicles that target osteoprogenitors. *Nat. Commun.* 12 (1), 6043. doi:10.1038/s41467-021-26302-y

Xiang, X. C., Guan, F. L., Jiao, F. L., Li, H., Zhang, W. J., Zhang, Y. J., et al. (2021). A new urinary exosome enrichment method by a combination of ultrafiltration and TiO2 nanoparticles. *Anal. Methods* 13 (13), 1591–1600. doi:10.1039/d1ay00102g

Xiao, Y., Wang, S. K., Zhang, Y., Rostami, A., Kenkare, A., Casella, G., et al. (2021). Role of extracellular vesicles in neurodegenerative diseases. *Prog. Neurobiol.* 201, 102022. doi:10.1016/j.pneurobio.2021.102022

Xie, H., Di, K. L., Huang, R. R., Khan, A., Xia, Y. Y., Xu, H. P., et al. (2020a). Extracellular vesicles based electrochemical biosensors for detection of cancer cells: A review. *Chin. Chem. Lett.* 31 (7), 1737–1745. doi:10.1016/j.cclet.2020.02.049

Xie, M., Xiong, W., She, Z., Wen, Z. C., Abdirahman, A. S., Wan, W. Q., et al. (2020b). Immunoregulatory effects of stem cell-derived extracellular vesicles on immune cells. *Front. Immunol.* 11, 13. doi:10.3389/fimmu.2020.00013

Xie, S., Niu, W., Xu, F., Wang, Y., Hu, S., and Niu, C. (2020c). Differential expression and significance of miRNAs in plasma extracellular vesicles of patients with Parkinson's disease. *Int. J. Neurosci.* 132, 673–688. doi:10.1080/00207454.2020.1835899

Xu, F., Fei, Z. Y., Dai, H. X., Xu, J. L., Fan, Q., Shen, S. F., et al. (2022). Mesenchymal stem cell-derived extracellular vesicles with high PD-L1 expression for autoimmune diseases treatment. *Adv. Mater.* 34 (1), e2106265. doi:10.1002/adma.202106265

Xu, S. Q., Nasr, S. H., Chen, D. Y., Zhang, X. X., Sun, L. L., Huang, X. F., et al. (2018). MiRNA extraction from cell-free biofluid using protein corona formed around carboxyl magnetic nanoparticles. *ACS Biomater. Sci. Eng.* 4 (2), 654–662. doi:10.1021/acsbiomaterials.7b00668

Xue, S., Liu, D. C., Zhu, W. J., Su, Z., Zhang, L. W., Zhou, C. Y., et al. (2019). Circulating MiR-17-5p, MiR-126-5p and MiR-145-3p are novel biomarkers for diagnosis of acute myocardial infarction. *Front. Physiol.* 10, 123. doi:10.3389/fphys.2019.00123

Yanez-Mo, M., Siljander, P. R., Andreu, Z., Zavec, A. B., Borras, F. E., Buzas, E. I., et al. (2015). Biological properties of extracellular vesicles and their physiological functions. *J. Extracell. vesicles* 4, 27066. doi:10.3402/jev.v4.27066

Yang, H. C., Ham, Y. M., Kim, J. A., and Rhee, W. J. (2021). Single-step equipment-free extracellular vesicle concentration using super absorbent polymer beads. *J. Extracell. Vesicles* 10 (4), e12074. doi:10.1002/jev2.12074

Yang, T. T., Liu, C. G., Gao, S. C., Zhang, Y., and Wang, P. C. (2018). The serum exosome derived MicroRNA-135a, -193b, and-384 were potential Alzheimer's disease biomarkers. *Biomed. Environ. Sci.* 31 (2), 87–96. doi:10.3967/bes2018.011

Yekula, A., Yekula, A., Muralidharan, K., Kang, K. K., Carter, B. S., and Balaj, L. (2020). Extracellular vesicles in glioblastoma tumor microenvironment. *Front. Immunol.* 10, 3137. doi:10.3389/fimmu.2019.03137

Yu, D., Li, Y. X., Wang, M. Y., Gu, J. M., Xu, W. R., Cai, H., et al. (2022). Exosomes as a new frontier of cancer liquid biopsy. *Mol. Cancer* 21 (1), 56. doi:10.1186/s12943-022-01509-9

Yu, W., Hurley, J., Roberts, D., Chakrabortty, S. K., Enderle, D., Noerholm, M., et al. (2021). Exosome-based liquid biopsies in cancer: Opportunities and challenges. *Ann. Oncol.* 32 (4), 466–477. doi:10.1016/j.annonc.2021.01.074

Yu, Y., Bai, F., Qin, N., Liu, W., Sun, Q., Zhou, Y., et al. (2018). Non-proximal renal tubule-derived urinary exosomal miR-200b as a biomarker of renal fibrosis. *Nephron* 139, 269–282. doi:10.1159/000487104

Yuan, L., and Li, J. Y. (2019). Exosomes in Parkinson's disease: Current perspectives and future challenges. *ACS Chem. Neurosci.* 10 (2), 964–972. doi:10.1021/acschemneuro.8b00469

Yuana, Y., Levels, J., Grootemaat, A., Sturk, A., and Nieuwland, R. (2014). Co-isolation of extracellular vesicles and high-density lipoproteins using density gradient ultracentrifugation. *J. Extracell. vesicles* 3, 23262. doi:10.3402/jev.v3.23262

Yue, B. L., Yang, H. Y., Wang, J., Ru, W. X., Wu, J. Y., Huang, Y. Z., et al. (2020). Exosome biogenesis, secretion and function of exosomal miRNAs in skeletal muscle myogenesis. *Cell Prolif.* 53 (7), e12857. doi:10.1111/cpr.12857

Zhai, L.-Y., Li, M.-X., Pan, W.-L., Chen, Y., Li, M.-M., Pang, J.-X., et al. (2018). *In situ* detection of plasma exosomal MicroRNA-1246 for breast cancer diagnostics by a Au nanoflare probe. *ACS Appl. Mat. Interfaces* 10, 39478–39486. doi:10.1021/acsami.8b12725

Zhang, H. Y., and Lyden, D. (2019). Asymmetric-flow field-flow fractionation technology for exomere and small extracellular vesicle separation and characterization. *Nat. Protoc.* 14 (4), 1027–1053. doi:10.1038/s41596-019-0126-x

Zhang, J., Li, S., Li, L., Li, M., Guo, C. Y., Yao, J., et al. (2015). Exosome and exosomal MicroRNA: Trafficking, sorting, and function. *Genomics Proteomics Bioinforma.* 13 (1), 17–24. doi:10.1016/j.gpb.2015.02.001

Zhang, T. R., and Huang, W. Q. (2021). Angiogenic exosome-derived microRNAs: Emerging roles in cardiovascular disease. *J. Cardiovasc. Transl. Res.* 14 (5), 824–840. doi:10.1007/s12265-020-10082-9

Zhao, Y., Chen, F., Li, Q., Wang, L., and Fan, C. (2015). Isothermal amplification of nucleic acids. *Chem. Rev.* 115 (22), 12491–12545. doi:10.1021/acs.chemrev.5b00428

Zheng, D. D., Huo, M., Li, B., Wang, W. T., Piao, H. L., Wang, Y., et al. (2021). The role of exosomes and exosomal MicroRNA in cardiovascular disease. *Front. Cell Dev. Biol.* 8, 616161. doi:10.3389/fcell.2020.616161

Zhou, J., Yu, L., Gao, X., Hu, J., Wang, J. P., Dai, Z., et al. (2011). Plasma MicroRNA panel to diagnose hepatitis B virus-related hepatocellular carcinoma. *J. Clin. Oncol.* 29 (36), 4781–4788. doi:10.1200/jco.2011.38.2697

Zhou, L. Y., Wang, W., Wang, F. F., Yang, S. Q., Hu, J. Q., Lu, B. J., et al. (2021). Plasma-derived exosomal miR-15a-5p as a promising diagnostic biomarker for early detection of endometrial carcinoma. *Mol. Cancer* 20 (1), 57. doi:10.1186/s12943-021-01352-4

Zhou, X., Wen, W., Shan, X., Zhu, W., Xu, J., Guo, R. H., et al. (2017). A six-microRNA panel in plasma was identified as a potential biomarker for lung adenocarcinoma diagnosis. *Oncotarget* 8 (4), 6513–6525. doi:10.18632/oncotarget.14311

frontiers | Frontiers in Bioengineering and Biotechnology

TYPE Original Research
PUBLISHED 16 December 2022
DOI 10.3389/fbioe.2022.1097363

OPEN ACCESS

EDITED BY
Guangli Li,
Hunan University of Technology, China

REVIEWED BY
Jinghua Chen,
Jiangnan University, China
Wenzhong Liu,
Huazhong University of Science and Technology, China

*CORRESPONDENCE
Mubashir Hussain,
mubashir@aa.seu.edu.cn
Bin Liu,
liubin@njmu.edu.cn

†These authors have contributed equally to this work

SPECIALTY SECTION
This article was submitted to Biosensors and Biomolecular Electronics, a section of the journal Frontiers in Bioengineering and Biotechnology

RECEIVED 13 November 2022
ACCEPTED 06 December 2022
PUBLISHED 16 December 2022

CITATION
He X, Wang C, Wang Y, Yu J, Zhao Y, Li J, Hussain M and Liu B (2022), Rapid classification of micro-particles using multi-angle dynamic light scatting and machine learning approach.
Front. Bioeng. Biotechnol. 10:1097363.
doi: 10.3389/fbioe.2022.1097363

Rapid classification of micro-particles using multi-angle dynamic light scatting and machine learning approach

Xu He[1†], Chao Wang[1†], Yichuan Wang[1], Junxiao Yu[1], Yanfeng Zhao[1], Jianqing Li[1,2], Mubashir Hussain[1,3*] and Bin Liu[1*]

[1]Jiangsu Province Engineering Research Center of Smart Wearable and Rehabilitation Devices, School of Biomedical Engineering and Informatics, Nanjing Medical University, Nanjing, China, [2]The State Key Laboratory of Bioelectronics, School of Instrument Science and Engineering, Southeast University, Nanjing, China, [3]Changzhou Medical Center, The Affiliated Changzhou Second People's Hospital of Nanjing Medical University, Changzhou Second People's Hospital, Nanjing Medical University, Changzhou, China

The rapid classification of micro-particles has a vast range of applications in biomedical sciences and technology. In the given study, a prototype has been developed for the rapid detection of particle size using multi-angle dynamic light scattering and a machine learning approach by applying a support vector machine. The device consisted of three major parts: a laser light, an assembly of twelve sensors, and a data acquisition system. The laser light with a wavelength of 660 nm was directed towards the prepared sample. The twelve different photosensors were arranged symmetrically surrounding the testing sample to acquire the scattered light. The position of the photosensor was based on the Mie scattering theory to detect the maximum light scattering. In this study, three different spherical microparticles with sizes of 1, 2, and 4 μm were analyzed for the classification. The real-time light scattering signals were collected from each sample for 30 min. The power spectrum feature was evaluated from the acquired waveforms, and then recursive feature elimination was utilized to filter the features with the highest correlation. The machine learning classifiers were trained using the features with optimum conditions and the classification accuracies were evaluated. The results showed higher classification accuracies of 94.41%, 94.20%, and 96.12% for the particle sizes of 1, 2, and 4 μm, respectively. The given method depicted an overall classification accuracy of 95.38%. The acquired results showed that the developed system can detect microparticles within the range of 1–4 μm, with detection limit of 0.025 mg/ml. Therefore, the current study validated the performance of the device, and the given technique can be further applied in clinical applications for the detection of microbial particles.

KEYWORDS

micro-particles detection, dynamic light scattering, MIE scattering, machine learning, features selection, shapley value

1 Introduction

Microparticles are small spherical particles with different size ranges within 1–1,000 μm (Li et al., 2013; Veremchuk et al., 2021). In the atmosphere, particles with a diameter less than 2.5 μm have the characteristics of strong activity, long residence time, and transport distance, which significantly harms human health and the quality of the atmosphere. The application of rapid classification of microparticles is to prevent damage to humans from airborne pollution and food contamination (Wieland et al., 2022). Particles can also be used as an effective drug delivery transmitter in cancer treatment and prevention (Nakane, 2012; Gong et al., 2015; Kumar et al., 2015). Light obscuration test (LOT) is an analytical method in which particles in a liquid are placed between a laser light source and a detector. A laser light source is used to illuminate the particles, thus creating a blocking light. The system processes the detected signal to display a calibration curve. The calibration curve quantifies the particles and determines their size (Hawe et al., 2013). Microparticle detection instruments commonly use LOT to detect insoluble particles in intravenous fluids for drug detection. The rapid classification of particles with different sizes is crucial for the human environment and the timely identification of microorganisms (Kumar et al., 2015). In the last decade, many microparticle detection techniques have been developed (Zhao et al., 2011; Dalili et al., 2019; Lengyel et al., 2019; Lerche, 2019), such as flow microscopy, spectroscopy, mass spectrometry (Zwicker, 2010; McNay et al., 2011; Kreimer et al., 2015). Recently, classifying particles using high-speed microscopy to acquire particle images by artificial intelligence algorithms has become a mainstream research method. Luo et al. (2020) developed a pipeline based on machine learning to identify images obtained from Charge Coupled Device (CCD) imaging and improved the accuracy of particle identification. Lugnan et al. (2020) developed a machine learning method for high-throughput single particle analysis using flow cytometry to achieve interference pattern classification of transparent PMMA microparticles with diameters of 15.2 and 18.6 μm. Bals et al. (2022) used scanning electron microscopy images to record contrast ratio and resolution, then classified the acquired images by machine learning based on the shape and size of micro-particles. The above methods are limited to imaging analysis and require more space for expensive detection instruments (Klug et al., 2019; Di et al., 2022; Yue et al., 2022).

In this study, we proposed an application of multi-angle dynamic light scattering (MDLS) method based on machine learning. The initial sample was diluted by mixing 1 μl of the original sample (25 mg/ml) with deionized water (DI). The prepared sample was placed in the device to collect scattered light for 30 min. The surrounding photodetector acquired the multi-angle dynamic light scattering signal and converted the acquired scattered light signal into a voltage wave. The power spectrum features were obtained from the signal waveform, and the principal component analysis (PCA) and recursive feature elimination (RFE) methods were applied to select the optimum features. Machine learning (ML) is an artificial intelligence technique that enables fast and automated classification of input features. ML has been widely applied in various applications, such as biomedical engineering and optical-based instruments (Lussier et al., 2020; Shin et al., 2020). Three machine learning algorithms, including logistic regression (LR), random forest (RF), and support vector machines (SVM) were applied for classifying features. The accuracy, precision, recall, and F1-score were used as evaluation metrics for classification performance. The overall schematic representation of the experiments and detection principle has been illustrated in Figure 1. The results demonstrated that the proposed technique is effective for the rapid detection and classification of microparticles. The proposed research aimed to shorten detection time, reduce detection costs, and simplify operation methods for classifying microparticles. The detection process did not require expensive equipment and complex operations to perform non-contact, non-invasive, and rapid detection of samples, which had great potential for optical and clinical applications.

2 Materials and methods

2.1 Micro-particles characteristics

Lumisphere polystyrene fluorescent microspheres from Tianjin Bessler Chromatography Technology Development Center (Tianjin, China) were used with a concentration of 25 mg/ml. The microscopic images of the microparticles with three different sizes were taken by scanning electron microscopy (SEM), as shown in Figure 2. The testing samples of different concentrations were prepared using series dilution to find the optimum concentration for acquiring data. The optimum concentration of the testing sample was obtained by getting the highest number of peaks/variations in the acquired waveform of respective sample. The testing samples with concentrations of 0.0125, 0.025, 0.05, 0.075, 0.1, and 0.125 mg/ml were mixed with DI water to acquire the optimal concentration. The solution was vortexed and centrifuged at 1,000 rpm for 10 min. The residue was removed from the sample to remove unwanted impurities. Then 1 ml of DI water was mixed with the supernatant to prepare the final sample for the experiment. All the experiments were performed at a room temperature (25–28°C).

2.2 MDLS prototype

Mie scattering theory describes the elastic scattering of light when the wavelength of the incident light is similar or smaller

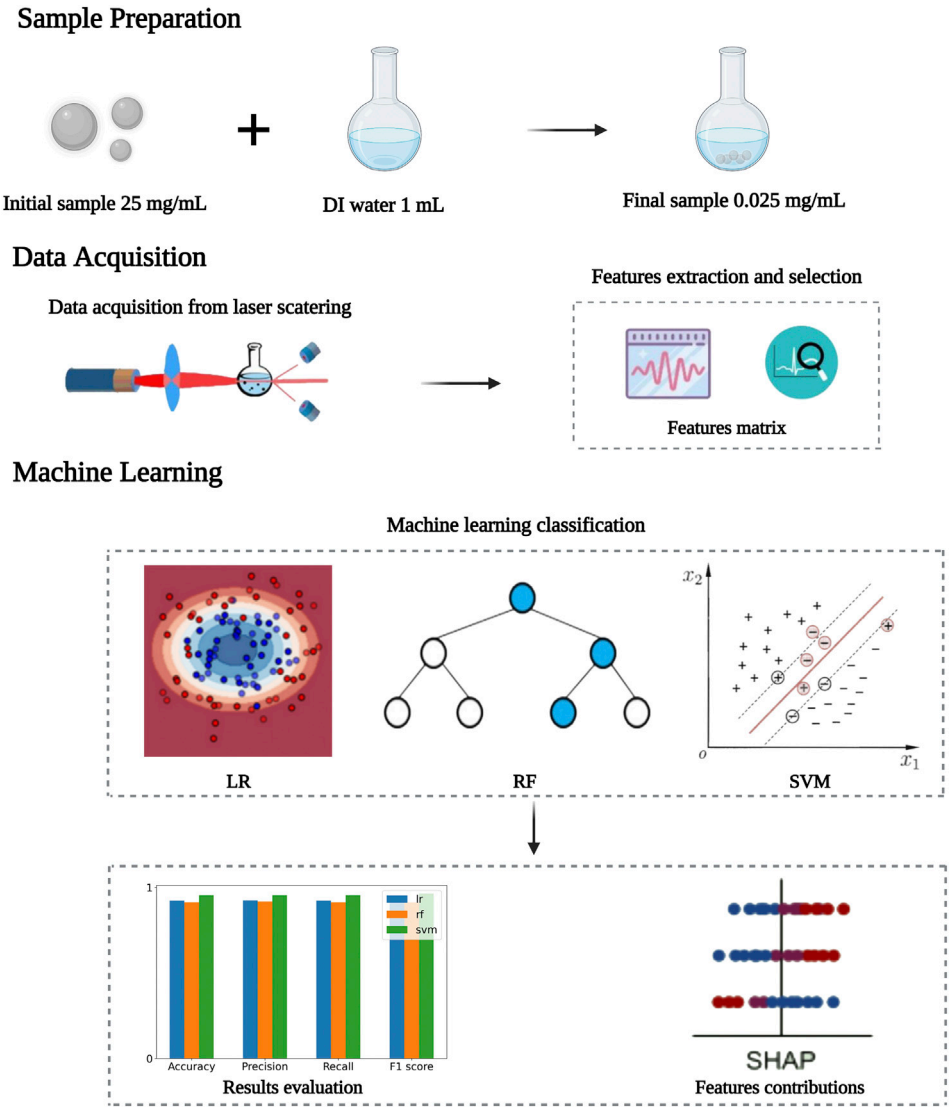

FIGURE 1
The flowchart for the detection principle for classifying microparticles based on MDLS and machine learning.

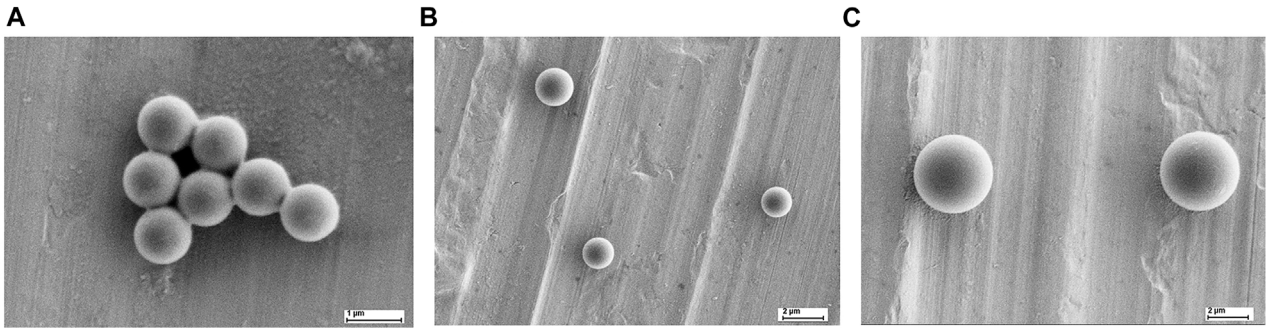

FIGURE 2
Images of three particles scanning under electron microscope **(A)** 1 μm **(B)** 2 μm and **(C)** 4 μm.

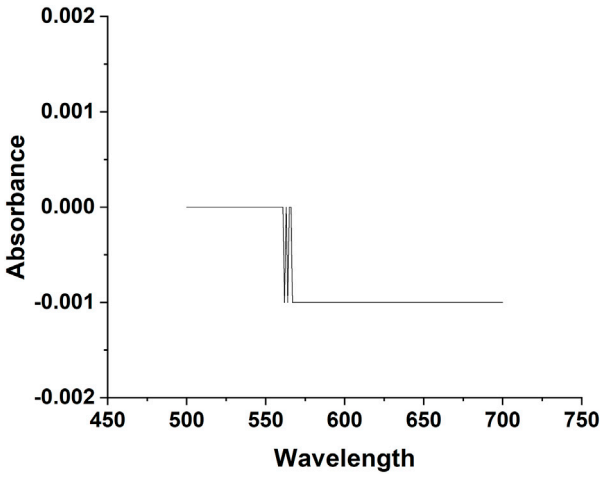

FIGURE 3
Testing the absorbance of glass flasks used for sample detection from 500 to 700 nm.

than the diameter size of spherical particles. Mie theory has been widely applied to laser diffraction analysis to detect particle size effects (Altug et al., 2022). MDLS combines the angular information of Mie scattering with dynamic light scattering to measure particle size. MDLS shows that the intensity of the scattered light fluctuates in a particular direction with time because the tiny particles in solution are in Brownian motion, and the distance between each scattered particle constantly changes with time. MDLS is a common method for detecting particle size and has been used in many medical detection devices (Guo et al., 2018). Optical methods were widely used as an important research tool for particle classification and qualitative detection (Fan et al., 2014; Olson et al., 2015).

The prototype contains three main parts: 1) a laser source, 2) an assembly of the photosensitive sensor, and 3) a data acquisition system (Hussain et al., 2020a). The designed prototype and the laser hardware were assembled by the Nanjing Institute of Advanced Laser Technology, Chinese Academy of Sciences (Nanjing, China). The laser source of the device has a wavelength of 660 nm at a rated power of 150 mW. The power rating of the laser source was measured by PM320E and S130C instruments developed by Thorlabs (New Jersey, United States). When the laser passes through the sample, the scattering light was detected by the high-speed silicon photodiodes FDS100 (wavelength ranges from 350 to 1,100 nm with rise time of 10 ns) manufactured by Thorlabs (New Jersey, United States). The AD8675 manufactured by Analog Devices (Massachusetts, United States) operational amplifier was used in the system to amplify the weak signal. A small flask made of round bottom silicon was used in the experiment (Celo Measure & Control Technology Co., Hefei). UV-1800 Spectrophotometer (SHIMADZU, Japan) measured the absorbance of the glass (Figure 3), which was approximately zero between 500–700 nm wavelength.

The original prototype was designed with 32 photoelectric sensors for signal acquisition (Hussain et al., 2020b). However, the initial number of 32 sensors consumed more computational power. The redundant data acquisition channels did not provide enough information, significantly deteriorating the classification results. The intensity of scattering light depends on the shape, size, and characteristics of the particles based on the Mie scattering theory. Particles of different sizes exhibited different scattered light patterns. The maximum scattering light intensity occurs in the incoming light's forward direction (Lock and Laven, 2011). Therefore, the number of sensors was tested and reduced from 32 to 12.

The 3D assembly of the developed prototype was designed using Solidworks 2020 software, as shown in Figure 4. The 3-axis positioning table controlled the "XYZ" 3-axial alignment of the light source to ensure that the laser is focused on the center of the sample. The laser beam positioning unit, laser collimator, sample flask and the direction of the incident light to the sample were optimized to acquire maximum signal energy from the forward scattering light. The calibrated system guarantees that no interference from external factors appears throughout the detection experiments. The signals were collected by NI data acquisition card (PCI-6225). The system showed zero voltage in the dark environment. The data collector maintained the calibrated zero signal waveform when the flask was filled with DI water as an empty sample. The collected data were further processed for features evaluation and data classification using MatlabR 2018a software.

2.3 Features extraction and features selection

2.3.1 Features extraction

Signal-to-noise ratio (SNR) gives the ratio between the power of the information signal carried in the acquired signal to the noise signal and measures the quality of the signal. Higher SNR indicates better signal quality and provides valid information for computational analysis (Szkulmowska et al., 2005). The SNR calculated the quality of the signal, where P_s denoted the total signal power and P_n denoted the noise power, as presented in Eq. 1:

$$SNR = 10lg\frac{P_s}{P_n} \quad (1)$$

Various time-domain feature extraction algorithms have been developed for signal classification tasks (pahuja et al., 2022; Wang et al., 2022). Rami et al. developed an Electromyography (EMG) signal-based feature extraction method to extract power spectrum features from the non-

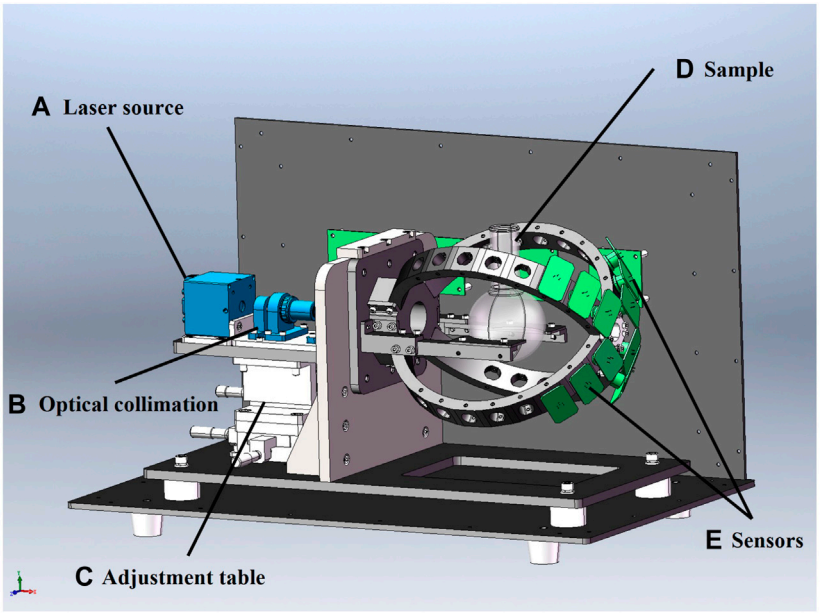

FIGURE 4
Prototype of the optical system designed by Soildworks 2020. **(A)** Laser source: Laser source with wavelength of 660 nm and power rating of 150 mW laser sources was used to emit laser beam; **(B)** Optical collimation: The optimized collimation system was used to ensure that the scattering light signal from the micro-particles was fully transmitted to the detector unit in real time. **(C)** Adjustment table: The 3-axis positioning system was used to adjust the position of the horizontal x and y axis and the vertical z axis so that the laser beam can be focused on the center of the sample. **(D)** Sample: Different concentrations of microparticle samples mixed with DI water was prepared as experimental samples. **(E)** Sensors: A photodiode with wavelength range of 350–1,100 nm and rise time of 10 ns was implemented to convert the light signal to an electrical signal.

stationary signal in time domain (Khushaba et al., 2014). The acquired data from the prototype also showed non-stationary behavior. In the feature extraction technique, the MDLS signal is denoted by x [j], the length of the signal is represented by N, and the sampling frequency is fs. The MDLS scattered signal can be expressed over time by a function of X [k] after the discrete Fourier transform (DFT). According to Parseval's theorem, the power contained in the signal is equal to the sum of the powers of the components of the signal from the complete orthogonal set. The Parseval's theorem is applied to the derivation of the power spectral characteristics:

$$\sum_{j=0}^{N-1} |\boldsymbol{x}[\boldsymbol{j}]|^2 = \frac{\boldsymbol{1}}{\boldsymbol{N}} \sum_{\boldsymbol{k}=\boldsymbol{0}}^{\boldsymbol{N}-\boldsymbol{1}} |\boldsymbol{X}[\boldsymbol{k}]\boldsymbol{X}^{*}[\boldsymbol{k}]| = \sum_{\boldsymbol{K}=\boldsymbol{0}}^{\boldsymbol{N}-\boldsymbol{1}} \boldsymbol{P}[\boldsymbol{k}] \tag{2}$$

The power spectrum characteristic P [k] is calculated by multiplying $\boldsymbol{X}^{*}[\boldsymbol{k}]$ and X [k], where k denotes the frequency of the signal. Eq. 2 represents the phase-excluded power spectrum.

According to the symmetry of the Fourier transform, all positive and negative frequencies were included to handle the whole spectrum. The given method used the time domain signal to evaluate the power spectrum features. All odd moments were set to zero by the FT. Therefore, according to the definition of the *nth* order moment m of the power spectral density P [k], all odd moments will be calculated as zero, which is defined as:

$$\boldsymbol{m}_{\boldsymbol{n}} = \sum_{\boldsymbol{k}=\boldsymbol{0}}^{\boldsymbol{N}-\boldsymbol{1}} \boldsymbol{k}^{\boldsymbol{n}} \boldsymbol{P}[\boldsymbol{k}] \tag{3}$$

Based on Eq. 2, Parseval's theorem can be used when $n = 0$. According to the time-differentiation property of the FT, when $n \neq 0$, the n^{th} order derivative of the discrete time signal equals the spectrum multiplied by the nth power of k as follows:

$$\boldsymbol{F}[\boldsymbol{\Delta}^{\boldsymbol{n}}\boldsymbol{x}[\boldsymbol{j}]] = \boldsymbol{k}^{\boldsymbol{n}}\boldsymbol{X}[\boldsymbol{k}] \tag{4}$$

Therefore, the number of extracted features is defined by the following properties:

2.3.1.1 Zero-order moments

The zero-order moment represented the total power in the frequency domain:

$$\boldsymbol{m}_{\boldsymbol{0}} = \sqrt{\sum_{\boldsymbol{j}=\boldsymbol{0}}^{\boldsymbol{N}-\boldsymbol{1}} \boldsymbol{x}[\boldsymbol{j}]^2} \tag{5}$$

2.3.1.2 Second-order moments and fourth-order moments

The second-order moment indicates the magnitude of the fluctuation of the power spectrum corresponding to the mean value. In the power spectrum characteristics, the power spectrum

with $k^2P[X]$ is correlated with spectrum related to $kX[k]$, and represented by Eq. 2:

$$m_2 = \sqrt{\sum_{k=0}^{N-1} k^2 P[k]} = \sqrt{\frac{1}{N}\sum_{j=0}^{N-1}(\Delta x[j^2])} \tag{6}$$

Similarly, the fourth-order moments can be expressed by the following equation:

$$m_4 = \sqrt{\sum_{k=0}^{N-1} k^4 P[k]} = \sqrt{\frac{1}{N}\sum_{j=0}^{N-1}(\Delta^2 x[j])^2} \tag{7}$$

The features were normalized (m_0, m_2 and m_4) to reduce the effect of noise on the features, where λ was routinely set to 0.1.

$$m_0 = \frac{m_0^\lambda}{\lambda}, \quad m_2 = \frac{m_2^\lambda}{\lambda}, \quad m_4 = \frac{m_4^\lambda}{\lambda} \tag{8}$$

Thus, the first three extracted features f_1,f_2,f_3 are defined as:

$$f_1 = log(m_0) \tag{9}$$

$$f_2 = log(m_0 - m_2) \tag{10}$$

$$f_3 = log(m_0 - m_4) \tag{11}$$

2.3.1.3 Sparsity

Sparsity defines the energy contained in a vector which is represented by:

$$f_4 = log\left(\frac{m_0}{\sqrt{m_0 - m_2}\sqrt{m_0 - m_4}}\right) \tag{12}$$

2.3.1.4 Wavelength ratio

The waveform length characteristic defines the sum of the absolute values of the second and fourth-order derivatives of the signal:

$$f_5 = log\left(\frac{\sum_{j=0}^{N-1}|\Delta^2 x|}{\sum_{j=0}^{N-1}|\Delta^4 x|}\right) \tag{13}$$

However, the sampling frequency of the data acquisition was set to 1 kHz for the 12 channels. The five features were collected from each channel to form the feature vector $f = [f_1,f_2,f_3,f_4,f_5]$. A total of 60 features were extracted from 12 channels, and the feature filtering algorithms were applied to filter the feature set.

2.3.2 Features selection method

The dimensionality of features affects the classification results, and irrelevant features may degrade the performance of the classifier (Li et al., 2017). Feature selection methods optimize the feature set and remove low relevance and redundant features. Feature selection methods are useful for removing irrelevant features affecting the training model and improving the classification accuracy of the model (Khaire and Dhanalakshmi, 2022). The PCA and RFE were used as dimensionality reduction algorithms.

2.3.2.1 PCA

PCA is a commonly used algorithm for data dimensionality reduction. PCA can project each data point onto only the first few principal components to obtain low-dimensional data while preserving as much variation as possible. In PCA, high-dimensional features are determined based on the eigenvectors and eigenvalues of the covariance matrix for K principal components and mapped to the K-dimensional space (K < N), where K-dimensional features are associated as new eigenvectors based on the magnitude of the eigenvalues (Yang et al., 2004).

2.3.2.2 RFE

Removing several features at a time often negatively impacts classifier performance, while using a small subset may yield better results. Therefore, RFE was introduced to overcome the drawback (Guyon et al., 2002). REF is a feature selection method with good generalization performance based on backward search of the model as features were removed in each iteration by using the feature importance metric within the model as a metric. RFE searches for a subset of features by starting with all features in the training dataset and successfully removing features until the desired numbers are obtained.

2.4 Machine learning

Machine learning represents a class of algorithms for data classification. With the development of artificial intelligence, machine learning technology has been widely applied in various fields, especially in biomedical engineering and life science (Goodswen et al., 2021). Among different machine learning algorithms, LR is a probabilistic non-linear regression with applications in prediction and discrimination. RF is an integrated learning model that contains multiple decision trees, and the output category is determined by the plurality of the categories output from the individual trees. SVM is a typical supervised learning classification algorithm in machine learning, which classifies data by finding the maximum interval in the feature space (Ghannam and Techtmann, 2021).

After acquiring the experimental data, the machine learning classification algorithms were applied based on Sklearn 0.19.0 package (Intel Core i7-10700 CPU processor, 2.90 Ghz, 32 GB RAM, RXT 3070). The SVM classifier acquired the highest classification accuracy compared with other classifiers. The machine learning classification process is presented in Figure 5, where the data set was divided into a training set and a test set in the ratio of 7:3. After denoising, the

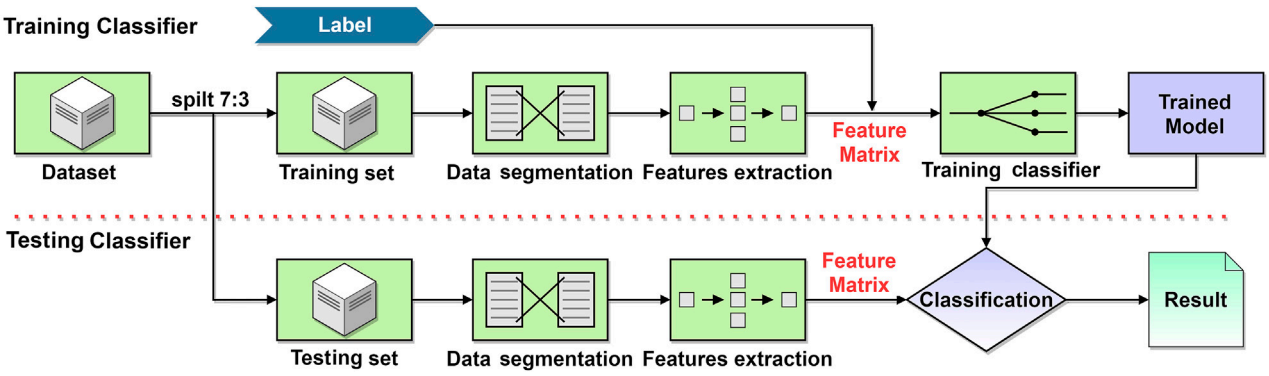

FIGURE 5
Flowchart of the microparticles classification based on machine learning.

data was segmented by adding a sliding window length of 250 ms and slid over the data signal with an increment of 150 ms. The power spectrum features were extracted for the signals in each window. The features extracted from three particle sizes of 1, 2, and 4 μm were labeled before training the machine learning classifier.

2.5 Performing analysis and features contribution

2.5.1 Performing analysis

Model evaluation metrics were applied to select a model with high generalization ability for machine learning classification tasks. Models with high generalization ability tend to adapt the unknown samples. Cross-validation is used to assess machine learning classifiers on the training set for checking their performance. In 5-fold cross-validation, the dataset is divided into 5 subsets that are not utilized in training the classifier. The 5-subsets were used for testing the model to evaluate the classifier (Bergmeir and Benitez, 2012; Wong and Yeh, 2020). The performance was assessed based on the average value generated from each result of the subset. In this research, the 5-fold cross-validation was performed to optimize the parameters of the classifier. The generalization performance of the model was tested on the test set.

The confusion matrix was plotted for subsequent computation of performance evaluation metrics. The confusion matrix is a class of tables used to visualize the classification results and evaluate classification performance. The values from the confusion matrix were represented by True Positive (*TP*), True Negative (*TN*), False Positive (*FP*), and False Negative (*FN*). The given characteristics were applied to evaluate the performance metrics, in which *TP* and *TN* denote the results of particle size that had been correctly classified, while *FP* and *FN* represent the results of particle size data classified incorrectly by the classifier. These parameters constituted the confusion matrix were used to evaluate the performance metrics, including precision, accuracy, recall, and F1 score. Precision represents the percentage of correctly predicted results to total outcomes. Recall is the probability that the predicted positive samples were positive samples. The F1 score was obtained from the weighted average of precision and recall.

The above metrics were used to evaluate the performance of the classifier and defined respectively:

$$Accuracy = \frac{TP + TN}{TP + TN + FP + FN} \tag{14}$$

$$Precision = \frac{TP}{TP + FP} \tag{15}$$

$$Recall = \frac{TP}{TP + FN} \tag{16}$$

$$F_1 score = \frac{2 \times TP}{2 \times TP + FP + FN} \tag{17}$$

2.5.2 Features contribution

Shapley value is a solution concept that involves the equitable distribution of benefits and costs to several actors working jointly in the game theory (Ribeiro et al., 2016; Lundberg and Lee, 2017). Shapley values are mainly applied to situations where the contribution of each actor is not equal but cooperates to obtain a benefit or reward. Shapley values have been widely used in artificial intelligence to provide good interpretability for machine learning and deep learning black box models (Rozemberczki et al., 2022). The proposed method can attribute the output value of the model to each Shapley value in the dataset at each sample level. Shapley values provide a natural way to calculate which features contribute to predictions, interpreting a model trained on a set of features as a coalition of players' value functions. The Shapley value explains the degree of contribution of each feature to the outcome.

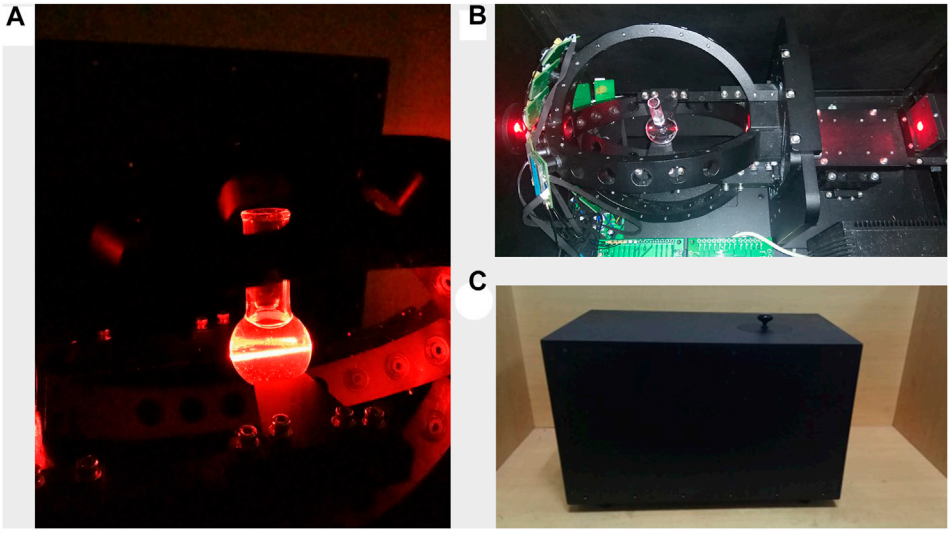

FIGURE 6
(A) Internal status of the prototype during the operation; **(B)** photodetectors are distributed in the backward direction; and **(C)** an external cover of the system is used to avoid external light (dimension: 50 cm × 30 cm × 30 cm).

3 Results

3.1 Prototype design

The prototype was successfully developed with a dimension of 50 cm × 30 cm × 30 cm. The testing sample was placed in the chamber of the prototype, as shown in Figure 6A. The sample was placed to focus the laser light on the center of the flask, as shown in Figure 6B. The particles that randomly moved in the flask scattered the detection beam while the sensor received the scattered signal in real-time. The pattern of scattering light was affected by the size and shape of the microparticles (Hussain et al., 2019). A black box was used to avoid external interference, improving the quality of the acquired signal, as shown in Figure 6C.

3.2 Optimized condition experiments

The testing samples with concentrations of 0.0125, 0.025, 0.05, 0.075, 0.1, and 0.125 mg/ml were mixed with DI water to acquire the optimal concentration. Each of the experiments was performed for 30 min. Samples with different concentrations were tested to obtain the average number of peaks (Figure 7). The scattering of the light was weak when the concentration was too low, so the number of detected peaks was less. At higher concentrations, the number of detected characteristic peaks was also too low due to particle-to-particle interaction.

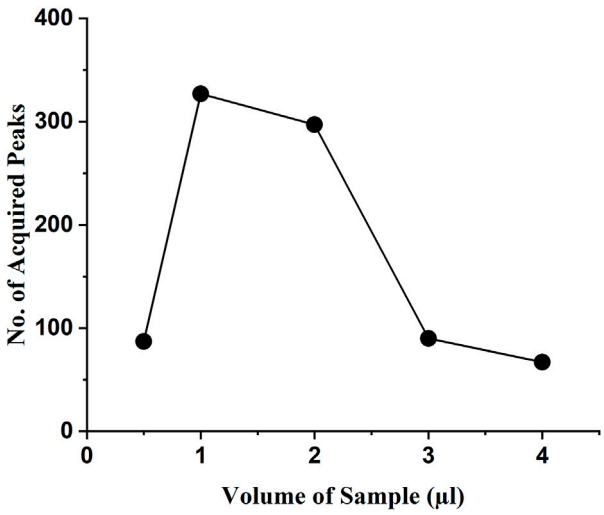

FIGURE 7
Average peak values were obtained using samples with different concentrations.

Overall, the experimental results showed that a higher number of peaks in the waveform were generated at a sample concentration of 0.025 mg/ml. The classification outcomes showed incorrect results for samples with concentrations below 0.025 mg/ml. Therefore, the sample concentration of 0.025 mg/ml is considered as the detection limit.

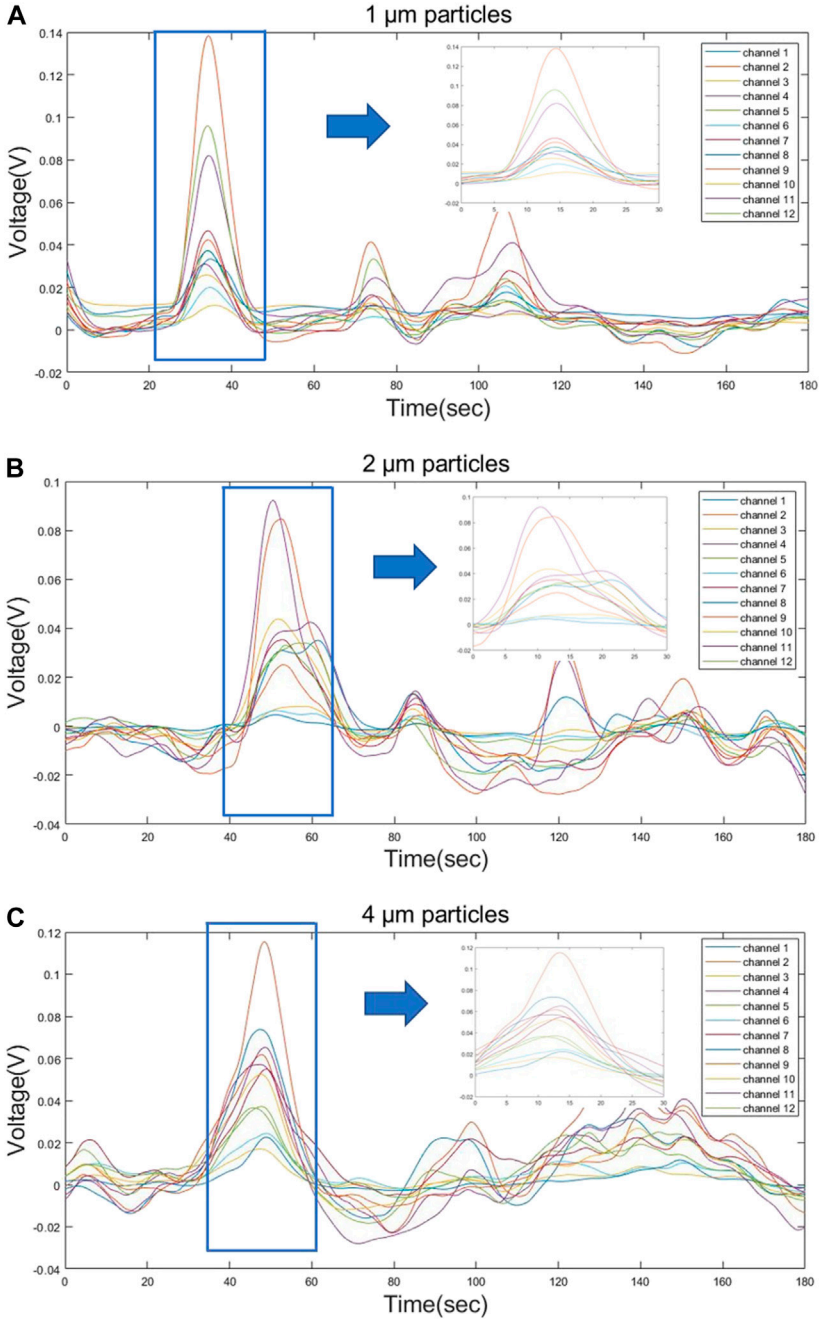

FIGURE 8
Partial waveform signals from three different sizes of particles **(A)** 1 μm **(B)** 2 μm and **(C)** 4 μm appeared during the 180 s of detection, during which the particles passing through the beam showed a significant voltage signal on the sensor.

3.3 Signal testing

The prepared samples with an optimum concentration were used to detect the MDLS. The time-domain light scattering signals from three different particles were obtained for 30 min. The SNR of the signal increased from 2.98 to 6.698 after applying the second order Butterworth filter to the acquired raw data. Figures 8A–C shows the test signal obtained from 12 channels for three particles with time duration of 3 min. An output signal shows significant variations in the peak values obtained from different particles sizes.

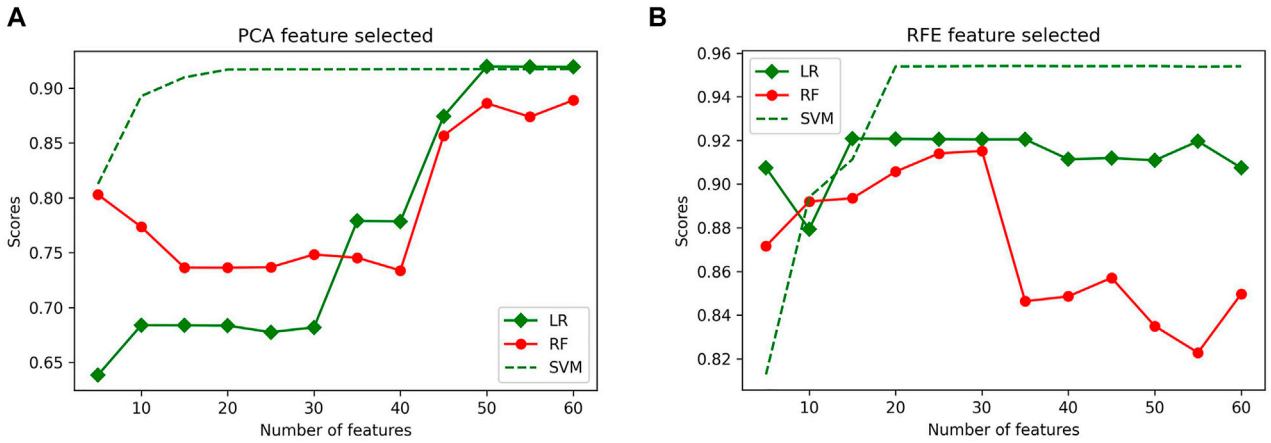

FIGURE 9
Average classification scores obtained from LR, RF and SVM classifiers using **(A)** PCA and **(B)** RFE for feature selection after 5-fold cross-validation.

A

Actual Class \ Predicted Class	1 μm particles	2 μm particles	4 μm particles
1 μm particles	10553	820	294
2 μm particles	293	5637	1652
4 μm particles	106	223	12404

B

Actual Class \ Predicted Class	1 μm particles	2 μm particles	4 μm particles
1 μm particles	10448	59	1115
2 μm particles	694	6182	623
4 μm particles	189	98	12574

C

Actual Class \ Predicted Class	1 μm particles	2 μm particles	4 μm particles
1 μm particles	11291	207	124
2 μm particles	459	6638	402
4 μm particles	84	201	12576

FIGURE 10
Confusion matrix of three different classifiers **(A)** RFE-LR **(B)** RFE-RF **(C)** RFE-SVM on testing set.

The peak values represent the time when the particles pass through the detection beam. The signal test significantly revealed the similarity of the particle signals of the three different particle sizes in terms of peak features and combinations of detection channels, so the feature extraction and machine learning approach can significantly improve the effectiveness of the classification task.

3.4 Features reduction and classification algorithms

PCA and RFE were used as feature selection algorithms, and then 5-fold cross-validation was applied to the features. Before training and testing the classifiers, the features matrix were labeled as 1 μm (class 0 label), 2 μm (class 1 label), and 4 μm (class 2 label). The number of features varied from 5 to 60, with an increment of 5 in each iteration. A 5-fold cross-validation evaluated the results of each feature selection. The highest accuracies of LR, RF, and SVM classifiers using 50 selected features with PCA were 91.97%, 88.89%, and 91.74%, respectively (Figure 9A). Similarly, the highest accuracies of LR, RF classifiers were 92.08%, 91.52%, using 30 selected features, the highest accuracy of SVM classifier were 95.38% using 50 selected features with RFE, (Figure 9B). Overall, the classification results using RFE were more accurate than PCA. The RFE feature selection method selected a subset of 50 features to obtain the highest classification accuracy.

The confusion matrix was plotted from the outcomes to evaluate the performance of the three classifiers. The row of the confusion matrix represented the actual sample classes, and the column represented the predicted sample classes (Figure 10). The green boxes in the diagonal line represented the outcomes that were correctly classified. The remaining feature data points represented the incorrectly classified values. The identification accuracy, precision, recall, and F1 score of the testing dataset were evaluated using Eqs 14–17, and the results are presented in

TABLE 1 Four evaluation metrics of different classifiers on test dataset.

Model evaluation metrics	LR	RF	SVM
Accuracy (%)	92.26	91.31	95.38
Precision	0.9238	0.9170	0.9536
Recall	0.9226	0.9131	0.9538
F1 score	0.9215	0.9125	0.9634

Table 1. Overall, the SVM(kernel = "linear", decision_function_shape = "ovr",C = 100, gamma = 0.0001, probability = True) classifier achieved higher classification accuracy than LR and RF classifiers.

3.5 Features contributions

The Shapley values were used to validate whether the 50 power spectrum features subset influenced the prediction results. We computed the Shapely values that were contributed from the power spectral features of the SVM classification model. The average Shapely values from each feature and the corresponding Shapley values for each data point were calculated and counted. The bar chart on the left (Figure 11A) showed the average Shapley values for the three classifiers, indicating each feature's average contribution to the final output. The scatter plot on the right (Figure 11B) demonstrated the distribution of Shapley values and their contribution to the model output structure. The color of each point represented the intensity of the feature value. Blue data points indicated low features, while red represented the opposite. The results showed a significant contribution of the first 12 features to the results, consistent with the proposed channel arrangement for the acquisition system. The first 12 features that corresponded to the zero-order moment features of the 12 channels played a crucial role in the contribution of the classification results.

4 Discussion

The objective of this paper is to develop a new system and to verify the ability of the proposed technique for the identification

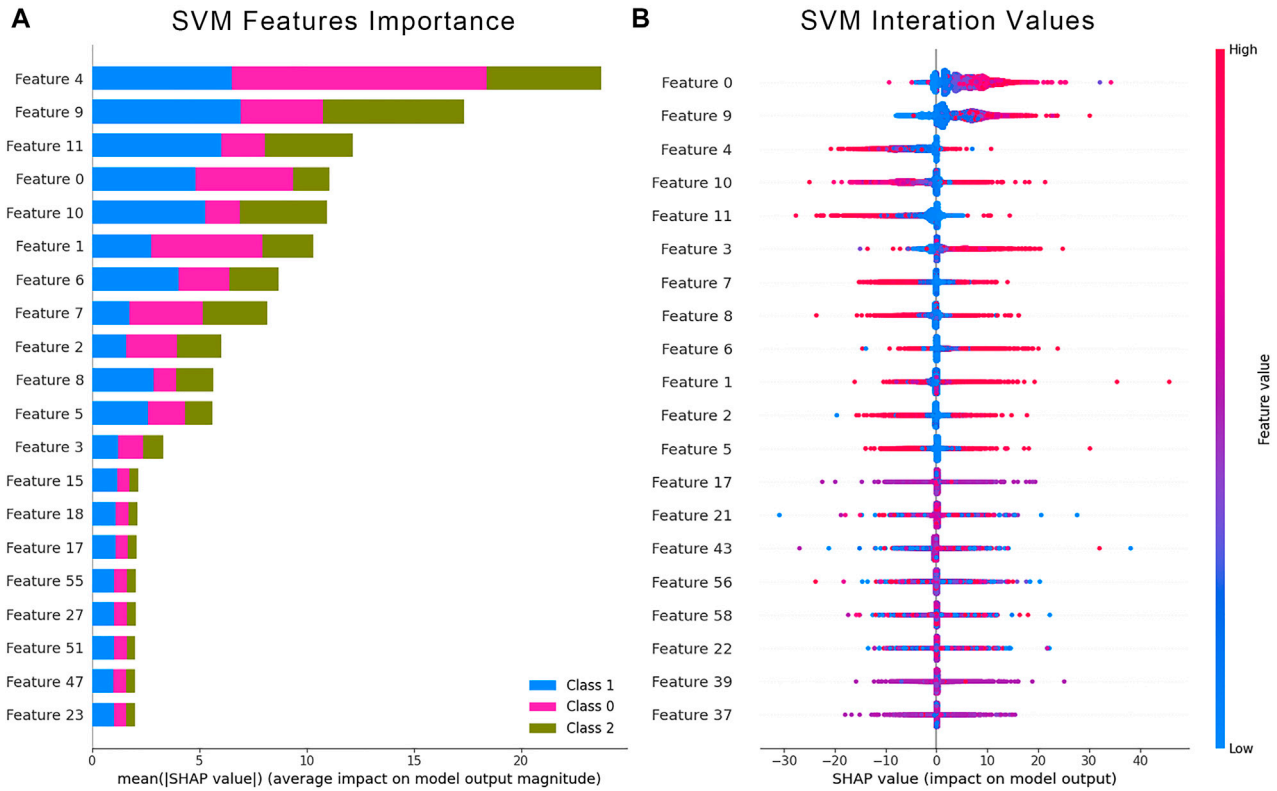

FIGURE 11
Quantification of feature impact on prediction through analysis of Shapley additive explanations (SHAP) values of the 20 most impactful features. **(A)** Averaged Shapley values of features with higher contribution indicate an average effect of these features on the output amplitude. **(B)** The scatter plot represents the distribution of Shapley values and the effect on the model output of all test samples.

of different particle sizes. With the continuous development of point-of-care testing (POCT) technology, detection techniques are gradually evolving with high accuracy and simplicity. The developed system can identify the size of microparticles with high accuracy in a short time. The given analysis was conducted by collecting a large amount of data based on the scattering light from particle samples of different sizes (1, 2, and 4 μm). The time-domain features were obtained from the acquired data, and the features were reduced the number of features to acquire higher classification accuracy. The RFE feature selection method selected a subset of 50 features, and gave best results compared with PCA features selection method. The selected features were trained using machine learning to automate the detection procedure. The logistic regression classifier gave classification accuracies of 95.30%, 92.38%, 89.17% for particle sizes of 1, 2 , and 4 μm, respectively. The random forest classifier gave classification accuracies of 92.59%, 96.71%, 76.62% for particle sizes of 1, 2, and 4 μm, respectively. The SVM classifier showed higher identification accuracy with prominent classification parameters. The SVM classifier gave the highest classification accuracies of 94.41%, 94.20%, 96.12% for particle sizes of 1, 2, and 4 μm, respectively. The trained SVM classifier gives an average classification accuracy of 95.38%. The detection limit of the given method is 0.025 mg/ml. The contribution and effect of each feature to the results were analyzed by features selection methods. Selected features identified by the RFE feature filter have shown superior classification results. The Shapley values of these features described a significant contribution to the results. In summary, the developed system based on MDLS and machine learning can quickly and accurately detect microparticles. Furthermore, the prototype was highly integrated, and the developed method did not require lengthy sample preparation. The given technique requires further validation for practical applications that can be applied to detect microbial particles within the range of 1–4 μm.

Data availability statement

The raw data supporting the conclusion of this article will be made available by the authors, without undue reservation.

Author contributions

Writing—original draft preparation original manuscript writing and algorithm: XH; investigation and methodology: CW; visualization: YW; language embellishment and algorithm: JY; validation: YZ; literature research and validation: JL; sample preparation and data acquisition: MH; project administration and supervision: BL. All authors have read and agreed to the published version of the manuscript.

Funding

This research was funded by NSFC (61401217, 62075098), the Key Research and Development Program of Jiangsu (BE2022160). NSFC (61401217, 62075098) provided funded for sample acquisition and the design of the light scattering prototype for this experiment. The Key Research and Development Program of Jiangsu (BE2022160) provided computer hardware support for this experiment.

Acknowledgments

We are thankful to MH and BL for providing technical guidance for this experiment. The authors are also very grateful to Southeast University for providing the instrumentation support for this experiment.

Conflict of interest

The authors declare that the research was conducted in the absence of any commercial or financial relationships that could be construed as a potential conflict of interest.

Publisher's note

References

Altug, H., Oh, S., Maier, S. A., and Homola, J. (2022). Advances and applications of nanophotonic biosensors. *Nat. Nanotechnol.* 17, 5–16. doi:10.1038/s41565-021-01045-5

Bals, J., Loza, K., Epple, P., Kircher, T., and Epple, M. (2022). Automated and manual classification of metallic nanoparticles with respect to size and shape by analysis of scanning electron micrographs. *Materialwiss. Werkst.* 53, 270–283. doi:10.1002/mawe.202100285

Bergmeir, C., and Benitez, J. M. (2012). On the use of cross-validation for time series predictor evaluation. *Inf. Sci.* 191, 192–213. doi:10.1016/j.ins.2011.12.028

Dalili, A., Samiei, E., and Hoorfar, M. (2019). A review of sorting, separation and isolation of cells and microbeads for biomedical applications: Microfluidic approaches. *Analyst* 144, 87–113. doi:10.1039/c8an01061g

Di, K., Fan, B., Gu, X., Huang, R., Khan, A., Liu, C., et al. (2022). Highly efficient and automated isolation technology for extracellular vesicles microRNA. *Front. Bioeng. Biotechnol.* 10, 948757. doi:10.3389/fbioe.2022.948757

Fan, X., Zheng, W., and Singh, D. J. (2014). Light scattering and surface plasmons on small spherical particles. *Light. Sci. Appl.* 3, e179. doi:10.1038/lsa.2014.60

Ghannam, R. B., and Techtmann, S. M. (2021). Machine learning applications in microbial ecology, human microbiome studies, and environmental monitoring. *Comput. Struct. Biotechnol. J.* 19, 1092–1107. doi:10.1016/j.csbj.2021.01.028

Gong, J., Jaiswal, R., Dalla, P., Luk, F., and Bebawy, M. (2015). Microparticles in cancer: A review of recent developments and the potential for clinical application. *Seminars Cell & Dev. Biol.* 40, 35–40. doi:10.1016/j.semcdb.2015.03.009

Goodswen, S. J., Barratt, J. L. N., Kennedy, P. J., Kaufer, A., Calarco, L., and Ellis, J. T. (2021). Machine learning and applications in microbiology. *FEMS Microbiol. Rev.* 45, fuab015. fuab0155. doi:10.1093/femsre/fuab015

Guo, L., Wang, T., Chen, Z., He, N., Chen, Y., and Yuan, T. (2018). Light scattering based analyses of the effects of bovine serum proteins on interactions of magnetite spherical particles with cells. *Chin. Chem. Lett.* 29, 1291–1295. doi:10.1016/j.cclet.2017.11.017

Guyon, I., Weston, J., Barnhill, S., and Vapnik, V. (2002). Gene selection for cancer classification using support vector machines. *Mach. Learn* 46, 389–422. doi:10.1023/A:1012487302797

Hawe, A., Schaubhut, F., Geidobler, R., Wiggenhorn, M., Friess, W., Rast, M., et al. (2013). Pharmaceutical feasibility of sub-visible particle analysis in parenterals with reduced volume light obscuration methods. *Eur. J. Pharm. Biopharm.* 85, 1084–1087. doi:10.1016/j.ejpb.2013.02.004

Hussain, M., Chen, Z., Lv, M., Xu, J., Dong, X., Zhao, J., et al. (2020a). Rapid and label-free classification of pathogens based on light scattering, reduced power spectral features and support vector machine. *Chin. Chem. Lett.* 31, 3163–3167. doi:10.1016/j.cclet.2020.04.038

Hussain, M., Lv, M., Dong, X., Shen, H., Wang, W., Li, S., et al. (2020b). Design of rapid bacterial identification system based on scattering of laser light and classification of binned plots. *J. Nanosci. Nanotechnol.* 20, 4047–4056. doi:10.1166/jnn.2020.17491

Hussain, M., Lv, M., Xu, J., Dong, X., Wang, T., Wang, Z., et al. (2019). "Rapid identification of pathogens based on MIE light scattering and machine learning approach," in IEEE International Symposium on Medical Measurements and Applications (MeMeA), Messina, Italy, June 22, 2022 – June 24, 2022 (IEEE Press), 1–5. doi:10.1109/MeMeA.2019.8802228

Khaire, U. M., and Dhanalakshmi, R. (2022). Stability of feature selection algorithm: A review. *J. King Saud Univ. - Comput. Inf. Sci.* 34, 1060–1073. doi:10.1016/j.jksuci.2019.06.012

Khushaba, R. N., Takruri, M., Miro, J. V., and Kodagoda, S. (2014). Towards limb position invariant myoelectric pattern recognition using time-dependent spectral features. *Neural Netw.* 55, 42–58. doi:10.1016/j.neunet.2014.03.010

Klug, K. E., Jennings, C. M., Lytal, N., An, L., and Yoon, J. (2019). Mie scattering and microparticle-based characterization of heavy metal ions and classification by statistical inference methods. *R. Soc. open Sci.* 6, 190001. doi:10.1098/rsos.190001

Kreimer, S., Belov, A. M., Ghiran, I., Murthy, S. K., Frank, D. A., and Ivanov, A. R. (2015). Mass-spectrometry-based molecular characterization of extracellular vesicles: Lipidomics and proteomics. *J. Proteome Res.* 14, 2367–2384. doi:10.1021/pr501279t

Kumar, M., Singh, R. S., and Banerjee, T. (2015). Associating airborne particulates and human health: Exploring possibilities. *Environ. Int.* 84, 201–202. doi:10.1016/j.envint.2015.06.002

Lengyel, M., Kállai-Szabó, N., Antal, V., Laki, A. J., and Antal, I. (2019). Microparticles, microspheres, and microcapsules for advanced drug delivery. *Sci. Pharm.* 87, 20. doi:10.3390/scipharm87030020

Lerche, D. (2019). Comprehensive characterization of nano- and microparticles by iIn-sSitu visualization of particle movement using advanced sedimentation techniques. *Kona* 36, 156–186. doi:10.14356/kona.2019012

Li, J., Fu, C., and Yang, C. F. (2013). Recent advances in micro/nano-particles for clinical detection of cancer biomarkers. *Anal. Methods* 5, 5862–5874. doi:10.1039/C3AY40791H

Li, Y., Li, T., and Liu, H. (2017). Recent advances in feature selection and its applications. *Knowl. Inf. Syst.* 53, 551–577. doi:10.1007/s10115-017-1059-8

Lock, J. A., and Laven, P. (2011). Mie scattering in the time domain. Part 1. The role of surface waves. *J. Opt. Soc. Am. A* 28, 1086–1095. doi:10.1364/JOSAA.28.001086

Lugnan, A., Gooskens, E., Vatin, J., Dambre, J., and Bienstman, P. (2020). Machine learning issues and opportunities in ultrafast particle classification for label-free microflow cytometry. *Sci. Rep.* 10, 20724. doi:10.1038/s41598-020-77765-w

Lundberg, S. M., and Lee, S. (2017). A unified approach to interpreting model predictions. *NeurIPS* 30, 4768–4777. doi:10.3390/mi11121084

Luo, S., Zhang, Y., Nguyen, K. T., Feng, S., Shi, Y., Liu, Y., et al. (2020). Machine learning-based pipeline for high accuracy bioparticle sizing. *Micromachines* 11, 1084. doi:10.3390/mi11121084

Lussier, F., Thibault, V., Charron, B., Wallace, G. Q., and Masson, J. (2020). Deep learning and artificial intelligence methods for Raman and surface-enhanced Raman scattering. *TrAC Trends Anal. Chem.* 124, 115796. doi:10.1016/j.trac.2019.115796

Mcnay, G., Eustace, D., Smith, W. E., Faulds, K., and Graham, D. (2011). Surface-Enhanced Raman scattering (sers) and surface-enhanced resonance Raman scattering (serrs): A review of applications. *Appl. Spectrosc.* 65, 825–837. doi:10.1366/11-06365

Nakane, H. (2012). Translocation of particles deposited in the respiratory system: A systematic review and statistical analysis. *Environ. Health Prev. Med.* 17, 263–274. doi:10.1007/s12199-011-0252-8

Olson, J., Dominguez-Medina, S., Hoggard, A., Wang, L., Chang, W., and Link, S. (2015). Optical characterization of single plasmonic nanoparticles. *Chem. Soc. Rev.* 44, 40–57. doi:10.1039/c4cs00131a

Pahuja, S. K., and Veer, K. (2022), "Recent approaches on classification and feature extraction of eeg signal: A review", *Robotica*. 40, 77–101. doi:10.1017/S0263574721000382

Ribeiro, M. T., Singh, S., and Guestrin, C. (2016). "Why should I trust you? Explaining the predictions of any classifier," in *Proceedings of the 22nd ACM SIGKDD international conference on knowledge discovery and data mining* (San Francisco, California, USA: Association for Computing Machinery), 1135–1144. doi:10.1145/2939672.2939778

Rozemberczki, B., Watson, L., Bayer, P., Yang, H., Kiss, O., Nilsson, S., et al. (2022), "The shapley value in machine learning", arXiv e-prints. arXiv:2202.05594.

Shin, H., Oh, S., Hong, S., Kang, M., Kang, D., Ji, Y., et al. (2020). Early-stage lung cancer diagnosis by deep learning-based spectroscopic analysis of circulating exosomes. *ACS Nano* 14, 5435–5444. doi:10.1021/acsnano.9b09119

Szkulmowska, A., Wojtkowski, M., Gorczynska, I., Bajraszewski, T., Szkulmowski, M., Targowski, P., et al. (2005). Coherent noise-free ophthalmic imaging by spectral optical coherence tomography. *J. Phys. D. Appl. Phys.* 38, 2606–2611. doi:10.1088/0022-3727/38/15/011

Veremchuk, L. V., Vitkina, T. I., Barskova, L. S., Gvozdenko, T. A., and Mineeva, E. E. (2021). Estimation of the size distribution of suspended particulate matters in the urban atmospheric surface layer and its influence on bronchopulmonary pathology. *Atmosphere* 12, 1010. doi:10.3390/atmos12081010

Wang, M., Yin, X., Zhu, Y., and Hu, J. (2022). Representation learning and pattern recognition in cognitive biometrics: A survey. *Sensors* 22, 5111. doi:10.3390/s22145111

Wieland, S., Balmes, A., Bender, J., Kitzinger, J., Meyer, F., Ramsperger, A. F. R. M., et al. (2022). From properties to toxicity: Comparing microplastics to other airborne microparticles. *J. Hazard. Mater.* 428, 128151. doi:10.1016/j.jhazmat.2021.128151

Wong, T., and Yeh, P. (2020). Reliable accuracy estimates from k-fold cross validation. *IEEE Trans. Knowl. Data Eng.* 32, 1586–1594. doi:10.1109/TKDE.2019.2912815

Yang, J., Zhang, D., Frangi, A. F., and Yang, J. Y. (2004). Two-dimensional PCA: A new approach to appearance-based face representation and recognition. *IEEE Trans. Pattern Anal. Mach. Intell.* 26, 131–137. doi:10.1109/TPAMI.2004.1261097

Yue, S., Fang, J., and Xu, Z. (2022). Advances in droplet microfluidics for SERS and Raman analysis. *Biosens. Bioelectron.* 198, 113822. doi:10.1016/j.bios.2021.113822

Zhao, X., Zhao, Y., and Gu, Z. (2011). Advances of multiplex and high throughput biomolecular detection technologies based on encoding microparticles. *Sci. China Chem.* 54, 1185–1201. doi:10.1007/s11426-011-4343-6

Zwicker, J. I. (2010). Impedance-based flow cytometry for the measurement of microparticles. *Semin. Thromb. Hemost.* 36, 819–823. doi:10.1055/s-0030-1267035

frontiers | Frontiers in Bioengineering and Biotechnology

TYPE Review
PUBLISHED 23 December 2022
DOI 10.3389/fbioe.2022.1112327

OPEN ACCESS

EDITED BY
Nongyue He,
Southeast University, China

REVIEWED BY
Guangyao Zhang,
Qingdao University, China
Shancheng Yan,
Nanjing University of Posts and Telecommunications, China

*CORRESPONDENCE
Libo Nie,
libonie@aliyun.com

†These authors have contributed equally to this work and share first authorship

SPECIALTY SECTION
This article was submitted to Biosensors and Biomolecular Electronics, a section of the journal Frontiers in Bioengineering and Biotechnology

RECEIVED 30 November 2022
ACCEPTED 08 December 2022
PUBLISHED 23 December 2022

CITATION
Wu K, He X, Wang J, Pan T, He R, Kong F, Cao Z, Ju F, Huang Z and Nie L (2022), Recent progress of microfluidic chips in immunoassay.
Front. Bioeng. Biotechnol. 10:1112327.
doi: 10.3389/fbioe.2022.1112327

Recent progress of microfluidic chips in immunoassay

Kaimin Wu[1†], Xuliang He[2†], Jinglei Wang[1], Ting Pan[1], Ran He[1], Feizhi Kong[1], Zhenmin Cao[1], Feiye Ju[1], Zhao Huang[1] and Libo Nie[1*]

[1]Hunan Key Laboratory of Biomedical Nanomaterials and Devices, Hunan University of Technology, Zhuzhou, China, [2]Zhuzhou People's Hospital, Zhuzhou, China

Microfluidic chip technology is a technology platform that integrates basic operation units such as processing, separation, reaction and detection into microchannel chip to realize low consumption, fast and efficient analysis of samples. It has the characteristics of small volume need of samples and reagents, fast analysis, low cost, automation, portability, high throughout, and good compatibility with other techniques. In this review, the concept, preparation materials and fabrication technology of microfluidic chip are described. The applications of microfluidic chip in immunoassay, including fluorescent, chemiluminescent, surface-enhanced Raman spectroscopy (SERS), and electrochemical immunoassay are reviewed. Look into the future, the development of microfluidic chips lies in point-of-care testing and high throughput equipment, and there are still some challenges in the design and the integration of microfluidic chips, as well as the analysis of actual sample by microfluidic chips.

KEYWORDS

microfluidic chip, immunoassay, fluorescence, chemiluminescence, surface-enhanced Raman spectroscopy, electrochemistry

1 Introduction

Microfluidic technology refers to the process or manipulation of a small amount of fluid (10-9-10-18 L) using microchannels with tens to hundreds of microns (Abe et al., 2010; Alix-Panabières and Pantel, 2014; Huang L. et al., 2021; Bai et al., 2022). It is a new research field developed from the technologies and principles of chemistry, physics, biology, materials science, fluid mechanics and microelectronics (Deng et al., 2013; Sackmann et al., 2014; Hamdallah et al., 2020). In the early 1990s, Manz et al. carried out the research on chip electrophoresis and first proposed the concept of microcomplete analysis system (Manz et al., 1990).

Microfluidic chip, also called microfluidic chip lab or lab-on-chip (LOC), is a technology platform that integrates the sample processing, reaction, separation, detection and other routine operations involved in chemical and biological experiments on a chip of several square centimeters to achieve low consumption, rapid and efficient analysis. Microfluidic chip is characterized by the its microstructure to accommodate the fluid, such as micro channels, micro reaction

chambers and other micro functional components, resulting in a series of special effects of micro fluid, such as laminar flow effect, surface tension and capillary effect, rapid heat conduction effect and diffusion effect, which is conducive to accurate fluid control and rapid reaction. Due to the micron-scale structure, the fluid displays special properties that are different from those in the macroscopic scale, which leads to unique analytical performance (Li et al., 2013b; Mou et al., 2016; Liu H. et al., 2017; Zhang Z. et al., 2022). Compared with traditional analysis methods, the prominent advantage of microfluidic chip lies in the flexible combination and integration of various unit, realizing the automatic operation, high throughput detection and low reagent consumption, preventing human interference and pollution, as well as completing efficient repeated experiments. Microfluidic chip is also of good compatibility that easy to integrate with other technical devices (Daw and Finkelstein, 2006). Using microfluidic chip technology, hundreds of samples can be simultaneously analyzed in a few minutes or even less time, and the whole process of sample pretreatment and analysis can be realized automatically (Li et al., 2013a; Liu et al., 2013; Lu et al., 2021).

With the development of materials science, the materials of microfluidic chips have emerged in a wide range from silicon, glass to paper-based, hydrogels, and polymers. At the same time, the preparation technology of microfluidic chip is also booming, including screen printing, inkjet printing, 3D printing and so on. Some advanced processing technologies, such as femtosecond laser processing technology and two-photon 3D printing technology, also provide more possibilities for the production of high-precision microfluidic chips.

Microfluidic chip technology has brought a subversive breakthrough in biomedical field. Due to the advantages of small reagent consumption, short reaction process, high sensitivity and low cost, microfluidic chips are easy to be developed into portable instruments and have significant advantages of real-time on-site detection, which can be widely used in gene, protein and microbiology assay. Microfluidic chip is also potentially used in portable instruments and point-of-care testing (POCT), which can be widely used in the field of biomedicine (Hale et al., 2010; van de Sandt et al., 2012; Wang H. et al., 2021; Huang Q. et al., 2021; Goldstein et al., 2021; Jalili et al., 2021; Ma et al., 2021; Yin et al., 2021; Dornhof et al., 2022; Sun et al., 2022; Yang et al., 2022).

2 Preparation of microfluidic chip

2.1 Materials of microfluidic chip

In the preparation of microfluidic chips, the durability, manufacturability, transparency, biocompatibility, as well as the possibility of surface functionalization of the materials must be considered (Pan et al., 2017; Sticker et al., 2020; Niculescu et al., 2021). At present, the materials of microfluidic chips include silicon, quartz, glass, polymer, hydrogel, paper and so on (Qin et al., 1998).

Silicon is one of the favored materials for microfluidic chip preparation, which is easy to obtain and has good chemical compatibility and thermal stability (Singh et al., 2011; Martins et al., 2018). At the same time, silicon has been the preferred material for microfluidic platform preparation for decades due to its simplicity of manufacturing, easy to be surface modified and the semiconductor properties (Nielsen et al., 2020).

Glass and quartz are also widely used as the materials of microfluidic chips due to their low cost and good biocompatibility, with the surface modification based on silicon hydroxyl (Jiang X. et al., 2020). In addition, glass is of excellent light transmittance which is convenient for optical detection (Hwang et al., 2019).

Polymer is a kind of important material used in microfluidic chip because of its variety, low cost, simple manufacturing process, good transparency, and modifiable performance. Polymer used in microfluidic chip involves of thermoplastic polymer, thermosetting polymer and solvent volatile polymer. Thermoplastic polymer includes polymethyl methacrylate (PMMA), polycarbonate (PC) and polyethylene (PE), etc. Thermosetting polymer includes polydimethylsiloxane (PDMS), epoxy resin and polyurethane (PU), *etc.* Solvent volatile polymer includes acrylic, rubber and fluorine plastics, *etc.* PDMS is hydrophobic organosilicon material, which has the advantages of no byproduct, low stress and modulus, excellent physiological inertia, and remaining elastic within the temperature range of −40–210°C (Syed et al., 2014). PMMA is also known as plexiglass, with the properties of easy processing, strong corrosion resistance, good insulation and high transparency. The density of PMMA is much less than that of glass, but the strength of PMMA is 10 times stronger than that of glass (Gabriel et al., 2014).

Hydrogel has become one of the matrix materials of microfluidic chips (Liu M. et al., 2017; Yang F. et al., 2018; Jing et al., 2019; Mofazzal Jahromi et al., 2019; Nielsen et al., 2020), which usually have a hydrophilic porous structure, and its porous structure is filled with water molecules, allowing biomacromolecules to pass through (Lee et al., 2014; Chen et al., 2016; Liu M. et al., 2017; Chen et al., 2017; Xu et al., 2019; Huang et al., 2020; Vera et al., 2021).

Paper materials have the history of use more than two thousand years, which usually has a loose porous hydrophilic structure. Water-based liquid dropped on the surface of the paper can flow autonomously in the paper fiber by capillary forces. The application of paper materials in microfluidic chips is mainly inspired by the application of paper chromatography in traditional chemical detection methods (Martinez et al., 2007; Hellmann, 2008). The microfluidic analysis platform prepared from paper (such as chromatography paper and nitrocellulose film) is called paper-based microfluidic chip, also known as paper

chip. Microfluidic paper-based chip is a miniature laboratory analysis system that uses paper substrates to replace the traditional substrates of microfluidic systems. By establishing hydrophilic/hydrophobic channels and analysis units on the surface, the sample on the chip carries out self-driven flow and corresponding reactions to realize sample pretreatment, separation, purification, and detection (Wu et al., 2016; Wu et al., 2017). Paper-based microfluidic chips are characterized by low cost, easy processing, disposable use and no external fluid pump, which greatly simplifies the requirements of chip structure for auxiliary equipment (Lin et al., 2020; Liu et al., 2020). In recent years, paper-based microfluidic chip has been applied to a certain extent in life science and medicine, food safety, environmental monitoring and other fields (Qi et al., 2018; Jiang H. et al., 2020; Yang et al., 2020). Except the advantages, there are still many constraints in the application of paper-based microfluidic chips. For example, the sample is volatile in the channel or in the flow process, resulting in the loss of the sample. The precision of the paper chip, as well as the sensitivity of colorimetric detection is relatively low. In addition, the sample may leak in the process of circulation. The performance of paper chip can be improved by selecting the appropriate paper substrate, reasonably designing the fluid channel and employing optimal processing method.

2.2 Fabrication of microfluidic chips

Different fabrication methods of microfluidic chips are adopted according to properties of the substrates. The surface of silicon materials can be modified by silanization to reduce "non-specific" adsorption (Wu et al., 2009; Muthusubramaniam et al., 2011). However, silicon materials also have the shortcomings such as poor light transmittance, fragility and poor electrical insulation. The process methods of silicon chip are mainly photolithography and etching (Chow et al., 2004). Due to their special surface properties, glass and quartz are difficult to be treated directly. The common processes are photoetching and lithography, which are divided into gluing, exposure, development, etching, degluing, drilling, and sealing (Nakanishi et al., 2001; Qiu et al., 2020). The application of glass and quartz chips in microfluidic devices is limited due to the high cost of micromachining, time consumption, and the requirement of a clean room in preparation process (Tang et al., 2021). The fabrication of polymer microfluidic chip mainly adopts hot pressing, moulding method, injection moulding method and so on. Only after the preparation of microchannel can the sample tube be modified, installed and sealed (Chen et al., 2001; Krishnan et al., 2004; Wu et al., 2005; Liu et al., 2009). The preparation of hydrogel microfluidic chip is significantly different from that of silicon/glass and polymer materials, which is mainly prepared by UV laser or 3D printing (Decock et al., 2018).

The preparation of paper-based microfluidic chips involves various methods to construct a hydrophilic/hydrophobic channel on the paper-based surface so that the dripping sample can flow directly through the preset channel. Initially, ultraviolet lithography was used to treat the paper and construct hydrophobic channels on the surface of cellulose paper (Martinez et al., 2007). With the development of technology, the processing methods of paper-based microfluidic chips have been greatly improved currently, which include inkjet printing, inkjet etching, wax printing, wax immersion, plasma treatment, etc., (Carrilho et al., 2009; Abe et al., 2010; Li et al., 2010a; Li et al., 2010b; Chitnis et al., 2011).

3 Application of microfluidic chip in immunoassay

Microfluidic chip not only realizes low reagent consumption and high throughput detection, but also has obvious advantages of easy integration and good compatibility with other technical equipment. Nowadays, microfluidic chips are widely used in bioassay. Immunoassay detects the analytes (mainly proteins) based on antibody-antigen reaction. Common immunoassay methods include enzyme linked immunosorbent assay (ELISA), radioimmunoassay, fluorescence immunoassay, chemiluminescence, etc. (Lai et al., 2018a; Lai et al., 2018b). Traditional immunoassay relies on large equipment and skilled operators, with complicated operation, expensive reagents, long assay time and low sensitivity. At the same time, with the demand increasing for real-time detection, clinical diagnosis need a high sensitivity, high accuracy, rapid, portable and real-time immunoassay method. The combination of immunoassay and microfluidic technology can greatly overcome the shortcomings of traditional immunoassay. For example, the high surface-to-volume ratio of micro-channels is able to accelerate the antibody-antigen binding to shorten the reaction time. Microfluidic immunoassay exhibits a lot of advantages such as fast response, low reagent consumption, high-throughput and portability (Zheng et al., 2020; Wang Y. et al., 2021; Reis et al., 2021; Rodriguez-Moncayo et al., 2021). Researchers have developed a variety of microfluidic immunoassay chips by combining microfluidic technology with various detection techniques such as fluorescent, chemiluminescence, surface-enhanced Raman spectroscopy (SERS), and electrochemical methods and so on.

3.1 Fluorescent microfluidic immunoassay

Among all kinds of detection methods, immunofluorescence detection is a technology with high sensitivity and easy to realize real-time diagnosis. In fluorescence immunoassays, fluorescent materials such as fluorescent dyes, quantum dots (QDs),

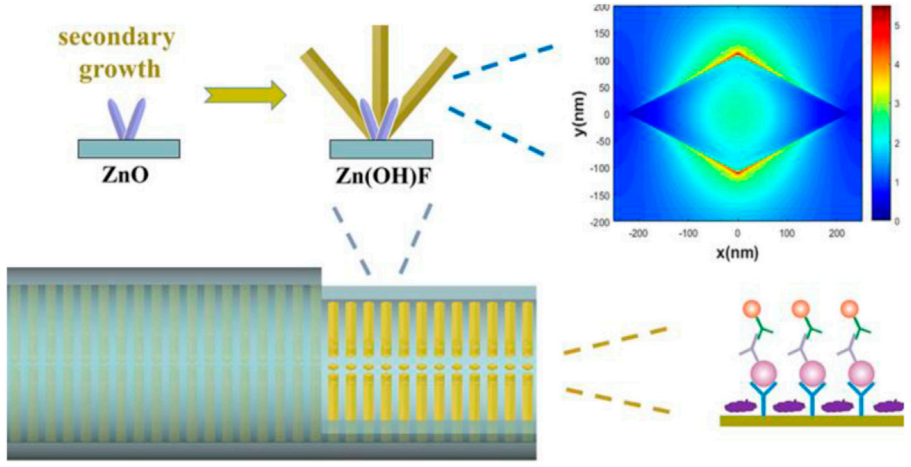

FIGURE 1
Zn(OH)F array-based microfluidic fluorescence assay (Zhao et al., 2021).

upconversion nanoparticles (UCNPs), fluorescent microspheres, aggregationinduced emission (AIE) luminogens are labeled with antigens or antibodies to achieve quantification of analytes, which can be used in the combination of fluorescence immunoassay with microfluidic chips (Zhou L. et al., 2016; Mao et al., 2016; Zhou et al., 2017; Li et al., 2019; Tan et al., 2019; Xie et al., 2019; Ding et al., 2020; Zuo et al., 2020; Chen Y. et al., 2021; Gong et al., 2021). To improve the sensitivity of fluorescent microfluidic immunoassay, integration of nanostructures with microchannels is a promising approach. At present, ZnO has been broadly used in fluorescence immunoassays because of its fluorescence amplification ability towards biomolecular (Hu et al., 2015; Liu et al., 2016; Piguillem et al., 2020). Guo et al. grew ZnO nanowires in microfluidic channels for enhanced fluorescent detection of cancer biomarkers. Due to the increase of the binding surface area and the fluorescence amplification of ZnO nanowires, the nanostructure integrated microfluidic chip attained a LOD of 1 pg/ml and 100 fg/ml in human α-fetoprotein (AFP) and carcinoembryonic antigen (CEA) detection, respectively (Guo et al., 2018). Duan's group designed a micro/nanostructure integrated microfluidic chip by combining ZnO nanorod arrays with *in situ* zeolitic imidazolate framework-8 (ZIF-8) coating for synergetic enhanced fluorescent detection. Taking advantage of the synergetic fluorescence enhancement of ZnO nanorod and ZIF-8 towards organic fluorescence labels, the microfluidic fluorescence detection of CEA exhibited a LOD as low as 0.01 pg ml^{-1} and a linear range of 0.01–100 pg ml^{-1} (Zhao et al., 2020). Furthermore, they proposed a rhombus-like Zn(OH)F array-based microfluidic device for fluorescence detection of human epididymis-specific protein 4 (HE4). The results showed that the fluorescence enhancement factor of the Zn(OH)F arrays toward Cy3 is approximately 4-fold that of the ZnO nanorod arrays, with a LOD of 9.3 fM and a linear range of 10 fM to 100 pM (Figure 1) (Zhao et al., 2021).

High throughput is an important developing direct for bioassay. To achieve high throughput immunoassay, Duan et al. combined fluorescence detection with microfluidic chips for rapid semi-quantitative detection of serum biomarker mesothelin, which allowed the simultaneous measurement of four samples with three repeats (Duan et al., 2019). Qiu et al. developed a fluorescent microfluidic immunoassay biochip based on self-assembly of Lys-AuNPs@MoS_2 nanocomposites with large contact surface, excellent stabilities and multiple binding sites (Figure 2). In this system, 60 samples such as inflammatory factors and cardiovascular biomarkers were simultaneously detected within 40 min with a limit of detection (LOD) of several to tens pg/mL (Qiu et al., 2022).

Roberto et al. developed a microfluidic device with a button valve located on each microchamber (Figure 3). Fluorescence signals were measured for four types of severe acute respiratory syndrome coronavirus 2 (SARS-COV-2) immunoglobulin in parallel from 50 serum samples, achieving a sensitivity of 95% and a specificity of 91%. In the third week after the onset of symptoms of COVID-19 infection, the sensitivity and specificity can reach 100% when assessing the serums of patients (Rodriguez-Moncayo et al., 2021).

Although with high sensitivity, the fluorescence signals of fluorescent microfluidic immunoassay are usually collected by fluorescence microscope or scanner. The application of these large instruments will increase the experimental cost and affect the portability of microfluidic devices. Therefore, the miniaturization of fluorescent microfluidic device is a goal to realize the whole process of sample pretreatment, immunobinding reaction and fluorescence signal collection on the chip, so as to realize the portable microfluidic immunofluorescence analysis system.

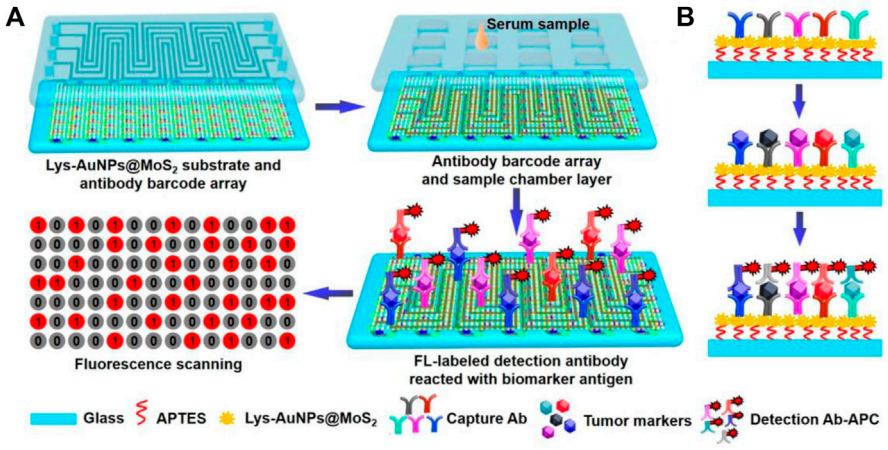

FIGURE 2
Schematic diagram of immunoassay microfluidic chip based on Lys-AuNPs@MoS_2 substrate. **(A)** Self-assembly of the Lys-AuNPs@MoS_2 substrate. **(B)** Mechanism of microfluidic incubation.

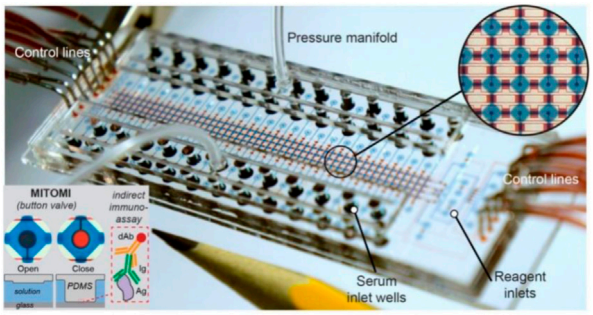

FIGURE 3
Microfluidic device using MITOMI for COVID-19 antibody detection (Rodriguez-Moncayo et al., 2021).

3.2 Chemiluminescent microfluidic immunoassay

The chemiluminescence immunoassay (CLIA) which combine chemiluminescence detection with a specific immunosorbent assay is widely used in clinical diagnostic (Zhou B. et al., 2016; Yao et al., 2016). The conventional CLIA is limited by the requirement of large equipment, cumbersome operation process, and high consumption. Integration of CLIA with microfluidic chip is promising to offer a simple, low reagent consumption and inexpensive platform for immunoassay, and promote high throughput screening and POCT diagnostics. Huang et al. developed an active droplet-array (ADA) microfluidics-based CLIA system for procalcitonin detection, which consists of a compact microchip analyzer and microfluidic chips with preloaded reagents. The detection can be completed automatically in 12 min, with a LOD of 0.044 ng ml^{-1} and a detection range from 0.044 to 100 ng ml^{-1} (Huang et al., 2022). Smartphone-enabled microfluidic CLIA is a promising portable system for POC applications, but it is suffered from the rather weak chemiluminescent light emitted from a limited sample volume in the microchannel when using the smartphone as a detector. Chen et al. proposed a novel acoustic streaming tweezers-enabled microfluidic CLIA (Figure 4). In this design, probe particles were enriched and the biomarker capture capability was enhanced under high-speed microscale vortexes, which increased the local chemiluminescent intensity and enable the direct capture of light signal by a common smartphone camera. The system reached a LOD of 0.2 ng/ml and a large linear range from 0.3 to 10 ng/ml for prostate-specific antigen (PSA) detection (Chen X. et al., 2021).

Up to now, multiplex CLIA for sensitive and simultaneous detection of biomarkers still remains a great challenge. Two strategies of CL multiplex microfluidic immunoassay in one detection run have been reported, including temporal-resolved and spatial-resolved detection. For temporal-resolved CLIA strategy, solution migration delays are created in microfluidic paper-based analytical devices (μPADs) to generate temporal-resolved CL signals for multiplex analysis. For spatial-resolved CLIA strategy, spatial-resolved CL arrays were fabricated by spotting different antibodies at defined positions for simultaneous determination, and the CL imaging signals are recorded simultaneously by a cooled low-light charge-coupled imaging device (CCD). Cui's group developed a CLIA strategy for simultaneous detection of copeptin, heart-type

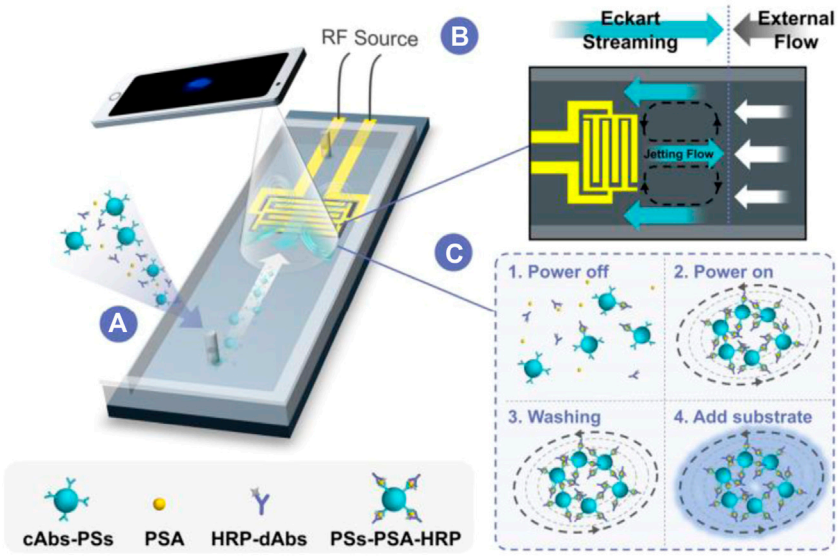

FIGURE 4
Acoustically enhanced microfluidic smartphone detection platform. **(A)** The platform enhances biomolecular binding and enriches the formed immunocomplexes simultaneously. **(B)** The opposite Eckart streaming and external flow determine the size of the vortex and the compactness of the particles in the vortex. **(C)** The interactions between reagents were enhanced by streaming and particle trapping, washing, reaction, and sensing are achieved on the same chip at continuous flow.

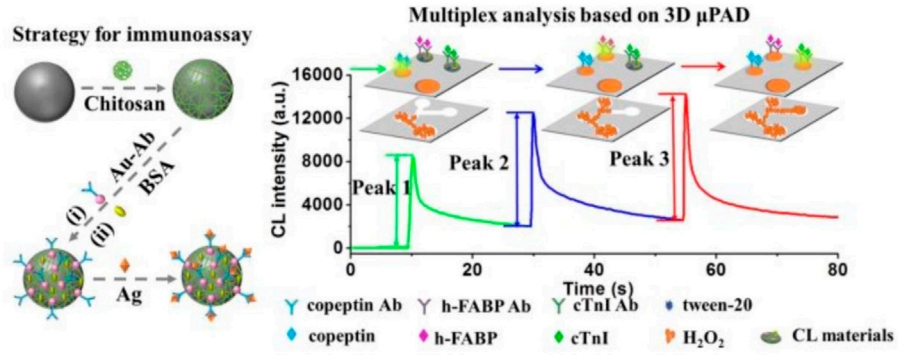

FIGURE 5
Schematic illustration of multiplex CLIA based on Co^{2+}-ABEI-Fe_3O_4@void@C and 3D μPAD (Yang et al., 2019).

fatty acid binding protein (h-FABP), and cardiac troponin I (cTnI) by using Co^{2+}/N-(aminobutyl)-N-(ethylisoluminol) (ABEI) functionalized magnetic carbon composite (Co^{2+}-ABEI-Fe_3O_4@void@C) as an interface and a three-dimensional paper-based analytical devices as a detection system (Figure 5). The antigen (Ag) were captured by the antibody on the sensing interface to increase CL intensity due to the catalysis of −COO−existing in Ag. After injecting H_2O_2, three time-resolved CL signals were generated in one CL detection run by virtue of time-delayed transport of H_2O_2 to different detection zones. The detection limit of copeptin, h-FABP, and cTnI was 0.40 pg/ml, 0.32 pg/ml, and 0.50 pg/ml respectively, which is at least one order of magnitude lower than most of the reported immunoassays (Yang et al., 2019).

Furthermore, they reported a temporal-spatial-color multi-resolved CL imaging method for multiplex immunoassay using a smartphone coupled with a microfluidic chip, which was performed by sequentially transporting coreactant H_2O_2 to the detection zones to initiate cobalt-based zeolitic imidazolate frameworks ZIF-67 catalyzed luminol-H_2O_2 CL and CL

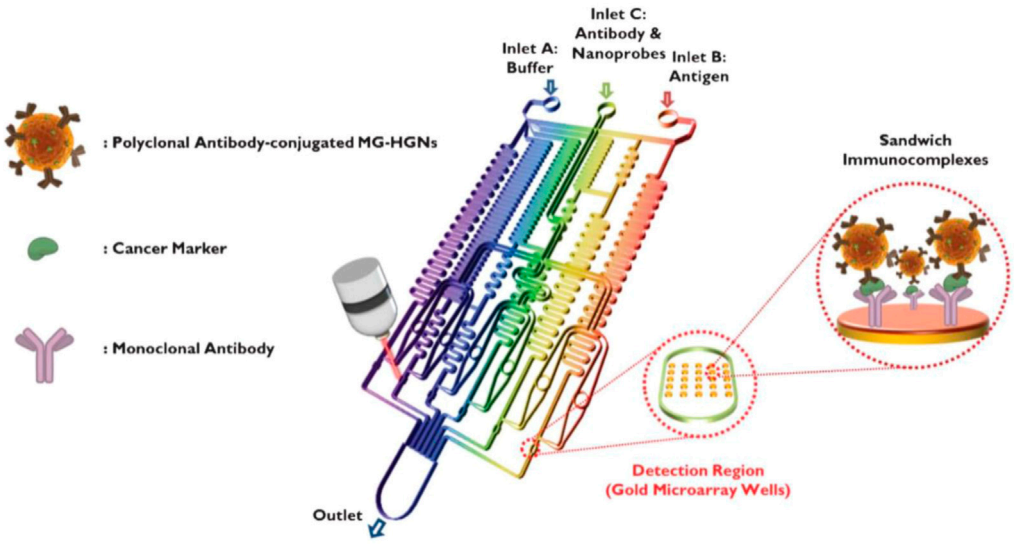

FIGURE 6
Schematic diagram of a gold array-embedded gradient chip for the SERS-based immunoassay. The illustrations in the enlarged circles represent the formation of sandwich immunocomplexes on the surface of 5*5 round gold wells embedded in the gradient channel (Lee et al., 2012).

resonance energy transfer reactions (Li et al., 2020). The strategy was applied for multiplex analysis of three cancer biomarkers with a low LOD of pg/mL to fg/mL, good selectivity, and low-cost.

CLIA based on μPADs has become an attractive method because of its simplicity, high sensitivity, and high compatibility. However, sandwich-type CLIA need two antibodies and labeling technology, which suffers from multistep reactions and purifications, resulting in complex operation, high cost and long analytical time. Thus, It's still challengeable to meet the requirement of rapid clinical diagnosis.

3.3 SERS-based microfluidic immunoassay

SERS detection is a powerful spectroscopy technology by providing ultrasensitive and intrinsic chemical fingerprint information (Liu et al., 2018; Zuo et al., 2018). SERS-based assays are promising methods for immunoassays due to their rapid and sensitive analytical capabilities. SERS has inherent advantages over fluorescence, including minimal photobleaching effect, wide excitation wavelength range, and multiplexing capability (Gao et al., 2016). To achieve rapid immunoassay and reproducible SERS signals, SERS-based microfluidic chips have been developed to improve the performance of immunoassay, which involve of continuous microfluidic system and microdroplet microfluidics. The most common serial microfluidic immunoassays are performed in microfluidic channels ranging in size from 10 to 1,000 μm. Microfluidic channels can be analyzed in parallel with multiple samples simultaneously. Combined with SERS technology, microfluidic immunoassays can improve the performance of immunoassays in terms of sensitivity, response time, throughput, and overall cost (Wang et al., 2017). In continuous microfluidic system, the samples and reagents continuously flow in the microchannel. Choo's group designed a SERS-based microfluidic immunoassay platform by combining a gradient microfluidic device with gold-patterned microarray wells (Figure 6) (Lee et al., 2012). A 5*5 gold microarray was embedded in the micro-channel to form sandwich immunocomplexes for SERS detection. They also utilized magnetic beads to form magnetic immunocomplexes which were trapped by yoke-type solenoids embedded within the microfluidic device. The SERS-based competitive immunoassay was performed within a microfluidic environment and the SERS signals of anthrax biomarker poly-γ-D-glutamic acid (PGA) were detected with a LOD of 100 pg/ml (Gao et al., 2015). Automating the immunoassay process in microfluidic channels increases the efficiency and control of manual operations. Recently, Li et al. reported a "magnetic focused" microfluidic immunoassay in which nanoprobes are magnetically focused to specific points in the microfluidic channel, enabling the enrichment of "hot spots" for SERS detection targeting carcinoembryonic antigen with a detection limit of 0.1 pM, achieving high sensitivity (Li et al., 2015). In addition, Kaminska et al. developed a gold-silver coated gallium nitride substrate as a novel immunofixation platform, which improved the efficiency of SERS-based microfluidic immunoassays and achieved a low detection limit

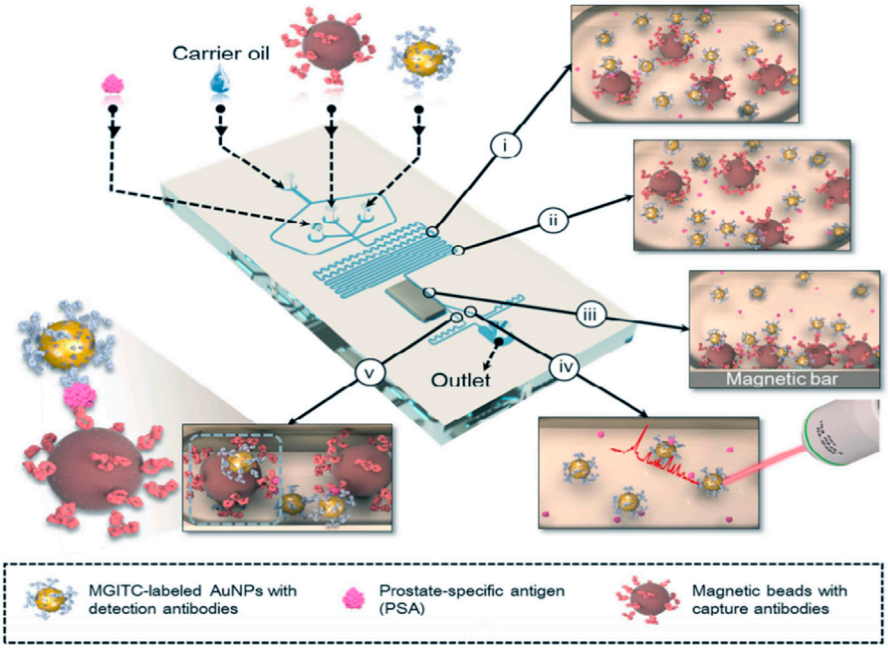

FIGURE 7
Schematic illustration of the SERS-based microdroplet sensor for wash-free magnetic immunoassay (Gao et al., 2016).

of 0.01 IU/ml for hepatitis B virus antigen (Kaminska et al., 2015).

To reduce the sensor size and improve the portability of microfluidic sensor, Gao et al. proposed a novel pump-free microfluidic system for SERS-based immunoassay which applied a capillary pump to replace heavy syringe pump in conventional microfluidic system. Using this chip for rapid analysis of PSA biomarker, the LOD is estimated to be below 0.01 ng ml^{-1}, with a good linear response in the range from 0.01 to 100 ng ml^{-1} (Gao et al., 2019). Furthermore, they developed another pump-free SERS-microfluidic chip for the simultaneous detection of creatine kinase MB isoenzyme (CK-MB) and cardiac troponin (cTnI) cardiac markers. In this study, the patterned SERS paper substrate was fabricated and then in-situ synthesized AuNPs on paper microchannel. The 3D fibre structure provided the capillarity force and compacted AuNPs deposition scaffold for sample flow and highly sensitive SERS detection, which simultaneously detected the concentrations of two cardiac markers ranging from 0.01 to 50 ng/ml (Gao et al., 2022).

Unlike the continuous microfluidic systems, the microdroplet microfluidics focuses on creating discrete microdroplet by utilizing immiscible phases. Droplet microfluidic systems perform miniaturization reactions by separating reaction components into discrete microliters to picoliter volumes (Berry et al., 2019). It enables fast and high-throughput analysis without increasing the complexity and size of microfluidic chips. The advantages offered by this platform include reduced reagent consumption, precise control of reaction time, and the ability to synthesize highly homogeneous micro/nanostructures. Droplet microfluidics can be combined with SERS technology for fast and reproducible analysis. To date, the droplet SERS platform has been used in a variety of biochemical applications (Wang et al., 2017). Gao et al. reported a novel wash-free SERS-based microdroplet sensor for sensitive immunoassay of PSA biomarker (Figure 7). In this strategy, a magnetic bar was embedded in the microfluidic system to split droplets into two parts: one magnetic immunocomplexes and the other the free SERS tags. The presence of PSA target lead more SERS tags to immunocomplex in one droplet so that the SERS signals were able to be measured for quantitative evaluation of PSA marker. The SERS signals were measured at 174 droplets/minute and the LOD was estimated to be below 0.1 ng/ml (Gao et al., 2016).

The emerging of novel techniques promotes the development of microfluidic immunoassay chips. Wang et al. proposed an immunoassay method based on a novel digital microfluidics (DMF) and SERS for detection of disease biomarkers (Figure 8). Based on the principle of electrowetting on dielectric, droplets were individually driven to transport, merge, split, and dispense from reservoirs by applying electrical potentials to an array of electrodes, which greatly simplified the analysis process while reducing the risk of

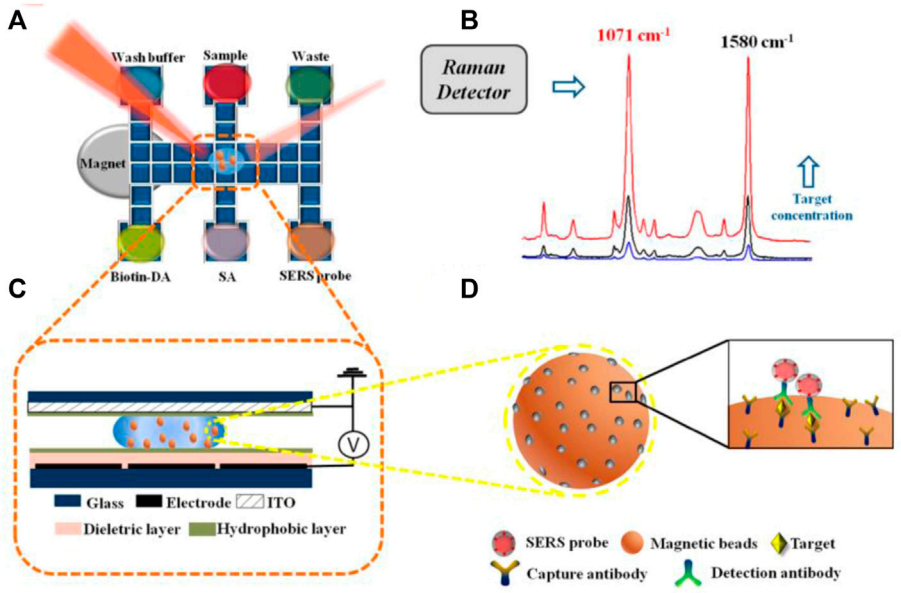

FIGURE 8
Schematic diagram of SERS immune analysis by DMF. **(A)** Illustration of DMF-SERS method and bottom plate of DMF chip. **(B)** Two characteristic Raman peaks of 4-MBA at 1071 cm^{-1} and 1580 cm^{-1}. **(C)** Side view of DMF chip containing a droplet with magnetic beads. **(D)** Immunocomplex functionalized with SERS tags on magnetic beads.

exposure to hazardous samples. Compared with the standard ELISA method, DMF-SERS method has high sensitivity (LOD 74 pg/ml) and good selectivity (Wang et al., 2018).

SERS based microfluidic chips provides an ideal mechanism for achieving homogeneous mixing, spatially defined detection areas, sensitive and reproducible measurements with low sample consumption. Because of the larger size of Raman detector, the miniaturization of SERS based microfluidic device is a challenge to achieve POCT immunoassay.

3.4 Electrochemical microfluidic immunoassay

Electrochemical detection integrated with microfluidic devices are promising for immunoassay due to the benefits such as low sample consumption, low detection limit, and rapid, simple and portable assay (He et al., 2018a; Yang G. et al., 2018; Lai et al., 2019; Xie et al., 2020; He et al., 2021; Schmidt-Speicher and Länge, 2021; Wang et al., 2022). To improve the sensitivity of electrochemical microfluidic immunoassay, surface modification of electrodes in the microchannels are widely used in order to increase the surface area and binding ability (He et al., 2015; He et al., 2018b; Ning et al., 2018; Deng et al., 2021a; Deng et al., 2021b; Zhang et al., 2021). MatÃas et al. produced a gold nanoporous structure on the gold electrode in the microchannel by using dynamic hydrogen bubble template (DHBT) method, which obtained outstanding properties, like high specific surface area, large pore volume, good conductivity, and excellent electrochemical activity. The selectivity and sensitivity of the sensor were improved, achieving a LOD of 30 pg ml^{-1} and a variation coefficient less than 4.75% for the detection of SOX-2 cancer biomarker (Regiart et al., 2020). Jofre et al. reported an electrochemical microfluidic immunosensor by modifying the gold electrode with an ordered mesoporous carbon in chitosan to increase the sensitivity of detection (Jofre et al., 2020). Zhang et al. proposed a miniaturized electrochemical microfluidic immunosensor for interleukin-6 (IL-6) detection. The electrode was modified with gold nanoparticles and graphene to increase surface area, and magnetic beads were employed to concentrate immunoassay on the electrode (Figure 9). This magneto-immunosensor achieved a LOD of 0.42 pg/ml and a linear range from 0.97–250 pg/ml (Zhang C. et al., 2022).

The advantages of electrochemical microfluidic devices such as being small and portable make them becoming the powerful candidates to construct POCT platform. In these devices, graphene oxide (GO) is usually coated on the electrodes using a screen-printing technique, which is beneficial to the covalent immobilization of proteins. Baldo et al. developed a disposable electrochemical microfluidic device (DEμD) for ultrasensitive detection of ovalbumin (OVA) in wine (Figure 10). In the

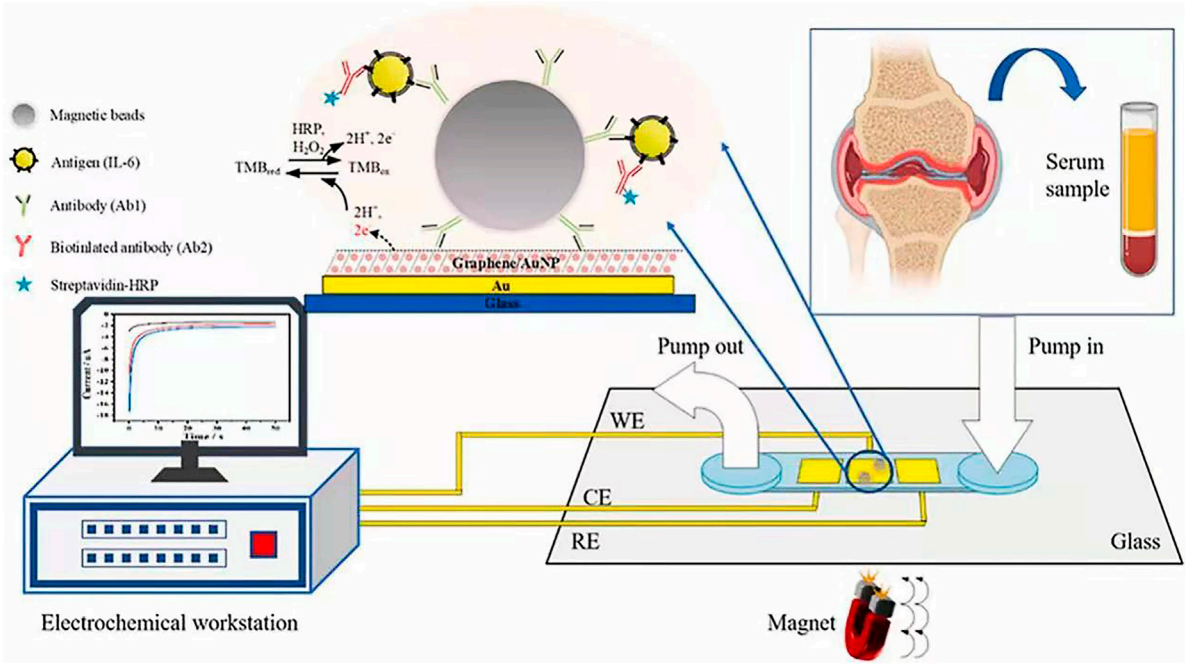

FIGURE 9
Microfluidic electrochemical magnetoimmunosensor based on hybrid of AuNPs and graphene (Zhang C. et al., 2022).

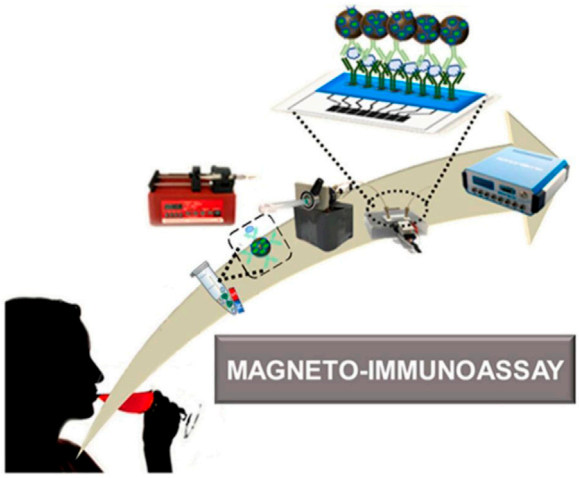

FIGURE 10
Schematic illustration of DEμD for OVA detection in wine samples (Baldo et al., 2021).

DEμD, 8 GO-based working electrodes (8-WEs) integrated with horseradish peroxidase (HRP) and anti-OVA antibody modified magnetic beads to achieve sandwich assay. The magneto-immunoassay obtained a ultralow LOD of 0.2 fg ml^{-1} and a wide linear range of 0.01~10 pg ml^{-1} for OVA detection, which allows eight simultaneous detections per device (Baldo et al., 2021).

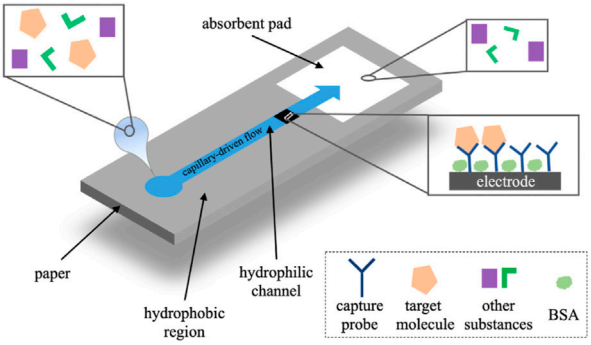

FIGURE 11
The operational principle of electrochemical μPADs (Yuan et al., 2022).

Paper-based analytical devices have the advantages of low cost, portable, eco-friendly, and high-throughput manufacturing, which makes it become an ideal alternative for POCT (Lim et al., 2019; Ruecha et al., 2019; Gutierrez-Capitan et al., 2020). Nowadays, microfluidic paper-based analytical devices (μPADs) integrated with electrochemical detection have been developed as typical POCT devices for immunoassay (Cate et al.,

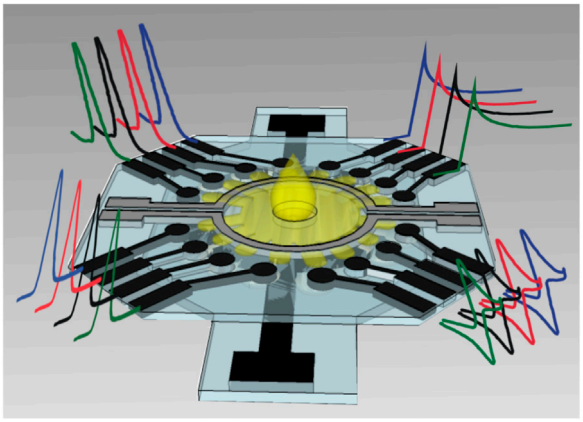

FIGURE 12
Schematic representation of multiplex μPAD based on 16 electrodes (Fava et al., 2019).

2015; Yuan et al., 2022). In electrochemical μPADs (Figure 11), samples flow through the micro-channel and the working electrode driven by the capillary. The target molecules are captured by the probes on the electrode and the electrochemical signals are detected (Yuan et al., 2022).

Cao et al. structured electrochemical μPADs for the detection of Human Chorionic Gonadotropin (HCG) based on the standard sandwich immunoreaction (Cao et al., 2017). Ruecha et al. developed a label-free electrochemical μPAD immunosensor in which the screen-printed electrodes were modified with polyaniline/graphene nanocomposites to provide high conductivity and large surface area, which obtained a LOD of 3.4 pg ml^{-1} and a linear range of 5–1,000 pg ml^{-1} for detection of human IFN-γ (Ruecha et al., 2019). For multiplex analysis, Wang et al. developed a multi-parameter μPAD for simultaneous detection of carcinoembryonic antigen (CEA) and neuron-specific enolase (NSE) (Yang et al., 2019). Fava et al. proposed a high-throughout

TABLE 1 Different immunoassay applications based on microfluidic chips.

Detection principle	Instrumentation for integration	Applications	Results (LOD: Limit of detection; DR: Dynamic range)	References
Fluorescence	Fluorescence microscope	Enzymatic assay (glucose), magnetic bead-based immunoassay (lgE)	DR: 26–150 mg L^{-1} (glucose); LOD: 150 nM (lgE)	Vergauwe et al. (2011)
Fluorescence	Microplate reader	Rhombus-like Zn(OH)F array-based immunoassay (Cy3)	DR: 10 fM-100 pM; LOD: 9.3 fM	Zhao et al. (2021)
Fluorescence	Fluorescence microscope	ZnO nanowires-based immunoassay	LOD: 1 pg mL^{-1} (AFP) 100 fg mL^{-1} (CEA)	Guo et al. (2018)
Chemiluminescence	PMT	Magnetic bead-based immunoassay to detect insulin and interleukin-6	DR:8–1,000 pmol L^{-1} (insulin); 1.5–750 pg mL^{-1} (IL-6)	Sista et al. (2008)
Chemiluminescence	Photodiode	Magnetic bead-based immunoassay to separate and detect protein, bacteria and virus	LOD: 30 ng mL^{-1} (HSA); 4×10^4 cfu mL^{-1} (*Bacillus atrophaeus*); 10^6 cfu mL^{-1} (MS2 bacteriophage); 2×10^7 cfu mL^{-1} (*Escherichia coli*)	Coudron et al. (2019)
Chemiluminescence	PMT	Magnetic bead-based immunoassay to quantitatively detect rubella IgG	DR: 0.15–100 μU mL^{-1} LOD: 0.15 μU mL^{-1}	Fobel et al. (2014)
Chemiluminescence	PMT	Magnetic bead-based immunoassay to detect rubella virus (RV) IgG directly from blood	LOD: 1.9 IU mL^{-1}	Dixon et al. (2020)
Surface enhanced Raman scattering (SERS)	Raman detector	Immunoassay on a DMF platform to detect avian influenza virus H5N1	LOD: 74 pg mL^{-1}	Wang et al. (2018)
Electrochemistry	Electrochemical potentiostat	Magnetic bead-based immunoassay to detect interleukin-6	DR: 0.97–250 pg mL^{-1} LOD: 0.42 pg mL^{-1}	Zhang et al. (2022a)
Electrochemistry	Electrochemical analyzer	Paper-based microfluidic device coupled with label-free electrochemical impedance immunosensor to detect human interferon-gamma (IFN-γ)	DR: 5–1,000 pg mL^{-1} LOD: 3.4 pg mL^{-1}	Ruecha et al. (2019)

μPAD based on 16 independent microfluidic channels for glucose determination in urine (Figure 12), obtaining a LOD of 3×10^{-5} mol L^{-1} and a linear range from 1.0×10^{-4} mol L^{-1} to 4×10^{-2} mol L^{-1} (Fava et al., 2019).

Electrochemical microfluidic devices provide an attractive strategy with low reagent consumption, sensitivity, ease of handling, cost-effectiveness, rapid analysis and miniaturization ability. Based on the simplicity of electrochemical detection, electrochemical microfluidic immunoasssay are promising in the development of POCT and multiplex detection devices.

In summary, different platforms have their own characteristics. Here, we list the representative configurations of each platform, including its detection mechanism, instrumentation, application, and detection limits, in Table 1 for a clear comparison.

4 Conclusion

In recent years, microfluidic chip technology has been applied across many fields and disciplines, and biomedical applications are one of the focuses of current researches. The advantages brought by the unique physical and chemical properties of reactions in microchannels continue to promote the development of microfluidic chip technology. In this review, microfluidic chip technology is summarized from the aspects of chip materials, preparation technologies and applications in immunoassay. The emergence of new materials has improved some of the performance of microfluidic chip, but there are also some shortcomings which can not completely replace the earlier materials. In the future, the material development of microfluidic chips should fully consider the precision of processing technology, the processing cost and the ease of mass production. With the advantage of good compatibility with other detection techniques, the development of microfluidic chip should focus on integrated, automated, miniaturized and high throughput equipment. One obvious developing trend is portable microfluidic devices, which is great potential in POCT detection of biological samples with low consumption, real-time monitoring, simple operation and low cost. In addition, the designs of simultaneous detection of multiple biomarkers will be popular in the application of microfluidic chip as biosensor. With the rapid development of microfluidic devices, single performance microfluidic chip could not meet the current demand. The application of diverse and multifunctional manufacturing technologies is urgent, which requires not only the innovation of microfluidic chip materials, but also the integration of various technologies such as microfluidics and microelectronics. The multidisciplinary nature of microfluidic technology requires continuous and coordinated development between different fields. In addition, the actual sample analysis by microfluidic chip, such as sample input and pretreatment, still face the challenge. With the progress of various technologies and further research, microfluidic chips are of great potentials in commercial applications in the field of biological detection.

Author contributions

KW and XH developed the review outline, wrote the manuscript, and developed the figures. LN supervised the content. JW, TP, RH, FK, ZC, FJ, and ZH critically contributed to the content and reviewed the manuscript to ensure accuracy and completeness. All authors contributed to the article and approved the submitted version.

Funding

This work was supported by the Natural Science Foundation of Hunan Province (2020JJ6102), and Scientific Research Fund of Hunan Provincial Education Department (19A144).

Conflict of interest

The authors declare that the research was conducted in the absence of any commercial or financial relationships that could be construed as a potential conflict of interest.

Publisher's note

References

Abe, K., Kotera, K., Suzuki, K., and Citterio, D. (2010). Inkjet-printed paperfluidic immuno-chemical sensing device. *Anal. Bioanal. Chem.* 398 (2), 885–893. doi:10.1007/s00216-010-4011-2

Alix-Panabières, C., and Pantel, K. (2014). Challenges in circulating tumour cell research. *Nat. Rev. Cancer* 14 (9), 623–631. doi:10.1038/nrc3820

Bai, Y., Ji, J., Ji, F., Wu, S., Tian, Y., Jin, B., et al. (2022). Recombinase polymerase amplification integrated with microfluidics for nucleic acid testing at point of care. *Talanta* 240, 123209. doi:10.1016/j.talanta.2022.123209

Baldo, T. A., Proenca, C. D. A., Felix, F. D. S., Freitas, T. A., Sakata, S. K., Angnes, L., et al. (2021). Disposable electrochemical microfluidic device for ultrasensitive detection of egg allergen in wine samples. *Talanta* 232, 122447. doi:10.1016/j.talanta.2021.122447

Berry, S. B., Lee, J. J., Berthier, J., Berthier, E., and Theberge, A. B. (2019). Droplet incubation and splitting in open microfluidic channels. *Anal. Methods* 11 (35), 4528–4536. doi:10.1039/c9ay00758j

Cao, L., Fang, C., Zeng, R., Zhao, X., Jiang, Y., and Chen, Z. (2017). Paper-based microfluidic devices for electrochemical immunofiltration analysis of human chorionic gonadotropin. *Biosens. Bioelectron.* 92, 87–94. doi:10.1016/j.bios.2017.02.002

Carrilho, E., Martinez, A. W., and Whitesides, G. M. (2009). Understanding wax printing: A simple micropatterning process for paper-based microfluidics. *Anal. Chem.* 81 (16), 7091–7095. doi:10.1021/ac901071p

Cate, D. M., Adkins, J. A., Mettakoonpitak, J., and Henry, C. S. (2015). Recent developments in paper-based microfluidic devices. *Anal. Chem.* 87 (1), 19–41. doi:10.1021/ac503968p

Chen, D.-c., Hsu, F.-L., Zhan, D.-Z., and Chen, C.-h. (2001). Palladium film decoupler for amperometric detection in electrophoresis chips. *Anal. Chem.* 73 (4), 758–762. doi:10.1021/ac000452u

Chen, X., Ning, Y., Pan, S., Liu, B., Chang, Y., Pang, W., et al. (2021a). Mixing during trapping enabled a continuous-flow microfluidic smartphone immunoassay using acoustic streaming. *ACS Sens.* 6 (6), 2386–2394. doi:10.1021/acssensors.1c00602

Chen, Y., Liu, W. Y., and Zeng, G. S. (2016). Stimulus-responsive hydrogels reinforced by cellulose nanowhisker for controlled drug release. *RSC Adv.* 6 (90), 87422–87432. doi:10.1039/c6ra14421g

Chen, Y., Liu, W., Zeng, G., and Liu, Y. (2017). Microporous PDMAEMA-based stimuli-responsive hydrogel and its application in drug release. *J. Appl. Polym. Sci.* 134 (38), 45326. doi:10.1002/app.45326

Chen, Y., Tang, Y., and Wang, H. (2021b). Quantification of ATP in cell by fluorescence spectroscopy based on generalized ratio quantitative analysis model. *Spectrochim. Acta A Mol. Biomol. Spectrosc.* 263, 120170. doi:10.1016/j.saa.2021.120170

Chitnis, G., Ding, Z., Chang, C. L., Savran, C. A., and Ziaie, B. (2011). Laser-treated hydrophobic paper: An inexpensive microfluidic platform. *Lab. Chip* 11 (6), 1161–1165. doi:10.1039/c0lc00512f

Chow, A. Y., Chow, V. Y., Packo, K. H., Pollack, J. S., Peyman, G. A., and Schuchard, R. (2004). The artificial silicon retina microchip for the treatment of VisionLoss from retinitis pigmentosa. *Archives Ophthalmol.* 122 (4), 460. doi:10.1001/archopht.122.4.460

Coudron, L., McDonnell, M. B., Munro, I., McCluskey, D. K., Johnston, I. D., Tan, C. K. L., et al. (2019). Fully integrated digital microfluidics platform for automated immunoassay; A versatile tool for rapid, specific detection of a wide range of pathogens. *Biosens. Bioelectron.* 128, 52–60. doi:10.1016/j.bios.2018.12.014

Daw, R., and Finkelstein, J. J. N. (2006). Lab on a chip. *Insight Lab a chip* 442 (7101), 367–418. doi:10.1038/442367a

Decock, J., Schlenk, M., and Salmon, J. B. (2018). *In situ* photo-patterning of pressure-resistant hydrogel membranes with controlled permeabilities in PEGDA microfluidic channels. *Lab. Chip* 18 (7), 1075–1083. doi:10.1039/c7lc01342f

Deng, P., Feng, J., Xiao, J., Wei, Y., Liu, X., Li, J., et al. (2021a). Application of a simple and sensitive electrochemical sensor in simultaneous determination of paracetamol and ascorbic acid. *J. Electrochem. Soc.* 168 (9), 096501. doi:10.1149/1945-7111/ac1e59

Deng, P., Xiao, J., Feng, J., Tian, Y., Wu, Y., Li, J., et al. (2021b). Highly sensitive electrochemical sensor for tyrosine detection using a sub-millimeter electrode. *Microchem. J.* 165, 106106. doi:10.1016/j.microc.2021.106106

Deng, Y., Wang, W., Ma, C., and Li, Z. (2013). Fabrication of an electrochemical biosensor array for simultaneous detection of L-glutamate and acetylcholine. *J. Biomed. Nanotechnol.* 9 (8), 1378–1382. doi:10.1166/jbn.2013.1633

Ding, S., Xu, A., Li, M., Sun, A., Zhang, Z., Xia, Y., et al. (2020). Theoretical study on the sensing mechanism of an ON(1)-OFF-ON(2) type fluoride fluorescent chemosensor. *Spectrochim. Acta A Mol. Biomol. Spectrosc.* 237, 118397. doi:10.1016/j.saa.2020.118397

Dixon, C., Lamanna, J., and Wheeler, A. R. (2020). Direct loading of blood for plasma separation and diagnostic assays on a digital microfluidic device. *Lab. Chip* 20 (10), 1845–1855. doi:10.1039/d0lc00302f

Dornhof, J., Kieninger, J., Muralidharan, H., Maurer, J., Urban, G. A., and Weltin, A. (2022). Microfluidic organ-on-chip system for multi-analyte monitoring of metabolites in 3D cell cultures. *Lab. Chip* 22 (2), 225–239. doi:10.1039/d1lc00689d

Duan, X., Zhao, L., Dong, H., Zhao, W., Liu, S., and Sui, G. (2019). Microfluidic immunoassay system for rapid detection and semi-quantitative determination of a potential serum biomarker mesothelin. *ACS Sens.* 4 (11), 2952–2957. doi:10.1021/acssensors.9b01430

Fava, E. L., Silva, T. A., Prado, T. M. D., Moraes, F. C., Faria, R. C., and Fatibello-Filho, O. (2019). Electrochemical paper-based microfluidic device for high throughput multiplexed analysis. *Talanta* 203, 280–286. doi:10.1016/j.talanta.2019.05.081

Fobel, R., Kirby, A. E., Ng, A. H., Farnood, R. R., and Wheeler, A. R. (2014). Paper microfluidics goes digital. *Adv. Mater* 26 (18), 2838–2843. doi:10.1002/adma.201305168

Gabriel, E. F. M., Coltro, W. K. T., and Garcia, C. D. (2014). Fast and versatile fabrication of PMMA microchip electrophoretic devices by laser engraving. *Electrophoresis* 35 (16), 2325–2332. doi:10.1002/elps.201300511

Gao, R., Chen, F., Yang, D., Zheng, L., Jing, T., Jia, H., et al. (2022). Simultaneous sers-based immunoassay of dual cardiac markers on pump-free hybrid microfluidic chip. *Sens. Actuators B Chem.* 369, 132378. doi:10.1016/j.snb.2022.132378

Gao, R., Cheng, Z., deMello, A. J., and Choo, J. (2016). Wash-free magnetic immunoassay of the PSA cancer marker using SERS and droplet microfluidics. *Lab. Chip* 16 (6), 1022–1029. doi:10.1039/c5lc01249j

Gao, R., Ko, J., Cha, K., Jeon, J. H., Rhie, G. E., Choi, J., et al. (2015). Fast and sensitive detection of an anthrax biomarker using SERS-based solenoid microfluidic sensor. *Biosens. Bioelectron.* 72, 230–236. doi:10.1016/j.bios.2015.05.005

Gao, R., Lv, Z., Mao, Y., Yu, L., Bi, X., Xu, S., et al. (2019). SERS-based pump-free microfluidic chip for highly sensitive immunoassay of prostate-specific antigen biomarkers. *ACS Sens.* 4 (4), 938–943. doi:10.1021/acssensors.9b00039

Goldstein, Y., Spitz, S., Turjeman, K., Selinger, F., Barenholz, Y., Ertl, P., et al. (2021). Breaking the third wall: Implementing 3D-printing techniques to expand the complexity and abilities of multi-organ-on-a-chip devices. *Micromachines (Basel)* 12 (6), 627. doi:10.3390/mi12060627

Gong, L., Zhao, L., Tan, M., Pan, T., He, H., Wang, Y., et al. (2021). Two-photon fluorescent nanomaterials and their applications in biomedicine. *J. Biomed. Nanotechnol.* 17 (4), 509–528. doi:10.1166/jbn.2021.3052

Guo, L., Shi, Y., Liu, X., Han, Z., Zhao, Z., Chen, Y., et al. (2018). Enhanced fluorescence detection of proteins using ZnO nanowires integrated inside microfluidic chips. *Biosens. Bioelectron.* 99, 368–374. doi:10.1016/j.bios.2017.08.003

Gutierrez-Capitan, M., Baldi, A., and Fernandez-Sanchez, C. (2020). Electrochemical paper-based biosensor devices for rapid detection of biomarkers. *Sensors (Basel)* 20 (4), 967. doi:10.3390/s20040967

Hale, B. G., Albrecht, R. A., and García-Sastre, A. (2010). Innate immune evasion strategies of influenza viruses. *Future Microbiol.* 5 (1), 23–41. doi:10.2217/fmb.09.108

Hamdallah, S. I., Zoqlam, R., Erfle, P., Blyth, M., Alkilany, A. M., Dietzel, A., et al. (2020). Microfluidics for pharmaceutical nanoparticle fabrication: The truth and the myth. *Int. J. Pharm.* 584, 119408. doi:10.1016/j.ijpharm.2020.119408

He, L., Huang, R., Xiao, P., Liu, Y., Jin, L., Liu, H., et al. (2021). Current signal amplification strategies in aptamer-based electrochemical biosensor: A review. *Chin. Chem. Lett.* 32 (5), 1593–1602. doi:10.1016/j.cclet.2020.12.054

He, Q., Liu, J., Liu, X., Li, G., Deng, P., Liang, J., et al. (2018a). Sensitive and selective detection of tartrazine based on TiO(2)-electrochemically reduced graphene oxide composite-modified electrodes. *Sensors (Basel)* 18 (6), 1911. doi:10.3390/s18061911

He, Q., Liu, J., Liu, X., Xia, Y., Li, G., Deng, P., et al. (2018b). Novel electrochemical sensors based on cuprous oxide-electrochemically reduced graphene oxide nanocomposites modified electrode toward sensitive detection of sunset yellow. *Molecules* 23 (9), 2130. doi:10.3390/molecules23092130

He, X., Li, C., Jiang, Y., Zhu, Q., Wang, W., Zhang, C., et al. (2015). Electrochemical mechanism of Cr(III) reduction for preparing crystalline chromium coatings based on 1-Ethyl-3-methylimidazolium bisulfate ionic liquid. *J. Electrochem. Soc.* 162 (9), D435–D443. doi:10.1149/2.0461509jes

Hellmann, J. (2008). Deciding to resuscitate extremely premature babies: How do parents and neonatologists engage in the decision? *Yearb. Neonatal Perinat. Med.* 2008, 334–336. doi:10.1016/s8756-5005(08)79269-2

Hu, W., Liu, Y., Chen, T., Liu, Y., and Li, C. M. (2015). Hybrid ZnO nanorod-polymer brush hierarchically nanostructured substrate for sensitive antibody microarrays. *Adv. Mater* 27 (1), 181–185. doi:10.1002/adma.201403712

Huang, E., Huang, D., Wang, Y., Cai, D., Luo, Y., Zhong, Z., et al. (2022). Active droplet-array microfluidics-based chemiluminescence immunoassay for point-of-care detection of procalcitonin. *Biosens. Bioelectron.* 195, 113684. doi:10.1016/j.bios.2021.113684

Huang, L., Su, E., Liu, Y., He, N., Deng, Y., Jin, L., et al. (2021a). A microfluidic device for accurate detection of hs-cTnI. *Chin. Chem. Lett.* 32 (4), 1555–1558. doi:10.1016/j.cclet.2020.09.055

Huang, Q., Shan, X., Cao, R., Jin, X., Lin, X., He, Q., et al. (2021b). Microfluidic chip with two-stage isothermal amplification method for highly sensitive parallel detection of SARS-CoV-2 and measles virus. *Micromachines (Basel)* 12 (12), 1582. doi:10.3390/mi12121582

Huang, X., Hu, J., Huang, J., Zhou, G., Tun, T., Tang, J., et al. (2020). Preparation of ultrahigh-water-content nanofiber composite hydrogel for Cd^{2+} removal. *J. Chem. Technol. Biot.* 96 (5), 1237–1245. doi:10.1002/jctb.6636

Hwang, J., Cho, Y. H., Park, M. S., and Kim, B. H. (2019). Microchannel fabrication on glass materials for microfluidic devices. *Int. J. Precis. Eng. Man.* 20 (3), 479–495. doi:10.1007/s12541-019-00103-2

Jalili, A., Bagheri, M., Shamloo, A., and Kazemipour Ashkezari, A. H. (2021). A plasmonic gold nanofilm-based microfluidic chip for rapid and inexpensive droplet-based photonic PCR. *Sci. Rep.* 11 (1), 23338. doi:10.1038/s41598-021-02535-1

Jiang, H., Yang, J., Wan, K., Jiang, D., and Jin, C. (2020a). Miniaturized paper-supported 3D cell-based electrochemical sensor for bacterial lipopolysaccharide detection. *ACS Sensors* 5 (5), 1325–1335. doi:10.1021/acssensors.9b02508

Jiang, X., Chen, J., Wei, M., Li, F., Ban, B., and Li, J. (2020b). Effect of impurity content difference between quartz particles on flotation behavior and its mechanism. *Powder Technol.* 375, 504–512. doi:10.1016/j.powtec.2020.07.107

Jing, X., Li, H., Mi, H.-Y., Liu, Y.-J., Feng, P.-Y., Tan, Y.-M., et al. (2019). Highly transparent, stretchable, and rapid self-healing polyvinyl alcohol/cellulose nanofibril hydrogel sensors for sensitive pressure sensing and human motion detection. *Sens. Actuators B Chem.* 295, 159–167. doi:10.1016/j.snb.2019.05.082

Jofre, C. F., Regiart, M., Fernandez-Baldo, M. A., Bertotti, M., Raba, J., and Messina, G. A. (2020). Electrochemical microfluidic immunosensor based on TES-AuNPs@Fe(3)O(4) and CMK-8 for IgG anti-Toxocara canis determination. *Anal. Chim. Acta* 1096, 120–129. doi:10.1016/j.aca.2019.10.040

Kaminska, A., Witkowska, E., Winkler, K., Dziecielewski, I., Weyher, J. L., and Waluk, J. (2015). Detection of hepatitis B virus antigen from human blood: SERS immunoassay in a microfluidic system. *Biosens. Bioelectron.* 66, 461–467. doi:10.1016/j.bios.2014.10.082

Krishnan, M., Agrawal, N., Burns, M. A., and Ugaz, V. M. (2004). Reactions and fluidics in miniaturized natural convection systems. *Anal. Chem.* 76 (21), 6254–6265. doi:10.1021/ac049323u

Lai, Y., Deng, Y., Yang, G., Li, S., Zhang, C., and Liu, X. (2018a). Molecular imprinting polymers electrochemical sensor based on AuNPs/PTh modified GCE for highly sensitive detection of carcinomaembryonic antigen. *J. Biomed. Nanotechnol.* 14 (10), 1688–1694. doi:10.1166/jbn.2018.2617

Lai, Y., Wang, L., Liu, Y., Yang, G., Tang, C., Deng, Y., et al. (2018b). Immunosensors based on nanomaterials for detection of tumor markers. *J. Biomed. Nanotechnol.* 14 (1), 44–65. doi:10.1166/jbn.2018.2505

Lai, Y., Zhang, C., Deng, Y., Yang, G., Li, S., Tang, C., et al. (2019). A novel α-fetoprotein-MIP immunosensor based on AuNPs/PTh modified glass carbon electrode. *Chin. Chem. Lett.* 30 (1), 160–162. doi:10.1016/j.cclet.2018.07.011

Lee, K. H., Lee, K. H., Lee, J., Choi, H., Lee, D., Park, Y., et al. (2014). Integration of microfluidic chip with biomimetic hydrogel for 3D controlling and monitoring of cell alignment and migration. *J. Biomed. Mater Res. A* 102 (4), 1164–1172. doi:10.1002/jbm.a.34772

Lee, M., Lee, K., Kim, K. H., Oh, K. W., and Choo, J. (2012). SERS-based immunoassay using a gold array-embedded gradient microfluidic chip. *Lab. Chip* 12 (19), 3720–3727. doi:10.1039/c2lc40353f

Li, F., Guo, L., Li, Z., He, J., and Cui, H. (2020). Temporal-spatial-color multiresolved chemiluminescence imaging for multiplex immunoassays using a smartphone coupled with microfluidic chip. *Anal. Chem.* 92 (10), 6827–6831. doi:10.1021/acs.analchem.0c01405

Li, J., Skeete, Z., Shan, S., Yan, S., Kurzatkowska, K., Zhao, W., et al. (2015). Surface enhanced Raman scattering detection of cancer biomarkers with bifunctional nanocomposite probes. *Anal. Chem.* 87 (21), 10698–10702. doi:10.1021/acs.analchem.5b03456

Li, S.-X., Wang, Y.-Q., Chen, Z.-P., and Chen, Y. (2019). Probe technique-based generalized multivariate standard addition strategy for the analysis of fluorescence signals with matrix effects. *Chemom. Intell. Lab.* 190, 41–47. doi:10.1016/j.chemolab.2019.05.006

Li, S., Liu, H., Deng, Y., Lin, L., and He, N. (2013a). Development of a magnetic nanoparticles microarray for simultaneous and simple detection of foodborne pathogens. *J. Biomed. Nanotechnol.* 9 (7), 1254–1260. doi:10.1166/jbn.2013.1610

Li, S., Liu, H., Jia, Y., Mou, X., Deng, Y., Lin, L., et al. (2013b). An automatic high-throughput single nucleotide polymorphism genotyping approach based on universal tagged arrays and magnetic nanoparticles. *J. Biomed. Nanotechnol.* 9 (4), 689–698. doi:10.1166/jbn.2013.1568

Li, X., Tian, J., Garnier, G., and Shen, W. (2010a). Fabrication of paper-based microfluidic sensors by printing. *Colloid. Surf. B* 76 (2), 564–570. doi:10.1016/j.colsurfb.2009.12.023

Li, X., Tian, J., and Shen, W. (2010b). Progress in patterned paper sizing for fabrication of paper-based microfluidic sensors. *Cellulose* 17 (3), 649–659. doi:10.1007/s10570-010-9401-2

Lim, H., Jafry, A. T., and Lee, J. (2019). Fabrication, flow control, and applications of microfluidic paper-based analytical devices. *Molecules* 24 (16), 2869. doi:10.3390/molecules24162869

Lin, D., Li, B., Qi, J., Ji, X., Yang, S., Wang, W., et al. (2020). Low cost fabrication of microfluidic paper-based analytical devices with water-based polyurethane acrylate and their application for bacterial detection. *Sens. Actuators B Chem.* 303, 127213. doi:10.1016/j.snb.2019.127213

Liu, B., Jia, Y., Ma, M., Li, Z., Liu, H., Li, S., et al. (2013). High throughput SNP detection system based on magnetic nanoparticles separation. *J. Biomed. Nanotechnol.* 9 (2), 247–256. doi:10.1166/jbn.2013.1483

Liu, C., Meng, F., Zheng, W., Xue, T., Jin, Z., Wang, Z., et al. (2016). Plasmonic ZnO nanorods/Au substrates for protein microarrays with high sensitivity and broad dynamic range. *Sens. Actuators B Chem.* 228, 231–236. doi:10.1016/j.snb.2016.01.019

Liu, H., Dong, H., Chen, Z., Lin, L., Chen, H., Li, S., et al. (2017a). Magnetic nanoparticles enhanced microarray detection of multiple foodborne pathogens. *J. Biomed. Nanotechnol.* 13 (10), 1333–1343. doi:10.1166/jbn.2017.2418

Liu, J., Chen, C.-F., Tsao, C.-W., Chang, C.-C., Chu, C.-C., and DeVoe, D. L. (2009). Polymer microchips integrating solid-phase extraction and high-performance liquid chromatography using reversed-phase polymethacrylate monoliths. *Anal. Chem.* 81 (7), 2545–2554. doi:10.1021/ac802359e

Liu, M., Zeng, X., Ma, C., Yi, H., Ali, Z., Mou, X., et al. (2017b). Injectable hydrogels for cartilage and bone tissue engineering. *Bone Res.* 5, 17014. doi:10.1038/boneres.2017.14

Liu, P., Li, B., Fu, L., Huang, Y., Man, M., Qi, J., et al. (2020). Hybrid three dimensionally printed paper-based microfluidic platform for investigating a cell's apoptosis and intracellular cross-talk. *ACS Sens.* 5 (2), 464–473. doi:10.1021/acssensors.9b02205

Liu, Q., Chen, Z. P., Shi, C. X., Chen, Y., and Yu, R. Q. (2018). Quantitation of cobalt in Chinese tea by surface-enhanced Raman spectroscopy in combination with the spectral shape deformation quantitative theory. *J. Raman Spectrosc.* 50 (3), 322–329. doi:10.1002/jrs.5528

Lu, S., Lin, S., Zhang, H., Liang, L., and Shen, S. (2021). Methods of respiratory virus detection: Advances towards point-of-care for early intervention. *Micromachines (Basel)* 12 (6), 697. doi:10.3390/mi12060697

Ma, J., Wu, Y., Liu, Y., Ji, Y., Yang, M., and Zhu, H. (2021). Cell-sorting centrifugal microfluidic chip with a flow rectifier. *Lab. Chip* 21 (11), 2129–2141. doi:10.1039/d1lc00217a

Manz, A., Graber, N., and Widmer, H. M. (1990). Miniaturized total chemical analysis systems: A novel concept for chemical sensing. *Sens. Actuators B Chem.* 1 (1-6), 244–248. doi:10.1016/0925-4005(90)80209-i

Mao, L., Lu, Z., He, N., Zhang, L., Deng, Y., and Duan, D. (2016). A new method for improving the accuracy of miRNA detection with NaYF4:Yb, Er upconversion nanoparticles. *Sci. China Chem.* 60 (1), 157–162. doi:10.1007/s11426-016-0021-0

Martinez, A. W., Phillips, S. T., Butte, M. J., and Whitesides, G. M. (2007). Patterned paper as a platform for inexpensive, low-volume, portable bioassays. *Angew. Chem. Int. Ed. Engl.* 46 (8), 1318–1320. doi:10.1002/anie.200603817

Martins, J. P., Torrieri, G., and Santos, H. A. (2018). The importance of microfluidics for the preparation of nanoparticles as advanced drug delivery

systems. *Expert Opin. Drug Del* 15 (5), 469–479. doi:10.1080/17425247.2018.1446936

Mofazzal Jahromi, M. A., Abdoli, A., Rahmanian, M., Bardania, H., Bayandori, M., Moosavi Basri, S. M., et al. (2019). Microfluidic brain-on-a-chip: Perspectives for mimicking neural system disorders. *Mol. Neurobiol.* 56 (12), 8489–8512. doi:10.1007/s12035-019-01653-2

Mou, X.-B., Ali, Z., Li, B., Li, T.-T., Yi, H., Dong, H.-M., et al. (2016). Multiple genotyping based on multiplex PCR and microarray. *Chin. Chem. Lett.* 27 (11), 1661–1665. doi:10.1016/j.cclet.2016.04.005

Muthusubramaniam, L., Lowe, R., Fissell, W. H., Li, L., Marchant, R. E., Desai, T. A., et al. (2011). Hemocompatibility of silicon-based substrates for biomedical implant applications. *Ann. Biomed. Eng.* 39 (4), 1296–1305. doi:10.1007/s10439-011-0256-y

Nakanishi, H., Nishimoto, T., Arai, A., Abe, H., Kanai, M., Fujiyama, Y., et al. (2001). Fabrication of quartz microchips with optical slit and development of a linear imaging UV detector for microchip electrophoresis systems. *Electrophoresis* 22 (2), 230–234. doi:10.1002/1522-2683(200101)22:2<230::aid-elps230>3.0.co;2-7

Niculescu, A. G., Chircov, C., Birca, A. C., and Grumezescu, A. M. (2021). Fabrication and applications of microfluidic devices: A review. *Int. J. Mol. Sci.* 22 (4), 2011. doi:10.3390/ijms22042011

Nielsen, J. B., Hanson, R. L., Almughamsi, H. M., Pang, C., Fish, T. R., and Woolley, A. T. (2020). Microfluidics: Innovations in materials and their fabrication and functionalization. *Anal. Chem.* 92 (1), 150–168. doi:10.1021/acs.analchem.9b04986

Ning, J., He, Q., Luo, X., Wang, M., Liu, D., Wang, J., et al. (2018). Rapid and sensitive determination of vanillin based on a glassy carbon electrode modified with Cu(2)O-electrochemically reduced graphene oxide nanocomposite film. *Sensors (Basel)* 18 (9), 2762. doi:10.3390/s18092762

Pan, L. J., Tu, J. W., Ma, H. T., Yang, Y. J., Tian, Z. Q., Pang, D. W., et al. (2017). Controllable synthesis of nanocrystals in droplet reactors. *Lab. Chip* 18 (1), 41–56. doi:10.1039/c7lc00800g

Piguillem, S. V., Regiart, M., Bertotti, M., Raba, J., Messina, G. A., and Fernández-Baldo, M. A. (2020). Microfluidic fluorescence immunosensor using ZnONFs for invasive aspergillosis determination. *Microchem. J.* 159, 105371. doi:10.1016/j.microc.2020.105371

Qi, J., Li, B., Wang, X., Fu, L., Luo, L., and Chen, L. (2018). Rotational paper-based microfluidic-chip device for multiplexed and simultaneous fluorescence detection of phenolic pollutants based on a molecular-imprinting technique. *Anal. Chem.* 90 (20), 11827–11834. doi:10.1021/acs.analchem.8b01291

Qin, D., Xia, Y., Rogers, J. A., Jackman, R. J., Zhao, X.-M., and Whitesides, G. M. (1998). Microfabrication, microstructures and microsystems. *Top. Curr. Chem.* 194, 1–20. doi:10.1007/3-540-69544-3_1

Qiu, J., Jiang, P., Wang, C., Chu, Y., Zhang, Y., Wang, Y., et al. (2022). Lys-AuNPs@MoS(2) nanocomposite self-assembled microfluidic immunoassay biochip for ultrasensitive detection of multiplex biomarkers for cardiovascular diseases. *Anal. Chem.* 94 (11), 4720–4728. doi:10.1021/acs.analchem.1c05061

Qiu, X., Li, Y., Wang, Y., Guo, H., and Nie, L. (2020). A novel molecularly imprinted nanosensor based on quartz crystal microbalance for specific recognition of α-amanitin. *Microchem. J.* 159, 105383. doi:10.1016/j.microc.2020.105383

Regiart, M., Gimenez, A. M., Lopes, A. T., Carreno, M. N. P., and Bertotti, M. (2020). Ultrasensitive microfluidic electrochemical immunosensor based on electrodeposited nanoporous gold for SOX-2 determination. *Anal. Chim. Acta* 1127, 122–130. doi:10.1016/j.aca.2020.06.037

Reis, N. M., Needs, S. H., Jegouic, S. M., Gill, K. K., Sirivisoot, S., Howard, S., et al. (2021). Gravity-driven microfluidic siphons: Fluidic characterization and application to quantitative immunoassays. *ACS Sens.* 6 (12), 4338–4348. doi:10.1021/acssensors.1c01524

Rodriguez-Moncayo, R., Cedillo-Alcantar, D. F., Guevara-Pantoja, P. E., Chavez-Pineda, O. G., Hernandez-Ortiz, J. A., Amador-Hernandez, J. U., et al. (2021). A high-throughput multiplexed microfluidic device for COVID-19 serology assays. *Lab. Chip* 21 (1), 93–104. doi:10.1039/d0lc01068e

Ruecha, N., Shin, K., Chailapakul, O., and Rodthongkum, N. (2019). Label-free paper-based electrochemical impedance immunosensor for human interferon gamma detection. *Sens. Actuators B Chem.* 279, 298–304. doi:10.1016/j.snb.2018.10.024

Sackmann, E. K., Fulton, A. L., and Beebe, D. J. (2014). The present and future role of microfluidics in biomedical research. *Nature* 507 (7491), 181–189. doi:10.1038/nature13118

Schmidt-Speicher, L. M., and Länge, K. (2021). Microfluidic integration for electrochemical biosensor applications. *Curr. Opin. Electrochem.* 29, 100755. doi:10.1016/j.coelec.2021.100755

Singh, A., Malek, C. K., and Kulkarni, S. K. (2011). Development in microreactor technology for nanoparticle synthesis. *IJN* 09, 93–112. doi:10.1142/s0219581x10006557

Sista, R. S., Eckhardt, A. E., Srinivasan, V., Pollack, M. G., Palanki, S., and Pamula, V. K. (2008). Heterogeneous immunoassays using magnetic beads on a digital microfluidic platform. *Lab. Chip* 8 (12), 2188–2196. doi:10.1039/b807855f

Sticker, D., Geczy, R., Hafeli, U. O., and Kutter, J. P. (2020). Thiol-ene based polymers as versatile materials for microfluidic devices for life sciences applications. *ACS Appl. Mater Interfaces* 12 (9), 10080–10095. doi:10.1021/acsami.9b22050

Sun, L., Lehnert, T., Li, S., and Gijs, M. A. M. (2022). Bubble-enhanced ultrasonic microfluidic chip for rapid DNA fragmentation. *Lab. Chip* 22 (3), 560–572. doi:10.1039/d1lc00933h

Syed, A., Mangano, L., Mao, P., Han, J., and Song, Y. A. (2014). Creating sub-50 nm nanofluidic junctions in a PDMS microchip via self-assembly process of colloidal silica beads for electrokinetic concentration of biomolecules. *Lab. Chip* 14 (23), 4455–4460. doi:10.1039/c4lc00895b

Tan, H., Gong, G., Xie, S., Song, Y., Zhang, C., Li, N., et al. (2019). Upconversion Nanoparticles@Carbon Dots@Meso-SiO(2) sandwiched core-shell nanohybrids with tunable dual-mode luminescence for 3D anti-counterfeiting barcodes. *Langmuir* 35 (35), 11503–11511. doi:10.1021/acs.langmuir.9b01919

Tang, T., Yuan, Y., Yalikun, Y., Hosokawa, Y., Li, M., and Tanaka, Y. (2021). Glass based micro total analysis systems: Materials, fabrication methods, and applications. *Sens. Actuators B Chem.* 339, 129859. doi:10.1016/j.snb.2021.129859

van de Sandt, C. E., Kreijtz, J. H., and Rimmelzwaan, G. F. (2012). Evasion of influenza A viruses from innate and adaptive immune responses. *Viruses* 4 (9), 1438–1476. doi:10.3390/v4091438

Vera, D., Garcia-Diaz, M., Torras, N., Alvarez, M., Villa, R., and Martinez, E. (2021). Engineering tissue barrier models on hydrogel microfluidic platforms. *ACS Appl. Mater Interfaces* 13 (12), 13920–13933. doi:10.1021/acsami.0c21573

Vergauwe, N., Witters, D., Ceyssens, F., Vermeir, S., Verbruggen, B., Puers, R., et al. (2011). A versatile electrowetting-based digital microfluidic platform for quantitative homogeneous and heterogeneous bio-assays. *J. Micromech. Microeng.* 21 (5), 054026. doi:10.1088/0960-1317/21/5/054026

Wang, H., Enders, A., Preuss, J. A., Bahnemann, J., Heisterkamp, A., and Torres-Mapa, M. L. (2021a). 3D printed microfluidic lab-on-a-chip device for fiber-based dual beam optical manipulation. *Sci. Rep.* 11 (1), 14584. doi:10.1038/s41598-021-93205-9

Wang, X., He, X., He, Z., Hou, L., Ge, C., Wang, L., et al. (2022). Detection of prostate specific antigen in whole blood by microfluidic chip integrated with dielectrophoretic separation and electrochemical sensing. *Biosens. Bioelectron.* 204, 114057. doi:10.1016/j.bios.2022.114057

Wang, Y., Ruan, Q., Lei, Z. C., Lin, S. C., Zhu, Z., Zhou, L., et al. (2018). Highly sensitive and automated surface enhanced Raman scattering-based immunoassay for H5N1 detection with digital microfluidics. *Anal. Chem.* 90 (8), 5224–5231. doi:10.1021/acs.analchem.8b00002

Wang, Y., Zhao, J., Zhu, Y., Dong, S., Liu, Y., Sun, Y., et al. (2021b). Monolithic integration of nanorod arrays on microfluidic chips for fast and sensitive one-step immunoassays. *Microsyst. Nanoeng.* 7, 65. doi:10.1038/s41378-021-00291-w

Wang, Z., Zong, S., Wu, L., Zhu, D., and Cui, Y. (2017). SERS-activated platforms for immunoassay: Probes, encoding methods, and applications. *Chem. Rev.* 117 (12), 7910–7963. doi:10.1021/acs.chemrev.7b00027

Wu, D., Luo, Y., Zhou, X., Dai, Z., and Lin, B. (2005). Multilayer poly(vinyl alcohol)-adsorbed coating on poly(dimethylsiloxane) microfluidic chips for biopolymer separation. *Electrophoresis* 26 (1), 211–218. doi:10.1002/elps.200406157

Wu, J., Chen, Q., Liu, W., He, Z., and Lin, J.-M. (2017). Recent advances in microfluidic 3D cellular scaffolds for drug assays. *TrAC* 87, 19–31. doi:10.1016/j.trac.2016.11.009

Wu, J., He, Z., Chen, Q., and Lin, J.-M. (2016). Biochemical analysis on microfluidic chips. *TrAC* 80, 213–231. doi:10.1016/j.trac.2016.03.013

Wu, Z., Chen, H., Liu, X., Zhang, Y., Li, D., and Huang, H. (2009). Protein adsorption on poly(N-vinylpyrrolidone)-Modified silicon surfaces prepared by surface-initiated atom transfer radical polymerization. *Langmuir* 25 (5), 2900–2906. doi:10.1021/la8037523

Xie, H., Di, K., Huang, R., Khan, A., Xia, Y., Xu, H., et al. (2020). Extracellular vesicles based electrochemical biosensors for detection of cancer cells: A review. *Chin. Chem. Lett.* 31 (7), 1737–1745. doi:10.1016/j.cclet.2020.02.049

Xie, S., Gong, G., Song, Y., Tan, H., Zhang, C., Li, N., et al. (2019). Design of novel lanthanide-doped core-shell nanocrystals with dual up-conversion and down-conversion luminescence for anti-counterfeiting printing. *Dalton Trans.* 48 (20), 6971–6983. doi:10.1039/c9dt01298b

Xu, J., Feng, Y., Wu, Y., Li, Y., Ouyang, M., Zhang, X., et al. (2019). Noninvasive monitoring of bone regeneration using NaYF4: Yb3+, Er3+ upconversion hollow microtubes supporting PLGA-PEG-PLGA hydrogel. *React. Funct. Polym.* 143, 104333. doi:10.1016/j.reactfunctpolym.2019.104333

Yang, B., Wang, P., Li, Z., Tao, C., You, Q., Sekine, S., et al. (2022). A continuous flow PCR array microfluidic chip applied for simultaneous amplification of target genes of periodontal pathogens. *Lab. Chip* 22 (4), 733–737. doi:10.1039/d1lc00814e

Yang, F., Ren, B., Cai, Y., Tang, J., Li, D., Wang, T., et al. (2018a). Mechanically tough and recoverable hydrogels via dual physical crosslinkings. *J. Polym. Sci. Pol. Phys.* 56 (19), 1294–1305. doi:10.1002/polb.24729

Yang, G., Lai, Y., Xiao, Z., Tang, C., and Deng, Y. (2018b). Ultrasensitive electrochemical immunosensor of carcinoembryonic antigen based on gold-label silver-stain signal amplification. *Chin. Chem. Lett.* 29 (12), 1857–1860. doi:10.1016/j.cclet.2018.11.030

Yang, N., Zhou, X., Yu, D., Jiao, S., Han, X., Zhang, S., et al. (2020). Pesticide residues identification by impedance time-sequence spectrum of enzyme inhibition on multilayer paper-based microfluidic chip. *J. Food Process Eng.* 43 (12). doi:10.1111/jfpe.13544

Yang, R., Li, F., Zhang, W., Shen, W., Yang, D., Bian, Z., et al. (2019). Chemiluminescence immunoassays for simultaneous detection of three heart disease biomarkers using magnetic carbon composites and three-dimensional microfluidic paper-based device. *Anal. Chem.* 91 (20), 13006–13013. doi:10.1021/acs.analchem.9b03066

Yao, P., Liu, Z., Tung, S., Dong, Z., and Liu, L. (2016). Fully automated quantification of insulin concentration using a microfluidic-based chemiluminescence immunoassay. *SLAS Technol.* 21 (3), 387–393. doi:10.1177/2211068215578822

Yin, B., Wan, X., Qian, C., Sohan, A., Zhou, T., and Yue, W. (2021). Enzyme method-based microfluidic chip for the rapid detection of copper ions. *Micromachines (Basel)* 12 (11), 1380. doi:10.3390/mi12111380

Yuan, Y., Liu, B., Wang, T., Li, N., Zhang, Z., and Zhang, H. (2022). Electrochemical microfluidic paper-based analytical devices for tumor marker detection. *TrAC* 157, 116816. doi:10.1016/j.trac.2022.116816

Zhang, C., Shi, D., Li, X., and Yuan, J. (2022a). Microfluidic electrochemical magnetoimmunosensor for ultrasensitive detection of interleukin-6 based on hybrid of AuNPs and graphene. *Talanta* 240, 123173. doi:10.1016/j.talanta.2021.123173

Zhang, J., Feng, J., Tian, Y., Wu, Y., Liu, X., and He, Q. (2021). Ultrasensitive electrochemical determination of tyrosine based on the α-Fe2O3@Co3O4-NRGO modified electrode. *Microchem. J.* 171, 106867. doi:10.1016/j.microc.2021.106867

Zhang, Z., Ma, P., Ahmed, R., Wang, J., Akin, D., Soto, F., et al. (2022b). Advanced point-of-care testing technologies for human acute respiratory virus detection. *Adv. Mater* 34 (1), e2103646. doi:10.1002/adma.202103646

Zhao, D., Wu, Z., Yu, J., Wang, H., Li, Y., and Duan, Y. (2020). Highly sensitive microfluidic detection of carcinoembryonic antigen via a synergetic fluorescence enhancement strategy based on the micro/nanostructure optimization of ZnO nanorod arrays and *in situ* ZIF-8 coating. *Chem. Eng. J.* 383, 123230. doi:10.1016/j.cej.2019.123230

Zhao, D., Wu, Z., Zhang, W., Yu, J., Li, H., Di, W., et al. (2021). Substrate-induced growth of micro/nanostructured Zn(OH)F arrays for highly sensitive microfluidic fluorescence assays. *ACS Appl. Mater. Inter.* 13 (24), 28462–28471. doi:10.1021/acsami.1c04752

Zheng, F., He, E., Wang, Z., Huang, J., and Li, Z. (2020). Mosaic immunoassays integrated with microfluidic channels for high-throughput parallel detection. *Anal. Chem.* 92 (8), 5688–5694. doi:10.1021/acs.analchem.0c00537

Zhou, B., Yang, H., Deng, Y., Liu, M., Liu, B., He, N., et al. (2016a). Ultrasensitive quantitation of MicroRNAs via magnetic beads-based chemiluminesent assay. *Sci. China Chem.* 59 (8), 1051–1058. doi:10.1007/s11426-015-0504-0

Zhou, L., Liu, Y., Hu, S., Wang, H., Sun, H., and Zhang, X. (2016b). A new ratiometric two-photon fluorescent probe for imaging of lysosomes in living cells and tissues. *Tetrahedron* 72 (31), 4637–4642. doi:10.1016/j.tet.2016.06.038

Zhou, L., Lu, D., Wang, Q., Liu, S., Lin, Q., and Sun, H. (2017). Molecular engineering of a mitochondrial-targeting two-photon in and near-infrared out fluorescent probe for gaseous signal molecules H(2)S in deep tissue bioimaging. *Biosens. Bioelectron.* 91, 699–705. doi:10.1016/j.bios.2016.12.055

Zuo, Q., Chen, Y., Chen, Z. P., and Yu, R. Q. (2020). A novel ratiometric fluorescent sensing method based on MnO(2) nanosheet for sensitive detection of alkaline phosphatase in serum. *Talanta* 209, 120528. doi:10.1016/j.talanta.2019.120528

Zuo, Q., Chen, Y., Chen, Z. P., and Yu, R. Q. (2018). Quantification of cadmium in rice by surface-enhanced Raman spectroscopy based on a ratiometric indicator and conical holed enhancing substrates. *Anal. Sci.* 34 (12), 1405–1410. doi:10.2116/analsci.18P342

frontiers | Frontiers in Bioengineering and Biotechnology

TYPE Original Research
PUBLISHED 05 January 2023
DOI 10.3389/fbioe.2022.1094028

OPEN ACCESS

EDITED BY
Mehmet Senel,
University of California, Irvine,
United States

REVIEWED BY
Guangyao Zhang,
Qingdao University, China
Jie Wu,
Nanjing University, China

*CORRESPONDENCE
Han Shen,
shenhan10366@sina.com
Zhiyang Li,
lizhiyangcn@qq.com

†These authors have contributed equally to this work and share first authorship

SPECIALTY SECTION
This article was submitted to Biosensors and Biomolecular Electronics, a section of the journal Frontiers in Bioengineering and Biotechnology

RECEIVED 09 November 2022
ACCEPTED 02 December 2022
PUBLISHED 05 January 2023

CITATION
Xu H, Peng L, Wu J, Khan A, Sun Y, Shen H and Li Z (2023), Clustered Regularly Interspaced Short Palindromic Repeats-Associated Proteins13a combined with magnetic beads, chemiluminescence and reverse transcription-recombinase aided amplification for detection of avian influenza a (H7N9) virus.
Front. Bioeng. Biotechnol. 10:1094028.
doi: 10.3389/fbioe.2022.1094028

Clustered Regularly Interspaced Short Palindromic Repeats-Associated Proteins13a combined with magnetic beads, chemiluminescence and reverse transcription-recombinase aided amplification for detection of avian influenza a (H7N9) virus

Hongpan Xu[1†], Lijun Peng[1,2†], Jie Wu[1†], Adeel Khan[3], Yifan Sun[1], Han Shen[1*] and Zhiyang Li[1*]

[1]Nanjing Drum Tower Hospital Clinical College of Jiangsu University, Nanjing, China, [2]Clinical Laboratory Center, Affiliated Hangzhou Chest Hospital, Zhejiang University School of Medicine, Hangzhou, Zhejiang, China, [3]State Key Laboratory of Bioelectronics, School of Biological Science and Medical Engineering, National Demonstration Center for Experimental Biomedical Engineering Education (Southeast University), Southeast University, Nanjing, China

Clustered Regularly Interspaced Short Palindromic Repeats (CRISPR) and Clustered Regularly Interspaced Short Palindromic Repeats-Associated Proteins (CRISPR-Cas) have promising prospects in the field of nucleic acid molecular diagnostics. However, Clustered Regularly Interspaced Short Palindromic Repeats-based fluorescence detection technology is mainly hindered by proteins with conjugated double bonds and autofluorescence, resulting in high fluorescence background, low sensitivity and incompatible reaction systems, which are not conducive to automatic clinical testing. Chemiluminescence (CL) detection technology has been applied mainly owing to its greatly high sensitivity, as well as low background and rapid response. Therefore, we developed a rapid, ultrasensitive and economical detection system based on Clustered Regularly Interspaced Short Palindromic Repeats-Clustered Regularly Interspaced Short Palindromic Repeats-Associated Proteins 13a combined with magnetic beads (MBs) and chemiluminescence (CL) (Cas13a-MB-CL) to detect Influenza A (H7N9), an acute respiratory tract infectious disease. The carboxyl functionalized magnetic beads (MBs-COOH) were covalently coupled with aminated RNA probe while the other end of the RNA probe was modified with biotin. Alkaline phosphatase labeled streptavidin (SA-ALP) binds with biotin to form magnetic beads composites. In presence of target RNA, the collateral cleavage activity of Cas13a was activated to degrade the RNA probes on MBs and released Alkaline phosphatase from the composites. The composites were then magnetically separated followed by addition of ALP substrate Disodium 2-chloro-5-{4-methoxyspiro [1,2-dioxetane-3,2′-(5′-chloro) tricyclo (3.3.1.13,7)

decan]-4-yl}-1-phenyl phosphate (CDP-star), to generate the chemiluminescence signal. The activity of Associated Proteins 13a and presence of target RNA was quantified by measuring the chemiluminescence intensity. The proposed method accomplished the detection of H7N9 within 30 min at 25°C. When combined with Reverse Transcription- Recombinase Aides Amplification (RT-RAA), the low detection limit limit of detection was as low as 19.7 fM (3S/N). Our proposed MB-Associated Proteins 13a-chemiluminescence was further evaluated to test H7N9 clinical samples, showing superior sensitivity and specificity.

KEYWORDS

H7N9, magnetic beads, LwCas13a, reverse transcription-recombinase aided amplification, chemiluminescence

1 Introduction

Clustered Regularly Interspaced Short Palindromic Repeats (CRISPR) and CRISPR-Associated Proteins (CRISPR-Cas)-based diagnostics have revolutionized in the field of nucleic acid molecular diagnostics (Abudayyeh et al., 2016; Gootenberg et al., 2017; Chen et al., 2018; Khan et al., 2019; Srivastava et al., 2020). Different types of promising CRISPR-Cas based system can combine fluorescence to achieve signal amplification (Abudayyeh et al., 2017; Liang et al., 2019; Peng et al., 2020). However, proteins have conjugated double bonds along with spontaneous fluorescence, thus having a high background (Chang et al., 2019; Guindani et al., 2019). And incompatible reaction systems often need to combine microfluidic or manually open the lid to take samples from the first step reaction, which is not conducive to clinical large-scale sample screening. (Peng et al., 2020; Wang et al., 2020; Zhou et al., 2022).

Chemiluminescence (CL) detection technology has completely avoided the shortcomings of high fluorescent signal background and easy to quench, which is becoming the most important area of biological analysis research and development (Yang et al., 2014; Huang; Zhang et al., 2021; Hu et al., 2022; Liu et al., 2022; Zhao et al., 2022). Also, the CL signal of antibody joint with typical horseradish peroxidase (HRP), Alkaline phosphatase (ALP) and magnetic beads (MBs) platforms have been perfectly employed to commercialized immunoassay diagnosis kits and effectively solving clinical problems (Huang; Speletas et al., 2020; Huang et al., 2019). Besides, methods for using CRISPR-Cas13a combined with CL and MBs have not been reported yet, so it is necessary to use CL with CRISPR-Cas13a to improve sensitivity also low the background.

Avian influenza A (H7N9) virus is classified into subtypes based on two surface proteins, namely Hemagglutinin (HA) and Neuraminidase (NA). It is a new recombinant virus which has the ability to bind to human receptors, and can invade the epithelial cells of human lower respiratory tract and lung cells, and in mammals (Zhou et al., 2013). Since human H7N9 infection was first discovered in 2013, there have been five human infections in China (Chen et al., 2013; Gao et al., 2013). Influenza caused by H7N9 virus has the characteristics of short incubation period and high mortality, which seriously threatens the safety of human life (Gao et al., 2013). Early diagnosis is very important to control the spread of diseases, improve the prognosis of patients and reduce medical expenses. The detection of H7N9 virus mainly includes three methods: 1) virus isolation and culture; 2) Detection of relevant antigens in serum (such as the detection of antigens by ELISA) (Yu et al., 2017); 3) the detection of viral nucleic acid. In recent years, H7N9 virus has been mainly detected by nucleic acid in clinical practice. The conventional nucleic acid detection method is quantitative reverse polymerase chain reaction (RT-qPCR) (Yang et al., 2018). However, it is difficult for grass-roots hospitals to meet the requirements due to the need for specific testing equipment, long time consuming, need of trained operators and special planning of the laboratory. Therefore, it is necessary to establish a reliable, sensitive and rapid H7N9 virus detection system.

In this study, we established a method for detecting H7N9 by recording the chemiluminescence signals of ALP utilizing RT-RAA-Cas13a-MB-CL to amplify nucleic acids. The schematic process can be seen in Scheme 1, a 5′-end amino-modified and 3′-end biotin-modified RNA probe was labeled on a carboxyl functionalized MB (MBs-COOH) by a condensation chemical reaction, and coupled with alkaline phosphatase labeled streptavidin (ALP-SA) to form MB-RNA-ALP complexes. Only when the target RNAs are present, CRISPR RNA (crRNA) of Cas13a binds and activates the collateral cleavage activity of Cas13a to cleave MB-RNA-ALP complexes and release ALP. Then, the solution was separated *via* external magnetic fields, followed by addition of ALP substrate in the supernatant to generate a chemiluminescence signals. When combined with Reverse Transcription- Recombinase Aided Amplification (RT-RAA) to amplify target RNA, this method showed superior sensitivity and specificity in short times.

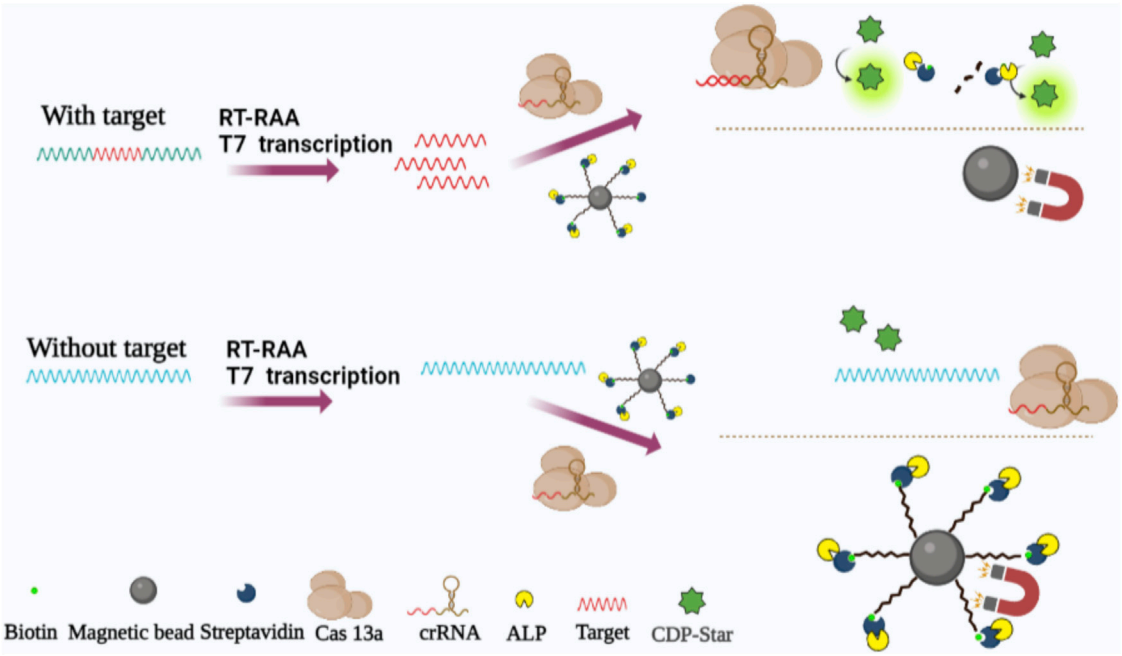

SCHEME 1
Schematic illustration of RT-TAA-Cas13a-MB-CL platform for the detection of nucleic acids. Target RNA was amplified with RT-RAA. The aminated RNA probes were coupled to MBs-COOH and through biotin conjugation SA-ALP. In addition, Cas13a bound target RNA under the guidance of crRNA degrading RNA probes and releasing ALP. CL signals were generated when added CDP-Star.

2 Materials

2-morpholinoethanesulfonic acid monohydrate (MES), 1-ethyl-3-(3-dimethylaminopropyl) carbodiimide hydrochloride (EDC·HCl), sodium chloride (NaCl), Tween-20, magnesium chloride ($MgCl_2$), peptone, yeast powder, agarose powder, ampicillin (Amp) and ALP-SA were purchased from Dalian Meilun Biological Technology Co., Ltd. (Suzhou, China, http://www.meilune.com). Tris-base, Tris hydrochloric acid (Tris HCl), Isopropyl β-D-1-thiogalactopyranoside (IPTG) and 4-hydroxyethyl piperazine ethanesulfonic acid (HEPES) were supplied by Sigma-Aldrich (St. Louis, United States, https://www.sigmaaldrich.com). Dynabeads® MyOne™ Carboxylic Acid (Life Technologies, United States) and HiScribe T7 Quick High Yield RNA Synthesis kit (New England Biolabs) were also used. RT-RAA nucleic acid amplification kit was purchased from Jiangsu Qitian Gene Biotechnology Co., Ltd. (Wuxi, China, http://www.qt-bio.com). The RNA probes and H7N9 gene were synthesized by was purchased from GenScript Biotech Co., Ltd. (Nanjing, China, https://www.genscript.com.cn/quick_order_menu.html). All the oligonucleotides (Sup. Table 1) and diethylpyrocarbonate (DEPC) treated water were obtained from Sangon (Shanghai, China, https://www.sangon.com). The pC013-Twinstrep-SUMO-huLwCas13a (Addgene plasmid #90097) was provided by Zhang Feng's laboratory. CDP-Star was served by Sysmex Corporation (Japan, https://www.sysmex.com.cn). All chemical reagents used in the study were of analytical grade and all solutions were prepared with DEPC treated water. All the hemagglutinin (HA) and neuraminidase (NA) sequences of H7N9 used in the present study were downloaded from the NCBI (National Center for Biotechnology Information), and the sequences of RNA probe, crRNA and H7N9 virus and other control viruses, including seasonal influenza viruses (A/H1N1 and A/H3N2), 2009 swine-origin influenza virus A/H1N1, and avian influenza viruses (A/H5N1 and A/H9N1) were donated by Jiangsu Provincial Center for Disease Prevention and Control are shown in Sup. Table 1. And nuclease assay buffer (NAB) was prepared using 20 mM HEPES, 60 mM NaCl, 6 mM $MgCl_2$, pH 6.8.

2.1 LwCas13a protein expression and purification

Extraction of PCO13-Twinstrep-SUMO-huLwCas13a-plasmid used the Plasmid Mini Kit (OMEGA). 50ng of plasmids were then transferred into E. coli competent cells

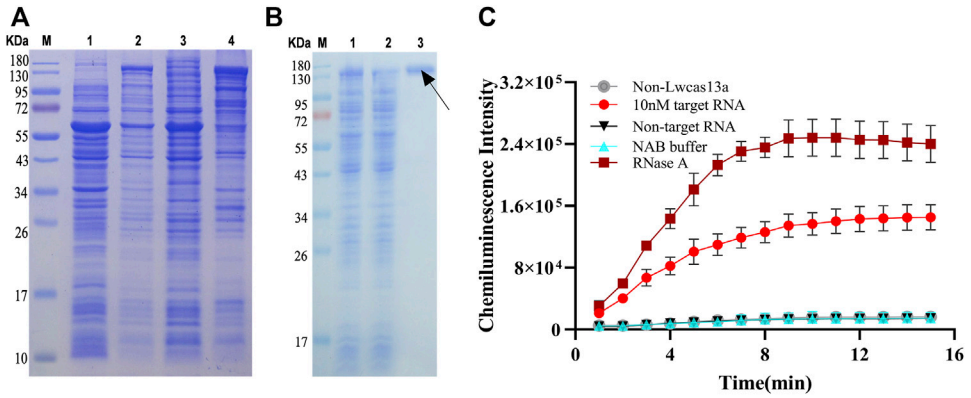

FIGURE 1
LwCas13a protein expression, purification and verification. **(A)** The expression of LwCas13a protein. M, marker; lane 1, E. coli wasn't induced by IPTG, lane 2, IPTG induced E. coli overnight; lane 3, precipitation of broken cells; lane 4, supernatant of broken cells. **(B)** The purification of LwCas13a protein. M, marker; lane 1, supernatant of broken cells; lane 2, flow-through treated with SUMO enzyme. Lane 3, Eluent. **(C)** Verification of LwCas13a activity.

BL21 (Cwbiotech). After transformation, 100 μL of dilutions of cells were plated on ampicillin (Amp) and Luria-Bertani (LB)-agar plate and incubated overnight at 37°C. The next day, a single colony was picked and plated in a 10 ml of LB medium (Containing 100 μL of Amp), which was used to inoculate 1 L of LB medium and shook overnight at speed of 220 r/min until the OD600 was 0.6 at 37°C. At this time, LwCas13a protein expression was induced by supplementation with IPTG to a final concentration of 500 μM. The culture was maintained at 16°C for 16 h, and the cells were then centrifuged at 4,500 g for 10 min at 4°C. Considering the stability of the Cas13a protein, all steps of protein purification were carried out at 4°C. After centrifugation, the cell pellet was harvested and resuspended in lysis buffer (20 mM Tris-HCl, 500 mM NaCl, 1 mM DTT, pH 7.4). Then, protease inhibitor (MCE) and lysozyme were added, followed by sonication (JX-650, Shanghai, China) with following conditions: 200 W of power, ultrasonic 2.5 s and 10 s of pause for 30 min. Centrifugation was carried at 10,000 g for 60 min at 4°C and filtered the supernatant through a 220 nm filter (Sterile Millex). The filtered supernatant was applied to a 5 ml HisTrapHP nickel ion affinity column (GE Healthcare Life Sciences) *via* Fast protein liquid chromatography (FPLC) (AKTA PURE, GE Healthcare Life Sciences). Then the protein bound column was washed three times using a buffer (20 mM Tris-HCl, 500 mM NaCl, 30 mM imidazole, pH 7.4). About 250 Units of SUMO protease (ThermoFisher) was then loaded onto the column and incubated overnight at 4°C with rotation. Finally, the column was washed with lysis buffer again and the collected solution was analyzed by 12% SDS-PAGE. Fractions containing pure LwCas13a were pooled and exchanged the buffer *via* a Millipore centrifugal ultrafiltration tube (Amicon Ultra) to a storage buffer (600 mM NaCl, 50 mM Tris-HCl, pH 7.5, 5% glycerol, 2 mM DTT). The final product was stored at −80°C.

2.2 Preparation of RNA standard and crRNA

Plasmid containing the HA or NA gene of the H7N9 virus was amplified using PrimeSTAR Max DNA Polymerase (TaKaRa), and then purified using a SanPrep PCR product purification kit (Sangon Biotech). Purified dsDNA was incubated with T7 polymerase overnight at 37°C using HiScribe T7 Quick High Yield RNA Synthesis Kit (New England Biolabs). The RNA was purified by RNA rapid concentration and purification kit (Sangon Biotech) and quantified by One drop (American Thermal Power Corporation) to prepare a gradient RNA standard solution. The crRNA was designed based on the target RNA sequence. Two complementary crRNA-DNA primers (with an appended T7 promoter sequence) were annealed with final concentration 10 μM. Then the dsDNAs were transcribed to crRNA, using the HiScribe T7 Quick High Yield RNA Synthesis kit (New England Biolabs).

2.3 Preparation of MB-RNA-ALP complexes

Taking 10 mg/ml carboxylated MBs was stored in a refrigerator at 4°C, followed by vortex on a vortex shaker for 5 min to mix the MBs. 100 μL of the mixed MBs were then washed twice with 1 ml of 100 mM MES buffer, resuspended in 800 μL of MES buffer. Then an appropriate amount of 1.25 M EDC and RNA probe were added to make a total volume of 1 ml, rotating and incubated overnight at 4°C. The next day, after blocking the MBs twice with 1 ml of TT buffer (0.25 M Tris, 0.01% Tween -20, pH 8.0, 30 min per round of incubation), the MBs were resuspend with 1 ml of NAB. At last, ALP was added (according to the

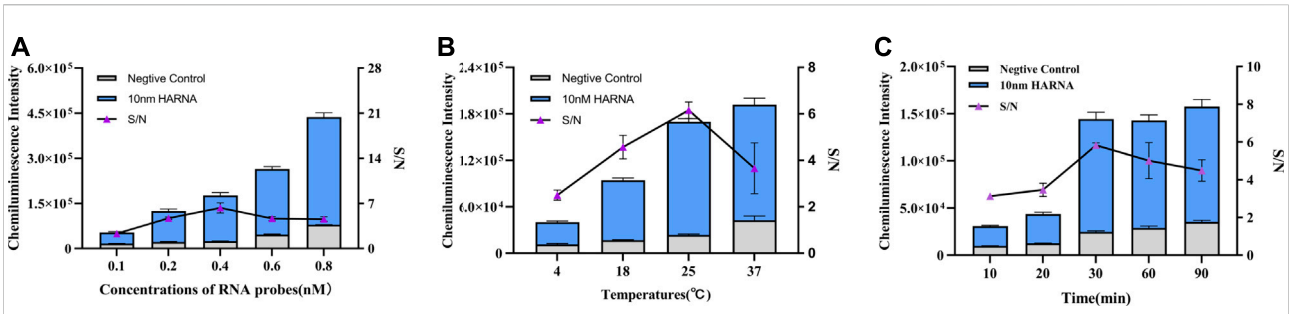

FIGURE 2
Optimization of experimental conditions. **(A)** Optimization of RNA probe concentration. **(B)** Optimization of reaction temperature. **(C)** Optimization of reaction time. The data are presented as mean ± S.D. of three replicate measurements.

volume ratio of ALP:MBs = 1:10) to the MBs and rotating for 1 h. The MB-RNA-ALP complexes were washed twice with 1 ml of TT buffer and stored in TT buffer at 4°C.

2.4 Chemiluminescent detection of MBs composites to verification of LwCas13a activity

For each test, 2 μL of primary MBs were added to the reaction solution (11.25 nM purified LwCas13a, 22.5 nM crRNA, 10 nM target RNA, 1 μL of murine RNase inhibitor (New England Biolabs), 100 ng of background total human RNA (purified from human PBMC), supplemented with NAB to 50 μL) and mixed on a roller mixer for 30 min. The activated LwCas13a cleaved the RNA probe and the ALP was released from the MB-RNA-ALP complexes. Non-target RNA or non-Cas13a protein served as a negative control (NC) in the detection system, and MBs complexes supplement 50 μL of NAB buffer served as background value. At the same time, MB-RNA-ALP complexes were incubated with RNase acting as a positive control, to confirm that the ALP could release from complexes and act as a signal molecule. After magnetic separation, 30 μL of the reaction solution and ALP substrate were incubated in a 96-well microplate format and the CL signal value was recorded using a microplate reader (SpectraMax M5) at 42°C for 15 min.

2.5 HA or NA gene RNA detection with Cas13a-MB-CL system

About 1 μL of mouse RNase inhibitor, 11.25 nM purified LwCas13a, 22.5 nM crRNA, 100 ng of background total human RNA and various concentrations of target RNA were mixed with MBs complexes and were further supplemented with NAB buffer to a final volume of 50 μL for HA RNA and NA RNA detection.

2.6 H7N9 detection with RT-TAA-Cas13a-MB -CL system

Improved detection assays were performed with RT-RAA nucleic acid amplification kit (Qitian Gene Biotechnology) and HiScribe T7 Quick High Yield RNA Synthesis kit (New England Biolabs) as follows: 0.48 μM forward primer, 0.48 μM reverse primer, 14 mM magnesium acetate anhydrous, 12.5 μL mM rNTP, 2.5 μLT7 Mix, various concentrations of target RNA, 2 μL murine RNase inhibitor and 25 μL Basic E-mix to 50 μL final volume. After completing optimization of the RT-RAA amplification system for the cleaving system, MB-RNA-ALP complexes were added into the reaction solution (11.25 nM purified LwCas13a, 22.5 nM crRNA, 1 μL RNase inhibitor, 100 ng RNA purified from human PBMC and various concentration gradients of the RT-RAA amplification products of HA RNA) and replenished with NAB buffer 50 μL to a final volume of 50 μL for HA RNA and NA RNA detection.

2.7 Specificity and clinical sample testing

H7N9 virus samples and other viruses samples, including seasonal influenza viruses (A/H1N1 and A/H3N2), 2009 swine-origin influenza virus A/H1N1, and avian influenza viruses (A/H5N1 and A/H9N1) donated by Jiangsu Provincial Center for Disease Prevention and Control were tested after amplification by RT-RAA. The testing was conducted using the same procedure as described in Section 2.6.

3 Results and discussion

3.1 LwCas13a protein expression and purification

In our study, based on the structural features of PCO13-Twinstrep-SUMO-huLwCas13a-plasmid, the LwCas13a protein

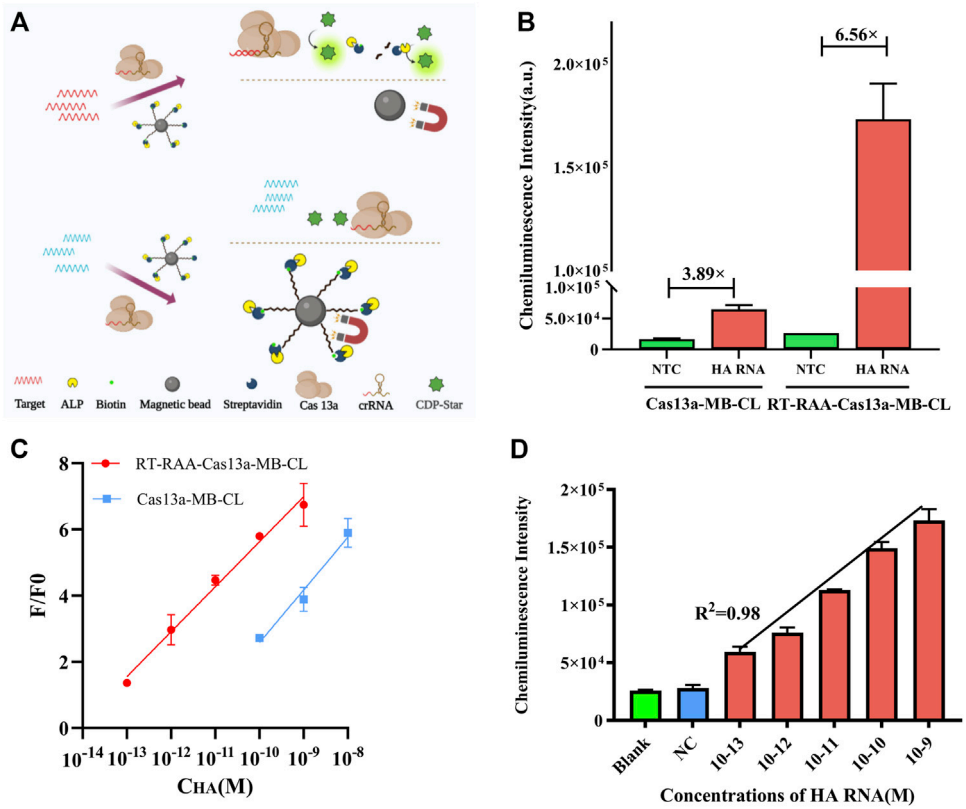

FIGURE 3
(A) Schematic illustration of Cas13a-MB-CL in response to HA RNA. **(B)** CL intensity responses of HA RNA (1 nM) in RT-RAA-Cas13a-MB-CL and Cas13a-MB-CL. **(C)** Calibration curve of RT-RAA-Cas13a-MB-CL (red) and Cas13a-MB-CL (blue) in response to different concentrations of HA RNA. F and F0 are the CL intensities with and without the presence of HA RNA. **(D)** Linear plot of RT-RAA-Cas13a-MB-CL of HA RNA at concentrations from 100 fM to 1 nM. The data are presented as mean ± S.D. of three replicate measurements.

was purified by the SUMO enzyme. The molecular weight of LwCas13a containing the SUMO site and the marker protein was 155.2 kD, but it was 138.5 kD after digestion with SUMO enzyme. LwCas13a expressed in E. coli was analyzed by SDS-PAGE. Coomassie blue stained gel results showed that the IPTG significantly induced the production of Cas13a protein in E. coli (Figure 1A, lane 2). The bacterial solution after IPTG induction was collected, centrifuged, and the cell pellet was disrupted by sonication and centrifuged again. SDS-PAGE analysis was performed on disrupted cell supernatant and cell pellet. It was found that the LwCas13a was mainly present in the supernatant (Figure 1A, lane three and 4). Because the LwCas13a protein contains a His-tag, we used nickel ion affinity chromatography to adsorb water-soluble proteins. A protein without multiple consecutive histidine was eluted from the column by the wash buffer, while LwCas13a was still on the column, and then the SUMO site in LwCas13a was digested with SUMO enzyme, and the LwCas13a lost 6 × His was easily eluted from the column by lysis buffer, pointed by the black arrow (Figure 1B, lane 3). By this purification method a highly pure LwCas13a protein can be obtained.

3.2 Chemiluminescent detection of MBs composites to verification of LwCas13a activity

RNase A can degrade RNA probes, so we used RNase A as a positive control to verify the RNase activity of LwCas13a. As shown in Figure 1C, the CL intensity increased with time and became stable after 10 min approximately. The CL intensity of positive sample (10 nM) was evidently higher than that of negative control (no target HA RNA or LwCas13a) and the blank, which indicated that Cas13a could non-specifically cleave RNA probes by binding the target RNA and its corresponding crRNA.

3.3 Optimization of experimental parameters

Given the non-specific absorption and steric hindrance effect, the density of probes on the surface of MBs may also affect the cleavage of RNA probes by Cas13a protein. About 1 mg MB and

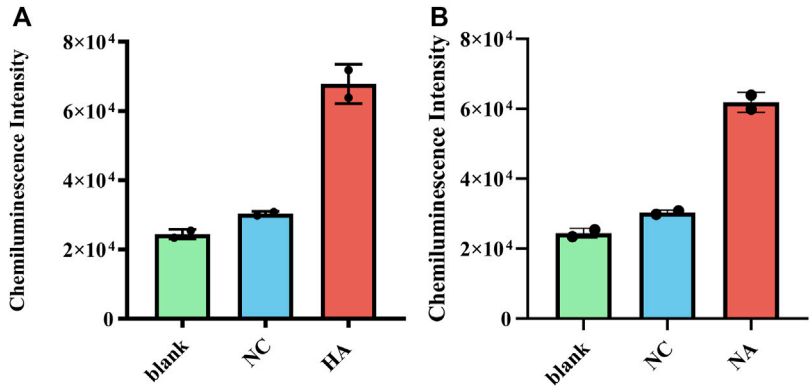

FIGURE 4
(A) Clinical samples using RT-RAA-Cas13a-MB-CL to detect HA RNA and **(B)** NA RNA of H7N9. The data are presented as mean ± S.D. of three replicate measurements; NC, negative control.

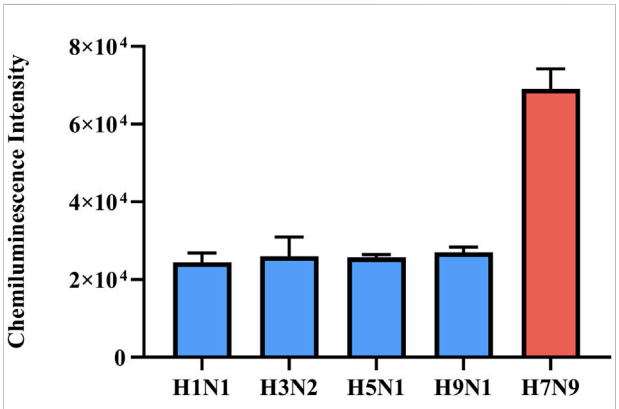

FIGURE 5
Specificity of RT-RAA-Cas13a-MB-CL detection of H7N9 virus samples against other influenza virus samples for HA. The data are presented as mean ± S.D. of three replicate measurements.

five different concentrations of RNA probes (0.1, 0.2, 0.4, 0.6 and 0.8 nM) were used to determine their effect on the CL intensity. We used 10 nM target RNA to activate Cas13a. Figure 2A showed that the CL intensity increased as the probe concentration increased. However, considering the positive judgment criterion, according to Figure 2A, there was a maximum S/N value at 0.4 nM, so 0.4 nM could be proposed as optimal concentration of RNA probes for the modification of MBs. The reaction temperature was investigated as a factor that may affect the cleaving efficiency of Cas13a. A temperature gradient (4, 18, 25, 37°C) was set to test the effect of the reaction temperature on the CL intensity. Figure 2B illustrated that as the temperature increased, the CL intensity increased, but the negative control and blank also increased. According to the change of S/N value, 25°C was selected as the optimal reaction temperature. Reaction time is another factor that affects the cleaving efficiency of Cas13a. A hybridization time gradient (10, 20, 30, 60, 90 min) was established to examine its effect on CL intensity. Figure 2C showed that in the range of 10–30 min, the CL intensity significantly increased with increased hybridization time and the CL intensity gradually stabilized after 30 min, but the negative control also increased with time. Therefore, 30 min was considered to be the best reaction time.

3.4 Sensitivity detection of H7N9 after RT-RAA amplification

The schematic of Cas13a-MB-CL detection system was illustrated in Figure 3A. The detection limit of Cas13a-MB-CL detecting HA RNA was 100 p.m. (Figure 3C). Besides, Cas13a-MB-CL was used to detect NA RNA, having the same detection limit (Supplementary Figure S1). RT-RAA assay is a newly developed technology which can react at constant temperature and within a short reaction time (30 min) (Wang et al., 2022; Wu et al., 2022). Hence, we combined the CRISPR/Cas system with RT-RAA to improve sensitivity to detect H7N9. The results in Supplementary Figure S2 showed that the RT-RAA amplification system (RT-RAA-Cas13a-MB-CL) did have an effect on the cleaving system, and the CL intensity of positive group was gradually enhanced from the original multiplier products to the 16-fold dilution of products, weakened in 32-fold dilution of products. Therefore, the products of the 16-fold dilution were selected as the optimal optimization condition to be added to the cleaving system (Supplementary Figure S2). The proposed RT-RAA-Cas13a-MB-CL has a much better detection sensitivity compared to Cas13a-MB-CL assay in theory. Then, we investigated CL signals between the two methods in response to different concentrations of HA RNA (Figures 3B,C) and NA

RNA (Supplementary Figure S1). In Figure 3B, the CL response signals of 1 nM HA RNA from RT-RAA-Cas13a-MB-CL and Cas13a-MB-CL assay were determined to be 6.56 and 3.89 compared to blank controls, respectively, suggesting an efficient signal gain in RT-RAA-Cas13a-MB-CL. And more importantly, RT-RAA-Cas13a-MB-CL was able to decrease the limit of detection (LOD) by approximately three orders of magnitude compared with the Cas13a-MB-CL assay (Figure 3C). Here, F/F0 was defined as the CL response signal, where F and F0 are the CL intensities of each assay with and without the presence of HA/NA RNA, respectively. Moreover, the LOD of RT-RAA-Cas13a-MB-CL is one to two orders of magnitude lower than that of Cas13a-fluorescence based RNA assays (Abudayyeh et al., 2016). To calculate the LOD of RT-RAA-Cas13a-MB-CL, a linear relationship between the CL response signal and the logarithmic value of H7N9 RNA concentration was obtained in the concentration range from 100 fM to 1 nM, with a LOD of 19.7 fM (3S/N, R^2 = 0.98) (Choengchan et al., 2006; nanocomposite, 2020) (Figure 3D, Supplementary Figure S3).

3.5 Clinical sample testing and specificity verification

The clinical performance of RT-RAA-Cas13a-MB-CL was evaluated using H7N9 virus samples donated by Jiangsu Provincial Center for Disease Prevention and Control. And the CL values of HA and NA in the two clinical samples were greater than that of negative controls (Figures 4A,B), showing a superior sensitivity and specificity.

In addition, the detection of H7N9 RNAs by the RT-RAA-Cas13a-MB-CL should be sequence-specific, so we tested seasonal influenza viruses (A/H1N1 and A/H3N2), 2009 swine-origin influenza virus A/H1N1, and avian influenza viruses (A/H5N1 and A/H9N1) donated by Jiangsu Provincial Center for Disease Prevention and Control (Sup. Table 1). The CL detection signals of H7N9 virus samples were significantly higher compared to other virus samples (Figure 5, Supplementary Figure S4). Above all, the proposed method had high specificity in the detection of H7N9 RNAs. Compared with RT-qPCR, the specificity of this method was comparable or even much better. Although slightly less sensitive than RT-qPCR, the entire detection process of this method can be completed in 30 min, while RT-qPCR needs more than 1 hour.

4 Conclusions

We successfully developed a novel method for detection of H7N9 virus based on MBs, CL and CRISPR-Cas13a, overcoming the problem of high fluorescence background in CRISPR combined with fluorescence detection technology. We improved sensitivity of detection methods with RT-RAA, a novel developed amplification technique which can react at constant temperature and is compatible with CRISPR. The LOD was as low as 19.7 fM at 25°C. Compared to the traditional fluorescence detection technology, it is an innovation in the method. Since MB-RNA-ALP complexes can be prepared and stored in advance, the entire detection process can be shortened to 30 min. More importantly, this method combined with magnetic bead method has proven to be applicable for influenza virus RNA detection in complex biological samples although having an incompatible reaction system. This assay has great promise for virus detection and can be adapted to clinical large-scale screening in the future. Thus, it is expected to scale up clinical applications and can be a valuable improvement towards achieving automated testing platforms for application in clinical setups in the near future.

Data availability statement

The raw data supporting the conclusions of this article will be made available by the authors, without undue reservation.

Author contributions

HX: Conceptualization, methodology, software, and investigation, data curation, writing-original draft. LP: Methodology, software, investigation, project administration, writing-review and editing. JW: Formal analysis, writing-original draft, writing-review, editing and software. AK organized the figures. HS: Supervision, methodology, data curation, and administration. ZL: Funding acquisition, supervision, administration, and data Curation.

Funding

This study was supported by the National Natural Science Foundation of China (61971216), the Key Research and Development Project of Jiangsu Province (BE2019603, BE2019761, BE2020768, and BE2022692), Nanjing Important Science and Technology Specific Projects (2021-11005), Nanjing Science and Technology Development Plan Project (202205066) and Natural Science Foundation of Zhejiang Province (LGC22H200013).

Conflict of interest

The authors declare that the research was conducted in the absence of any commercial or financial relationships that could be construed as a potential conflict of interest.

The reviewer JW declared a shared parent affiliation with the authors to the handling editor at the time of review.

Publisher's note

All claims expressed in this article are solely those of the authors and do not necessarily represent those of their affiliated organizations, or those of the publisher, the editors and the reviewers. Any product that may be evaluated in this article, or claim that may be made by its manufacturer, is not guaranteed or endorsed by the publisher.

Supplementary material

The Supplementary Material for this article can be found online at: https://www.frontiersin.org/articles/10.3389/fbioe.2022.1094028/full#supplementary-material

References

Abudayyeh, O. O., Gootenberg, J. S., Essletzbichler, P., Han, S., Joung, J., Belanto, J. J., et al. (2017). RNA targeting with CRISPR-Cas13. *Nature* 550 (7675), 280–284. doi:10.1038/nature24049

Abudayyeh, O. O., Gootenberg, J. S., Konermann, S., Joung, J., Slaymaker, I. M., Cox, D. B. T., et al. (2016). C2c2 is a single-component programmable RNA-guided RNA-targeting CRISPR effector. *Science* 353 (6299), aaf5573. doi:10.1126/science.aaf5573

Chang, H.-Y., Ko, T. P., Chang, Y. C., Huang, K. F., Lin, C. Y., Chou, H. Y., et al. (2019). Crystal structure of the blue fluorescent protein with a Leu-Leu-Gly tripeptide chromophore derived from the purple chromoprotein of Stichodactyla haddoni. *Int. J. Biol. Macromol.* 130, 675–684. doi:10.1016/j.ijbiomac.2019.02.138

Chen, J. S., Ma, E., Harrington, L. B., Da Costa, M., Tian, X., Palefsky, J. M., et al. (2018). CRISPR-Cas12a target binding unleashes indiscriminate single-stranded DNase activity. *Science* 360 (6387), 436–439. doi:10.1126/science.aar6245

Chen, Y., Liang, W., Yang, S., Wu, N., Gao, H., Sheng, J., et al. (2013). Human infections with the emerging avian influenza A H7N9 virus from wet market poultry: Clinical analysis and characterisation of viral genome. *Lancet* 381 (9881), 1916–1925. doi:10.1016/s0140-6736(13)60903-4

Choengchan, N., Mantim, T., Wilairat, P., Dasgupta, P., Motomizu, S., and Nacapricha, D. (2006). A membraneless gas diffusion unit: Design and its application to determination of ethanol in liquors by spectrophotometric flow injection. *Anal. Chim. Acta X.* 579 (1), 33–37. doi:10.1016/j.aca.2006.07.018

Gao, R., Cao, B., Hu, Y., Feng, Z., Wang, D., Hu, W., et al. (2013). Human infection with a novel avian-origin influenza A (H7N9) virus. *N. Engl. J. Med.* 368 (20), 1888–1897. doi:10.1056/NEJMoa1304459

Gootenberg, J. S., Abudayyeh, O. O., Lee, J. W., Essletzbichler, P., Dy, A. J., Joung, J., et al. (2017). Nucleic acid detection with CRISPR-Cas13a/C2c2. *Science* 356 (6336), 438–442. doi:10.1126/science.aam9321

Guindani, C., Frey, M., Simon, J., Koynov, K., Schultze, J., Ferreira, S. R. S., et al. (2019). Covalently binding of bovine serum albumin to unsaturated poly(globalide-Co-epsilon-Caprolactone) nanoparticles by thiol-ene reactions. *Macromol. Biosci.* 19 (10), 1900145. doi:10.1002/mabi.201900145

Hu, T., Ke, X., Ou, Y., and Lin, Y. (2022). CRISPR/Cas12a-Triggered chemiluminescence enhancement biosensor for sensitive detection of nucleic acids by introducing a tyramide signal amplification strategy. *Anal. Chem.* 94 (23), 8506–8513. doi:10.1021/acs.analchem.2c01507

Huang, J., Li, J., Lyu, Y., Miao, Q., and Pu, K. (2019). Molecular optical imaging probes for early diagnosis of drug-induced acute kidney injury. *Nat. Mater.* 18 (10), 1133–1143. doi:10.1038/s41563-019-0378-4

Huang, J. New hybridoma cell line, useful in kit, e.g. radioimmunoassay kit, for detecting human immunoglobulin M that is produced in early stage of pathogenic infection caused by cytomegalovirus, and for diagnosis cytomegalovirus infection. *Sichuan Maccura Biol. New Mater.*

Khan, H., Khan, A., Liu, Y., Wang, S., Bibi, S., Xu, H., et al. (2019). CRISPR-Cas13a mediated nanosystem for attomolar detection of canine parvovirus type 2. *Chin. Chem. Lett.* 30 (12), 2201–2204. doi:10.1016/j.cclet.2019.10.032

Liang, M., Li, Z., Wang, W., Liu, J., Liu, L., Zhu, G., et al. (2019). A CRISPR-Cas12a-derived biosensing platform for the highly sensitive detection of diverse small molecules. *Nat. Commun.* 10 (1), 3672. doi:10.1038/s41467-019-11648-1

Liu, Y., Cao, M., Huang, Z., Yu, C., Yang, N., Wu, Q., et al. (2022). Ultrasensitive detection of IgE levels based on magnetic nanocapturer linked immunosensor assay for early diagnosis of cancer. *Chin. Chem. Lett.* 33 (4), 1855–1860. doi:10.1016/j.cclet.2021.08.117

nanocomposite (2020). *Nanocomposite magnetite kaolin for rh preconcent source anal sci.* jan 10 36 1 87 90.pdf.

Peng, S., Tan, Z., Chen, S., Lei, C., and Nie, Z. (2020). Integrating CRISPR-Cas12a with a DNA circuit as a generic sensing platform for amplified detection of microRNA. *Chem. Sci.* 11 (28), 7362–7368. doi:10.1039/d0sc03084h

Speletas, M., Kyritsi, M. A., Vontas, A., Theodoridou, A., Chrysanthidis, T., Hatzianastasiou, S., et al. (2020). Evaluation of two chemiluminescent and three ELISA immunoassays for the detection of SARS-CoV-2 IgG antibodies: Implications for disease diagnosis and patients' management. *Front. Immunol.* 11, 609242. doi:10.3389/fimmu.2020.609242

Srivastava, S., Upadhyay, D. J., and Srivastava, A. (2020). Next-generation molecular diagnostics development by CRISPR/Cas tool: Rapid detection and surveillance of viral disease outbreaks. *Front. Mol. Biosci.* 7, 4. doi:10.3389/fmolb.2020.00004

Wang, G., Tian, W., Liu, X., Ren, W., and Liu, C. (2020). New CRISPR-derived microRNA sensing mechanism based on Cas12a self-powered and rolling circle transcription-unleashed real-time crRNA recruiting. *Anal. Chem.* 92 (9), 6702–6708. doi:10.1021/acs.analchem.0c00680

Wang, Y., Nie, M., Deng, H., Lai, S., Zhou, Y., Sun, X., et al. (2022). Establishment of a reverse transcription recombinase-aided amplification detection method for porcine group a rotavirus. *Front. Vet. Sci.* 9, 954657. doi:10.3389/fvets.2022.954657

Wu, X., Liu, Y., Gao, L., Yan, Z., Zhao, Q., Chen, F., et al. (2022). Development and application of a reverse-transcription recombinase-aided amplification assay for porcine epidemic diarrhea virus. *Viruses* 14 (3), 591. doi:10.3390/v14030591

Yang, H. W., Guo, Y., Li, S., Lan, G., Jiang, Q., Yang, X., et al. (2014). Magnetic beads-based chemiluminescent assay for ultrasensitive detection of pseudorabies virus. *J. Nanosci. Nanotechnol.* 14 (5), 3337–3342. doi:10.1166/jnn.2014.8254

Yang, Y., Li, S., Wong, G., Ma, S., Xu, Z., Zhao, X., et al. (2018). Development of a quadruple qRT-PCR assay for simultaneous identification of highly and low pathogenic H7N9 avian influenza viruses and characterization against oseltamivir resistance. *BMC Infect. Dis.* 18, 406. doi:10.1186/s12879-018-3302-7

Yu, Y. Y., Zhang, X., Zhao, B., Sun, Y., Zhang, X., Bai, T., et al. (2017). A sandwich ELISA for the detection of neuraminidase of avian influenza A(H7N9) virus. *J. Virological Methods* 247, 58–60. doi:10.1016/j.jviromet.2017.05.014

Zhang, C., Jin, J., Liu, K., Ma, X., and Zhang, X. (2021). Carbon dots-peroxyoxalate micelle as a highly luminous chemiluminescence system under physiological conditions. *Chin. Chem. Lett.* 32 (12), 3931–3935. doi:10.1016/j.cclet.2021.05.050

Zhao, H., Su, E., Huang, L., Zai, Y., Liu, Y., Chen, Z., et al. (2022). Washing-free chemiluminescence immunoassay for rapid detection of cardiac troponin I in whole blood samples. *Chin. Chem. Lett.* 33 (2), 743–746. doi:10.1016/j.cclet.2021.07.017

Zhou, J., Lin, Q., Huang, Z., Xiong, H., Yang, B., Chen, H., et al. (2022). Aptamer-initiated catalytic hairpin assembly fluorescence assay for universal, sensitive exosome detection. *Anal. Chem.* 94 (15), 5723–5728. doi:10.1021/acs.analchem.2c00231

Zhou, J., Wang, D., Gao, R., Zhao, B., Song, J., Qi, X., et al. (2013). Biological features of novel avian influenza A (H7N9) virus. *Nature* 499 (7459), 500–503. doi:10.1038/nature12379

frontiers | Frontiers in Bioengineering and Biotechnology

TYPE Methods
PUBLISHED 17 January 2023
DOI 10.3389/fbioe.2023.1022066

OPEN ACCESS

EDITED BY
Hongna Liu,
iRepertore Inc., United States

REVIEWED BY
Hongxing Liu,
First Affiliated Hospital of Guangzhou Medical University, China
Luxi Jiang,
Zhejiang Provincial People's Hospital, China

*CORRESPONDENCE
Yi Wang,
wildwolf0101@163.com

†These authors have contributed equally to this work

SPECIALTY SECTION
This article was submitted to Biosensors and Biomolecular Electronics, a section of the journal Frontiers in Bioengineering and Biotechnology

RECEIVED 18 August 2022
ACCEPTED 09 January 2023
PUBLISHED 17 January 2023

CITATION
Jia N, Zhou J, Xiao F, Zheng B, Huang X, Sun C, Fu J, Xu Z, Chen M and Wang Y (2023), A CRISPR-Cas12a—Based platform for ultrasensitive, rapid, and highly specific detection of *Mycoplasma pneumonia* in clinical application.
Front. Bioeng. Biotechnol. 11:1022066.
doi: 10.3389/fbioe.2023.1022066

A CRISPR-Cas12a—Based platform for ultrasensitive, rapid, and highly specific detection of *Mycoplasma pneumonia* in clinical application

Nan Jia[1†], Juan Zhou[1†], Fei Xiao[1†], Baoying Zheng[2], Xiaolan Huang[1], Chunrong Sun[1], Jin Fu[1], Zheng Xu[1], Min Chen[1] and Yi Wang[1*]

[1]Experimental Research Center, Capital Institute of Pediatrics, Beijing, China, [2]Respiratory Medicine, Capital Institute of Pediatrics, Beijing, China

Mycoplasma pneumoniae (MP), which is responsible for a majority of community-acquired pneumonia (CAP) in children, has been largely underestimated. Here, we coupled multiple cross displacement amplification (MCDA) technique with CRISPR-Cas12a-based biosensing system to design a novel detection platform termed MP-MCDA-CRISPR assay for MP infection diagnosis and clinical application. The MP-MCDA-CRISPR assay amplified the CARDS gene of MP by MCDA method, followed by *trans*-cleavage of the reporter molecular upon the formation of CRISPR-Cas12a-gRNA-target DNA complex, which was confirmed by the release of fluorescent signals. A set of standard MCDA primers, an engineered CP1 primer, a quenched fluorescent ssDNA reporter, and a gRNA were designed targeting the CARDS gene of MP. The optimal temperature for MCDA pre-amplification is 64°C, and the time for CRISPR-Cas12a-gRNA biosensing process is 5 min. The limit of detection (LoD) of the MP-MCDA-CRISPR assay is 50 fg per reaction without any cross-reaction with other non-MP pathogens. The MP-MCDA-CRISPR assay accurately identified the 50 real time-PCR positive clinical samples and 78 negative ones. Taken together, the MP-MCDA-CRISPR assay designed here is a promising diagnostic tool for point-of care (POC) testing of MP infection.

KEYWORDS

***Mycoplasma pneumoniae*, multiple cross displacement amplification, CRISPR, Cas12a, community-acquired pneumonia**

Introduction

Lower respiratory tract infection has been recognized as a major cause of morbidity and mortality in children, and *Mycoplasma pneumoniae* (MP) was the most commonly detected bacterial pathogen among children <18 years old hospitalized with community-acquired pneumonia (CAP) (Jain et al., 2015). Apart from pneumonia, MP was also associated with upper respiratory infections and a wide range of extrapulmonary manifestations, such as mucositis (Vujic et al., 2015), encephalitis (Daxboeck et al., 2004), and Stevens-Johnson syndrome (SJS) (Olson et al., 2015). Although MP infection was usually considered as mild and self-limited (Waites and Talkington, 2004) for which the burden of MP infection was usually underestimated, it was reported that more than 10% children hospitalized for MP infection were admitted to the ICU (Kutty et al., 2019). Along with the emergence and wide spread of macrolide-resistant MP isolates (Li et al., 2009; Yamada et al., 2012), identification and surveillance of MP infection needs to further strengthen.

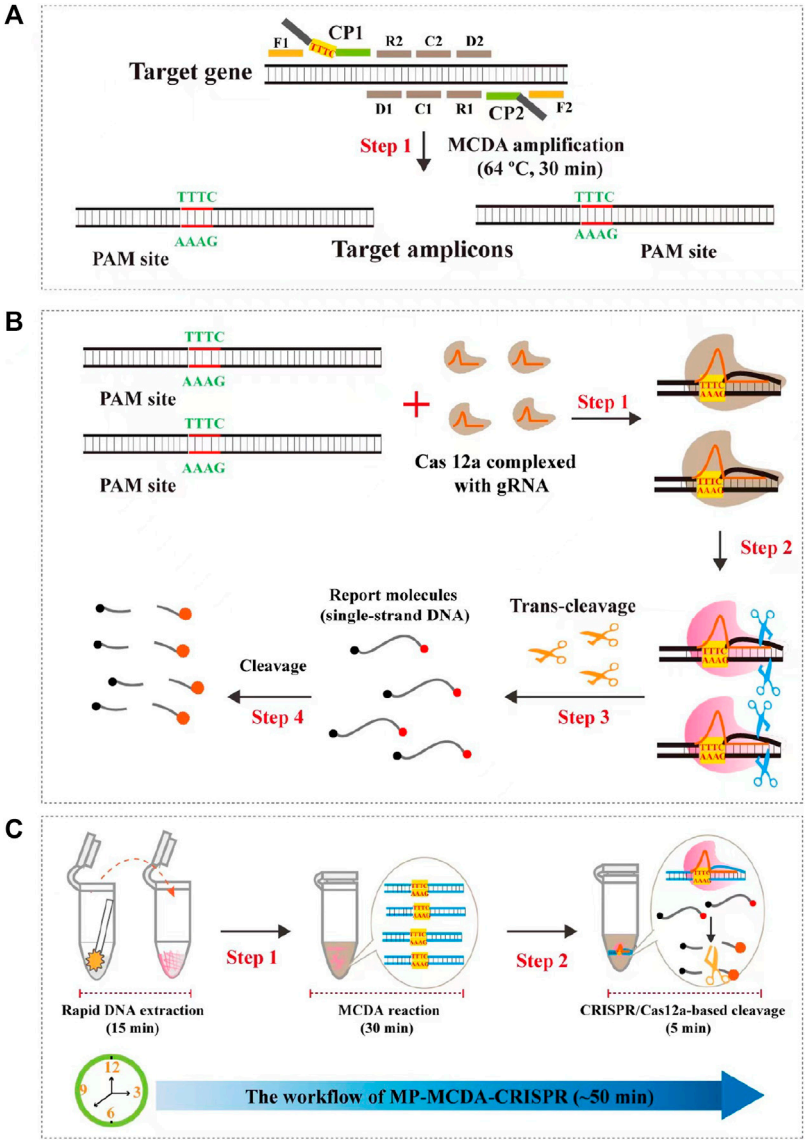

FIGURE 1
Schematic illustration of the principle of the MP-MCDA-CRISPR assay. **(A)** Schematic illustration of the principle of MCDA with the modified primer. The primer CP1 was modified with a PAM site (TTTC) at the linker region. After amplification, a CRISPR-Cas12a recognition site was constructed in the target amplicons. **(B)** Schematic illustration of the CRISPR-Cas12a detection system. Upon recognition of the target DNA, the CRISPR-Cas12a-gRNA complex cleaves the single stranded DNA reporter molecule and responds with release of fluorescence signal. **(C)** Overview of the MP-MCDA-CRISPR workflow. MP-MCDA-CRISPR assay employs three closely linked steps: DNA extraction (step 1), MCDA pre-amplification (step 2), CRISPR-Cas12a cleavage and data report (step 3). The whole process could be completed in 50 min.

Due to the clinical characteristics of MP infection are non-specific (Kutty et al., 2019), identification and confirmation of MP infection is mainly based on laboratory diagnosis. At present, there are three methods commonly used for detection of MP infection, i.e., culture, serology and molecular-based methods. Although culture is the traditional "gold standard" for identification of MP infection (specificity is 100%), long time and fastidious cultivation requirements makes it impractical (Waites et al., 2017). Optimum serological testing of MP infection usually needs two sera specimens collected at least 2 weeks apart (Bajantri et al., 2018), which is time-consuming; besides, insufficient immunological responses of the infant and elderly (Bajantri et al., 2018) and cross-activity with cytomegalovirus or Epstein-Barr virus infections (Medjo et al., 2014) also limit the sensitivity and specificity of MP testing, making this method not readily available. Molecular-based methods have been considered as "new gold standard" credited with their superior sensitivity and time-effectiveness (Waites et al., 2012; Loens and Ieven, 2016; Waites et al., 2017), and a series of commercially diagnostic methods are available for MP infection detection, such as the real-time PCR-based method RespiFinder SMART 22 (Patho Finder, Maastrict, the Netherlands) (Pillet et al., 2013), loop-mediated isothermal amplification (LAMP)-based method *illumigene Mycoplasma* (Meridian BioScience, Inc., Cincinnati, OH, United States) (Ratliff et al., 2014) and strand displacement assays (SDA)-based method BD Probe Tec ET (BD Diagnostics, Sparks, MD, United States) (Loens et al., 2010). Real-time

10.3389/fbioe.2023.1022066

TABLE 1 The strains used in this study.

Strains	Source of strains[a]	No. of strains	MP-MCDA-CRISPR[b]
M. pneumoniae	Isolated strains (CIP)	10	P
Bacillus cereus	Isolated strains (CDC)	1	N
Citrobacter	Isolated strains (CDC)	2	N
Corynebacterium striatum	Isolated strains (CDC)	1	N
Enteroadherent Escherichia coli	Isolated strains (CDC)	1	N
Enterococcus faecalis	Isolated strains (CDC)	2	N
Enteroinvasive E. coli	Isolated strains (CDC)	1	N
Enteropathogenic E. coli	Isolated strains (CDC)	1	N
Enterotoxic E. coli	Isolated strains (CDC)	1	N
Klebsiella pneumoniae	Isolated strains (CDC)	2	N
Listeria innocua	Isolated strains (CDC)	1	N
Listeria ivanovii	Isolated strains (CDC)	1	N
Listeria monocytogenes	Isolated strains (CDC)	1	N
Monilia albican	Isolated strains (CDC)	2	N
Moraxella catarrhalis	Isolated strains (CDC)	1	N
Mycobacterium tuberculosis	Isolated strains (CDC)	2	N
Mycoplasma hominis	Isolated strains (CDC)	2	N
Mycoplasma penetrans	Isolated strains (CDC)	2	N
Mycoplasma primatus	Isolated strains (CDC)	2	N
Mycoplasma genitalium	Isolated strains (CDC)	2	N
Mycoplasma urealytium	Isolated strains (CDC)	3	N
Neisseria meningitidis	Isolated strains (CDC)	1	N
Nocardia asteroides	Isolated strains (CDC)	1	N
Pseudomonas aeruginosa	Isolated strains (CDC)	1	N
Salmonella sp.	Isolated strains (CDC)	2	N
Shiga toxin-producing E. coli	Isolated strains (CDC)	1	N
Shigella baumannii	Isolated strains (CDC)	1	N
Shigella sonnei	Isolated strains (CDC)	1	N
Staphylococcus amber	Isolated strains (CDC)	1	N
Staphylococcus epidermidis	Isolated strains (CDC)	1	N
Staphylococcus haemolyticus	Isolated strains (CDC)	2	N
Stenotrophomonas maltophilia	Isolated strains (CDC)	1	N
Steptococcus salivarius	Isolated strains (CDC)	1	N
Streptococcus aureus	Isolated strains (CDC)	1	N
Streptococcus pneumoniae	Isolated strains (CDC)	1	N
Streptococcus pyogenes	Isolated strains (CDC)	1	N
Streptococcus suis	Isolated strains (CDC)	2	N

[a]CIP, Capital Institute of Pediatrics; CDC, Chinese center for disease control and prevention.
[b]P, positive; N, negative.

TABLE 2 The primers, probe, and gRNAs used in the current study.

Primers/Probes/gRNA	Sequence and modification (5′-3′)[a]	Length[b]
MCDA primers		
F1	TCAAAGACAAGTAGTATTTGACTC	24 nt
F2	TGAGGGTTGTGCATTTCC	18 nt
CP1	TGATACGCAAAGGAAGTGCG**TTTC**TGGTGATCGAGAAATGGCA	43 nt
CP2	GACTAGTAGATGCTGTTCCCGTTGAGGTTCATTAATTCTAGTAGTCTCT	49 nt
C1	TGATACGCAAAGGAAGTGCG	20 nt
C2	GACTAGTAGATGCTGTTCCCGTTGA	25 nt
D1	AAGCTCTAATTCCCATTTG	19 nt
D2	ACCTGGTCATGCTCACCA	18 nt
R1	TGGACCATCGGTAAACCA	18 nt
R2	CAGCTAATGTCCGTAGTG	18 nt
gRNA	UAAUUUCUACUAAGUGUAGAUUGGUGAUCGAGAAAUGGCA	40 mer
Probe[c]	FAM-TATTATTATTATTATTT-BHQ1	17 mer

[a]CP1 primer was modified in linker region with a PAM site (TTTC).
[b]nt, nucleitide; mer, monomeric unit.
[c]5′end of probe was labeled with FAM, and 3′end was labeled with BHQ1.

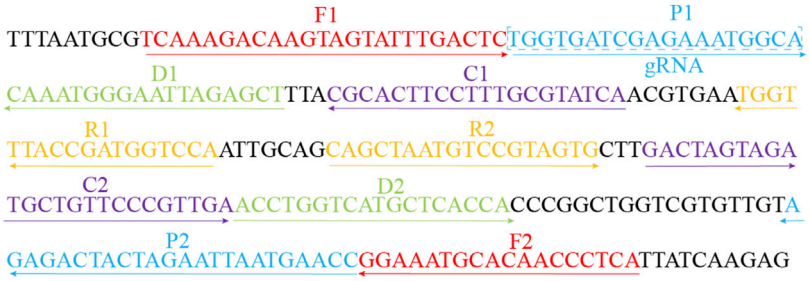

FIGURE 2
Sequences and locations of the CARDS gene of MP used to design the MCDA primers and gRNA. Locations of MCDA primers are underlined and gRNA is in the box. The right arrow and left arrow represent the sense and complementary sequence used in this study, respectively.

PCRs had lower likelihood of contamination, could provide quantitative data and detect antimicrobial resistance genes (Waites et al., 2017); however, their highly dependence of high-precision apparatus and skilled technicians hampered their widely utilization. LAMPs and SDAs are less expensive and equipment requirement, more easy-to-perform, specific and sensitive than real-time PCR-based methods (Kakuya et al., 2014; Waites et al., 2017), however, the product analysis methods are somewhat labor-consuming or subjective (Li et al., 2020). Therefore, an accurate, rapid, ultrasensitive and highly specific assay for MP detection is sorely needed for case and outbreak identification and treatment and infection prevention guidance.

In recent years, a variety of CRISPR/Cas (clustered regularly interspaced short palindromic repeats and CRISPR associated protein)-related technologies have been harnessed for use in fields of research (Liu et al., 2022), including the nucleic acid detection field (Gootenberg et al., 2017), owing to their merit in terms of efficiency, specificity, and precision for biosensing (Liu et al., 2022). CRISPR/Cas systems are widely distributed in prokaryotic genomes and confer prokaryote acquired immunity against foreign nuclei acids (Barrangou et al., 2007; Brouns et al., 2008; Marraffini and Sontheimer, 2008). The principle of nuclei acid detection with CRISPR/Cas system is based on the collateral cleavage activities of Cas effectors (such as Cas12a, Cas12b, Cas13a, and Cas14), which enable non-specific and indiscriminate cleavage of surrounding non-target single strand RNA and DNA following the guidance of gRNA (guide RNA) (Li et al., 2019a; Li et al., 2019b; Shihong Gao et al., 2021). Up to now, there have been several CRISPR/Cas biosensing systems applied in nuclei acid analysis, such as DETECTR (DNA Endonuclease-Targeted CRISPR Trans Reporter) (Chen et al., 2018), SHERLOCK (Specific High-sensitivity Enzymatic Reporter UnLOCKing) (Gootenberg et al., 2017), HOLMES (One-Hour-Low cost Multipurpose highly Efficient System) (Li et al., 2018b), CRISPR-top (Li et al., 2021) and CRISPR-MCCD, which are proven cost-effective, easily accessible, and widely applicable.

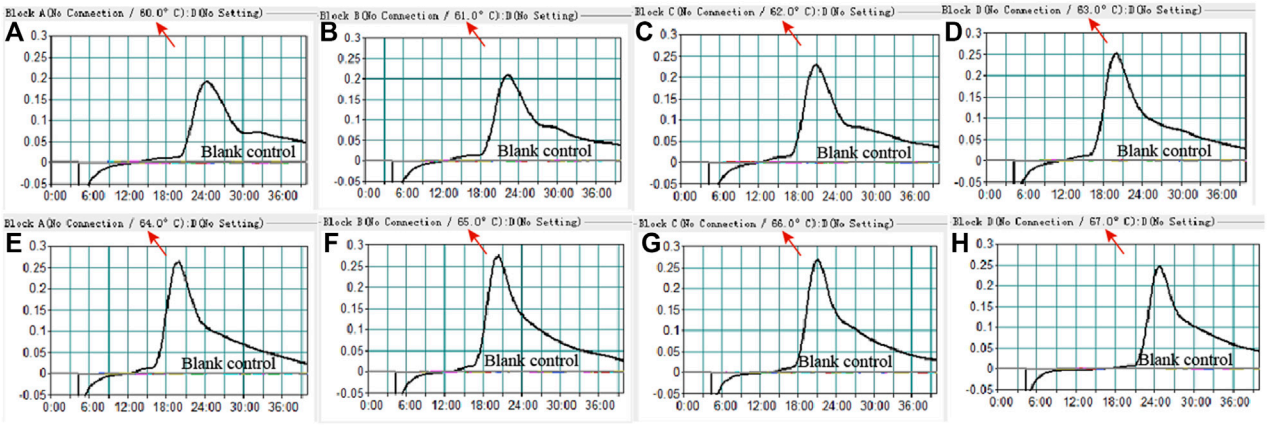

FIGURE 3
Temperature optimization for the MCDA assay. The MCDA method was used to detect pre-amplification of the CARDS gene of MP. The dynamic curves **(A–H)** were obtained at different temperatures ranging from 60°C to 67°C, with 64°C as the optimal MCDA reaction temperature for MP testing.

In the current study, we incorporated the CRISPR-Cas12a biosensing system with a relatively new and promising nucleic acid isothermal amplification technology termed multiple cross displacement amplification (MCDA) for timely, accurate, robust, ultrasensitive and highly specific diagnosis of MP infection, and named as MP-MCDA-CRISPR. Furthermore, a protospacer adjacent motif (PAM) site (TTTC) for the CRISPR-Cas12a–related assay was engineered onto the MCDA primers for detecting sequences that lack of PAM sites. Thereafter, we illustrated the principle of the MP-MCDA-CRISPR assay (Figure 1) and validated its feasibility in clinical specimens.

Materials and methods

Reagents and instruments

The primers used in this study were synthesized by AOKE Biotech Co., Ltd. (Beijing, China), and the probe and gRNA were by Tianyi-Huiyuan Bioscience & Technology Co., Ltd. (Beijing, China). Genomic DNA kit for nucleic acid extraction and purification was purchased from Beijing TransGen Biotech Co., Ltd. (Beijing, China). The universal isothermal amplification kits, visual detection reagent (VDR), and CRISPR-Cas12a protein (Cpf1) were obtained from HuiDeXin Biotechnology (Tianjin, China). A real-time turbidimeter (LA-320C) was purchased from Eiken Chemical Co., Ltd. (Japan) and the Applied Biosystems® 7500 Real Time PCR System was from ThermoFisher Scientific (United States).

Bacterial strain and clinical samples

Bacterial strains used in this study were shown in Table 1, including pure cultures of 10 MP strains and 40 other pathogens. Additionally, 128 nasopharyngeal swabs collected from 128 patients suspected of MP infection in the capital institute of pediatrics (CIP) were employed in this study as well for clinical feasibility assessment. Nucleic acid of all the pure cultures and clinical samples were extract and purified by using the genomic DNA kit.

Design of multiple cross displacement amplification primers and gRNA

According to the principle of MCDA assay, the primers of MP were designed based on the CARDS gene (community-acquired respiratory distress syndrome toxin gene) by using the PRIMER PREMIER 5.0 software. BLAST analysis was used to verify the specificity of MP-MCDA primers. In addition, the gRNA of MP CARDS gene was designed according to the CRISPR-Cas12a detection mechanism. The positions of MCDA primers and gRNA are shown in Table 2 and Figure 2. PAM sites (TTTC) were added into the linker region of the regular CP1 primer of MCDA for CRISPR-Cas12a biosensing. The principle of analysis based on MCDA and CRISPR-Cas12a is shown in Figure 1. The MCDA primers, gRNA and probe sequences are shown in Table 2.

Multiple cross displacement amplification

The pre-amplification step of MCDA was performed with an isothermal amplification kit as per the manufacturer's instructions (HuiDeXing Biotech. Co., Ltd., Tianjing, China). The reaction system of MP-MCDA was 25 μL, including 12.5 μL of 2× reaction buffer, 0.4 μM each of F1 and F2, 1.6 μM each of CP1 and CP2, 0.8 μM each of C1, C2, D1, D2, R1, and R2, 1.0 μL of Bst 2.0 DNA polymerase (8 U), 1 μL (pure bacteria) or 5 μL (clinical sample) DNA template, and appropriate volume of distilled water (DW) to 25 μL. The reaction process was conducted with the real-time turbidity (LA-320C) to monitor the amplification results and optimize the amplification temperature.

CRISPR-Cas12a based assay

In this study, Cas12a (Cpf1) was used for CRISPR-Cas-based *trans*-cleavage detection. The CRISPR-Cas12a-gRNA complex was formed by incubating 100 nM CRISPR-Cas12a (Cpf1) (Cat No: 10148305) with 100 nM gRNA in 2× HDX buffer at 37°C for

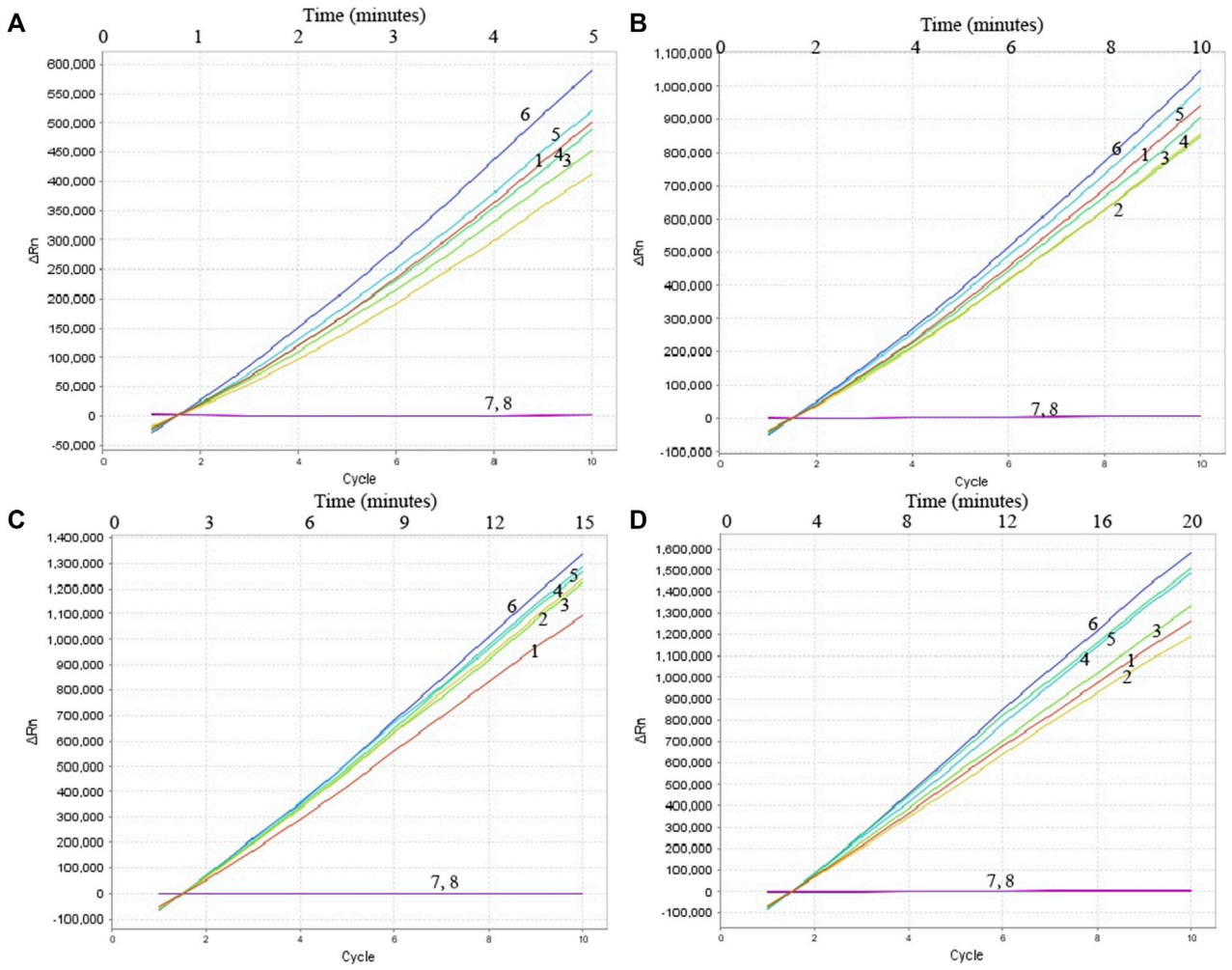

FIGURE 4
Optimization of reaction time of CRISPR-Cas12a-based biosensing system. Real-time fluorescence detection was used for reporting the CRISPR-Cas12a-gRNA cleavage results at 5 min **(A)**, 10 min **(B)**, 15 min **(C)**, and 20 min **(D)**. Stable fluorescence signal can be detected within 5 min. Curves 1–7, the fluorescence signal of the MP-MCDA reaction products yield from 5 ng, 500 pg, 50 pg, 5 pg, 500 fg, 50 fg, and 5 fg of MP genomic DNA; Curve 8, fluorescence signal of the blank control (DW).

10 min. Then, the complex should be used immediately or stored at low temperature (0°C–4°C) for no more than 12 h.

The CRISPR-Cas12a-based *trans*-cleavage assay was conducted in a 100 μL mixture, including 2 μL of MCDA products, 2.5 μL of probe, 18 μL of CRISPR-Cas12a-gRNA complex, 50 μL of 2× HDX buffer, and 27.5 μL of DW, following a process of incubation at 37°C for 10 min. The results were monitored by real-time fluorescence (RTF) method, with the probe (5′-Fam-TATTATTATTATTATTT-BHQ1-3′, 10 μM) utilized for CRISPR-Cas12a *trans*-cleavage detection (Zhu et al., 2021).

Sensitivity and specificity of the MP-MCDA-CRISPR assay

To verify the specificity of MP-MCDA-CRISPR assay, a total of 10 MP strains and 40 non-MP strains were used (Table 1), with distilled water (DW) applied as the blank control. Nucleic acid of all the strains were extracted and purified by using the Beijing TransGen Genomic DNA kit. In addition, nucleic acids of MP strains were also serially diluted from 5 ng to 5 pg per reaction with 10-fold attenuation for sensitivity analysis. In both kind of analysis, the MP-MCDA-CRISPR assay was performed as described above, and the results were reported by both RTF and VDR methods. Each test was repeated triple.

Validation of the feasibility of MP-MCDA-CRISPR assay in clinical samples

To further verify the feasibility of MP-MCDA-CRISPR assay in clinical settings, we collected 128 nasopharyngeal swabs suspected of MP infection based on clinical symptoms from CIP. The MP-MCDA-CRISPR assay was conducted as described above. All the clinical specimens were tested by real-time PCR method as well. Results of both methods were compared. Particularly, all the procedures were approved by the ethics committee of CIP, and all the samples obtained the informed consent signed by the participant's guardian.

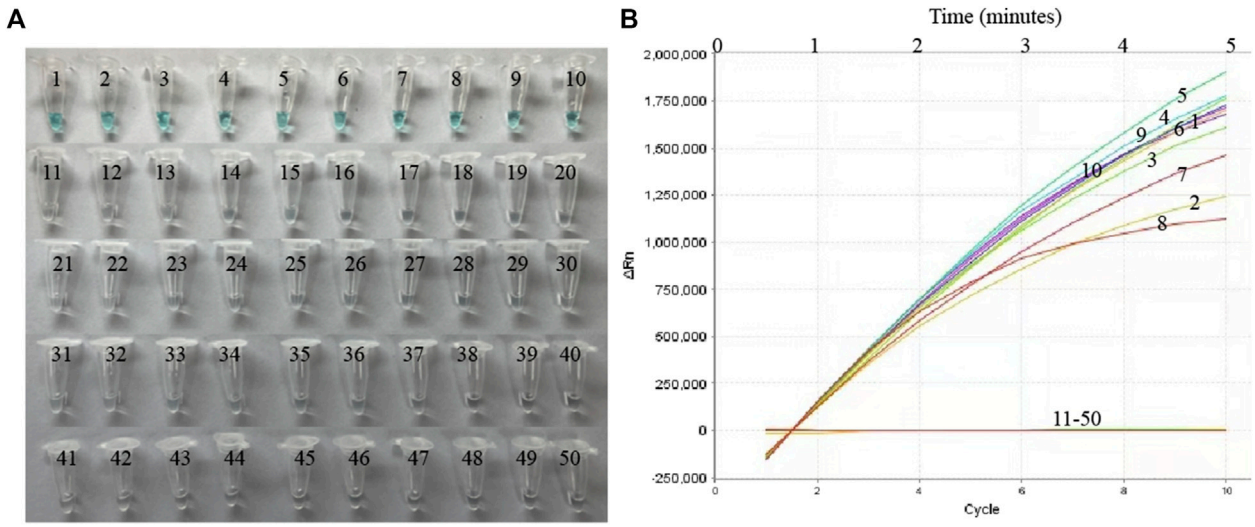

FIGURE 5
The specificity of the MP-MCDA-CRISPR assay. The specificity of the MP-MCDA-CRISPR assay reported by VDR method **(A)** and RTF method **(B)**, respectively. Tubes/Curves 1–10 represent the MP agents, and Tubes/Curves 11–50 represent non-MP pathogens.

Results

Overview of MP-MCDA-CRISPR detection system

The principle of MP-MCDA-CRISPR assay is shown in Figure 1. Firstly, the extracted MP DNA templates were exponentially pre-amplificated by the MCDA method within 30 min, of which the core primer CP1 was engineered with a PAM site (TTTC) for Cas12a effector at its linker region (Figure 1A). Then the gRNA, which formed a complex with CRISPR-Cas12a effector (Figure 1B, step 1), guided Cas12a molecules to recognize the target amplicons by the PAM site (Figure 1B, step 2). Finally, the trans-cleavage activity of the CRISPR-Cas12a effector was activated and the single-strand DNA (ssDNA) reporter molecules (5′-FAM-TATTATTATTATTATTT-BHQ1-3′) were ultrafast digested (Figure 1B, step 3, step 4), which was detected by the Applied Biosystems® 7500 Real Time PCR System. For the negative results, the ssDNA reporting molecules were not digested and the fluorescence signals could not be detected.

Optimal reaction conditions for MP-MCDA-CRISPR assay

To confirm the optimal temperature of MP-MCDA, temperatures ranging from 60°C to 67°C with an interval of 1°C were tested. As shown in Figure 3, 64°C was detected to be the optimal reaction temperature for the MP-MCDA reaction. Afterwards, the reaction time for CRISPR-Cas12a detection step was also optimized by comparing the results at 5, 10, 15, 20 min, respectively. As shown in Figure 4, a reaction time of 5 min was recommended for the CRISPR-Cas12a cleavage step of MP-MCDA-CRISPR assay.

Specificity of MP-MCDA-CRISPR assay

Nucleic acid templates extracted from 10 MP and 40 non-MP strains were used to evaluate the specificity of the MP-MCDA-CRISPR assay. The MP-MCDA-CRISPR was conducted under optimal reaction conditions, and the results were further confirmed using visual MCDA technique (VDR-based method). Readouts of both methods demonstrated that the 10 MP strains were positive, while all the non-MP strains were negative (Figure 5), implying that the specificity of MP-MCDA-CRISPR assay was 100%. Therefore, the MP-MCDA-CRISPR assay designed in this study has a high selectivity to the target nucleic acid.

Sensitivity of MP-MCDA-CRISPR assay

To evaluate the sensitivity of MP-MCDA-CRISPR assay, the serially diluted MP DNA (ranging from 5 ng to 5 fg per microliter) were used. As shown in Figure 6, readouts of the real-time turbidity, CRISPR and VDR methods indicated that the limit of detection (LoD) of MP-MCDA-CRISPR assay was 50 fg per reaction.

Feasibility of MP-MCDA-CRISPR assay in clinical samples

To further verify whether MP-MCDA-CRISPR assay could be used for MP detection in clinical samples, 128 nasopharyngeal swab samples suspected of MP infection were simultaneously detected by MP-MCDA-CRISPR and RT-PCR methods. Identical to the RT-PCR results, the 50 positive samples were confirmed as MP infection by MP-MCDA-CRISPR assay, while the 78 negative ones were

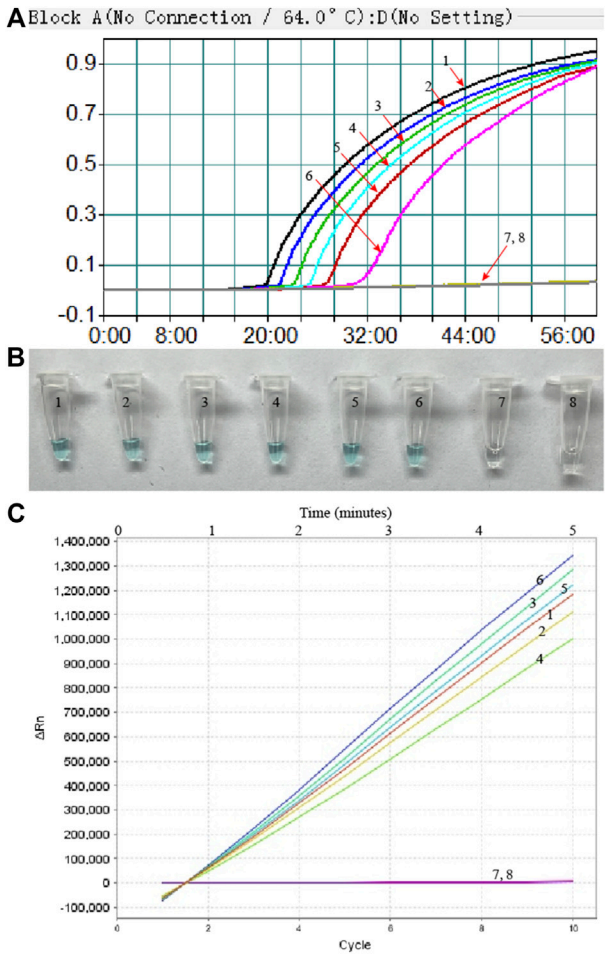

FIGURE 6
The sensitivity of the MP-MCDA-CRISPR assay. Real-time turbidity **(A)**, VDR **(B)** and RTF **(C)** methods were used to report the MP-MCDA-CRISPR assay results, respectively. Curves/Tubes 1–8 represent the MP genomic DNA concentrations of 5 ng, 500 pg, 50 pg, 5 pg, 500 fg, 50 fg, and 5 fg per reaction, and the blank control (DW), respectively. The LoD of the MP-MCDA-CRISPR assay was 50 fg per reaction.

considered as non-MP infection likewise (Figure 7), suggesting a consistency of 100% between the two methods (Table 3). These results suggested that the MP-MCDA-CRISPR assay established in this study could be used as a valuable technique for detecting MP infection in clinical settings.

Discussion

Here, a novel MP-MCDA-CRISPR assay, which combined the CRISPR-Cas12a-based biosensing system with MCDA, was established and evaluated for rapid detection of MP infection in clinical settings. Hitherto, various isothermal amplification techniques coupled with different biosensing systems have been developed for MP infection diagnosis, such as MCDA combined with nanoparticle-based lateral flow biosensor (LFB) (Wang et al., 2019), LAMP combined with LFB (Xiao et al., 2022), and recombinase polymerase amplification (RPA) combined with real-time fluorescent probe (Jiang et al., 2022), incarnating the advantages of sensitivity, specificity, simplicity and rapidity. Discovery of the CRISPR-Cas system provided a superior alternative for nucleic acid detecting platform for the high specificity (single base pair specificity) and sensitivity (only several copies) (Zhu et al., 2021), and the CRISPR-Cas9, CRISPR-Cas12, and CRISPR-Cas13 systems had been applied for detection of a variety of pathogens, such as hepatitis B virus (Chen et al., 2021) and SARS-CoV-2 (Zhu et al., 2021). In this report, the CRISPR-Cas12a system was first applied as the biosensing platform for MP detection for its highly sensitive, specific, and accurate. Particularly, the CP1 primer of standard MCDA method was modified by adding an engineered PAM site (TTTC) at the linker region (Figure 1) to circumvent the limitation of lack of PAM site which is essential for CRISPR-Cas12a-based biosensing platforms. Thus, the newly developed MCDA-CRISPR assay could detected any target sequences which were dearth of PAM sites.

An ideal laboratory diagnostic technique should be rapid, specific, sensitive, and easy to operate. In order to improve the sensitivity of MP-MCDA-CRISPR detection, CARDS gene of MP was pre-amplified by MCDA method. MCDA is a relatively new isothermal amplification technique which is independence of complex and expensive thermal cycling instruments and skilled personnel (Wang et al., 2015). The MCDA method contained a set of 10 primers extending 10 different regions of the target gene, i.e., a pair of replacement primers (F1 and F2), a pair of cross primers (CP1 and CP2) and three pairs of amplification primers (C1, C2, D1, D2, R1, and R2) (Figure 1A), endowing this method a high specificity (Wang et al., 2015). Another great virtue of MCDA assay is its high amplification efficiency, for which only within 30 min and minor amounts of templates (as low as 50 fg) the MCDA assay could reach to the cut-off value of detection (Zhang et al., 2020). More importantly, the MCDA-CP1 primer was engineered with a CRSIPR-Cas12a PAM site (TTTC), which played an important role for location of CRISPR-Cas12a-gRNA complex to the specific amplicons (Figure 1). Hence, the target gene located in the genome of MP could be sensitively, timely and accurately detected by the MP-MCDA-CRISPR assay.

In this study, the MCDA products were detected by the CRISPR-Cas12a-based biosensing system. For this biosensing system, the pivotal component is the CRISPR-Cas12a effector, which could perform collateral cleavage on non-targeted ssDNA upon the formation of the CRISPR-Cas12a-gRNA-target DNA ternary complex following the guidance of gRNA to the target DNA (Li et al., 2018a). Besides, a quenched fluorescent ssDNA reporter (FAM-TATTATTATTATTATTT-BHQ1) was applied as the probe, which released fluorescent signals upon *trans*-cleaved by the Cas12a effector (Figure 1B). The RTF method was used in this study for reporting the MP-MCDA-CRISPR outcomes. In positive reactions, the reporter molecule was cleaved and the produced fluorescent signals was captured by a real-time fluorescent detector. While in the negative reactions, none fluorescent signal was detected for the failure of cleavage of reporter molecule owing to the lack of target DNA. Last but not least, the newly devised MP-MCDA-CRISPR assay was specific enough and had no cross-reaction with other non-MP pathogens.

The newly devised MP-MCDA-CRISPR assay was verified for clinical feasibility as well. The 50 real-time quantitative PCR-positive samples were tested positive by the MP-MCDA-CRISPR assay, so did

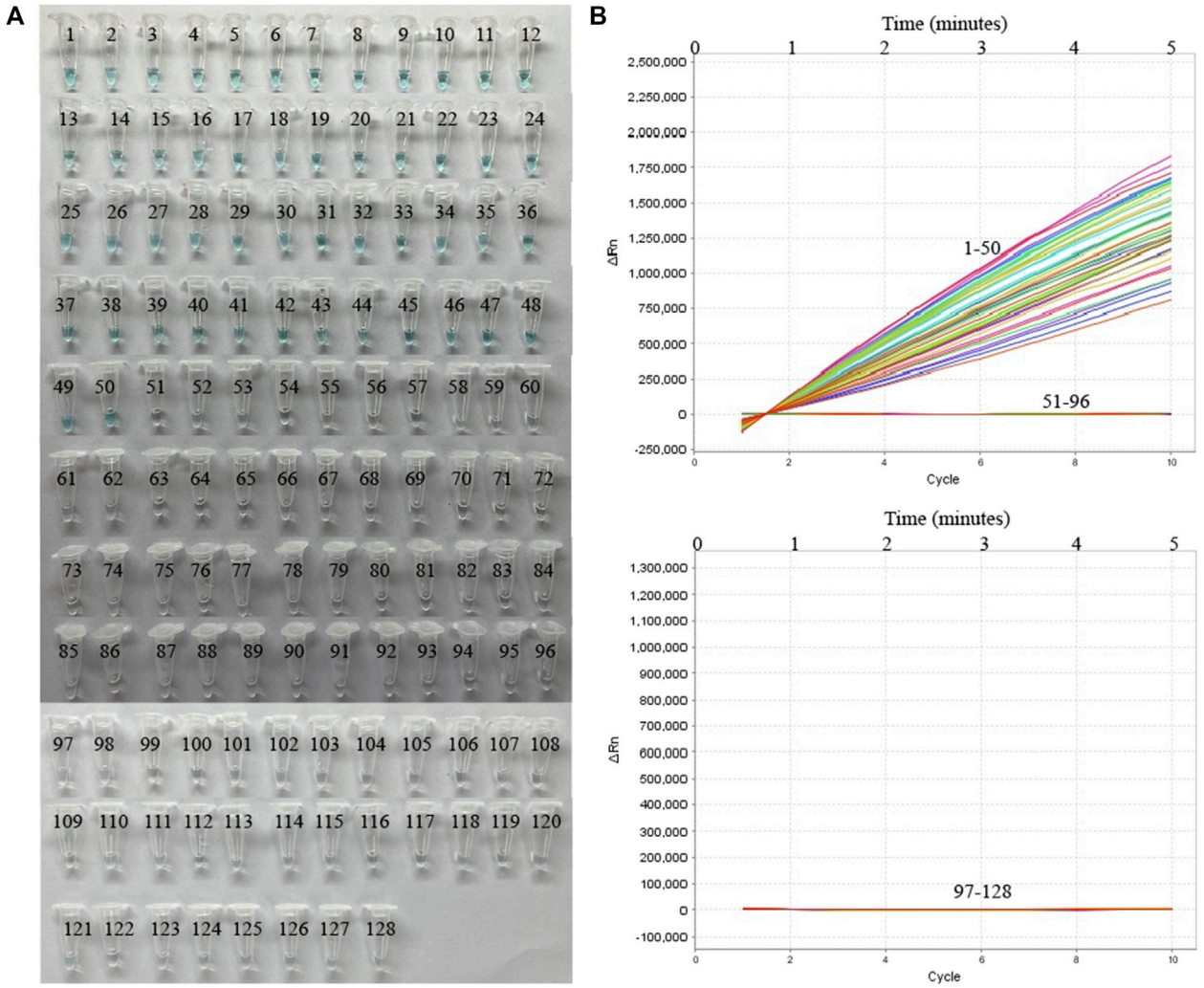

FIGURE 7
MP-MCDA-CRISPR results of 128 clinical samples suspected of MP infection. VDR **(A)** and RTF **(B)** methods were used to report the MP-MCDA-CRISPR assay results, respectively. Tubes/Curves 1–50 represent the 50 real-time PCR positive samples; Tubes/Curves 51–128 represent the 78 real-time PCR negative samples.

TABLE 3 Results comparison of MP-MCDA-CRISPR assay and real-time PCR for MP detection in clinical specimens.

Detection assay	Nasopharyngeal swab samples	
	Positive	Negative
MP-MCDA-CRISPR	50 (39%)	78 (61%)
Real-time PCR	50 (39%)	78 (61%)

the 78 real-time quantitative PCR-negative samples as negative in MP-MCDA-CRISPR assay. The concordance between the MP-MCDA-CRISPR assay and the real-time quantitative PCR test demonstrated the reliability of MP-MCDA-CRISPR assay in MP detection for clinical application. The whole detection procedure, including a 15 min process for genomic DNA template preparation, a 30 min process for MCDA pre-amplification, and a 5 min process for CRISPR-Cas12a-gRNA detection and results readout, could be completed within 50 min (Figure 1C). To sum up, with the advantages of low degree of instrument dependence, rapid turnaround time, and accurate detection capability, the MP-MCDA-CRISPR assay is expected to become point of care (POC) diagnosis method for MP infection detection, especially in the low-income countries and regions in the world. Further optimization for this newly proposed MP-MCDA-CRISPR assay could be devising a readout system simpler and easier to perform.

Taken together, we combined MCDA method and CRISPR-Cas12a-based biosensing system to develop a novel assay called "MP-MCDA-CRISPR" for the sensitive, specific and rapid detection of MP infections. The MP-MCDA-CRISPR assay could detect as low as 50 fg genomic DNA of MP and had no cross-reaction with other pathogens. The whole test could be completed within 50 min without complicated instruments and experienced technicians. Herein, the newly developed MP-MCDA-CRISPR assay is expected to become an important POC method for MP infection detection in clinical settings, especially in the resource-limited areas.

Data availability statement

The raw data supporting the conclusion of this article will be made available by the authors, without undue reservation.

Ethics statement

Studies involving human participants were reviewed and approved by the Capital Institute of Pediatrics Ethics Committee (Ethics approval number: SHERLL2021010). The patient/participant (legal guardian/near relative) provided written informed consent to participate in the study.

Author contributions

YW conceived and supervised this study. NJ performed the experiments. NJ, JZ, and FX analyzed the data. CS, FX, JF, XH, NJ, MC, and ZX provided reagents and materials. YW performed the software. BZ provided clinical guidance. NJ and JZ drafted the manuscript. YW and JZ revised the manuscript.

Funding

This study was funded by Beijing Nova Program (Grant No. Z211100002121042), National Key Research and Development Program of China (Grant Nos. 2021YFC2301101 and 2021YFC2301102).

Conflict of interest

The authors declare that the research was conducted in the absence of any commercial or financial relationships that could be construed as a potential conflict of interest.

Publisher's note

All claims expressed in this article are solely those of the authors and do not necessarily represent those of their affiliated organizations, or those of the publisher, the editors and the reviewers. Any product that may be evaluated in this article, or claim that may be made by its manufacturer, is not guaranteed or endorsed by the publisher.

References

Bajantri, B., Venkatram, S., and Diaz-Fuentes, G. (2018). Mycoplasma pneumoniae: A potentially severe infection. *J. Clin. Med. Res.* 10 (7), 535–544. doi:10.14740/jocmr3421w

Barrangou, R., Fremaux, C., Deveau, H., Richards, M., Boyaval, P., Moineau, S., et al. (2007). CRISPR provides acquired resistance against viruses in prokaryotes. *Science* 315 (5819), 1709–1712. doi:10.1126/science.1138140

Brouns, S., Jore, M. M., Lundgren, M., Westra, E. R., Slijkhuis, R., Snijders, A., et al. (2008). Small CRISPR RNAs guide antiviral defense in prokaryotes. *Science* 321 (5891), 960–964. doi:10.1126/science.1159689

Chen, J. S., Ma, E., Harrington, L. B., Da Costa, M., Tian, X., Palefsky, J. M., et al. (2018). CRISPR-Cas12a target binding unleashes indiscriminate single-stranded DNase activity. *Science* 360 (6387), 436–439. doi:10.1126/science.aar6245

Chen, X., Tan, Y., Wang, S., Wu, X., Liu, R., Yang, X., et al. (2021). A CRISPR-cas12b-based platform for ultrasensitive, rapid, and highly specific detection of hepatitis B virus genotypes B and C in clinical application. *Front. Bioeng. Biotechnol.* 9, 743322. doi:10.3389/fbioe.2021.743322

Daxboeck, F., Blacky, A., Seidl, R., Krause, R., and Assadian, O. (2004). Diagnosis, treatment, and prognosis of Mycoplasma pneumoniae childhood encephalitis: Systematic review of 58 cases. *J. Child. Neurol.* 19 (11), 865–871. doi:10.1177/08830738040190110401

Gootenberg, J. S., Abudayyeh, O. O., Lee, J. W., Essletzbichler, P., Dy, A. J., Joung, J., et al. (2017). Nucleic acid detection with CRISPR-Cas13a/C2c2. *Science* 356 (6336), 438–442. doi:10.1126/science.aam9321

Jain, S., Williams, D. J., Arnold, S. R., Ampofo, K., Bramley, A. M., Reed, C., et al. (2015). Community-acquired pneumonia requiring hospitalization among US children. *N. Engl. J. Med.* 372 (9), 835–845. doi:10.1056/NEJMoa1405870

Jiang, T., Wang, Y., Jiao, W., Song, Y., Zhao, Q., Wang, T., et al. (2022). Recombinase polymerase amplification combined with real-time fluorescent probe for Mycoplasma pneumoniae detection. *J. Clin. Med.* 11 (7), 1780. doi:10.3390/jcm11071780

Kakuya, F., Kinebuchi, T., Fujiyasu, H., Tanaka, R., and Kano, H. (2014). Genetic point-of-care diagnosis of M ycoplasma pneumoniae infection using LAMP assay. *Pediatr. Int.* 56 (4), 547–552. doi:10.1111/ped.12327

Kutty, P. K., Jain, S., Taylor, T. H., Bramley, A. M., Diaz, M. H., Ampofo, K., et al. (2019). Mycoplasma pneumoniae among children hospitalized with community-acquired pneumonia. *Clin. Infect. Dis.* 68 (1), 5–12. doi:10.1093/cid/ciy419

Li, L., Li, S., Wang, J., and Liu, G. (2019b). CRISPR/Cas systems towards next-generation biosensing. *Trends Biotechnol.* 37 (7), 730–743. doi:10.1016/j.tibtech.2018.12.005

Li, L., Li, S., Wu, N., Wu, J., Wang, G., Zhao, G., et al. (2019a). HOLMESv2: A CRISPR-cas12b-assisted platform for nucleic acid detection and DNA methylation quantitation. *ACS Synth. Biol.* 8 (10), 2228–2237. doi:10.1021/acssynbio.9b00209

Li, S., Huang, J., Ren, L., Jiang, W., Wang, M., Zhuang, L., et al. (2021). A one-step, one-pot CRISPR nucleic acid detection platform (CRISPR-top): Application for the diagnosis of COVID-19. *Talanta* 233, 122591. doi:10.1016/j.talanta.2021.122591

Li, S., Jiang, W., Huang, J., Liu, Y., Ren, L., Zhuang, L., et al. (2020). Highly sensitive and specific diagnosis of COVID-19 by reverse transcription multiple cross-displacement amplification-labelled nanoparticles biosensor. *Eur. Respir. J.* 56 (6), 2002060. doi:10.1183/13993003.02060-2020

Li, S. Y., Cheng, Q.-X., Liu, J.-K., Nie, X.-Q., Zhao, G.-P., and Wang, J. (2018a). CRISPR-Cas12a has both cis-and trans-cleavage activities on single-stranded DNA. *Cell Res.* 28 (4), 491–493. doi:10.1038/s41422-018-0022-x

Li, S. Y., Cheng, Q. X., Wang, J. M., Li, X. Y., Zhang, Z. L., Gao, S., et al. (2018b). CRISPR-Cas12a-assisted nucleic acid detection. *Cell Discov.* 4, 20. doi:10.1038/s41421-018-0028-z

Li, X., Atkinson, T. P., Hagood, J., Makris, C., Duffy, L. B., and Waites, K. B. (2009). Emerging macrolide resistance in Mycoplasma pneumoniae in children: Detection and characterization of resistant isolates. *Pediatr. Infect. Dis. J.* 28 (8), 693–696. doi:10.1097/INF.0b013e31819e3f7a

Liu, G., Lin, Q., Jin, S., and Gao, C. (2022). The CRISPR-Cas toolbox and gene editing technologies. *Mol. Cell* 82 (2), 333–347. doi:10.1016/j.molcel.2021.12.002

Loens, K., and Ieven, M. (2016). Mycoplasma pneumoniae: Current knowledge on nucleic acid amplification techniques and serological diagnostics. *Front. Microbiol.* 7, 448. doi:10.3389/fmicb.2016.00448

Loens, K., Mackay, W., Scott, C., Goossens, H., Wallace, P., and Ieven, M. (2010). A multicenter pilot external quality assessment programme to assess the quality of molecular detection of Chlamydophila pneumoniae and Mycoplasma pneumoniae. *J. Microbiol. Methods* 82 (2), 131–135. doi:10.1016/j.mimet.2010.05.006

Marraffini, L. A., and Sontheimer, E. J. (2008). CRISPR interference limits horizontal gene transfer in staphylococci by targeting DNA. *Science* 322 (5909), 1843–1845. doi:10.1126/science.1165771

Medjo, B., Atanaskovic-Markovic, M., Radic, S., Nikolic, D., Lukac, M., and Djukic, S. (2014). Mycoplasma pneumoniae as a causative agent of community-acquired pneumonia in children: Clinical features and laboratory diagnosis. *Ital. J. Pediatr.* 40 (1), 104–107. doi:10.1186/s13052-014-0104-4

Olson, D., Watkins, L. K. F., Demirjian, A., Lin, X., Robinson, C. C., Pretty, K., et al. (2015). Outbreak of Mycoplasma pneumoniae–associated Stevens-Johnson syndrome. *Pediatrics* 136 (2), e386–e394. doi:10.1542/peds.2015-0278

Pillet, S., Lardeux, M., Dina, J., Grattard, F., Verhoeven, P., Le Goff, J., et al. (2013). Comparative evaluation of six commercialized multiplex PCR kits for the diagnosis of respiratory infections. *PloS one* 8 (8), e72174. doi:10.1371/journal.pone.0072174

Ratliff, A. E., Duffy, L. B., and Waites, K. B. (2014). Comparison of the illumi gene Mycoplasma DNA amplification assay and culture for detection of Mycoplasma pneumoniae. *J. Clin. Microbiol.* 52 (4), 1060–1063. doi:10.1128/JCM.02913-13

Shihong Gao, D., Zhu, X., and Lu, B. (2021). Development and application of sensitive, specific, and rapid CRISPR-Cas13-based diagnosis. *J. Med. Virol.* 93 (7), 4198–4204. doi:10.1002/jmv.26889

Vujic, I., Shroff, A., Grzelka, M., Posch, C., Monshi, B., Sanlorenzo, M., et al. (2015). Mycoplasma pneumoniae-associated mucositis–case report and systematic

review of literature. *J. Eur. Acad. Dermatol Venereol.* 29 (3), 595–598. doi:10.1111/jdv.12392

Waites, K. B., and Talkington, D. F. (2004). Mycoplasma pneumoniae and its role as a human pathogen. *Clin. Microbiol. Rev.* 17 (4), 697–728. doi:10.1128/CMR.17.4.697-728.2004

Waites, K. B., Xiao, L., Liu, Y., Balish, M. F., and Atkinson, T. P. (2017). Mycoplasma pneumoniae from the respiratory tract and beyond. *Clin. Microbiol. Rev.* 30 (3), 747–809. doi:10.1128/CMR.00114-16

Waites, K. B., Xiao, L., Paralanov, V., Viscardi, R. M., and Glass, J. I. (2012). Molecular methods for the detection of Mycoplasma and ureaplasma infections in humans: A paper from the 2011 william beaumont hospital symposium on molecular pathology. *J. Mol. Diagn* 14 (5), 437–450. doi:10.1016/j.jmoldx.2012.06.001

Wang, Y., Wang, Y., Ma, A. J., Li, D. X., Luo, L. J., Liu, D. X., et al. (2015). Rapid and sensitive isothermal detection of nucleic-acid sequence by multiple cross displacement amplification. *Sci. Rep.* 5, 11902. doi:10.1038/srep11902

Wang, Y., Wang, Y., Quan, S., Jiao, W., Li, J., Sun, L., et al. (2019). Establishment and application of a multiple cross displacement amplification coupled with nanoparticle-based lateral flow biosensor assay for detection of Mycoplasma pneumoniae. *Front. Cell Infect. Microbiol.* 9, 325. doi:10.3389/fcimb.2019.00325

Xiao, F., Zhou, J., Sun, C., Huang, X., Zheng, B., Fu, J., et al. (2022). Loop-mediated isothermal amplification coupled with nanoparticle-based biosensor: A rapid and sensitive method to detect Mycoplasma pneumoniae. *Front. Cell Infect. Microbiol.* 12, 882855. doi:10.3389/fcimb.2022.882855

Yamada, M., Buller, R., Bledsoe, S., and Storch, G. A. (2012). Rising rates of macrolide-resistant Mycoplasma pneumoniae in the central United States. *Pediatr. Infect. Dis. J.* 31 (4), 409–411. doi:10.1097/INF.0b013e318247f3e0

Zhang, X., Payne, M., Wang, Q., Sintchenko, V., and Lan, R. (2020). Highly sensitive and specific detection and serotyping of five prevalent Salmonella serovars by multiple cross-displacement amplification. *J. Mol. Diagn* 22 (5), 708–719. doi:10.1016/j.jmoldx.2020.02.006

Zhu, X., Wang, X., Li, S., Luo, W., Zhang, X., Wang, C., et al. (2021). Rapid, ultrasensitive, and highly specific diagnosis of COVID-19 by CRISPR-based detection. *ACS Sens.* 6 (3), 881–888. doi:10.1021/acssensors.0c01984

frontiers | Frontiers in Bioengineering and Biotechnology

TYPE Methods
PUBLISHED 07 February 2023
DOI 10.3389/fbioe.2023.1131840

OPEN ACCESS

EDITED BY
Zhiyang Li,
Nanjing Drum Tower Hospital, China

REVIEWED BY
Guangyao Zhang,
Qingdao University, China
Jie Wu,
Nanjing University, China

*CORRESPONDENCE
Hongbin Zhang,
zhangwater@hotmail.com

SPECIALTY SECTION
This article was submitted to Biosensors and Biomolecular Electronics, a section of the journal Frontiers in Bioengineering and Biotechnology

RECEIVED 26 December 2022
ACCEPTED 30 January 2023
PUBLISHED 07 February 2023

CITATION
Yuan S, Xie G, Yang X, Chen Y and Zhang H (2023), Portable paper-based electrochemiluminescence test incorporating lateral-flow immunosensors for detection of interferon-γ levels. *Front. Bioeng. Biotechnol.* 11:1131840. doi: 10.3389/fbioe.2023.1131840

Portable paper-based electrochemiluminescence test incorporating lateral-flow immunosensors for detection of interferon-γ levels

Shichao Yuan[1], Guihua Xie[2], Xiang Yang[2], Yu Chen[1] and Hongbin Zhang[1]*

[1]Department of Basic Medical Research, General Hospital of Southern Theater Command of PLA, Guangzhou, China, [2]Guangzhou Leide Biotechnology Co, Ltd, Guangzhou, China

Tuberculosis (TB) poses a serious threat to human health and social development. Accurate diagnosis of *mycobacterium tuberculosis* infection plays a critical role in the prevention and treatment of tuberculosis. Interferon-γ (INF-γ) release assay (IGRA) is currently the only quantitative tuberculosis infection diagnosis method. An accurate, fast, and easily handled INF-γ detection method is the key to obtaining accurate results. Herein, we report a novel paper-based electrochemiluminescence (ECL) method based on lateral flow immunosensors that combines the easy handling characteristics of immunochromatography and the high sensitivity of electrochemiluminescence to detect IFN-γ. To our knowledge this is the first INF-γ detection method that combines immunochromatography with electrochemiluminescence. The paper-based ECL-LFI test consists of a sample pad, conjugation pad (with binding antibody IFN-γ-Ab1 conjugated with ruthenium tripyridine), detection pad (with capture antibody IFN-γ-Ab2 immobilized on nanospheres), absorbent pad, and electrode for signal activation. The ECL signal is obtained by cyclic voltammetry scanning at a speed of 0.1 V/s in the detection area of the paper-based ECL-LFI test. In our experiments, the paper-based ECL-LFI test exhibited a minimum detection limit of 2.57 pg/mL within 12 min, and a broad detection range of 2.57–5,000 pg/mL, with repeatability of 8.10% and stability of 4.97%. With the advantage of high accuracy and sensitivity, easy handling, and low user training requirements, this ECL-LFI test might be used as point-of-care testing (POCT) in the IGRA for tuberculosis diagnosis.

KEYWORDS

electrochemiluminescence, interferon-γ, lateral flow immunosensors, paper-based, POCT (point-of-care testing)

1 Introduction

Interferon gamma (IFN-γ) is a major immunoregulatory cytokine predominantly produced by T cells and innate lymphoid cells (Petermann et al., 2019). IFN-γ not only has antiviral, anti-microbial infection, antitumor, and other biological functions, but also plays a crucial role in innate immunity and acquired immunity (Hawerkamp et al., 2020; Thibaut et al., 2020; Caputa et al., 2022). It can also be used to detect immune levels or certain diseases, such as tuberculosis (TB) (Bergamaschi et al., 2021; Hlaca et al., 2022).

The IFNB-γ release assay (IGRA) method is commonly used in the diagnosis of TB infection (Sloot et al., 2020). The traditional IGRA method requires professional operation, instruments, and experimental platforms, and the process is time-consuming and laborious (Hamada et al., 2021; Petnak et al., 2022). Therefore, an accurate, fast point-of-care testing (POCT) method for the IGRA is urgently needed.

Electrochemiluminescence (ECL) sensors incorporate a combination of electrochemistry and measurement of visual luminescence, and have the advantages of being highly sensitive, non-hazardous, and inexpensive; moreover, they exhibit a linear response over a wide range (Zhang and Liu, 2020; Ahmadi et al., 2021; Rizzo et al., 2021). Several electrochemical luminescence immunoassays have been established to detect tuberculosis markers Lipoarabinomannan (LAM), ESAT-6, IFN-γ and Interleukin (IL-2) (Zhou et al., 2017a; Zhou et al., 2017b; Sigal et al., 2018; Broger et al., 2019). The luminous substances emit light only under electrical stimulation, which reduces the sensitivity of ECL to interference by external factors (Bauer et al., 2021). Several reported ECL assays for IFN-γ adopt only paper-based circular detection (Sennikov et al., 2003; Li et al., 2020). The lateral-flow immunoassay (LFI) is a paper-based platform that is inexpensive, simple to perform, rapid, and portable, and thus is ideal for use in point-of-care (POC).

In this report, a lateral flow immunosensor combined with ECL was developed to detect IFN-γ. Nanospheres combined with capture antibodies were adopted to improve the capture efficiency and ECL intensity. The entire testing process takes only 12mins.The ECL-LFI adopts dry chemical diagnosis, which is different from traditional wet chemical diagnosis. Moreover, there is no need to add samples many times, samples can be added at once to detect the IFN-γ concentration without other operations, which is highly desirable for new and sudden infectious diseases. The combination of paper and screen printed electrode (SPE) makes ECL-LFI portable and mass producible. Moreover, the RPEL-B POCT electrochemical luminescence detector we used is close to a notebook, and the weight is only 1 kg, which is highly conducive to application in remote areas with poor medical conditions.

2 Materials and methods

2.1 Materials

IFN-γ-Ab1, IFN-γ-Ab2, and antigen were purchased from Guangzhou Leide Biotechnology Co., Ltd. (China). N-Hydroxy succinimide (NHS), 1-(3-Dimethylaminopropyl)-3-ethylcarbodiimide hydro (EDC), Ru $(bpy)_2$ (mcbpy-O-Su-ester) $(PF_6)_2$ (Ru-NHS ester), Butyldiethanolamine (BDEA), Tripropylamine (TPA), and TWEEN-20 were purchased from Sigma–Aldrich (United States of America). Elecsys buffer was purchased from Roche (Switzerland). Nanospheres (200-nm diameter) were purchased from Biotron Biotechnology Co., Ltd. (China). Centrifugal tubes (15 mL) and 5-mL 7K MWCO Zeba™ spin desalting columns were purchased from Thermo Fisher Scientific (United States of America). A Three Screen Printed Electrodes (SPEs) were purchased from Zensor Technology (China). Glass fiber RB-45 and absorbent paper ABP-S270 were purchased from Shanghai KingBio Biotechnology (China). Whatman No. One and Whatman No. 102 filters were purchased from Whatman (United States of America). PT-0.45 μm was purchased from Cytiva (United States of America). Biodyne C was purchased from PALL (United States of America). Heterophilic antibody blocker (HBR) and dimethyl sulfoxide (DMSO) were purchased from Bio Liye Technology (China).

2.2 Instruments

A RPEL-B POCT electrochemical luminescence detector was purchased from Xi'an Remex Analysis Instruments (China). An HGS210 high-speed cutting machine and HGS510-1 bench-type gold spraying marking machine were purchased from Hangzhou AutoKun Technology (China). A rotary disc mixer was purchased from Aquapro International Co. (United States of America).

2.3 Preparation of antibody-functionalized ECL nanoprobes

The method of labeling the antibody with Ru-NHS ester was based on a previously reported method with some modifications (Zhou et al., 2014). First, 1 mg of Ru-NHS ester was dissolved in DMSO to 10 mmol/L and then diluted with distilled water to 1 mmol/L. IFN-γ-Ab1 was diluted with phosphate buffered saline (PBS) to 25 μmol/L. Second, 500 μL of antibody solution and 1,000 μL, 500 μL, and 250 μL of Ru-NHS ester solution were mixed in separate samples; the molar ratio of Ru-NHS ester to antibody was 80:1, 40:1, and 20:1, respectively. The samples were then wrapped with tin foil and rotated on the rotary disc mixer for 12 h. Following the reaction, a 5-mL 7K MWCO Zeba™ spin desalting column was used to remove free Ru-NHS ester from the Ru-labeled IFN-γ-Ab1 (labeled antibodies). See Figure 1B.

Preparation of captured antibodies IFN-γ-Ab2 coupled nanospheres was performed as shown in Figure 1B.

Diluted capture antibodies was added to activated microspheres and then blocked with 0.05-M Tris-HCl and 1% Bovine albumin (BSA) before being resuspended in a resuspend solution.

2.4 Preparation of immunochromatographic strips

To determine the paper suitable for detection, different papers were cut into several discs with a diameter of 6 mm. Each disc was placed in the circular detection pad of the three-electrode SPE. Labeled antibodies was diluted to 0.2 mg/mL according to the method described in Section 2.3 and mixed with Elecsys buffer. Subsequently, 6 μL of diluted antibody was added to the disc for the electrochemiluminescence test.

The captured antibodies was sprayed on the detection pad using the HGS510-1 bench-type gold spraying marking machine. Following that, a 2% sucrose solution was added to protect the antibody adsorbed on the paper.

Each sample pad was pretreated with 0.05 M Tris (pH 7.4), 1% BSA, 0.5% sodium casein, 0.5% trehalose, 2% sucrose, 0.5 mg/mL HBR, and 0.9% NaCl. Following overnight drying in an oven at 37°C, the labeled antibodies was sprayed on the bonding pad with the HGS510-1, followed by oven drying again. The labeled antibodies was sprayed onto the conjugation pad using the HGS510-1 machine and then oven-dried again.

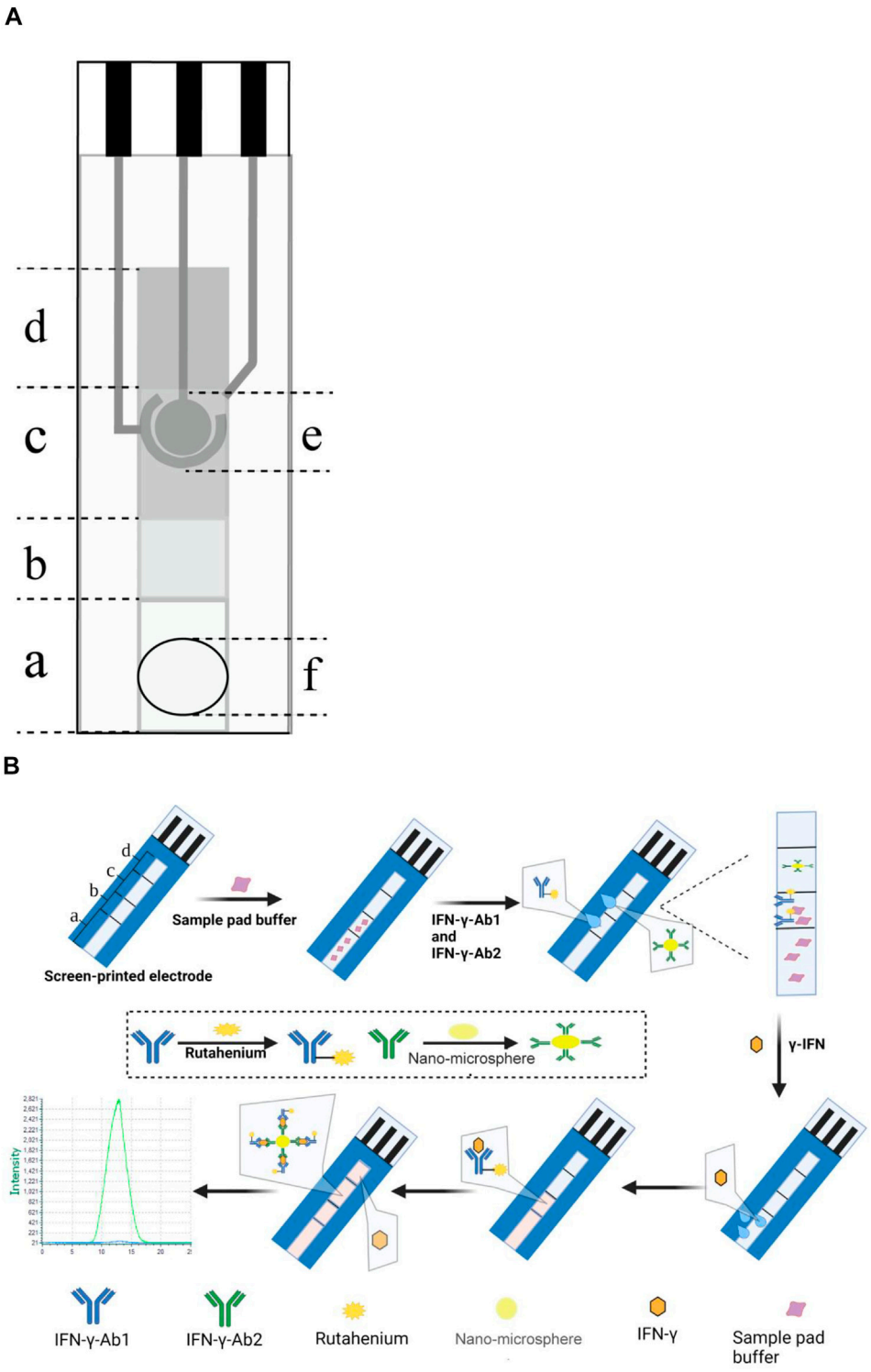

FIGURE 1
(A) Schematic diagram of the three-electrode SPE ECL-LFI; **(a)** Sample pad, **(b)** conjugation pad, **(c)** detection pad, **(d)** absorbent pad, **(e)** electrodes (reference electrode, working electrode, and counter electrode), and **(f)** sample loading hole. **(B)** Illustration of the ECL-LFI for detection of IFN-γ; **(a)** sample pad, **(b)** conjugation pad, **(c)** detection pad, and **(d)** absorbent pad.

The entire paper-based channel is 7 cm long and 6 mm wide. The sample pad is 2.5 cm long. The conjugation pad is 1.0 cm long. The detection pad is 1.5 cm long, and the absorbent pad is 2 cm long (Figure 1A).

2.5 ECL detection of IFN-γ

The immunoassay was based on the double-antibody sandwich method. To begin, the sample was diluted with 0.1-M PBS (pH 7.4) and

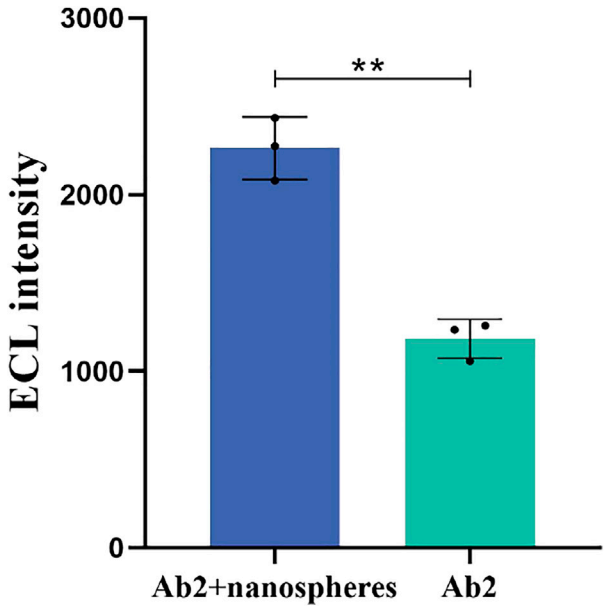

FIGURE 2
Effect of IFN-γ-Ab2 coupled nanospheres on ECL intensity. The concentration of IFN-γ is 200 pg/mL $p < 0.05$ was considered significant; $p < 0.01$.

50 μL Elecsys buffer to a final volume of 150 μL. The diluted sample was then dropped into the loading hole of the paper-based ECL-LFI. Through optimization of reaction time, following a reaction in the dark for 12 min, ECL detection was carried out as shown in Figure 2. Potential scanning was performed by cyclic voltammetry scanning from 0.2 to 1.5 V; the photomultiplier tube voltage was set at 800 V.

2.6 Statistical analysis

Standard deviations were determined by relative expression ratios of three replicates for each measurement. In the case of a normal distribution, a *t*-test or analysis of variance (ANOVA) test with Bonferonni correction was applied. A *p*-value less than 0.05 was considered significant (*$p < 0.05$; **$p < 0.01$). All statistical analyses were performed using SPSS 21.0 software (SPSS Inc., United States of America).

3 Results and discussion

3.1 Characterization of antibody-functionalized ECL nanoprobes

The OD value of the ECL nanoprobe was measured with a spectrophotometer. According to the formula [Label ratio] = $A_{\text{antibody absorption}} \times$dilution factor/13700 $M^{-1}cm^{-1} \times C_{\text{antibody concentration}}$ (Zhou et al., 2014), the labeling rates of the 20:1,40:1, and 80:1 Ru-NHS ester to antibody molar ratios were 45.5%, 53.1%, and 44.8%, respectively. Thus, the labeling rate is the highest when the molar ratio is 40:1.

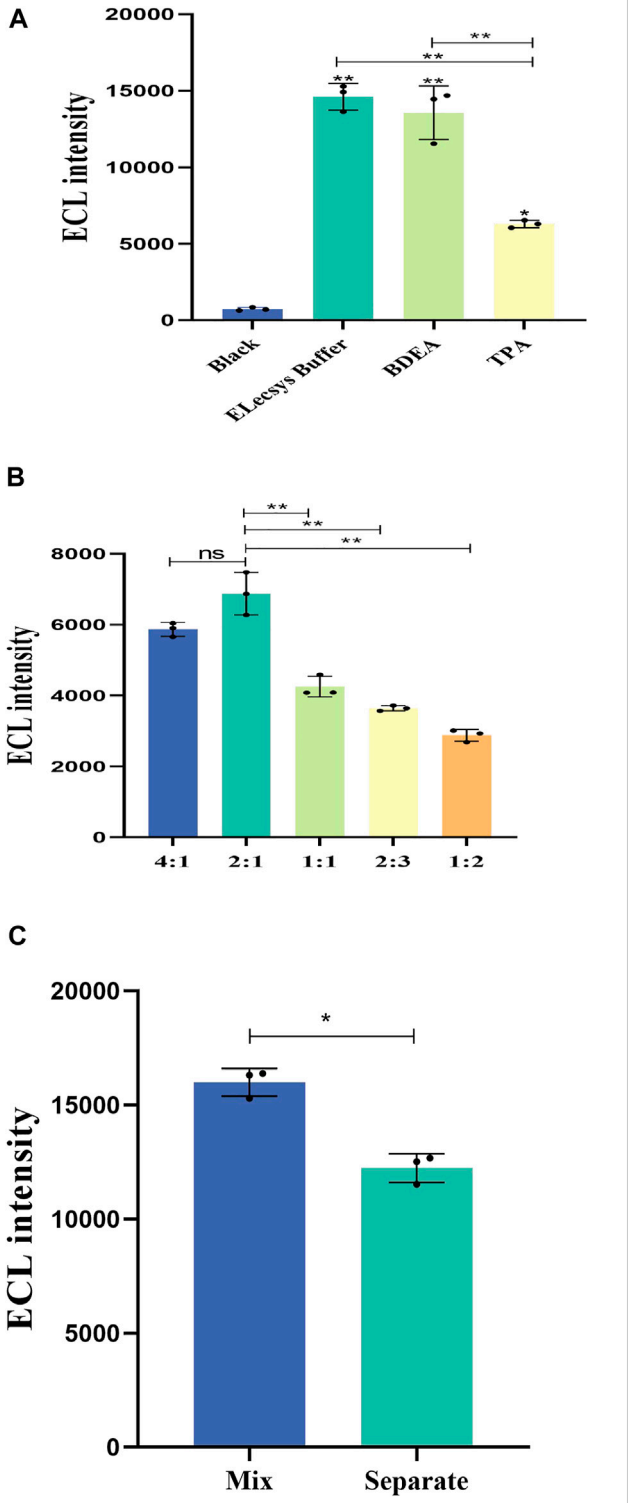

FIGURE 3
(A) Influence of the different co-reactants on the ECL intensity. The concentration of IFN-γ is 10 ng/mL. **(B)** Effect of different proportions of the volume of Elecsys buffer on the ECL intensity of the sample. The concentration of IFN-γ is 5,000 pg/mL. **(C)** Difference among methods of adding co-reactants. The concentration of IFN-γ is 10 ng/mL $p < 0.05$ was considered significant; A, $p < 0.01$; B, $p < 0.01$; C, $p < 0.05$.

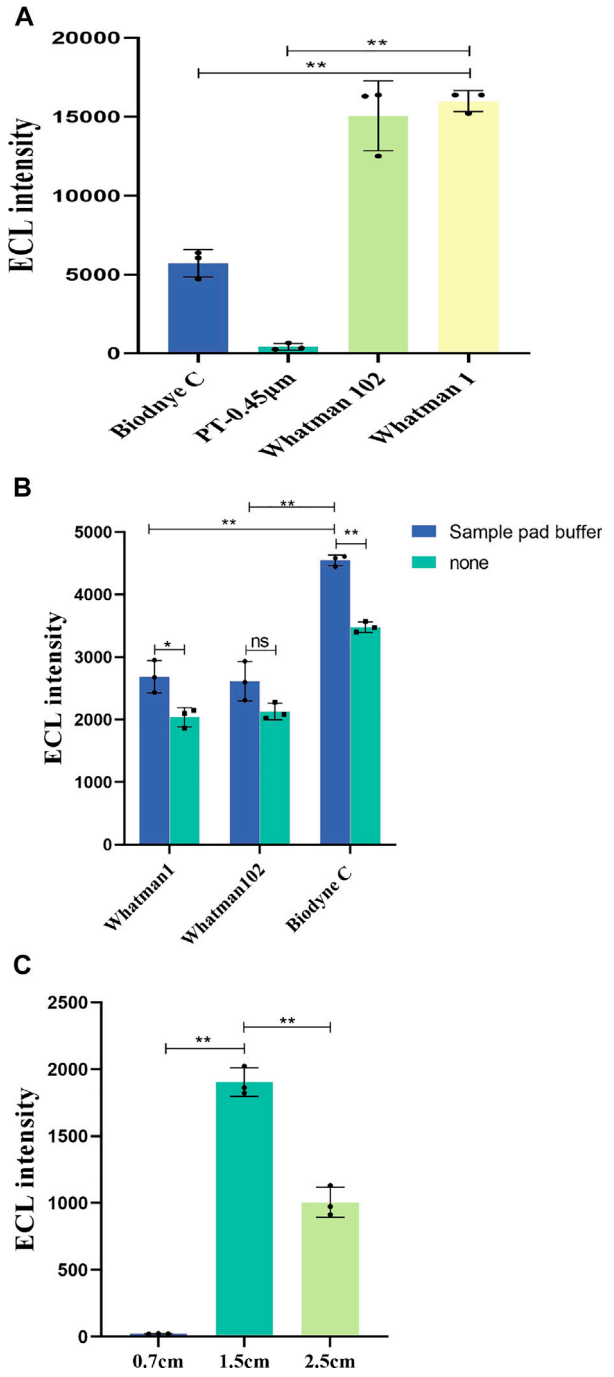

FIGURE 4
(A) ECL characteristics of different papers. The concentration of labeled antibodies is 0.2 mg/mL. **(B)** Effect of sample pad buffer on ECL intensity and ECL intensity of different detection pads in immunochromatography. The concentration of IFN-γ is 5000 pg/mL. **(C)** ECL intensity for different detection pad lengths. The concentration of IFN-γ is 200 pg/mL $p < 0.05$ was considered significant; A, $p < 0.01$; B, $p < 0.01$; C, $p < 0.01$.

RPEL-B was used to measure the effect of IFN-γ-Ab2 coupled to nanospheres. The average ECL intensity of IFN-γ-Ab2 coupled with nanospheres and IFN-γ-Ab2 was 2,264 and 1,184, respectively (n = 3). Figure 2A presents a comparison with the spraying of detection antibody IFN-γ-Ab2 alone; a higher ECL intensity was obtained after IFN-γ-Ab2 was bound to the nanospheres and then sprayed onto the detecting area of the strip; the difference was statistically significant ($p < 0.01$).

The ECL intensity of the materials used in the ECL-LFI test was detected to eliminate the signal interference to the Ru-NHS ester. The average ECL intensity of Ru-NHS ester, IFN-γ, IFN-γ-Ab1, IFN-γ-Ab2, nanospheres, and Elecsys buffer are 4,158.7, 79.3, 62.3, 79.8, and 113.3, respectively (n = 3). Figure 2B illustrates that the materials used in ECL-LFI do not interfere with the ECL intensity of Ru-NHS ester ($p < 0.01$).

3.2 Effect of co-reactants on ECL intensity

In this study we optimized several crucial parameters of the reaction of co-reactants with Ru-NHS ester. The experiment was carried out on Whatman No. 1 filter medium, and the blank group was 6 μL of 0.2 mg/mL labeled antibodies.

Figure 3A shows the ECL intensity result of different co-reactants during antibody labeling. The average ECL intensity of Black, Elecsys buffer, BDEA, and TPA were 732.3, 14,613, 13,565.7, and 6,297, respectively (n = 3). Compared with the blank, BDEA, and TPA groups, the ECL intensity of Elecsys buffer was higher by a factor of 19.95,1.08, and 2.32, respectively ($p < 0.01$).

Figure 3B shows the ECL intensity of different volumes of Elecsys buffer. The average ECL intensity for Sample: Elecsys buffer ratios of 4:1, 2:1, 1:1, 2:3, and 1:2 are 5,869, 6,875.3, 4,252.7, 3,643.3, and 2,878.3 respectively (n = 3). When the volume ratio of Sample: Elecsys buffer was 2:1, the ECL intensity was significantly higher than for the other groups ($p < 0.01$).

Figure 3C shows the difference among methods of adding co-reactants. "Mix" means buffer solution and sample mixed in advance for detection. "Separate" means buffer solution and sample dropped into the sample hole sequentially. The average ECL intensity of Mix and Separate are 15,993.7 and 12,235.7, respectively (n = 3). In summary, mixing samples and Elecsys buffer in advance is better than dropping them separately ($p < 0.05$).

3.3 Optimization of the paper-based test

The ECL performance for Whatman No. One and Whatman No. 102 filter media, Biodyne C, and PT-0.45 μm was tested. A 6-μL mixture of Elecsys buffer and 0.2 mg/mL labeled antibodies was dropped on each paper, and the ECL intensity was detected. The results in Figure 4A present the ECL characteristics for the different papers. The average ECL intensity of Biodyne C, PT-0.45 μm, Whatman No. 102, and Whatman No. One were 5,713, 411.7, 15,068, and 15,993.7, respectively (n = 3). The ECL intensity of Whatman No. One was higher than that of any other paper ($p < 0.01$).

Once the sample pad was treated by sample pad buffer, the treated sample pads were assembled in the paper-based channels with detection pads made of Whatman No. 1, Whatman No. 102, and Biodyne C, and the ECL intensity was measured under the same conditions for each paper. The sample pad buffer can increase the hydrophilicity of the paper and the pretreatment of samples, balance the pH of the sample to be tested, and adjust the salt ion strength. Figure 4B shows the effect of sample pad buffer on ECL intensity. The

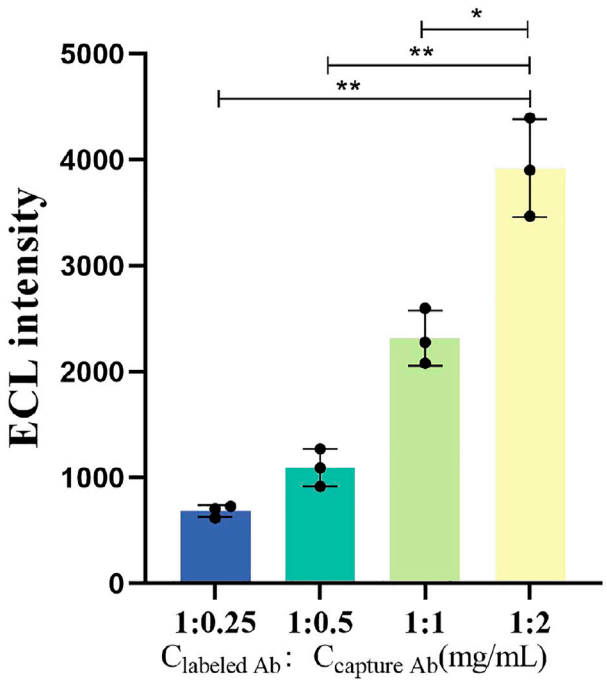

FIGURE 5
ECL intensity when the labeled antibodies reacts with the captured antibodies at different concentrations. The concentration of IFN-γ is 5000 pg/mL $p < 0.05$ was considered significant; $p < 0.01$.

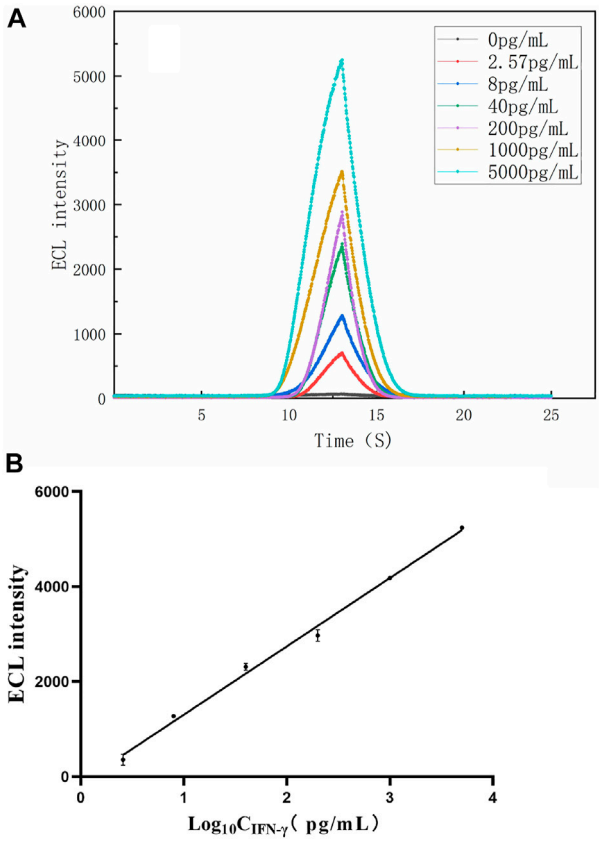

FIGURE 6
(A) ECL intensity-time curves of the paper-based ECL-LFI with different concentrations of IFN-γ **(B)** Linear relationship between the ECL intensity and IFN-γ concentrations of 2.57, 8, 40, 200, 1,000, and 5,000 pg/mL.

average ECL intensity of sample pad buffer group and "none" group for Whatman No. One are 2,686 and 2035.7; for Whatman No. 102 they are 2,613 and 2,127; and for Biodyne C they are 4,546 and 3,479.7, respectively (n = 3). The ECL intensity is higher after the sample pad buffer treatment ($p < 0.01$).

The results in Figure 4B show the ECL intensity for different detection pads in immunochromatography. Through experimental comparison, Biodyne C film exhibited higher ECL strength and more suitability for detection in the ECL-LFI test. Although the ECL characteristics of Whatman No. One and Whatman No. 102 are better than those of Biodyne C, in this work it is also necessary to consider the protein adsorption capacity, porosity, and wettability of the paper, as well as the capillary flow of the water-based samples. The low porosity and high protein adsorption capacity of Biodyne C are more conducive to immunochromatography. Therefore, Biodyne C was finally selected as the paper for the detection pad.

Figure 4C shows the influence of different lengths of test pads on ECL intensity. The average ECL intensity for test pad lengths of 0.7, 1.5, and 2.5 cm are 22.1, 1903.3, and 1,005.3 respectively (n = 3). Since the detection pad is a circle with a diameter of 6 mm, we set up three groups of detection pads with different lengths (0.7 cm, 1.5 cm, and 2.5 cm) for comparison. The results show that the 1.5-cm length is more suitable for the proposed ECL-LFI test ($p < 0.01$). No significant ECL intensity was found in the 0.7-cm group. The reason is that the detection pad should cover the electrodes completely, and it also should overlap the front and rear combination pads and water absorption pad by a small amount. Since the 0.7-cm detection pad length is too short, the normal flow measurement and chromatography process cannot be completed.

3.4 Effect of the concentration of labeled antibodies and captured antibodies on the ECL intensity

To obtain higher ECL intensity, we set four groups of labeled antibodies to capture antibodies concentration ratios as follows for the ECL intensity test: 1 mg/mL:0.25 mg/mL, 1 mg/mL:0.5 mg/mL, 1 mg/mL:1 mg/mL, and 1 mg/mL:2 mg/mL. All were joined to 150 μL 1,000 pg/mL samples. Figure 5 illustrates the ECL intensity of labeled antibodies and captured antibodies with different concentration ratios. The average ECL intensity for concentration ratios of 1:0.25, 1:0.5, 1:1, and 1:2 are 684.3, 1,093.7, 2,318, and 3,921, respectively (n = 3). When the concentrations of labeled antibodies and captured antibodies were 1 mg/mL and 2 mg/mL, respectively, the corresponding signal was better ($p < 0.01$). Considering the cost of the paper-based ECL-LFI test, no more experiments were conducted on other concentrations.

3.5 Analytical performance of the paper-based ECL-LFI test

The ECL-LFI test was used to quantitatively detect the content of IFN-γ-Ag, as shown in Figures 6A, B. With increasing Ag concentration, the ECL intensity increases gradually. The

TABLE 1 Results of the detection of IFN-γ in human serum.

Sample	Added (pg/mL)	Found (pg/mL, n = 3)	Recovery (%)	RSD (%, n = 3)	ELISA (pg/mL, n = 3)
Serum + IFN-γ	0	7.6 ± 1.2			6.1 ± 1.0
	200	206.5 ± 17.6	103.2	8.5	201.3 ± 10.2
	1,000	1,073.2 ± 60.5	107.8	5.6	1,028.6 ± 43.5
	5,000	5,412.9 ± 310.2	108.3	5.7	5,309.2 ± 198.5

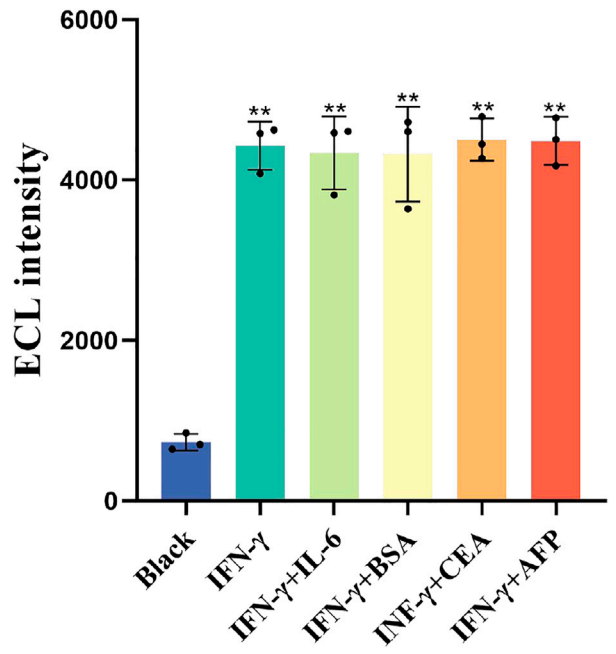

FIGURE 7
Specificity of paper-based ECL-LFI test. $P < 0.05$ was considered significant; $p < 0.01$.

calibration plots exhibited a good linear relationship between the ECL intensity and the logarithm of IFN-γ concentrations in the range of 2.57–5,000 pg/mL. The linear regression equations were IECL = 1439lg CIFN-γ-Ag − 135.5, with a correlation coefficient R^2 = 0.9932. Moreover, the detection limit for IFN-γ was 2.57 pg/mL (S/N = 3) according to the Guidelines of the Clinical and Laboratory Standards Institute (NCCLS) (Satlin et al., 2020). The results show that the paper-based ECL-LFI test can quantitatively detect IFN-γ during one potential scanning and exhibited wide linear ranges and low detection limits, indicating that it has significant value in improving the accuracy and reliability of TB infection diagnosis.

3.6 Analysis of IFN-γ in human serum

The reliability of the paper-based ECL-LFI test was verified by using a commercial ELISA test. Upon adding serum of unknown concentration, ECL-LFI found a result of 206.5 ± 17.6 pg/mL; the ELISA result was 201.3 ± 10.2 pg/mL. Table 1 indicates that the detection results of the ECL-LFI test for IFN-γ in human sera agreed closely with those from the ELISA test. Moreover, the recovery of IFN-γ was 106.3%. Relative standard deviation (RSD) was 5.6% for IFN-γ (n = 3). ELISA is often used alone or in combination with other methods to detect TB (Mungmunpuntipatip and Wiwnaitkit, 2020). These results show that the paper-based ECL-LFI test can reliably determine IFN-γ in human serum.

TABLE 2 Reproducibility of the paper-based ECL-LFI test.

Concentration	M	Sd	RSD (%)
1,000 pg/mL	4,162.3	336.9	8.1

TABLE 3 Stability of the paper-based ECL-LFI test.

Concentration	M Of each batch	M	Sd	RSD (%)
1,000 pg/mL	4,417.6	4,163.5	207.02	4.97
	4,162.3			
	3,910.5			

3.7 Specificity, reproducibility, and stability of the paper-based ECL-LFI test

The as-prepared ECL-LFI test was investigated to evaluate its specificity, reproducibility, and stability. Figure 7 shows the influence of external interference on ECL intensity. The average ECL intensity of Black, IFN-γ, IL-6, BSA, CEA, and AFP were 732.3, 4,396, 4,336.7, 4,322.3, 4,504.3, and 4,488, respectively (n = 3). The results indicate that BSA, CEA, AFP, and IL6 had no significant effect on the standard solution of IFN-γ, indicating that the ECL-LFI had a satisfactory specificity ($p < 0.01$).

Ten paper-based ECL-LFI tests were used to detect 1,000 pg/mL IFN-γ. RSD for IFN-γ is 8.1%, indicating an acceptable reproducibility of the paper-based ECL-LFI (Table 2). The stability of the ECL paper-based ECL-LFI test was calculated by preparing ECL-LFI tests in three batches, with 10 pieces in each batch, and testing the ECL intensity: RSD for ECL IFN-γ is 4.97% (Table 3), in compliance with the Guidelines of the (NCCLS). These results demonstrate that the paper-based ECL-LFI test exhibited satisfactory specificity, reproducibility, and stability.

4 Conclusion

The paper-based ECL-LFI test we developed enabled us to use a linear channel for electrochemical detection of IFN-γ in human serum, for the first time. This development enables us to add samples at one time and

detect IFN-γ concentration in human serum without other operations. The proposed paper-based ECL-LFI test provides highly sensitive ECL signals. Moreover, the commercial ELISA test results demonstrate that the paper-based ECL-LFI test is highly reliable. Therefore, the paper-based ECL-LFI provides an effective approach for detection of IFN-γ in human serum and has potential application in facilitating accurate and reliable clinical diagnosis of TB. In addition, the successful preparation of the proposed ECL-LFI test can be applied to the detection of other diseases and lays a foundation for the preparation of multiple ECL paper-based ECL-LFI tests with multiple channels and multiple detection projects in the future.

Data availability statement

The raw data supporting the conclusions of this article will be made available by the authors, without undue reservation.

Author contributions

SY and YC: Methodology, Validation. Writing original draft. GX: Investigation, Data curation. XY: Writing review and editing. HZ: Conceptualization, Methodology, Supervision.

Funding

This research was supported by Special Projects in Key pads of Guangdong Province (No. 2022B1111020006).

Conflict of interest

Authors GX and XY were employed by Guangzhou Leide Biotechnology Co, Ltd.

The remaining authors declare that the research was conducted in the absence of any commercial or financial relationships that could be construed as a potential conflict of interest.

Publisher's note

All claims expressed in this article are solely those of the authors and do not necessarily represent those of their affiliated organizations, or those of the publisher, the editors and the reviewers. Any product that may be evaluated in this article, or claim that may be made by its manufacturer, is not guaranteed or endorsed by the publisher.

References

Ahmadi, A., Khoshfetrat, S. M., Kabiri, S., Dorraji, P. S., Larijani, B., and Omidfar, K. (2021). Electrochemiluminescence paper-based screen-printed electrode for HbA1c detection using two-dimensional zirconium metal-organic framework/Fe_3O_4 nanosheet composites decorated with Au nanoclusters. *Microchim. Acta* 188 (9), 296–311. doi:10.1007/s00604-021-04959-y

Bauer, M., Wunderlich, L., Weinzierl, F., Lei, Y., Duerkop, A., Alshareef, H. N., et al. (2021). Electrochemical multi-analyte point-of-care perspiration sensors using on-chip three-dimensional graphene electrodes. *Anal. Bioanal. Chem.* 413 (3), 763–777. doi:10.1007/s00216-020-02939-4

Bergamaschi, C., Terpos, E., Rosati, M., Angel, M., Bear, J., Stellas, D., et al. (2021). Systemic IL-15, IFN-γ, and IP-10/CXCL10 signature associated with effective immune response to SARS-CoV-2 in BNT162b2 mRNA vaccine recipients. *Cell Rep.* 36 (6), 109504. doi:10.1016/j.celrep.2021.109504

Broger, T., Tsionksy, M., Mathew, A., Lowary, T. L., Pinter, A., Plisova, T., et al. (2019). Sensitive electrochemiluminescence (ecl) immunoassays for detecting lipoarabinomannan (lam) and esat-6 in urine and serum from tuberculosis patients. *Plos One* 14 (4), e0215443. doi:10.1371/journal.pone.0215443

Caputa, G., Matsushita, M., Sanin, D. E., Kabat, A. M., Edwards-Hicks, J., Grzes, K. M., et al. (2022). Intracellular infection and immune system cues rewire adipocytes to acquire immune function. *Cell Metab.* 34 (5), 747–760.e6. doi:10.1016/j.cmet.2022.04.008

Hamada, Y., Cirillo, D. M., Matteelli, A., Penn-Nicholson, A., Rangaka, M. X., and Ruhwald, M. (2021). Tests for tuberculosis infection: Landscape analysis. *Eur. Resp. J.* 58 (5), 2100167. doi:10.1183/13993003.00167-2021

Hawerkamp, H. C., van Geelen, L., Korte, J., Di Domizio, J., Swidergall, M., Momin, A. A., et al. (2020). Interleukin-26 activates macrophages and facilitates killing of *Mycobacterium tuberculosis*. *Sci. Rep.* 10 (1), 17178. doi:10.1038/s41598-020-73989-y

Hlaca, N., Zagar, T., Kastelan, M., Brajac, I., and Prpic-Massari, L. (2022). Current concepts of vitiligo immunopathogenesis. *Biomedicines* 10 (7), 1639. doi:10.3390/biomedicines10071639

Li, F., You, M., Li, S., Hu, J., Liu, C., Gong, Y., et al. (2020). Paper-based point-of-care immunoassays: Recent advances and emerging trends. *Biotechnol. Adv.* 39, 107442. doi:10.1016/j.biotechadv.2019.107442

Mungmunpuntipatip, R., and Wiwnaitkit, V. (2020). IGRA-ELISA for tuberculosis diagnosis. *Clin. Lab. Heidelb.* 66 (4). doi:10.7754/clin.lab.2019.190830

Petermann, F., Pekowska, A., Johnson, C. A., Jankovic, D., Shih, H. Y., Jiang, K., et al. (2019). The magnitude of IFN-γ responses is fine-tuned by DNA architecture and the non-coding transcript of Ifng-as1. *Mol. Cell* 75 (6), 1229–1242. doi:10.1016/j.molcel.2019.06.025

Petnak, T., Eksombatchai, D., Chesdachai, S., Lertjitbanjong, P., Taweesedt, P., Pornchai, A., et al. (2022). Diagnostic accuracy of interferon-gamma release assays for diagnosis of smear-negative pulmonary tuberculosis: A systematic review and meta-analysis. *BMC Pulm. Med.* 22 (1), 219–9. doi:10.1186/s12890-022-02013-y

Rizzo, F., Polo, F., Sojic, N., and Xu, G. (2021). Editorial: Electrochemiluminescence: From fundamentals to applications. *Front. Chem.* 9, 706465. doi:10.3389/fchem.2021.706465

Satlin, M. J., Lewis, J. S., Weinstein, M. P., Patel, J., Humphries, R. M., Kahlmeter, G., et al. (2020). Clinical and laboratory standards institute and European committee on antimicrobial susceptibility testing position statements on polymyxin b and colistin clinical breakpoints. *Clin. Infect. Dis.* 71 (9), e523–e529. doi:10.1093/cid/ciaa121

Sennikov, S. V., Krysov, S. V., Injelevskaya, T. V., Silkov, A. N., Grishina, L. V., and Kozlov, V. A. (2003). Quantitative analysis of human immunoregulatory cytokines by electrochemiluminescence method. *J. Immunol. Methods* 275 (1-2), 81–88. doi:10.1016/s0022-1759(03)00007-3

Sigal, G. B., Pinter, A., Lowary, T. L., Kawasaki, M., Li, A., Mathew, A., et al. (2018). A novel sensitive immunoassay targeting the 5-methylthio-d-xylofuranose-lipoarabinomannan epitope meets the who's performance target for tuberculosis diagnosis. *J. Clin. Microbiol.* 56 (12), 013388–e1418. doi:10.1128/JCM.01338-18

Sloot, R., Shanaube, K., Claassens, M., Telisinghe, L., Schaap, A., Godfrey-Faussett, P., et al. (2020). Interpretation of serial interferon-gamma test results to measure new tuberculosis infection among household contacts in Zambia and South Africa. *BMC Infect. Dis.* 20 (1), 760–819. doi:10.1186/s12879-020-05483-9

Thibaut, R., Bost, P., Milo, I., Cazaux, M., Lemaitre, F., Garcia, Z., et al. (2020). Bystander IFN-γ activity promotes widespread and sustained cytokine signaling altering the tumor microenvironment. *Nat. Cancer* 1 (3), 302–314. doi:10.1038/s43018-020-0038-2

Zhang, S., and Liu, Y. (2020). Recent progress of novel electrochemiluminescence nanoprobes and their analytical applications. *Front. Chem.* 8, 626243. doi:10.3389/fchem.2020.626243

Zhou, B., Zhu, M., Hao, Y., and Yang, P. (2017). Potential-resolved electrochemiluminescence for simultaneous determination of triple latent tuberculosis infection markers. *Acs Appl. Mat. Interfaces* 9 (36), 30536–30542. doi:10.1021/acsami.7b10343

Zhou, B., Zhu, M., Qiu, Y., and Yang, P. (2017). Novel electrochemiluminescence-sensing platform for the precise analysis of multiple latent tuberculosis infection markers. *Acs Appl. Mat. Interfaces* 9 (22), 18493–18500. doi:10.1021/acsami.7b03211

Zhou, X., Zhu, D., Liao, Y., Liu, W., Liu, H., Ma, Z., et al. (2014). Synthesis, labeling and bioanalytical applications of a tris(2,2'-bipyridyl)ruthenium(II)-based electrochemiluminescence probe. *Nat. Protoc.* 9 (5), 1146–1159. doi:10.1038/nprot.2014.060

frontiers | Frontiers in Bioengineering and Biotechnology

TYPE Original Research
PUBLISHED 08 February 2023
DOI 10.3389/fbioe.2023.1144463

OPEN ACCESS

EDITED BY
Yanqi Wu,
Jamhuriya University of Science and Technology, Somalia

REVIEWED BY
Hui Chen,
Hunan University of Technology, China
Zhu Chen,
Hunan University of Technology, China
Zhishan Yuan,
Guangdong University of Technology, China

*CORRESPONDENCE
Huan Yang,
yanghuang2015@tmu.edu.cn
Li Wang,
jsxzwdl@163.com

†These authors have contributed equally to this work

SPECIALTY SECTION
This article was submitted to Biosensors and Biomolecular Electronics, a section of the journal Frontiers in Bioengineering and Biotechnology

RECEIVED 14 January 2023
ACCEPTED 30 January 2023
PUBLISHED 08 February 2023

CITATION
Chen Y, Sha L, Li W, Zhou L, Pei B, Bian X, Ji Y, Liu Y, Wang L and Yang H (2023), Rapid quantitative detection of *Klebsiella pneumoniae* in infants with severe infection disease by point-of-care immunochromatographic technique based on nanofluorescent microspheres. *Front. Bioeng. Biotechnol.* 11:1144463. doi: 10.3389/fbioe.2023.1144463

Rapid quantitative detection of *Klebsiella pneumoniae* in infants with severe infection disease by point-of-care immunochromatographic technique based on nanofluorescent microspheres

Ying Chen[1†], Lulu Sha[1†], Wenqing Li[1], Liuyan Zhou[1], Bing Pei[2], Xinyu Bian[1], Yongxin Ji[3], Yiping Liu[1], Li Wang[4*] and Huan Yang[1*]

[1]School of Medical Technology, Xuzhou Medical University, Xuzhou, China, [2]Department of Clinical Laboratory, Suqian First People's Hospital, Suqian, China, [3]Nanjing Nanoeast Biotech Co., Ltd., Nanjing, China, [4]Department of Clinical Laboratory, Xuzhou First People's Hospital, Xuzhou, China

Background: *Klebsiella pneumoniae* (KP, *K. pneumoniae*) is one of the most important nosocomial pathogens that cause severe respiratory infections. As evolutionary high-toxic strains with drug resistance genes increase year by year, the infections caused by it are often accompanied by high mortality, which may be fatal to infants and can cause invasive infections in healthy adults. At present, the traditional clinical methods for detecting *K. pneumoniae* are cumbersome and time-consuming, and the accuracy and sensitivity are not high. In this study, nanofluorescent microsphere (nFM)-based immunochromatographic test strip (ICTS) quantitative testing platform were developed for point-of-care testing (POCT) method of *K. pneumoniae*.

Methods: 19 clinical samples of infants were collected, the genus-specific gene of *mdh* was screened from *K. pneumoniae*. Polymerase chain reaction (PCR) combined with nFM-ICTS based on magnetic purification assay (PCR-ICTS) and strand exchange amplification (SEA) combined with nFM-ICTS based on magnetic purification assay (SEA-ICTS) were developed for the quantitative detection of *K. pneumoniae*. The sensitivity and specificity of SEA-ICTS and PCR-ICTS were demonstrated by the existing used classical microbiological methods, the real-time fluorescent quantitative PCR (RTFQ-PCR) and PCR assay based on agarose gel electrophoresis (PCR-GE).

Results: Under optimum working conditions, the detection limits of PCR-GE, RTFQ-PCR, PCR-ICTS and SEA-ICTS are 7.7×10^{-3}, 2.5×10^{-6}, 7.7×10^{-6}, 2.82×10^{-7} ng/μL, respectively. The SEA-ICTS and PCR-ICTS assays can quickly identify *K. pneumoniae*, and could specifically distinguish *K. pneumoniae* samples from non-*K. pneumoniae* samples. Experiments have shown a diagnostic agreement of 100% between immunochromatographic test strip methods and the traditional clinical methods on the detection of clinical samples. During the purification process, the Silicon coated magnetic nanoparticles (Si-MNPs) were used to removed false positive results effectively from the products, which showed of great screening ability. The SEA-ICTS method was developed based on PCR-ICTS, which is a more rapid (20 min), low-costed method compared with PCR-ICTS assay for the detection of *K. pneumoniae* in infants. Only need

a cheap thermostatic water bath and takes a short detection time, this new method can potentially serve as an efficient point-of-care testing method for on-site detection of pathogens and disease outbreaks without fluorescent polymerase chain reaction instruments and professional technicians operation.

KEYWORDS

PCR, immunochromatographic test strip (ICTS), POCT, strand exchange amplification (SEA), *Klebsiella pneumoniae*, rapid detection, nanofluorescent microsphere (nFM)

1 Introduction

Klebsiella pneumoniae (KP, *K. pneumoniae*) is one of the most harmful opportunistic bacteria and one of the main causes of nosocomial infections (Kong et al., 2018). It can cause bacterial pneumonia, liver abscesse (Chen et al., 2011; Nordmann and Poirel, 2014), sepsis and even other life-threatening consequences. In clinical investigations, drug-resistant *K. pneumoniae* was found to be highly contagious (Nordmann et al., 2012), especially in infants (Lee et al., 2020), because their immune system is fragile. The infections caused by *K. pneumoniae* are usually accompanied by high mortality (Arena et al., 2020), which could make severe challenges to clinical anti-infection treatment (Xu et al., 2017; Jia et al., 2022) and endanger infants' health in developing countries (Zaidi et al., 2005; Li et al., 2021). At present, traditional microbial culture and drug resistance detection technologies consume a long time and are insensitive (Khan et al., 2014). Compared with the culture method, the molecular detection method is fast, sensitive and specific (Hooi et al., 2001). Among them, polymerase chain reaction (PCR) and immunochromatography are more commonly used. Traditional PCR detection methods based on agarose gel electrophoresis (PCR-GE) and real-time fluorescence quantitative PCR (RTFQ-PCR) (Chen et al., 2011; Nordmann and Poirel, 2014) have been widely used in the detection of pathogenic microorganism. However, PCR-GE can only be used for qualitative testing, and the following nucleic acid dyes in the agarose gel electrophoresis step are also toxic. RTFQ-PCR equipment is expensive (Glupczynski et al., 2016; Glupczynski et al., 2017; Song et al., 2020), which is not conducive to widespread clinical application.

In 2000, a study have developed a method, termed loop-mediated isothermal amplification (LAMP), that amplifies DNA under isothermal conditions (Notomi et al., 2000). This method employs a DNA polymerase and a set of four specially designed primers that recognize a total of six distinct sequences on the target DNA. Recently, a study using N.BspD6I nickel enzyme further explored the possible mechanism of DNA synthesis based on Bst DNA polymerase under non-template conditions (Zyrina et al., 2007). In 2016, strand exchange amplification (SEA) based on double-stranded DNA (dsDNA) degeneration bubbles was reported (Shi et al., 2016), which is the same with LAMP assay. However, the LAMP technology generally needs multiple pairs of primers and the primer design of LAMP is difficult, while SEA only uses one pair of primers. In SEA, a pair of primers (as shown in Figure 1) has been used to amplify DNA efficiently and steadily at a single temperature. As shown in the figure, a double-stranded DNA (dsDNA) exchanges one of its strands by a homologous single-stranded DNA (ssDNA) to form a heteroduplex product after completing the first primer expansion. DNA base have been added randomly by Bst DNA polymerase to the 3′ suspension due to its inherent nucleotide transferase activity. In the following rounds, more and more shift DNA strands with random 3′ suspension bases accumulate rapidly by the action of primers and Bst DNA polymerase. A new double strand can be formed if the newly synthesized strand has a 3′ drape DNA base, which complements the 3′ drape base of the previous replacement strand.

Immunochromatography test paper technology was first introduced in the 1980s. The design of immunochromatographic test strip (ICTS) can be currently used for pathogens' nucleic acid detection, and is called "nucleic acid lateral flow immunoassay" (NALFIA) (Duong and Rhee, 2007; Chen et al., 2008; Chen et al., 2019; Zhuang et al., 2019; Chen et al., 2022). Immunochromatography test strip technology is currently widely used in fields requiring rapid antigen testing, especially in clinical medicine (Lin et al., 2022), agriculture (Dong et al., 2022; Lu et al., 2022), drug abuse (Suryoprabowo et al., 2021), food (Wang et al., 2022; Xing et al., 2022) and environmental semi-antigen pollutants (Ren et al., 2021), and microbial pollutants (Gao et al., 2021). In recent years, scientists have been working to develop ICTS methods for pathogen detection (Li et al., 2020a), but its low sensitivity has made it a bottleneck worldwide. With the advancement of nanotechnology, functional magnetic nanomaterials are gradually applied to biological detection due to their large specific surface area, superparamagnetism, and controllable size (Duong and Rhee, 2007; Chen et al., 2019). The magnetic beads enable the isolation or extraction of target molecule or substance due to the good biocompatibility and adequate functional groups for chemical

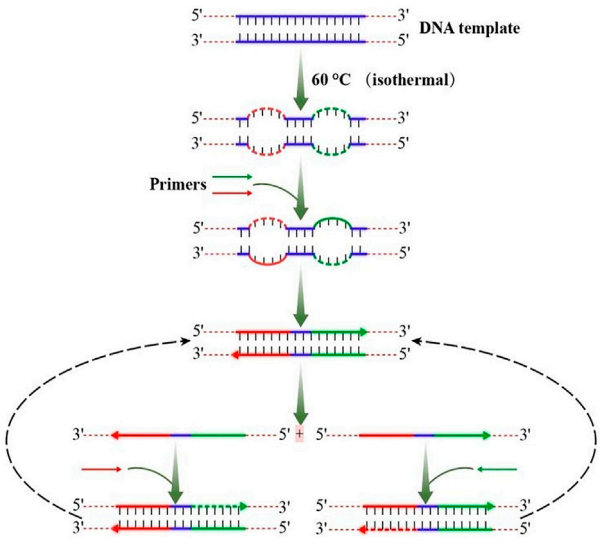

FIGURE 1
Schematic diagram of SEA.

TABLE 1 Bacterial strains of infants used for SEA-ICTS and PCR-ICTS in this study.

No.	Sample	Age (months)	Sex	Disease	Species/strain
1	A12	1–5	F	Ventricular septal defect	*K. pneumoniae*
2	A17	1–5	M	Bronchopneumonia	*K. pneumoniae*
3	A18	1–5	M	Severe pneumonia	*K. pneumoniae*
4	A21	1–5	M	Septicopyemia	*K. pneumoniae*
5	A23	1–5	M	Bronchopneumonia	*K. pneumoniae*
6	A24	1–10 days	M	Neonatalpneumonia	*K. pneumoniae*
7	A28	1–5	M	Necrotizing enteritis	*K. pneumoniae*
8	A33	1–5	M	Bronchopneumonia	*K. pneumoniae*
9	A35	1–5	M	Neonatalpneumonia	*K. pneumoniae*
10	A37	1–10 days	M	Neonatalpneumonia	*K. pneumoniae*
11	A39	1–5	M	Bronchopneumonia	*K. pneumoniae*
12	A49	20–25 days	F	Sepsis	*K. pneumoniae*
13	A57	1–5	M	Bronchopneumonia	*K. pneumoniae*
14	A58	1–5	M	Pneumonia; sepsis	*K. pneumoniae*
15	A61	1–5	M	Bronchitis	*K. pneumoniae*
16	A62	1–5	M	Septicopyemia; severe pneumonia	*K. pneumoniae*
17	A65	1–5	M	Bronchopneumonia	*K. pneumoniae*
18	A66	1–5	M	Bronchitis; sepsis	*K. pneumoniae*
19	A127	6–10	M	Bronchopneumonia	*K. pneumoniae*

fixation which have been applied to immunoassay. Silicon coated magnetic nanoparticles (Si-MNPs) we made can be used for specific bioaffinity capture of molecules. Moreover, nanofluorescent microsphere (nFM) have good thermal stability, dispersibility, biocompatibility, high fluorescence stability, surface modification, narrow particle size and high luminous efficiency, and nFM are rarely employed for the immunochromatography methods (Zhang et al., 2015; Chen et al., 2019; Zhuang et al., 2019; Chen et al., 2022; Chen et al., 2023).

In order to enable detection *in situ* or without expensive instrument conditions, we developed and validated a novel, rapid and sensitive immunoassay combined with strand exchange amplification (SEA) for isothermal and quantitative detection of *K. pneumoniae* in infants with severe infection disease by a point-of-care immunochromatographic technique based on nanofluorescent microspheres (SEA-ICTS) in this study. With the use of functional nanoparticles as signal amplifiers greatly increases the sensitivity of ICTS for fluorescence sensing, the entire process can be completed in 30 min and the results can be quantified by ICTS sensor reader without false positives or negatives.

The genus-specific gene of *mdh* (Sun et al., 2008; Thong et al., 2011) was screened from *K. pneumoniae* to investigate the application potential of new immune chromatography technology in early clinical detection as well as to compare the existing used classical microbiological methods, PCR-GE and the RTFQ-PCR method. The SEA-ICTS method was optimized based on PCR-ICTS we established in this study; However, the optimized SEA-ICTS method is a more rapid, low-costed method compared with PCR-ICTS assay for the detection of *Klebsiella pneumoniae* (KP, *K. pneumoniae*) in infants and can potentially serve as an efficient point-of-care testing (POCT) method for on-site detection of pathogens and disease outbreaks.

2 Material and methods

2.1 Bacterial culture and genomic DNA extraction

The bacterial strains used in this study included 19 clinical strains of *Klebsiella pneumoniae* (KP, *K. pneumoniae*) in infants collected from Nanjing Children's Hospital (as shown in Table 1), one standard strain of *K. pneumonia* (ATCC 700603) and 14 clinical strains of non-*Klebsiella pneumoniae* (NKP) were provided from the Affiliated Hospital of Xuzhou Medical University and Xuzhou First People's Hospital. Strains identification was performed by the traditional methods of bacteria culture and Vitek 2 Compact (BioMerieux, France), and all pathogenic strain DNA specimens are kept in the −80°C refrigerator. DNA extraction of all samples was carried out by TIANamp bacterial DNA kit (TIANGEN, Beijing, China) according to the manufacturer's instructions. Ultraviolet spectrophotometer (Merinton SMA 1000, Beijing) was used to determine the ratio of A260/A280, and agarose electrophoresis was used to detect DNA integrity and evaluate DNA quality. The genome DNA (gDNA) of the above strain is stored at −80°C until it is thawed before analysis.

2.2 Reagents, chemicals and ICTS construction

All oligonucleotides, including target-specific primer sets (PCR and SEA) were synthesized by Sangon Biotech (Shanghai) Co., Ltd. (Shanghai, China). ICTS consists of six parts: sample pad, nitrocellulose membrane (NC), conjugate pad, absorption pad, polystyrene support card and detection area with test (T), and control line (C). Streptavidin-modified fluorescent microspheres were added into 1 mL of 0.01 mol/L PBS solution (pH 7.4) containing 0.9% Nacl, 1% BSA and 0.09% Proclin, then the mixture was centrifugated at 14,000 rpm for 15 min at 4°C. The supernatant was discarded and the residue was reconstituted in 1 ml of resuspension by vortex mixing and sonication. Repeat the above cleaning steps three times. Finally, 10 μL of Streptavidin-modified Fluorescent Microspheres were reconstituted in 100 μL of resuspension.

The sample pad was first treated with PBS solution (pH 7.4) containing 6% trehalose, 0.5% (v/v) Tween 20, 1% BSA, 0.5% pvpk30, 0.5% Tetronic 1,307 and 0.05% proclin300 followed by drying at 37°C for 10 h. The conjugate pad was saturated with Streptavidin-modified Fluorescent Microspheres and then dried at 37°C for 2 h. To obtain the detection area, Biotin–BSA and Anti-digoxin antibodies were diluted to the proper concentrations, filtered, and dispensed at the test line (T line) and control line (C line) respectively. The strip was assembled by laminating the sample pad, conjugate pad, NC membrane, and absorbent pad onto a backing card. The conjugate pad and the absorbent pad were separately attached to the ends of the NC membrane with overlaps of 2 mm. The sample pad was pasted onto the conjugate pad with a 2 mm overlap. The assembled backing was cut into the width of 4 mm and placed in a sealed bag with desiccant. In the end, it should be kept away from light and stored at 4°C.

2.3 Establish and optimize the nucleic acid amplification reaction conditions of SEA and PCR

2.3.1 Design of SEA and PCR primers

The genus-specific gene of *mdh* sequence of *Klebsiella pneumoniae* strain was obtained from GenBank nucleotide sequence database (http://www.ncbi.nlm.nih.gov). The specific primers for SEA (sF and sR) and PCR (F and R) were designed by NUPACK network software and Primer Premier 5.0 (Premier Biosoft International, Palo Alto, CA). Forward primer of sF and F were labeled with biotin at the 5′ end and reverse primer of sR and R were labeled with digoxigenin at the 3′ end. The primers above were synthesized by Sangon Biotech (Shanghai) Co., Ltd.

2.3.2 Establish and optimize of SEA and PCR

The SEA reaction was carried out within the final volume of 25 μL reaction system containing 7.5 μL primer, 2.5 μL DNA template, 4 μL buffer B of DNA polymerase and 11 μL buffer A of isothermal amplification buffer (Qingdao Naide Biotechnology Co., Ltd.) to form a reaction system, blow and mix well, and briefly centrifuge to remove bubbles. The product is visualized under ultraviolet light through 3% agarose gel electrophoresis. SEA's identification and experimental procedures are auxiliary information. In order to optimize the reaction conditions, the fluorescence values of *K. pneumoniae* (ATCC 700603) genomic DNA (gDNA) were measured in a constant temperature of water bath of 60°C, 61°C, 62°C, 63°C, 64°C and 65°C. Each SEA reaction contains a positive and negative control, and all SEA experiments are repeated.

The PCR reaction was performed in a final volume of 25 μL containing 12.5 μL green *Taq* mixture (Vazyme, Nanjing), 1 μL forward primer (10 μmol/L), 1 μL reverse primer (10 μmol/L), 1 μL sample DNA and sterile deionized water. The PCR reaction was carried out on a Bio-Rad PCR system under the following conditions: 95°C 5 min, 30 cycles of 95°C 30 s, 58.5°C 30 s and 72°C 30 s, finally extend for 7 min at 72°C. The products were visualized under ultraviolet light through 1.5% (w/v) agarose gel electrophoresis (PCR-GE) to minimize the possibility of non-specific amplification.

2.4 Purification SEA/PCR products

Add 5 μL SEA or PCR products and 9 μL Si-MNPs, the mixture was hatched at room temperature (RT), and slowly mix for 5 min to fully adsorb DNA fragments. The Si-MNPs-DNA complex was then fixed with magnets for 2 min and washed twice with alcohol solution (85%). Suspend Si-MNPs with 15 μL of sterile deionized water, and then remove Si-MNPs from the nucleic acid products. Then the purified SEA or PCR products can be used for ICTS detection or stored at −20°C. The whole process is shown in Figure 2.

2.5 Establish SEA-ICTS and PCR-ICTS for the detection of *Klebsiella pneumoniae*

Add the reaction mixture of 100 μL containing purified 15 μL SEA or PCR products and 85 μL PBS (pH 7.4) to the reaction tube. Then, the mixed solution were directly added into our ICTS sample pad, which was the specific positions designated as the capture test lines on the strip, and 100 μL PBS solution was used as the blank control. The fluorescence value was read by ICTS sensor reader of Nanoeasy 1700 (Nanoeast, Nanjing, China) which we made after 2 min and the relevant image was recorded by fluorescence imager. The quantification of SEA or PCR products can be completed in 3 min.

2.6 Detection of sensitivity and specificity of SEA-ICTS and PCR-ICTS

The genus-specific gene of *mdh* was used to detect the specificity of microorganisms of *K. pneumoniae,* and other pathogenic samples (as shown in Table 1) of SEA-ICTS and PCR-ICTS methods as well as to evaluate the specificity of the test paper. The SEA amplification were carried out using 28.2 to 2.82×10^{-8} ng/μL standard DNA to evaluate the detection limits of SEA-GE and SEA-ICTS (Figure 7). The PCR amplification were carried out with standard DNA of 7.7 to 7.7×10^{-7} ng/μL to evaluate the detection limits of PCR-GE and PCR-ICTS (Figure 7). Sterile deionized water is used as a negative control, and the concentration is repeated three times per concentration. The ICTS sensor reader is used for detection. In the fluorescence threshold test, the signal value is defined as 500 (detection limit). If the signal value is greater than 500, the result is positive, otherwise the signal value is less than 500, which is negative.

K. pneumoniae standard strain (ATCC 700603), 19 clinical isolates and 14 non-*Klebsiella pneumoniae* reference strains were used to evaluate the specificity of SEA-ICTS and PCR-ICTS assays (as shown in Table 1). And sterile phosphate-buffered saline (PBS buffer, pH 7.4) was used as a negative control for DNA extraction. The reaction was carried out under optimized conditions. All samples were performed in duplicate.

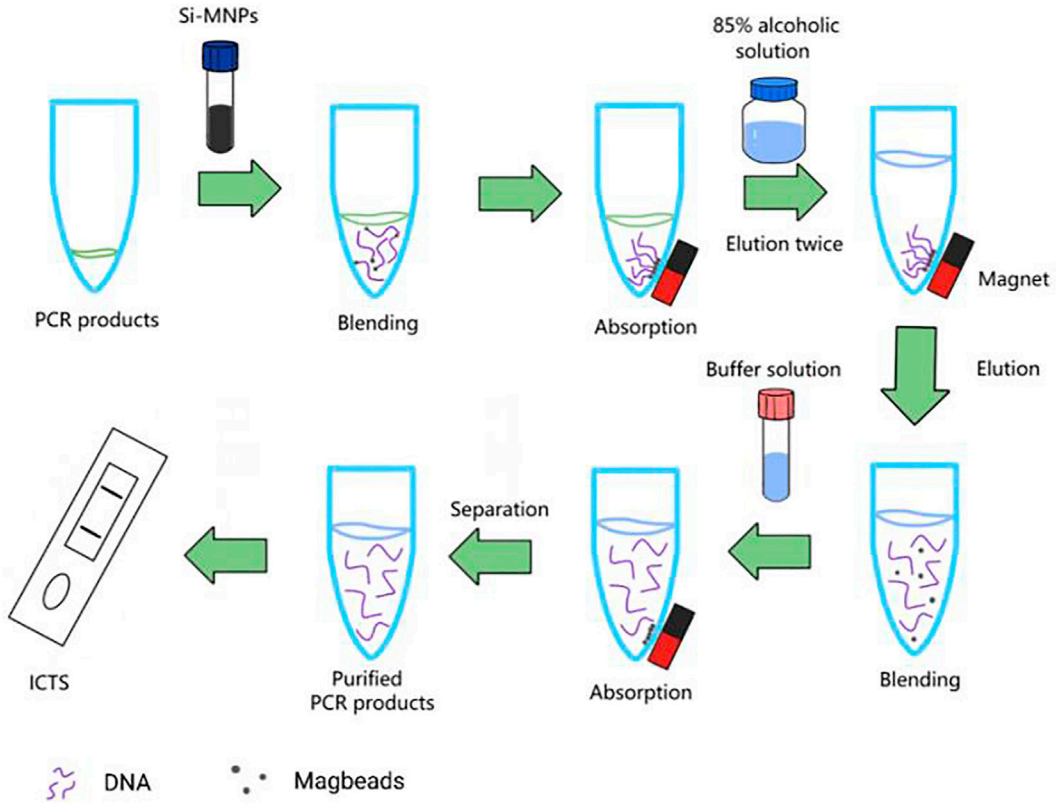

FIGURE 2
The illustration of Si-MNPs purified SEA/PCR products.

2.7 RTFQ-PCR quantitative detection

RTFQ-PCR reaction was carried out on the StepOne PULS fluorescence quantitative PCR analyzer (ABI, Foster, CA, United States) using a 2X SG Fast qPCR Master Mix (High Rox, BBI, ABI). Each 20 μL reaction mixture contains 10 μL 2X SybrGreen qPCR main mixture (High Rox, B639273, BBI, ABI), 0.4 μL primer F (10 μmol/L), 0.4 μL primer R (10 μmol/L), 2 μL DNA template and sterile deionized water with a volume of up to 20 μL. The cyclic conditions are as follows: 95°C 3 min, 45 cycles of 95°C 5 s, 60°C 30 s. The sensitivity of RTFQ-PCR (*mdh*) was evaluated using gDNA (1.74×10^7–1.74×10^3 copies/μL) of different concentrations of *K. pneumoniae* strains. All processes were repeated three times, including negative and positive control.

3 Results

3.1 The principle of ICTS quantitative testing platform based on nanofluorescent microsphere (nFM)

Genomic DNA is extracted, and then performed to nucleic acid isothermal amplification of SEA and variable temperature amplification of PCR, respectively (Figure 3). The specific primers of genus-specific gene *mdh* for SEA (sF and sR) and PCR (F and R) were labelled on 5′-end with biotin and digoxigenin, respectively. After purification of SEA or PCR products, the reaction mixture was directly loaded on the immunochromatographic test strips based on nFM. One end of the enlarged products is marked with biotin and bound to FM-labeled streptavidin, and the other end is marked with digoxin, which binds to the anti-digoxin antibody on the test line (T), redundant streptavidin-coated nFM can be combined with biotin-labeled BSA on the control line (C), thereby a portable test paper reader of fluorescence detection system can receive fluorescence signal. Using the ICTS sensor reader to detect stronger fluorescence signals, and the results can be quantified and shared in real time through the network. In the presence of the target, the positive result appeared with two data at the T and C line positions on the strip, while in the absence of the target, the negative result with a very low value (value < 500) at the T line position on the strip. Negative control using PBS instead of SEA or PCR products did not result in any value on the T lines. So the SEA-ICTS and PCR-ICTS methods can be used to rapid and specific analysis of gDNA isolated from *K. pneumoniae*. No false-positive or false-negative results were ever seen, and the results were comparable to PCR-GE and RTFQ-PCR (as shown in Table 1).

3.2 Characterization of nanofluorescent microspheres-streptavidin (nFM-SA)

The nanofluorescent microspheres-streptavidin (nFM-SA) conjugates was prepared based on coupling method and the corresponding characterization was performed. Figure 4A

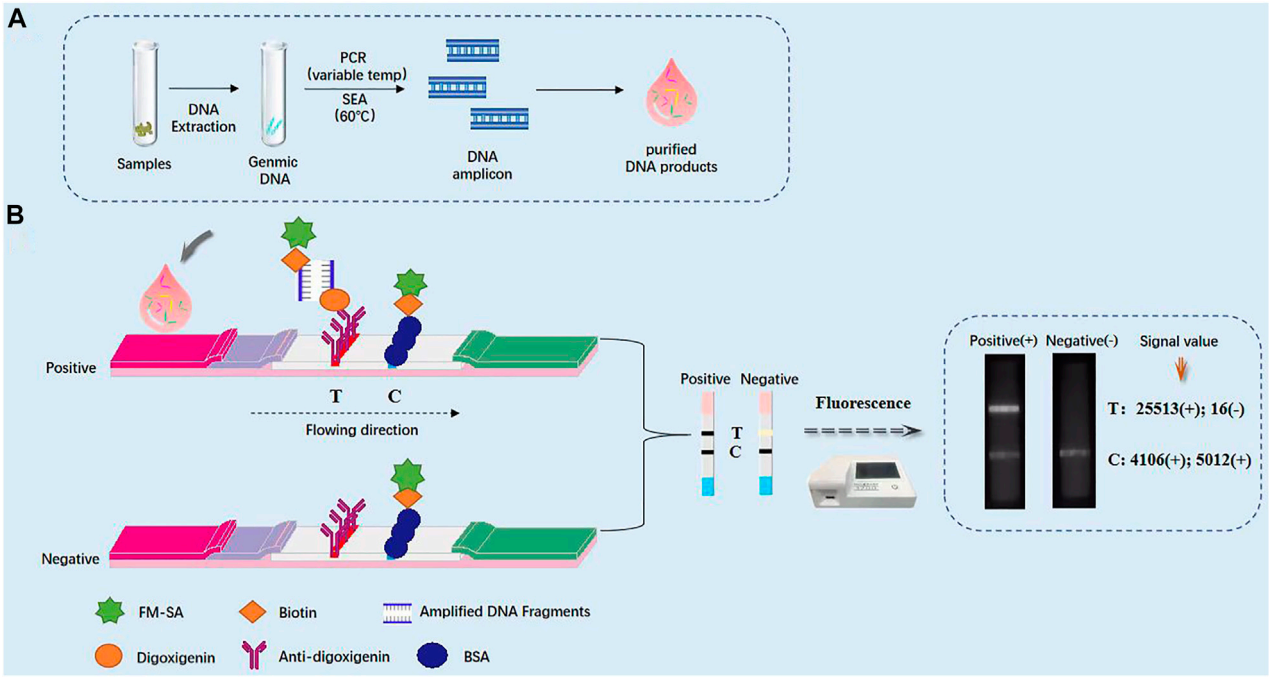

FIGURE 3
Schematic diagram of immunochromatographic test strip (ICTS). **(A)** Schematic diagram of immunochromatographic test strip for the detection of *Klebsiella pneumoniae*. **(B)** Photograph of the packaged ICTS and its internal structure, consisting of a sample pad, a conjugate pad, a detection region with test and control lines, and an absorbent pad.

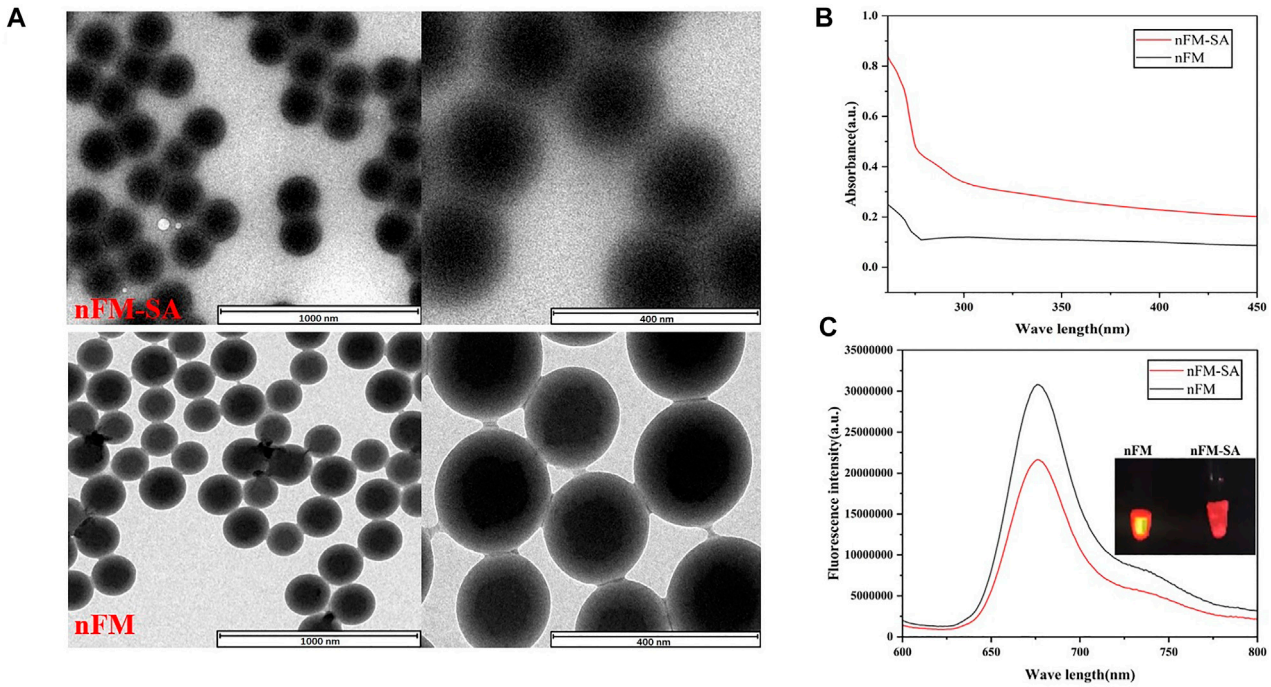

FIGURE 4
Characterization of nFM and nFM-SA conjugates. **(A)** Transmission electron microscopy (TEM) images of synthesized nFM and nFM-SA conjugates, **(B)** Ultraviolet visible (UV–vis) absorption, and **(C)** fluorescence emission spectra of free nFM and nFM-SA conjugates.

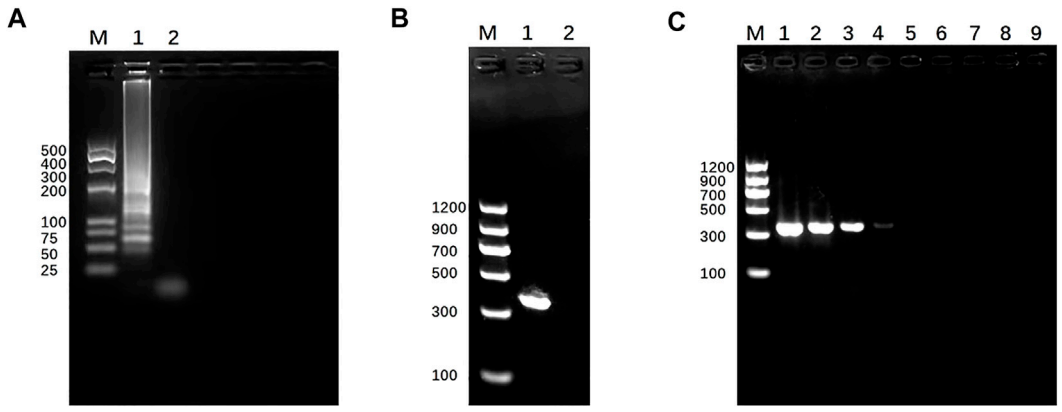

FIGURE 5
Establishment and identification of SEA and PCR. **(A)** SEA result. Lane M, DL 500 DNA marker. Lane 1, SEA product of *mdh* for *Klebsiella pneumoniae* by 3% (w/v) agarose gel electrophoresis. Lane 2, negative control. **(B)** PCR result. Lane M, DL 2000 DNA marker. Lane 1, PCR products of *mdh* for *Klebsiella pneumoniae* determined by 1.5% (w/v) agarose gel electrophoresis. Lane 2, negative control.**(C)** Detection sensitivity of PCR-GE using serially diluted *Klebsiella pneumoniae* (*mdh*); lane M, DL1200 marker; lanes 1–8, DNA concentration from 7.7 to 7.7 × 10^{-7} ng/μL. Lane 9, negative control. The size of the PCR products (*mdh*) was 364 bp.

shows that the nFM have a standard spherical structure before and after SA modification. From the transmission electron microscopy image, compared with free-nFM, the surface of the nFM-SA microspheres was covered with a membrane-like structure. Both nFM and nFM-SA have good uniformity and dispersibility and are soluble in water and other common solvents. To confirm the success of cross-linking, fluorescence spectra and ultraviolet visible (UV-Vis) absorption were used. Compared with unmodified nFM, nFM-SA has obvious a protein characteristic peak near 280 nm in UV–visible absorption spectra, indicating that SA has successfully combined with nFM (Figure 4B). As shown the fluorescence spectroscopy in Figure 4C, the maximum emission wavelength of nFM is 676 nm, and the fluorescence intensity of nFM-SA decreased compared with that of the unmodified nFM. The main reason is attributed to the fact that the organic structure of SA wrapped on the surface of the fluorescent microspheres absorbs part of the fluorescence of the nFM (Shang et al., 2021). These data indicate that the nFM-SA complex were successfully prepared and fully met the test strip requirements.

3.3 Verification of the SEA and PCR technique for nucleic acid detection

To test the feasibility of the SEA-ICTS and PCR-ICTS platform for nucleic acid detection, a genus-specific gene of *mdh* for *K. pneumoniae* was selected. The SEA and PCR products were visualized under ultraviolet light through agarose gel electrophoresis (GE), and compared to DNA Marker (TaKaRa, Dalian, China) to verify the products or the size of amplicons in order to minimize the possibility of non-specific amplification. The results showed that the PCR and SEA products were successfully amplified, while negative control did not show any amplification results (Figure 5).

3.4 The results of before and after purification of SEA/PCR products

In order to correctly detect SEA or PCR products, Si-MNPs were used as a purification and signal amplifier to remove false positive results. As shown in Table 2, the test line value in the dilution group (blank control) showed that the background signal value of the fluorescence intensity is relatively low, indicating that the test strip itself does not produce false positive. In the negative control groups, the fluorescence intensity of the pre-purification signal of the negative samples were 5,643 and 4,548, indicating that the amplification of the non-target band caused false positive results. The signal intensity after purification were reduced to 176 and 187, indicating that most non-target strips have been cleared during purification, and ICTS can be used to detect *K. pneumoniae* as an effective tool. There is no significant difference in signal values between S1, S2 and S3 positive samples before and after purification, which are similar to the results of P1, P2 and P3. These results are consistent with the results of agarose gel electrophoresis. Therefore, the ICTS strips had good repeatability and strong screening ability, which can eliminate false positive results.

3.5 Optimize the reaction conditions of SEA-ICTS

In order to optimize the reaction conditions of temperature and time, the standard strain of *K. pneumoniae* was used as a target to optimize the reaction temperature in a constant temperature of water bath of 58°C, 59°C, 60°C, 61°C and 62°C. All SEA-ICTS experiments were repeated and contain negative control. As shown in Figure 6A, the optimum reaction temperature was 60°C. Then, the fluorescence values of SEA amplicons were collected every 5 min from 0 to 60 min under 60°C as the optimize the reaction temperature. As shown in Figure 6B, when the reaction time reached 20 min, the fluorescence values

10.3389/fbioe.2023.1144463

TABLE 2 The fluorescence intensity results of before and after purification of SEA/PCR products.

Variable	SEA product (before purification)		SEA product (after purification)	
	T line	C line	T line	C line
Diluent	53	6,978		
Negative control	2,590	5,643	176	6,523
S1	47,368	5,319	50,483	6,409
S2	44,648	6,214	47,521	5,432
S3	43,211	5,980	43,790	4,320
Variable	PCR product (before purification)		PCR product (after purification)	
	T line	C line	T line	C line
Diluent	46	7,223		
Negative control	2,312	4,548	187	4,381
P1	35,604	4,727	26,936	4,709
P2	29,396	6,465	22,720	4,392
P3	36,292	5,743	29,874	4,507

S1, S2, S3 represent SEA amplified products of *mdh* gene. P1, P2, P3 represent PCR amplified products of *mdh* gene.

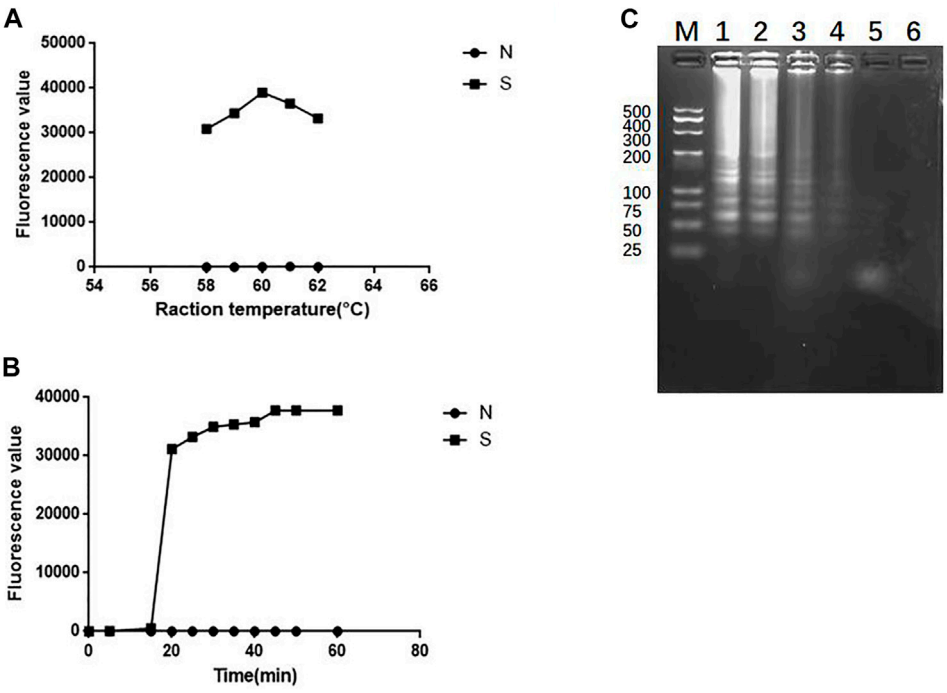

FIGURE 6
Optimize the reaction conditions of SEA. **(A)** Fluorescence values of standard strain of *Klebsiella pneumonia* at 58°C, 59°C, 60°C, 61°C and 62°C, respectively by SEA-ICTS; **(B)** Fluorescence values of parallel samples collected by SEA-ICTS every 5 min from 0 to 60 min at 60°C; **(C)** SEA product determined by 3% agarose gel electrophoresis. Lane M, DL 500 DNA marker. Lane 1, 35 min. Lane 2, 30 min. Lane 3, 25 min. Lane 4, 20 min. Lane 5, 15 min, Lane 6, negative control.

was 31,153, which was significantly different from the negative control. The SEA products were also visualized by agarose gel electrophoresis (SEA-GE), the results were consistent with SEA-ICTS (Figure 6C). Therefore, 60°C reaction for 20 min was determined as the optimal reaction conditions for SEA-ICTS assay.

3.6 Detection of sensitivity and of SEA-ICTS and PCR-ICTS

In SEA-ICTS method, the *mdh* gene was detected by using a concentration of 28.2 ng/μL and ten times continuously diluted. The

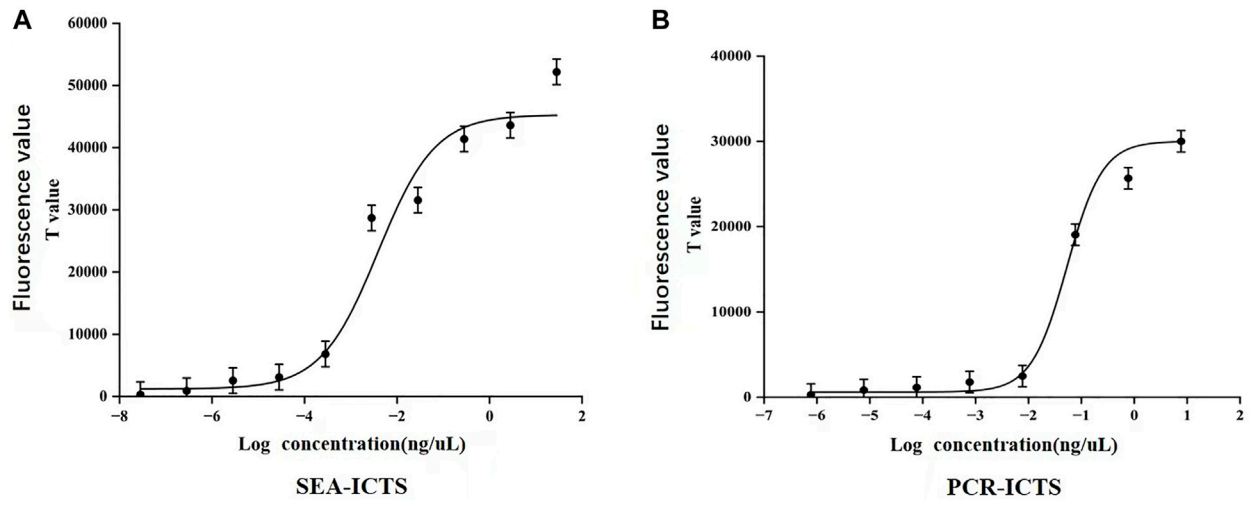

FIGURE 7
Sensitivity detection of *Klebsiella pneumoniae*. **(A,B)**, The correlation curves were established with the logarithmic value of DNA concentration as the abscissa and the signal value (T value) of ICTS as the ordinate. Each value was derived from three independent experiments, and the error bars mean standard deviations.

results determine the sensitivity of SEA-ICTS. In SEA-ICTS, the fluorescence signal values of standard DNA dilution range from 51686.88 to 310.07, and the concentration of *mdh* decreased from 28.2 to 2.82 × 10^{-8} ng/μL. The relationship between different concentrations and the test value was observed {Y = 45286.1 − 44072.9/(1 + exp[(x+2.4)/0.6])}, the correlation analysis shows that the Pearson correlation coefficient (Pearson's r) between DNA concentration and ICTS results is R^2 = 0.9396 (Figure 7A). The results showed that the sensitivity of SEA-ICTS for the detection of *mdh* was 2.82 × 10^{-7} ng/μL.

In PCR-ICTS method, the *mdh* gene was detected by using a standard strain concentration of 7.7 ng/μL and diluted ten times continuously. The results determine the sensitivity of PCR-GE and PCR-ICTS (Figure 5C, 7). In PCR-ICTS, the fluorescence signal values of standard DNA dilution range from 286.52 to 30,462. The relationship between different concentrations and the test value was observed {Y = 30008.6 − 29388/(1 + exp[(x + 1.3)/0.3])}, and *mdh* concentration decreased from 7.7 to 7 × 10^{-7}ng/μL. Correlation analysis shows that the Pearson correlation coefficient (Pearson's r) between DNA concentration and ICTS results is R^2 = 0.9411. The results show that the detection limits of the *mdh* gene used by PCR-ICTS is 7.7 × 10^{-6} ng/μL, which is 1,000 times that measured by PCR-GE of 7.7 × 10^{-3} ng/μL (Figure 5C). However, the detection limits of the *mdh* gene used by SEA-ICTS is 2.82 × 10^{-7} ng/μL, which is 10 times that measured by PCR-ICTS.

3.7 Specificity detection of clinical sample by SEA-ICTS and PCR-ICTS

To verify the specificity of new methods, *Klebsiella pneumoniae* (KP, *K. pneumoniae*) specimens from infants and 14 cases of non-*Klebsiella pneumoniae* (nKP) biopathogens were tested. The results showed that only *K. pneumoniae* strains showed characteristic amplification band, while nKP strains and negative control did not show any amplicon (Figure 8). Then, 19 cases *Klebsiella pneumoniae* (KP, *K. pneumoniae*) specimens from infants and 14 cases of non-*Klebsiella pneumoniae* (nKP) biopathogens were tested by SEA-ICTS and PCR-ICTS. The results showed that the detection of KP and nKP with ICTS technology were consistent with traditional detection methods, which showed a high degree of specificity (Table 3).

3.8 RTFQ-PCR quantitative detection

The genus-specific gene of *mdh* of *K. pneumoniae* was detected by the gold standard detection method of RTFQ-PCR. According to Figure 9A, there is a good linear relationship between the logarithm of DNA concentration and the periodic threshold (Ct) value of RTFQ-PCR. The linear equation is y = −3.211x + 38.869, and the R^2 value exceeds 0.99. The minimum detection limit for plasmids containing the target gene is 67.3 copies/uL, which is converted to a DNA concentration with the sensitivity of 2.5 × 10^{-6} ng/uL. From Figure 9B, it can be judged that the detection results of different DNA concentrations of *K. pneumoniae* are very repetitive and sensitive.

4 Discussion

In recent years, due to long-term excessive and improper clinical use of carbapenem antibiotic etc., the detection rate of *K. pneumoniae* has been increasing, especially in hospital-born infants (Yu et al., 2016) with serious infectious diseases (Lôme et al., 2018; Porreca et al., 2018; Huang et al., 2020).

In this study, 19 samples used SEA-ICTS, PCR-ICTS, qualitative testing of agarose gel electrophoresis, and traditional clinical methods as well as the molecular gold standard technology of RTFQ-PCR for the detection of the genus-specific gene of *K. pneumoniae* from infants.

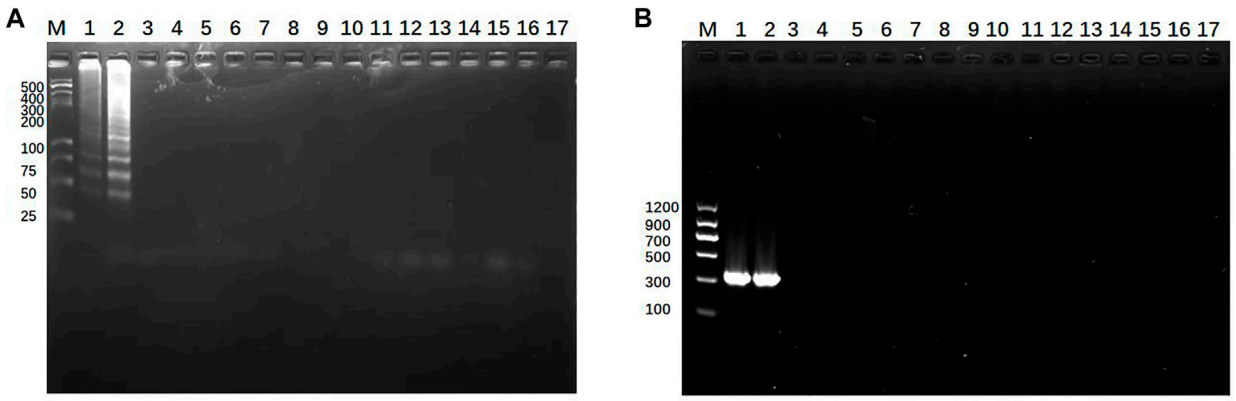

FIGURE 8
Specificity detection of *Klebsiella pneumoniae*. **(A)** Detection specificity of SEA-GE using *Klebsiella pneumoniae* (*mdh*) and non-*Klebsiella pneumoniae*: lane M, DL 500 DNA marker; lanes 1-2, *Klebsiella pneumoniae* with different DNA concentrations; lanes 3–16, non-*Klebsiella pneumoniae,* Lane 17, negative control. **(B)** Detection specificity of PCR-GE using *Klebsiella pneumoniae* and non-*Klebsiella pneumoniae*: lane M, DL 1200 DNA marker; lanes 1-2, *Klebsiella pneumoniae*; lanes 3–16, non-*Klebsiella pneumoniae*. Lane 17, negative control.

TABLE 3 Comparison of SEA-ICTS and PCR-ICTS results with PCR-GE and Vitek 2 compact results (*mdh*).

NO.	Sample type and species	NAA-ICTS		NAA-GE		Vitek 2 compact
		SEA-ICTS	PCR-ICTS	SEA-GE	PCR-GE	
1	*Klebsiella pneumoniae* (ATCC 700603)	+	+	+	+	+
2–20	*Klebsiella pneumoniae* (19 clinical isolates of infants)	+	+	+	+	+
21	*E. faecium*	–	–	–	–	–
22	*S. mitis*	–	–	–	–	–
23	*S. pneumoniae*	–	–	–	–	–
24	*S. epidermidis*	–	–	–	–	–
25	*S. aureus*	–	–	–	–	–
26	*A. baumannii*	–	–	–	–	–
27	*A. cloacae*	–	–	–	–	–
28	*E. coli*	–	–	–	–	–
29	*P. Aeruginosa*	–	–	–	–	–
30	*S.maltophilia*	–	–	–	–	–
31	*S. boydii*	–	–	–	–	–
32	*Y. enterocolitia*	–	–	–	–	–
33	*Salmonella*	–	–	–	–	–
34	*C. albicans*	–	–	–	–	–

NAA, nucleic acid amplification.

Under optimum working conditions, the detection limits of PCR-GE, RTFQ-PCR, PCR-ICTS and SEA-ICTS are 7.7×10^{-3}, 2.5×10^{-6}, 7.7×10^{-6}, 2.82×10^{-7} ng/μL, respectively. The PCR-ICTS and the SEA-ICTS assays have detected *K. pneumoniae*, and could specifically distinguish *K. pneumoniae* samples from non-*Klebsiella pneumoniae* samples. Moreover, the fluorescence intensity by ICTS was higher than electrophoretic band in agarose gel electrophoresis detection. The results showed that SEA-ICTS and PCR-ICTS detection platform in this study have high sensitivity and strong screening ability, which can eliminate false negative results.

Immune chromatography can only detect specific bacterial antibodies based on monoclonal or polyclonal (Li et al., 2020b), and most test strips are only used for qualitative experiments. In this study, streptavidin-modified nFM were used to capture

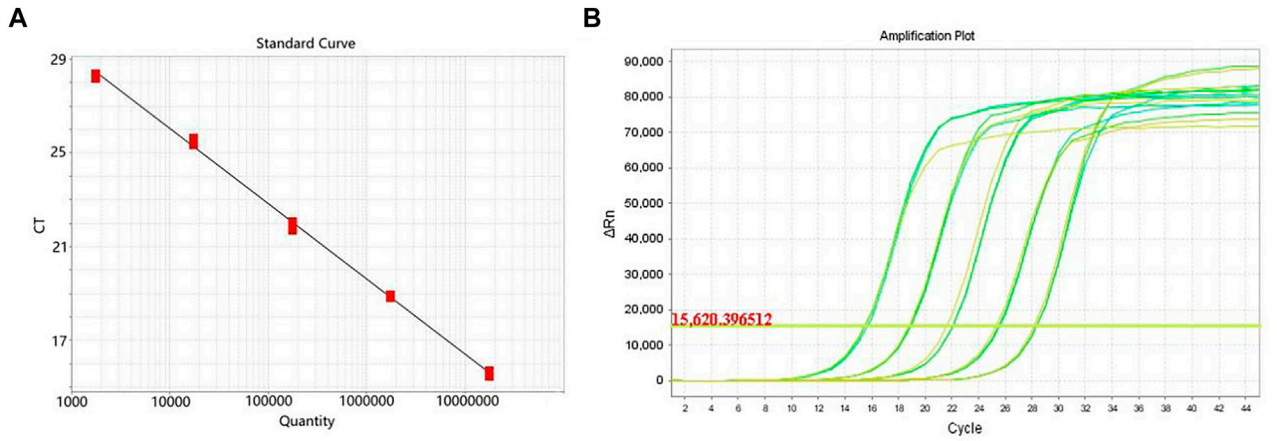

FIGURE 9
Detection sensitivity of RTFQ-PCR using standard strain of *Klebsiella pneumoniae*. **(A)** The standard curve of the RTFQ-PCR for the detection of 5 *Klebsiella pneumoniae* DNA samples from 5.8×10^{-2} to 5.8×10^{-6} ng/μL; **(B)** The amplification curves of RTFQ-PCR method of these 5 *Klebsiella pneumoniae* samples with different concentrations. Numbers 1–5 represent the different concentrations.

TABLE 4 Parameters comparison of methods used for detection of *Klebsiella pneumoniae* of infants.

Method	Sensitivity	Demands for instrumentation	Potential for specific DNA sequence	Inspection cost	Times
Traditional microbiological method	Low	Medium	No	Medium	2–3 days
PCR-GE	Medium	Medium	No	Medium	220 min (30 + 100+90)[b]
PCR-ICTS[a]	High	Medium	Yes	Low	160 min (30 + 100+30)[c]
SEA-ICTS[a]	High	Low	No	Low	80 min (30 + 20+30)[d]
RTFQ-PCR	High	High	Yes	High	160 min (30 + 130)[e]

[a]The asterik represents the research methods developed by this study.
[b]220 min include the time of DNA extraction for 30 min, PCR for 100 min, electrophoresis for 90 min.
[c]DNA extraction for 30 min, PCR for 100 min, purification and ICTS for 30 min.
[d]DNA extraction for 30 min, SEA for 20 min, purification and ICTS for 30 min.
[e]DNA extraction for 30 min, RTFQ-PCR for 130 min.

amplification products labeled with biotin. Compared with colloidal gold, nFM has higher signal values, a wider linear range, better interoperability and repeatability, and is also suitable for quantitative detection. In addition, the high degree of specific affinity and multi-stage amplification between biotin and nFM can be used to improve the sensitivity of detection lines to immune binding and trace analysis.

In recent years, new ICTS-based detection methods have emerged, which means that ICTS methods are practical in many fields. These methods reduce the detection workload and the possibility of bacterial contamination (Kuo et al., 2015; Vyas et al., 2015). The ICTS method, combined with some special equipment, can process large-volume samples in complex analytical processes. For example, Xu et al. (2013) proposed a new information and communication technology that uses multiclonal antibodies to label FMs to detect *C. jejuni*, which can only qualitatively detect *clostridium difficile*. Zhang et al. (2013) developed a plant pathogens (Cmn and Pss) detection method based on microsphere-based fluorescent immunoassay, which analysis time (1 h) was much shorter compared with ELISA (6–8 h). However, flow cytometry and more samples are required in this method. Blavikova et al. (2011) developed an ICTS detection method requiring special equipment and complex analytical processes (total analysis time is 16 h).

However, the ICTS quantitative testing platform developed in this study have advantages such as being simple to operate, low-cost, high sensitivity and specificity as well as rapid quantitative detection. It can achieve quantitative detection of target DNA sequences through low-costed and small-sized detection equipment. After purification process of magnetic beads, the false positive can also be reduced; Therefore, the ICTS quantitative testing platform are popularized and used in areas with poor clinical and medical equipment where vulnerable to *K. pneumoniae* pathogens. In contrast, traditional microbial methods usually take 2–3 days to obtain qualitative results, which is time-consuming and laborious. PCR assay based on agarose gel electrophoresis (PCR-GE)

takes a relatively long time (220 min:30 + 100 + 90), but it has low sensitivity, toxic nucleic acid dyes used, and cannot obtain quantitative results; RTFQ-PCR method has advantages of faster (160 min: 30 + 130) and high sensitivity, however, this assay requires skilled technicians and expensive nucleic acid amplification instrument, which limited the application scope of this method (Table 4).

In fact, after purification of nucleic acid amplification products (SEA or PCR products), the ICTS detection time only need 2–3 min. In this article, we choose 30 min as a comparative benchmark for the whole process including purification and ICTS. Especially, in our ICTS quantitative testing platform, the SEA-ICTS method was optimized based on PCR-ICTS we established in this study, which is a more rapid, low-costed method compared with PCR-ICTS assay for the detection of *Klebsiella pneumoniae* (KP, *K. pneumoniae*) (KP) in infants. Only needs cheap thermostatic water bath and takes a short detection time, this new method can potentially serve as an efficient POCT method for on-site detection of pathogens and disease outbreaks without fluorescent PCR instruments and professional technicians operation.

In summary, this study aims to eliminate the application of gel electrophoresis in nucleic acid amplification product analysis and replace it with a faster, quantitative and cost-effective ICTS testing platform of SEA-ICTS and PCR-ICTS. The detection sensitivity of these two methods is nearly the same with RTFQ-PCR, but the cost is lower than that of RTFQ-PCR, which is cheaper and more suitable for testing clinical samples, especially in poor working conditions in hospitals. SEA-ICTS and PCR-ICTS methods can be used as alternatives to complement each other, according to the test working conditions. Therefore, due to its high sensitivity, strong specificity, simple operation, low-costed and strong detectability, the new ICTS quantitative testing platform can be used as an ideal tool to quantitatively and accurately determine whether patients, especially infants are infected with *K. pneumoniae*.

5 Conclusion

This paper introduces an nFM-based ICTS quantitative testing platform (SEA-ICTS and PCR-ICTS) that can detect *Klebsiella pneumonia* in infants as low as 2.82×10^{-7} ng/μL of SEA-ICTS method and 7.7×10^{-6} ng/μL of PCR-ICTS method. The results have showed that the new ICTS methods were fast, non-toxic, simple and low-costed. In particular, the SEA-ICTS method does not require special and expensive equipment and complex technologies to achieve high specificity and sensitivity, facilitate the rapid detection of *K. pneumoniae*, and may become an alternative fast and easy clinical sample detection tool to RTFQ-PCR and the traditional clinical detection methods.

Data availability statement

The original contributions presented in the study are included in the article/Supplementary Material, further inquiries can be directed to the corresponding authors.

Ethics statement

Ethical review and approval was not required for the study on human participants in accordance with the local legislation and institutional requirements.

Author contributions

YC and HY: conception and design. YC and LW: administrative support; LW, BP, and YJ: provision of study materials or patients; LS, WL, and LZ: collection and assembly of data; LS, XB, and YL: data analysis and interpretation. All authors: manuscript writing and final approval of manuscript.

Funding

This work was supported by grants from “Qinglan Project” in Jiangsu Province, Xuzhou Science and Technology Planning Project (KC22115).

Conflict of interest

Author YJ was employed by Nanjing Nanoeast Biotech Co., Ltd.

The remaining authors declare that the research was conducted in the absence of any commercial or financial relationships that could be construed as a potential conflict of interest.

Publisher’s note

References

Arena, F., Di Pilato, V., Vannetti, F., Fabbri, L., Antonelli, A., Coppi, M., et al. (2020). Population structure of KPC carbapenemase-producing *Klebsiella pneumoniae* in a long-term acute-care rehabilitation facility: identification of a new lineage of clonal group 101, associated with local hyperendemicity. *Microb. Genom.* 6 (1), e000308. doi:10.1099/mgen.0.000308

Blazkova, M., Javurkova, B., Fukal, L., and Rauch, P. (2011). Immunochromatographic strip test for detection of genus Cronobacter. *Biosens. Bioelectron.* 26 (6), 2828–2834. doi:10.1016/j.bios.2010.10.001

Chen, W. J., Tsai, P. J., and Chen, Y. C. (2008). Functional nanoparticle-based proteomic strategies for characterization of pathogenic bacteria. *Anal. Chem.* 80 (24), 9612–9621. doi:10.1021/ac802042x

Chen, L., Mediavilla, J. R., Endimiani, A., Rosenthal, M. E., Zhao, Y., Bonomo, R. A., et al. (2011). Multiplex real-time PCR assay for detection and classification of *Klebsiella pneumoniae* carbapenemase gene (bla KPC) variants. *J. Clin. Microbiol.* 49 (2), 579–585. doi:10.1128/JCM.01588-10

Chen, Y., Zhang, L., Xu, L., Guo, X., Yang, H., Zhuang, L., et al. (2019). Rapid and sensitive detection of Shigella flexneri using fluorescent microspheres as label for immunochromatographic test strip. *Ann. Transl. Med.* 7 (20), 565. doi:10.21037/atm.2019.09.46

Chen, Z., Zhao, K., He, Z., Luo, X., Qin, Z., Tan, Y., et al. (2022). Development and evaluation of a thermostatic nucleic acid testing device based on magnesium pyrophosphate precipitation for detecting Enterocytozoon hepatopenaei. *Chin. Chem. Lett.* 33 (8), 4053–4056. doi:10.1016/j.cclet.2022.01.072

Chen, H., Ma, X., Zhang, X., Hu, G., Deng, Y., Li, S., et al. (2023). Novel aerosol detection platform for SARS-CoV-2: Based on specific magnetic nanoparticles adsorption sampling

and digital droplet PCR detection. *Chin. Chem. Lett.* 34 (1), 107701. doi:10.1016/j.cclet.2022.07.044

Dong, H., Xu, D., Wang, G., Meng, X., Sun, X., Yang, Q., et al. (2022). Broad-specificity time-resolved fluorescent immunochromatographic strip for simultaneous detection of various organophosphorus pesticides based on indirect probe strategy. *Anal. Methods* 14 (10), 1051–1059. doi:10.1039/D2AY00067A

Duong, H. D., and Rhee, J. I. (2007). Use of CdSe/ZnS core-shell quantum dots as energy transfer donors in sensing glucose. *Talanta* 73 (5), 899–905. doi:10.1016/j.talanta.2007.05.011

Gao, S., Wu, J., Wang, H., Hu, S., and Meng, L. (2021). Highly sensitive detection of Cronobacter sakazakii based on immunochromatography coupled with surface-enhanced Raman scattering. *J. Dairy Sci.* 104 (3), 2748–2757. doi:10.3168/jds.2020-18915

Glupczynski, Y., Evrard, S., Ote, I., Mertens, P., Huang, T. D., Leclipteux, T., et al. (2016). Evaluation of two new commercial immunochromatographic assays for the rapid detection of OXA-48 and KPC carbapenemases from cultured bacteria. *J. Antimicrob. Chemother.* 71 (5), 1217–1222. doi:10.1093/jac/dkv472

Glupczynski, Y., Jousset, A., Evrard, S., Bonnin, R. A., Huang, T.-D., Dortet, L., et al. (2017). Prospective evaluation of the OKN K-SeT assay, a new multiplex immunochromatographic test for the rapid detection of OXA-48-like, KPC and NDM carbapenemases. *J. Antimicrob. Chemother.* 72 (7), 1955–1960. doi:10.1093/jac/dkx089

Hooi, L. N., Looi, I., and Ng, A. J. (2001). A study on community acquired pneumonia in adults requiring hospital admission in Penang. *Med. J. Malays.* 56 (3), 275–284.

Huang, J., Chen, X., Zhao, Y., Shi, Y., Zhao, Z., Ding, H., et al. (2020). Outbreak of KPC-producing *Klebsiella pneumoniae* ST15 strains in a Chinese tertiary hospital: resistance and virulence analyses. *J. Med. Microbiol.* 71 (2). doi:10.1099/jmm.0.001494

Jia, X., Zhu, Y., Jia, P., Liu, X., Yu, W., Li, X., et al. (2022). Emergence of a superplasmid coharboring hypervirulence and multidrug resistance genes in *Klebsiella pneumoniae* poses new challenges to public health. *Microbiol. Spectr.* 10 (6), e0263422. doi:10.1128/spectrum.02634-22

Khan, F. Y., Abukhattab, M., AbuKamar, M., and Anand, D. (2014). Adult *Klebsiella pneumoniae* meningitis in Qatar: clinical pattern of ten cases. *Asian Pac J. Trop. Biomed.* 4 (8), 669–672. doi:10.12980/APJTB.4.201414B100

Kong, Z., Shen, J., Li, X., Kang, H., Sun, D., and Gu, B. (2018). Analysis of drug resistance genes of carbapenem-resistant *Klebsiella pneumoniae* in children. *Chin. J. Nosocomiol.* 28 (20). doi:10.11816/cn.ni.2018-182834

Kuo, Y. B., Li, Y. S., and Chan, E. C. (2015). Rapid identification of HPV 16 and 18 by multiplex nested PCR-immunochromatographic test. *J. Virol. Methods* 212, 8–11. doi:10.1016/j.jviromet.2014.10.009

Lee, J. H., Jang, Y. R., Ahn, S. J., Choi, S. J., and Kim, H. S. (2020). A retrospective study of pyogenic liver abscess caused primarily by *Klebsiella pneumoniae* vs. non-Klebsiella pneumoniae: CT and clinical differentiation. *Abdom. Radiol. (NY)* 45 (9), 2669–2679. doi:10.1007/s00261-019-02389-2

Li, G., Rong, Z., Wang, S., Zhao, H., Piao, D., Yang, X., et al. (2020). Rapid detection of brucellosis using a quantum dot-based immunochromatographic test strip. *PLoS Neglected Trop. Dis.* 14 (9), e0008557. doi:10.1371/journal.pntd.0008557

Li, C., He, X., Yang, Y., Gong, W., Huang, K., Zhang, Y., et al. (2020). Rapid and visual detection of African swine fever virus antibody by using fluorescent immunochromatography test strip. *Talanta* 219, 121284. doi:10.1016/j.talanta.2020.121284

Li, Y., Li, D., Xue, J., Ji, X., Shao, X., and Yan, J. (2021). The epidemiology, virulence and antimicrobial resistance of invasive *Klebsiella pneumoniae* at a Children's medical center in eastern China. *Infect. Drug Resist* 14, 3737–3752. doi:10.2147/IDR.S323353

Lin, L., Xu, X., Song, S., Xu, L., Zhu, Y., Kuang, H., et al. (2022). Immunological quantitative detection of dicofol in medicinal materials. *Analyst* 147 (15), 3478–3485. doi:10.1039/D2AN00462C

Lôme, V., Brunel, J. M., Pages, J. M., and Bolla, J. M. (2018). Multiparametric profiling for identification of chemosensitizers against gram-negative bacteria. *Front. Microbiol.* 9, 204. doi:10.3389/fmicb.2018.00204

Lu, Y., Shan, Y., Huang, H., Zhu, L., Li, B., Wang, S., et al. (2022). Quantum dot microsphere-based immunochromatography test strip enabled sensitive and quantitative on-site detections for multiple mycotoxins in grains. *Food Chem.* 376, 131868. doi:10.1016/j.foodchem.2021.131868

Nordmann, P., and Poirel, L. (2014). The difficult-to-control spread of carbapenemase producers among Enterobacteriaceae worldwide. *Clin. Microbiol. Infect.* 20 (9), 821–830. doi:10.1111/1469-0691.12719

Nordmann, P., Gniadkowski, M., Giske, C. G., Poirel, L., Woodford, N., and Miriagou, V. (2012). Identification and screening of carbapenemase-producing Enterobacteriaceae. *Clin. Microbiol. Infect.* 18 (5), 432–438. doi:10.1111/j.1469-0691.2012.03815.x

Notomi, T., Okayama, H., Masubuchi, H., Yonekawa, T., Watanabe, K., Amino, N., et al. (2000). Loop-mediated isothermal amplification of DNA. *Nucleic Acids Res.* 28 (12), e63. doi:10.1093/nar/28.12.e63

Porreca, A. M., Sullivan, K. V., and Gallagher, J. C. (2018). The epidemiology, evolution, and treatment of KPC-producing organisms. *Curr. Infect. Dis. Rep.* 20 (6), 13. doi:10.1007/s11908-018-0617-x

Ren, S., Li, Q., Wang, J., Fan, B., Bai, J., Peng, Y., et al. (2021). Development of a fast and ultrasensitive black phosphorus-based colorimetric/photothermal dual-readout immunochromatography for determination of norfloxacin in tap water and river water. *J. Hazard. Mater.* 402, 123781. doi:10.1016/j.jhazmat.2020.123781

Shang, Y., Cai, S., Ye, Q., Wu, Q., Shao, Y., Qu, X., et al. (2021). Quantum dot nanobeads-labelled lateral flow immunoassay strip for rapid and sensitive detection of Salmonella Typhimurium based on strand displacement loop-mediated isothermal amplification. *Engineering*. doi:10.1016/j.eng.2021.03.024

Shi, C., Shang, F., Zhou, M., Zhang, P., Wang, Y., and Ma, C. (2016). Triggered isothermal PCR by denaturation bubble-mediated strand exchange amplification. *Chem. Commun.* 52 (77), 11551–11554. doi:10.1039/c6cc05906f

Song, W., Park, M. J., Jeong, S., Shin, D. H., Kim, J. S., Kim, H. S., et al. (2020). Rapid identification of OXA-48-like, KPC, NDM, and VIM carbapenemase-producing enterobacteriaceae from culture: Evaluation of the RESIST-4 O.K.N.V. Multiplex lateral flow assay. *Ann. Lab. Med.* 40 (3), 259–263. doi:10.3343/alm.2020.40.3.259

Sun, Z., Chen, Z., Hou, X., Li, S., Zhu, H., Qian, J., et al. (2008). Locked nucleic acid pentamers as universal PCR primers for genomic DNA amplification. *PLoS ONE* 3 (11), e3701. doi:10.1371/journal.pone.0003701

Suryoprabowo, S., Liu, L., Kuang, H., Cui, G., and Xu, C. (2021). Fluorescence based immunochromatographic sensor for rapid and sensitive detection of tadalafil and comparison with a gold lateral flow immunoassay. *Food Chem.* 342, 128255. doi:10.1016/j.foodchem.2020.128255

Thong, K. L., Lai, M. Y., Teh, C. S. J., and Chua, K. H. (2011). Simultaneous detection of methicillin-resistant,*Staphylococcus aureus*, Acinetobacter baumannii,*Escherichia coli*, *Klebsiella pneumoniae* and *Pseudomonas aeruginosa* by multiplex PCR. *Trop. Biomed.* 28 (1), 21–31.

Vyas, S. S., Jadhav, S. V., Majee, S. B., Shastri, J. S., and Patravale, V. B. (2015). Development of immunochromatographic strip test using fluorescent, micellar silica nanosensors for rapid detection of B. abortus antibodies in milk samples. *Biosens. Bioelectron.* 70, 254–260. doi:10.1016/j.bios.2015.03.045

Wang, L., Sun, J., Ye, J., Wang, L., and Sun, X. (2022). One-step extraction and simultaneous quantitative fluorescence immunochromatography strip for AFB1 and Cd detection in grain. *Food Chem.* 374, 131684. doi:10.1016/j.foodchem.2021.131684

Xing, G., Sun, X., Li, N., Li, X., Wu, T., and Wang, F. (2022). New advances in lateral flow immunoassay (LFI) technology for food safety detection. *Molecules* 27 (19), 6596. doi:10.3390/molecules27196596

Xu, D., Wu, X., Li, B., Li, P., Ming, X., Chen, T., et al. (2013). Rapid detection of Campylobacter jejuni using fluorescent microspheres as label for immunochromatographic strip test. *Food Sci. Biotechnol.* 22, 585–591. doi:10.1007/s10068-013-0118-5

Xu, L., Sun, X., and Ma, X. (2017). Systematic review and meta-analysis of mortality of patients infected with carbapenem-resistant *Klebsiella pneumoniae*. *Ann. Clin. Microbiol. Antimicrob.* 16 (1), 18. doi:10.1186/s12941-017-0191-3

Yu, J., Tan, K., Rong, Z., Wang, Y., Chen, Z., Zhu, X., et al. (2016). Nosocomial outbreak of KPC-2- and NDM-1-producing *Klebsiella pneumoniae* in a neonatal ward: a retrospective study. *BMC Infect. Dis.* 16 (1), 563. doi:10.1186/s12879-016-1870-y

Zaidi, A. K., Huskins, W. C., Thaver, D., Bhutta, Z. A., Abbas, Z., and Goldmann, D. A. (2005). Hospital-acquired neonatal infections in developing countries. *Lancet* 365 (9465), 1175–1188. doi:10.1016/S0140-6736(05)71881-X

Zhang, F., Li, J., Zou, M., Chen, Y., Wang, Y., and Qi, X. (2013). Simultaneous detection of Clavibacter michiganensis subsp. nebraskensis and Pantoea stewartii subsp. stewartii based on microsphere immunoreaction. *J. Biomol. Screen.* 18 (4), 474–480. doi:10.1177/1087057112467818

Zhang, X., Wu, C., Wen, K., Jiang, H., Shen, J., Zhang, S., et al. (2015). Comparison of fluorescent microspheres and colloidal gold as labels in lateral flow immunochromatographic assays for the detection of T-2 toxin. *Molecules* 21 (1), E27. doi:10.3390/molecules21010027

Zhuang, L., Ji, Y., Tian, P., Wang, K., Kou, C., Gu, N., et al. (2019). Polymerase chain reaction combined with fluorescent lateral flow immunoassay based on magnetic purification for rapid detection of canine parvovirus 2. *BMC Vet. Res.* 15 (1), 30. doi:10.1186/s12917-019-1774-3

Zyrina, N. V., Zheleznaya, L. A., Dvoretsky, E. V., Vasiliev, V. D., Chernov, A., and Matvienko, N. I. (2007). N.BspD6I DNA nickase strongly stimulates template-independent synthesis of non-palindromic repetitive DNA by Bst DNA polymerase. *Biol. Chem.* 388 (4), 367–372. doi:10.1515/BC.2007.043

frontiers | Frontiers in Bioengineering and Biotechnology

TYPE Original Research
PUBLISHED 31 March 2023
DOI 10.3389/fbioe.2023.1066391

OPEN ACCESS

EDITED BY
Zhiyang Li,
Nanjing Drum Tower Hospital, China

REVIEWED BY
Lei Li,
St. Jude Children's Research Hospital, United States
Robert H. Austin,
Princeton University, United States

*CORRESPONDENCE
Michael A. Lynes,
Michael.Lynes@uconn.edu

SPECIALTY SECTION
This article was submitted to Biosensors and Biomolecular Electronics, a section of the journal Frontiers in Bioengineering and Biotechnology

RECEIVED 10 October 2022
ACCEPTED 21 March 2023
PUBLISHED 31 March 2023

CITATION
Maltz-Matyschsyk M, Melchiorre CK, Herbst KW, Hogan AH, Dibble K, O'Sullivan B, Graf J, Jadhav A, Lawrence DA, Lee WT, Carson KJ, Radolf JD, Salazar JC, Lynes MA and Connecticut Children's COVID Collaborative (2023), Development of a biomarker signature using grating-coupled fluorescence plasmonic microarray for diagnosis of MIS-C.
Front. Bioeng. Biotechnol. 11:1066391.
doi: 10.3389/fbioe.2023.1066391

Development of a biomarker signature using grating-coupled fluorescence plasmonic microarray for diagnosis of MIS-C

Michele Maltz-Matyschsyk[1], Clare K. Melchiorre[1], Katherine W. Herbst[2], Alexander H. Hogan[2,3], Kristina Dibble[1], Brandon O'Sullivan[1], Joerg Graf[1], Aishwarya Jadhav[4], David A. Lawrence[4,5], William T. Lee[4,5], Kyle J. Carson[4], Justin D. Radolf[3], Juan C. Salazar[2,3], Michael A. Lynes[1]* and Connecticut Children's COVID Collaborative

[1]Department of Molecular and Cell Biology, University of Connecticut, Storrs, CT, United States, [2]Connecticut Children's Medical Center, Hartford, CT, United States, [3]University of Connecticut Health Center, Farmington, CT, United States, [4]Wadsworth Center, New York State Department of Health, Albany, NY, United States, [5]University at Albany School of Public Health, Rensselaer, NY, United States

Multisystem inflammatory syndrome in children (MIS-C) is a rare but serious condition that can develop 4–6 weeks after a school age child becomes infected by SARS-CoV-2. To date, in the United States more than 8,862 cases of MIS-C have been identified and 72 deaths have occurred. This syndrome typically affects children between the ages of 5–13; 57% are Hispanic/Latino/Black/non-Hispanic, 61% of patients are males and 100% have either tested positive for SARS-CoV-2 or had direct contact with someone with COVID-19. Unfortunately, diagnosis of MIS-C is difficult, and delayed diagnosis can lead to cardiogenic shock, intensive care admission, and prolonged hospitalization. There is no validated biomarker for the rapid diagnosis of MIS-C. In this study, we used Grating-coupled Fluorescence Plasmonic (GCFP) microarray technology to develop biomarker signatures in pediatric salvia and serum samples from patients with MIS-C in the United States and Colombia. GCFP measures antibody-antigen interactions at individual regions of interest (ROIs) on a gold-coated diffraction grating sensor chip in a sandwich immunoassay to generate a fluorescent signal based on analyte presence within a sample. Using a microarray printer, we designed a first-generation biosensor chip with the capability of capturing 33 different analytes from 80 μL of sample (saliva or serum). Here, we show potential biomarker signatures in both saliva and serum samples in six patient cohorts. In saliva samples, we noted occasional analyte outliers on the chip within individual samples and were able to compare those samples to 16S RNA microbiome data. These comparisons indicate differences in relative abundance of oral pathogens within those patients. Microsphere Immunoassay (MIA) of immunoglobulin isotypes was also performed on serum samples and revealed MIS-C patients had several COVID antigen-specific immunoglobulins that were significantly higher than other cohorts, thus identifying potential new targets for the second-generation biosensor chip. MIA also identified additional biomarkers for our second-generation chip, verified biomarker signatures generated on the first-generation chip, and aided in second-generation chip optimization. Interestingly, MIS-C samples from the United States had a more diverse and

robust signature than the Colombian samples, which was also illustrated in the MIA cytokine data. These observations identify new MIS-C biomarkers and biomarker signatures for each of the cohorts. Ultimately, these tools may represent a potential diagnostic tool for use in the rapid identification of MIS-C.

KEYWORDS

COVID-19, MIS-C, diagnostic, biomarkers, microarray

Introduction

Acute pediatric SARS-CoV-2 infections, although usually mild, have hospitalized over 150,000 children since the coronavirus disease-2019 (COVID-19) pandemic began (https://covid.cdc.gov/covid-data-tracker/#new-hospital-admissions). In rare instances, two to 6 weeks after an acute infection, children can develop a severe inflammatory disorder known as multisystem inflammatory syndrome in children (MIS-C) (Guimarães et al., 2021; Radia et al., 2021). The syndrome is non-specific and is associated with, but not limited to, the following symptoms: abdominal pain, diarrhea, vomiting, rashes, red eyes, red or swollen hands/feet, red cracked lips, cough, sore throat, fever, cardiovascular dysfunction, and respiratory dysfunction (Feldstein et al., 2020; Ramaswamy et al., 2020; Guimarães et al., 2021; Radia et al., 2021; Algarni and Alghamdi. 2022). According to the CDC as of 30 January 2023 in the US there have been 9,344 MIS-C patients ("CDC COVID Data Tracker: Multisystem Inflammatory Syndrome in Children (MIS-C)" n.d.). Half of children with MIS-C are admitted to the intensive care unit (ICU) and 76 children have died from MIS-C. Unfortunately, MIS-C symptoms and the associated immune response mimics other inflammatory diseases. For example, Kawasaki disease (an acute and self-limited vasculitis of unknown etiology) shares many clinical and laboratory markers with MIS-C (e.g., fever, rash, red eyes, inflammatory markers) leading to misdiagnosis and delaying definitive management (Newburger et al., 2016; Phamduy et al., 2021).

Diagnosing MIS-C and Kawasaki (and atypical Kawasaski Disaease) often depends on blood laboratory markers; however, venipunctures can be invasive and traumatic, and it can be difficult to collect substantial blood volumes in pediatric patients (Bagnasco et al., 2012). The development of a simple and fast diagnostic tool that requires small volumes of serum or saliva to distinguish between these inflammatory diseases would help decrease diagnostic time and allow for optimized treatment options. (Li et al., 2020; Mahmoud et al., 2021). Current approaches to the analysis of biofluids using bead-based multiplex ELISA immunoassays, multi-parameter flow cytometry, reverse phase arrays, 2-D gel electrophoresis, 2-D differential in-gel electrophoresis (2-D DIGE), and antibody (Ab) microarrays can be time consuming, demanding of larger sample sizes, and labor intensive. (Amanullah et al., 2002; Noordin and Nurulhasanah, 2013). In this study, we created a novel grating-coupled fluorescent plasmonics (GCFP) microarray assay using 33 analytes to define the biosignatures of children effected by SARS-CoV-2 infection. In previous studies, GCFP has been demonstrated to be a highly sensitive tool for exploring proteomic profiles in both serum and saliva (Molony et al., 2012; Rice et al., 2012; Chou et al., 2020; Cady et al., 2021). In brief, this technology is on based surface plasmon resonance (SPR): the physical phenomenon of energy transfer at a metal-dielectric interface (Figures 1A,B) (Unfricht et al., 2005; Jin et al., 2006; Marusov et al., 2012; Molony et al., 2012; Chou et al., 2020). Under specific optical conditions, the energy of the light excites electron density oscillation (the plasmon) within the metal coating on the sensor chip, reducing the intensity of the reflected light. Using the diffraction grating on the chip, the wave vector of the illuminating beam of light can be matched with the plasmon wave vector. The gold grating plus the use of a fluorophore increases the collected light, thereby enhancing the signal (Figure 1B) (Reilly et al., 2006). Here we describe a new approach to MIS-C diagnostics that can be applied to both serum and saliva analysis. We demonstrate that the modification of a gold-coated nanoscale grating surface chip with capture antibodies targeting different analytes in a biofluid sample, combined with the use of surface plasmon resonance-enhanced fluorescence, assesses biomarkers simultaneously creating a biomarker signature (including both positive and negative detection), which can potentially distinguish MIS-C from other diseases. This assay combines the detection of several biomarkers into a biomarker signature, and we hypothesize that testing numerous biomarkers increases the likelihood of developing a robust biosignature for MIS-C. We also identify potential new markers of MIS-C and optimize sensitivity of current analytes within the microarray, which along with ongoing studies will inform the design of a second-generation chip that is more specific to MIS-C.

Materials and methods

Biological samples

Our prospective observational study included 260 subjects, birth to ≤21 years of age, enrolled 1 April 2020, through 1 May 2022, at sites in Connecticut, United States and Cali, Colombia. After obtaining IRB approval (#21-004), subjects were enrolled in two cohorts: an experimental cohort (Cohort A) and a reference cohort (Cohort B). The experimental cohort was comprised of subjects who were positive for SARS-CoV-2 infection per antigen or PCR testing and hospitalized for COVID-19 symptoms (subgroup A1); hospitalized and meeting the Center for Disease Control's criteria for MIS-C (subgroup A2); and non-hospitalized subjects testing positive for SARS-CoV-2 by antigen or PCR, (subgroup A3). The reference cohort was comprised of SARS-CoV-2 negative subjects who were: hospitalized with a diagnosis of Kawasaki disease (subgroup B1); hospitalized because of an acute viral infection (subgroup B2); or healthy controls undergoing routine ambulatory surgery (subgroup B3). To ensure correct subgroup assignment, cases were independently reviewed and adjudicated by three pediatric specialists. Demographic data, health history, current

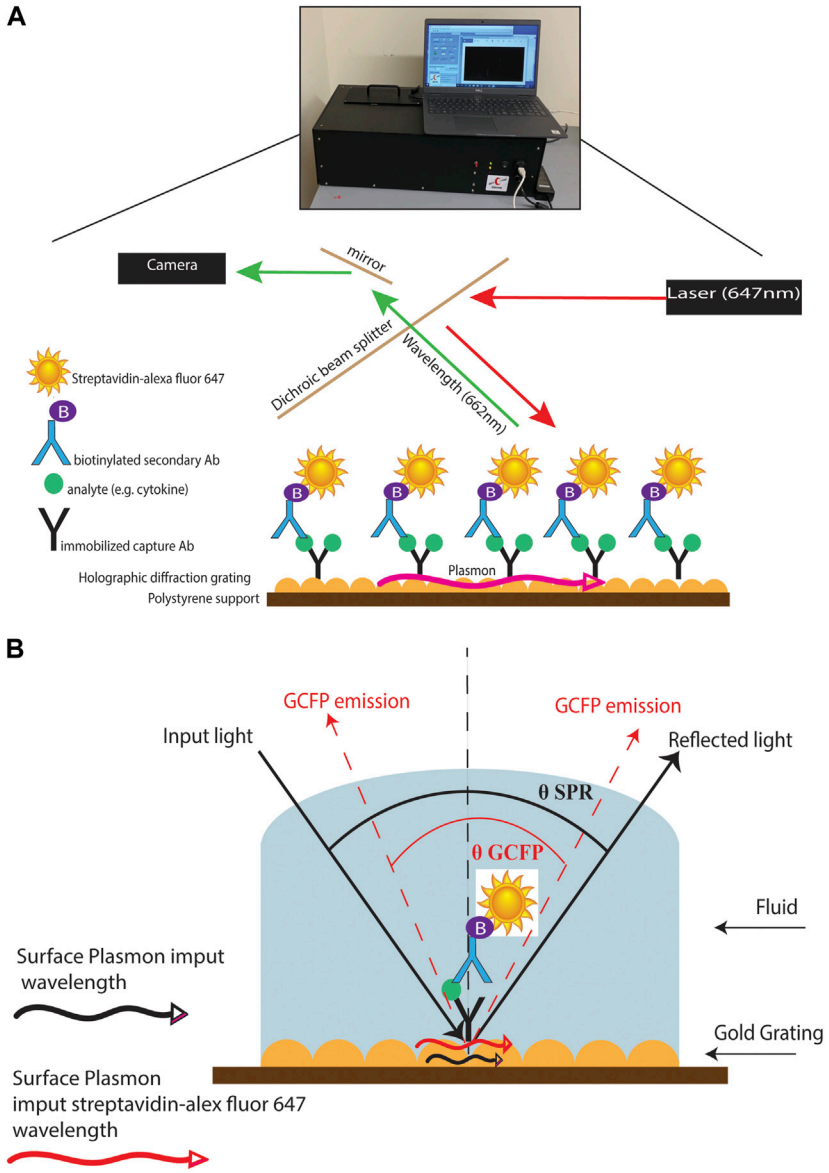

FIGURE 1
GCFP assay and wavelength pathway. **(A)** Capture antibodies are immobilized onto a gold-coated nanoscale grating surface chip by pin spotting. Chips were then fitted with plexiglass windows and gaskets to create a flow cell for fluid to pass over the surface of the printed chip. Fluid containing potential analytes can then be run over the assembled chip, followed by biotinylated secondary antibodies and then streptavidin-Alexafluor647, with washes in between steps with PSB-T. The chip can then be placed in a GCFP reader where a laser illuminates the chip and the fluorescence intensity is collected with a camera and each ROI is analyzed using Enhanced Fluorescence Reader software, V2.3. **(B)**. Under normal SPR optical conditions, the energy of the light excites electron density oscillation (the plasmon) within the metal coating on the sensor chip, reducing the intensity of the reflected light (Black lines). Using the diffraction grating on the chip, the wave vector of the illuminating beam of light can be matched with the plasmon wave vector (red lines). The gold grating plus the use of a fluorophore increases the collected light, thereby enhancing the signal (red lines).

symptoms, and in-patient treatments and diagnostic testing results were collected at baseline. Subjects will be followed for up to 4 years *via* survey for health and SARS-CoV-2 vaccine status.

Patient saliva processing

Patient saliva samples were stored at −80°C for at least 24 h prior to processing. The samples were placed in the biosafety cabinet and allowed to thaw at room temperature for approximately 20 min. Once thawed, the tubes were cleaned with alcohol wipes and centrifuged at 200 *g* for 15 min at 4°C. For samples to be analyzed with the grating-coupled fluorescent plasmonic biosensor chip, 500 µL of supernatant was aliquoted and 35 µL of protease inhibitor dissolved in 1 mL PBS was added (Pierce™ protease inhibitor tablet, Thermo Fisher Scientific, MA, USA) was added. For samples intended to be used in 16S RNA PacBio sequencing, 250 µL of supernatant was aliquoted and heat-inactivated for 30 min at 56°C. Once processed, samples were stored at −80°C until use.

TABLE 1 Regions of interest used on first generation chip.

Marker class	Analytes
Cytokines	IL-7, IL-21, IFNg, IL-15, IL-6, IL-10, IL-17, IL-2, IL-4, IL-1b, TNFa, IL-33, IL-18 (total), IL-18BPa
Chemokines	CCL20, CXCL11, CCL24, CCL2, CCL3, CCL7, CXCL10, CXCL9, CCL5, CCL17, CXCL8, CX3CL1
Interleukin receptor	sCD25
Kidney function	Cystatin C
Indicator of Inflammation	CRP
Range of biological processes	Galectin-3
Infection indicator	Procalcitonin
Type 1 membrane protein	B7-1/CD80
Protein found on antigen presenting cells	Perforin
Peptide involved in central and peripheral nervous systems	Neuropeptide Y
Serine protease that is expressed strongly in the pancreas	Marapsin/Pancreasin
Cell death	LDH(A)
Protein fragments produced when a blood clot	D-Dimer
Tissue damage	Cardiotrophin-1
Spike protein receptor	ACE-2
Heat shock protein	HSP70
Iron levels	Ferritin

Patient serum processing

Sera were isolated from patient blood samples by resting the blood for approximately 30 min after collection to allow for coagulation. The non-coagulated fraction was transferred into a 15 mL tube and centrifuged at 1000 *g* for 15 min. Supernatant was then transferred to a new tube and centrifuged at 1000 *g* for 5 min. Supernatants were aliquoted into 200 µL cryovials and stored at −80°C until transferred to participating laboratories.

Printing of grating-coupled fluorescence plasmonic (GCFP) biosensor chip

Biosensor chips were fabricated and processed as described previously with the following modifications (Molony et al., 2012; Rice et al., 2012; Chou et al., 2020; Cady et al., 2021). Capture antibodies were diluted to 250 µg/mL with PBS (Table 1) and printed on the GCFP chips using a 0.35 mm diameter microarray pin and a SpotBot II microarray printer (ArrayIt, CA, United States) or an XactII microarray printer (LabNEXT, NJ, United States). Each capture antibody was spotted to create five individual regions of interest (ROI) per analyte on each biosensor chip. During printing, microarrays were kept at a relative humidity of 70% and at ambient temperature (AT) (−25°C). After printing, chips were allowed to dry at a relative humidity of 70% and AT (−25°C) for 1 h. Chips were then transferred to a 50 mL polypropylene tube containing desiccant and stored at AT for up to 4 weeks, with no significant signal loss (data not shown).

Grating-coupled fluorescence plasmonic detection assay

Biosensor chips were processed as previously described with the following modifications (Molony et al., 2012; Rice et al., 2012; Chou et al., 2020) (Figure 1). Chips were fitted with plexiglass windows and gaskets to allow fluid to pass over the surface of the chip. The chip was then blocked with 80 µL of Superblock™ T20 (PBS) blocking buffer (Thermo Fisher Scientific, MA, United States) in a static incubation for 1 h. Each chip was then washed with PBS-T at a flow rate of 0.5 mL/min for 3 min using a peristaltic pump. PBS doped with recombinant protein (20 ng/mL) or patient samples (80 µL of serum or saliva samples diluted with PBS to 1.5 mL) were then recirculated over the chip for 90 min at 0.5 mL/min for 3 min. Each chip was then washed with PBS-T at 0.5 mL/min for 3 min. Biotinylated secondary antibody mixtures were created with all detection antibodies at a concentration of 200 ng/mL and then recirculated over the chip for 90 min. The chip was then washed with PBS-T at 0.5 mL/min for 3 min and then PBS containing 500 ng/mL of streptavidin-AlexaFluor 647 (Thermo Fisher) was recirculated over the chip for 1 h. The chip was then washed for a final time with PBS-T at 0.5 mL/min for 3 min and 70 µL of PBS was injected into the flow cell. ROIs were then identified using Ciencia software, Enhanced fluorescence Reader V2.3, and fluorescence intensity for each ROI was collected using a GCFP reader (Ciencia, Inc.). A GCFP detection ratio was used to normalize each ROI value as previously described (Cady et al., 2021)

16S-23S rRNA microbiome sequencing

DNA was extracted using the Complete Lyse & Purify kit (Shoreline Biome, Farmington, CT, United States). Saliva samples were thawed on ice, and between 50 µL and 200 µL of saliva was pelleted by centrifuged at 5,500 rpm for 10 min. Pellets were resuspended in nuclease-free water, then purified according to the manufacturer's protocol. Extracted DNA was amplified with the StrainID Amplify kit according to manufacturer protocol and as previously described (Graf et al., 2021). Briefly, 10 µL of DNA and 10 µL of PCR mix (Shoreline Biome, United States) were added to each well with barcoded primers. The PCR reaction was carried out on a thermocycler (BioRad, Hercules, CA, United States) according to manufacturer protocol. Amplicons were screened on a QIAxcel (Qiagen, Germantown, MD, United States) Advanced system using the Fast Analysis protocol. Samples were then pooled together based on band intensity. Samples were cleaned using the GeneRead Size Selection Kit (Qiagen, United States) according to manufacturer protocol and resuspended in 50 µL of elution buffer. After verifying that both pools were pure, amplicons were pooled and sequenced on a PacBio Sequel IIe. Sequences were demultiplexed with SBAnalyzer, then split into groups of approximately 35 samples. DADA2 software (https://benjjneb.github.io/dada2/) was used to call ASVs, and taxonomy was assigned using the Athena database (Graf et al., 2021; Callahan et al., 2016). Data analysis was performed in QIIME2 and R (McMurdie and Holmes, 2013; Bolyen et al., 2019). Visualizations were made with GraphPad Prism and microViz (Barnett et al., 2021). The code used is available at https://github.com/brandon-osullivan/Code-for-Maltz-Matyschsyk-et-al-2022.

Microsphere immunoassay for cytokines identification

Cytokines/Chemokine levels in the serum samples were measured in duplicate using the Luminex® 200™ instrument and Milliplex®MAP kits from EMD Millipore (Cat #HSTCMAG-28SK, HCYTA-60K, HCYP2MAG-62K and HCYP4MAG-64K) according to manufacturer's protocol. A 96 well plate provided with the kit was first washed with 200 µl per well of wash buffer. The wash buffer was then discarded, and 25 µl of serum sample was added to the plate in duplicate along with 50 µl of standards and controls as provided with each kit. Assay buffer (25 µl) was then added to the sample wells followed by 25 µl of premixed magnetic beads (provided with the kit) to each well. The plate was covered with a dark lid and placed on a plate shaker (200 rpm on a Barnstead 4625 Titer plate shaker) overnight at 4°C in a dark room. On the following day, the plate was washed 3X with 200 µl of wash buffer using BioTek ELx405™ microplate washer with magnetic capture: after washing, detection antibodies (50 µl) were added to each well and the plate was incubated for 1 h on a plate shaker covered with a foil. Streptavidin-Phycoerythrin (50 µl) was added to each well and the plate was incubated for 30 min on a plate shaker covered with foil. Finally, the plate was washed 3 × with 200 µl of wash buffer using BioTek ELx405™ microplate washer and analyzed using the Luminex® 200™ instrument (Calibrated each week with Luminex 200 Calibration and Performance Verification kits: Cat # LX2R-CAL-K25, LX2R-PVER-K25) with 150 µl of Sheath Fluid present in each well. Standard curves were generated using the Luminex xPONENT® software and the concentrations of cytokines/chemokines in the serum samples were calculated using these standard curves in pg/mL.

Microsphere immunoassay for Ig response to Sars-CoV-2 epitopes

Specimens were assessed for the presence of antibodies reactive with SARS-CoV-2 using an MIA as previously described (Yates et al., 2021). Briefly, recombinant SARS-CoV-2 N protein antigen (Native Antigen Company, United Kingdom) and the receptor binding domain (RBD) of the SAR-CoV-2 spike protein (MassBiologics, MA, USA) were covalently linked to the surface of fluorescent microspheres (Luminex Corporation, TX, USA). Additional target antigens (S1 or S2 domain (Native Antigen, United Kingdom) of SARS-CoV-2 were included in the multiplexed microsphere assay. Serum samples (25 µl) and antigen-conjugated microspheres (25 µl) were mixed and incubated before washing and further incubation with phycoerythrin-conjugated antisera. The antisera used were chosen to specifically recognize, as indicated, total antibodies (pan-Ig), or, individually IgM, IgA, IgG, IgG1, IgG2, IgG3, IgG4. After washing, the microsphere fluorescence intensity (MFI) was quantified with a FlexMap 3D Luminex analyzer (Luminex Corporation, TX, United States). Results were either direct MFI values with reactivity based upon a defined cutoff MFI, or, were normalized by comparison to the MFI of the negative controls and expressed as the ratio between the two (P/N). Positive reactivity is determined by a result that is ≥6 SD above the cutoff; results that fall between 3 SD and 6 SD are considered "Indeterminate".

Optimization of biosensor chip

We set out to optimize the initial biosensor chip configuration by comparison to an established Luminex assay. First, we performed a dose response curve examining the limit of detection for the 11 analytes that were evaluated in both the GCFP assay and the Luminex data using parameters that had been employed with the first-generation GCFP chip. Chips were spotted as described above with the capture antibodies for the following analytes: TNF-α, IL-7, IL-6, IL-4, IL-21, IL-2, IL-1β, IL-17A, IFN-δ, CCL-3, CCL20. Recombinant proteins (R&D Systems, MN, USA; Shenandoah Biotechnology, Inc, PA, United States) were then diluted to 5 ng/mL, 1 ng/mL, 200 pg/mL, and 1 pg/mL and recirculated over the chip as described above. Detection ratios were calculated, and the limit of detection was determined for each matched pair set by GCFP. We then optimized the capture and secondary antibodies to reach values detectable with the Luminex MIA assay.

Results

Identification and validation of regions of interest

Since MIS-C and COVID-19 are relativity new disease states, we set out to develop our first generation GCFP biosensor chip based on literature available early in the pandemic (Cabrero-Hernandez, 2020; Bar-Meir et al., 2021; Consiglio et al., 2020; Ramaswamy et al., 2020; Whittaker et al., 2020; Buszko et al., 2021; Filbin et al., 2021). These

10.3389/fbioe.2023.1066391

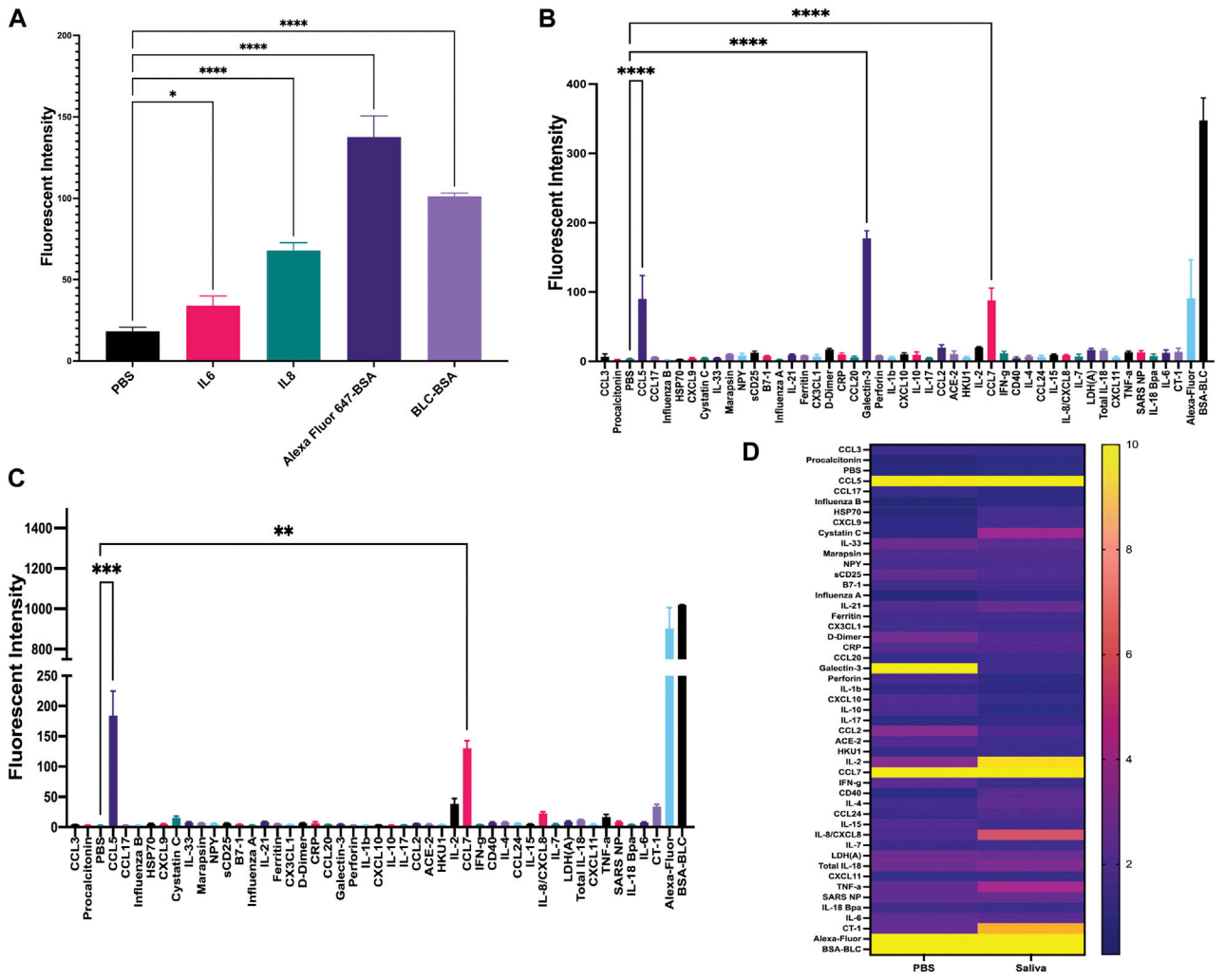

FIGURE 2
Development of sandwich-based ELISA assay on a gold-coated nanoscale grating surface chip. **(A)** Capture antibodies for IL-6 and IL-8 were immobilized onto the chip, along with the negative control (PBS) and two positive controls; biotin-BSA (BLC-BSA, to show streptavidin binding) and Alexafluor 647-BSA (to show stabilization during washing), 20 ng/mL of recombinant IL-6 and IL-8 were flowed over the chip. The fluorescence intensity was collected as previously described. Fluorescent intensity within the ROIs for IL-6, IL-8 and positive controls was significantly higher than the negative control. **(B)** Forty-two capture antibodies were immobilized onto the chip, 20 ng/mL each of recombinant CCL5, galactin-3 and CCL7 diluted in PBS was run over the chip and the fluorescence intensity was collecting for each ROI as previously described. The fluorescent intensity within the ROIs for CCL5, galactin-3 and CCL7 were significantly higher than the negative control. **(C)** Forty-two capture antibodies were immobilized onto the chip, 20 ng/mL of recombinant protein CCL5 and CCL7 diluted in human saliva was run over the chip and the fluorescence intensity was collected for each ROI as previously described. The fluorescent intensity within the ROIs for CCL5 and CCL7 were significantly higher than the negative control. **(D)** A heat map was generated using the detection ratio, which was normalized to the negative control to compare data in B and **(C)**. One-way ANOVA analysis was performed (* = $p < 0.05$, ** = $p < 0.01$, *** = $p < 0.001$, **** = $p < 0.0001$. The data are presented as the average of five ROIs for each analyte ($\pm$ standard error of the mean).

studies showed an array of cytokines, chemokines, tissue damage markers, and inflammatory indicators that differed significantly in children with MIS-C, COVID-19, and Kawasaki (Table 1). Our goals with the first-generation chip were to: 1) identify commercially available matched pair antibodies for our ROIs to differentiate MIS-C from COVID-19, Kawasaki, and healthy controls and 2) develop a GCFP assay to simultaneously evaluate if these markers could be used as a disease-specific biosignature. We validated 42 commercially available matched pair antibodies by ELISA using recombinant proteins (Supplementary Figure S1). Nine commercially available kits that did not meet our ELISA standards when performed following manufacture protocols, and were omitted from further analysis (Supplementary Figure S1).

Development of the grating-coupled fluorescence plasmonic biosensor chip assay

Once matched-pair kits were validated using ELISA, we then tested their ability to perform a sandwich-based immunoassay on the gold-coated nanoscale grating surface chip using IL-6, IL-8 and

both positive (Alexafluor-647 and biotin-BSA) and negative (PBS) controls (Figures 1, 2A). When compared to PBS (negative control), the fluorescent intensity within the ROIs for IL-6, IL-8 and positive controls was significantly higher, indicating 20 ng/mL of IL-6 and IL-8 recombinant proteins could be detected with GCFP technology. Next, we examined the specificity of the ROIs by spotting all the capture antibodies in Table 1 onto the chip and recirculating 20 ng/mL of recombinant CCL5, galactin-3 and CCL7 diluted in PBS over the biosensor chip (Figure 2B). When compared to PBS (negative control ROIs), the fluorescent intensity within the ROIs for CCL5, galactin-3 and CCL7 were significantly higher, indicating that the GCFP assay was able to capture and detect these recombinant proteins at cognate ROIs and that there was no significant cross-reactivity between these recombinant proteins and unrelated ROIs. To evaluate the use of human salvia as the sample matrix, CCL5 and CLL7 (20 ng/mL) were spiked into commercially available pooled human saliva (Innovative Research, MI, United States) (Figure 2C). Spiked samples in pooled saliva matrix produced higher values than when the same analytes were diluted in PBS owing to the presence of endogenous CCL5 and CCL7 in the saliva pool. A heat map was created using the detection ratio for each set of 5 ROIs (Figure 2D). The heat map shows the detection ratio and indicates positive detection of all recombinant proteins when normalizing to the negative control ROIs on the same chip.

Analysis of patient samples by grating-coupled fluorescence plasmonic imaging

The first-generation GCFP chip was then evaluated to identify a candidate biomarker signature of disease using data from each of our 6 cohorts. Patient saliva and serum were analyzed with the biosensor chips and the fluorescent intensities were captured using GCFP reader (Ciencia, Inc., CT, United States) (Figure 1). For each patient sample, an image was produced from the reader; Ciencia software was used to identify ROIs, and then the fluorescent intensities for each ROI were measured and the corresponding detection ratios calculated. Figure 3 shows representative saliva data generated from a randomly selected patient from cohort B2. The image generated from patient ID 210041005 shows that five capture antibodies and the two positive controls (Biotin-BSA and alexafluor-647 labeled BSA) have a positive signal (Figure 3A). Cystatin C, Marapsin, CRP, Galectin-3, and IL-8 ROIs were each significantly different from the negative control, indicating that these analytes are present at high levels in this patient's saliva (Figure 3B). The fluorescent intensities were then normalized to the negative control and a heat map was generated to visualize the biomarker signature (Figure 3C). Cystatin C, Marapsin, CRP, Galectin-3, and IL-8 all had high detection ratios. Saliva from the six cohorts (A1 = 15, A2 = 9, A3 = 6, B1 = 4, B2 = 13, B3 = 7) were similarly analyzed, and results are displayed as heatmaps (Figures 4A,B). Figure 4A shows the mean for each analyte from all the patient samples in each of the 6 cohorts. From this initial small data set we can begin to identify potential biomarkers for A2 (CXCL10), A3 (sDC25) and B1(IL-1 β and IL-2). Interestingly, when comparing individual patients from each cohort we can see variation in these biomarker signatures, suggesting variation in disease state presentation (Figure 4B). From the serum cohorts, 56 samples (A1 = 13, A2 = 12, B1 = 12, B2 = 12, B3 = 7) were analyzed with the first-generation biosensor chip configuration and heat maps were generated for each group and for each individual patient (Figure 5A) shows the mean for each analyte from all the patient samples run in each of the 5 cohorts and indicates potential biomarker signatures for each cohort. In A2 (MIS-C group) biomarker sCD25 was found to be a potential unique biomarker for this group, while IL-21 was a unique biomarker for B1 (Kawasaki). Again, variation between individuals' biomarker signatures within the different cohorts indicates heterogeneous disease presentation (Figure 5B).

Interrogation of grating-coupled fluorescence plasmonic saliva outliers using 16S-23S rRNA gene amplicon sequence analysis

We noted some analyte outliers within individual saliva samples (Figure 4B). To further analyze the saliva from these samples, we performed 16S-23S' rRNA PacBio sequencing. For this study, we singled out sequencing data for the samples that were run over the first-generation biosensor chip and compared the relative abundances of different bacterial species. To identify bacterial species that were more abundant in the samples that were analyte outliers, we applied a 99% confidence interval, and confirmed outliers with the ROUT method. These data revealed a difference in relative abundance of several bacterial species, some of which could be linked to immunocompromised status, oral hygiene or other diseases (Figure 6). For example, sample 2100410014 from cohort A3 had an inflammatory profile that more closely resembled a sample from the MIS-C or Kawasaki cohorts. This sample also had highly elevated levels of *P. endodontalis*, a known oral pathogen, with a relative abundance of 19.26% of the overall community (median = 0.0%) (Figure 6B). In sample 2100410113, another saliva sample that was an outlier in the biomarker analysis, we found that the community was composed primarily of *Streptococcus* sp. A12 (63.45%, median = 0.74%) (Figure 6C). Sample 2100430008 had high levels of *Gemella sanguinis* (17.61%, median = 0.59%) and *Streptococcus* sp. A12 (8.00%, median = 0.74%) (Figures 6C,D). Sample 2100440031 had raised levels of *Porphorymonas endodontalis* (0.64%, median = 0.0%) and *G. haemolysans* (4.65%, median = 0.84%) (Figures 6B,E). In sample 2100410044, the majority of the community was *Streptococcus salivarius* (61.67%, median = 2.05%) (Figure 6F). Sample 2100410011 had elevated levels of *Streptococcus pneumoniae* (6.77%, median = 0.0%) (Figure 6G). 2100410072 also had elevated levels of *S. pneumoniae* (2.20%, median 0.0%), as well as above average levels of *Gemella haemolysans* (7.26%, median = 0.84%) (Figures 6E,G). In sample 2100410018, we observed elevated levels of *Streptococcus* sp. ChDC B345 (28.39%, median = 1.34%) (Figure 6H). Our last GCFP analyte outlier, sample 2100410034, had elevated levels of *S. salivarius* (18.09%, median = 2.05%) and *Schaalia odontolytica* (17.07%, median = 3.36%) (Figures 6F,I).

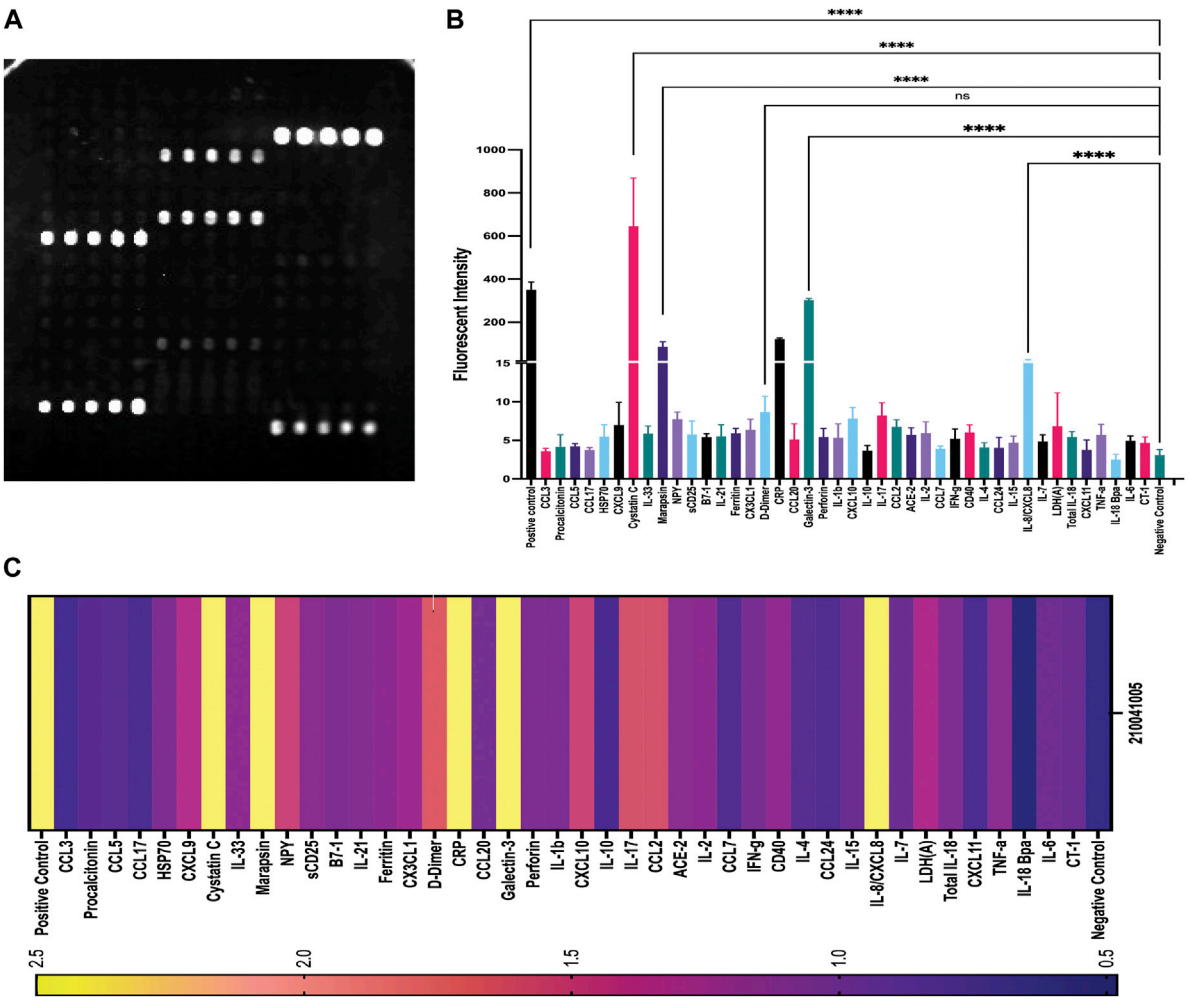

FIGURE 3
Example of patient (210041005) data generated from GCFP assay. **(A)** Forty-two unique capture antibodies were immobilized on regions of interest in sets of 5 ROIs on the chip and patient sample number 210041005 was run over the chip and an image of the GCFP sensor chip output was captured. **(B)** Fluorescent intensity within the ROIs were collected as previously described, detecting cystatin C, Marapsin, D-dimer, galaectin-3, and IL-8. **(C)** A heat map of the detection ratio was generated and shows detection of the same analytes as in **(B)**. One-way ANOVA analysis was performed (* = $p < 0.05$, ** = $p < 0.01$, *** = $p < 0.001$, **** = $p < 0.0001$. The data are presented as the average of five ROIs for each analyte (± standard error of the mean).

Refining the composition of a second-generation chip using Microsphere Immunoassay

Concurrent with these microarray studies, candidates for inclusion on a second generation GCFP sensor chip were evaluated. We examined 249 serum samples (180 from the United States and 69 from Colombia) from five different cohorts (A1, A2, B1, B2, and B3). Patient samples were analyzed for levels of 26 cytokines/chemokines using the Luminex xMAP® multiplex assay. IL-4, IL-6, IL-10, and IL-13, known to be involved in Th_2 type immune response and promoting B cell differentiation to plasma cells, were significantly elevated in the A2 (MIS-C cohort) when compared to most other cohorts (Figure 7A). Furthermore, chemokines IL-8 and CXCL11 were also found to be expressed at higher levels in the A2 cohort. By comparison, the first-generation GCFP chip detected higher IL-8 for cohorts A1, A2, B1 and IL-4 in cohorts A1 and A2 (Figure 5A), while it did not detect IL-6 for any of the cohorts. It is important to note that MIA may use different proprietary antibodies or conditions or recognize different epitopes on these targets. The results from the Luminex studies were representative of a higher sample size than the GCFP analysis, which may also contribute to differences in the results. MIA data did confirm IL-10, IL-13 and CXCL11 as possible new targets for the second-generation chip.

The antibody response to the SARS-CoV-2 nucleocapsid and spike components (full spike, RBD, S1, S2) were measured using a MIA to separately detect anti-viral IgM, IgA, and all four IgG subclasses. Figures 7B–G shows that responses in the MIS-C cohort were substantially different from standard COVID-19 infections and from healthy controls. Note that some sera in the control cohort had antibodies to either the spike proteins or nucleocapsid, indicating previously undetected SARS-CoV-2 infection or an unreported vaccination. The predominant IgG

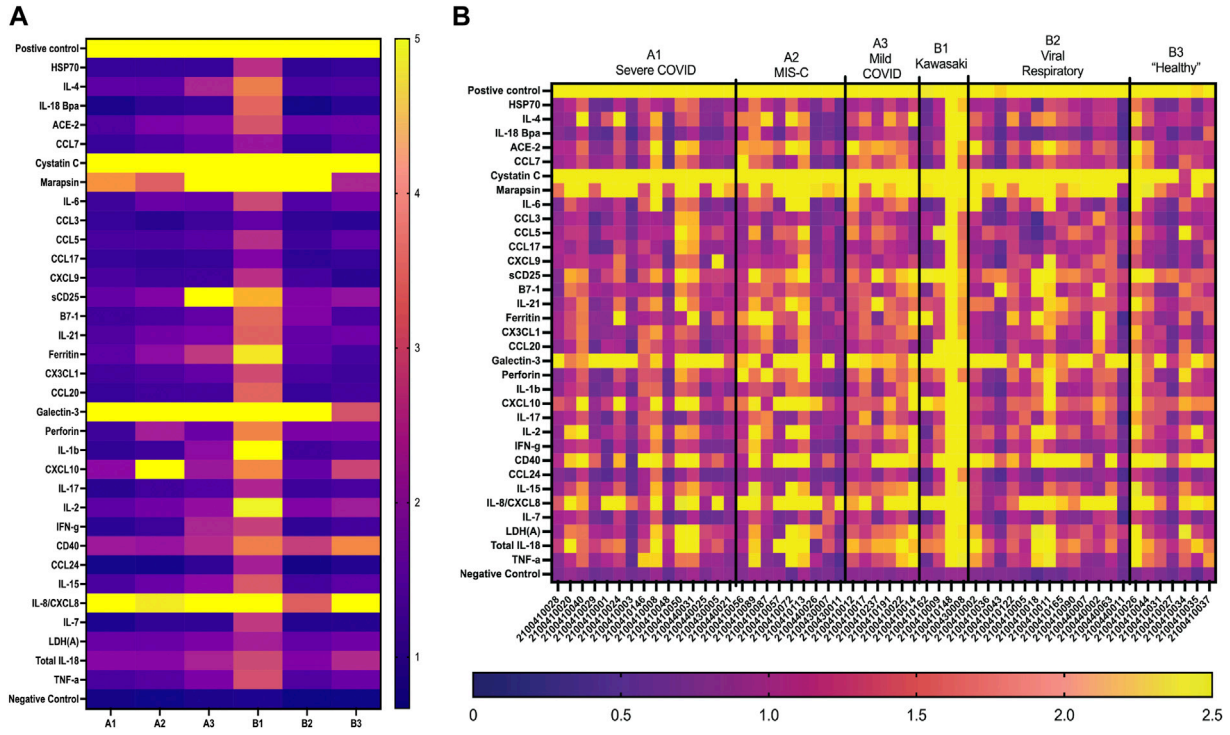

FIGURE 4
GCFP detection ratio for patient saliva samples. Saliva samples obtained from each of the patient cohorts; 54 samples (A1 = 15, A2 = 9, A3 = 6, B1 = 4, B2 = 13, B3 = 7) were run over the first-generation biosensor chip. **(A)** Heat maps generated for each cohort using the mean detection ratio for each analyte, showing candidate biomarkers for the A2 (CXCL10), A3 (sDC25) and B1(IL-1β and IL-2) cohorts. **(B)** Heat maps generated for each individual patient demonstrate individual variation in disease state.

subclasses produced in response to COVID-19 infection are IgG_1 (Yates et al., 2021; 2021); both the COVID-19 and MIS-C cohorts had prominent IgG_1 response centered around the RBD/S1 components of SARS-CoV-2 spike protein. The MIS-C cohort generally made a stronger IgG_1 response as compared to the COVID-19 cohort. Notably, the MIS-C cohort made a significantly higher IgA response to SARS-COV-2 spike domains as compared to the COVID-19 cohort (Figure 7G), indicating SARS-COV-2 spike antigen as a possible target for the second generation GCFP chip.

Comparison of grating-coupled fluorescence plasmonic biosensor chip biomarker signature to Cytokine Microsphere Immunoassay results

We compared US serum samples with Colombia serum samples using both GCFP biomarker signature data and cytokine microbead assay (Figure 8A; Table 2). In cohort A2 (MIS-C), the biomarkers detected by the GCFP chip in US serum samples produced a more complex and robust signature when compared to the Colombia serum samples (Figure 8A). We also compared US patient saliva samples with Colombia saliva samples: biomarker signatures produced by GCFP microarray had a trend similar to that observed with serum samples (Figure 8B). Correspondingly, MIA performed on serum samples showed lower levels of cytokine in Cohort A2 Colombia samples compared to US samples (Table 2). Taken together these data indicate a difference in immune response between these two populations.

To compare MIA data directly with the biomarker signature generated on the first-generation chip, 11 analytes that had been included in both assays and detection ratios were log transformed to visualize the data by cohort and as individual patients (Figure 9). The heat map reveals that most of the analytes were detected within both biomarker signatures generated from MIA and GCFP for the cohorts with the exception of IL-4, IL-6, CCL20 and IL-21. When we compare individual samples, similar signature patterns were found in the following samples for both MIA and GCFP; 2100410146, 2100410150, 2100410042, 2100410049, 2100410131, 2100410168, 2100410184, 2100440014, 2100410153, 2100410114, 2100410208, 2100440008, 21004400062, 2100410094, 2100410139, and 2100410165. When noting the quantified analyte levels (pg/mL) in the microbead assay dataset (Supplementary Table S1) it also becomes clear that some of the analytes (IL-4, IL-6 and CCL20) were not detected on the GCFP chip while others, like IL-1 β, were detected on the chip but not within the microbead assay. To address this, we performed a dose response curve on the first-generation chip for analytes that were measured both by MIA and GCFP using PBS that was doped with different amounts of recombinant proteins (10ng, 5ng, 1ng, 200pg, 1 pg/mL) (Figure 10A). These data indicate that for many of the analytes analyzed by both MIA and GCFP, the

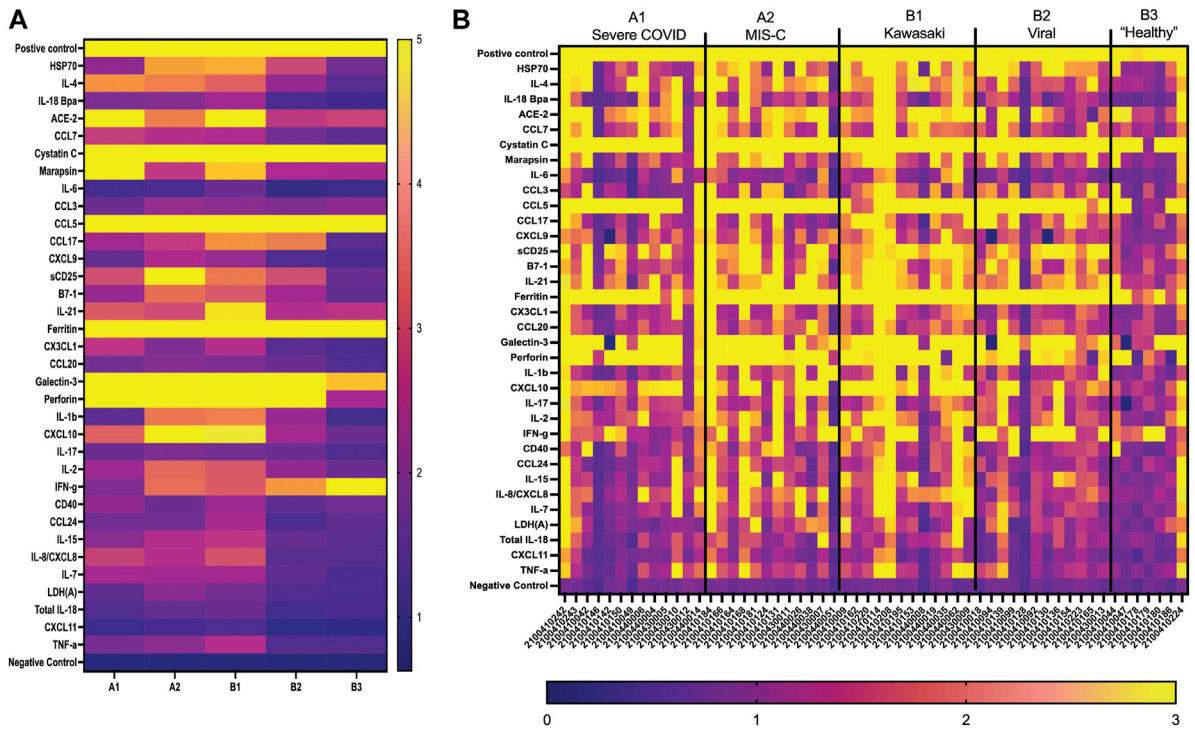

FIGURE 5
GCFP detection ratio for serum samples from patient cohorts. Serum samples from each of the cohorts were tested on the first generation GCFP biosensor chip. 56 samples (A1 = 13, A2 = 12, B1 = 12, B2 = 12, B3 = 7) were tested. **(A)** Heat maps generated for each cohort using the mean detection ratio for each analyte, showing a more robust signature per cohort then within saliva. **(B)** Heat maps generated for each patient, showing individual variation in disease state.

first-generation chip has a detection limit of 1 ng/mL while MIA could detect levels as low as 1 pg/mL, which could explain the analytes that were undetected by GCFP. We further optimized the GCFP chip to improve the assay's limit of detection (Figure 10B). We first increased the amount of secondary antibody to 10-fold the amount recommended by the manufacturers for ELISA. We did not see an improvement with this change (Figure 10B). We then increased the amount of capture antibody immobilized on the GCFP chip by twofold (500 µg/mL) and we were able to see an improvement in limit of detection for most analytes, indicating that manipulating capture reagents can further improve detection limits. Future studies for the next-generation chip will not only be focused on adding other reported analytes now known to be important for MIS-C, but also optimizing each analyte reagent set to allow for detection in the pg/mL range.

Discussion

Clinicians need a rapid, accurate test for MIS-C to guide treatment decisions. Here we show that using GCFP technology we can characterize two biomarker signatures within two different biofluids (serum and saliva), one for a group/cohort and one for an individual patient. In saliva, the GCFP biomarker analytes found in all disease state cohorts were Cystatin C, Marapsin, Galactin-3, and IL-8. When designing the chip we included Cystatin C for its potential as being predicative of renal injury and due to its observed elevated levels in COVID-19 patients (Li et al., 2020). We were able to detect Cystatin C in all our cohorts; only one patient did not produce detectable Cystatin C. The normal range of Cystatin C is 10–12 mg/mL in saliva and, 0.63–8.0 mg/mL in serum; and has been shown to be upregulated in people with poor oral hygiene (Lie et al., 2001; Dickinson, 2002; Ziegelasch et al., 2019). This suggested that Cystatin C may present at levels exceeding the upper limit of GCFP detection under the conditions tested. Marapsin/pancreasin is a trypsin-like serine protease that has been described in pancreatic tissue; little is known about its role in other systems although it can be expressed in stratified squamous epithelium tissues (esophagus, cervix and larynx) (Bhagwandin et al., 2003; Li et al., 2009). We included this analyte to potentially predict pancreatic health since reduced pancreatic function increases risk of developing severe COVID-19 (Abramczyk et al., 2022). Our biosensor chip was able to detect marapsin in all of the infected cohorts (A1-3 & B1-2), but not in the healthy cohort (B3). Interestingly, marapsin has been found to be upregulated in the epidermis of patients with psoriasis and/or regenerating wound infections, suggesting a possible role in infection (Li et al., 2009). Galectin-3 is a ß-galactoside binding lectin that can drive neutrophil chemotaxis, bind TLR4, and increase production of pro-inflammatory cytokines during viral infections (Joo et al., 2001; Filer et al., 2009; Henderson and Sethi, 2009; Burguillos et al., 2015). Increased serum levels of galectin-3 (>30 ng/mL) have been correlated with severe COVID-19 outcomes (Eduardo et al., 2022). Our biomarker signature showed galectin-3 was present in all cohorts, while lower in healthy controls,

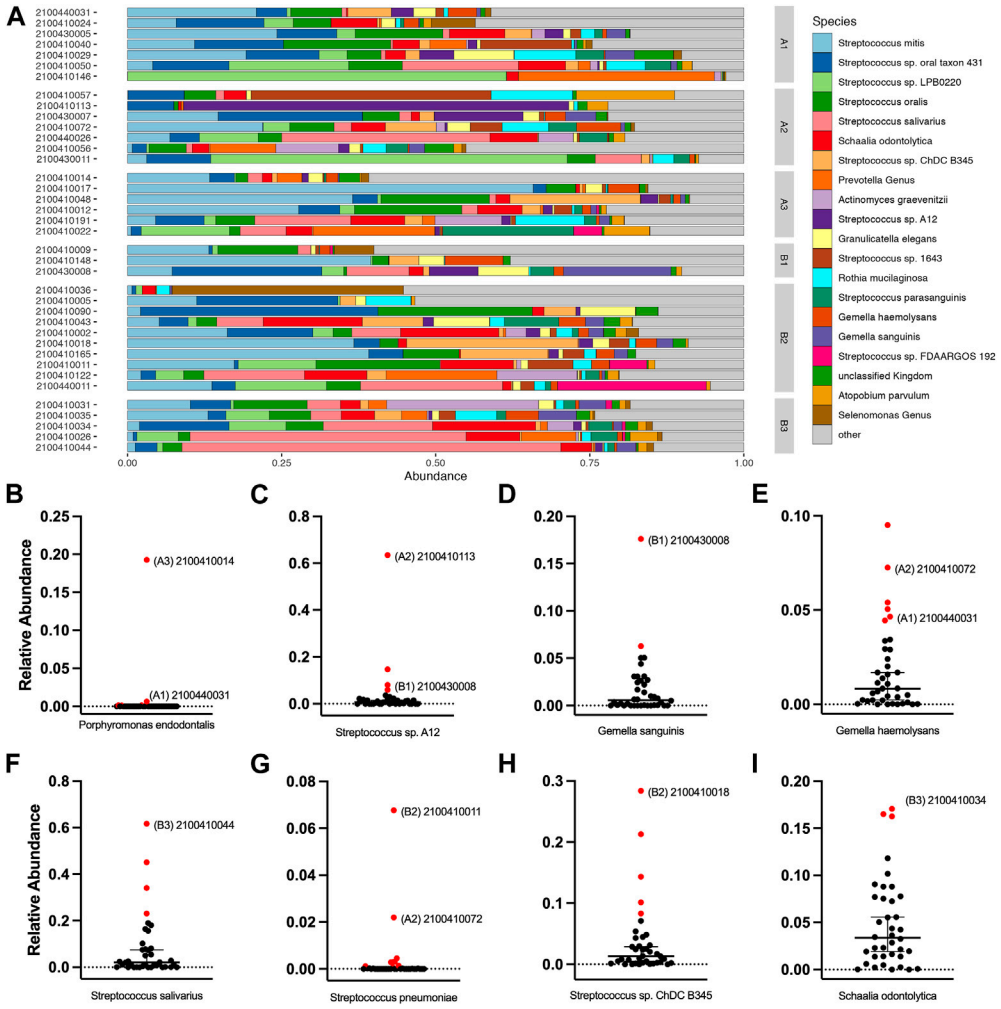

FIGURE 6
Salivary microbiome of samples analyzed using GCFP. From saliva samples analyzed by GCFP using the first generation GCFP biosensor chip, 34 samples were also analyzed by 16S RNA high throughput sequencing. Relative abundance at species level was calculated. **(A)** Relative abundance of the top 20 most abundant taxa across all samples. **(B–I)** Plots of the relative abundance for 8 bacterial species that were elevated in one or more outlier samples from analyte data. Error bars represent a 95% confidence interval of the median. Points in red were identified as outliers by the ROUT method. Samples that were analyte outliers and had an increase in that species are labeled with their cohort.

indicating a role in infection. Galectin-3 may be upregulated in COVID-19 cohorts (A1,2,3) but the amount found in saliva were near saturation for the GCFP assay as configured. Finally, IL-8 cytokines are produced by a wide range of cells including oral keratinocytes and are a potential biomarker for predicting oral disease (Finoti et al., 2017; Lopez-Labady et al., 2021). IL-8 was also reported early in the pandemic to be a sensitive serum biomarker in both mild and severe COVID-19 patients (Li et al., 2020). Interestingly, GCFP detected salivary IL-8 in all cohorts, while in serum it was detected only in the A1, A2 and B1 cohorts.

There were some cohort-unique saliva biomarkers contributing to the biomarker signature from each of the different cohorts. GCFP detection of CXCL10 was only seen in Cohort A2 (MIS-C). CXCL10 is a chemokine that is produced by many different cell lines and tissues (Jong-Ho Lee et al., 2020). This chemokine has been identified in several studies as a contributing factor to the modulation and intensity of inflammation caused by SARS-CoV2 and recently was shown to be at higher levels in MIS-C patients (Callahan et al., 2021; Caldarale et al., 2021). sCD25 was solely detected on the GFCP chip in sera from cohort A3 (mild COVID). sCD25 is the soluble form of IL-2R alpha chain, has been linked to T-cell proliferation and inflammatory disease, and is a driver of disease pathogenesis (Russell et al., 2012). sCD25 was reported to be upregulated in the serum of pediatric patients with SARs-CoV2 infections and MIS-C (Mostafa et al., 2022). It is interesting to note that sCD25 is present in the saliva from the A3 cohort and present in the serum biomarker signature from A1, A2, and B1 cohorts. In Kawasaki patient serum, sCD25 has been found to be 3-100x higher than in healthy controls, which is consistent with our observations (Teraura et al., 2016). In cohort B1, we observe the most diverse saliva biomarker signature when compared to the other cohorts, with ferritin, IL-1β and IL-2 being uniquely found at elevated levels in this cohort. Studies have indicated that high serum levels of ferritin are present in Kawasaki patients and ferritin is a predictor of

10.3389/fbioe.2023.1066391

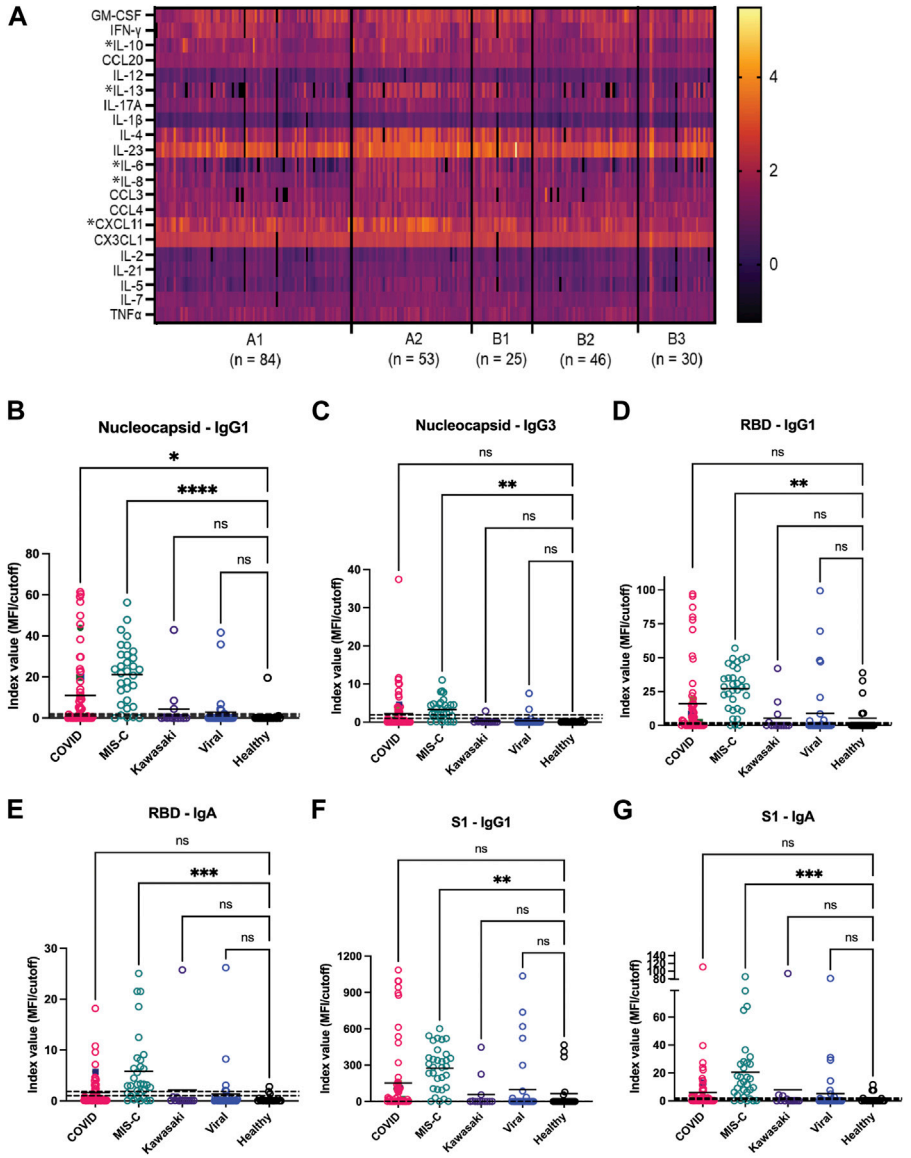

FIGURE 7
Potential analytes found by MIA can inform the evolving composition of a second generation GCFP biosensor chip. **(A)** A heat map was generated from microsphere immunoassay from serum samples for each cohort. * Indicates a significant difference in that cytokine for the A2 cohort for CXCL11, IL-8, IL-6, IL-4, IL-13, & IL-10 analytes. **(B–G)** The antibody response to the SARS-CoV-2 nucleocapsid and spike components (full spike, RBD, S1, S2), the MIS-C cohort had a significantly higher IgA response to SARS-COV-2 spike domains as compared to the COVID-19 cohort. One-way ANOVA analysis was performed (* = $p < 0.05$, ** = $p < 0.01$, *** = $p < 0.001$, **** = $p < 0.0001$.

non-responsiveness to intravenous immunoglobulin (IVIG) therapy (Yamamoto et al., 2015; Kim et al., 2021; Qiu et al., 2022). IL-1β has previously been reported to play a key role in the inflammatory profile of Kawasaki disease, and IL-2 is significantly higher in children with Kawasaki than in healthy controls (Okada et al., 2003; Hoang et al., 2014; Alphonse et al., 2016). These findings indicate that data obtained by GCFP in saliva samples are consistent with recent scientific studies and show potential for this assay as a diagnostic tool. We showed that there was variation between individual saliva samples in patients within the same cohort, indicating differences in immune responsiveness.

The microbiome 16S RNA data helped to decipher potential reasons for some of the observed differences within cohorts by demonstrating imbalances in the microbial community or the presence of oral pathogens. In future studies, we plan on designing an approach to detect these imbalances and/or pathogens by using an oligonucleotide based GCFP biosensor chip to characterize the oral microbiome. Ultimately, it will be interesting to explore the possibility of doing both protein capture, antibody capture, and oligonucleotide analyte capture on the same sensor chip to further improve the efficiency and versatility of the assay.

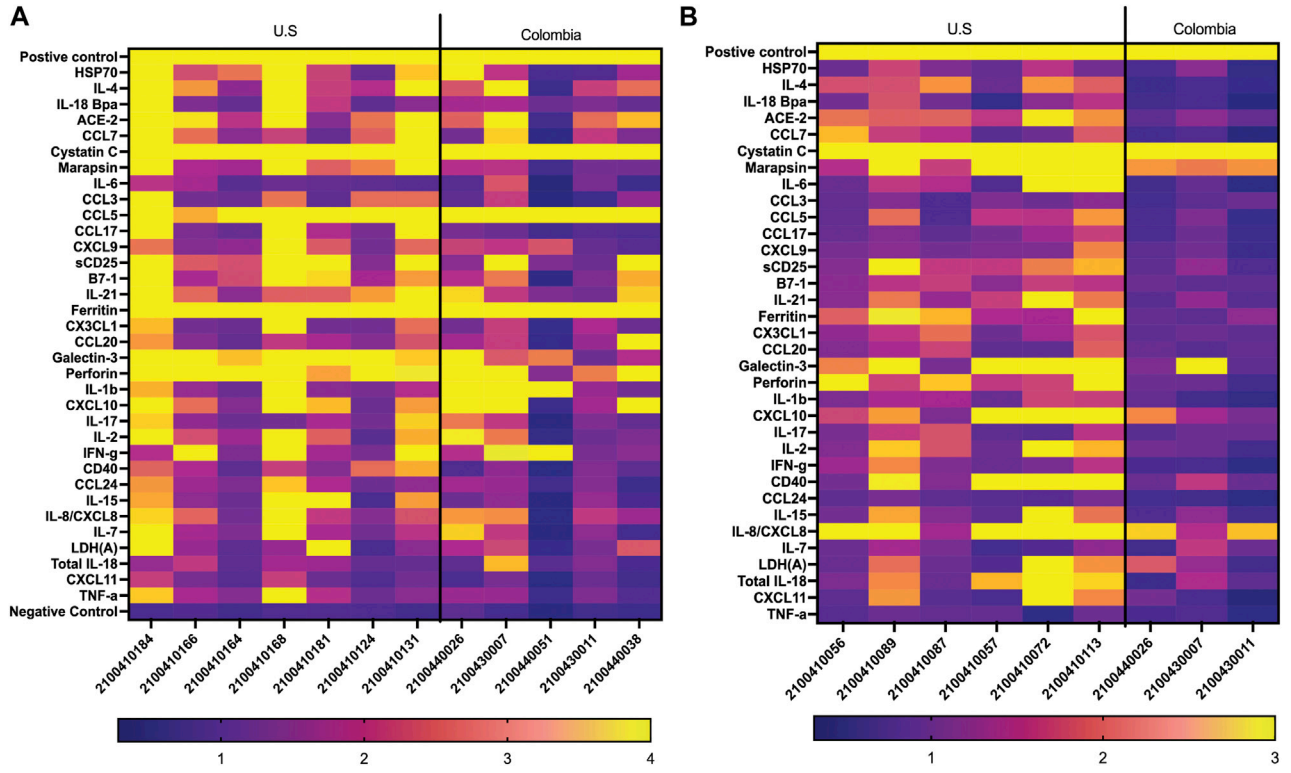

FIGURE 8
Comparison of USA vs. Colombia MIS-C patient samples by GCFP microarray. **(A)** Heat map of A2 serum samples comparing USA to Colombia samples. The USA patient population has a more robust signature. **(B)** Heat of A2 saliva samples comparing USA to Colombia samples, USA has a more robust signature.

Serum samples demonstrated a more complex biomarker signature than saliva samples, on both individual and inter-cohort levels (Figures 4, 5), which could be due to increased analyte presence in serum compared to saliva, better preservation of analyte in serum, or the choices of analytes included on the first-generation chip. The salivary proteome has 3,074 unique human proteins and only shares 1,234 proteins with blood plasma (https://www.salivaryproteome.org). GCFP biomarker analytes found in all disease state cohorts were cystatin C, ferritin, galectin 3, and perforin. As noted above, cystatin C, galectin-3 and ferritin are all found in serum at levels >250 ng/mL which could be at the limit of saturation for these assays. As expected, perforin, a glycoprotein responsible for pore formation in cell membranes of target cells, which plays an important role in cytotoxic activity, was not a marker within our healthy control group, thus showing selectivity of disease states on our chip (Osińska et al., 2014). A2 and B1 serum cohorts shared 3 analytes not found in other cohorts: HSP70, IL-1β, and IL-2. HSP70, a stress protein known to induce inflammation and has been linked to pathogenesis of Kawasaki disease (Lu et al., 1998; Hulina et al., 2018) was not present in A2 saliva but was present in B1 saliva samples. ACE2 (angiotensin converting enzyme-2) is a monocarboxypeptidase found within cell membranes or as a soluble protein throughout the body (Jiang et al., 2014). It is a member of the renin-angiotensin system (RAS) and has been implicated in diabatic cardiovascular complications and chronic heart failure; elevated expression has been linked to severe COVID-19, and it is a receptor for SARS-CoV2 entry into the cell (Patel et al., 2013; Jiang et al., 2014; Beyerstedt et al., 2021).We detected ACE2 in the serum biomarker signatures for A1, A2, and B1. While ACE2 levels in cohorts A1 and A2 are consistent with recent scientific literature, it is not a known biomarker in Kawasaki disease, despite the fact that cardiac disease (coronary artery aneurysms, myocarditis, pericarditis, congestive heart failure, pericardial effusion, and arrhythmias) is a complication in these patients (Tizard, 2005). The detection of ACE2 within cohort B1 could suggest the presence of cardiac disease within individuals of this group.

We have demonstrated the versatility of the GCFP microarray, the option to manipulate the composition of the microarray features, and the potential to detect over 1000 analytes in one assay (Guignon, and Lynes, 2014; Yuk et al., 2013; Molony et al., 2012; Unfricht et al., 2005; Marusov et al., 2012; Reilly et al., 2006). In the current study, using a small sample volume (70–80 μL) of either saliva or serum, we were able to begin to identify an initial biomarker signature for the different cohorts studied, showing that GCFP microarrays can be a potential novel approach for MIS-C disease diagnosis. ELISA or microsphere immunoassay (MIA), the gold standards for analyte measurement, use larger sample volume than GCFP, an especially important consideration with pediatric patients. We were also able to modify the protocol to increase assay sensitivity. MIA data in this study revealed four potential new GCFP targets, IL-10, IL-13, CXCL11 and SARS-COV-2 spike antigen, that can be added to

TABLE 2 MIA Cytokine levels US vs. Colombia.

	A1		A2		B1		B2	
Cytokine (pg/mL)	US	Colombia	US	Colombia	US	Colombia	US	Colombia
CXCL11	262.8	359.2	1123	520.2	379.3	466.5	181	195.6
GM-CSF	120.6	239.4	203.1	163.2	250.3	291.4	111.6	228.7
CX3CL1	236.1	246.3	272	254.2	246.9	268.3	213.6	244.9
IFN-γ	105	113.1	137.3	150.4	92.00	87.81	56.72	106.5
IL-10	46.3	174.6	187.4	157	71.07	79.41	26.82	75.5
CCL20	33.2	49.1	59.7	151.4	43.72	64.38	27.83	42.6
IL-12(p70)	5.3	7.6	5.2	5.9	6.6	5.2	6.052	6.3
IL-13	34.1	14.03	119.2	24.53	114.4	20.26	19.98	27.4
IL-17A	21.9	24.18	26.2	18.50	27.45	21.86	15.84	25.8
IL-1β	3.7	4.1	5	4.3	5.4	4.3	3.779	4.3
IL-2	6	7.4	6.8	6.4	6.9	7.1	4.4	7.3
IL-21	7.1	9.2	10.1	7.1	10.17	11.80	7.2	11
IL-4	250	71.05	689.4	125.6	532.0	106.6	146.0	129
IL-23	1103	792.4	1302	768.8	1530	43,016	532.5	1031
IL-5	8.4	6.068	19.4	7.8	20.49	6.8	24.93	6.6
IL-6	27.3	8.9	77.0	150.4	61.24	12.35	23.08	11.28
IL-7	15	14.14	18.5	15.5	18.59	30.50	13.68	14.66
IL-8	39.6	18.3	104	35.9	76.84	29.86	24.11	29.98
CCL3	32.7	43.86	48.5	26.4	37.11	28.67	73.93	32.95
CCL4	45.7	54.39	64.8	47.61	58.97	61.19	44.98	69.87
TNF-α	16.5	30.7	33.4	35.2	27.31	33.32	19.92	33.33
IFN-α2	124.7	227	214	153.6	267.7	183.5	465.2	234.5
IL-15	27.8	17.3	26.6	11.94	16.58	6.47	22.66	9.795
IL-18	270.7	362.7	835	1846	599.4	507.3	574.5	557.6
IL-33	422.8	85.4	831.4	163.2	930.3	712	355.5	250.4
IFN-β	1421	527	3446	468	3158	156.8	2750	647.4

the second-generation GCFP chip. By including more biomarkers on the chip, we can establish a more specific signature for each disease state tested, including indicators of individual organ function as well as systemic health. We are also able to detect disease state variation between patients within a disease group, which could potentially help with individualized diagnostics and treatment and provide faster treatment options per patient. It is important to note that negative markers (ones that do not appear as signals in these cohorts) are also informative and may be useful in excluding patients as belonging to one of these cohorts who present with those markers. We started building the first-generation GCFP chip at the beginning of the COVID pandemic. In future studies, ongoing research will be utilized to design a microarray in the second-generation chip that will produce biosignature that is even more specific and sensitive to MIS-C. Our data demonstrate GCFP microarrays as a novel, professional point of care diagnostic tool.

The Connecticut Children's COVID Collaborative

Salazar, Juan C, Connecticut Children's Medical Center, Hartford, Connecticut 06106, United States, and University of Connecticut Health Center, Farmington, Connecticut 06030, United States; **Lynes, Michael A**, University of Connecticut, Storrs, Connecticut 06269, United States; **Lawrence David A,** Wadsworth Center, New York State Department of Health, Albany, New York 12208, United States, and University at Albany School of Public Health,

10.3389/fbioe.2023.1066391

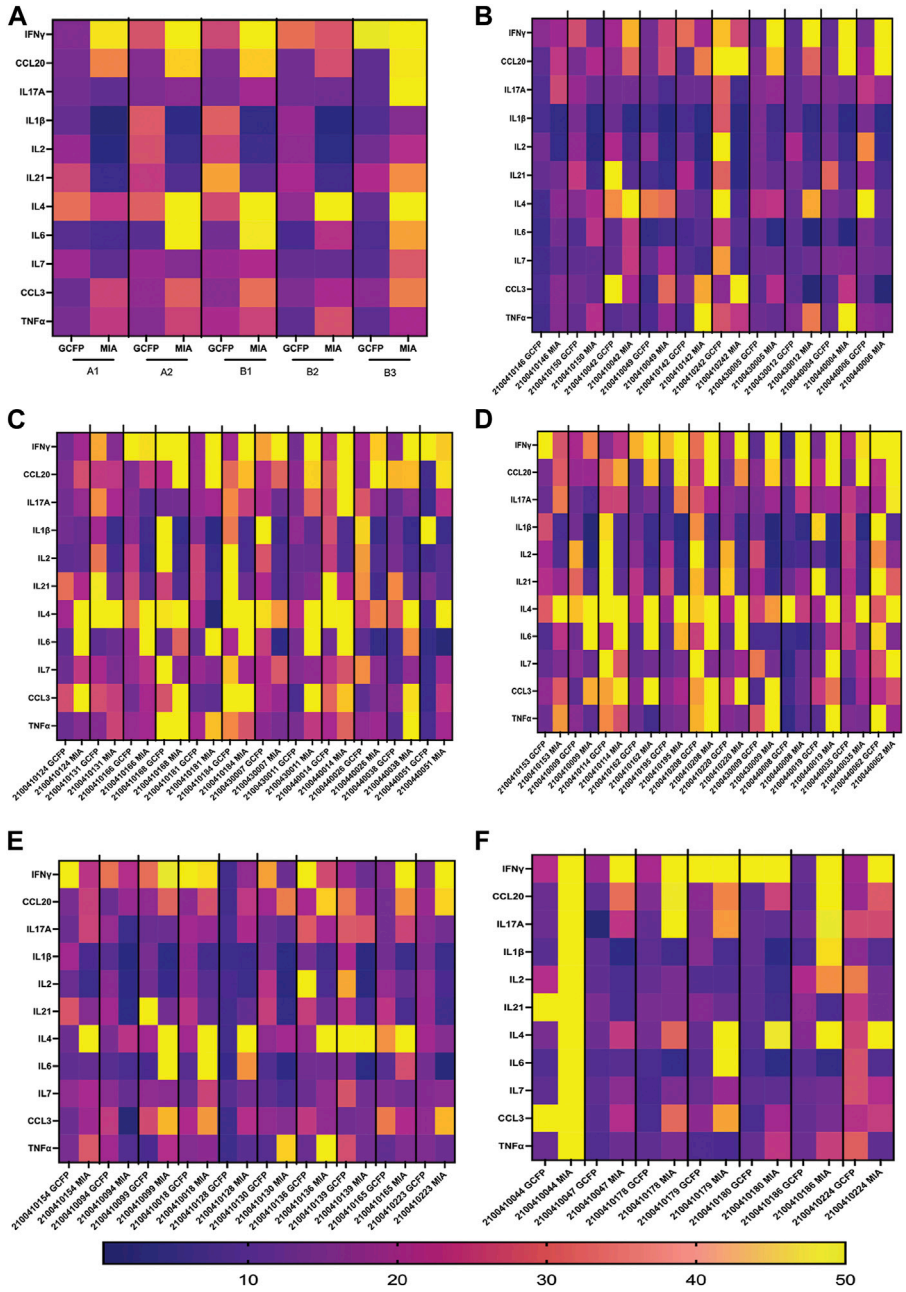

FIGURE 9
Serum from Cohorts and individual patient comparison of GCFP microarray assay to MIA. To compare a traditional MIA with the GCFP microarray, 11 analytes were included in both assays. **(A)** A heat map was generated by log transforming GCFP detection ratios and using the mean of each analyte detection ratio for each cohort. Of the 11 analytes, 5 were below the detection limit of the GCFP first generation biosensor chip. **(B)** A heat map generated by log transforming GCFP detection ratios from individual serum samples from cohort A1. **(C)** A heat map generated by log transforming GCFP detection ratios from individual serum samples from cohort A2. **(D)** A heat map generated by log transforming GCFP detection ratios from individual serum samples from cohort B1. **(E)** A heat map generated by log transforming GCFP detection ratios from individual serum samples from cohort B2. **(F)** A heat map generated by log transforming GCFP detection ratios from individual serum samples from cohort B3. 16 of the 44 shared serum samples had similar biomarker signatures, while IL-4, IL-6 and CCL20 were not consistently detected on the GCFP chip.

Rensselaer, New York 12144, United States; **Brimacombe, Michael**, Connecticut Children's Medical Center, Hartford, Connecticut 06106, United States, and University of Connecticut Health Center, Farmington, Connecticut 06030, United States; **Carroll, Christopher L,** onnecticut Children's Medical Center, Hartford, Connecticut 06106, United States, and University of Connecticut Health Center, Farmington, Connecticut 06030, United States; **Carson, Kyle J**, Wadsworth Center, New York State Department of Health, Albany, New York 12208, United States; **Dagenais, Taylor RT**, Big Rose Web Design LLC, Middleton, Wisconsin 53562, United States; **De La Cruz Macías, Catalina**, Centro de Estudios en Infectología Pediátrica, Cali, Colombia; **El Chebib, Hassan**, Connecticut Children's Medical Center,

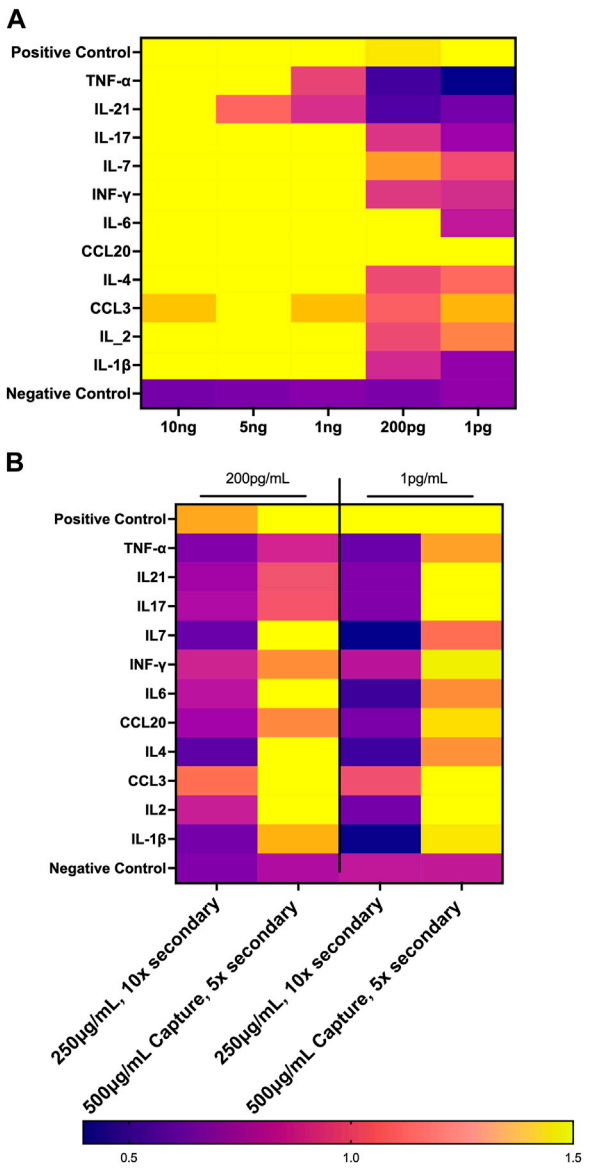

FIGURE 10
Optimization of First Generation GCFP Chip. **(A)** Measurements of the limit of detection for 11 analytes from the first-generation biosensor chip. 1 ng/mL is the limit of detection for most analytes in this assay. **(B)** Optimizing reagents can increase the limit of detection.

Hartford, Connecticut 06106, United States, and University of Connecticut Health Center, Farmington, Connecticut 06030, United States; **George, Joshy**, The Jackson Laboratory for Genomic Medicine, Farmington, Connecticut 06032, United States; **Ghassabian, Akhgar**, New York University Grossman School of Medicine, New York, New York 10016, United States; **Giles, Steven S**, Big Rose Web Design LLC, Middleton, Wisconsin 53562, United States; **Graf Jeorg**, University of Connecticut, Storrs, Connecticut 06269, United States; **Gunter, Courtney**, The Jackson Laboratory for Genomic Medicine, Farmington, Connecticut 06032, United States; **Herbst, Katherine W**, Connecticut Children's Medical Center, Hartford, Connecticut 06106, United States; **Hawley, Kelly L**, Connecticut Children's Medical Center, Hartford, Connecticut 06106, United States, and University of Connecticut Health Center, Farmington, Connecticut 06030, United States; **Hogan, Alexander H**, Connecticut Children's Medical Center, Hartford, Connecticut 06106, United States, and University of Connecticut Health Center, Farmington, Connecticut 06030, United States; **Jadhav, Aishwarya**, Wadsworth Center, New York State Department of Health, Albany, New York 12208, United States; **Kozhaya, Lina**, The Jackson Laboratory for Genomic Medicine, Farmington, Connecticut 06032, United States; **Lee, William T**, Wadsworth Center, New York State Department of Health, Albany, New York 12208, United States, and University at Albany School of Public Health, Rensselaer, New York 12144, United States; **López, Eduardo L**, Centro de Estudios en Infectología Pediátrica, Cali, Colombia; **Maltz-Matyschsyk**, Michele, University of Connecticut, Storrs, Connecticut 06269, United States; **Melchiorre, Clare K**, University of Connecticut, Storrs, Connecticut 06269, United States; **O'Sullivan, Brandan**, University of Connecticut, Storrs, Connecticut 06269, United States; **Radolf, Justin D**, University of Connecticut Health Center, Farmington, Connecticut 06030, United States; **Unutmaz, Derya**, The Jackson Laboratory for Genomic Medicine, Farmington, Connecticut 06032, United States.

Data availability statement

The original contributions presented in the study are included in the article/Supplementary Material, further inquiries can be directed to the corresponding author.

Ethics statement

The studies involving human participants were reviewed and approved by the IRB. Written informed consent to participate in this study was provided by the participants' legal guardian/next of kin.

Author contributions

MM-M Planned experiments, developed GCFP assay, ran GCFP patient samples, analysed GCFP data, and wrote the manuscript. CM Planned experiments, developed GCFP assay, organized and supervised reagent validation, discussed experiments, and helped writing of the manuscript. KH planned, organized, supervised sample collection, discussed experiments, helped with writing of the manuscript. AH planned, organized, and supervised sample diagnostics, discussed experiments, and helped with writing of the manuscript. BO'S ran, analysed 16S-23S rRNA microbiome sequencing and helped with writing of the manuscript. JG Planned, discussed experiments, and helped writing of the manuscript. AJ ran and analysed MIA for cytokine identification and helped with writing of the manuscript. DAL Planned, discussed experiments, and helped writing of the manuscript. KC performed MIS for Ig response to Sars-CoV-2 epitopes. WTL Planned, discussed experiments, and helped writing of the manuscript. JR

Planned, discussed experiments, and helped writing of the manuscript. JS Planned, discussed experiments, and helped writing of the manuscript. ML Supervised, planned, discussed experiments, and helped writing of the manuscript. All authors contributed to the article and approved the submitted version.

Funding

Research reported in this publication was supported by the Eunice Kennedy Shriver National Institute of Child and Human Development of the National Institutes of Health under award number 1R61HD105613-01 We would also like to acknowledge Robert and Francine Shanfield for their generous donation in support of this research, without which this article would not be possible.

Acknowledgments

We would like to thank Christina Aglieco and Berivan Hamoto for collecting and processing saliva samples. We would also like to thank our colleagues Adriana Camacho, Carlie DeFelice, Hilda Giraldo, Stephanie Lesmes, Isabel Orbe, Celina Porcaro, Jessika Rodrígueza, Noah Schulman, and Beatriz Vanegas for their vital contribution to the project, including participant recruitment and biospecimen collection and processing.

Conflict of Interest

ML has intellectual property (U.S. Patent #7,655,421) related to functional phenotyping of leukocytes by SPR microarray. ML, MM-M, DL, and JG have ongoing, NIH-funded, collaborations with Ciencia, Inc.

The remaining authors declare that the research was conducted in the absence of any commercial or financial relationships that could be construed as a potential conflict of interest.

Publisher's Note

All claims expressed in this article are solely those of the authors and do not necessarily represent those of their affiliated organizations, or those of the publisher, the editors and the reviewers. Any product that may be evaluated in this article, or claim that may be made by its manufacturer, is not guaranteed or endorsed by the publisher.

Supplementary material

The Supplementary Material for this article can be found online at: https://www.frontiersin.org/articles/10.3389/fbioe.2023.1066391/full#supplementary-material

References

Abramczyk, U., Nowaczyński, M., Adam, S., Wojnicz, P., Zatyka, P., and Kuzan, A. (2022). Consequences of COVID-19 for the pancreas. *Int. J. Mol. Sci.* 23 (2), 864. doi:10.3390/ijms23020864

Algarni, A. S., NjoudAlamri, M. N Z. K, R A., Alghamdi, S. H., Alsubhi, R. S., and Alghamdi, S. H. (2022). Clinical practice guidelines in multisystem inflammatory syndrome (MIS-C) related to COVID-19: A critical review and recommendations. *World J. Pediatr.* 18 (2), 83–90. doi:10.1007/s12519-021-00499-w

Alphonse, T., Prince, M., Trang, T. D., Shumitzu, C., Hoang, T L., McCrindle, B W., et al. (2016). Inositol-triphosphate 3-kinase C mediates inflammasome activation and treatment response in Kawasaki disease. *J. Immunol.* 197 (9), 3481–3489. LP – 3489. doi:10.4049/jimmunol.1600388

Amanullah, A., Hewitt, C. J., Nienow, A. W., Lee, C., Chartrain, M., Buckland, B. C., et al. (2002). Application of multi-parameter flow cytometry using fluorescent probes to study substrate toxicity in the indene bioconversion. *Biotechnol. Bioeng.* 80 (3), 239–249. doi:10.1002/BIT.10477

Bagnasco, A., Pezzi, E., Rosa, F., Fornonil, L., and Sasso, L. (2012). Distraction techniques in children during venipuncture: An Italian experience. *J. Prev. Med. Hyg.* 53 (1), 44–48. doi:10.15167/2421-4248/JPMH2012.53.1.314

Bar-Meir, M.t, Godfrey, M. E., Shack, A. R., Hashkes, P. J., Goldzweig, O, and Megged, O (2021). Characterizing the differences between multisystem inflammatory syndrome in children and Kawasaki disease. *Sci. Rep.* 11, 13840–13845. doi:10.1038/s41598-021-93389-0

Barnett, D., Ilja, A., and Penders, J. (2021). MicroViz: An R package for microbiome data visualization and statistics. *J. Open Source Softw.* 6 (63), 3201. doi:10.21105/joss.03201

Beyerstedt, S., Barbosa Casaro, E., and Érika, B. R. (2021). COVID-19: Angiotensin-converting enzyme 2 (ACE2) expression and tissue susceptibility to SARS-CoV-2 infection. *Eur. J. Clin. Microbiol. Infect. Dis. Official Publ. Eur. Soc. Clin. Microbiol.* 40 (5), 905–919. doi:10.1007/s10096-020-04138-6

Bhagwandin, V., Hau, L., Clair, J M-S., Paul, W., and George, C. (2003). Structure and activity of human pancreasin, a novel tryptic serine peptidase expressed primarily by the pancreas. *J. Biol. Chem.* 278, 3363–3371. doi:10.1074/jbc.M209353200

Bolyen, E, Rideout, J R., Dillon, M. R., Bokulich, N. A., Abnet, C C., Al-Ghalith, G. A., et al. (2019). Reproducible, interactive, scalable and extensible microbiome data science using QIIME 2. *Nat. Biotechnol.* 37 (8), 852–857. doi:10.1038/s41587-019-0209-9

Burguillos, M A., Svensson, M., Tim, S., Boza-Serrano, A., Garcia-Quintanilla, A, Kavanagh, E, et al. (2015). Microglia-secreted galectin-3 acts as a toll-like receptor 4 ligand and contributes to microglial activation. *Cell Rep.* 10 (9), 1626–1638. doi:10.1016/j.celrep.2015.02.012

Buszko, M., Nita-Lazar, A., Park, J-H., Schwartzberg, P. L., Verthelyi, Da, Young, H A., et al. (2021). Lessons learned: New insights on the role of cytokines in COVID-19. *Nat. Immunol.* 22 (4), 404–411. doi:10.1038/s41590-021-00901-9

Cabrero-Hernandez, M., Garcia-Salido, A., Leoz-Gordillo, I., Alonso-Cadenas, J. A., Gochi-Valdovinos, A., Gonzalez Brabin, A., et al. (2020). Severe SARS-CoV-2 infection in children with suspected acute abdomen: A case series from a tertiary hospital in Spain. *Pediatr. Infect. Dis. J.* 39 (8), e195–e198. doi:10.1097/inf.0000000000002777

Cady, N. C., Tokranova, N, Minor, A, Nikvand, N, Klemen, S., Lee, W T., et al. (2021). Multiplexed detection and quantification of human antibody response to COVID-19 infection using a plasmon enhanced biosensor platform. *Biosens. Bioelectron.* 171, 112679. doi:10.1016/J.BIOS.2020.112679

Caldarale, F., Giacomelli, M., Garrafa, E., Tamassia, N., Morreale, A., Poli, P., et al. (2021). Plasmacytoid dendritic cells depletion and elevation of IFN-γ dependent chemokines CXCL9 and CXCL10 in children with multisystem inflammatory syndrome. Available at: https://www.frontiersin.org/articles/10.3389/fimmu.2021.654587.

Callahan, B. J., McMurdie, P. J., Rosen, M.l J., Han, A. W., Johnson, A., and Holmes, S. P. (2016). DADA2: High-Resolution sample inference from illumina amplicon data. *Nat. Methods* 13 (7), 581–583. doi:10.1038/nmeth.3869

Callahan, V., Seth, H., Crawford, M. A., Lehman, C. W., Morrison, H. A., Ivester, H. M., et al. (2021). The pro-inflammatory chemokines CXCL9, CXCL10 and CXCL11 are upregulated following SARS-CoV-2 infection in an AKT-dependent manner. *Viruses* 13 (6), 1062. doi:10.3390/v13061062

Chou, E., Lasek-Nesselquist, E., Taubner, B., Pilar, A., Guignon, E., Page, W., et al. (2020). A fluorescent plasmonic biochip assay for multiplex screening of diagnostic serum antibody targets in human lyme disease. *PLOS ONE* 15 (2), e0228772. doi:10.1371/JOURNAL.PONE.0228772

Consiglio, C. R., Cotugno, N., Sardh, F., Pou, C., Amodio, D., Rodriguez, L., et al. (2020). The immunology of multisystem inflammatory syndrome in children with COVID-19. *Cell* 183 (4), 968–981.e7. doi:10.1016/J.CELL.2020.09.016

Dickinson, D. P. (2002). Salivary (SD-Type) cystatins: Over one billion years in the making—but to what purpose? *Crit. Rev. Oral Biol. Med.* 13 (6), 485–508. doi:10.1177/154411130201300606

Eduardo, C-A., Limon-de la Rosa, N., Salgado-de la Mora, M., Valdez-Sandoval, P., Palacios-Jimenez, M., Rodriguez-Alvarez, F., et al. (2022). Galectin-3 as a potential prognostic biomarker of severe COVID-19 in SARS-CoV-2 infected patients. *Sci. Rep.* 12 (1), 1856. doi:10.1038/s41598-022-05968-4

Feldstein, L. R., EricaRoseNewhams, B. S M. H P. C, M M., Son, M B F., Newburger, J W., Son, M. B. F., et al. (2020). Multisystem inflammatory syndrome in U.S. Children and adolescents. *N. Engl. J. Med.* 383 (4), 334–346. doi:10.1056/NEJMOA2021680

Filbin, M R., Mehta, A, Schneider, A. M., Kyle, R., Kays, J R. G., Gentili, M., et al. (2021). Longitudinal proteomic analysis of severe COVID-19 reveals survival-associated signatures, tissue-specific cell death, and cell-cell interactions. *Cell Rep. Med.* 2 (5), 100287. doi:10.1016/J.XCRM.2021.100287

Filer, A., Bik, M., Parsonage, G N., Fitton, J, Trebilcock, E, Howlett, K, et al. (2009). Galectin 3 induces a distinctive pattern of cytokine and chemokine production in rheumatoid synovial fibroblasts via selective signaling pathways. *Arthritis & Rheumatism* 60 (6), 1604–1614. doi:10.1002/art.24574

Finoti, L. S., Nepomuceno, R., Pigossi, S C., Corbi, S C. T., Rodrigo, S., and Scarel-Caminaga, R. M. (2017). Association between interleukin-8 levels and chronic periodontal disease: A PRISMA-compliant systematic review and meta-analysis. *Medicine* 96 (22), e6932. Available at: https://journals.lww.com/md-journal/Fulltext/2017/06020/Association_between_interleukin_8_levels_and.18.aspx.

Graf, L. N., Caimano, M. J., Jackson, E., Gratalo, D., Fasulo, D., Driscoll, M. D., et al. (2021). High-resolution differentiation of enteric bacteria in premature infant fecal microbiomes using a novel RRNA amplicon. *MBio* 12 (1), 036566–e3720. doi:10.1128/mBio.03656-20

Guignon, E. F., and Lynes, M. A. (2014). Sensitivity enhancement of a grating-based surface plasmon-coupled emission (SPCE) biosensor chip using gold thickness. *Chem. Phys. Lett.* 591, 5–9. doi:10.1016/j.cplett.2013.10.081

Guimarães, D., Pissarra, R., Reis-Melo, A., and Guimarães, H. (2021). Multisystem inflammatory syndrome in children (misc): A systematic review. *Int. J. Clin. Pract.* 75 (11), e14450. doi:10.1111/IJCP.14450

Henderson, N C., and Sethi, T. (2009). The regulation of inflammation by galectin-3. *Immunol. Rev.* 230 (1), 160–171. doi:10.1111/j.1600-065X.2009.00794.x

Hoang, L. T., Shimizu, C., Ling, L., Adriana, H. T W, Levin, M., Hibberd, M L., et al. (2014). Global gene expression profiling identifies new therapeutic targets in acute Kawasaki disease. *Genome Med.* 6 (11), 541. doi:10.1186/s13073-014-0102-6

Hulina, A., Rajković, M G., Daniela, J. D., Jelić, D., Dojder, A., Čepelak, I., and Rumora, L. (2018). Extracellular Hsp70 induces inflammation and modulates LPS/LTA-Stimulated inflammatory response in THP-1 cells. *Cell Stress & Chaperones* 23 (3), 373–384. doi:10.1007/s12192-017-0847-0

Jiang, F., Yang, J., Zhang, Y., Dong, M., Wang, S., Zhang, Q., et al. (2014). Angiotensin-converting enzyme 2 and angiotensin 1–7: Novel therapeutic targets. *Nat. Rev. Cardiol.* 11 (7), 413–426. doi:10.1038/nrcardio.2014.59

Jin, G b., Unfricht, D. W., Fernandez, S. M., and Lynes, M. A. (2006). Cytometry on a chip: Cellular phenotypic and functional analysis using grating-coupled surface plasmon resonance. *Biosens. Bioelectron.* 22 (2), 200–206. doi:10.1016/J.BIOS.2005.12.021

Joo, H-G., Goedegebuure, P S., Sadanaga, N, Nagoshi, M., von Bernstorff, W, and Eberlein, T J. (2001). Expression and function of galectin-3, a β-galactoside-binding protein in activated T lymphocytes. *J. Leukoc. Biol.* 69 (4), 555–564. doi:10.1189/jlb.69.4.555

Kim, S H., Song, E S., Yoon, S., Eom, G. H., Kang, G., and YoungCho, K. (2021). Serum ferritin as a diagnostic biomarker for Kawasaki disease. *Alm* 41 (3), 318–322. doi:10.3343/alm.2021.41.3.318

Lee, J-H., Han, H-S., and Joon, K. L. (2020). The importance of early recognition, timely management, and the role of healthcare providers in multisystem inflammatory syndrome in children. *Jkms* 36 (2), 177–e20. doi:10.3346/jkms.2021.36.e17

Li, L., Li, J., Gao, M., Fan, H., Wang, Y., Xu, X., et al. (2020). Interleukin-8 as a biomarker for disease prognosis of coronavirus disease-2019 patients. *Front. Immunol.* 11, 602395. doi:10.3389/fimmu.2020.602395

Li, W., Dimitry, M., Stuart, B., Ganesan, R, Sa, S, Ferrando, R, et al. (2009). The serine protease marapsin is expressed in stratified squamous epithelia and is up-regulated in the hyperproliferative epidermis of psoriasis and regenerating wounds. *J. Biol. Chem.* 284 (1), 218–228. doi:10.1074/jbc.M806267200

Li, Y., Yang, S., Ding, P., Zhu, H.-M., Li, B-Y., Yang, X., et al. (2020). Predictive value of serum cystatin C for risk of mortality in severe and critically ill patients with COVID-19. *World J. Clin. Cases* 8 (20), 4726–4734. doi:10.12998/wjcc.v8.i20.4726

Lie, M. A., Loos, B. G., Henskens, Y. M., Timmerman, M. F., Veerman, E. C., van der Velden, U., et al. (2001). Salivary cystatin activity and cystatin C in natural and experimental gingivitis in smokers and non-smokers. *J. Clin. Periodontology* 28 (10), 979–984. doi:10.1034/j.1600-051x.2001.028010979.x

Lopez-Labady, T, JeanethBologna-Molina, R., and Villarroel-Dorrego, M. (2021). Expression of interleukin-1ß and interleukin-8 in oral potentially malignant disorders and carcinomas. *Front. Oral Health* 2, 649406–6. doi:10.3389/froh.2021.649406

Lu, W., Cheng, P., and Chen, S. (1998). HSP60, HSP70 in the pathogenesis of Kawasaki disease: Implication and action. *J. Tongji Med. Univ. = Tong Ji Yi Ke Da Xue Xue Bao* 18 (3), 145–148. doi:10.1007/BF02888523

Mahmoud, S., EmanFouda, M., Kotby, A., Ibrahim, H. M., Gamal, M., el Gendy, Y. G., et al. (2021). The 'golden hours' algorithm for the management of the multisystem inflammatory syndrome in children (MIS-C). *Glob. Pediatr. Health* 8, 2333794X2199033. doi:10.1177/2333794X21990339

Marusov, G., Sweatt, A., Pietrosimone, K., Benson, D., Geary, S. J., Silbart, L. K., et al. (2012). A microarray biosensor for multiplexed detection of microbes using grating-coupled surface plasmon resonance imaging. *Environ. Sci. Technol.* 46 (1), 348–359. doi:10.1021/ES201239F

McMurdie, P. J., and Holmes, S. (2013). Phyloseq: An R package for reproducible interactive analysis and graphics of microbiome census data. *PLOS ONE* 8 (4), e61217. doi:10.1371/journal.pone.0061217

Molony, R. D., Rice, J. M., Shetty, V., Dey, D., Lawrence, D. A., and Lynes, M. A. (2012). Mining the salivary proteome with grating-coupled surface plasmon resonance imaging and surface plasmon coupled emission microarrays *current Protocols in toxicology* chapter. *Curr. Protoc. Toxicol.* 18 (53), Unit 18.16.1-19. doi:10.1002/0471140856.TX1816S53

Mostafa, G A., Mohamed Ibrahim, H., and Abeer Al, S S., (2022). Up-regulated serum levels of soluble CD25 and soluble CD163 in pediatric patients with SARS-CoV-2. *Eur. J. Pediatr.* 181 (6), 2299–2309. doi:10.1007/s00431-022-04398-8

Newburger, J. W., Takahashi, M., and Burns, J. C. (2016). Kawasaki disease. *J. Am. Coll. Cardiol.* 67 (14), 1738–1749. doi:10.1016/J.JACC.2015.12.073

Noordin, R., and Nurulhasanah, O. (2013). Proteomics technology – a powerful tool for the biomedical scientists. *Malays. J. Med. Sci. MJMS* 20 (2), 1–2.

Okada, Y., Shinohara, M., Kobayashi, T., Inoue, Y., Tomomasa, T., Kobayashi, T, et al. (2003). Effect of corticosteroids in addition to intravenous gamma globulin therapy on serum cytokine levels in the acute phase of Kawasaki disease in children. *J. Pediatr.* 143 (3), 363–367. doi:10.1067/S0022-3476(03)00387-1

Osińska, Iw., Popko, K., and Demkow, U. (2014). Perforin: An important player in immune response. *Central-European J. Immunol.* 39 (1), 109–115. doi:10.5114/ceji.2014.42135

Patel, V. B., Parajuli, N., and Oudit, G. Y. (2013). Role of angiotensin-converting enzyme 2 (ACE2) in diabetic cardiovascular complications. *Clin. Sci.* 126 (7), 471–482. doi:10.1042/CS20130344

Phamduy, T. T., Smith, S., Herbst, K. W., Phamduy, P. T., Brimacombe, M, Alexander, H., et al. (2021). Kawasaki disease hospitalizations in the United States 2016–2020: A comparison of before and during the coronavirus disease 2019 era.Pediatr. *Infect. Dis. J.* 40 (11), e407–e412. doi:10.1097/INF.0000000000003289

Qiu, Z., Liu, H., GuoFan, Z., Chen, W. X., and Hu, P. (2022). The clinical implications of serum ferritin in Kawasaki disease: A helpful biomarker for evaluating therapeutic responsiveness, coronary artery involvement and the tendency of macrophage activation syndrome. *Archives Med. Sci. AMS* 18 (1), 267–274. doi:10.5114/aoms/144293

Radia, T, Williams, N., Agrawal, P., Harman, K., Jonathan, W., Cook, J., et al. (2021). Multi-system inflammatory syndrome in children & adolescents (MIS-C): A systematic review of clinical features and presentation. *Paediatr. Respir. Rev.* 38, 51–57. doi:10.1016/J.PRRV.2020.08.001

Ramaswamy, A.i, Brodsky, N. N., Tomokazu, S. S., Comi, M., Asashima, H., Hoehn, K. B., et al. (2020). Post-infectious inflammatory disease in MIS-C features elevated cytotoxicity signatures and autoreactivity that correlates with severity. *MedRxiv Prepr. Serv. Health Sci.* 2020, 20241364. doi:10.1101/2020.12.01.20241364

Reilly, M. T., Nessing, P. A., Guignon, E. F., Lynes, M A., and Fernandez, S. M. (2006). SPR surface enhanced fluorescence with a gold-coated corrugated sensor chip. *Proc. SPIE* 6099, 60990E. doi:10.1117/12.646165

Rice, J. M., Lawrence, J., Stern, E. F. G., D A. L., Lynes, M A., and Lynes, M. A. (2012). Antigen-specific T cell phenotyping microarrays using grating coupled surface plasmon resonance imaging and surface plasmon coupled emission. *Biosens. Bioelectron.* 31 (1), 264–269. doi:10.1016/J.BIOS.2011.10.029

Russell, S. E., Anne C Moore, P. G. F, Walsh, P. T., and Walsh, P. T. (2012). Soluble IL-2rα (SCD25) exacerbates autoimmunity and enhances the development of Th17 responses in mice. *PLOS ONE* 7 (10), e47748. doi:10.1371/journal.pone.0047748

Teraura, H., Kotani, K., Minami, T., Takeshima, T., Shimooki, O., and Kajii, E. (2016). The serum concentration of soluble interleukin-2 receptor in patients with Kawasaki disease. *Ann. Clin. Biochem.* 54 (2), 209–213. doi:10.1177/0004563216677583

Tizard, E. J. (2005). Complications of Kawasaki disease. *Curr. Paediatr.* 15 (1), 62–68. doi:10.1016/j.cupe.2004.09.002

Unfricht, D. W., Colpitts, S. L., Fernandez, S.M., and Lynes, M. A. (2005). Grating-coupled surface plasmon resonance: A cell and protein microarray platform. *Proteomics* 5 (17), 4432–4442. doi:10.1002/PMIC.200401314

Whittaker, E., Bamford, A., Kenny, J., Kaforou, M., Jones, C. E., Shah, P., et al. (2020). Clinical characteristics of 58 children with a pediatric inflammatory multisystem syndrome temporally associated with SARS-CoV-2. *JAMA* 324 (3), 259–269. doi:10.1001/JAMA.2020.10369

Yamamoto, N., Sato, K., Hoshina, T., Kojiro, M., and Kusuhara, K. (2015). Utility of ferritin as a predictor of the patients with Kawasaki disease refractory to intravenous immunoglobulin therapy. *Mod. Rheumatol.* 25 (6), 898–902. doi:10.3109/14397595.2015.1038430

Yates, J. L., Ehrbar, D. J., Hunt, D. T., Girardin, R. C., Dupuis, A. P., Payne, A. F., et al. (2021). Serological analysis reveals an imbalanced IgG subclass composition associated with COVID-19 disease severity. *Cell Rep. Med.* 2 (7), 100329. doi:10.1016/j.xcrm.2021.100329

Yates, J. L., DylanEhrbar, J., Hunt, D. T., Girardin, R. C., AlanDupuis, P., Payne, A. F., et al. (2021). Serological analysis reveals an imbalanced IgG subclass composition associated with COVID-19 disease severity. *Cell Rep. Med.* 2 (7), 100329. doi:10.1016/j.xcrm.2021.100329

Yuk, J S., Guignon, E. F., and Lynes, M. A. (2013). Highly sensitive grating coupler-based surface plasmon-coupled emission (SPCE) biosensor for immunoassay. *Analyst* 138 (9), 2576–2582. doi:10.1039/C3AN00135K

Ziegelasch, N., Vogel, M., Müller, E., Tremel, N., Jurkutat, A., Löffler, M., et al. (2019). Cystatin C serum levels in healthy children are related to age, gender, and pubertal stage. *Pediatr. Nephrol. Berl. Ger.* 34 (3), 449–457. doi:10.1007/s00467-018-4087-z

frontiers | Frontiers in Bioengineering and Biotechnology

TYPE Original Research
PUBLISHED 03 May 2023
DOI 10.3389/fbioe.2023.1169424

OPEN ACCESS

EDITED BY
Mehmet Senel,
Biruni University, Türkiye

REVIEWED BY
Yue Cao,
Nanjing University of Posts and Telecommunications, China
Andrea Idili,
University of Rome Tor Vergata, Italy

*CORRESPONDENCE
Zhiyang Li,
lizhiyangcn@qq.com
Han Shen,
shenhan10366@sina.com

†These authors have contributed equally to this work and share first authorship

RECEIVED 19 February 2023
ACCEPTED 19 April 2023
PUBLISHED 03 May 2023

CITATION
Wu J, Xu H, Hu F, Jiang Y, Fan B, Khan A, Sun Y, Di K, Gu X, Shen H and Li Z (2023), CRISPR-Cas and catalytic hairpin assembly technology for target-initiated amplification detection of pancreatic cancer specific tsRNAs.
Front. Bioeng. Biotechnol. 11:1169424.
doi: 10.3389/fbioe.2023.1169424

CRISPR-Cas and catalytic hairpin assembly technology for target-initiated amplification detection of pancreatic cancer specific tsRNAs

Jie Wu[1†], Hongpan Xu[1†], Fenghua Hu[1†], Yiyue Jiang[1], Boyue Fan[1], Adeel Khan[2], Yifan Sun[1], Kaili Di[3], Xinrui Gu[3], Han Shen[1*] and Zhiyang Li[1*]

[1]Department of Clinical Laboratory, Nanjing Drum Tower Hospital Clinical College of Jiangsu University, Nanjing, China, [2]State Key Laboratory of Bioelectronics, National Demonstration Center for Experimental Biomedical Engineering Education (Southeast University), School of Biological Science and Medical Engineering, Southeast University, Nanjing, China, [3]Department of Clinical Laboratory, Nanjing Drum Tower Hospital, Affiliated Hospital of Medical School, Nanjing University, Nanjing, China

Transfer RNA-derived small RNAs (tsRNAs) tRF-LeuCAG-002 (ts3011a RNA) is a novel class of non-coding RNAs biomarker for pancreatic cancer (PC). Reverse transcription polymerase chain reaction (RT-qPCR) has been unfit for community hospitals that are short of specialized equipment or laboratory setups. It has not been reported whether isothermal technology can be used for detection, because the tsRNAs have rich modifications and secondary structures compared with other non-coding RNAs. Herein, we have employed a catalytic hairpin assembly (CHA) circuit and clustered regularly interspaced short palindromic repeats (CRISPR) to develop an isothermal and target-initiated amplification method for detecting ts3011a RNA. In the proposed assay, the presence of target tsRNA triggers the CHA circuit that transforms new DNA duplexes to activate collateral cleavage activity of CRISPR-associated proteins (CRISPR-Cas) 12a, achieving cascade signal amplification. This method showed a low detection limit of 88 aM at 37 °C within 2 h. Moreover, it was demonstrated for the first time that, this method is less likely to produce aerosol contamination than RT-qPCR by simulating aerosol leakage experiments. This method has good consistency with RT-qPCR in the detection of serum samples and showed great potential for PC-specific tsRNAs point-of-care testing (POCT).

KEYWORDS

pancreatic cancer, tsRNAs, CRISPR-Cas12a, catalytic hairpin assembly, target-initiated amplification

Highlights

- Catalytic hairpin assembly (CHA) circuit and clustered regularly interspaced short palindromic repeats (CRISPR) (CHA-CRISPR) is a simple, isothermal, ultrasensitive, and target-initiated amplification method to detect ts3011a RNA, a novel class of non-coding RNAs biomarkers for pancreatic cancer (PC).

Based on CHA-CRISPR method, this assay achieved simple, isothermal, ultrasensitive and target-initiated amplification of ts3011a RNA with a low detection limit of 88 aM in 2 h at 37 °C. Moreover, it was demonstrated for the first time that, this method is less likely to produce aerosol contamination than Reverse transcription polymerase chain reaction (RT-qPCR) by simulating aerosol leakage experiments. This method has good consistency with RT-qPCR in detection of serum samples and showed great potential for PC specific tsRNAs point-of-care testing (POCT). Its diagnostic performance was found to be similar to that of RT-qPCR, and it is more suitable in community hospitals without precision instruments and PCR testing standard environments.

1 Introduction

Pancreatic cancer (PC) is the cancer with the lowest 5-year survival rate (Siegel et al., 2022). Because of the lack of markers for early diagnosis, most patients are in an advanced stage when they are diagnosed (Pereira et al., 2020). As a kind of transfer RNA-derived small RNAs (tsRNAs) (Li et al., 2018a; Jin and Guo, 2019), tRF-Leu-CAG-002 (ts3011a) was found to be a potential diagnostic marker for early pancreatic cancer (Jin et al., 2021). TsRNAs are newly discovered non-coding RNA that account for the vast majority of total small RNA in mammalian tissues and cells, and their existence ratios are much higher than that of the miRNAs (Zhang et al., 2014). The concentrations of ts3011a were between pM and fM in the clinically relevant ranges (Jin et al., 2021). Therefore, the development of point-of-care testing (POCT) technology using tsRNA as a marker will make it possible to carry out early pancreatic cancer screening in the community.

At present, reverse transcription PCR (RT-qPCR) is a commonly used non-coding RNA detection technology (Liu et al., 2012; Li et al., 2018b; Xiong et al., 2018). This technique requires sophisticated equipment and specialized laboratories that are susceptible to aerosol contamination by leakage of high-concentration amplification products (Chen et al., 2005; Ye et al., 2019). Because tsRNAs have more abundant modifications and secondary structures than other non-coding RNA (Li et al., 2018a), it has not been reported whether the isothermal technology can be used for detection. The combination of clustered regularly interspaced short palindromic repeats associated (CRISPR-Cas) system with target isothermal amplification methods, such as reverse transcription loop-mediated isothermal amplification (RT-LAMP) (Rezaei et al., 2021) and reverse transcription recombinase polymerase amplification (RT-RPA) (Chen et al., 2022a), can detect non-coding RNA such as miRNA and lncRNA without precision instruments, but they are prone to aerosol pollution (Borst et al., 2004). Target-initiated amplification methods like hybridization chain reaction (HCR) (Wang et al., 2019) and catalytic hairpin assembly (CHA) (Chen et al., 2022b) combined with CRISPR-Cas are not easy to cause aerosol pollution in theory, and CHA (Peng et al., 2020; Zeng et al., 2022) technology takes less time than HCR technology (Xing et al., 2020; Zhou et al., 2022a), making it more suitable for POCT diagnosis. However, whether CHA can be used for tsRNAs detection, and whether it can produce aerosol pollution needs further experimental verification.

Herein, we illustrated a simple method by coupling CRISPR/Cas12a and CHA to realize the detection of ts3011a RNA. In our experiment, two hairpins from the CHA circuit were triggered by tsRNAs and transformed into new DNA duplexes. The new DNA duplexes consisted of protospacer adjacent motif (PAM) and protospacer sequence that can be recognized by Cas12a/CRISPR RNA (crRNA) complexes. Therefore, the collateral cleavage activity of CRISPR/Cas12a was initiated, and cascade signal amplification was realized through the cleavage events of fluorescent ssDNA reporter molecules (Scheme 1). Based on the above principle, the experimental conditions were optimized, and a simulated aerosol leakage experiment was designed to verify whether the method would produce aerosol pollution. And for the detection of pancreatic cancer, the diagnostic efficiency was evaluated.

2 Experiment section

2.1 Materials and instruments

NaCl, KCl, $MgCl_2$, and glycerol were purchased from Macklin Biochemical Co., Ltd., Shanghai, China. Tris hydrochloric acid (TrisHCl) was purchased from Dalian Meilun Biological Technology Co., Ltd., Suzhou, China. Dithiothreitol (DTT) was purchased from SaiGuo Biotech Co., Ltd., Guangzhou, China. Lachnospiraceae bacterium (LbCas12a) was purchased from GenScript Biotech Co., Ltd., Nanjing, China, and the protein was stored at −80 °C until later use. Agarose powder, ×10 Trizma base boric acid ethylene diamine tetra acetic acid (TBE) buffer, and ×6 Loading buffer were obtained from Sangon Biotech, Shanghai, China. All oligonucleotides (Supplementary Table S1) and diethylpyrocarbonate (DEPC) treated water were obtained from Sangon (Shanghai, China). All chemical reagents used in the study were of analytical grade, and all the solutions were prepared with DEPC-treated water. Human pancreatic carcinoma cells (PANC-1), and human pancreatic duct cells (hTERT-HPNE) were bought from Zhong Qiao Xin Zhou Biotechnology Co., Ltd. (Shanghai, China). Cell culture medium, fetal bovine serum (FBS), trypsin,penicillin–streptomycin, and dulbecco's modified eagle medium (DMEM) were bought from Invitrogen (Gibco, United States). TRIzol RNA isolation reagents were bought from Thermo Fisher Scientific (Wilmington, United States). Primer Script ™ RT reagent Kit and TB Green Premix Ex Taq ™ II qPCR Kit were provided by Takara Biomedical Technology Co., Ltd. (Beijing, China). The primers (Supplementary Table S1) were designed and synthesized by Sangon (Shanghai, China). The humidified incubator was used for cell culture (Thermo Fisher Scientific, United States). The annealing buffer used in the annealing step was bought from Beyotime Biological Technology Co., Ltd. (Shanghai, China) and Gel Imaging System used Tanon 2500R for photographing (Shanghai, China). DNA annealing process, RT-qPCR, and fluorescence intensity (FL) testing were carried out on C1000™ Thermal Cycler (Bio-Rad Laboratories, Inc., United States). A cyclone air sampler (ASP-200p, Shenzhen Lemniscare Medical Technology Co., Ltd., China) was used for sampling.

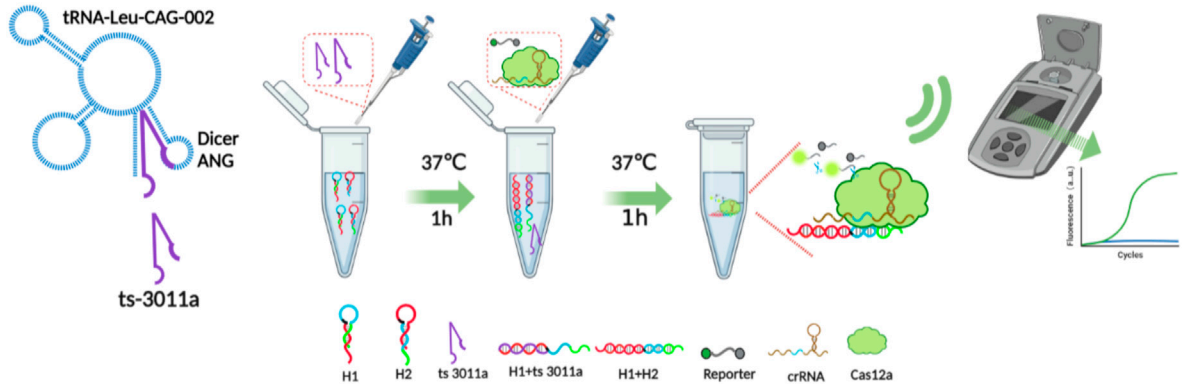

SCHEME 1
Schematic of fluorescence assay for tsRNA based on CHA reaction and CRISPR-Cas12a system.

2.2 Performing tsRNA-triggered CHA circuits in solution

The structures of H1 and H2 were predicted by https://sg.idtdna.com/calc/analyzer. The H1 and H2 were annealed at 95 °C for 5 min and then gradually cooled down at 4 °C for 1 h to obtain the desired stem-loop structure using a thermal cycler respectively. The CHA reaction buffer consisted of 5 mM KCl, 20 mM Tris-HCl, and 140 mM NaCl, pH 7.5. A 10 μL CHA reaction system contained 2 μM H1, 2 μM H2, and different concentrations of tsRNA to conduct the reaction at 37 °C for 1 h. Besides, we used fluorescence quenching H1 to detect time-dependent fluorescent signals of CHA in the presence of different targets, mainly including ts3011a, tRF-3, tRF-4, and tRF-10 (Supplementary Figure S1).

2.3 Gel electrophoresis analysis

Native PAGE analysis was performed to characterize the CHA products. A measure of 2 μL of ×6 loading buffer was mixed with 10 μL of each sample, and then 10 μL of the above-mixed solution was loaded into a 12% PAGE, running at 100 V for 2 h in ×1 TBE buffer. After that, the gel was stained for 10 min in 50 mL ×1 TBE buffer with 5 μL ×10,000 Gel-Red nucleic acid gel stain. The gels were then photographed.

2.4 Detection of ts3011a with CRISPR-CHA assay

Subsequently, 1 μL of the above CHA reaction solution was added into the cleavage buffer (5% glycerol, 1 mM DTT, 5 mM $MgCl_2$, 20 mM tris HCl, and 100 mM KCl, pH 7.5) containing 400 nM CRISPR-Cas12a, 200 nM crRNA, and 1 μM FAM-TTATT-BHQ1 reporter molecules (FQ), making a final volume of 10 μL. The fluorescence emission measurements were recorded at 518 nm in the thermal cycler at 37 °C for 1 h. The stem length, CHA reaction time, temperature, and concentration of crRNA and Cas enzyme in 10 μL volume were optimized.

2.5 Cell culture and ts3011a extraction

PANC-1 and hTERT-HPNE were grown in DMEM supplemented with 10% FBS, 1%penicillin–streptomycin (100 U/mL penicillin and 100 μg/mL streptomycin) and cultured at 37 °C in a humidified incubator containing 95% air and 5% CO_2. Total RNA was extracted using TRIzol RNA isolation reagents. cDNA was prepared by Primer Script™ RT reagent Kit. Each measure of 10 μL of reaction system included 2 μL of primer script buffer (×5) and 0.5 μL of primer script enzyme, which were mixed with 0.5 μL primer, 2 μL of total RNA, and 5 μL of DEPC treated water. The reactions were then incubated at 42 °C for 15 min, 85 °C for 5 s, and cDNA was stored at −20 °C until further use.

2.6 RT-qPCR analysis of ts3011a expression

RT-qPCR analysis of ts3011a expression was conducted by qPCR Kit. The whole 25 μL of reaction volume contained 12.5 μL of ×2 Premix Ex Taq II, 1 μL of both forward and reverse primers, 2 μL of cDNA, and 8.5 μL of DEPC treated water. The reaction was conducted using a thermal cycler according to the guidelines of the manufacturer (at 95 °C for 30 s, followed by 40 cycles of 95 °C for 5 s and 60 °C for 30 s). The relative expression of cell samples was evaluated by referring to the expression of the mir39 (external control for miRNAs) using the $^{2-\Delta\Delta}$ Ct method (Supplementary Table S2).

2.7 Simulated aerosol detection experiment

CHA, CHA-CRISPR, and RT-qPCR were performed with 1 nM ts3011a, respectively, to simulate the possible release of aerosol after CHA, CHA-CRISPR, and RT-qPCR reaction. The closed hood was

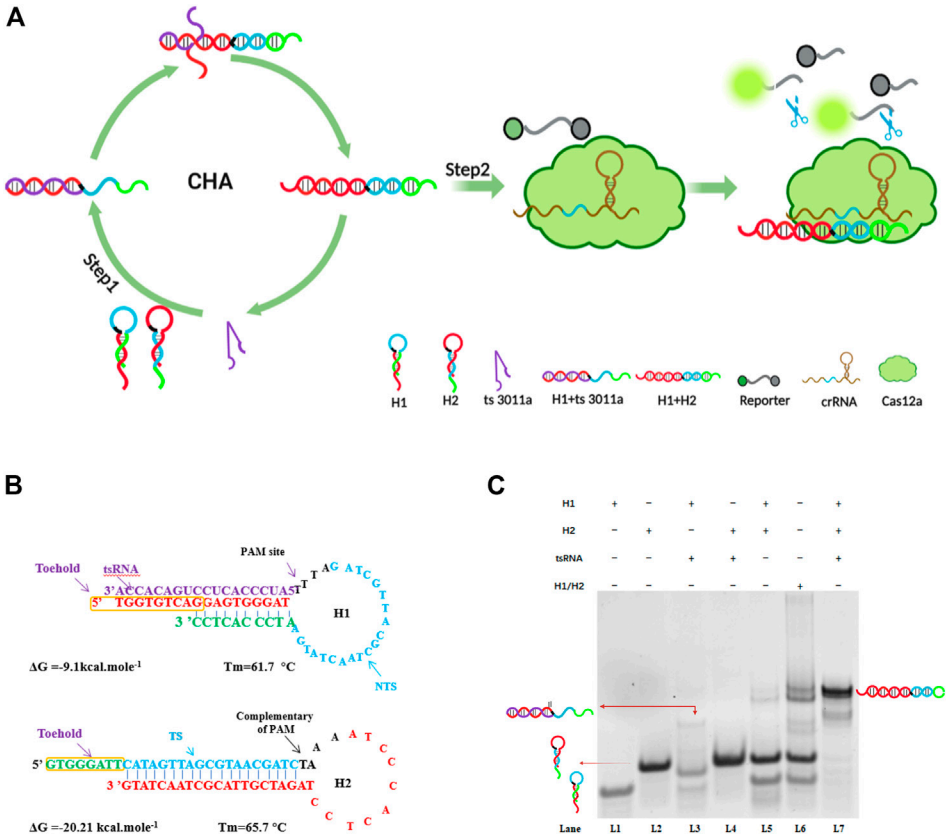

FIGURE 1
(A) Specific demonstration of CHA-CRISPR mechanism for detecting tsRNAs. **(B)** Detailed sequences of H1 and H2 in the CHA circuit for detection of tsRNAs. TS, target sequence; NTS, non-target sequence. **(C)** Electrophoresis analysis of the CHA system; H1 (2 μM); H2 (2 μM); ts3011a RNA (100 nM). H1/H2 were not annealed, H1 + H2 were annealed.

opened to ventilate for 0.5 h. The air sampler with 2 mL of sampling liquid (CHA or RT-qPCR reaction buffer) was put into the closed hood. The 8-strip tubes with CHA or CHA-CRISPR or RT-qPCR products were then put into the closed hood and uncapped. The closed-hood lead was closed and left for 5 min. The sampler was then turned on for 15 min with an air velocity of 200 L/min (Chen et al., 2023). CHA or CHA-CRISPR or RT-qPCR respectively were then performed using 1 μL of the sample liquid according to steps 2.4 and 2.6. After each aerosol collection experiment, the inner wall of the closed cover and the sampler were wiped twice with water and 75% alcohol.

2.8 Quantification of ts3011a in serum samples with CHA-CRISPR

All the pancreatic cancer serum samples and healthy serum samples were collected from consented patients at the Nanjing Drum Tower Hospital (Nanjing, China) from January to October 2022. Approval was obtained from our hospital ethics committee. 200 μL of serum samples were centrifuged at 1700 g for 20 min at 4 °C. The TRIzol RNA isolation reagents were used to extract the total RNA. 1 μL of total RNA was added to the CHA-CRISPR system to validate its potential feasibility.

3 Results and discussion

3.1 Principle of CHA-CRISPR

In the first step of amplification, CHA cycles contained the following three main elements: two hairpins (H1 and H2) and target ts3011a RNAs as initiators (Figure 1A). Both designed H1 and H2 had a stem-loop DNA containing majority complementary regions and an 8-nt 5′overhang as a toehold, which remained at metastable state that coexisted in the absence of ts3011a RNAs. As illustrated in Figure 1B, H1 contained the sequence "TGGTGTCAGGAGTGG GAT", which was perfectly complementary to the sequence of the target tsRNA, and the loop region contained the 5′-TTTA-3′ protospacer adjacent motif (PAM) of Cas12a, as well as a non-target strand (NTS) "TTTAGATCGTTACGCTAACTATGA". The length of NTS was 20 nt (Feng et al., 2021; Kaminski et al., 2021). The target tsRNA binding to the exposed toehold domain of H1 triggered a branch migration, generating an H1-tsRNA intermediate through domain hybridization. The exposed toehold domain "ATCCCACTCC" in the H1/tsRNA complex further triggered strand displacement on domain "GTGGGATTCATAGTTAGC GTAACGATCTAAAATCCCACTCC" of H2, which led to the dynamic assembly of H1 and H2, forming mass H1/H2 duplexes and releasing target ts3011a RNAs (Figure 1A). The Cas12a

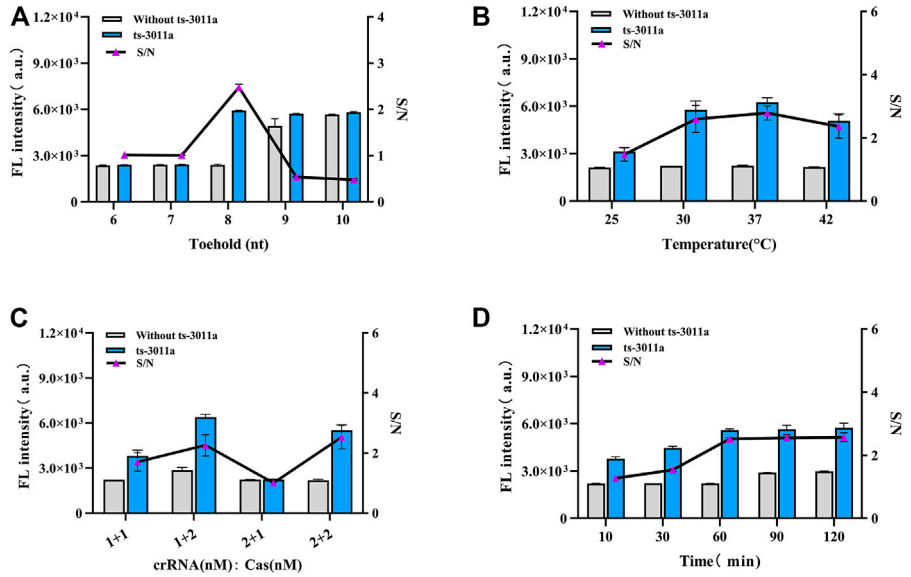

FIGURE 2
Optimization of experimental parameters. **(A)** Different base numbers of toeholds for H1 and H2. **(B)** Cleavage temperature. **(C)** The concentrations of crRNA and Cas12a, 1 + 1 (crRNA 200 nM, Cas12a 200 nM); 1 + 2 (crRNA 200 nM, Cas12a 400 nM); 2 + 1 (crRNA 400 nM, Cas12a 200 nM); 2 + 2 (crRNA 400 nM, Cas12a 400 nM). **(D)** CHA reaction time. Concentrations of H1 and H2 from A to D groups were 2 μM; ts3011a RNA (10 pM). Data are presented as mean ± S.D from three replicates measurements.

proteins, crRNA, and FQ were introduced in the second step of amplification to mix with H1/H2 duplexes. The Cas12a/crRNA recognized the PAM-TTTA and bound to the protospacer sequence of H1/H2 duplexes, resulting in the activation of collateral cleavage activity of Cas12a to cleave the reporter molecules, hence, generating intense fluorescence signals for tsRNA quantification (Figure 1A).

To verify the feasibility of the assay, we conducted gel electrophoresis (Figure 1C). Only when H1, H2, and target ts3011a RNAs coexisted in the reaction solution, did obvious hybridization bands with higher molecular weight appear as lane 7 (Figure 1C), suggesting the formation of H1/H2 duplexes. Moreover, hybridization bands were the same size as H1/H2 duplexes when H1 and H2 did not form hairpins, as seen in lane 6 (Figure 1C). The H1 and H2 did form hairpins after annealing, remaining at a metastable state which coexisted as shown in lane 5 (Figure 1C). A negligible band of the H1/H2 duplex was observed in the absence of ts3011a (Figure 1C, lane 5), which indicated low background leakage in the CHA circuit, as demonstrated in previous reports (Wang et al., 2020; Zhou et al., 2022b). An obvious band for ts3011a RNAs/H1 duplex was observed in lane 3, indicating effective initiation of the CHA cycles by ts3011a RNAs. To show the effect of target concentration on H1/H2 and H1/ts3011a complex formation, we added FQ-H1 experiments (Supplementary Figure S1). When the target concentration was 10 nM, the fluorescence increased significantly, and with the decrease of the target concentration, the fluorescence intensity decreased (Supplementary Figure S1A). Besides, CHA has good specificity and can distinguish homologous RNA (Supplementary Figure S1B).

3.2 Experimental optimization

The stem length was vital in the design of H1 and H2 (Shen et al., 2020; Cui et al., 2021). The complementary stem length was too long to facilitate the opening of the hairpin, and when too short, complementary bases have poor specificity. As investigated from 6 to 10 nt toehold length of H1 and H2 in the presence of 1 nM ts3011a RNAs, the FL intensity results showed that 8-nt 5′overhang toeholds were best for initiation of reaction as shown in Figure 2A. The toehold length (8 nt) had the lowest background in electrophoresis (Supplementary Figure S2). And 37 °C was the best temperature (Figure 2B). In addition, the concentration optimization results for crRNA and Cas enzyme showed that the fluorescence intensity increased with the efficiency of the Cas enzymes. There was maximum S/N (signal/noise) at crRNA 200 nM and Cas 400 nM (Figure 2C). The results from CHA reaction time showed that the FL intensity increased significantly with increased hybridization time and the FL intensity gradually stabilized after 60 min (Figure 2D). Therefore, 60 min was selected as the best CHA reaction time.

3.3 Linear range and specificity of the proposed circuit

The detection of ts3011a RNAs by the DNA circuit should be sequence-specific, so we evaluated the other three kinds of tsRNA (sequences shown in Supplementary Table S1). Among them, the sequence of tRF-4 was similar to that of ts3011a RNAs, with 12 same nucleotides, thus showing a higher fluorescence detection signal

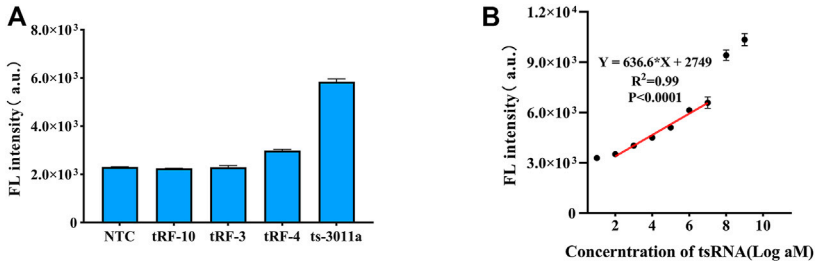

FIGURE 3
(A) Specificity of CHA-CRISPR detection of ts3011a (10 pM) against different kinds of tsRNAs (10 pM). **(B)** Linear plot for CHA-CRISPR vs. logarithm of ts3011a at 100 aM to 1 nM concentrations. NTC, No Template Control. Data are presented as mean ± S. D from three replicate measurements.

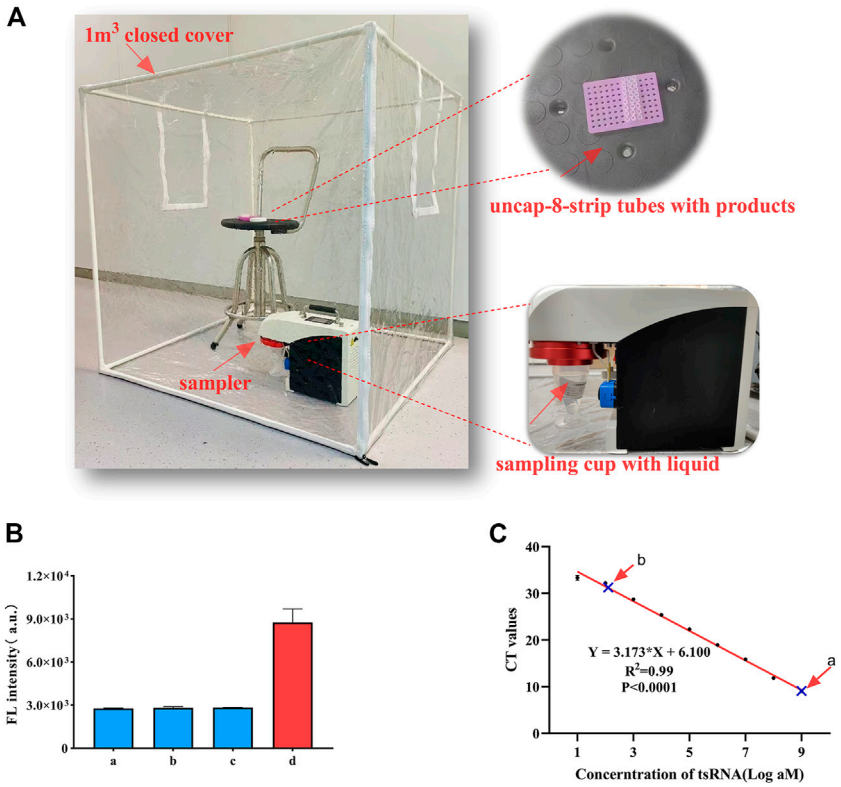

FIGURE 4
(A) Sampling scene (including the sampler device and samples). **(B)** Aerosol detection of CHA-CRISPR. a, blank control (without ts3011a); b, collected sampling liquid of CHA products; c, collected sampling liquid of CHA-CRISPR products; d, ts3011a (1 nM). **(C)** Aerosol detection of RT-qPCR. a, ts-3011a (1 nM); b, collected sampling liquid of RT-qPCR products. Data are presented as mean ± S.D. from three replicate measurements.

(Figure 3A). However, it also confirmed that the CHA-CRISPR assay achieved highly specific detection of ts3011a RNAs.

The standard ts3011a RNA samples were diluted with DEPC and quantified by RT-qPCR (Supplementary Figure S3). Fluorescence signals were collected from 0 to 1 nM in 1 h cleavage of excessive FQ reporter molecules. With the increase of target concentration, the fluorescence intensity also increased (Supplementary Figure S4). As illustrated in Figure 3B, an obvious linear relationship of CHA-CRISPR ranging from 100 aM to 10 pM (R^2 = 0.99), with a limit of detection (LOD) of 88 aM (3δ/S, δ indicating the standard deviation of the blank control and S indicating the slope of calibration curve) (Choengchan et al., 2006). The sensitivity of the proposed method was comparable to the RT-qPCR (Supplementary Figure S3).

3.4 Simulated aerosol detection experiment

The detection device is shown in Figure 4A. The aerosol was generated by a momentary shock, and we chose to open the lids for

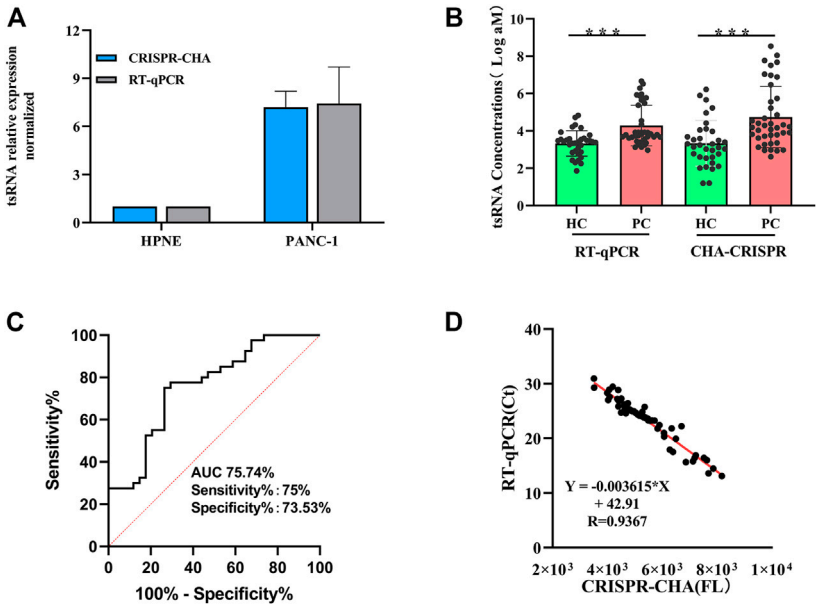

FIGURE 5
Diagnostic efficiency evaluation results. **(A)** Expression levels of ts3011a in cells using CHA-CRISPR and RT-qPCR. **(B)** Serum ts3011a expression level was detected by CHA-CRISPR and RT-qPCR. HC, healthy control (including 40 PC patients and 34 control individuals). $p < 0.001$. **(C)** Receiver Operating Characteristic (ROC) curves for CHA-CRISPR for ts3011a concentrations in serum samples (including 40 PC patients and 34 control individuals). **(D)** Correlation of CHA-CRISPR assay fluorescence intensity with clinical RT-qPCR Ct values. Data are presented as mean ± S. D from three replicate measurements.

5 min because the aerosol was still floating in the air and was not completely settled to be captured by the sampler. The results showed that the fluorescence generated by the collected sampling liquid of 1 nM ts3011a CHA-CRISPR and CHA products did not cause a significant increase compared to blank control (Figure 4B). RT-qPCR was performed with 1 nM ts3011a collected sampling liquid of RT-qPCR products can cause amplified contamination of 0.21 fM (Figure 4C; Supplementary Table S3). These results suggested that the CHA-CRISPR can avoid aerosol contamination caused by amplified products.

3.5 Quantification of ts-3011a in cells and serum samples with CHA-CRISPR

The expression levels of ts3011a RNA in PANC-1 and hTERT-HPNE were analyzed with CHA-CRISPR and RT-qPCR (Supplementary Table S2). The quantification results showed that the CHA-CRISPR was consistent with RT-qPCR (Figure 5A). The level of ts3011a RNAs in the serum samples was also detected (Figure 5B). These results showed that the levels of ts3011a RNAs from PC patients were much higher than those from healthy individuals, which was consistent with recently reported results (Jin et al., 2021). Besides, the CHA-CRISPR demonstrated a significantly superior diagnostic accuracy for early PC patients, with an area under the curve (AUC) of 0.7574, exhibiting 75% sensitivity and 75.53% specificity (Figure 5C), which is consistent with RT-qPCR (which showed the sensitivity of 66.67% and specificity of 77.78%, Supplementary Figure S5). From Figure 5D, the fluorescence intensity of the CHA-CRISPR assay demonstrated a good agreement with the Ct values of RT-qPCR in the detection of serum samples (R = 0.9367).

4 Conclusion

In summary, based on CHA and CRISPR-Cas12a, we have first developed a target-initiated amplification detection of pancreatic-cancer-specific tsRNAs. Under simulated experimental conditions, aerosol pollution was not produced by products of CHA-CRISPR with 1 nM tsRNA. The detection was achieved at 37 °C within 2 h, with a detection limit of 88 aM. Its diagnostic performance was found to be similar to that of RT-qPCR, and it is more suitable in community hospitals without precision instruments and PCR testing standard environments.

Data availability statement

The original contributions presented in the study are included in the article/Supplementary Material, further inquiries can be directed to the corresponding authors.

Ethics statement

The studies involving human participants were reviewed and approved by Nanjing Drum Tower Hospital Clinical College of Jiangsu University. The patients/participants provided their written informed consent to participate in this study.

Author contributions

JW: conceptualization, methodology, software, and investigation, data curation, writing-original draft. HX: methodology, software, investigation, project administration, writing-review, and editing. FH, YJ, BF, and AK: formal analysis and software. YS: resources and software. KD: conceptualization and data curation. XG: resources and validation. HS: supervision and administration. ZL: funding acquisition, supervision, administration, and data curation.

Funding

This study was supported by the Nanjing Important Science & Technology Specific Projects (2021-11005), the National Natural Science Foundation of China (61971216), the Key Research and Development Project of Jiangsu Province (BE2022692 and BE2020768), Nanjing Science and Technology Development Plan Project (202205066).

Conflict of interest

The authors declare that the research was conducted in the absence of any commercial or financial relationships that could be construed as a potential conflict of interest.

Publisher's note

All claims expressed in this article are solely those of the authors and do not necessarily represent those of their affiliated organizations, or those of the publisher, the editors and the reviewers. Any product that may be evaluated in this article, or claim that may be made by its manufacturer, is not guaranteed or endorsed by the publisher.

Supplementary material

The Supplementary Material for this article can be found online at: https://www.frontiersin.org/articles/10.3389/fbioe.2023.1169424/full#supplementary-material

References

Borst, A., Box, A. T., and Fluit, A. C. (2004). False-positive results and contamination in nucleic acid amplification assays: Suggestions for a prevent and destroy strategy. *Eur. J. Clin. Microbiol. Infect. Dis.* 23 (4), 289–299. doi:10.1007/s10096-004-1100-1

Chen, C., Ridzon, D. A., Broomer, A. J., Zhou, Z., Lee, D. H., Nguyen, J. T., et al. (2005). Real-time quantification of microRNAs by stem-loop RT-PCR. *Nucleic Acids Res.* 33 (20), e179. doi:10.1093/nar/gni178

Chen, H., Ma, X., Zhang, X., Hu, G., Deng, Y., Li, S., et al. (2023). Novel aerosol detection platform for SARS-CoV-2: Based on specific magnetic nanoparticles adsorption sampling and digital droplet PCR detection. *Chin. Chem. Lett.* 34 (1), 107701. doi:10.1016/j.cclet.2022.07.044

Chen, P., Wang, L., Qin, P., Yin, B-C., and Ye, B-C. (2022). An RNA-based catalytic hairpin assembly circuit coupled with CRISPR-Cas12a for one-step detection of microRNAs. *Biosens Bioelectron* 207, 114152. doi:10.1016/j.bios.2022.114152

Chen, Z., Li, J., Li, T., Fan, T., Meng, C., Li, C., et al. (2022). A CRISPR/Cas12a-empowered surface plasmon resonance platform for rapid and specific diagnosis of the Omicron variant of SARS-CoV-2. *Nati Sci. Rev.* 9 (8), nwac104. doi:10.1093/nsr/nwac104

Choengchan, N., Mantim, T., Wilairat, P., Dasgupta, P. K., Motomizu, S., and Nacapricha, D. (2006). A membraneless gas diffusion unit: Design and its application to determination of ethanol in liquors by spectrophotometric flow injection. *Anal. Chim. Acta* 579 (1), 33–37. doi:10.1016/j.aca.2006.07.018

Cui, Y., Fan, S., Yuan, Z., Song, M., Hu, J., Qian, D., et al. (2021). Ultrasensitive electrochemical assay for microRNA-21 based on CRISPR/Cas13a-assisted catalytic hairpin assembly. *Talanta* 224, 121878. doi:10.1016/j.talanta.2020.121878

Feng, W., Newbigging, A. M., Tao, J., Cao, Y., Peng, H., Le, C., et al. (2021). CRISPR technology incorporating amplification strategies: Molecular assays for nucleic acids, proteins, and small molecules. *Chem. Sci.* 12 (13), 4683–4698. doi:10.1039/d0sc06973f

Jin, F., and Guo, Z. (2019). Emerging role of a novel small non-coding regulatory RNA: tRNA-derived small RNA. *ExRNA* 1 (1), 39. doi:10.1186/s41544-019-0036-7

Jin, F., Yang, L., Wang, W., Yuan, N., Zhan, S., Yang, P., et al. (2021). A novel class of tsRNA signatures as biomarkers for diagnosis and prognosis of pancreatic cancer. *Mol. Cancer* 20 (1), 95. doi:10.1186/s12943-021-01389-5

Kaminski, M. M., Abudayyeh, O. O., Gootenberg, J. S., Zhang, F., and Collins, J. J. (2021). CRISPR-based diagnostics. *Nat. Biomed. Eng.* 5 (7), 643–656. doi:10.1038/s41551-021-00760-7

Li, B., Mao, R., Liu, C., Zhang, W., Tang, Y., and Guo, Z. (2018). LncRNA FAL1 promotes cell proliferation and migration by acting as a CeRNA of miR-1236 in hepatocellular carcinoma cells. *Life Sci.* 197, 122–129. doi:10.1016/j.lfs.2018.02.006

Li, S., Xu, Z., and Sheng, J. (2018). tRNA-derived small RNA: A novel regulatory small non-coding RNA. *Genes (Basel).* 9 (5), 246. doi:10.3390/genes9050246

Liu, R., Chen, X., Du, Y., Yao, W., Shen, L., Wang, C., et al. (2012). Serum MicroRNA expression profile as a biomarker in the diagnosis and prognosis of pancreatic cancer. *Clin. Chem.* 58 (3), 610–618. doi:10.1373/clinchem.2011.172767

Peng, S., Tan, Z., Chen, S., Lei, C., and Nie, Z. (2020). Integrating CRISPR-Cas12a with a DNA circuit as a generic sensing platform for amplified detection of microRNA. *Chem. Sci.* 11 (28), 7362–7368. doi:10.1039/d0sc03084h

Pereira, S. P., Oldfield, L., Ney, A., Hart, P. A., Keane, M. G., Pandol, S. J., et al. (2020). Early detection of pancreatic cancer. *Lancet Gastroenterol.* 5 (7), 698–710. doi:10.1016/s2468-1253(19)30416-9

Rezaei, M., Bazaz, S. R., Rad, D. M., Shimoni, O., Jin, D., Rawlinson, W., et al. (2021). A portable RT-LAMP/CRISPR machine for rapid COVID-19 screening. *Biosensors-Basel* 11 (10), 369. doi:10.3390/bios11100369

Shen, J., Zhou, X., Shan, Y., Yue, H., Huang, R., Hu, J., et al. (2020). Sensitive detection of a bacterial pathogen using allosteric probe-initiated catalysis and CRISPR-Cas13a amplification reaction. *Nat. Commun.* 11 (1), 267. doi:10.1038/s41467-019-14135-9

Siegel, R. L., Miller, K. D., Fuchs, H. E., and Jemal, A. (2022). Cancer statistics, 2022. *CA Cancer J. Clin.* 72 (1), 7–33. doi:10.3322/caac.21708

Wang, J., Sun, Y., Lau, C., and Lu, J. (2020). Target-fueled catalytic hairpin assembly for sensitive and multiplex microRNA detection. *Anal. Bioanal. Chem.* 412 (13), 3019–3027. doi:10.1007/s00216-020-02531-w

Wang, X., Yang, D., Liu, M., Cao, D., He, N., and Wang, Z. (2019). Highly sensitive fluorescence biosensor for intracellular telomerase detection based on a single patchy gold/carbon nanosphere via the combination of nanoflare and hybridization chain reaction. *Biosens Bioelectron.* 137, 110–116. doi:10.1016/j.bios.2019.05.004

Xing, S., Lu, Z., Huang, Q., Li, H., Wang, Y., Lai, Y., et al. (2020). An ultrasensitive hybridization chain reaction-amplified CRISPR-Cas12a aptasensor for extracellular vesicle surface protein quantification. *Theranostics* 10 (22), 10262–10273. doi:10.7150/thno.49047

Xiong, D-D., Dang, Y-W., Lin, P., Wen, D-Y., He, R-Q., Luo, D-Z., et al. (2018). A circRNA-miRNA-mRNA network identification for exploring underlying pathogenesis and therapy strategy of hepatocellular carcinoma. *J. Transl. Med.* 16 (1), 220. doi:10.1186/s12967-018-1593-5

Ye, J., Xu, M., Tian, X., Cai, S., and Zeng, S. (2019). Research advances in the detection of miRNA. *J. Pharm. Anal.* 9 (4), 217–226. doi:10.1016/j.jpha.2019.05.004

Zeng, R., Xu, J., Lu, L., Lin, Q., Huang, X., Huang, L., et al. (2022). Photoelectrochemical bioanalysis of microRNA on yolk-in-shell Au@CdS based on the catalytic hairpin assembly-mediated CRISPR-Cas12a system. *Chem. Commun.* 58 (54), 7562–7565. doi:10.1039/d2cc02821b

Zhang, Y., Zhang, Y., Shi, J., Zhang, H., Cao, Z., Gao, X., et al. (2014). Identification and characterization of an ancient class of small RNAs enriched in serum associating with active infection. *J. Mol. Cell Biol.* 6 (2), 172–174. doi:10.1093/jmcb/mjt052

Zhou, H., Bu, S., Xu, Y., Xue, L., Li, Z., Hao, Z., et al. (2022). CRISPR/Cas13a combined with hybridization chain reaction for visual detection of influenza A (H1N1) virus. *Anal Bioanal Chem* 414, 8437–8445. doi:10.1007/s00216-022-04380-1

Zhou, J., Lin, Q., Huang, Z., Xiong, H., Yang, B., Chen, H., et al. (2022). Aptamer-initiated catalytic hairpin assembly fluorescence assay for universal, sensitive exosome detection. *Anal. Chem.* 94 (15), 5723–5728. doi:10.1021/acs.analchem.2c00231

Frontiers in
Bioengineering and Biotechnology

Accelerates the development of therapies, devices, and technologies to improve our lives

A multidisciplinary journal that accelerates the development of biological therapies, devices, processes and technologies to improve our lives by bridging the gap between discoveries and their application.

Discover the latest Research Topics

See more →

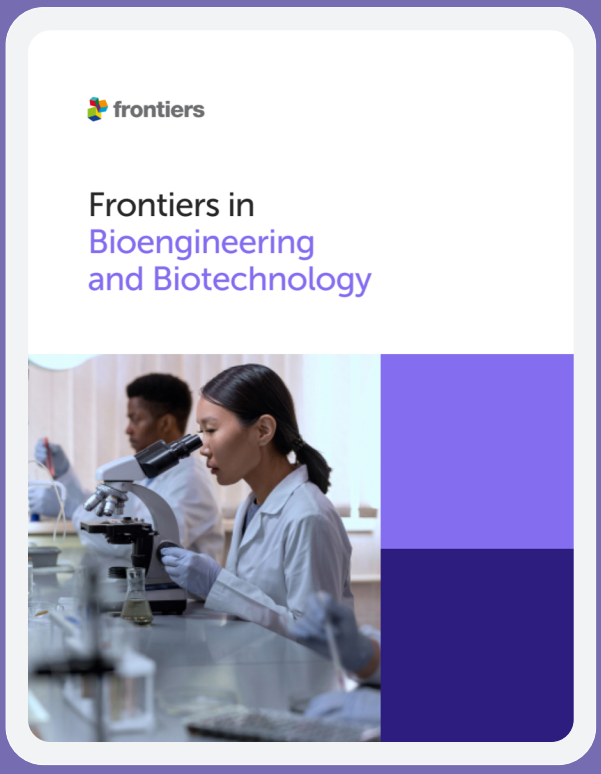

Frontiers

Avenue du Tribunal-Fédéral 34
1005 Lausanne, Switzerland
frontiersin.org

Contact us

+41 (0)21 510 17 00
frontiersin.org/about/contact